

---

# **XXVIII PHYSICS IN COLLISIONS**

Proceedings of the International Symposium held in  
Perugia, Italy, June 25-28, 2008

---

Cover artwork: S. Ciprini.

Cover image credits: Higgs boson production and decay event at LHC picture courtesy of Cavendish HEP-Group Cambridge. Drawing of the Major Fountain (*Fontana Maggiore*, completed in 1278 and designed by Nicola e Giovanni Pisano) the main monument in Perugia, sketched by S. Ciprini. Three-disk diagram courtesy of P5/Symmetry magazine/Sandbox Studio.

This volume is based on SLAC eConf L<sup>A</sup>T<sub>E</sub>X package modified by S. Ciprini.

FORUM

Editrice Universitaria Udinese Srl

[www.forumeditrice.it](http://www.forumeditrice.it)

Based on SLAC National Accelerator Laboratory eConf  
(Electronic Conference Proceedings Archive System).

[www.slac.stanford.edu/econf/C080625](http://www.slac.stanford.edu/econf/C080625)

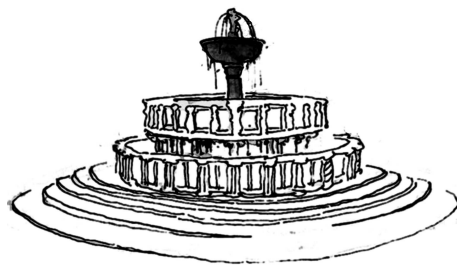
Udine, 2009

ISBN .....

Printed in Italy

# **XXVIII PHYSICS IN COLLISIONS**

**Proceedings of the International Symposium held in  
Perugia, Italy, June 25-28, 2008**



Editors

S. Ciprini, G. Mantovani and G. Anzivino

Organized by  
Physics Department, University of Perugia  
and I.N.F.N. Section of Perugia

Sponsored by  
Fondazione Cassa di Risparmio di Perugia,  
University of Perugia, I.N.F.N., and CAEN S.p.A

✠ This Volume is dedicated to the memory of Prof. Beate Naroska.

# Foreword

The XXVIII Physics in Collision International Conference was held in Perugia (Italy), June 25-28, 2008 at the Congress Hotel Giò. According to the tradition established in 1981, the Conference reviewed and updated key topics in all branches of particle and astroparticle physics. Informal discussions on new experimental results and their implications were an important part of the Conference.

This edition of PIC was dedicated to a recently deceased member of the International Advisory Committee, Prof. Beate Naroska, from DESY, Hamburg.

The previous PIC conferences were held in various countries , the most recent three in France, Brazil and Czech Republic, the first one (1981) in Virginia (USA). PIC2008 was organized jointly by the I.N.F.N., Sezione di Perugia and the Dipartimento di Fisica of the Università di Perugia.

Twenty seven invited talks were presented, covering the main results from all areas of particle physics, ranging from neutrino physics to the most recent results obtained from accelerators and astrophysics results from underground labs, earth-based and space-borne detectors. Twenty three posters were also submitted, out of which eleven were selected to give a short presentation.

The social part of the conference included a Welcome Party on June 25<sup>th</sup>, a reception by the Local authorities in the Perugia Town Hall (Palazzo dei Priori), a visit to the Perugia historical center and to the National Gallery of Umbria on June 26<sup>th</sup>, a trip to Assisi followed by the Conference dinner on June 27<sup>th</sup>.

The meeting was sponsored mainly by I.N.F.N. and locally by the Fondazione Cassa di Risparmio di Perugia. To both we express our most grateful thanks. I would like to deeply thank all members of the IAC for having collaborated with me to shape a very interesting and complete program for this XXVIII edition of the conference, the members of the Local Committee and the technicians and students of our Physics Department for their help in making PIC2008 a truly unforgettable event.

The complete proceedings of the The XXVIII Physics in Collision International Conference is available at SLAC web-site as [econf/C080625](http://econf.C080625).

Giancarlo Mantovani  
Chairman of the Conference Committees

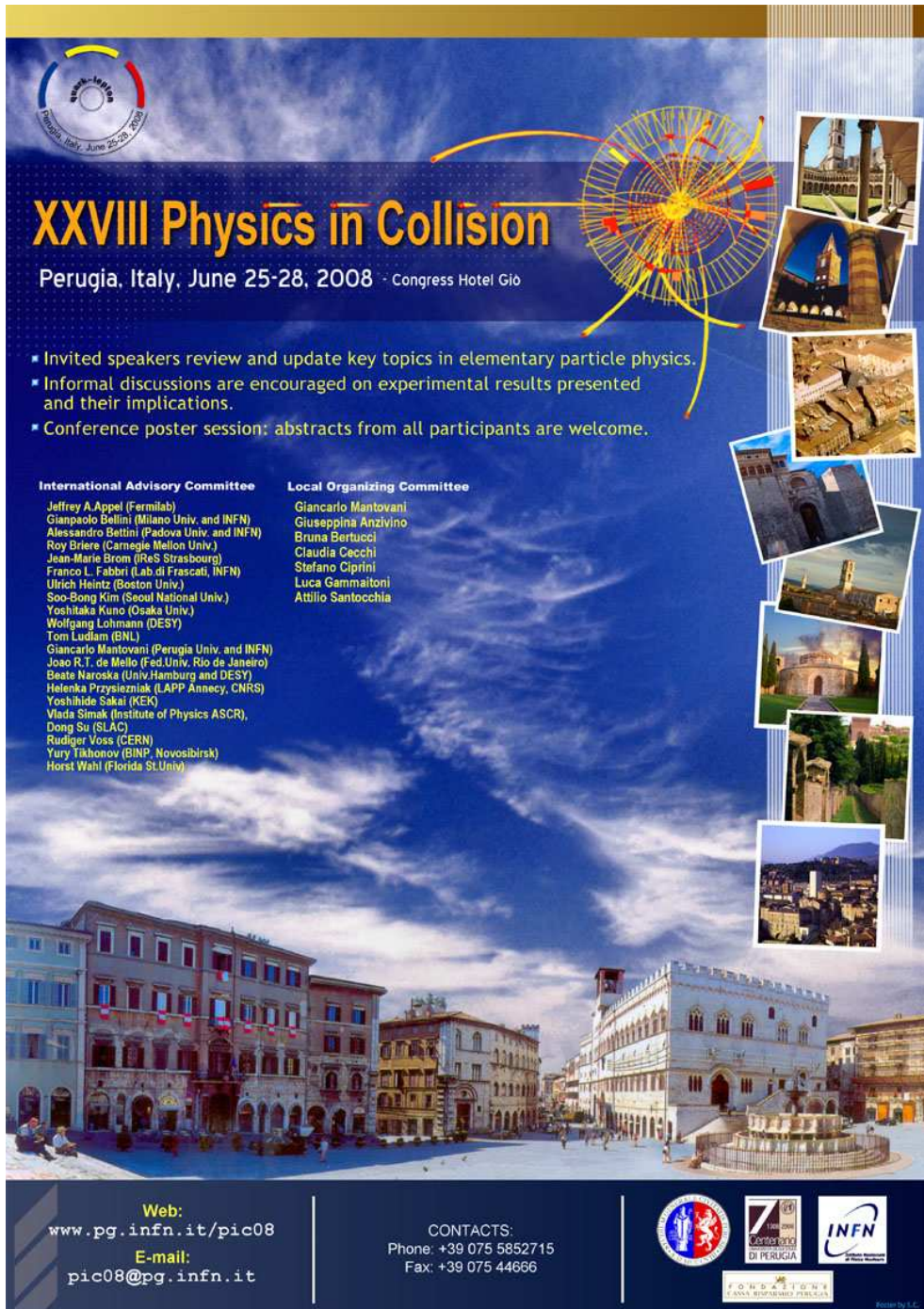


Figure 1: The conference poster.



## INTERNATIONAL ADVISORY COMMITTEE

Jeffrey A.Appel	(Fermilab)
Gianpaolo Bellini	(Milano Univ. and INFN)
Alessandro Bettini	(Padova Univ. and INFN)
Roy Briere	(Carnegie Mellon Univ.)
Jean-Marie Brom	(IReS Strasbourg)
Franco L. Fabbri	(Lab.di Frascati, INFN)
Ulrich Heintz	(Boston Univ.)
Soo-Bong Kim	(Seoul National Univ.)
Yoshitaka Kuno	(Osaka Univ.)
Wolfgang Lohmann	(DESY)
Tom Ludlam	(BNL)
Giancarlo Mantovani	(Perugia Univ. and INFN) Chair
Joao R.T. de Mello	(Fed.Univ. Rio de Janeiro)
Beate Naroska	(Univ.Hamburg and DESY)
Helenka Przysiezniak	(LAPP Annecy, CNRS)
Yoshihide Sakai	(KEK)
Vlada Simak	(Institute of Physics ASCR)
Dong Su	(SLAC)
Rudiger Voss	(CERN)
Yury Tikhonov	(BINP, Novosibirsk)
Horst Wahl	(Florida St.Univ)

## LOCAL ORGANIZING COMMITTEE

Giancarlo Mantovani (Chair)  
Giuseppina Anzivino  
Bruna Bertucci  
Claudia Cecchi  
Stefano Ciprini  
Luca Gammaitoni  
Attilio Santocchia

## EDITORS

Stefano Ciprini  
Giancarlo Mantovani  
Giuseppina Anzivino

## SECRETARIAT & ASSISTANCE

Benedetta Caponeri  
Gianfranco Chiocci  
Roberta Volpe





Figure 2: Participants of the XXVIII Physics in Collision Conference, held in Perugia, Italy, June 25-28, 2008. Group photo taken at the social dinner.



Figure 3: Other group photos.

# Table of Contents

<b>Foreword</b>	iii
<b>Conference poster and sponsors</b>	iv
<b>Committees</b>	v
<b>Group photos</b>	vii
<b>Table of Contents</b>	ix
<b>Electroweak Physics</b>	1
<b>Top Quark Cross Sections</b>	2
<i>Frédéric Déléot</i>	
<b>Top Quark Properties</b>	13
<i>Mousumi Datta</i>	
<b>W-Z physics from the Tevatron</b>	14
<i>Tim Bolton</i>	
<b>Electroweak constraints from HERA</b>	15
<i>Elisabetta Gallo</i>	
<b>Neutrino Physics</b>	27
<b>New developments in Solar Neutrino Physics</b>	28
<i>Gianpaolo Bellini</i>	
<b>Short-baseline Neutrinos: Recent Results and Future Prospects</b>	42
<i>Ryan B. Patterson</i>	
<b>Ultra high-energy neutrinos</b>	52
<i>Ryan Nichol</i>	

<b>Long Baseline Neutrino Oscillation Experiments</b>	53
<i>Mark Thomson</i>	
<b>Underground nuclear astrophysics and the Sun</b>	67
<i>Carlo Broggini</i>	
<b>OPERA: waiting for the <math>\tau</math></b>	76
<i>Andrea Longhin</i>	
<b>Heavy Flavour and Strange Particle Physics</b>	82
<b>B decay and CP violation: CKM angles and sides at the BABAR and BELLE B-Factories</b>	83
<i>Marc Verderi</i>	
<b>New Physics Effects in B decays</b>	96
<i>Yuan Chao</i>	
<b>Heavy B Hadrons</b>	101
<i>Stefano Giagu</i>	
<b>The Charm Renaissance: D-Physics – a Selective Review</b>	113
<i>Guy Wilkinson</i>	
<b>D<sup>0</sup> – <math>\overline{D}^0</math> Mixing: An Overview</b>	130
<i>Jörg Marks</i>	
<b>Strange Quark Physics at Sixty-Four</b>	142
<i>Bradley Cox</i>	
<b>Measurement of <math>K^+ \rightarrow \pi^+ \nu \bar{\nu}</math> at NA62 experiment</b>	154
<i>Spasimir Balev</i>	
<b> <math>V_{us}</math>  from kaon decays with the KLOE detector</b>	160
<i>Mario Antonelli</i>	
<b>Early physics with the LHCb detector</b>	166
<i>Dirk Wiedner</i>	

<b>Astroparticle Physics</b>	172
<b>Ultra High Energy Cosmic Rays from earth-based observatories</b>	173
<i>Sergio Petrera</i>	
<b>Dark Matter Detection and the XENON experiment</b>	184
<i>Elena Aprile</i>	
<b>Cosmic rays from the space based observatories</b>	193
<i>Piero Spillantini</i>	
<b>Very High-Energy Gamma Ray Astronomy</b>	209
<i>Ullrich Schwanke</i>	
<b>FERMI/GLAST and the Future of Gamma Ray Astronomy</b>	218
<i>Vincenzo Vitale</i>	
<b>Ultra-High Energy Particles Astronomy with a space-based experiment</b>	224
<i>Roberto Pesce</i>	
<b>Antimatter and DM search in space with AMS-02</b>	230
<i>Francesca R. Spada</i>	
 <b>QCD and Heavy ion Physics</b>	 236
<b>Jet Physics at HERA, Tevatron and LHC</b>	237
<i>Christophe Royon</i>	
<b>QCD at the HERAscale and implications at the Terascale</b>	251
<i>Achim Geiser</i>	
<b>Exotic hadron spectroscopy</b>	266
<i>Jolanta Brodzicka</i>	
<b>Longitudinal Structure Function Measurements from HERA</b>	278
<i>Vladimir Chekelian</i>	
<b>Spin structure of the nucleon</b>	288
<i>Krystof Kurec</i>	

<b>What is the matter created in heavy ion collisions?</b>	299
<i>Raphael Granier de Cassagnac</i>	
<b>Higgs Searches and BSM Physics</b>	310
<b>Higgs Searches at the Tevatron</b>	311
<i>Anyes Taffard</i>	
<b>Higgs Searches at LHC</b>	324
<i>Giorgia Mila</i>	
<b>Beyond the Standard Model - Searches at HERA and the Tevatron</b>	330
<i>Stefan Grünendahl</i>	
<b>BSM measurements with Top at LHC :</b>	
<b>CMS sensitivity to Flavour Changing Neutral Currents</b>	343
<i>Leonardo Benucci</i>	
<b><math>ZZ</math> into <math>4\ell</math> expected sensitivity with the first ATLAS data</b>	351
<i>Ilektra A. Christidi</i>	
<b>ATLAS RPC commissioning status and cosmic ray test results</b>	358
<i>Michele Bianco</i>	
<b>Poster Session</b>	365
<b>Study of the Behavior of the Nuclear Modification Factor in Freeze-out State</b>	366
<i>Muhammad Ajaz et al.</i>	
<b>Hidden Valley Higgs Decays in the ATLAS Detector</b>	370
<i>Guido Ciapetti</i>	
<b>Mini-Bias and Underlying Event Studies at CMS</b>	376
<i>Yuan Chao</i>	
<b>ATLAS Trigger Menu for Early Data-Taking</b>	381
<i>Marc-André Dufour and Bilge Demirköz</i>	

<b>Level-3 Calorimetric Resolution available for the Level-1 and Level-2 CDF Triggers</b>	<b>386</b>
<i>Virginia Greco et al.</i>	
<b>Measurement of Branching Fractions of the inclusive decay <math>D^0 \rightarrow \Phi X</math> and of the exclusive decays of the <math>D^0</math> involving a <math>K^+K^-</math></b>	<b>391</b>
<i>Gerhard Leder and Franz Mandl</i>	
<b>The Liquid Argon Jet Trigger of the H1 Experiment at HERA</b>	<b>396</b>
<i>Bob Olivier</i>	
<b>A new very inclusive trigger selection for the SM WH discovery channel at CDF</b>	<b>401</b>
<i>Pierluigi Totaro</i>	
<b>Scientific Program</b>	<b>408</b>
<b>List of Participants</b>	<b>412</b>



# Electroweak Physics

Session Convener: *Giancarlo Mantovani*  
Session Convener: *Helenka Przysiezniak*

Top Quark Cross Sections *Frédéric Déliot*

Top Quark Properties *Mousumi Datta*

W-Z physics from the Tevatron *Tim Bolton*

Electroweak constraints from HERA *Elisabetta Gallo*

# Top Quark Cross Sections

*Frédéric Déliot*

*CEA-Saclay, IRFU/SPP, bât. 141, 91191 Gif sur Yvette Cedex, France*

*Frederic.Deliot@cea.fr*

*On Behalf of the CDF and DO Collaborations.*

## 1 Introduction

The top quark is the latest quark of the Standard Model (SM) that was discovered, discovery that was made in 1995 by the CDF and D0 collaborations [1]. It is the “youngest” quark of the SM and many of its properties remain to be studied in detail.

Since it is also the heaviest elementary particle known so far, its status in the SM is special. Indeed, the top quark is 40 times heavier than its weak isospin partner the  $b$  quark and its Yukawa coupling to the Higgs boson is close to 1. The large top quark mass induces large contributions in virtual fermionic loops of radiative corrections. Since its decay time is smaller than the hadronization time, the top quark is the only quark that decays before hadronizing and so it can be used to probe the properties of a bare quark. All these characteristics may indicate that the top quark could play a special role in the SM.

Top physics is a rich and still developing field in particular at the Tevatron, the proton-antiproton collider at Fermilab with a center of mass energy of 1.96 TeV, which is currently the only place where the top quark can be produced directly. Two multipurpose detectors are located around the Tevatron accelerator: CDF D0. The Tevatron running period can be divided into three data taking periods: first the Run I from 1993 to 1996 with a center of mass energy of 1.8 TeV and a delivered integrated luminosity of  $120 \text{ pb}^{-1}$  per experiment, secondly the Run IIa from 2002 to March 2006 with an increased center of mass energy of 1.96 TeV and a delivered integrated luminosity of  $1.5 \text{ fb}^{-1}$  per experiment. Finally the third period from August 2006 is expected to last until 2009 or 2010 with an expected delivered integrated luminosity from 6 to  $8 \text{ fb}^{-1}$ . The typical data taking efficiency of the experiments is above 85%. The analyses presented in this article use from 0.9 to  $2.2 \text{ fb}^{-1}$  of data and are documented in [2, 3]. The results are quoted as they were presented at the time of the conference regardless on any later updates.

The top quark can be produced via two modes, either via the strong interaction leading to a production by  $t\bar{t}$  pair or via the electroweak interaction leading to the single top production. The pair production is the dominant mode at hadron colliders.

## 2 Top Quark Pair Production: $t\bar{t}$ Cross Sections

### 2.1 Top Quark Pair Production

At Tevatron, the top quark pair production occurs by quark-antiquark annihilation in 85% of the cases while the remaining part is provided by gluon fusion. The theoretical prediction for a top quark mass of  $M_{top} = 175$  GeV and the CTEQ6.5 PDF set [3] is:  $\sigma_{t\bar{t}} = 6.73 \text{ pb} \pm 10\%$  at Tevatron [5] (it is  $\sigma_{t\bar{t}} = 908 \text{ pb} \pm 10\%$  at LHC). Typically for  $1 \text{ fb}^{-1}$  of data, we expect to see around 300  $t\bar{t}$  events in the lepton+jets channel per experiment at Tevatron.

Within the framework of the SM, the top quark decays approximately 100% of the time into a  $W$  boson and a  $b$  quark. The  $t\bar{t}$  final states are classified according to the  $W$  boson decay modes. When the two  $W$  bosons coming from the top and the antitop decay hadronically, the final state is called the alljets or full hadronic final state. This decay channel has the largest branching ratio but also suffers from the largest background coming from multijet events. The lepton+jets channel occurs 30% of the time when one  $W$  boson decays leptonically and one hadronically. This mode has reasonable statistics and reasonable background. The two  $W$  bosons decaying leptonically in 4% of the cases lead to the dilepton channel that has low statistics but low background (here lepton denotes electron or muon). Finally in 20% of the cases, the final state contains a  $\tau$  which is challenging to identify in an hadronic environment.

### 2.2 Motivations and Method

The inclusive  $t\bar{t}$  cross section  $\sigma_{t\bar{t}}$  is a quantity that allows to test the SM by comparing the experimental measurements with the QCD Next-to-Leading Order (NLO) prediction. It also allows to extract the top quark mass by comparing these two values. Measuring  $\sigma_{t\bar{t}}$  enables as well as the possibility to probe for new physics that can manifest itself in anomalous  $t\bar{t}$  production rate or different cross section values for different top decay channels.  $t\bar{t}$  events are also an important background for Higgs boson searches.

The  $t\bar{t}$  cross section is extracted using the following formula:

$$\sigma_{t\bar{t}} = \frac{N_{observed} - N_{background}}{\epsilon_{t\bar{t}}(M_{top})L} \quad (1)$$

where  $N_{observed}$  and  $N_{background}$  are the number of observed data events and predicted number of background events.  $N_{observed} - N_{background}$  can be evaluated either from a counting experiment or using a fit of a discriminating variable shape.  $L$  is the recorded integrated luminosity that is channel dependent and  $\epsilon_{t\bar{t}}$  is the signal efficiency which

is evaluated using  $t\bar{t}$  Monte Carlo (MC) samples correcting for any differences between data and MC.

### 2.3 Cross Section Results in the Lepton+jets Channel

The signature of  $t\bar{t}$  events in the lepton+jets channel consists of one high  $p_T$  isolated lepton, large missing transverse energy ( $\cancel{E}_T$ ) and four jets among which two are  $b$  quark jets. Tagging  $b$  quark jets is very useful to select signal events. Two main analysis strategies can be followed: either a topological approach where a multivariable discriminant is formed using kinematic variables (aplanarity, sphericity, angles, invariant masses, ...) to separate signal from background or an approach based on b-tagging where b-tagging is used to enhance the sample purity. The typical signal over background ratio is 2:3 for analysis without b-tagging and 4:1 in analysis with b-tagging requesting four jets. The main backgrounds in this channel come from  $W$ +jets events which is evaluated using MC but normalized to data before b-tagging and from multijet events where one jet fakes an isolated lepton. This later background is evaluated from data. Backgrounds coming from diboson,  $Z$ +jet and single top events are evaluated using MC.

Both D0 and CDF measured this cross section with respectively  $0.9 \text{ fb}^{-1}$  and  $1.12 \text{ fb}^{-1}$  using b-tagging separating events depending on the lepton flavor, number of jets and number of b-tagged jets. The results are indicated in Figure 1 and show a 12% relative total error. The errors are already dominated by the systematic uncertainties. The dominant ones, except the luminosity error (6%), come from the b-tagging uncertainty (6%), MC modeling (4%) and jet energy scale (4%).

CDF also performed a measurement using soft lepton tagging. In the analysis, instead of using track impact parameters or secondary vertex reconstruction to tag  $b$  quarks, the semileptonic  $b$  quark decay into either a soft electron or muon is exploited. In this case the total cross section error is still dominated by the statistical uncertainty (Figure 1) while the dominant source of systematic uncertainties comes from lepton tagging acceptance (8% to 15%) and fake rate (5%).

Alternatively both D0 and CDF performed a lepton+jets topological analysis where D0 is using a likelihood discriminant while CDF is using a neural network (NN). The discriminant output is fitted to extract the cross section (see Figure 1). In these analyses, the statistical error is still important. D0 combines the topological with the b-tagging result that are 31% correlated leading to a cross section measurement with 11% total uncertainty.

The cross section results can be used to extract the top quark properties or to probe for new physics, particularly in the lepton+jets channel which provides the most precise measurement. Comparing the combined topological and b-tagging D0 cross section measurement described above with the computation from QCD, the top quark mass ( $M_{top}$ ) can be extracted in a well defined renormalization scheme. In

order to do so, a joint likelihood is constructed resulting in the product of a theory likelihood (that takes both the factorization or renormalization scale uncertainties and the PDF error into account) times an experimental likelihood formed using the total experimental uncertainty as a function of  $M_{top}$ . The theory and experimental errors are assumed to be independent. The resulting top mass after integrating over the cross section is  $M_{top} = 170 \pm 7$  GeV in agreement with the world average value [6].

The  $t\bar{t}$  cross section value can also be evaluated simultaneously with the ratio  $R$  of  $b$  quark to light quark branching ratios defined as:

$$R = \frac{Br(t \rightarrow Wb)}{Br(t \rightarrow Wq)} = \frac{|V_{tb}|^2}{|V_{tb}|^2 + |V_{ts}|^2 + |V_{td}|^2} \quad (2)$$

where  $q$  stands for any down type quark. Indeed the standard cross section measurements assume  $R \approx 1$  as predicted by the SM. A simultaneous extraction of  $\sigma_{t\bar{t}}$  and  $R$  allows to relax this assumption and to put a limit on the CKM matrix element  $V_{tb}$  assuming three quark families and the matrix unitarity. D0 performed this measurement and finds:  $R = 0.97^{+0.09}_{-0.08}$  (stat+sys) and  $|V_{tb}| > 0.89$  at 95% confidence level (CL).

## 2.4 Cross Section Results in the Dilepton Channel

The signature of  $t\bar{t}$  events in the dilepton channel consists of two high  $p_T$  isolated leptons, large missing transverse energy ( $\cancel{E}_T$ ) and two  $b$  quark jets. The typical signal over background ratio is 3:1 without applying b-tagging. Complementary to the selection of two well identified leptons, one single lepton with an isolated track can also be requested to enhance the signal acceptance. While b-tagging is not necessary to select a rather pure signal sample in the standard case, the lepton+track selection needs b-tagging to enhance the signal purity. The main background in this channel comes from Drell-Yan production with fake  $\cancel{E}_T$ . This background is estimated using data or MC. Multijet or  $W+jets$  events can also lead to the same final state when one or two jets fake an isolated lepton. This type of background is estimated using data. Finally the diboson background is evaluated using MC.

Both D0 and CDF measured this cross section with respectively  $1.1 \text{ fb}^{-1}$  and  $2 \text{ fb}^{-1}$  without requesting b-tagging. The results are indicated in Figure 1 and show a 17% relative total error. The total error is still dominated by the statistical uncertainty. The dominant systematic uncertainties, except the luminosity error (6%), come from the jet energy scale uncertainty (3%) and MC normalization (3%).

CDF also measured the dilepton cross section with b-tagging as well as the lepton+track cross section with and without b-tagging (see Figure 1).

Using both the dilepton cross section measurement described here and the lepton+jets one described in the previous section, the  $R_\sigma$  cross section ratio can be

computed:

$$R_\sigma = \frac{\sigma(t\bar{t} \rightarrow l + jets)}{\sigma(t\bar{t} \rightarrow dilepton)}. \quad (3)$$

The SM predicts  $R_\sigma = 1$  and any deviation from 1 is sensitive to  $W$  disappearance: i.e.  $t \rightarrow Xb$ . For instance, in the minimal supersymmetric extension of the SM (MSSM), a charged Higgs boson can be lighter than the top quark and the following decay can occur:  $t \rightarrow Hb$  with  $H^+ \rightarrow c\bar{s}$  which leads to  $R_\sigma > 1$ . D0 combined its lepton+jets and dilepton cross section results to extract:  $R_\sigma = 1.21^{+0.27}_{-0.26}$  (stat+sys) using a Feldman Cousins method [7]. Assuming a charged Higgs boson mass of  $m_{H^\pm} = 80$  GeV which decays exclusively into  $c\bar{s}$ , a limit on the branching ratio of top decaying to charged Higgs bosons can be set:  $Br(t \rightarrow Hb) < 0.35$  at 95% CL.

Another interesting dilepton channel arises when one of the lepton is a  $\tau$ . Final states with  $\tau$  leptons are challenging to identify in an hadronic environment but they are also the most sensitive channels to new physics. Indeed for instance in the MSSM, when a charged Higgs boson is lighter than the top quark, it can also decay into a  $\tau$ :  $H^+ \rightarrow \tau\nu$  therefore competing with the standard top decay into a  $W$  boson.

At D0 the identification of  $\tau$  decaying hadronically is performed using three different NNs depending on the decay products of the  $\tau$  classified in three cases: one charged pion or kaon and a neutrino, one charged pion or kaon with a neutral pion and a neutrino or finally several charged pions or kaons and a neutrino. D0 performed a  $t\bar{t}$  cross section measurement in the lepton+ $\tau$  channel using  $1 \text{ fb}^{-1}$  with b-tagging. The main background in this channel comes from  $W$ +jets events and is estimated from MC normalized to data. The multijet background where one jet fakes a  $\tau$  and another one fakes an isolated lepton is estimated using same sign data events. The other backgrounds are evaluated using MC. The result is shown in Figure 1 and has a total relative uncertainty of 28 % dominated by the statistical error. The dominant systematic uncertainties, except the luminosity error (6%), come from background estimation (20%), the b-tagging uncertainty (6%) and from the estimation of the  $\tau$  fake rate (4%).

## 2.5 Cross Section Results in the Full Hadronic Channel

The signature of  $t\bar{t}$  events in the full hadronic channel consists of six jets among which two are  $b$  quark jets. The typical signal over background ratio is 1:2 before applying b-tagging. b-tagging is thus necessary to help separating signal from background. With six jets in this channel, the combinatoric background is important.

CDF performed a  $t\bar{t}$  cross section measurement in this channel using  $1 \text{ fb}^{-1}$ . The selection requires from six to eight jets. The main background comes from multijet events estimated from data calibrating the tagging rate in the four jet bin which a background dominated sample. The signal from background separation is achieved using a NN that combines jet invariant masses, sphericity, aplanarity, ... The result

is shown in Figure 1. The total uncertainty of 25% is dominated by systematic uncertainties where the jet energy scale error (16%) and the b-tagging uncertainty (7%) are the dominant ones.

## 2.6 Summary and Perspectives for Top Quark Pair Production

All the  $t\bar{t}$  cross section measurements performed by the D0 and CDF collaborations are summarized in Figure 1. All the measurements are in agreement with each other as well as with the theoretical predictions. The current best single measurement shows a total uncertainty of 11% which is of the same order as the theoretical one. The systematic uncertainties dominate for the lepton+jets and full hadronic channels and future works will concentrate on reducing them. With the full luminosity that will be available at the end of Run II, a 6% total uncertainty could be achieved. The expected uncertainty at the LHC using  $10 \text{ fb}^{-1}$  is from 5% to 10% dominated by the luminosity error.

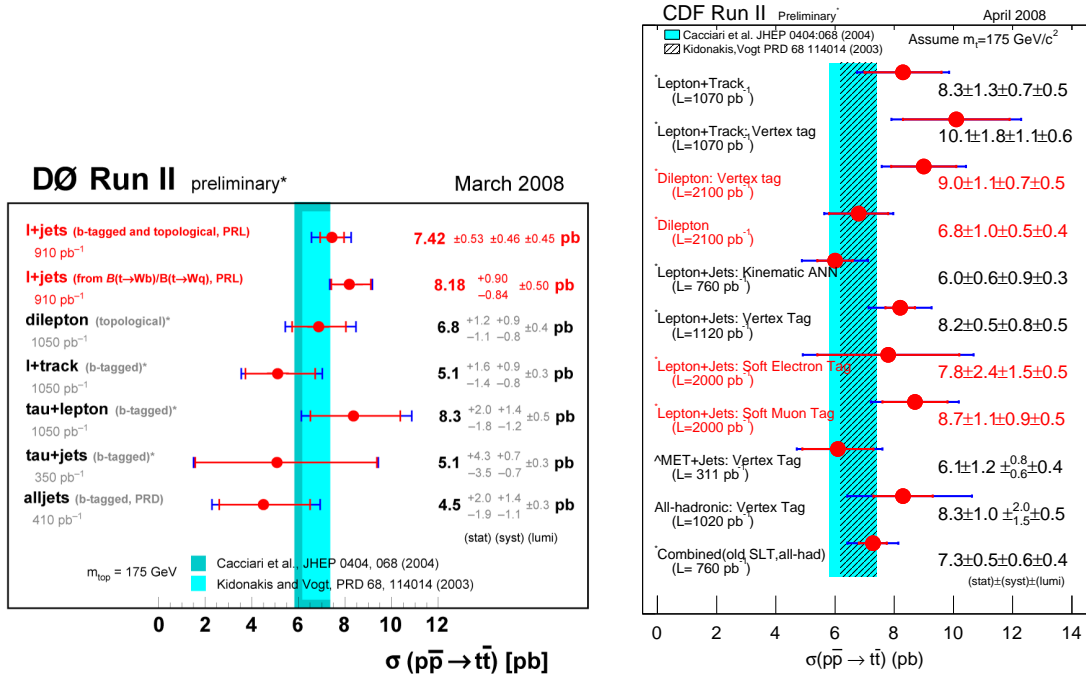


Figure 1: Summary of the D0 (left) and CDF (right)  $t\bar{t}$  cross section measurements.

### 3 Single Top Quark Cross Sections

#### 3.1 Production and Motivations

At Tevatron, the top quark can be produced by electroweak processes via three types of Feynman diagrams: the s-channel where a quark and an antiquark annihilate, the t-channel where a light quark interacts with a  $b$  quark from gluon splitting, and the  $W$  associated production where a gluon interacts with a light quark and produces a top quark in association with a  $W$  boson. At Tevatron, the main channel is the t-channel (65%) followed by the s-channel (30%) while the  $W$  associated production is too small to be seen. Since only one top quark is produced in the final state, only leptonic decay of the  $W$  boson from the top quark can be considered. Thus the t-channel final state consists of one lepton, two  $b$  quark jets including a very forward one and one light quark jet. The s-channel final state consists of one lepton and two  $b$  quark jets. The combined s+t channel NLO theoretical prediction for a top quark mass of  $M_{top} = 175$  GeV and CTEQ5M1 PDF set [3] is:  $\sigma_{t\bar{t}} = 2.9 \text{ pb} \pm 14\%$  at Tevatron while it is  $\sigma_{t\bar{t}} = 314 \text{ pb} \pm 20\%$  at LHC [8]. Typically for  $1 \text{ fb}^{-1}$  of data, we expect to see around 50  $t\bar{t}$  events per experiment at Tevatron.

It is important to measure the single top cross section first because this mode is predicted by the SM, and the measured cross section should be compared with the prediction to test the model. Since the single top cross section is directly proportional to  $|V_{tb}|^2$ , it also allows a direct measurement of this CKM matrix element. In addition this mode is sensitive to non standard processes like contribution from heavy  $W'$  boson, charged Higgs boson, flavour changing neutral currents (FCNC) or anomalous  $Wtb$  coupling like  $V+A$  contribution. The single top production is also a background for Higgs boson searches since it leads to the same final state as the Higgs boson associated production  $WH \rightarrow Wb\bar{b}$ . However measuring the single top cross section is difficult since the cross section is low and suffers from high background from  $t\bar{t}$ ,  $Wb\bar{b}$  and multijet events. Indeed after the preselection cuts, the typical signal over background ratio is 1:15. That's why multivariate techniques need to be used to extract the signal.

#### 3.2 Results

The preselection of single top events requires one isolated electron or muon with  $p_T > 15 - 20$  GeV, large  $\cancel{E}_T$ :  $\cancel{E}_T > 15 - 15$  GeV and from two to four jets with  $p_T > 15 - 25$  GeV among which one or two are b-tagged. The typical signal efficiency for the s-channel is around 3% and for the t-channel around 2%.

The diboson, Drell-Yan and  $t\bar{t}$  backgrounds are estimated using MC. The  $W$ +jets kinematics and flavor composition are evaluated using MC while its normalization comes from data before applying b-tagging. The multijet background is evaluated

from data either using sideband or non isolated lepton samples.

Both D0 and CDF performed single top measurements using respectively  $0.9 \text{ fb}^{-1}$  and  $2.2 \text{ fb}^{-1}$ . The total number of selected data events by D0 is 697 events in the 2 jet sample and 455 events in the 3 jet sample. The total number of selected data events by CDF is 1535 in the 2 jet sample and 712 in the 3 jet sample.

Systematic uncertainties affect the normalization and/or the shapes of the distributions. The main normalization systematic errors come from  $t\bar{t}$  pairs and  $W+\text{jets}$  normalization uncertainty, jet energy scale and b-tagging uncertainties. The total cross section uncertainty is however dominated by the statistical error.

The D0 collaboration already published a first  $3\sigma$  evidence for single top production [9]. Three analyses are currently performed [10] that differ from the multivariate technique which is used after the preselection. D0 uses methods based on boosted decision tree, on bayesian neural network and on matrix element. The results are summarized in Table 1. D0 uses the Best Linear Unbiased Estimate method [11] to combine the three analyses. The correlations amoung them are around 60%. The combined results are also shown in table 1.

	Decision Tree	NN	Matrix Element	Combined
Expected significance	$2.1\sigma$	$2.2\sigma$	$1.9\sigma$	$2.3\sigma$
Observed significance	$3.4\sigma$	$3.1\sigma$	$3.2\sigma$	$3.6\sigma$
Cross section	$4.9^{+1.4}_{-1.4} \text{ pb}$	$4.4^{+1.6}_{-1.4} \text{ pb}$	$4.8^{+1.6}_{-1.4} \text{ pb}$	$4.7 \pm 1.3 \text{ pb}$

Table 1: D0 single top results s and t channel combined using  $0.9 \text{ fb}^{-1}$  for  $M_{top} = 175 \text{ GeV}$  [10].

The CDF collaboration uses a large dataset of  $2.2 \text{ fb}^{-1}$  and four analyses based on a likelihood function, neural network, matrix element and boosted decision tree. The results are summarized in Table 2. CDF uses a neural network optimized using neuro-evolution of augmentation topologies [12] to combine the likelihood, neural network and matrix element analyses. The combined results are also shown in table 2.

	Likelihood	NN	ME	BDT	Combined
Expected significance	$3.4\sigma$	$4.4\sigma$	$4.5\sigma$	$4.6\sigma$	$5.1\sigma$
Observed significance	$2.0\sigma$	$3.2\sigma$	$3.4\sigma$	$2.8\sigma$	$3.7\sigma$
Cross section	$1.8^{+0.9}_{-0.8} \text{ pb}$	$2.0^{+0.9}_{-0.8} \text{ pb}$	$2.2^{+0.8}_{-0.7} \text{ pb}$	$1.9^{+0.8}_{-0.7} \text{ pb}$	$2.2 \pm 0.7 \text{ pb}$

Table 2: CDF single top results s and t channel combined using  $2.2 \text{ fb}^{-1}$  for  $M_{top} = 175 \text{ GeV}$ . ME stands for Matrix Element, and BDT for Boosted Decision Tree. The last column combines the likelihood, neural network and matrix element analyses.

Both D0 and CDF also reported separate measurements of the s and t channels. D0 uses the s+t channel boosted decision tree where the s and t channel cross sections are allowed to float. CDF uses neural network output templates for s and t channel separately and a 2-dimensional NN discriminant for the 2 jet 1 b-tag channel. Hence D0 measures:  $\sigma(s-ch) = 0.9 \text{ pb}$  and  $\sigma(t-ch) = 3.8 \text{ pb}$ . CDF measures:  $\sigma(s-ch) = 1.6^{+0.9}_{-0.8} \text{ pb}$  and  $\sigma(t-ch) = 0.8^{+0.7}_{-0.8} \text{ pb}$ . Figure 2 shows these measurements with their uncertainties.

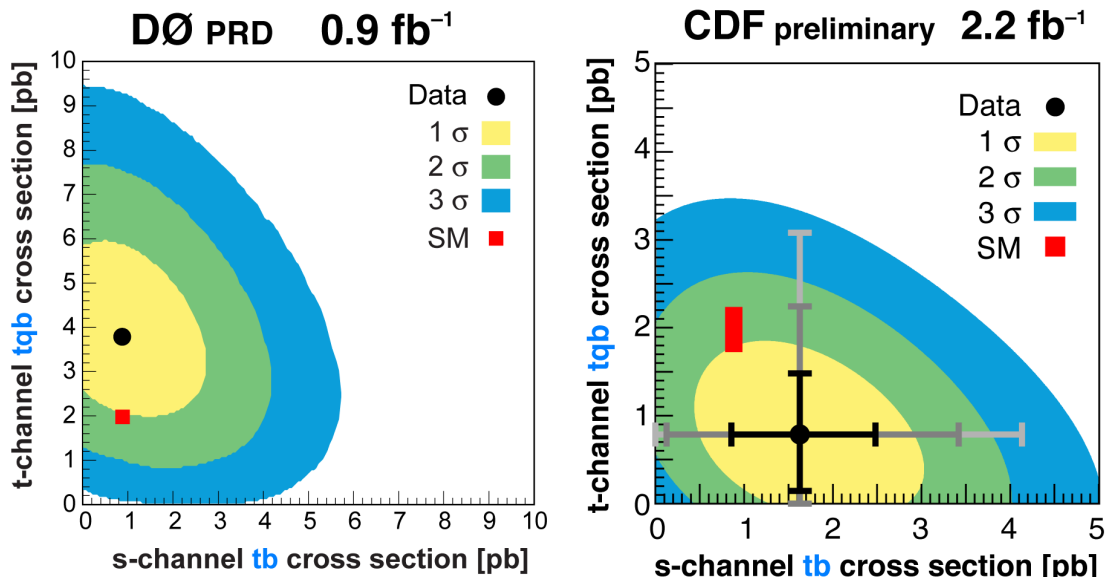


Figure 2: D0 (left) and CDF (right) s and t channel single top measurements

As already noticed, the single top cross section measurement allows to measure directly the CKM matrix element  $V_{tb}$  since it is proportional to  $|V_{tb}|^2$ . To extract  $V_{tb}$ , several assumptions are made. First the single top production is supposed to come exclusively from interaction with a  $W$  boson (ie. no FCNC are considered), the top quark is assumed to decay as predicted by the SM (ie.  $|V_{td}|^2 + |V_{ts}|^2 \ll |V_{tb}|^2$ ). Finally the  $Wtb$  coupling is assumed to be purely  $V - A$  (ie. no anomalous  $Wtb$  couplings). Under these hypotheses but without any assumption regarding the number of quark families or CKM unitarity, the following lower bounds are extracted:  $|V_{tb}| \geq 0.68$  at 95% CL by D0 and  $|V_{tb}| \geq 0.66$  at 95% CL by CDF both using a flat prior for  $V_{tb}$  from 0 to 1.

### 3.3 Summary and Perspectives for Single Top Production

Even though single top cross section measurements are challenging, both D0 and CDF report  $3\sigma$  evidence for single top production (see Tables 1 and 2). By analyzing more statistics and based on the current analysis sensitivity, a  $5\sigma$  observation of this electroweak top quark production is expected soon (see Figure 3 left). Analyzing the full run II dataset will also allow to exclude an extended range of models beyond the SM that manifest themselves in the single top sector if no sign of new physics appears (see Figure 3 right). LHC experiments will need around  $10 \text{ fb}^{-1}$  to see the t-channel and to discover the  $W$  associated production channel. The s-channel will be more difficult to see at the LHC.

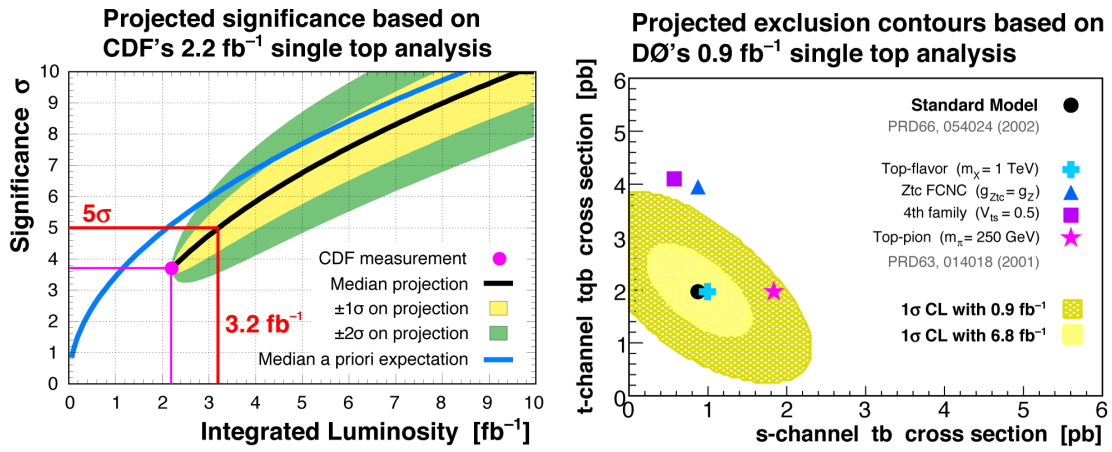


Figure 3: CDF projected significance (left) and D0 exclusion contours perspectives (right).

## 4 Conclusion

At the Run II of the Tevatron, top physics entered a precision area. Indeed the statistics is not the limiting factor anymore for the measurement of the  $t\bar{t}$  cross section in the lepton+jets and full hadronic channels. The best measurement currently achieves a 11% total relative uncertainty which is of the same order as the theoretical prediction uncertainty. Because of the precision achieved, the SM has been tested in the top quark sector by measuring the  $t\bar{t}$  cross section in all the possible channels and by reporting evidence for single top production.

The Tevatron will deliver from 6 to  $8 \text{ fb}^{-1}$  of data by the end of 2009 or 2010. At this time, even the dilepton  $t\bar{t}$  cross section will become limited by the systematic uncertainties. Future work to improve the  $t\bar{t}$  cross section measurements will then

focus on decreasing the systematic uncertainties. At the end of Run II, we also expect the discovery the single top in both the s and t channels. Of course with this statistics in hand, we can not exclude to see surprises in the top quark physics sector.

## References

- [1] F. Abe *et al.* [CDF Collaboration], Phys. Rev. Lett. **74** (1995) 2626 [arXiv:hep-ex/9503002]; S. Abachi *et al.* [D0 Collaboration], Phys. Rev. Lett. **74** (1995) 2632 [arXiv:hep-ex/9503003].
- [2] [http://www-d0.fnal.gov/Run2Physics/top/top\\_public\\_web\\_pages/top\\_public.html](http://www-d0.fnal.gov/Run2Physics/top/top_public_web_pages/top_public.html)
- [3] <http://www-cdf.fnal.gov/physics/new/top/top.html>
- [4] W. K. Tung, H. L. Lai, A. Belyaev, J. Pumplin, D. Stump and C. P. Yuan, JHEP **0702** (2007) 053 [arXiv:hep-ph/0611254];  
H. L. Lai, P. Nadolsky, J. Pumplin, D. Stump, W. K. Tung and C. P. Yuan, JHEP **0704** (2007) 089 [arXiv:hep-ph/0702268].
- [5] M. Cacciari, S. Frixione, M. L. Mangano, P. Nason and G. Ridolfi, JHEP **0809** (2008) 127 [arXiv:0804.2800 [hep-ph]].
- [6] [CDF Collaboration and D0 Collaboration], arXiv:0803.1683 [hep-ex].
- [7] G. J. Feldman and R. D. Cousins, Phys. Rev. D **57** (1998) 3873 [arXiv:physics/9711021].
- [8] Z. Sullivan, Phys. Rev. D **70** (2004) 114012 [arXiv:hep-ph/0408049].
- [9] V. M. Abazov *et al.* [D0 Collaboration], Phys. Rev. Lett. **98** (2007) 181802 [arXiv:hep-ex/0612052].
- [10] V. M. Abazov *et al.* [D0 Collaboration], Phys. Rev. D **78** (2008) 012005 [arXiv:0803.0739 [hep-ex]].
- [11] L. Lyons, D. Gibaut and P. Clifford, Nucl. Instrum. Meth. A **270** (1988) 110;  
A. Valassi, Nucl. Instrum. Meth. A **500** (2003) 391.
- [12] K. O. Stanley and Risto Miikkulainen, Evolutionary Computation, **10 (2)** (2002) 99-127.

# Top Quark Properties

*Mousumi Datta  
Fermi National Accelerator Laboratory*

paper not submitted

# **W-Z physics from the Tevatron**

*Tim Bolton  
Kansas State University*

paper not submitted

# Electroweak constraints from HERA

*Elisabetta Gallo  
INFN Firenze  
Via G. Sansone 1  
I-50019 Sesto Fiorentino, ITALY*

## 1 Introduction

The  $ep$  accelerator HERA at the laboratory DESY in Hamburg terminated activity on 30th June 2007. The two experiments H1 and ZEUS collected each  $0.5 \text{ fb}^{-1}$  of deep inelastic scattering (DIS)  $ep$  collisions at  $\sqrt{s} = 300,319 \text{ GeV}$ , for a total of  $1 \text{ fb}^{-1}$  of integrated luminosity for combined results. The data taking can be divided in two periods: the HERA I period, corresponding to the years 1994-2000, in which each experiment collected mainly  $e^+p$  data ( $\simeq 110 \text{ pb}^{-1}$  for  $e^+p$  and  $\simeq 15 \text{ pb}^{-1}$  for  $e^-p$ ); the HERA II period, corresponding to the years 2004-2007, after the machine performed a luminosity upgrade and installed spin rotators to provide longitudinally polarised lepton beams. Approximately equal amounts of integrated luminosity for electron- and positron-proton collisions, with either left- or right-handed polarisation, were provided by the end of data taking. The detectors are now dismantled but there is intense activity for the publication of results on the whole statistics, as most of the analyses published up to now involve only the HERA I data.

The legacy of H1 and ZEUS is a precise determination of the proton parton densities functions (PDFs), which is fundamental for the prediction of Standard Model (SM) cross sections at other colliders, like at the LHC. The region covered by HERA in the kinematic plane in Bjorken  $x$  and  $Q^2$  is shown in fig. 1. Here  $x$  is the fraction of proton momentum carried by the struck quark and  $Q^2$  is the virtuality of the exchanged boson: the higher the  $Q^2$ , the deeper we can look inside the proton. At HERA,  $x$  spans values between  $10^{-5}$  and  $10^{-1}$ , thus providing predictions for LHC, which covers similar  $x$  ranges but at higher  $Q^2$ . The values of  $Q^2$  are up to few  $\times 10^4 \text{ GeV}^2$ , corresponding to distances inside the proton smaller than  $10^{-18} \text{ m}$ . At these values of  $Q^2 \simeq M_Z^2, M_W^2$ , HERA can probe DIS processes at the electroweak scale, providing important results as described in the following.

The double differential (reduced) cross section for DIS neutral current (NC),  $e^\pm p \rightarrow e^\pm X$ , can be written at HERA as:

$$\tilde{\sigma}_r^\pm(x, Q^2) = \frac{d^2\sigma^\pm}{dx dQ^2} \frac{Q^4 x}{2\pi\alpha^2 Y_+} = \tilde{F}_2^\pm \mp \frac{Y_-}{Y_+} x \tilde{F}_3^\pm - \frac{y^2}{Y_+} \tilde{F}_L, \quad (1)$$

where  $Y_{\pm} = 1 \pm (1 - y)^2$  and  $y$  is the inelasticity of the reaction and is the fraction of the lepton momentum transferred to the hadronic system in the proton rest frame. The two proton structure functions  $\tilde{F}_2$  and  $x\tilde{F}_3$  are discussed in this report in the high- $Q^2$  range. The longitudinal structure function  $\tilde{F}_L$  is only relevant at high  $y$  and is negligible in the kinematic range reported here. The low- $Q^2$  data constrain the sea and gluon at low  $x$  (Fig. 1), while the neutral current and charged current (CC) data constrain the  $u$ -valence and  $d$ -valence at high- $x$ .

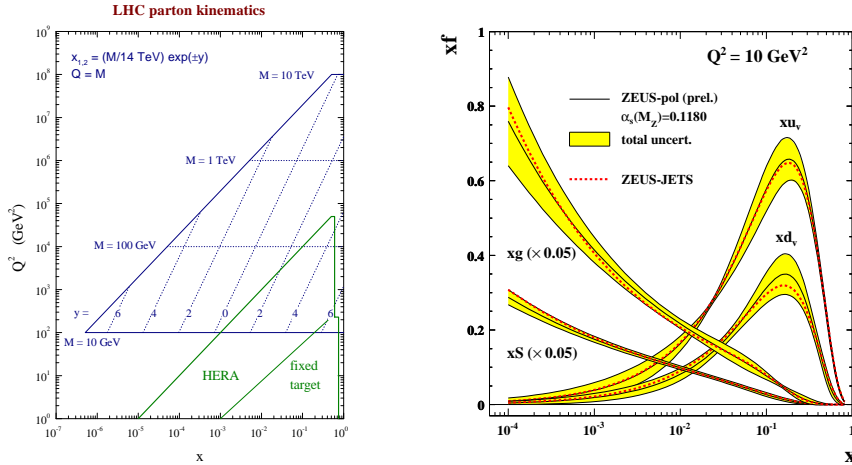


Figure 1: On the left: kinematic plane for the measurement of parton densities at HERA and other colliders. On the right: example of parton densities extracted from fits to the ZEUS data. The ZEUS-pol fit, discussed in this report, is shown together with a previous fit (ZEUS-JETS). The densities for the  $u$ -valence,  $d$ -valence, sea and gluon are shown as a function of  $x$  at the scale  $Q^2 = 10 \text{ GeV}^2$ . The sea and gluon are multiplied by 1/20 for better visibility.

## 2 Neutral current cross sections at high $Q^2$

Neutral current events are characterized by the presence of the scattered  $e^\pm$  detected at large angle in the calorimeters. The NC structure functions can be related to the quark distributions in leading order as:

$$\tilde{F}_2^\pm = F_2 + k_Z(-v_e \mp Pa_e) \cdot F_2^{\gamma Z} + k_Z^2(v_e^2 + a_e^2 \pm 2Pv_e a_e) \cdot F_2^Z \quad (2)$$

$$x\tilde{F}_3^\pm = k_Z(\pm a_e + Pv_e) \cdot xF_3^{\gamma Z} + k_Z^2(\mp 2v_e a_e - P(v_e^2 + a_e^2)) \cdot xF_3^Z \quad (3)$$

$$(F_2, F_2^{\gamma Z}, F_2^Z) = x \sum (e_q^2, 2e_q v_q, v_q^2 + a_q^2)(q + \bar{q}) \quad (4)$$

$$(xF_3^{\gamma Z}, xF_3^Z) = 2x \sum (e_q a_q, v_q a_q)(q - \bar{q}), \quad (5)$$

where  $k_Z = 1/4(\sin^2 \theta_W \cos^2 \theta_W) \cdot (Q^2)/(Q^2 + M_Z^2)$ ,  $a_e = -1/2$  and  $v_e = -1/2 + 2 \sin^2 \theta_W \simeq 0.04$ .

In the equations above,  $v_i$  and  $a_i$  denote the vector and axial weak couplings of the fermions ( $e$  and quarks  $q$ ) to the  $Z$ , while  $P$  is the longitudinal polarisation of the lepton beam. In the expression for  $\tilde{F}_2$  (Eq. (2)), the first term corresponds to pure  $\gamma$  exchange and dominates at low and medium  $Q^2$ . At high  $Q^2$  the second term, corresponding to the  $\gamma/Z$  interference, becomes relevant, while the third one, due to pure  $Z$  exchange, is always small. The parity violating structure function  $x\tilde{F}_3$  (Eq. (3)) is dominated by the  $\gamma/Z$  interference.

The unpolarised (corrected to  $P = 0$ )  $d\sigma/dQ^2$  cross section is shown in Fig. 2 where H1 and ZEUS results from  $e^\pm p$  HERA II data are shown. The cross section is measured over six orders of magnitude and agrees well with the SM prediction, which is shown here using the CTEQ6M PDFs. The positron and electron cross sections are equal at low  $Q^2$  where the photon exchange dominates, and start to differ at  $Q^2 \simeq M_Z^2$  where the  $\gamma/Z$  interference and the contribution of  $xF_3$  become sizeable.

As can be seen from Eq. (1), the parity violating structure function  $x\tilde{F}_3$  can be extracted from the difference between the  $e^+p$  and  $e^-p$  cross sections. The difference is dominated by the interference part which, as  $v_e$  is small, is proportional to  $a_e a_q$  and a parity conserving quantity. In terms of quark densities it can be formulated as

$$xF_3^{\gamma Z} = x/3(2u_v + d_v + \Delta), \quad (6)$$

(where  $\Delta$  is a small correction) and thus gives information on  $u_v$ ,  $d_v$ , the valence distributions for the up and down quarks. The quantity is shown, for a combination of H1 and ZEUS data [1], in Fig. 2, compared to two different parton density parametrizations. For the first time, the valence distribution is measured down to  $x \simeq 0.01$ . Note that LHC will measure the valence densities down to  $x \simeq 0.005$  in  $W$ -production.

### 3 Charged current cross section

Charged current events ( $ep \rightarrow \nu X$ ) are characterized by the presence of a neutrino in the final state and are therefore selected requiring high missing transverse momentum. The differential cross section in  $Q^2$  can be written as

$$\frac{d\sigma^{e^+p}}{dx, dQ^2} = (1 + P) \frac{G_F}{2\pi} \frac{(M_W^2)^2}{(M_W^2 + Q^2)^2} [\bar{u}_i(x, Q^2) + (1 - y)^2 d_i(x, Q^2)] \quad (7)$$

$$\frac{d\sigma^{e^-p}}{dx, dQ^2} = (1 - P) \frac{G_F}{2\pi} \frac{(M_W^2)^2}{(M_W^2 + Q^2)^2} [u_i(x, Q^2) + (1 - y)^2 \bar{d}_i(x, Q^2)]. \quad (8)$$

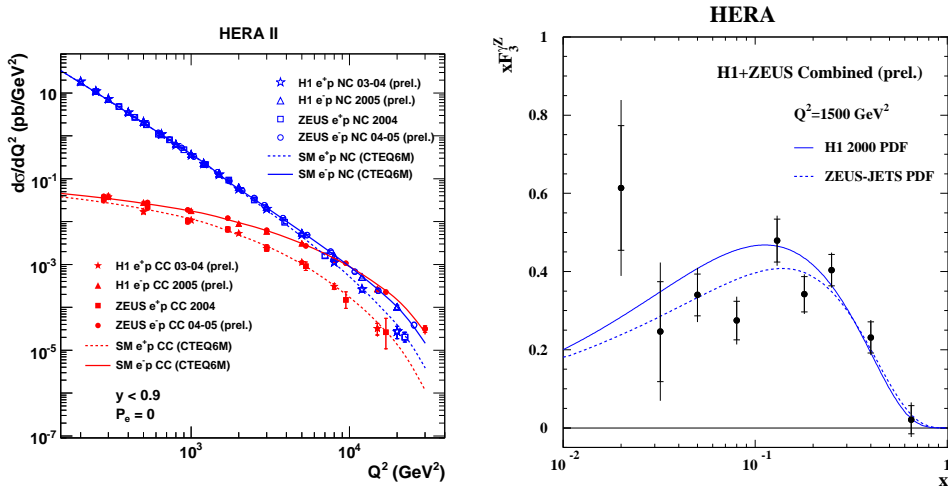


Figure 2: Results on NC and CC cross sections at HERA. The left plot shows the differential cross section in  $Q^2$  for both reactions. The cross sections are corrected here to polarisation  $P = 0$ . The right plot shows the combined H1+ZEUS results on the NC structure function  $x F_3$ . The data of the two Collaborations (total of  $480 \text{ pb}^{-1}$ ) have been here averaged and adjusted to a fixed  $Q^2$  value of  $1500 \text{ GeV}^2$ .

The cross sections for  $e^+$  and  $e^-$  have different dependences on the  $u$ -type and  $d$ -type parton densities, providing an important flavour separation at high  $x$ . As shown in Fig. 2, the CC cross section for  $e^- p$  is higher than that of  $e^+ p$  due to the fact that the  $u$  density is larger and in addition the  $d$  density in Eq. (7) is suppressed by the helicity factor  $(1 - y)^2$ . The  $d\sigma/dQ^2$  is flat for  $Q^2 \ll M_W^2$ , while for  $Q^2 > \sim M_W^2$  it decreases and its size becomes similar to that of the NC interaction. This text-book plot is one of the confirmation of the unification of the electromagnetic and weak interactions at the scale of the masses of the  $W$  or  $Z$ .

The term  $(1 \pm P)$  in Eqs. (7) and (8) refers to the strong dependence of the CC cross section on the lepton-beam polarisation. At HERA, leptons became naturally transversely polarised through synchrotron radiation via the Sokolov-Ternov effect. Spin rotators were installed during the luminosity upgrade in order to provide longitudinally polarised beams for the experiments. The build-up time for the polarisation was approximately 30 minutes at the beginning of the machine fills. The polarisation, here defined as  $P = (N_R - N_L)/(N_R + N_L)$ , where  $N_R$  ( $N_L$ ) is the number of right-handed (left-handed) electrons, reached typically values of 30-40% and its sign was changed every two-three months. It was measured by three different devices, exploiting the dependence on  $P$  of the Compton scattering cross section of circularly-polarised photons with the lepton beam.

The linear dependence of the total CC cross section versus  $P$  is shown in Fig. 3,

another text-book plot, which shows that the  $e^-p$  ( $e^+p$ ) cross sections tends to zero for  $P = +1$  ( $P = -1$ ). This is expected from the absence of right-handed currents in the weak interaction.

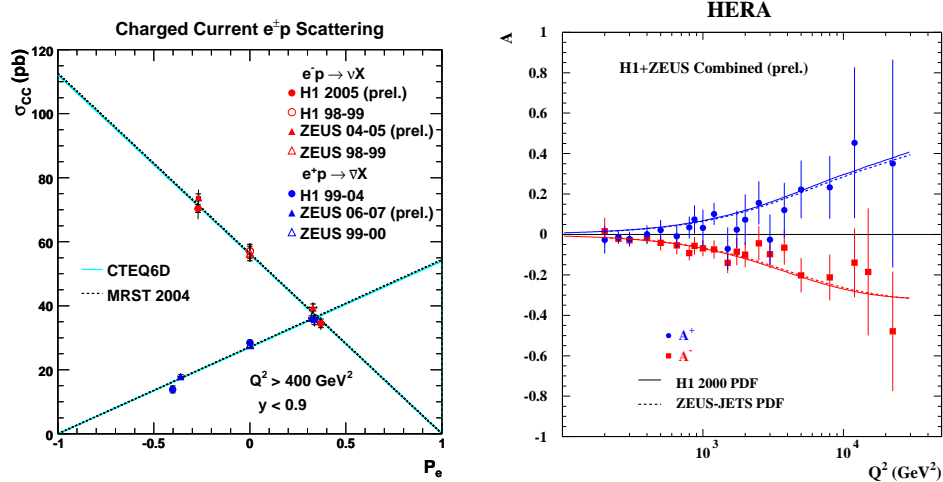


Figure 3: Results on CC and NC polarised cross sections at HERA. The left plot shows the total cross section for charged current  $e^\pm p$  versus the lepton beam polarisation. The right plot shows the combined H1+ZEUS results for the asymmetry in NC interactions.

## 4 Electroweak couplings

The effect of the polarisation in NC is much weaker than in CC and visible only at very high  $Q^2$ . In order to enhance it, the asymmetry

$$A^\pm = \frac{2}{P_R - P_L} \cdot \frac{\sigma^\pm(P_R) - \sigma^\pm(P_L)}{\sigma^\pm(P_R) + \sigma^\pm(P_L)} \simeq \mp k_Z a_e \frac{F_2^{\gamma Z}}{F_2} \quad (9)$$

is measured. This quantity is proportional to combinations  $a_e v_q$ , thus it provides a direct measurement of parity violation in neutral current at high  $Q^2$ . The asymmetry is shown in Fig. 3, where it can be seen that  $A^+$  is positive and  $\simeq -A^-$ , as predicted by the theory [1]. This asymmetry is the first measurement of parity violating effects in weak interactions at distances down to  $10^{-18}$  m.

The neutral current polarised data can also be employed to perform a QCD fit and extract simultaneously the parton densities and the electroweak parameters. The next-to-leading-order (NLO) QCD fits parametrise the parton densities at an initial scale  $Q_0^2$  and evolve them in  $Q^2$  with the DGLAP evolution equations. The new

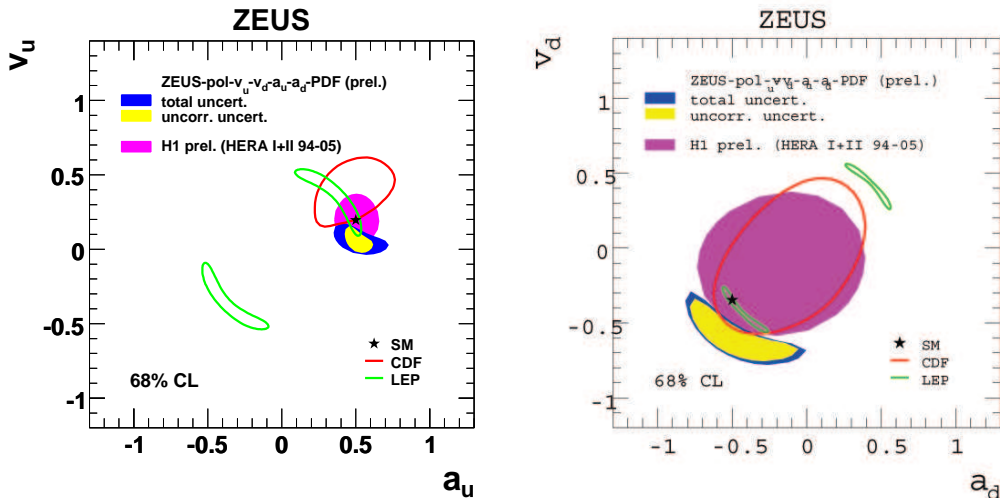


Figure 4: Contour plots at the 68% confidence level ( $CL$ ) of the limits on the electroweak couplings of the  $u$  (left) and  $d$  (right) quarks to the  $Z$ . The H1 and ZEUS results are shown together with CDF and LEP contours.

polarised NC data from HERA II provide a better constraint on the  $u$ -density, thanks to the much higher statistics ( $\simeq 176 \text{ pb}^{-1}$ ) of the  $e^-p$  sample compared to HERA I ( $\simeq 16 \text{ pb}^{-1}$ ). In addition, the polarisation allows the determination of the axial and vector couplings of the  $u$  and  $d$  quarks to the  $Z$ , which are still not very well constrained by other colliders data.

From the Eqs. (2-5), as  $v_e$  and  $k_Z^2$  are very small, it can be seen that the unpolarised term in  $xF_3$  is sensitive to the product  $e_q a_e a_q$  and thus to the axial coupling of the quarks. The polarised term in  $F_2$ , instead, is sensitive to the product  $e_q v_q a_e$  and thus to the vector coupling to the quarks. The new ZEUS-pol fit [2] provides information on the parton densities (Fig. 1) and on the quark couplings at the same time. The quark couplings are shown in Fig. 4, together with results from CDF and LEP II. The H1 results are also shown. The precision of the HERA data is competitive and the sign ambiguity of the LEP II data is resolved. All four couplings are in good agreement with the SM expectation.

## 5 Search for new physics at high $Q^2$

The HERA data at high  $Q^2$  have triggered the search for new physics in  $eq$  interactions down to distances of  $10^{-18} \text{ m}$ . A classical search is that for leptoquarks (LQs) coupling to first generation fermions, that can be produced in the  $s-$  and  $u-$ channels from the fusion of the lepton beam with one of the valence quarks in the protons. The

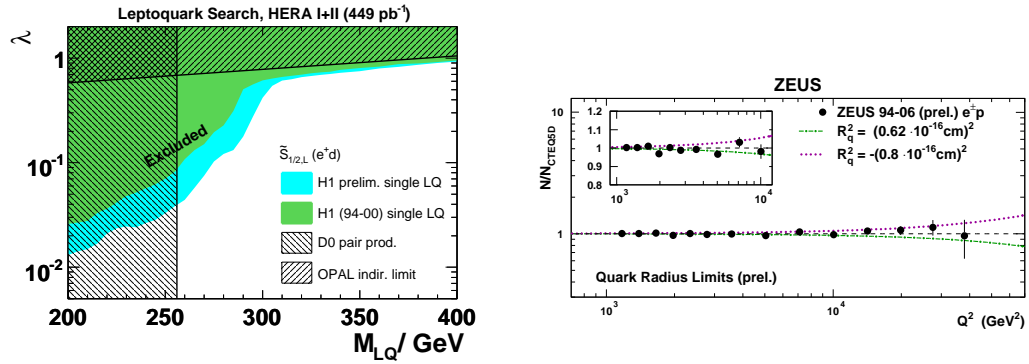


Figure 5: On the left: example of limit on one of the leptoquark types from the H1 data, based on the HERA I+II statistics. The H1 exclusion limit is shown for the leptoquark  $\tilde{S}_{1/2,L}(e^+d)$ , as a function of its mass and its Yukawa coupling  $\lambda$  to the positron and quark. On the right: Limit on the quark radius from the 1994-2006 ZEUS data. The differential cross section versus  $Q^2$  is shown divided by the SM expectation using CTEQ5D, a parametrisation which does not include the latest HERA data. The line shows the expectation for a quark radius corresponding to the obtained limit at 95%  $CL$ .

leptoquarks decay then to an electron/positron and a quark, or to a neutrino and a quark, with a signature similar to that of DIS NC or CC events at high  $Q^2$ . For masses of the leptoquark  $M_{LQ} < \sqrt{s}$ , the LQ signal appears as a narrow resonance at a certain Bjorken  $x \simeq M_{LQ}^2/s$ . For masses greater than  $\sqrt{s}$ , it manifests itself as a contact interaction, causing deviations of the cross sections at high  $x$  and  $Q^2$  from the SM expectation. The LQ signal can be distinguished also thanks to the different angular distribution of the lepton and jet in the final state in the LQ rest frame, compared to that of the DIS background. H1 has recently presented a search in the whole statistics from HERA I+II ( $\simeq 450 \text{ pb}^{-1}$ ) [3], but no deviation from the SM was observed in the final state lepton-jet mass spectra. Limits were set on LQ production, an example is shown in Fig. 5, together with recent results from other colliders. For masses in the range between 260 and 300 GeV, HERA excludes the production of leptoquarks with LQ-fermions Yukawa couplings in the range  $10^{-2}$ - $10^{-1}$ , in a region not covered by other experiments.

The substructure of quarks is another classical type of new physics that could be visible in the HERA data. It would manifest itself as a contact interaction, which decreases the  $Q^2$  spectrum with a form factor of the form  $(1 - R_q^2/6 \cdot Q^2)^2$ , where  $R_q$  is the finite quark radius and the electron is assumed to be pointlike. The  $d\sigma/dQ^2$  spectrum, normalized to the theory, is shown for the ZEUS 1994-2006 data [4] in Fig. 5. The ratio is consistent with one, thus no evident sign of a quark substructure

is seen in these data. A limit of  $R_q < 0.62 \times 10^{-18}$  m is obtained at 95%  $CL$ . This is the most stringent limit to date, and not very far from the electron radius limit [5] determined at LEP.

## 6 Constraints from events with high $p_T$ leptons

The observation of particular events in H1, with high transverse-momentum ( $P_T^l$ ) leptons in the final state, has attracted quite some attention from the HERA community for many years and triggered investigations of possible new physics.

The first search was the observation by H1 in 1994 of an event with an isolated high- $P_T^l$  muon, large missing transverse momentum ( $P_T^{\text{miss}}$ ) and a jet with large transverse energy  $P_T^X$ . Since then H1 has reported regularly on the observation of an excess of this type of events, both with an electron/positron or a muon in the final state, exclusively in  $e^+p$  interactions. In the Standard Model, such events are due to  $W$  production,  $ep \rightarrow (e)WX \rightarrow (e)l\nu X$ , where the  $W$  is radiated from one of the quarks in the proton. The  $W$  can decay then to a lepton and neutrino, while the struck quark produces the hadronic final state  $X$ . The scattered electron/positron can be seen in the detector if it is scattered at large angle (for  $Q^2$  typically  $> 4$  GeV $^2$ ) or escapes in the beam pipe in the lepton-beam direction. In  $W$  production, however, the hadronic system  $X$  has typically a low transverse energy, while the events observed by H1 showed an excess over the prediction at  $P_T^X > 25$  GeV. The ZEUS Collaboration has never confirmed this excess and recently the two Collaborations have defined a common phase space to compare the results [6]. The final state leptons are restricted to a common acceptance region corresponding to the polar-angle range  $15^\circ < \theta^l < 120^\circ$  (where  $\theta^l$  is measured with respect to the proton-beam direction) and  $P_T^l > 10$  GeV. The cut on the missing transverse energy of the event was chosen at  $P_T^{\text{miss}} > 12$  GeV. The full HERA I+II data set was combined (0.97 fb $^{-1}$ ) and in total 64 electron events and 23 muon events were selected, in good agreement with the SM expectation of  $72.9 \pm 8.9$  and  $19.9 \pm 2.6$ , respectively.

The combined  $P_T^X$  spectrum is shown in Fig. 6 for the  $e^+p$  data only. Selecting

$e^+p, P_T^X > 25$ GeV	$e + \mu$ Data	$e + \mu$ SM
H1 0.29 fb $^{-1}$	17	$7.1 \pm 0.9$
ZEUS 0.29 fb $^{-1}$	6	$7.5 \pm 1.1$
H1+ZEUS 0.58 fb $^{-1}$	23	$14.6 \pm 1.9$

Table 1: Data yields for the isolated lepton events at high  $P_T^X$  in the full  $e^+p$  H1+ZEUS data set. The selection refers to the common acceptance region in the two detectors.

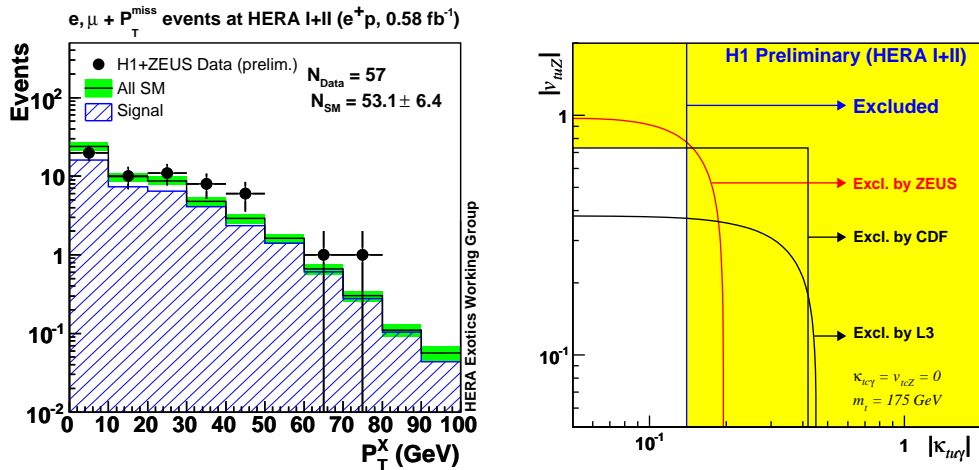


Figure 6: On the left: distribution of the  $P_T^X$  in the HERA combined  $e^+p$  data. On the right: Limits on the FCNC coupling for single top production from the latest H1 data, compared to previous published results. The contribution from charm quark is negligible in this kinematic regime at HERA and it is therefore neglected in the extraction of the limit ( $k_{tc\gamma} = 0$ ). The couplings to the  $Z$  are also neglected in the latest H1 results.

the region at high  $P_T^X$ , H1 observed 17 events with  $P_T^X > 25 \text{ GeV}$ , compared to a SM expectation of  $7.1 \pm 0.9$ , corresponding to a  $2.9\sigma$  deviation. The ZEUS data yield is shown in Table 1. No excess is observed by ZEUS and when the two data sets are combined, a total of 23 events is observed, for a SM prediction of  $14.6 \pm 1.9$ . The deviation is reduced to  $1.8\sigma$  and it is therefore not significant.

One of the possible processes giving rise to events at high  $P_T^X$  is the production of single top at HERA,  $ep \rightarrow (e)tX$ , where the top decays as  $t \rightarrow bW \rightarrow bl\nu$ . The SM cross section for such process is very small, of the order of  $1 \text{ fb}$ , therefore the observed event yield could be only due to new physics. A possible process is the flavour changing neutral current (FCNC) transition of a  $u$  quark in the proton to a  $t$  quark. This anomalous single-top production is described by an effective Lagrangian where the interaction of a top with a  $u$  quark and the photon is characterized by the magnetic coupling  $k_{tu\gamma}$ . H1 analysed their interesting events optimizing the cuts for single-top search [7]. The selected events distributions resulted to be compatible with the SM expectations and a limit at  $95\% CL$  on the cross section of  $\sigma(ep \rightarrow etX) < 0.16 \text{ pb}$  was extracted. The corresponding limit on  $k_{tu\gamma} < 0.14$  is shown in Fig. 6, where also previous published results from other colliders are shown. The H1 preliminary limit is the strictest limit to date.

On the other hand, the events selected by H1 and ZEUS are a good starting sample

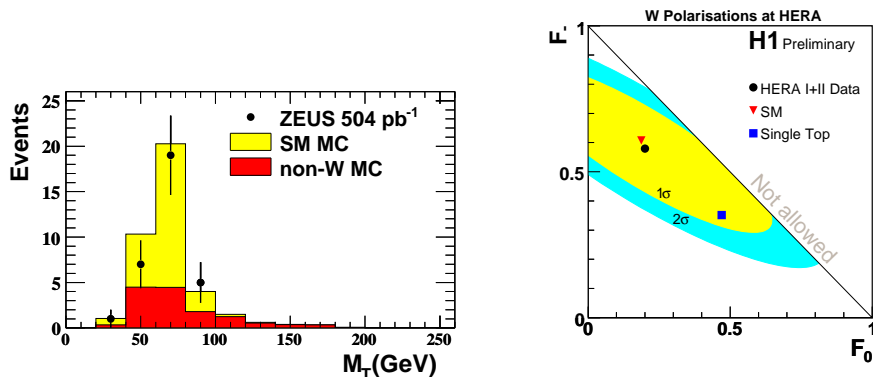


Figure 7: On the left: distribution of the transverse mass in  $W$ -candidate events in ZEUS. The data (dots) are superimposed to the SM expectation which is dominated by  $W$  production (light shaded histogram). On the right: Contour plots at  $1\sigma$  and  $2\sigma$  for the fitted  $F_-$  and  $F_0$  polarisation fractions of the  $W$ , from the H1 data.

to select  $W$  events at HERA. The transverse mass in the  $W \rightarrow e\nu$  channel is shown for the ZEUS data in Fig. 7, where the data clearly show the reconstructed  $W$ -mass peak. ZEUS measured a cross section [8] for  $\sigma(W \rightarrow l\nu X)$  of  $0.89^{+0.25}_{-0.22}(\text{stat.}) \pm 0.10(\text{syst.})$  pb, in good agreement with the SM calculation of 1.2 pb.

Additional selection cuts were also applied in H1, selecting a total of 31  $W$  candidates with very high purity. These events were analysed in terms of the polarisation fractions of the  $W$  boson [9], which were defined as a function of the angle  $\theta^*$  between the  $W$  momentum in the laboratory frame and the charged decay lepton in the rest frame of the  $W$ . The left-handed  $F_-$ , the longitudinal  $F_0$  and the right-handed  $F_+$  fractions have to satisfy the relation  $F_+ + F_- + F_0 = 1$  and can be extracted fitting the measured  $\cos \theta^*$  distributions from the relation (*i.e.* for  $W^+$ ):

$$\frac{dN}{d \cos \theta^*} \propto (F_+) \cdot \frac{3}{8}(1 + \cos \theta^*)^2 + F_0 \cdot \frac{3}{4}(1 - \cos^2 \theta^*) + F_- \cdot \frac{3}{8}(1 - \cos \theta^*)^2. \quad (10)$$

The optimal values for  $F_0$  and  $F_-$  extracted from a simultaneous fit are shown in Fig. 7, showing values very close to the ones predicted by the SM, but also compatible with single-top production within  $1\sigma$ .

The H1 Collaboration also reported the observation, in the HERA I data, of outstanding multielectron/positron events, with either two ( $2e$ ) or three ( $3e$ ) isolated high- $P_T^l$   $e$  in the final state. Six of these events had an invariant mass of the two highest-transverse energy leptons ( $M_{12}$ ) greater than 100 GeV, compared to a SM expectation of  $\simeq 0.53$ . Such events are predicted in the SM from the Bethe-Heitler reaction  $\gamma\gamma \rightarrow l^+l^-$ , where one of the photons is radiated from the initial quark and the other from the electron/positron beam. An excess could be due to new

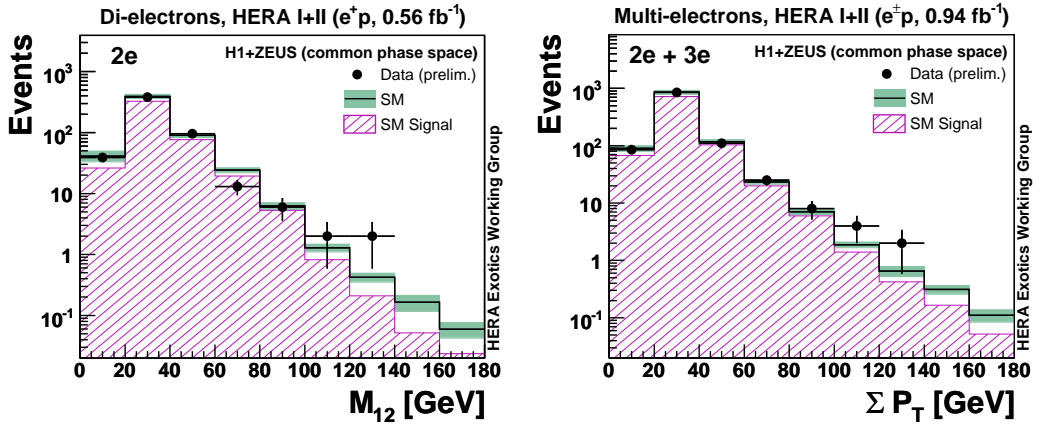


Figure 8: On the left: distribution of the mass of the two highest-energy leptons in  $2e$  events in the  $e^+p$  combined HERA data. On the right: distribution of the sum of the transverse momentum in  $(2e)+(3e)$  events in the full HERA sample.

physics, like for instance doubly-charged Higgs production. A coherent combination of H1 and ZEUS data was performed on the full HERA statistics [10], choosing a common phase space for the selection. At least two  $e$  candidates in an event had to be central ( $20^\circ < \theta^l < 150^\circ$ ), of which one must have  $P_T^l > 10$  GeV and the other  $P_T^l > 5$  GeV. The distribution of the invariant mass  $M_{12}$  is shown for the  $e^+p$  HERA sample in Fig. 8. For  $M_{12} > 100$  GeV, a total of 4 ( $2e$ ) events and 4 ( $3e$ ) events were observed in  $e^+p$ , for an expectation of  $1.97 \pm 0.22$  and  $1.10 \pm 0.12$ , respectively. Another interesting distribution is shown in Fig. 8, the scalar sum of the transverse momentum  $\sum P_T$ , where a marginal excess is seen at values greater than 100 GeV. From Table 2 it can be seen that the excess is in the  $e^+p$  data, where 5 events are observed, while  $1.8 \pm 0.2$  are expected. The study of multileptons is being extended also to muons and taus, the analysis is still in progress.

Data sample	Data	SM
$e^+p$ ( $0.56 \text{ fb}^{-1}$ )	5	$1.82 \pm 0.21$
$e^-p$ ( $0.38 \text{ fb}^{-1}$ )	1	$1.19 \pm 0.14$
$e^\pm p$ ( $0.94 \text{ fb}^{-1}$ )	6	$3.00 \pm 0.34$

Table 2: Data yields for the  $2e$  and  $3e$  events for  $\sum P_T > 100$  GeV in the full HERA data set.

## 7 Summary

The H1 and ZEUS Collaborations are completing the analysis of the cross sections in NC and CC interactions. The full HERA data set will be combined and a more precise determination of the PDFs and of the electroweak couplings will derive.

I would like to thank Stefan Schmitt, Matthew Wing and James Ferrando for a careful reading of this report and the organizers for a very enjoyable time in Perugia.

## References

- [1] H1 and ZEUS Collaborations, Electroweak Neutral Currents at HERA, contributed paper to the ICHEP06 conference.
- [2] ZEUS Collaboration, Combined EW and QCD Analysis of ZEUS Data Inclusive DIS Cross Sections with Longitudinally Polarised Leptons, contributed paper to the Lepton Photon 2007 Symposium, and references therein.
- [3] H1 Collaboration, Search for Leptoquark Bosons in  $ep$  Collisions at HERA, presented at the DIS2008 workshop, and references therein.
- [4] ZEUS Collaboration, Search for Contact Interactions, Leptoquarks, Large Extra Dimensions and Finite Quark Radius in  $ep$  Collisions, contribution to the Lepton Photon 2007 Symposium.
- [5] See *i.e.* D. Bourilkov, Search for TeV Strings and New Phenomena in Bhabha Scattering at LEP2, preprint hep-ph/0002172, for a limit on the electron radius  $< 2.8 \times 10^{-19}$  m at 95%  $CL$ .
- [6] H1 and ZEUS Collaborations, Isolated Leptons and Missing  $P_T$ , contributed paper to the EPS07 conference.
- [7] H1 Collaboration, Search for Anomalous Single Top Production in  $ep$  Collisions at HERA, contributed paper to the EPS07 conference.
- [8] ZEUS Collaboration, Search for Events with an Isolated Lepton and Missing Transverse Momentum and a Measurement of  $W$  Production at HERA, DESY-08-089.
- [9] H1 Collaboration, Measurement of  $W$  Production and  $W$  Polarisations at HERA, contributed paper to the EPS07 conference.
- [10] H1 and ZEUS Collaborations, Multi-Electron Events at HERA, contributed paper to the Lepton Photon 2007 Symposium.

# Neutrino Physics

Session Convener:

*Jeffrey A.Appel*

Session Convener:

*Vlada Simak*

New developments in Solar Neutrino Physics

*Gianpaolo Bellini*

Short-baseline Neutrinos:

Recent Results and Future Prospects

*Ryan B. Patterson*

Ultra high-energy neutrinos

*Ryan Nichol*

Long Baseline Neutrino Oscillation Experiments

*Mark Thomson*

Underground nuclear astrophysics and the Sun

*Carlo Broggini*

OPERA: waiting for the  $\tau$

*Andrea Longhin*

# New developments in Solar Neutrino Physics

Gianpaolo Bellini

Department of Physics

Universita' di Milano

Istituto Nazionale di Fisica Nucleare - Sezione di Milano

I-20133 Milano, ITALY

## 1 Introduction

In this paper I summarize the experimental results obtained in this last year on the solar neutrino physics; in addition the open problems in the Solar Standard Model are briefly discussed. The new experimental results concern SNO, third phase, Kamland and especially Borexino, which started to take data in may 2007, opening a window on the solar neutrino spectrum at very low energy.

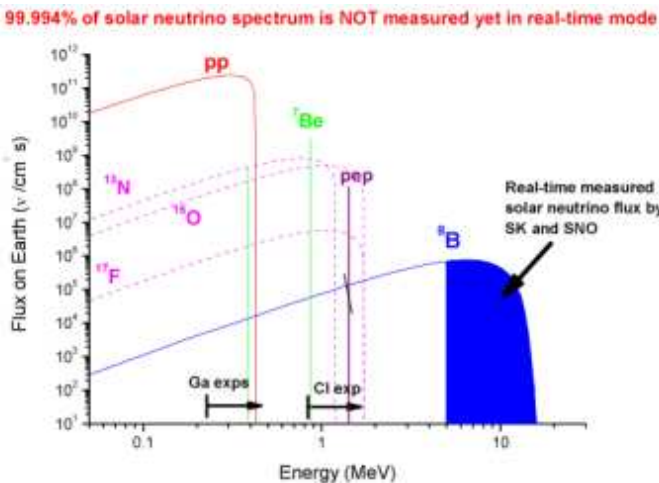


Figure 1:

Until now the experiments in real time (SNO and Superkamiokande) studied the solar neutrino flux only over a 4.5-5. MeV, exploring only about 1/10000 of the total solar spectrum (Figure 1). The reason of the choice of a so high threshold is the low rate of the neutrino events compared to the background produced by the natural

radioactivity, which is present everywhere, in the environment, in the construction and in the detecting materials. The threshold at 4.5-5. MeV is over the highest energy of radioactive decay of the two natural families, the Tl decay into  $e^- + \gamma$ .

The start up of the Borexino experiment, able to measure in real time the  $\nu$  events with a threshold down to 200-250 keV, opens a new era in the study of the solar neutrinos.

I will try also to show that the study of the solar neutrinos is able to produce important insights both in the elementary particle physics and in the Sun physics.

## 2 Open problems in the Solar Standard Model.

The fluxes of the solar neutrinos are predicted by the Solar Standard model, which has been developed in the last 40 years, together with the density profile and the He abundances. These evaluations can be checked by means of the results of the neutrino experiments, of the solar Luminosity and by studying the helioseismology. The input data of the model are the Opacity (the photon mean free path in the Sun), the metal abundances and the cross sections of the various nuclear reactions taking place in the Sun. As an example the flux of the neutrinos from  $^7Be$  depends from:

$$\Phi(^7Be) \approx S_{33}^{-0.43} \cdot S_{34}^{-0.86} \cdot L^{+3.40} \cdot O^{-1.49} \cdot (Z/X)^{-0.62} \quad (1)$$

where  $S_{ij}$  are the cross section factors, L the solar luminosity, O the Opacity, (Z/X) the metal abundances. The solar neutrino experiments can improve the parameter errors of the Solar Standard Model by measuring the neutrino fluxes, corrected with the oscillation model, to determine Opacity, Diffusion, S-factors, Z/X ratio. But the S factors can be measured also directly in high precision experiments in Laboratory.

It is the case of Luna [1], which measured  $S_{34}$  and  $S_{33}$  for the reactions  $^3He + ^4He \rightarrow \alpha + 2p$  and  $^3He + ^3He \rightarrow ^7Be + \gamma$ , respectively. These two reactions belong to the pp chain: the first controls the  $^7Be$  neutrino flux, while the second determines the pp chain branching ratio.  $S_{34}$  has been measured at 93 keV, allowing a good extrapolation to the Gamow peak: this precise value makes possible an important reduction of the uncertainty affecting the  $^7Be$  and  $^8B$  fluxes.  $S_{33}$  has been measured directly at the Gamow peak and its value confirmed the pp B.R., adopted until now by the Solar Model.

In addition LUNA obtained a good determination of  $S_{1,14}$ , which is connected to the reaction  $^{14}N(p, \gamma)^{15}O$ , the slowest process in the CNO chain. This experimental determination reduces the CNO flux of  $\approx 50\%$ .

Recently  $S_{34}$  has been measured also by Brown at al. [2], but at higher energy (330 keV); their results are consistent with the LUNA data.

An important open problem in the SSM is the metallicity. The solar surface abundances of metals are determined from the analysis of the photospheric atomic and

Source	BPS <sub>high</sub> Z	BPS <sub>low</sub> Z	Difference
PP	5.97( $1 \pm 0.007$ )	6.04( $1 \pm 0.007$ )	$0.07 \pm 0.06$
pep	1.41( $1 \pm 0.011$ )	1.45( $1 \pm 0.011$ )	$0.04 \pm 0.02$
hep	7.90( $1 \pm 0.16$ )	8.22( $1 \pm 0.16$ )	$0.30 \pm 1.70$
<sup>7</sup> Be	5.08( $1 \pm 0.06$ )	4.55( $1 \pm 0.05$ )	$0.53 \pm 0.35$
<sup>8</sup> B	5.95( $1^{+0.10}_{-0.09}$ )	4.72( $1^{+0.10}_{-0.09}$ )	$1.2 \pm 0.8$
<sup>13</sup> N	2.93( $1^{+0.15}_{-0.13}$ )	1.93( $1^{+0.15}_{-0.13}$ )	$1.0 \pm 0.6$
<sup>15</sup> O	2.20( $1^{+0.17}_{-0.14}$ )	1.37( $1^{+0.17}_{-0.14}$ )	$0.8 \pm 0.4$
<sup>17</sup> F	5.82( $1^{+0.17}_{-0.14}$ )	3.25( $1^{+0.17}_{-0.14}$ )	$2.6 \pm 1.2$

Table 1:

molecular spectral lines. Until the beginning of 2000, the associated solar atmospheric modeling has been done in one dimension, using a time-independent hydrostatic analysis, which incorporates the convection [3]. This treatment produces results in good agreement with the helioseismology observations.

More recently [4] a much improved three-dimensional treatment of the solar atmosphere reproduces better the profiles and brings the Solar abundances into a better agreement with other stars in the neighborhood. But the agreement with the helioseismology observations is much worse in comparison to the one-dimensional model. Following this improved analysis, the solar surface should contain 30-40% less carbon, nitrogen, oxygen, neon and argon, than previously believed.

The different values of the metallicity change the  $\nu$  flux of solar reactions. In table 1 the neutrino fluxes expected with high and low metallicity are shown [5]. In the table the following units are used:  $10^{10} \text{ cm}^{-2} \text{ s}^{-1}$  for pp,  $10^9$  for <sup>7</sup>Be,  $10^8$  for pep, <sup>13</sup>N, <sup>15</sup>O,  $10^6$  for <sup>8</sup>B and <sup>17</sup>F,  $10^3$  for hep.

In some cases the differences between high and low metallicity are larger than the model errors; in the case of <sup>7</sup>Be and <sup>8</sup>B they are borderline, while for the CNO cycle the difference is  $\sim 50\%$ . Then precise experimental measurements of solar neutrino fluxes can help in fixing the Z/X problem.

### 3 Recent results on solar neutrinos over 5 MeV.

SNO and Kamland have recently released new results. The SNO new data concern the so-called phase 3. As it is well known SNO is a Cherenkov experiment using heavy water; three different neutrino interactions are detected: Charged currents, CC ( $\nu_e + d \rightarrow p + p + e^-$ ), Neutral currents, NC ( $\nu_x + d \rightarrow n + p + \nu_x$ ), elastic scattering on electron, ES. The neutral current interactions are tagged by the neutron capture with the emission of  $\gamma$ s; the neutron is captured by the deuterium in the first phase (just  $D_2O : n + d \rightarrow t + \gamma + 6.25\text{MeV}$ ), by the <sup>35</sup>Cl in the second phase( $D_2O + 2$

tons of NaCl:  $n + {}^{35}Cl \rightarrow {}^{36}Cl + \gamma + 8.6\text{MeV}$ ), by  ${}^3\text{He}$  in the third phase ( ${}^{36}{}^3\text{He}$  proportional counters inserted in the detector:  $n + {}^3\text{He} \rightarrow p + t + 0.76\text{MeV}$ ).

The data of the third phase are collected in 387.17 live days [6]. The detection efficiencies are determined by a neutron calibration source ( ${}^{252}\text{Cf}$ ,  ${}^{241}\text{AmBe}$ ) and via  $\gamma$ s produced by activated NaCl.

The rates of the three reactions are compared with the first and second phase in Figure 2 (from left to right: CC, NC, ES). The agreement is in general good but for the elastic scattering where the results differ  $\sim 1.5 \sigma$ . The ratio between the CC and NC reactions is in good agreement with the ones obtained in the first two phases ( $\frac{\Phi_{CC}}{\Phi_{NC}} = 0.301 \pm 0.033$ ).

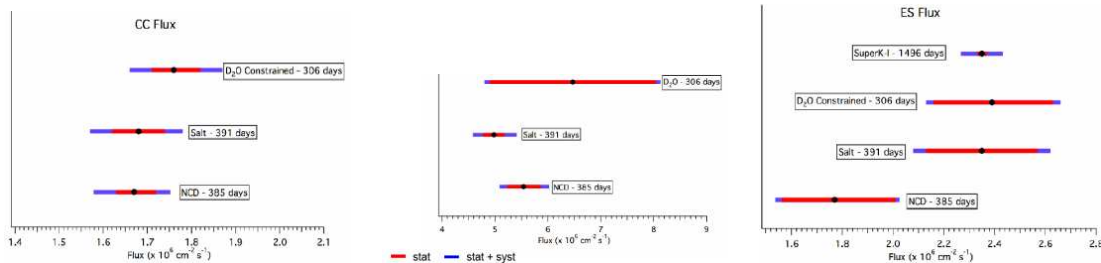


Figure 2:

As it is known, Kamland is a scintillator experiment which studies the antineutrinos produced by the Japanese reactors, with an average distance of 180 km and average energy of  $\approx 1.8$  MeV. The reaction detected is  $\bar{\nu} + p \rightarrow e^+ + n$ , with a prompt signal due to the  $e^+$  annihilation, and a delayed one (about  $200\mu\text{s}$ ) due to the neutron capture from  ${}^{12}\text{C}$  or H nuclei. In  $1490.8 \pm 0.5$  days of data taking they observe 1609  $\bar{\nu}$  interactions, to be compared with the expected number with no oscillation of  $2179 \pm 89$ . The background is estimated to be  $276.1 \pm 23.5$  [7].

In Figure 3 the energy spectrum of the detected interactions is compared with the expected one in the hypothesis of no oscillation, and with the background. In Figure 4 two oscillation periods are shown plotting the  $\bar{\nu}_e$  survival probability vs  $L_0/E_{\bar{\nu}_e}$ , profiting of the relatively wide energy spectrum of the reactors antineutrinos.

The best fit values of the oscillation parameters,  $\Delta m^2$ ,  $\tan^2\theta$ , obtained from the results of Kamland released in 2008, from the SNO all data collected in the three phases, from all solar experiments data collected until 2005 plus the Kamland data, from solar experiments including 2008 results + Kamland, are quoted in Figure 5.

In general there is a certain agreement among the various best fit values, except for SNO total, which is quoted without errors. As it is shown in Figure 6 (a), when the total SNO data are fitted, the allowed regions include oscillation parameters that are outside the LMA region, and the  $\Delta m^2$  parameter has two minima that are widely separated: this creates a problem in obtaining reasonable errors.

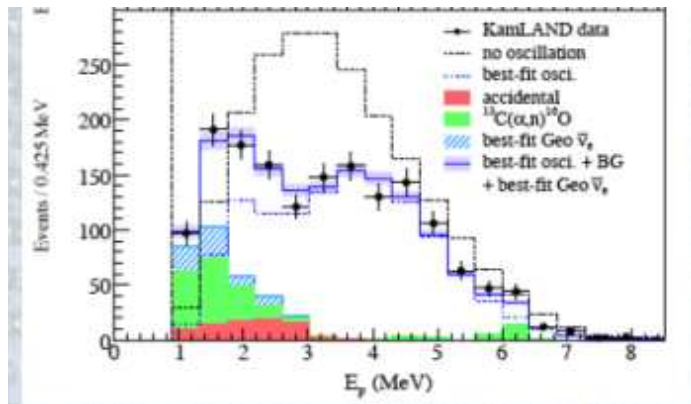


Figure 3:

The allowed regions are shown in Figure 6(b), for all data produced by the solar experiments (Cl, Ga, Superkamiokande, SNO, Borexino) and in Figure 6(c) for all solar plus Kamland. There is a disagreement in the best fit value for  $\Delta m^2$ ; the difference between solar only and solar plus Kamland is due more probably to  $\theta_{13}$ , which could be not zero [8].

In Figure 7 the survival probability of  $\nu_e$  as a function of the neutrino energy is shown. The continuous line reproduces the oscillation model calculated for  ${}^8\text{B}$  neutrinos by using, for the oscillation parameters, the best fit values quoted in the last line of Figure 5. The points refer to the data obtained by the real time solar neutrino experiments before the Borexino start up (high metallicity has been assumed), and the constraints that all the experiments on solar neutrinos produced on pp and  ${}^7\text{Be}$  fluxes.

## 4 Borexino.

### 4.1 The detector

Borexino is the first and only experiment, until now, able to study in real time the solar neutrino flux at or below 1 MeV of energy. It is installed in the Gran Sasso underground laboratory.

The Borexino design and layout are shown in Figure 8. The design is based on the principle of graded shielding and increasing radiopurity going from the external to the more internal shells. The detecting material of 300 tons is a binary scintillator (Pseudocumene [Pc] plus PPO), surrounded by a liquid buffer, consisting of Pseudocumene added with a quencher (DMP) [9].

The main feature of the Borexino detector is the very low radiopurity, never

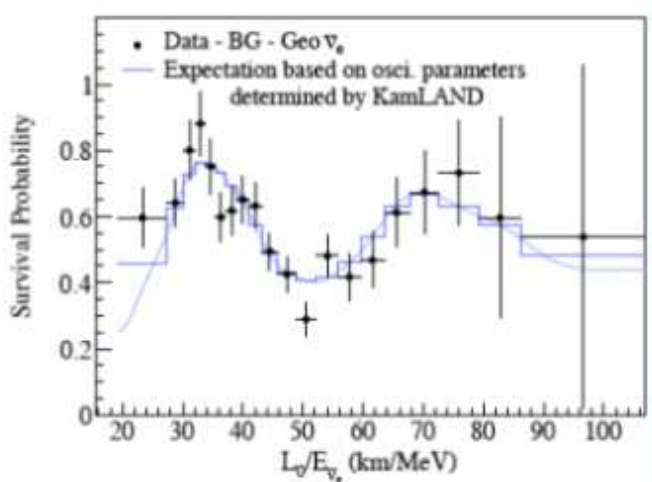


Figure 4:

achieved until now in experiments at ton level. To reach this goal, many special methods and tools have been developed, along five years of R&D. The main items concern: a) the scintillator cleaning by means of: water extraction, low temperature distillation (80 mbar, 90-95 °C), nitrogen stripping, ultrafine filtration; b) use of ultrapure N<sub>2</sub>, at record levels, for stripping: Rn free Nitrogen (Rn<0.1  $\mu Bq/m^3$ ), LAK Nitrogen (Ar content: 0.01 ppm, Kr: 0.03 ppt); c) special care in the Pe procurement: old layers crude oil (to minimize the <sup>14</sup>C), special loading station (maintained in N<sub>2</sub> atmosphere) directly connected to the production plant, special shipping vessels, rapid transport to the underground laboratory (to minimize the cosmogenic production of radioactive nuclides, as <sup>7</sup>Be); d) extreme precaution in the fabrication and assembly of the Nylon Vessels: selection and extrusion of the material in controlled area, construction in clean room with Rn control, special bag for shipping; e) all surface electropolished of: detector components, lines, fittings, valves; f) special developments and selection of the components (as for the PMTs); g) any operation in clean room or in N<sub>2</sub>, Ar atmosphere.

In addition, in order to check the ultra-low radioactive levels, a very high sensitivity detector (down to  $5 \cdot 10^{-16}$  g/g U, Th equivalent,  $\approx 10^{-18}$  <sup>14</sup>C/<sup>12</sup>C) has been installed underground, the Counting Test Facility (C.T.F.).

The background measured in Borexino during about 200 days of data taking is the following: <sup>14</sup>C/<sup>12</sup>C:  $(2.7 \pm 0.6) \cdot 10^{-18}$ ; <sup>232</sup>Th equivalent:  $(6.8 \pm 1.5) \cdot 10^{-18}$  g/g from the coincidence <sup>212</sup>Bi-<sup>212</sup>Po; <sup>238</sup>U equivalent:  $(1.6 \pm 0.1) \cdot 10^{-17}$  g/g from the coincidences <sup>214</sup>Bi-<sup>214</sup>Po. In addition two contaminants have been found in the detector: <sup>85</sup>Kr, despite the very high purity N<sub>2</sub> used for the stripping, and <sup>210</sup>Po without any evidence of <sup>210</sup>Bi.

	$\Delta m^2 (eV)^2 \cdot 10^{-5}$	$\tan^2 \theta$
Kamland 08	$7.58^{+0.14}_{-0.13} \pm 0.15$	$0.56^{+0.10+0.10}_{-0.07-0.06}$
SNO total 08	4.57	0.447
Solar 05 + Kamland	$7.59 \pm 0.21$	$0.47^{+0.06}_{-0.05}$
Cl-Ar, SK, Sage, Gallex SNO 08, Borex Kamland.	$7.94^{+0.42}_{-0.26}$	$0.448^{+0.05}_{-0.04}$

Figure 5:

The Kr is measured via the coincidences of the two following decays:  $^{85}Kr \rightarrow ^{85m}Rb \rightarrow ^{85}Rb$ , with the emission of a 173 keV  $\beta$ , followed by a 514 keV  $\gamma$ , with  $\tau = 1.46\mu s$ . Unfortunately this decay has a B.R. of only 0.43%: 8 events have been measured in the data taking period, corresponding to  $29 \pm 14$  c/d.

The nuclide  $^{210}Po$  is present despite the precision cleaning of the lines; this nuclide is very mobile and easily sticks on the internal surface of the pipes, and it is released little by little. At the beginning its rate was  $\sim 80$  c/d/ton; now it is reduced to  $\sim 10$  c/d/ton with a decay time very close to the nominal one (200 d).

## 4.2 The Borexino science goal.

The main reaction studied in Borexino is the  $\nu - e$  elastic scattering.

The first observation of sub-Mev neutrinos in real time is the first design goal of Borexino, with the aim of testing the MSW effect with the LMA solution at very low energy, and then the existence of two regimes of oscillation: in vacuum and in matter. A good determination of the  $^7Be$  flux, at or below 5%, would provide also a strong constraint on the pp flux, allowing a check of the balance between photon and neutrino luminosities in the Sun. Another item included in the original project is the measurement of the 7% seasonal variation of the neutrino signal, following the Earth's orbital eccentricity.

But the radio-purity measured with the first Borexino data is much better than the design prescriptions; this extraordinary achievement opens further possibilities,

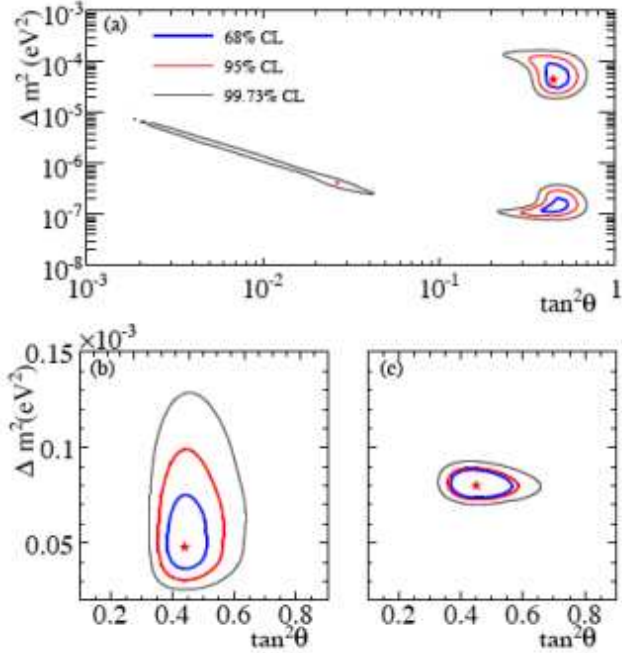


Figure 6:

as the experimental determination of the pep neutrino flux, possibly the pp flux, and the neutrinos from  ${}^8\text{B}$  with a threshold down to 2.8 MeV.

Other items of the Borexino scientific program are: the study of the  $\bar{\nu}_e$  emitted by the Earth; the detection of a Supernova explosion, if any; a competitive upper limit for the neutrino magnetic moment.

### 4.3 Measurement of the ${}^7\text{Be}$ neutrino flux and check of the existence of a vacuum regime in the oscillation model.

In Figure 9 all data are shown (black line), once vetoed or subtracted the muons, the events muon induced (within 2 ms after the muon) and the  ${}^{222}\text{Rn}$  daughters. In the same figure the blue line shows the data after the fiducial cut, and the red line, after  $\alpha s$  subtraction via the  $\alpha/\beta$  discrimination. The blue bump, shown before the  $\alpha s$  subtraction, is due to the  ${}^{210}\text{Po}$  (which has a  $Q=5.41$  MeV, quenched in the Borexino scintillator with a factor  $\approx 13$ ).

The  $\alpha/\beta$  is carried out by means of the Gatti parameter [10] [11], based upon references curves obtained in Borexino from the analysis of the  ${}^{222}\text{Rn}$  decay, during the filling operations.

In Figure 10 (left) the neutrino event distribution, once subtracted the  $\alpha s$ , is fitted

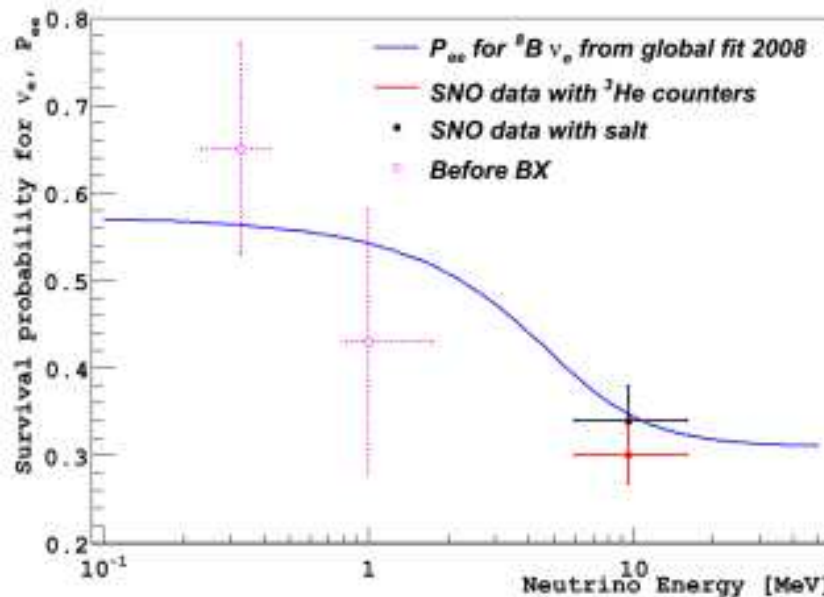


Figure 7:

living  ${}^7\text{Be}$ ,  ${}^{14}\text{C}$ , CNO+ ${}^{210}\text{Bi}$ ,  ${}^{11}\text{C}$ ,  ${}^{83}\text{Kr}$  and the light yield as free parameters, while the pp and pep fluxes are fixed at the values predicted by the Solar Standard Model. The CNO and the possible  ${}^{210}\text{Bi}$  are fitted together because their spectra are very similar. The  ${}^{11}\text{C}$  is produced by the residual muons in the underground Gran Sasso Laboratory (see later).

It has been preferred to leave as free parameters the  ${}^{83}\text{Kr}$  and the light yield, even if they are measured directly. The first is determined, as already explained, via the decay coincidence  ${}^{85}\text{Kr} \rightarrow {}^{85m}\text{Rb} \rightarrow {}^{85}\text{Rb}$ , but, due to its very small B.R., the statistics is still not enough for a precise measurement; the second is fitted directly by exploiting the well known spectrum of  ${}^{14}\text{C}$ ,  ${}^{210}\text{Po}$  and the position of the  ${}^7\text{Be}$  shoulder, due to the Compton edge. The fit results for both are fully consistent with the direct measurements.

In Figure 10 (right) a similar fit is carried out on the neutrino spectrum, but without  $\alpha$  subtractions: a threshold is imposed at 250 keV of energy, while the free parameters are the same as in the previous fit, with the difference that now the  ${}^{210}\text{Po}$  is added.

The results of the two fits are fully consistent each other. In particular for the  ${}^7\text{Be}$  flux the rate in both cases is:  $49 \pm 3$  cpd/100 tons [12]. Here the quoted error is statistical only.

The systematic errors concern the definition of the Inner Vessel position and the

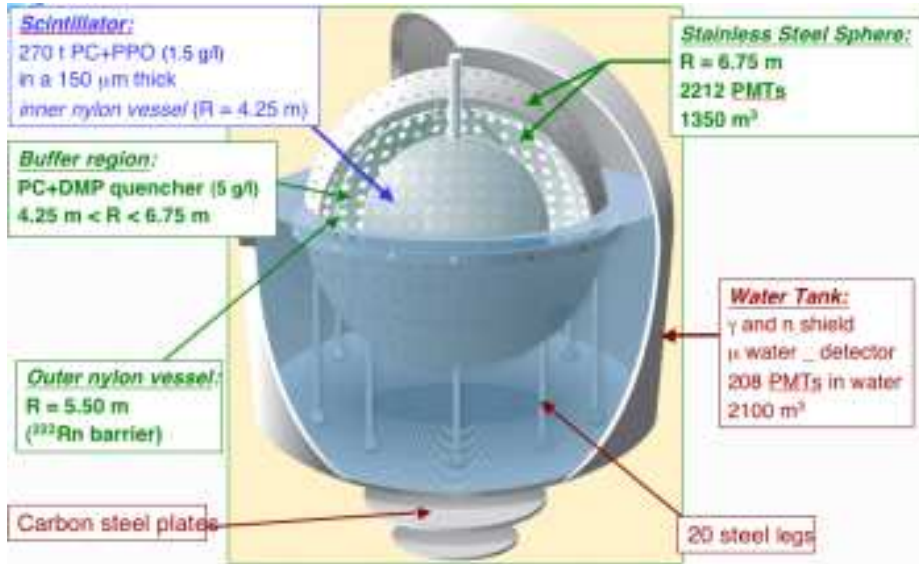


Figure 8:

detector response function. Both are determined until now exploiting internal signals and the ones emitted by the Inner vessel walls; the precision in fixing these two parameters will be much improved with a calibration campaign, already scheduled, by means of external sources.

Finally the 862 keV  ${}^7\text{Be}$  solar  $\nu$  rate in Borexino is:  $49 \pm 3_{\text{stat}} \pm 4_{\text{syst}}$  cpd/100 tons, corresponding to a flux:  $\Phi({}^7\text{Be}) = (5.12 \pm 0.51) \cdot 10^9 \text{ cm}^{-2} \text{ s}^{-1}$ , which has to be compared to the high metallicity prevision of  $(5.8 \pm 0.56) \cdot 10^9 \text{ cm}^{-2} \text{ s}^{-1}$  and to the low metallicity one,  $(4.55 \pm 0.5) \cdot 10^9 \text{ cm}^{-2} \text{ s}^{-1}$ . The quoted errors do not allow, for the moment, to discriminate between the two SSM expectations. The goal of Borexino is to reach a total error for the  ${}^7\text{Be}$  flux below 5%.

In Figure 11 the  $\nu_e$  survival probability as function of the neutrino energy is plotted. The MSW previsions (continuous and dashed lines) are calculated following the LMA solution with  $\Delta m_{12}^2 = 7.94 \cdot 10^{-5} \text{ eV}^2$  and  $\tan^2 \theta = 0.447$ , as obtained from the global fit on the data up-to-dated to 2008. The points for  ${}^7\text{Be}$  are the Borexino results, calculated for both the SSM hypotheses of high and low metallicity, while the ones for pp correspond to the pp flux constrained by the Borexino data.

The pp and CNO fluxes, as constrained by the Borexino data, are shown also in Figure 12.

The  ${}^7\text{Be}$   $\nu$  spectral shape vs the recoiled electron energy has been studied to find possible e.m. components due to the  $\nu$  magnetic moment: the limit of 5.4 Bohr magneton has been found, which is the lowest limit obtained until now.

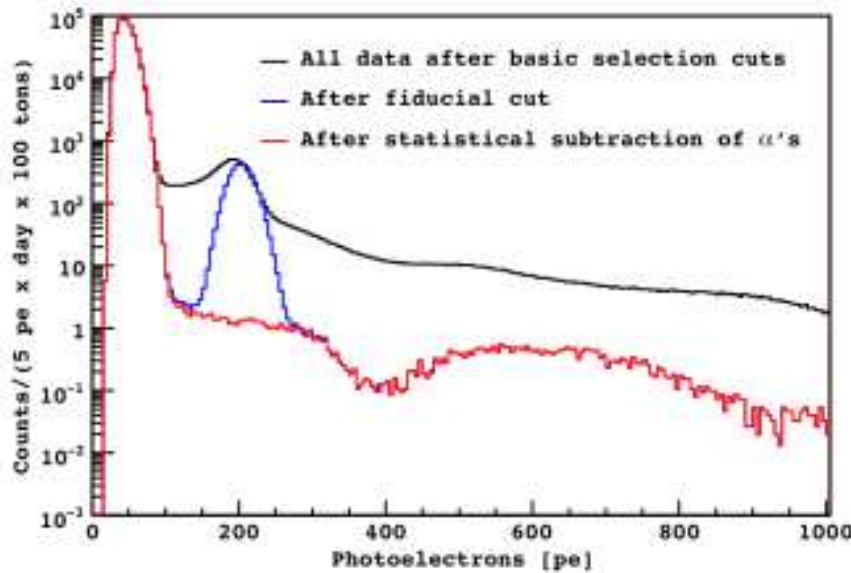


Figure 9:

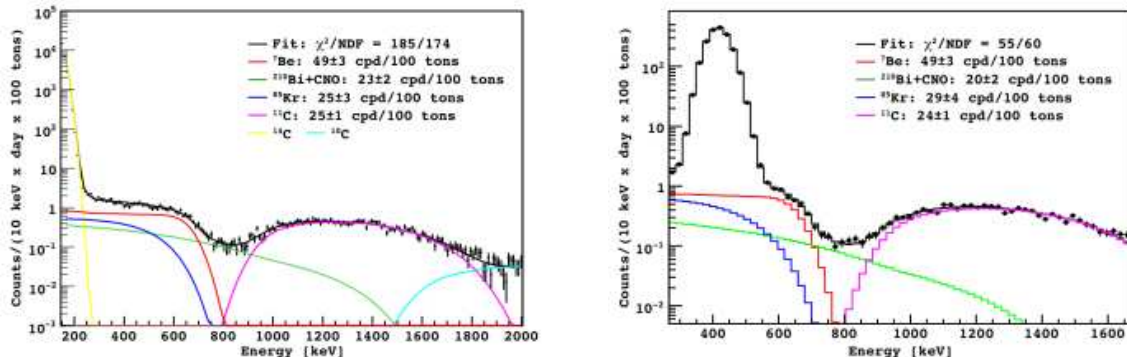


Figure 10:

#### 4.4 What next.

The next goals of Borexino are: the  $^{7}\text{Be}$  measurement with a total error at or below 5%, and possibly the direct determination of the pp flux. This last measurement could be obtained analyzing the energy window 190-230 keV, where the background is under control.

The pep flux is a further goal. To achieve it, much more statistics is needed (2 cpd/100 tons are expected in Borexino, following the SSM prevision), and a good

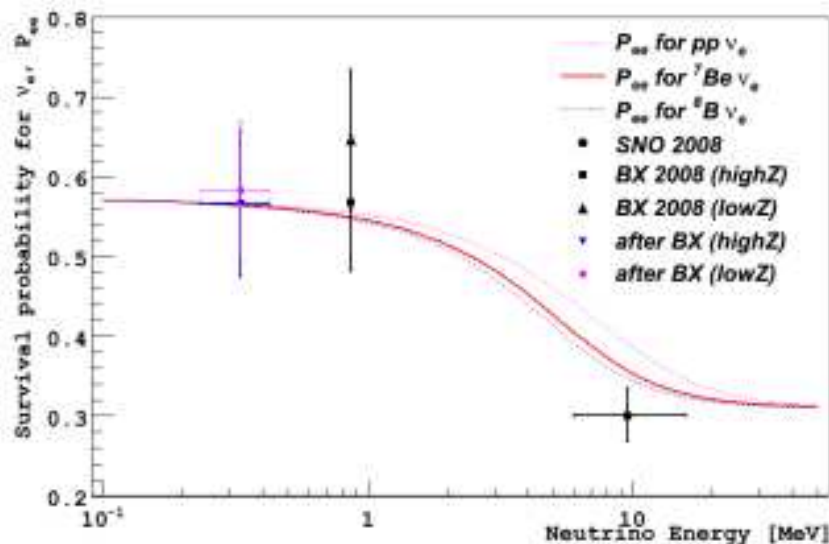


Figure 11:

identification of the  $^{11}C$  nuclides, produced by the cosmic muons in the Gran Sasso underground laboratory ( $1.1 \mu m^{-2}h^{-1}$  with  $\langle E_\mu \rangle = 325$  GeV) is necessary. The cosmogenic  $^{11}C$  are identified via a threefold coincidence among: the muon (which produces the  $^{11}C : \mu + ^{12}C = ^{11}C + n + \mu$ ), the  $^{11}C$  decay ( $^{11}C \rightarrow ^{11}B + e^+ + \nu_e$ ), and the n capture (with the emission of a 2.2 MeV  $\gamma$ ). This method has been tested successfully in C.T.F. [13]. The read out electronics has been implemented in Borexino to detect all the neutrons produced by each incident muon, which in some cases reach the number of 100. A rejection percentage of about 90% has been already achieved, but the work is still in progress.

Another study in progress is the detection of antineutrinos from the Earth, which is made easier in Gran Sasso due to the very low background of antineutrinos emitted by nuclear reactors on that site.

## 5 Conclusions.

There are still open problems in the Standard Solar Model, as it is the case for the metallicity, and many parameters are still unknown. Some important S factors have been measured in laboratory; precise experimental determinations of the neutrino fluxes can provide important insights in the Model.

Until now the scheme MSW-LMA has not been denied at low energy by the Borexino data on the  $^7Be$  flux, but more efforts and statistics are needed to give a

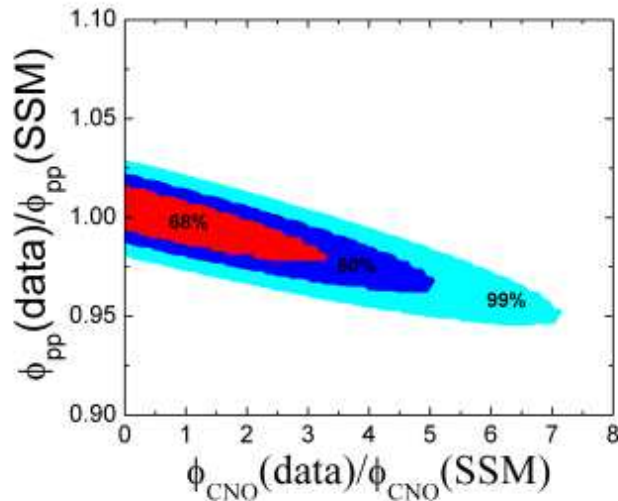


Figure 12:

final check of the oscillation model. In the meantime the vacuum oscillation regime has been found experimentally by Borexino.

Due to the very high radiopurity, Borexino seems able to measure other low energy solar neutrino fluxes, as pep and probably pp; the Borexino data produced already a strong constraint on the pp flux. But these measurements need a lot of care: Borexino estimates other two years to reach the final results.

## References

- [1] C. Broggini, talk at this Conference.
- [2] T.A.D. Brown et al., Phys. Rev. **C76**, 055801 (2007).
- [3] N. Grevesse et al., Space Sci. Rev. **85**, 161 (1998).
- [4] C. Allende Prieto et al., Astrophys. J. **573** L137 (2002); C. Allende et al., Astrophys. J. **556**, L63 (2001).
- [5] C. Pena-Garay and A.M. Serenelli, private communication.
- [6] SNO collaboration; B. Aharmin et al., arXiv: 0806.0989v1, June 2008.

- [7] J. Shirai, New Kamland results, Neutrino Oscillations in Venice, Proceedings Istituto Veneto di Scienze, Lettere ed Arti, pag. 447.
- [8] G.L. Fogli et al., Phys. Rev. Lett. **101**, 141861 (2008).
- [9] Borexino Collaboration, G. Alimonti et al., arXiv: 0806.2400, oct. 2008, to be published at N.I.M.
- [10] E. Gatti et al., Nuclear Electronics, **2** IAEA, Wein 265 (1962).
- [11] Borexino Collaboration, E. Back et al., Nucl. Instr. and Methods **A584**, 98 (2008).
- [12] Borexino Collaboration, C. Arpesella et al., PRLB **101**, 091302 (2008).
- [13] Borexino Collaboration, Phys. Rev. **C74**, 045805 (2006).

# Short-baseline Neutrinos: Recent Results and Future Prospects

*Ryan B. Patterson  
Physics Department  
California Institute of Technology  
Pasadena, California 91125  
U.S.A.*

## 1 Oscillations

The evidence is compelling that neutrinos undergo flavor change as they propagate. In recent years, experiments have observed the phenomenon of neutrino oscillations using disparate neutrino sources: the sun, fission reactors, accelerators, and secondary cosmic rays. The standard model of particle physics needs only simple extensions – neutrino masses and mixing – to accommodate all neutrino oscillation results to date, save one. The  $3.8\sigma$ -significant  $\bar{\nu}_e$  excess reported by the LSND collaboration [1] is consistent with  $\bar{\nu}_\mu \rightarrow \bar{\nu}_e$  oscillations with a mass-squared splitting of  $\Delta m^2 \sim 1 \text{ eV}^2$ . This signal, which has not been independently verified, is inconsistent with other oscillation evidence unless more invasive standard model extensions (*e.g.*, sterile neutrinos) are considered.

The Mini Booster Neutrino Experiment (MiniBooNE) is designed to search for  $\nu_\mu \rightarrow \nu_e$  oscillations with sufficient sensitivity to confirm or refute the LSND signal. MiniBooNE uses the Fermilab Booster neutrino beam, which begins with 8 GeV protons impinging on a beryllium target. The positively charged secondary mesons (mostly  $\pi^+$ , but some  $K^+$ ) produced in the target are magnetically focused forward into a 50 m air-filled decay region. Their subsequent decay chains lead to the high intensity  $\sim 1 \text{ GeV}$  neutrino source. The neutrinos are predominantly  $\nu_\mu$ , but  $K$  and  $\mu$  decays lead to a 0.6%  $\nu_e$  contamination that represents a large irreducible background to the  $\nu_\mu \rightarrow \nu_e$  search (as the best-fit LSND oscillation probability is  $\sim 0.3\%$ ).

The MiniBooNE detector sits 541 m downstream of the proton target, with most of the space in between occupied by earth. The detector is a 6.1 m radius spherical steel tank filled with 800 tons of mineral oil. An opaque shell of diameter 5.75 m, concentric with the steel tank, divides the oil into two optically isolated regions. The thin outer region is instrumented with 240 8-inch PMTs and serves as a veto shield for incoming cosmic rays and for partially contained neutrino events. The inner

main region is viewed by 1280 8-inch PMTs. The Cherenkov (and, at a lower level, scintillation) photons produced by high energy charged particles in the mineral oil lead to light patterns on the PMT array.

Charged current neutrino interactions in the MiniBooNE detector are identified by the characteristic ring of Cherenkov light created by the outgoing charged lepton. A muon's long, straight track leads to a sharp ring that fills in as the muon ranges out. An electron induces an electromagnetic shower, leading to a diffuse, but still ring-like, pattern.

High energy photons, such as those coming from  $\pi^0$  decay, also produce electron-like ring patterns. Neutral current production of  $\pi^0$ 's, usually proceeding through a  $\Delta$  resonance, leads to the largest misidentification background in MiniBooNE. This misidentification occurs when one of the two photons from the  $\pi^0$  decay goes unnoticed, either by having too little energy or by having its ring pattern obscured by the other's. In such cases, the event appears to contain a single electromagnetic shower and will be classified as a  $\nu_e$  charged current event. A related photon-based background comes from the rare ( $\sim 0.5\%$ ) electromagnetic decay  $\Delta \rightarrow N\gamma$ .

Further analysis details can be found in the first MiniBooNE oscillation paper, published in early 2007 [2]. Using a data sample of  $1.7 \times 10^6$  neutrino interactions from  $5.58 \times 10^{20}$  protons-on-target, MiniBooNE found no evidence for LSND-like  $\nu_\mu \rightarrow \nu_e$  oscillations, neither in the count of  $\nu_e$  candidates [data: 380, expectation:  $358 \pm 19_{\text{stat}} \pm 35_{\text{syst}}$ ] nor in the shape of the neutrino energy spectrum. The spectrum is shown in Figure 1, and the MiniBooNE limit contour for two-neutrino mixing parameters is shown in Figure 2. MiniBooNE also published a combined analysis of Bugey, KARMEN2, LSND, and MiniBooNE data, concluding that the four experiments are mutually compatible at only 3.9% C.L. [3]

The MiniBooNE oscillation analysis used a low-energy threshold of 475 MeV. A look below this threshold, down to 300 MeV, reveals a  $3.7\sigma$  discrepancy between data and expectation. The data excess is not consistent with two-neutrino oscillations. About 25% of the excess has been explained by the lack of photonuclear absorption in the simulation. (This process can remove one of the  $\pi^0 \rightarrow \gamma\gamma$  photons from an event, leaving behind an electron-like signature.) The remainder of the excess is as yet unexplained. Anomaly-mediated  $\gamma$  production was noted in Ref. [4] as a potential solution, but the rate and photon spectrum for this standard model process have not yet been well determined.

Although MiniBooNE was the higher profile experiment, the CHORUS collaboration also presented short-baseline oscillation results this year. CHORUS searched for  $\nu_\mu \rightarrow \nu_\tau$  oscillations at high  $\Delta m^2$  ( $> 1 \text{ eV}^2$ ) by looking for  $\tau$  lepton appearance in a 770 kg emulsion detector exposed to a 26 GeV broadband  $\nu_\mu$  beam. The vertex detection provided by the emulsion was supplemented by a fiber tracker, hadron and muon spectrometers, and hadronic and electromagnetic calorimeters.

The recent paper reports an updated analysis of the complete 1994-1997 CHO-

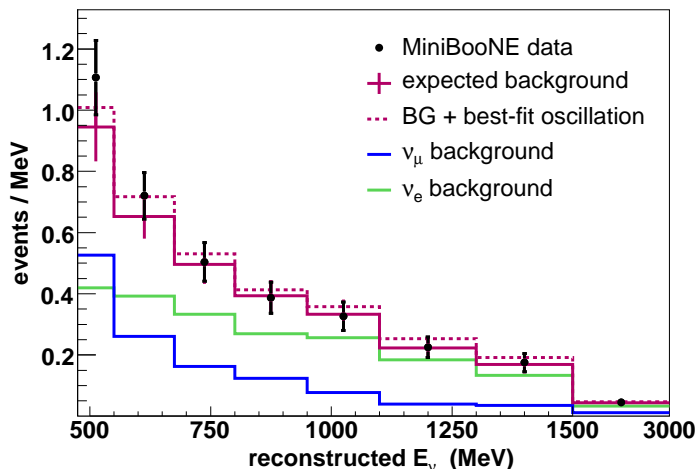


Figure 1: Reconstructed neutrino energy spectrum for the MiniBooNE  $\nu_e$  candidate sample. The black points show the data with statistical error bars. The magenta curves show the expected background-only spectrum (solid) and best-fit oscillation spectrum (dashed). The separate  $\nu_\mu$  and  $\nu_e$  components of the background are also shown (blue and green). The null and best-fit scenarios are insignificantly different ( $\Delta\chi^2 = 0.83$ ).

RUS data set using improved event reconstruction algorithms and a new automated system for scanning the emulsion plates [5]. No  $\nu_\tau$  appearance was observed, and the oscillation limits were improved by 30% over their earlier result. Figure 3 shows the oscillation parameters excluded by CHORUS.

## 2 Cross sections

The continuing surge of neutrino oscillation experiments brings an urgent need for precision neutrino cross sections. Cross sections for many relevant channels and energies have never been measured, and those that have are often decades old and imprecise. Further, existing measurements are rarely on nuclear targets. To give a sense of the situation, Figure 4 shows high-statistics cross section data for charged current  $\nu$  scattering over a wide energy range. Lest the picture look too rosy, neutral current data below 3 GeV are nearly non-existent, with only a handful of usually spectrum-specific measurements available.

The K2K collaboration is providing some help. K2K is a long-baseline oscillation experiment that uses a 1.3 GeV broadband  $\nu_\mu$  beam (97% purity) created at KEK in Tsukuba, Japan, and directed toward the Super-Kamiokande detector 250 km away.

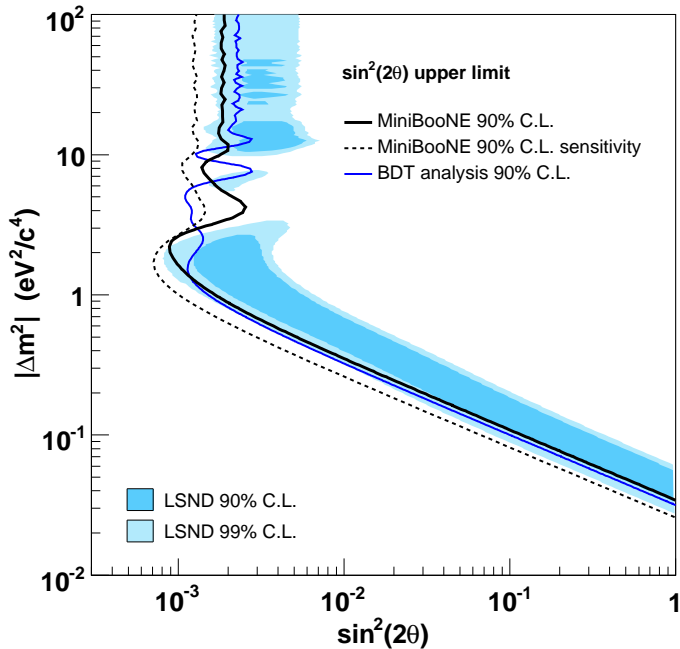


Figure 2: MiniBooNE exclusion contours. The filled regions show the LSND 90% and 99% C.L. allowed regions in oscillation parameter space ( $\sin^2(2\theta)$ ,  $\Delta m^2$ ). MiniBooNE excludes at 90% C.L. the oscillation parameters above the thick black line. Also shown are the MiniBooNE sensitivity contour (dashed) and the limit contour from a second, fairly independent analysis (thin blue).

A near detector on the KEK site measures the neutrino flux for the oscillation search and, relevant for this note, provides a large sample of neutrino interactions from which cross sections can be extracted. The near detector has four components: a 1 kton water Cherenkov detector, a scintillating fiber tracker (“SciFi”, water target), a scintillator bar tracker (“SciBar”, CH target), and a muon range stack (Fe). The scintillator tracker has been replaced by a lead glass array, but no cross section results have yet come from the latter.

A generic feature of conventional GeV-scale neutrino beams is that the absolute rate of neutrinos, and often the energy spectrum, is poorly known. This stems from the lack of quality cross section data for the production of pions in the beam targets. K2K therefore reports ratios of neutrino cross sections, with the reference channel being either inclusive or quasi-elastic charged current scattering.

Several recent K2K results relate to pion production and taken together they reveal a murky situation. Figure 5 shows the reconstructed  $\pi^0$  mass peak from neutral

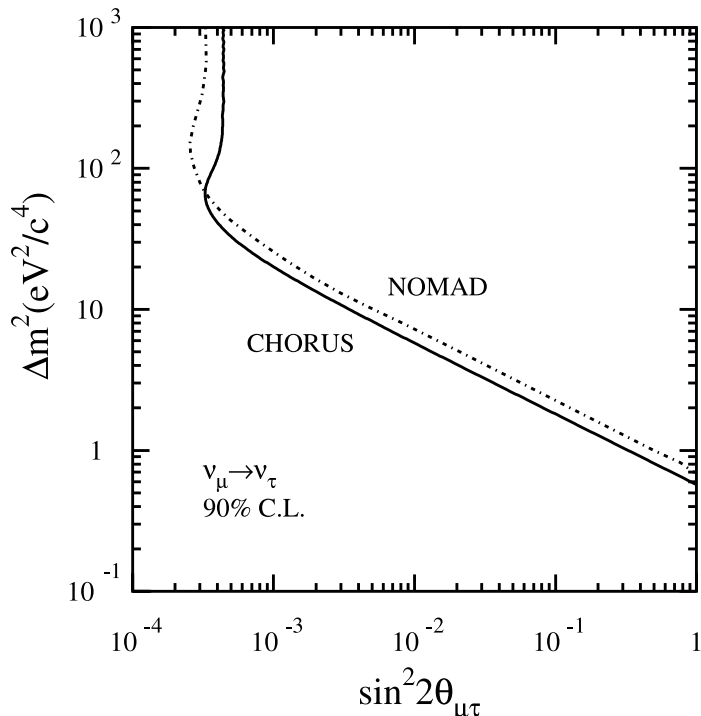


Figure 3: 90% C.L. limit in oscillation parameter space established by CHORUS. Points above the curve are excluded. The similar NOMAD limit is also shown. Figure from Ref. [5].

current interactions in the near water Cherenkov detector. From the event rate in the peak they extract the neutral current single- $\pi^0$  production cross section in ratio with the total charged current cross section [7]:

$$\sigma_{\text{NC}1\pi^0}/\sigma_{\text{CC}} = 0.063 \pm 0.001_{\text{stat}} \pm 0.006_{\text{stat}} . \quad (1)$$

This value agrees well with the Monte Carlo expectation of 0.064. However, the analysis of *charged* current  $\pi^0$  production in SciBar yields a number that is 40% higher than the Monte Carlo prediction [7],

$$\sigma_{\text{CC}1\pi^0}/\sigma_{\text{CCQE}} = 0.306 \pm 0.023_{\text{stat}} \pm 0.025_{\text{stat}} . \quad (2)$$

Three things changed from the first measurement to the second: (1) neutral to charged current, (2) water to hydrocarbon target, (3) inclusive to quasi-elastic charged current reference channel. Adding one further change ( $\pi^+$  production rather than  $\pi^0$ ) brings data and Monte Carlo *back into agreement*, although the errors are somewhat large [8]. The K2K  $\sigma_{\text{CC}1\pi^+}/\sigma_{\text{CCQE}}$  data also agrees with previous Argonne bubble

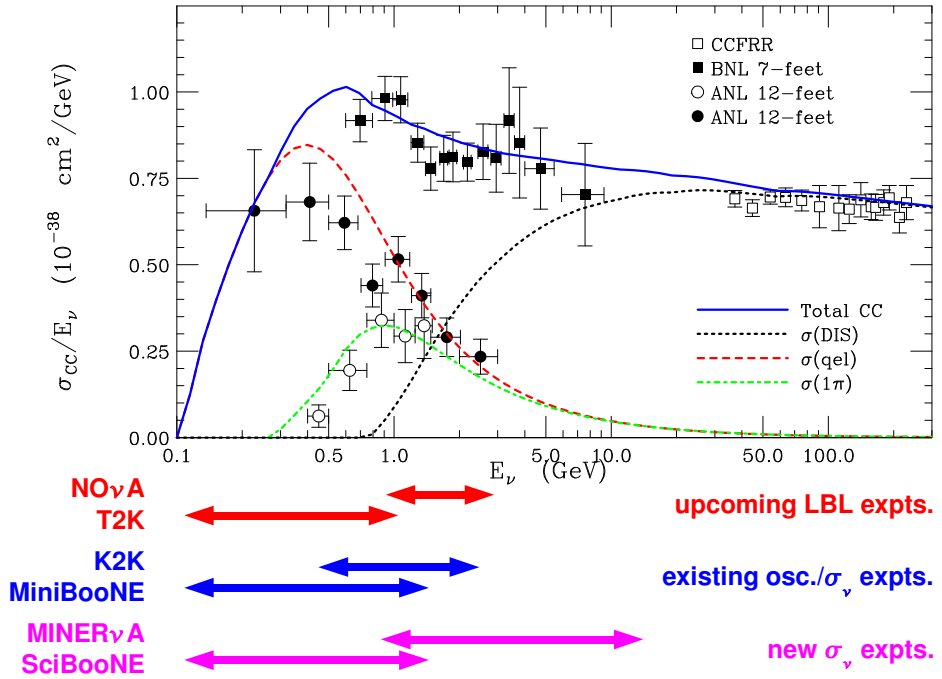


Figure 4: Charged current  $\nu$  cross section data. The top portion of the figure is taken from Ref. [6]. The upcoming long-baseline experiments NO $\nu$ A and T2K will benefit from improved low energy cross section measurements. As discussed in the text, K2K and MiniBooNE, both oscillation experiments, are providing additional data, but the next big steps in cross section precision will come with MINER $\nu$ A and SciBooNE.

chamber data [8], as Figure 6 shows. The upcoming dedicated cross section experiments discussed below are needed to clarify this situation.

MiniBooNE has added to the pion production data set by publishing the first ever measurement of coherent  $\pi^0$  production below 2 GeV. In coherent production, the target nucleus (in this case,  $^{12}\text{C}$ ) stays intact and in the ground state after the interaction. The MiniBooNE detector cannot observe the nuclear state directly, so the analysis uses the angular distribution (relative to the neutrino direction) of the outgoing  $\pi^0$  to extract a coherent fraction. (The detector also cannot resolve few-MeV de-excitation photons, so ‘‘coherent’’ here includes possible  $^{12}\text{C}^*$  final states.) MiniBooNE finds that  $(19.5 \pm 1.1_{\text{stat}} \pm 2.5_{\text{syst}})\%$  of its  $\pi^0$  production is coherent, significantly below the Rein/Sehgal-based [11] Monte Carlo expectation of 30% [12]. Preliminary  $\bar{\nu}$  data shows a similar coherent  $\pi^0$  discrepancy [13].

In addition to pion production results, MiniBooNE and K2K have both published measurements of the axial mass  $M_A$  index  $M_A$ . This free parameter of the charged current quasi-elastic (CCQE) cross section appears in the (usually taken as dipole)

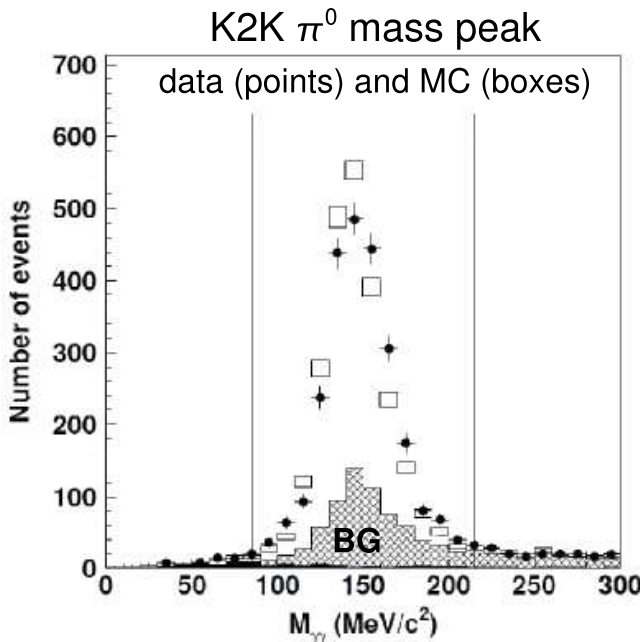


Figure 5: Data and Monte Carlo expectation for the  $\pi^0$  mass peak reconstructed from neutral current single- $\pi^0$  events in the K2K 1-kton water Cherenkov detector. The integrals between the vertical lines agree well within errors. Figure adapted from Ref. [7].

axial-vector form factor

$$F_A(Q^2) = \frac{F_A(0)}{\left(1 + \frac{Q^2}{M_A^2}\right)^2}, \quad (3)$$

where  $-Q^2 = q^2$  is the square of the four-momentum transfer. With the two-body final state of CCQE scattering,  $Q^2$  can be determined from the outgoing lepton's kinematics and the incoming neutrino's direction.  $M_A$  can subsequently be extracted from the observed  $Q^2$  distribution. Two difficulties arise. The first is that the absolute rate of neutrinos is not well understood. This is handled by doing a shape-only fit to the  $Q^2$  distribution (*i.e.*, by assigning an infinite normalization uncertainty). The second is that nuclear effects are poorly modeled. K2K excludes the lowest  $Q^2$  values (where nuclear effects appear) and MiniBooNE includes empirical nuclear model parameters in the fit to absorb model deficiencies.

Figure 7 shows the MiniBooNE  $Q^2$  fit alongside a table of  $M_A$  results. Note that the bubble chamber experiments yield a significantly lower  $M_A$  than the three recent measurements, all on nuclear targets. So far, this discrepancy evades explanation.

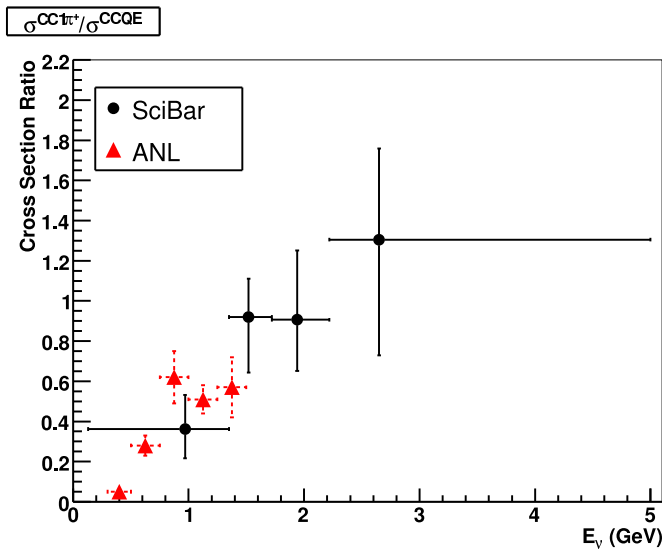


Figure 6: The ratio  $\sigma_{CC1\pi^+}/\sigma_{CCQE}$  versus neutrino energy. The black circles show the K2K SciBar measurement. The red triangles show Argonne data taken from [9] and [10]. Figure taken from Ref. [8], which also includes a graph of data and Monte Carlo together showing excellent agreement.

### 3 Upcoming

Two new experiments, SciBooNE and MINER $\nu$ A, will help clarify the above inelastic and quasi-elastic situations while reducing the errors on several relevant neutrino cross sections.

SciBooNE [18] is a transplant of K2K’s SciBar detector into the path of the Fermilab Booster neutrino beam, partway between the proton target and the MiniBooNE detector. In addition to working in concert with MiniBooNE to improve oscillation sensitivity by acting as a near detector, SciBooNE has over 100k  $\nu$  and  $\bar{\nu}$  interactions from which to extract cross sections.

The SciBooNE detector consists of a 10-kton, 14 000-channel scintillator bar tracker followed by an electromagnetic calorimeter and muon range stack. With its fine-grained tracking, SciBooNE can directly measure the kinematics of recoil nucleons and can distinguish  $\nu$  from  $\bar{\nu}$  charged current scattering via the displacement of the latter’s recoil track. (The recoil neutron is invisible until it undergoes a hard scatter). The collaboration is working to produce charged and neutral current pion production and (quasi-)elastic scattering cross sections, with first results expected in the coming year.

MINER $\nu$ A [19], also at Fermilab, will view the energy-tunable broadband NuMI

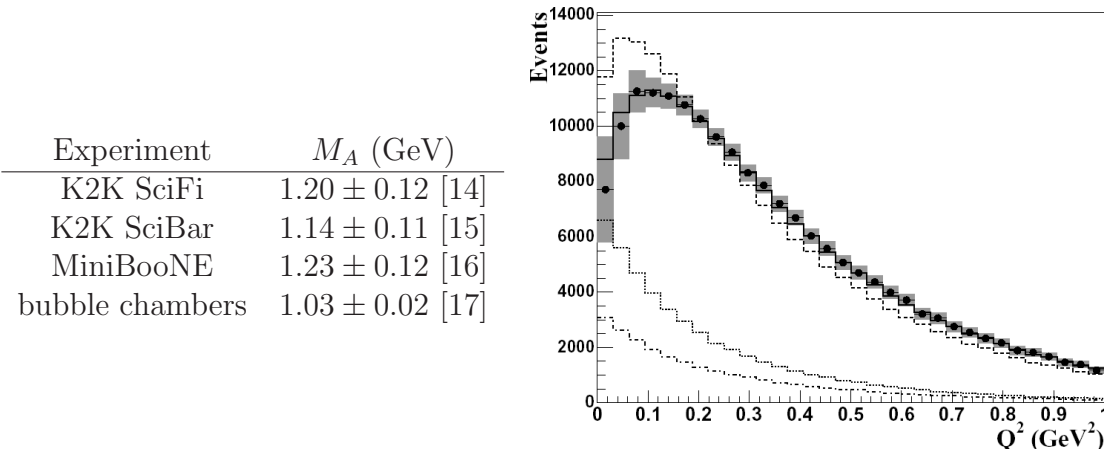


Figure 7: (Left)  $M_A$  values from recent measurements by K2K and MiniBooNE along with the average of two decades' worth of bubble chamber experiments. (Right) The MiniBooNE  $Q^2$  distribution. The points are the data and the shaded bars reflect the systematic errors. The topmost dashed and solid histograms show the Monte Carlo expectation before and after the  $M_A$  and nuclear model fit. Two classes of non-CCQE background are shown by the lower two histograms. Figure from Ref. [16].

neutrino beam, typically operating in the 1 to 15 GeV range. Its highly segmented detector (31 000 channels) will provide tracking resolutions of 2.5 mm, allowing for excellent final state identification. An important feature of the detector is the presence of multiple nuclear targets (Fe, Pb, C, and He) allowing nuclear effects and  $A$ -dependences to be studied. Data taking is expected to begin in 2009.

Looking further into the future, the NuSOnG collaboration proposes to convert the to-be-decommissioned Tevatron at Fermilab into a 100 GeV neutrino beam to look for TeV-scale modifications to standard model processes and to provide some degree of LHC complementarity [20].

Finally, several groups [21] [22] [23] look to place neutrino detectors near the Spallation Neutron Source being constructed at Oak Ridge National Laboratory, USA. A by-product of the neutron production is a  $10^{15} \nu/s$  pulsed neutrino source with a well-understood decay-at-rest spectrum. Proposals include low energy cross section measurements, improved sensitivity to LSND-like oscillations, and searches for beyond-the-standard-model components of the weak interaction (via modifications to the  $\nu_e$ -from- $\mu$ -decay energy spectrum).

## References

- [1] A. Aguilar *et al.* [LSND Collaboration], Phys. Rev. D **64**, 112007 (2001)

- [2] A. A. Aguilar-Arevalo *et al.* [MiniBooNE Collaboration], Phys. Rev. Lett. **98**, 231801 (2007)
- [3] A. A. Aguilar-Arevalo *et al.* [MiniBooNE Collaboration], Phys. Rev. D **78**, 012007 (2008)
- [4] J. A. Harvey, C. T. Hill and R. J. Hill, Phys. Rev. Lett. **99**, 261601 (2007)
- [5] E. Eskut *et al.* [CHORUS Collaboration], Nucl. Phys. B **793**, 326 (2008)
- [6] P. Lipari, M. Lusignoli and F. Sartogo, Phys. Rev. Lett. **74**, 4384 (1995)
- [7] C. Mariani [for the K2K Collaboration], AIP Conf. Proc. **967**, 174 (2007).
- [8] A. Rodriguez *et al.* [K2K Collaboration], Phys. Rev. D **78**, 032003 (2008)
- [9] G. M. Radecky *et al.*, Phys. Rev. D **25**, 1161 (1982) [Erratum-ibid. D **26**, 3297 (1982)].
- [10] S. J. Barish *et al.*, Phys. Rev. D **16**, 3103 (1977).
- [11] D. Rein and L. M. Sehgal, Nucl. Phys. B **223**, 29 (1983).
- [12] A. A. Aguilar-Arevalo *et al.* [MiniBooNE Collaboration], Phys. Lett. B **664**, 41 (2008)
- [13] V. T. Nguyen, arXiv:0806.2347 [hep-ex].
- [14] R. Gran *et al.* [K2K Collaboration], Phys. Rev. D **74**, 052002 (2006)
- [15] K2K Collaboration, in preparation.
- [16] A. A. Aguilar-Arevalo *et al.* [MiniBooNE Collaboration], Phys. Rev. Lett. **100**, 032301 (2008)
- [17] V. Bernard, L. Elouadrhiri and U. G. Meissner, J. Phys. G **28**, R1 (2002)
- [18] <http://www-sciboone.fnal.gov>
- [19] <http://minerva.fnal.gov>
- [20] <http://www-nusong.fnal.gov>
- [21] I. Stancu, AIP Conf. Proc. **981**, 34 (2008).
- [22] <http://www.phy.ornl.gov/nusns>
- [23] K. Scholberg, APS April Meeting, abstract M13.0009 (2008)

# Ultra high-energy neutrinos

*Ryan Nichol*  
*University College London*

paper not submitted

# Long Baseline Neutrino Oscillation Experiments

*Mark Thomson  
Cavendish Laboratory  
Department of Physics  
JJ Thomson Avenue  
Cambridge, CB3 0HE  
United Kingdom*

## 1 Introduction

In the last ten years the study of the quantum mechanical effect of neutrino oscillations, which arises due to the mixing of the weak eigenstates  $\{\nu_e, \nu_\mu, \nu_\tau\}$  and the mass eigenstates  $\{\nu_1, \nu_2, \nu_3\}$ , has revolutionised our understanding of neutrinos. Until recently, this understanding was dominated by experimental observations of atmospheric [1, 2, 3] and solar neutrino [4, 5, 6] oscillations. These measurements have been of great importance. However, the use of naturally occurring neutrino sources is not sufficient to determine fully the flavour mixing parameters in the neutrino sector. For this reason, many of the current and next generation of neutrino experiments are based on high intensity accelerator generated neutrino beams. The first generation of these long-baseline (LBL) neutrino oscillation experiments, K2K, MINOS and CNGS, are the main subject of this review. The next generation of LBL experiments, T2K and NO $\nu$ A, are also discussed.

## 2 Theoretical Background

For two neutrino weak eigenstates  $\{\nu_\alpha, \nu_\beta\}$  related to two mass eigenstates  $\{\nu_i, \nu_j\}$ , by a single mixing angle  $\theta_{ij}$ , it is simple to show that the survival probability of a neutrino of energy  $E_\nu$  and flavour  $\alpha$  after propagating a distance  $L$  through the vacuum is

$$P(\nu_\alpha \rightarrow \nu_\alpha) = 1 - \sin^2 2\theta_{ij} \sin^2 \left( \frac{1.27 \Delta m_{ji}^2 (\text{eV}^2) L (\text{km})}{E_\nu (\text{GeV})} \right), \quad (1)$$

where  $\Delta m_{ji}^2$  is the difference of the squares of the neutrino masses,  $m_j^2 - m_i^2$ . From the Z lineshape measurements at LEP [7], we know that there are exactly three active

flavours of neutrinos (assuming  $m_\nu < m_Z/2$ ) and it is straightforward to extend the two flavour treatment of neutrino oscillations to three flavours. Assuming neutrinos are Dirac particles, the single mixing angle of Equation 1 is replaced by the three mixing angles  $\{\theta_{12}, \theta_{13}$  and  $\theta_{23}\}$ , and a phase angle,  $\delta$ . The relation between the weak and mass eigenstates is described by the PMNS matrix [8, 9] which can be expressed in the convenient form

$$U_{\text{PMNS}} = \begin{pmatrix} 1 & 0 & 0 \\ 0 & c_{23} & s_{23} \\ 0 & -s_{23} & c_{23} \end{pmatrix} \begin{pmatrix} c_{13} & 0 & s_{13}e^{i\delta} \\ 0 & 1 & 0 \\ -s_{13}e^{i\delta} & 0 & c_{13} \end{pmatrix} \begin{pmatrix} c_{12} & s_{12} & 0 \\ -s_{12} & c_{12} & 0 \\ 0 & 0 & 1 \end{pmatrix}, \quad (2)$$

where  $c_{ij} = \cos \theta_{ij}$  and  $s_{ij} = \sin \theta_{ij}$ . Hence the phenomenology of neutrino oscillations is described by four angles  $\{\theta_{12}, \theta_{13}, \theta_{23}$  and  $\delta\}$  and two independent mass-squared differences,  $\Delta m_{21}^2$  and  $\Delta m_{32}^2$ . A non-zero value for  $\delta$  leads to CP violation in the lepton sector provided  $\sin \theta_{13}$  is also non-zero.

## 2.1 Atmospheric, Solar and Reactor Neutrino Data

In the limit that  $|\Delta m_{32}^2| \gg |\Delta m_{21}^2|$ , for many experiments it is a reasonable approximation to reduce the full three flavour treatment of neutrino oscillations to the two flavour form of Equation 1. In the treatment of solar neutrino data matter effects have to be included. In the two-flavour approximation, solar neutrino data from SNO [6] and reactor neutrino data from KamLAND [10] determine the relevant solar  $\Delta m^2$  scale to be  $|\Delta m_\odot^2| = (7.59 \pm 0.21) \times 10^{-5} \text{ eV}^2$  and  $\tan^2 \theta_\odot = 0.47^{+0.06}_{-0.05}$ . In the two-flavour approximation, the atmospheric neutrino data [1, 2, 3] yield  $|\Delta m_{\text{atm}}^2| \approx 2.5 \times 10^{-3} \text{ eV}^2$  and the mixing angle  $\sin^2 2\theta_{\text{atm}} \approx 1$ . These results can be placed in the context of three neutrino flavours. The mass eigenstates dominating solar neutrino oscillations are defined to be  $\nu_1$  and  $\nu_2$ , where  $m_1 < m_2$ . Hence, the solar neutrino data determine  $\Delta m_{21}^2$  and  $\tan^2 \theta_{12}$ . The atmospheric neutrino data place a lower limit on  $\sin^2 2\theta_{23} > 0.95$  (90 % C.L.) and provide a measurement of  $|\Delta m_{32}^2|$ . The data do not determine the mass hierarchy, *i.e.* whether  $m_3 > m_2$  or  $m_3 < m_2$ . In addition, the CHOOZ [11] reactor data constrains  $\sin^2 2\theta_{13} < 0.15$  (the exact value depends on  $|\Delta m_{32}^2|$ ).

In summary, solar and atmospheric neutrino experiments have provided measurements of  $\Delta m_{21}^2$ ,  $|\Delta m_{32}^2|$  and  $\theta_{12}$ . Currently there is no experimental constraint on the phase  $\delta$ , only a lower limit on  $\sin^2 2\theta_{23}$  and an upper limit on  $|\theta_{13}|$ .

## 3 Long-baseline Neutrino Oscillation Experiments

LBL experiments use intense  $\nu_\mu$  beams to investigate neutrino oscillations. The main parameters of the past (K2K), present (MINOS, OPERA), and future (T2K, NO $\nu$ A)

LBL experiments are summarised in Table 1. Each of the experiments has specific physics goals: K2K was designed to verify the atmospheric neutrino oscillation results from SK; MINOS was designed to perform precise measurements of the atmospheric oscillation parameters and may have sensitivity to  $\theta_{13}$ ; OPERA is designed to make the first observation of  $\nu_\tau$  appearance in  $\nu_\mu \leftrightarrow \nu_\tau$  oscillations; T2K is designed for the observation of  $\nu_\mu \leftrightarrow \nu_e$  and the measurement of  $\theta_{13}$  (depending on the value of  $\theta_{13}$ , phase II of the T2K experiment may have sensitivity to  $\delta$ ); NO $\nu$ A has similar goals to T2K but, due to the longer baseline, may also determine of the mass hierarchy. Before discussing these five experiments it is first worth considering how the intense neutrino beams are produced.

Experiment	Operational	Peak $E_\nu$	Baseline	Detector
K2K	1999 – 2004	1 GeV	250 km	Water Čerenkov
NuMI/MINOS	2005 – 2011(?)	3 GeV	735 km	Steel/Scintillator
CNGS/OPERA	2008–	17 GeV	732 km	Emulsion
T2K	2010–	0.7 GeV	295 km	Water Čerenkov
NO $\nu$ A	2012(?)–	1.8 GeV	810 km	Liquid Scintillator

Table 1: Summary of the main parameters of past, present and future long-baseline neutrino oscillations experiments. It should be noted that at this time the schedule for NO $\nu$ A is uncertain.

### 3.1 Neutrino Beams

All long-baseline experiments adopt the same basic approach to produce a collimated  $\nu_\mu$  beam. Firstly, an intense beam of protons is focused onto a target. The target is designed to maximise the production of secondary hadrons whilst minimising the number of secondary interactions. The secondary particles produced from the target are then focused by magnetic horns, shown schematically in Figure 1. Neutrino horns (typically) consist of shaped inner conductors joined to a cylindrical outer conductor. In coincidence with the beam spill, the horns are pulsed with large current,  $O(100\text{ kA})$ , which circulates via the inner and outer conductors. By a simple application of Ampere’s law it can be seen that this generates a large magnetic field proportional to  $1/r$  in the region between the inner and outer conductors. Because particles at larger angles to the primary beam axis traverse more of the region between the conductors where the field exists, they receive a larger transverse momentum kick. In this way, positive particles, such as  $\pi^+$  and  $K^+$ , tend to be focused and negative particles are defocused. Different experiments use one, two or three horns to achieve the optimal focusing for the desired neutrino beam energy. The focused particles, predominantly  $\pi^+$ , then traverse a long (hundreds of metres) decay region where

neutrinos are produced from  $\pi^+ \rightarrow \mu^+ \nu_\mu$  decays. Muon neutrinos are also produced in  $K^+ \rightarrow \mu^+ \nu_\mu$  decays. The  $\nu_e/\bar{\nu}_e$  contamination in the beam, which arises from  $\mu^+$  and  $K^0$  decays, is typically of order 1 %.

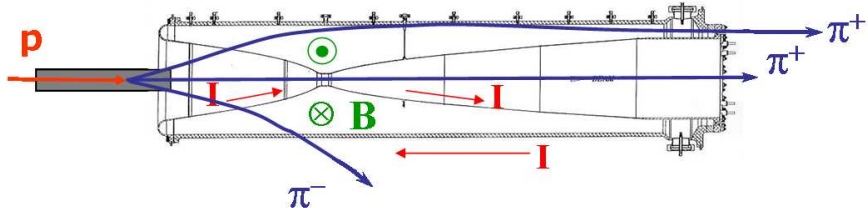


Figure 1: A schematic diagram showing the focusing (de-focusing) of secondary  $\pi^+$  ( $\pi^-$ ) by the magnetic field in between the inner and outer conductors of a neutrino horn (in this case MINOS horn 1).

### 3.2 Interaction Rate Uncertainties

It is important to note that it is not possible to predict the neutrino flux and energy spectrum with high accuracy since the process of hadron production from the target is not well modelled in the Monte Carlo simulations. This reflects the lack of hadron production data in the relevant kinematic regions. This situation should improve to some extent with the publication of MIPP data [12]. There are also significant uncertainties in low energy neutrino cross sections and interaction kinematics. As a result, the expected neutrino interaction rate in a LBL experiment is a combination of the imperfectly modelled beam spectrum and the imperfectly modelled neutrino cross sections. Consequently measurement of the unoscillated beam, *i.e.* in a near detector close to production, is essential to accurately predict the expectation at the far detector.

### 3.3 K2K

The KEK to Kamioka (K2K) experiment, which took data from 1999 until 2004, was the first LBL neutrino oscillation experiment. The main goal was to confirm the Super-Kamiokande atmospheric neutrino observations in a controlled beam experiment. An almost pure muon neutrino beam was created from 12 GeV proton synchrotron (KEK-PS) with a typical intensity of about  $5 \times 10^{12}$  protons per pulse. The beam was directed towards the Super-Kamiokande (SK) water Čerenkov detector located 250 km away. Two near detectors were employed; a 1 kton water Čerenkov detector and fine-grained detector system consisting of a scintillating-fibre/water target

tracker) and a lead-glass calorimeter which was upgraded to a totally active fine-segmented scintillator tracker (Sci-Bar). The neutrino beam direction and unoscillated energy spectrum were measured by the near detector system. K2K accumulated  $9.2 \times 10^{19}$  protons-on-target (PoT) of data for the physics analysis. A total of 112 neutrino beam induced events were observed in 22.5 kton fiducial volume of the SK detector, while  $158.1^{+9.2}_{-8.6}$  were expected without oscillation [13].

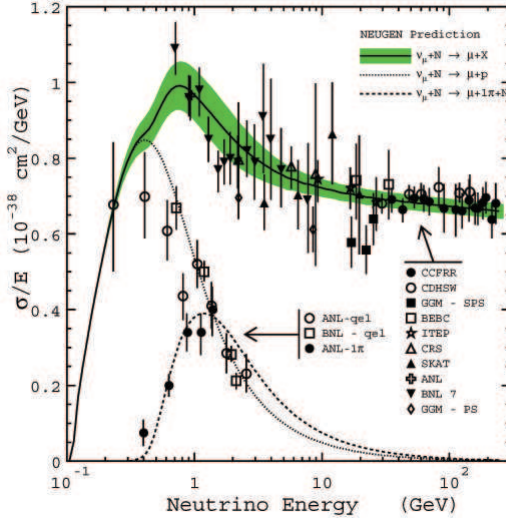


Figure 2: Neutrino cross-section data [14] compared to the prediction from the Neugen program [15]. The dotted curve indicates the quasi-elastic ( $\nu_\mu + n \rightarrow \mu^- + p$ ) contribution and the dashed curve indicates the resonance contribution with a single pion in the final state, (e.g.  $\nu_\mu + n \rightarrow \mu^- + \Delta^+ \rightarrow \mu^- + \pi^+ + n$ ) contribution. At higher energies deep inelastic scattering dominates. Plot taken from [16].

For the K2K baseline and the measured value of  $\Delta m_{\text{atm}}^2$ , the  $\nu_\mu \rightarrow \nu_\mu$  oscillation minimum is expected at approximately 0.6 GeV. For this energy, the neutrino cross section (see Figure 2) is dominated by quasi-elastic scattering,  $\nu_\mu + n \rightarrow \mu^- + p$ , resulting in a single Čerenkov ring from the relativistic muon. The next most important process is resonance production, e.g.  $\nu_\mu + n \rightarrow \mu^- + \Delta^+ \rightarrow \mu^- + n + \pi^+$ , resulting in Čerenkov two rings. For quasi-elastic interactions, the event kinematics ( $x = 1$ ) enable the neutrino energy to be determined from the measured energy and direction of the muon alone,

$$E_\nu^{\text{rec}} = \frac{m_N E_\mu - m_\mu^2/2}{m_N - E_\mu + p_\mu \cos \theta_\mu}, \quad (3)$$

where  $E_\mu$  and  $p_\mu$  are the muon energy and momentum, and  $\cos \theta_\mu$  is the muon scat-

tering angle with respect to the beam direction. Note that in Equation 3 the Fermi motion of the struck nucleon has been neglected. To measure the effect of neutrino oscillations on the neutrino energy spectrum, quasi-elastic interaction events are selected by requiring a single reconstructed Čerenkov ring consistent with originating from a muon. The neutrino energy spectrum from 58 single-ring muon-like events is shown in Figure 3a. A distortion of the energy spectrum is observed, consistent with neutrino oscillations. Since  $\theta_{13}$  is known to be small, Equation 1 is used to fit the data. The allowed oscillation parameter region from the measurements of the number of events and energy spectrum is shown in Figure 3b, along with the SK atmospheric neutrino results. The K2K results discriminated against the null oscillation hypothesis at the  $4.3\sigma$  level and provided verification of  $\Delta m_{\text{atm}}^2$  obtained from SK.

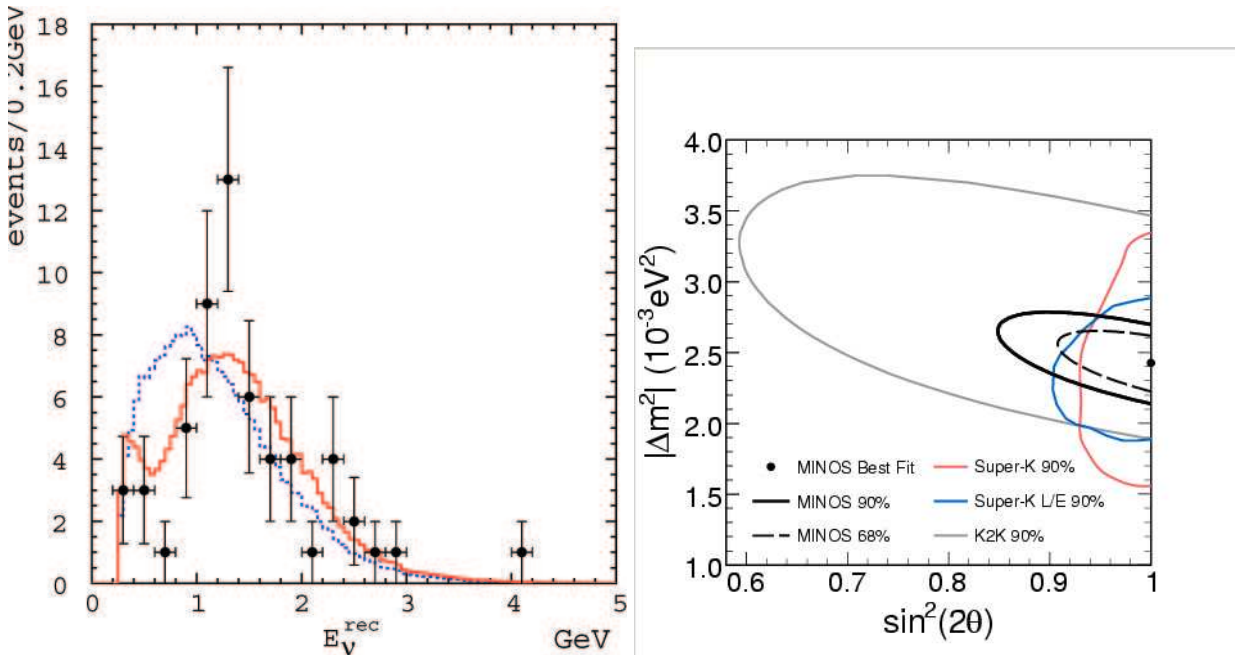


Figure 3: **a)** Energy spectrum for the observed 58 single-ring muon-like events from the K2K experiment. The solid red line is the expectation without oscillations and the dashed blue line shows the expectation for the best fit oscillation parameters. In both cases the expected spectra are normalised to the data. Taken from [13]. **b)** A comparison of 90 % C.L. contours in  $|\Delta m^2|$  and  $\sin^2 2\theta$  from two-flavour fits to atmospheric neutrino (SK) and LBL (K2K and MINOS) data. Taken from [18].

### 3.4 MINOS

Whilst K2K provided impressive confirmation of the SK atmospheric neutrino results, the measurements of the oscillation parameters were statistically limited. The main goal of the MINOS experiment [17] is the precise measurement of  $|\Delta m_{32}^2|$  and discrimination against alternative hypotheses such as neutrino decay and quantum decoherence. To achieve this, the NuMI beam is an order of magnitude more intense than that of the K2K experiment. In addition, MINOS may have sensitivity to  $\theta_{13}$  through sub-dominant  $\nu_\mu \rightarrow \nu_e$  oscillations and may be able to further constrain  $\theta_{23}$ .

The MINOS experiment has been taking data from the NuMI beam at Fermilab (FNAL) since 2005. The neutrino beam is produced using 120 GeV protons from the FNAL Main Injector incident on a graphite target. Pions are focused using two magnetic horns. The neutrino energy spectrum can be changed by adjusting either the horn current or the position of the target relative to the horns. The majority of the MINOS data has been taken in the lowest energy configuration (LE), for which the peak of the neutrino energy spectrum is at 3.3 GeV. The typical beam intensity is  $\sim 2.5 \times 10^{13}$  protons per pulse with a 2.4 s cycle time. By the end of 2008 MINOS had recorded  $6 \times 10^{20}$  PoT. The results reported here are based on an exposure of  $3.4 \times 10^{20}$  PoT [18].

For the MINOS baseline of 735 km, the  $\nu_\mu \rightarrow \nu_\mu$  oscillation minimum occurs at approximately 1.6 GeV (higher than for K2K). Hence for the MINOS experiment quasi-elastic, resonance and deep-inelastic scattering interactions all play a role (see Figure 2), and it is no longer possible to reconstruct the neutrino energy from the reconstructed muon alone. The MINOS detectors are magnetised steel-scintillator sampling calorimeters with alternating layers of 2.54 cm thick steel and 1 cm thick plastic scintillator strips. The detector is able measure the muon momentum (from curvature or range) and the energy of the recoiling hadronic system in charged-current (CC) interactions,  $\nu_\mu + \text{Fe} \rightarrow \mu^- + X$ . The 5.4 kton MINOS far detector (FD) is located in the Soudan Underground Laboratory 735 km away from the NuMI target. The 0.98 kton Near Detector (ND) is located 1.04 km from target. The ND and FD use the same basic detector technology and are functionally very similar. By comparing the neutrino energy spectrum in the near and far detectors systematic uncertainties associated with neutrino beam flux, interaction cross sections and detector response largely cancel.

Candidate  $\nu_\mu$  CC interaction events are selected using a multivariate technique using variables related to the (muon) track properties. The neutrino energy is reconstructed as the sum of the muon track momentum and hadronic shower energies. The measured near detector neutrino energy spectrum is used to predict the unoscillated spectrum at the far detector. However, from the point of view of the decaying mesons which produce the neutrino beam the near detector subtends a much larger solid angle than the far detector. Consequently, even in the absence of neutrino oscillations,

the near and far detector energy spectra are not identical. This is corrected for by extrapolating the measured neutrino energy spectrum in the near detector to that in the far detector using the Beam Matrix method [16].

For LE beam data, 730 CC  $\nu_\mu$  events are observed in the FD compared to the unoscillated expectation of  $936 \pm 53$ . The energy spectrum is shown in Figure 4a. A fit to the data using Equation 1 gives  $|\Delta m^2| = (2.43 \pm 0.13) \times 10^{-3} \text{ eV}^2$  and  $\sin^2 2\theta > 0.95$  at the 68 % C.L. The fit  $\chi^2 = 90$  for 97 degrees of freedom. The 68 % C.L. and 90 % C.L. contours are shown in Figure 3b. The ratio of the observed FD energy spectra to that expected in the absence of neutrino oscillations is shown in Figure 4b. Here the data are also compared to fits using alternative models that have been proposed to explain the disappearance of neutrinos in flight, namely, the decay of neutrinos to lighter particles (Equation 13 of [19]) and the decoherence of the neutrino quantum-mechanical wave packet (Equation 5 of [20]). These alternative models are disfavoured with respect to the oscillation hypothesis at the 3.7 and 5.7 standard deviation level.

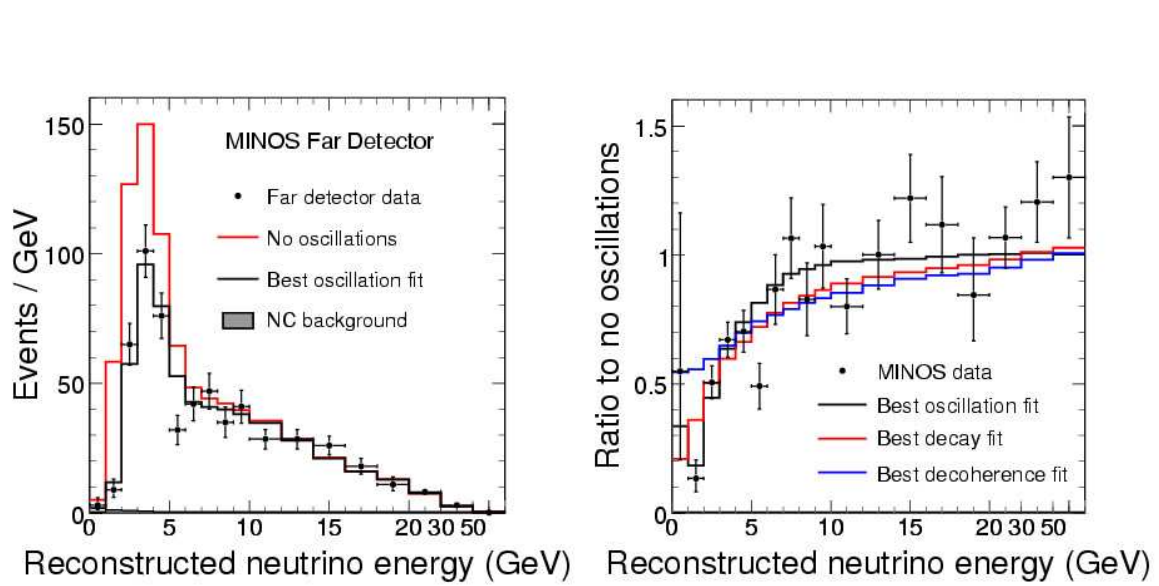


Figure 4: **a)** Reconstructed neutrino energy spectrum for selected  $\nu_\mu$  CC interactions in the MINOS FD. The data are compared to the unoscillated expectation and the best fit. **b)** The ratio of the observed energy spectrum of selected  $\nu_\mu$  CC interactions in the MINOS FD to the expected spectrum in the absence of oscillations (null hypothesis). The data are compared to the best fit and also to the hypotheses of neutrino decay and neutrino decoherence. Both plots taken from [18].

MINOS may have sensitivity to sub-dominant  $\nu_\mu \rightarrow \nu_e$  oscillations. Because  $\theta_{13}$  is

known to be small, the event rate is low (at most  $\sim 20$  events are expected in the current data sample). The measurement of this small signal is complicated by the large potential background from neutral current interactions with one or more  $\pi^0$ 's in the final state; the decays of  $\pi^0$ 's produce electromagnetic (EM) showers which can mimic the signal, *i.e.* an EM shower from the electron in  $\nu_e + \text{Fe} \rightarrow e^- + X$ . Furthermore, the coarse sampling of the MINOS detector is far from optimal for identifying electrons from  $\nu_e$  CC interactions. Nevertheless, the MINOS collaboration has developed sophisticated event identification algorithms and techniques to determine the expected background from the near detector data. First results based on  $3.25 \times 10^{20}$  PoT are expected early in 2009 with preliminary expected sensitivity shown in Figure 5. By 2010, MINOS will have sensitivity to  $\sin^2 2\theta_{13}$  down to  $\sim 0.06$ , *i.e.* roughly a factor two better than the current limit [11].

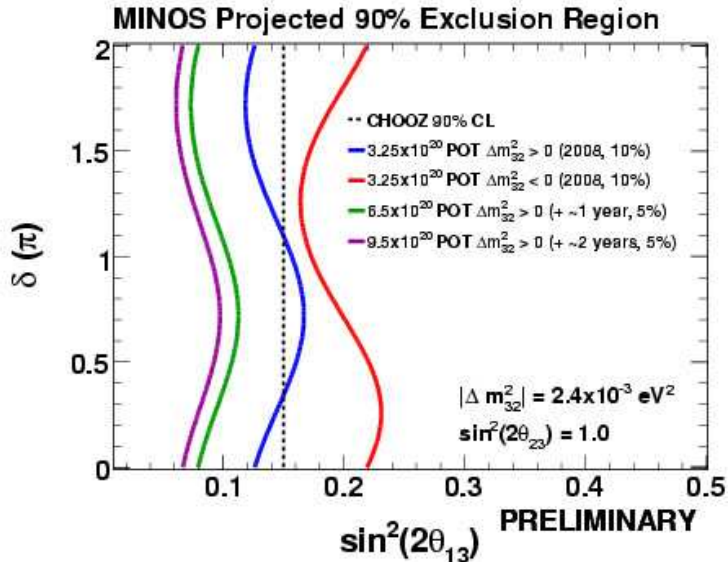


Figure 5: The MINOS projected 90 % C.L. sensitivity to  $\theta_{13}$  from the search for sub-dominant  $\nu_\mu \rightarrow \nu_e$  oscillations. The sensitivities are shown for an exposure of  $3.25 \times 10^{20}$  PoT assuming a 10 % systematic error on the background and for  $6.5 \times 10^{20}$  PoT and  $9.5 \times 10^{20}$  PoT assuming a 5 % background systematic uncertainty. The expected background is derived from the ND data.

In summary, MINOS provides a high statistics test of the neutrino oscillation hypothesis and yields a precise measurement ( $\pm 5\%$ ) of  $|\Delta m_{32}^2|$ . With the final MINOS data the lower bound on  $\theta_{23}$  may exceed the current limits from SK. MINOS also has sensitivity to  $\theta_{13}$  beyond the current limits from the CHOOZ experiment.

### 3.5 OPERA

The OPERA [21] experiment uses the CERN to Gran Sasso (CNGS) beam. The main goal of the experiment is to observe  $\tau$  leptons from  $\nu_\tau$  CC interactions arising from  $\nu_\mu \rightarrow \nu_\tau$  oscillations. At the CNGS baseline of 732 km the first oscillation minimum occurs at  $\sim 1.6$  GeV. This is lower than the kinematic threshold,  $E_{\nu_\tau} > 3.5$  GeV, for  $\nu_\tau + n \rightarrow \tau^- + p$ . Consequently  $\nu_\tau$  CC interactions can only be observed at energies where the oscillation probability is relatively small. To some extent, this is compensated by the rising  $\nu_\tau$  CC interaction cross section. For this reason the CNGS beam is relatively high energy, with the majority of the neutrino flux between 5 GeV and 25 GeV.

The expected number of  $\nu_\tau$  interactions is relatively small and detecting neutrino induced  $\tau$  leptons is challenging. The OPERA detector has 150,000 bricks with a layered structure of 1 mm thick lead plates followed by two emulsion layers. The high precision point resolution of the emulsion enables kinked tracks from  $\tau$  lepton decays to be cleanly identified. Bricks with candidate interactions are identified by scintillator tracking chambers which are located between walls formed from the lead/emulsion bricks. The bricks are robotically removed from the stack for automatic analysis of the emulsion. OPERA commenced its first full physics run in June 2008. For a nominal five year run (at an intensity of  $4.5 \times 10^{19}$  PoT/year) 10 identified  $\nu_\tau$  are expected (assuming the standard oscillation scenario) with a background of approximately 1 event. The OPERA experiment is discussed in more detail elsewhere in these proceedings [22].

## 4 Future Long Baseline Experiments

The past and current generation LBL neutrino experiments (K2K, MINOS, OPERA) utilise “on-axis” beams, where the beam points towards the far detector. This is the optimal configuration for maximising the neutrino flux. However, the resulting energy spectrum is rather broad as can be seen in Figure 4a. This is non-ideal for the  $\nu_\mu \rightarrow \nu_e$  appearance analysis where NC interactions of relatively high energy neutrinos can be a significant (and poorly modelled) background. The next generation of experiments (T2K and NO $\nu$ A) are designed to improve the sensitivity to  $\sin^2 2\theta_{13}$  by an order of magnitude compared to CHOOZ. These experiments employ an “off-axis” beam, where neutrino beam is aligned such that the far detector is a few degrees from the beam axis. Due to the pion decay kinematics producing the beam via  $\pi^+ \rightarrow \mu^+ \nu_\mu$ , the off-axis neutrino beam has a relatively narrow energy spectrum. The peak of the energy spectrum is chosen to correspond to the  $\nu_\mu \rightarrow \nu_e$  oscillation maximum, thus maximising the signal. The lack of higher energy neutrinos in the off-axis beam means that the NC background to the  $\nu_e$  appearance measurement is greatly reduced.

## 4.1 T2K

The Tokai-to-Kamioka (T2K) experiment will use an intense  $\nu_\mu$  beam produced at the J-PARC facility in Tokai. The main goals of the experiment are to observe  $\nu_e$  appearance and to measure or set improved lower limits on  $\theta_{23}$ . First beam is expected in April 2009 with the intensity gradually increasing to the design beam power of 750 kW. First results are anticipated in 2010. T2K employs a  $2.5^\circ$  off-axis beam. The peak energy is approximately 0.6 GeV. The energy spectrum is relatively narrow with a FWHM of approximately 0.3 GeV.

The T2K far detector, located 295 km from the beam, is the 50 kton (22.5 kton fiducial) Super-Kamiokande water Čerenkov detector. T2K has two main near detector systems 280 m from the beam. The on-axis near detector (INGRID) will be used to monitor the beam. It consists of modules with alternating layers of scintillating bars and iron plates. The off-axis detector is more complex. It is divided into three main parts: a tracker, a  $\pi^0$  detector, and an electromagnetic calorimeter. The tracker consists of three Time Projection Chambers (TPCs) with two fine-grained scintillating bar detectors in between. The main purpose of the tracking detector is to measure the beam flux and energy spectrum and to make measurements of neutrino cross sections and kinematics in order to constrain the far detector expectations. The  $\pi^0$  detector consists of layers of triangular scintillating bars. In between a number of the layers there are water targets. The main purpose of the  $\pi^0$  detector is to study  $\pi^0$  production in NC interactions; such events form the main background for the  $\nu_e$  appearance measurement.

Phase I of the T2K experiment assumes a 5 year run with a 0.75 MW beam, corresponding to  $5 \times 10^{21}$  PoT. With this exposure, it is estimated that the uncertainty on  $\sin^2 2\theta_{23}$  will be 0.01 and that on  $|\Delta m_{32}^2|$  will be  $10^{-4}$  eV $^2$ . Figure 6a shows the T2K expected sensitivity to  $\theta_{13}$  (which depends on  $\delta$ ). The limit of the sensitivity is  $\sin^2 2\theta_{13} \sim 0.01$  where approximately 10 signal events are expected, compared to the background of approximately 10 electromagnetic shower-like events from NC interactions and 13 events from the residual  $\nu_e$  component of the beam. Whether T2K can achieve this sensitivity will depend on how well these backgrounds can be constrained by the ND data.

## 4.2 NO $\nu$ A

The proposed NO $\nu$ A project at FNAL is designed to search for  $\nu_e$  appearance by comparing electron neutrino rates in a large off-axis detector 810 km from Fermilab with the rates in the near detector. In the first stage of the project the NuMI beam would be upgraded to between 400 kW and 700 kW. At the time of writing the schedule for NO $\nu$ A (and indeed whether the project will go ahead) is unclear. Optimistically one might anticipate first meaningful data in 2013/2014. The planned NO $\nu$ A detector [24]

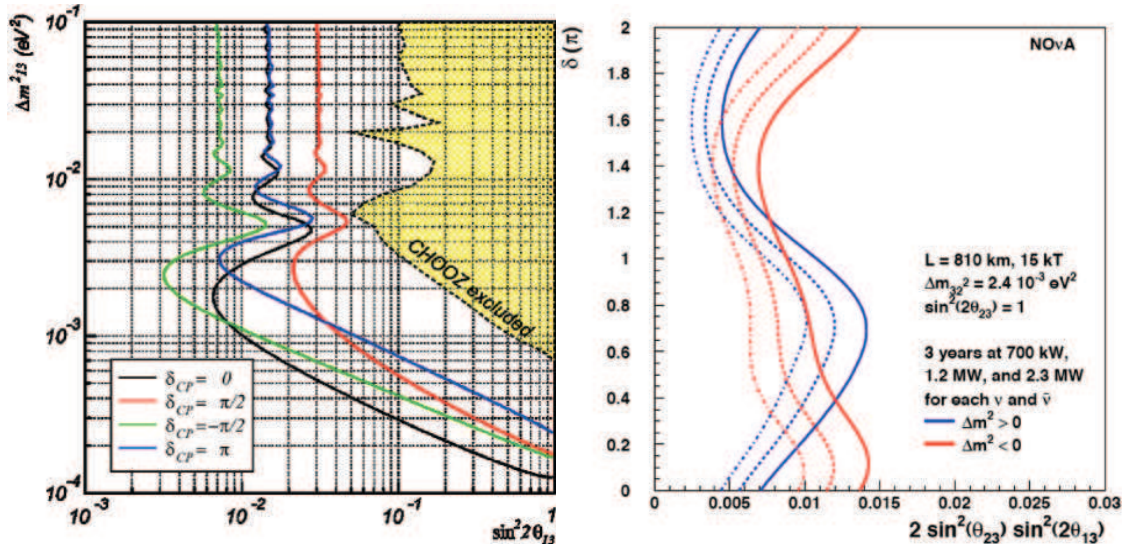


Figure 6: **a)** The expected T2K sensitivity to  $\sin^2 2\theta_{13}$  assuming the nominal Phase I run of 5 years at 0.75 MW. The plot is shown for four values of  $\delta$ . **b)** The expected NO $\nu$ A sensitivity to  $\sin^2 2\theta_{13}$  shown as a function of  $\delta$  and mass hierarchy. Taken from [25].

consists of approximately 1000 planes made up of  $4\text{ cm} \times 6\text{ cm} \times 15.5\text{ m}$  extruded plastic cells containing liquid scintillator. The cells would be read out using avalanche photo-diodes attached to wavelength-shifting fibres. The entire detector would be  $15.7\text{ m} \times 15.7\text{ m} \times 67\text{ m}$  in volume, giving a total mass of 15 kton. The totally active detector is optimised for the identification of electro-magnetic showers produced by  $\nu_e$  CC interactions. The 0.2 kton near detector would be constructed from identical components.

NO $\nu$ A would be sensitive to  $\theta_{13}$  down to  $\sin^2 2\theta_{13} \sim 0.01$ , although a simple interpretation in terms of  $\theta_{13}$  alone is not possible as the expected  $\nu_e$  event rates depend not only on  $\theta_{13}$  but also on the mass hierarchy and the CP phase  $\delta$ . The current estimated sensitivity is shown in Figure 6b. The final sensitivity will depend on beam intensity for which there are a number of options; upgrade NuMI to 0.4 – 0.7 MW, Super-NuMI (SNuMI) *i.e.* an upgrade to 1.2 MW or the 2.3 MW beam of Project-X which is currently under discussion.

## 5 Summary

High intensity long baseline experiments have opened up a new era in the study of neutrino oscillations. The feasibility of LBL neutrino experiments was first demon-

strated by K2K. MINOS has provided a precise measurement of  $|\Delta m_{32}^2|$  and a high precision test of the oscillation hypothesis. OPERA is currently searching for the first direct evidence of  $\nu_\tau$  appearance in  $\nu_\mu \rightarrow \nu_\tau$  oscillations. The next challenge for LBL experiments is the measurement of  $\theta_{13}$  which will ultimately pave the way to the experimental investigation of CP violation in the lepton sector. The T2K experiment (and hopefully NO $\nu$ A), along with the next generation of reactor experiments, will be central to the future experimental neutrino physics programme. The next ten years are likely to be every bit as exciting and pivotal for neutrino physics as the last ten years - and that is saying something!

## References

- [1] Y. Ashie *et al.*, Super-Kamiokande Collaboration, Phys. Rev. Lett. **93**, 101801 (2004).
- [2] Y. Ashie *et al.*, Super-Kamiokande Collaboration, Phys. Rev. **D 72**, 112005 (2005).
- [3] J. Hosaka *et al.*, Super-Kamiokande Collaboration, Phys. Rev. **D 74**, 032002 (2006).
- [4] J. Fukuda *et al.*, Super-Kamiokande Collaboration, Phys. Lett. **B 539**, 179 (2002).
- [5] J. P. Cravens *et al.*, Super-Kamiokande Collaboration, Phys. Rev. **D 78**, 032002 (2008).
- [6] B. Aharmim *et al.*, SNO Collaboration, Phys. Rev. **C 72**, 055502 (2005).
- [7] M. Acciarri *et al.*, L3 Collaboration, Phys. Lett. **B 431**, 199 (1998);  
P. Abreu *et al.*, Delphi Collaboration, Z. Phys. **C 74**, 577 (1997);  
R. Akers *et al.*, OPAL Collaboration, Z. Phys. **C 65**, 47 (1995);  
D. Buskulic *et al.*, Aleph Collaboration, Phys. Lett. **B 313**, 520 (1993).
- [8] Pontecorvo, B., Sov. Phys. JETP **6**, 429 and Zh. Eksp. Teor. Fiz. **33**, 549 (1957).
- [9] Maki, Z., Nakagawa, M. and Sakata, S., Progr. Theor. Phys. **28**, 870 (1962).
- [10] S. Abe *et al.*, KamLAND Collaboration, Phys. Rev. Lett. **100**, 221803 (2008).
- [11] M. Apollonio *et al.*, CHOOZ Collaboration, Phys. Lett. **B 466**, 415 (1999).
- [12] H. Meyer for the MIPP Collaboration, J. Phys. Conf. Ser. **69** 012025 (2007).

- [13] M. H. Ahn *et al.*, K2K Collaboration, Phys. Rev. **D 74**, 072003 (2006).
- [14] Durham Database Group, HEPDATA: Reaction Data Database,  
<http://durpdg.dur.ac.uk/HEPDATA/REAC>.
- [15] H. Gallagher, Nucl. Phys. B Proc. Suppl. **112**, 188 (2002).
- [16] P. Adamson *et al.*, MINOS Collaboration, Phys. Rev. **D 77**, 072002 (2008).
- [17] D. Michael *et al.*, MINOS Collaboration, Nucl. Instrum. Meth. **A596**, 190 (2008).
- [18] P. Adamson *et al.*, MINOS Collaboration, Phys. Rev. Lett. **101**, 131802 (2008).
- [19] V. Barger *et al.*, Phys. Rev. Lett. **82**, 2640 (1999).
- [20] G. L. Fogli *et al.*, Phys. Rev. **D 67**, 093006 (2003).
- [21] M. Guler *et al.*, CERN/SPSC 2000-028, SPSC/P318, LNGS P25/2000), “An appearance experiment to search for oscillations of the CNGS beam” (2000).
- [22] A. Longhin, these proceedings.
- [23] Y. Itow *et al.*, T2K Collaboration, KEK-REPORT-2001-4, ICRR-REPORT-477-2001-7, TRI-PP-01-05, [hep-ex/0106019](http://hep-ex.web.cern.ch/hep-ex/0106019), (2001).
- [24] NO $\nu$ A, NuMI Off-Axis  $\nu_e$  Appearance Experiment, TDR, October 2007;  
[http://www-nova.fnal.gov/nova\\_cd2\\_review/tdr\\_oct\\_23/tdr.htm](http://www-nova.fnal.gov/nova_cd2_review/tdr_oct_23/tdr.htm).
- [25] G. Feldman, “The NO $\nu$ A Experiment”, talk at the P5 meeting, SLAC, February 2008; <http://www-group.slac.stanford.edu/ppa/Reviews/p5/>.

# Underground nuclear astrophysics and the Sun

*Carlo Broggini  
(the LUNA Collaboration)  
Istituto Nazionale di Fisica Nucleare  
Sezione di Padova  
I-35131 Padova, ITALY*

## 1 Introduction

Thermonuclear reactions that generate energy and synthesize elements take place inside the stars in a relatively narrow energy window: the Gamow peak. In this region, which is far below the Coulomb energy, the reaction cross-section  $\sigma(E)$  drops almost exponentially with decreasing energy  $E$ :

$$\sigma(E) = \frac{S(E)}{E} \exp(-2\pi\eta) \quad (1)$$

where  $S(E)$  is the astrophysical factor and  $\eta$  is given by  $2\pi\eta = 31.29 Z_1 Z_2 (\mu/E)^{1/2}$ .  $Z_1$  and  $Z_2$  are the charges of the interacting nuclei in the entrance channel,  $\mu$  is the reduced mass (in amu), and  $E$  is the center of mass energy (in keV).

The extremely low value of the cross-section has always prevented its measurement within the Gamow peak mainly because of the cosmic ray induced background. Instead, the observed energy dependence of the cross-section at high energies is extrapolated to low energy, leading to large uncertainties. In order to explore this new domain of nuclear astrophysics two electrostatic accelerators have been installed underground in the Gran Sasso Laboratory by the LUNA (Laboratory for Underground Nuclear Astrophysics) Collaboration: a 50 kV accelerator [1] and a 400 kV one [2]. The mountain provides a natural shielding equivalent to at least 3800 meters of water which reduces the muon and neutron fluxes by a factor  $10^6$  and  $10^3$ , respectively. After 18 years LUNA still remains the only underground accelerator facility existing in the world. During this period its activity has been mainly devoted to the study of the key reactions of the proton-proton chain and of the CNO cycle.

## 2 In search of the resonance

The initial underground activity has been focused on the  ${}^3\text{He}({}^3\text{He},2\text{p}){}^4\text{He}$  cross section measurement within the solar Gamow peak (16-28 keV). A resonance at the thermal

energy of the Sun was suggested long time ago [3] [4] to explain the observed  ${}^8\text{B}$  solar neutrino flux: it would decrease the relative contribution of the alternative reaction  ${}^3\text{He}(\alpha, \gamma){}^7\text{Be}$ , which generates the branch responsible for  ${}^7\text{Be}$  and  ${}^8\text{B}$  neutrino production in the Sun. A narrow resonance with a peak S-factor 10-100 times the value extrapolated from high energy measurements could not be ruled out with the pre-LUNA data (such an enhancement is required to reduce the  ${}^7\text{Be}$  and  ${}^8\text{B}$  solar neutrinos by a factor 2-3).

Briefly, the 50 kV accelerator facility consisted of a duoplasmatron ion source, an extraction/acceleration system, a double-focusing 90° analyzing magnet, a windowless gas-target system and a beam calorimeter. The beam energy spread was very small (the source spread was less than 20 eV, acceleration voltage known with an accuracy of better than  $10^{-4}$ ), and the beam current was high even at low energy (about 300  $\mu\text{A}$ ). Eight thick (1 mm) silicon detectors of  $5\times 5\text{ cm}^2$  area were placed around the beam inside the target chamber, where there was a constant  ${}^3\text{He}$  gas pressure of 0.5 mbar.

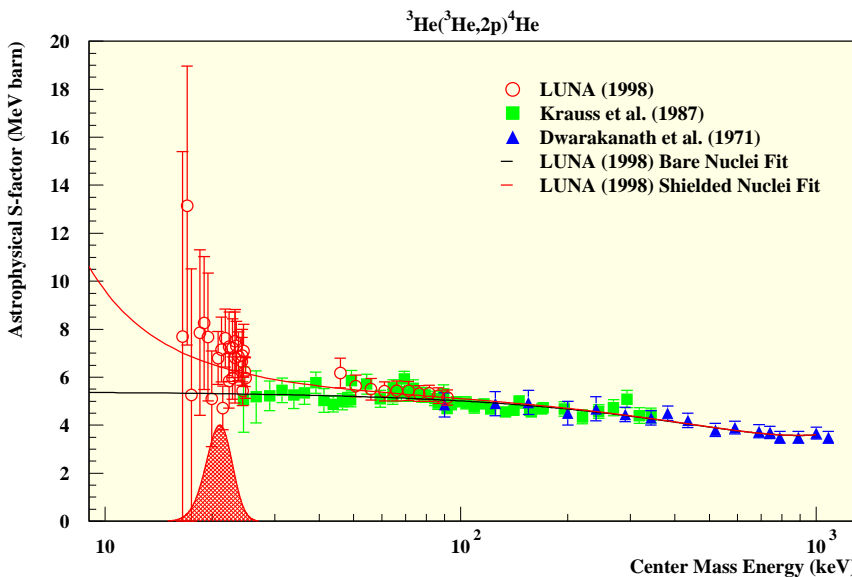


Figure 1: Astrophysical S(E)-factor of  ${}^3\text{He}({}^3\text{He}, 2\text{p}){}^4\text{He}$ .

The simultaneous detection of 2 protons has been the signature which unambiguously identified a  ${}^3\text{He}({}^3\text{He}, 2\text{p}){}^4\text{He}$  fusion reaction (detection efficiency:  $5.3 \pm 0.2$ , Q-value of the reaction: 12.86 MeV). No event fulfilling the selection criteria was detected during a 23 day background run with a  ${}^4\text{He}$  beam on a  ${}^4\text{He}$  target. Fig-

ure 1 shows the obtained results together with two existing measurements [5][6] of the astrophysical factor  $S(E)$ . The cross section varies by more than two orders of magnitude in the measured energy range. At the lowest energy of 16.5 keV it has the value of 0.02 pb, which corresponds to a rate of about 2 events/month, rather low even for the "silent" experiments of underground physics. The obtained result [7] showed that the  ${}^3\text{He}({}^3\text{He},2\text{p}){}^4\text{He}$  cross section does not have any narrow resonance within the Gamow peak of the Sun. Consequently, the astrophysical solution of the  ${}^8\text{B}$  and  ${}^7\text{Be}$  solar neutrino problem based on its existence has been ruled out. With  ${}^3\text{He}({}^3\text{He},2\text{p}){}^4\text{He}$  LUNA provided the first cross section measurement of a key reaction of the proton-proton chain at the thermal energy of the Sun. In this way it also showed that, by going underground and by using the typical techniques of low background physics, it is possible to measure nuclear cross sections down to the energy of the nucleosynthesis inside stars.

### 3 The ${}^7\text{Be}$ and ${}^8\text{B}$ solar neutrino flux

${}^3\text{He}(\alpha, \gamma){}^7\text{Be}$  ( $Q$ -value=1.586 MeV) is the key reaction for the production of  ${}^7\text{Be}$  and  ${}^8\text{B}$  neutrinos in the Sun since their flux depends almost linearly on the  ${}^3\text{He}(\alpha, \gamma){}^7\text{Be}$  cross section. The error on  $S_{3,4}$ , 9.4% [8] is the main nuclear limitation to the extraction of physics from the  ${}^8\text{B}$  and  ${}^7\text{Be}$  neutrino flux measurements [9] [10]. The capture reaction is dominated, at low energies, by the non-resonant direct capture mechanism to the ground state and to the 429 keV first excited state of  ${}^7\text{Be}$ . The cross section can be determined either from the detection of the prompt  $\gamma$  ray or from the counting of the produced  ${}^7\text{Be}$  nuclei. The latter requires the detection of the 478 keV  $\gamma$  due to the excited  ${}^7\text{Li}$  populated in the EC decay of  ${}^7\text{Be}$  (branching ratio of  $10.44 \pm 0.04\%$ ,  $T_{1/2} = 53.22 \pm 0.06$  days). Both methods have been used in the past to determine the absolute cross section in the energy range  $E_{c.m.} \geq 107$  keV (see [11] [12] and references therein) but the  $S_{3,4}$  extracted from the measurements of the induced  ${}^7\text{Be}$  activity are 13% higher [8] than the values obtained from the detection of the prompt  $\gamma$ -rays.

The underground experiment has been performed with the  ${}^4\text{He}^+$  beam from the 400 kV accelerator in conjunction with a windowless gas target made of oxygen free high conductivity copper, chosen because of its radioactive cleanliness, and filled with  ${}^3\text{He}$  at 0.7 mbar. The beam enters the target chamber through a 7 mm diameter collimator and it is stopped on a power calorimeter placed 35 cm downstream. The  ${}^7\text{Be}$  nucleus produced by the  ${}^3\text{He}(\alpha, \gamma){}^7\text{Be}$  reaction inside the  ${}^3\text{He}$  gas target are implanted into the calorimeter cap (thanks to the forward kinematics and low lateral straggling). After the irradiation, this cap (7 cm diameter) is removed and placed in front of a germanium detector for the measurement of the  ${}^7\text{Be}$  activity.

In the first phase of the experiment we obtained the  ${}^3\text{He}(\alpha, \gamma){}^7\text{Be}$  cross section

from the activation data [13] [14] alone, i.e. by counting the  ${}^7\text{Be}$  nuclei collected on the calorimeter cap. Their uncertainty of 4% (systematic and statistical combined in quadrature) is comparable to or lower than previous activation studies at high energy and lower than prompt- $\gamma$  studies at comparable energy. However, the claimed discrepancy between the results obtained with the two different methods can not be solved by activation (or prompt  $\gamma$ ) data only, even if very precise.

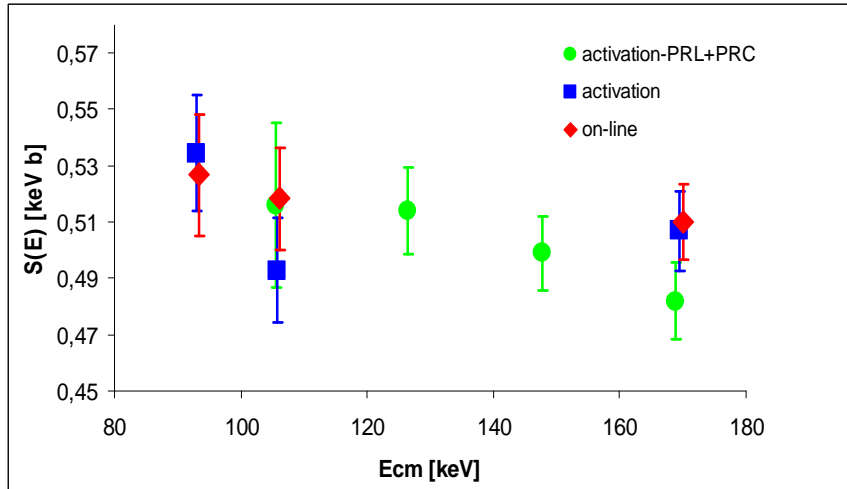


Figure 2: Astrophysical S-factor for  ${}^3\text{He}(\alpha, \gamma){}^7\text{Be}$  obtained with the activation method only (circles) and with activation (squares) and prompt  $\gamma$  (diamonds) simultaneously

As a matter of fact, in the second phase of the experiment we performed a new high accuracy measurement using simultaneously prompt and activation methods. The prompt capture  $\gamma$ -ray is detected by a 135 % relative efficiency ultra-low background HPGe detector placed in close geometry with the target. The germanium detector is surrounded by a 5 cm copper + 25 cm lead shielding and everything is closed inside an anti-radon box. At energies higher than 0.5 MeV we measured a background rate of 4.1 count/h/kg, one order of magnitude only worse than the best ultra-low background germanium set-up running in Gran Sasso (in spite of the presence of the beam-pipe entering our shielding and of the calorimeter inside the target chamber). Data have been collected at  $E_{c.m.} = 170, 106, 93$  keV. In this interval the cross section varies from 10.25 nbarn to 0.23 nbarn, with a total error of about 4%. Beam induced background has been measured with a 400 keV  $\alpha$  beam on a  ${}^4\text{He}$  gas target: no counts have been observed in addition to laboratory background. Figure 2 shows the astrophysical factor obtained with both methods simultaneously [15] and with activation only, during the first phase of the experiment. As we can see, the two methods give the same result within the quoted experimental error. Recently, similar conclusions have

been reached in a new simultaneous activation and prompt experiment [16] which covers the  $E_{c.m.}$  energy range from 330 keV to 1230 keV.

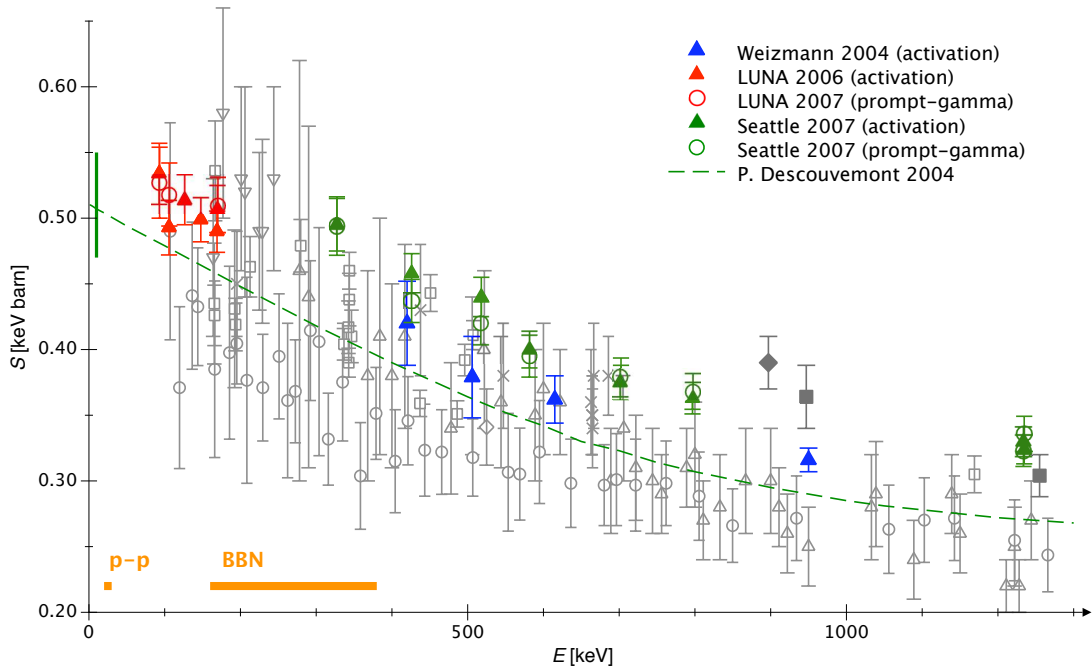


Figure 3: Astrophysical S-factor for  ${}^3\text{He}(\alpha, \gamma){}^7\text{Be}$ . The results from the modern, high precision experiments are highlighted. Horizontal bars show the Gamow peak of the Sun and of the Big Bang Nucleosynthesis.

The energy dependence of the  ${}^3\text{He}(\alpha, \gamma){}^7\text{Be}$  cross section seems to be theoretically well determined [8]. The only free parameter is the normalization. If we rescale the fit of [17] in Figure 3 to our data we obtain  $S_{3,4}(0)=0.560\pm 0.017$  keV barn, to be compared to the value of  $0.53\pm 0.05$  used in the Standard Solar Model. Thanks to our small error, the total uncertainty on the  ${}^8\text{B}$  solar neutrino flux goes from 12 to 10%, whereas the one on the  ${}^7\text{Be}$  flux goes from 9.4 to 5.5% [18]. This is particularly important for the Borexino experiments which is now running to achieve a precise measurement of the  ${}^7\text{Be}$  neutrino flux from the Sun.

## 4 The CNO cycle and the metallicity of the Sun

In our Sun the CNO cycle accounts for just a small fraction of the nuclear energy production, whereas the main part is supplied by the proton-proton chain.  ${}^{14}\text{N}(\text{p}, \gamma){}^{15}\text{O}$  (Q-value of the reaction: 7.3 MeV) is the slowest reaction of the cycle and it rules

its energy production rate. In particular, it is the key reaction to know the  $^{13}\text{N}$  and  $^{15}\text{O}$  solar neutrino flux, which depends almost linearly on this cross section. The energy region studied so far in nuclear physics laboratories is well above the region of interest for the CNO burning in astrophysical conditions (in particular, the solar Gamow peak is between 20 and 33 keV).

In the first phase of the LUNA study, data have been obtained down to 119 keV energy [19] [20] with solid targets of TiN (typical thickness of 80 keV). A 126% HpGe, placed at  $55^\circ$  from the beam direction and at distances between 1.5 and 20.5 cm from the target, detected the  $\gamma$  rays. A detector with excellent energy resolution is necessary in order to unambiguously separate the different contribution to the cross section. As a matter of fact, five different radiative capture transitions contribute to the  $^{14}\text{N}(\text{p},\gamma)^{15}\text{O}$  cross section at low energy: ground state, 6.79, 6.17, 5.24 and 5.18 MeV. Since they differently depend on the energy, each of them has to be measured and extrapolated to the low energy region. Finally, the total cross section is given by the sum of the different contributions.

The total cross section can be measured at very low energies by using a  $\gamma$  ray detector with very high efficiency (to compensate for the rapidly decreasing cross section) as well as a very pure, thin and stable  $^{14}\text{N}$  target. All this has been achieved in the second phase of the LUNA study with a large  $4\pi$  BGO summing detector (about 70% efficiency and 8% resolution in the energy region between 6 and 8 MeV) and with a windowless gas target [21] (the chamber is designed to fit inside the central hole of the BGO crystal detector). Figure 4 shows our results [22], corrected for the electron screening effect [23] (10% and 3% effect at 70 and 150 keV, respectively). At the lowest energy of 70 keV we measured a cross section of 0.24 pb, with an event rate of 11 counts/day from the reaction. In Figure 4 we see that our data starts at a much lower energy than the previous direct experiments [24][25][26], while overlapping over a wide energy range. We remark the excellent agreement with the R-matrix fit from the LUNA study with the germanium detector set-up [20].

The results we obtained first with the germanium detector data [19][20] and then with the BGO set-up [22] are about a factor two lower than the existing extrapolation at very low energy [8][27]. As a consequence the CNO neutrino yield in the Sun is decreased by about a factor two [28, 10], with respect to the estimates. The lower cross section is affecting also stars which are more evolved than our Sun. In particular, the age of the Globular Clusters is increased by 0.7-1 Gyr [28, 29] and the dredge-up of carbon to the surface of AGB stars is much more efficient [8].

The main conclusion from the LUNA data has been confirmed by an independent study at higher energy [26]. However, there is a 15% difference between the total S-factor extrapolated by the two experiments at the Gamow peak of the Sun. In particular, this difference arises from the extrapolation of the capture to the ground state in  $^{15}\text{O}$ , a transition strongly affected by interference effects between several resonances and the direct capture mechanism. In order to provide precise data for

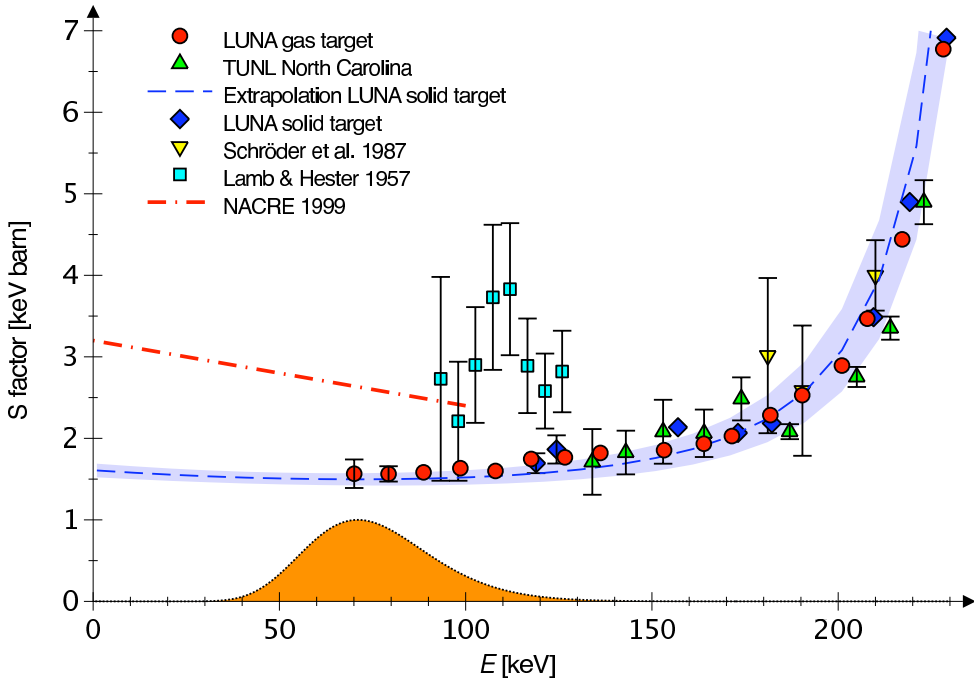


Figure 4: Astrophysical  $S(E)$ -factor of  $^{14}\text{N}(\text{p},\gamma)^{15}\text{O}$  as function of the center of mass energy  $E$ . The errors are statistical only. The Gamow peak for  $T_6=60$  is also shown.

the ground state capture we performed a third phase of the  $^{14}\text{N}(\text{p},\gamma)^{15}\text{O}$  study.

Low energy measurements of the radiative capture to the ground state in  $^{15}\text{O}$  are hampered by the systematic uncertainty due to the correction for the summing effect: primary and secondary gamma rays from the strong cascade transitions which are detected in coincidence and have the same signature as a true ground state capture gamma ray. In the new experiment we used a segmented Clover germanium detector [31] to reduce the summing correction and, in order to obtain sufficient statistics, we concentrate on the beam energy region immediately above the 259 keV resonance, where precise data effectively constrain the R-matrix fit for the ground state transition. Thanks to these improvements we could finally reduce to 8% the total error on the  $S$ -factor:  $S_{1,14}(0)=1.57\pm 0.13$  keV barn [32]. Thanks to this relatively small error it will soon be possible to measure the metallicity of the central region of the Sun by comparing the detected CNO neutrino flux with the predicted one [33]. As a matter of fact, the CNO neutrino flux is decreased by about 35% in going from the high to the low metallicity scenario [34].

The solar phase of LUNA has almost reached the end and a new and rich program of nuclear astrophysics mainly devoted to study the Mg-Al and Ne-Na cycles has already started about 2 years ago. There is only one reaction, which we are studying

now, still significant for solar neutrinos:  $^{15}\text{N}(\text{p},\gamma)^{16}\text{O}$ , which is the leak reaction from the first CNO cycle to the second one, where  $^{17}\text{F}$  neutrinos are produced (their flux from the Sun is expected to be about 2 orders of magnitude lower than the  $^{13}\text{N}$  and  $^{15}\text{O}$  ones).

## 5 Conclusions

Underground nuclear astrophysics started almost 18 years ago with the goal of exploring the fascinating domain of nuclear astrophysics at very low energy. During these years LUNA has proved that, by going underground and by using the typical techniques of low background physics, it is possible to measure nuclear cross sections down to the energy of the nucleosynthesis inside stars. In particular, the measurements of  $^3\text{He}(^3\text{He},2\text{p})^4\text{He}$  within the Gamow peak of the Sun has shown that nuclear physics was not the origin of the solar neutrino puzzle.

The cross section of  $^3\text{He}(\alpha,\gamma)^7\text{Be}$  has been measured with two different experimental approaches and with a 4% total error. Thanks to this small error, the total uncertainty on the  $^7\text{Be}$  solar neutrino flux has been reduced to 5.5%. Many years after the pioneering measurement of the  $^3\text{He}(\alpha,\gamma)^7\text{Be}$  cross section performed in 1959 [35], nuclear physics does not give anymore a dominant contribution to the uncertainties of the solar neutrino flux.

Finally, the study of  $^{14}\text{N}(\text{p},\gamma)^{15}\text{O}$  has shown that the expected CNO solar neutrino flux has to be decreased by about a factor two, with an error small enough to pave the way for a measurement of the central metallicity of the Sun.

## References

- [1] U. Greife et al., Nucl. Instr. Meth. A **350**, 327 (1994).
- [2] A. Formicola et al., Nucl. Instr. Meth. A **507**, 609 (2003).
- [3] W.A. Fowler, Nature **238**, 24 (1972).
- [4] V.N. Fetysov and Y.S. Kopysov, Phys. Lett. B **40**, 602 (1972).
- [5] A. Krauss et al., Nucl. Phys. A **467**, 273 (1987).
- [6] M.R Dwarakanath and H. Winkler, Phys. Rev. C **4**, 1532 (1971).
- [7] R. Bonetti et al., Phys. Rev. Lett. **82**, 5205 (1999).
- [8] E.G. Adelberger et al., Rev. Mod. Phys. **70**, 1265 (1998).
- [9] G. Fiorentini et al., astro-ph/0310753.

- [10] J.N. Bahcall and M. Pinsonneault, Phys. Rev Lett. **92**, 121301 (2004).
- [11] M.Hilgemeier et al., Z. Phys. A **329**, 243 (1988).
- [12] B.S. Nara Singh et al., Phys. Rev. Lett. **93**, 262503 (2004).
- [13] D. Bemmerer et al., Phys. Rev. Lett. **97**, 122502 (2006).
- [14] G. Gyurky et al., Phys. Rev. C **75**, 035805 (2007).
- [15] F. Confortola et al., Phys. Rev. C **75**, 065803 (2007).
- [16] T.A.D. Brown et al., Phys. Rev. C **76**, 055801 (2007).
- [17] P. Descouvement et al., Data Nucl. Data Tables **88**, 203 (2004).
- [18] C. Pena Garay, private communication,(2006).
- [19] A. Formicola et al., Phys. Lett. B **591**, 61 (2004).
- [20] G. Imbriani et al., Eur. Phys. J.A **25**, 455 (2005).
- [21] C. Casella et al., Nucl. Instr. Meth. A **489**, 160 (2002).
- [22] A. Lemut et al., Phys. Lett. B **634**, 483 (2006).
- [23] H. Assenbaum et al., Z. Phys. A **327**, 461 (1987).
- [24] W. Lamb and R. Hester, Phys. Rev. **108**, 1304 (1957).
- [25] U. Schroeder et al., Nucl. Phys. A **467** 240 (1987).
- [26] R.C. Runkle et al., Phys. Rev. Lett. **94** 082503 (2005).
- [27] C. Angulo et al., Nucl. Phys. A **656**, 3 (1999).
- [28] S. Degl'Innocenti et al., Phys. Lett. B **591**, 61 (2004).
- [29] G. Imbriani et al., Astronomy and Astrophysics **420**, 625 (2004).
- [30] F. Herwig and S.M. Austin, Astrophysical Journal **613**, L73 (2004).
- [31] Z. Elekes et al., Nucl. Instr. Meth. A **503**, 580 (2003).
- [32] M. Marta et al., Phys. Rev. C **78**, 022802 (2008).
- [33] W.C. Haxton and A.M. Serenelli., arXiv: 0805.2013, (2008).
- [34] J.N. Bahcall et al., Astrophysical Journal **621**, L85 (2005).
- [35] H.D. Holmgren and R.L. Johnston, Phys. Rev. **113**, 1556 (1959).

# OPERA: waiting for the $\tau$

*Andrea Longhin*

*(on behalf of the OPERA Collaboration)*

*Physics Department “M. Merlin”,*

*Bari University*

*via Amendola 173,*

*I-70126 Bari, Italy*

## 1 Overview and physics reach

OPERA[1] is a long baseline (730 Km) neutrino oscillation experiment located in Italy at the Gran Sasso underground laboratory (3500 m.w.e. overburden, residual  $\mu$  flux  $\sim 1 \text{ h}^{-1}\text{m}^{-2}$ ). The detector is conceived to observe  $\nu_\mu \rightarrow \nu_\tau$  oscillations in the parameter region indicated by Super-Kamiokande[2]<sup>1</sup> through direct observation (appearance) of  $\nu_\tau$  in an almost pure  $\nu_\mu$  beam (contaminations:  $\sim 4\% \bar{\nu}_\mu$ ,  $\lesssim 1\% \nu_e + \bar{\nu}_e$  and negligible  $\nu_\tau$ ). The CERN Neutrinos to Gran Sasso (CNGS [3]) high energy neutrino beam ( $\langle E_{\nu_\mu} \rangle \simeq 17 \text{ GeV}$ ) has been designed in order to maximize the possible number of  $\nu_\tau$  charged current interactions at destination taking into account the energy dependance of the oscillation probability and the  $\tau$  production cross section.

The OPERA detector is a massive (1.35 kton) and highly modular lead-nuclear emulsion target composed of 154750 units called Emulsion Cloud Chambers (ECCs or “bricks”). Each brick is a 56-layer stack of lead plates interleaved with nuclear emulsions providing the  $\mu\text{m}$  and the mrad level precision tracking needed for detecting the  $\tau$  decay topology.

At CNGS energies the average  $\tau$  decay length is  $\sim 450 \mu\text{m}$ .  $\nu_\tau$  appearance will be identified by the detection of the peculiar  $\tau$  lepton decay topology through its decay modes into electron (17.8%), muon (17.7%), and single (50%) or three charged hadrons (14%). In the case of a decay in the same lead plate of production, the impact parameter of the daughter track with respect to primary vertex can be used while for longer decays in which the  $\tau$  traverses at least one emulsion layer, the kink angle in space between the charged decay daughter and the parent direction will be employed.

---

<sup>1</sup>and confirmed by K2K and MINOS, not to speak about Kamiokande, SOUDAN-2 and MACRO.

Each one of the two targets is instrumented by 31 planes of electronic detectors (horizontal and vertical arrays of  $2.6 \times 1$  cm thick scintillator strips read by WLS fibres and multi-anode PMT at both ends) that allow the location of the brick in which the interaction occurred and drive the scanning of the emulsions by providing information on the outgoing tracks. The trigger efficiency is as large as 99%.

A magnetic spectrometer follows the instrumented target and measures the charge and momentum of penetrating tracks. Each spectrometer is composed by a bipolar iron magnet ( $\sim 990$  tons,  $B = 1.52$  T) instrumented with 22 RPC planes ( $\sim 70$  m $^2$  each) which act as inner trackers and six fourfold drift tubes (8 m long) planes which provide high precision tracking with a point resolution better than 300  $\mu\text{m}$ . Precise charge measurement is particularly important for the efficient suppression of the charm background. A resolution  $\Delta p/p < 0.25$  and charge mis-identification of a few % up to  $\sim 25$  GeV can be obtained.

The  $\tau$  search sensitivity calculated for 5 years of data taking with a total number of  $4.5 \cdot 10^{19}$  integrated p.o.t./year (200 days runs) is given in Table 1. The number of signal events essentially scales like  $(\Delta m_{13}^2)^2$ .

The main background sources are given by large angle scattering of muons produced in ordinary charged current interactions, hadronic interactions of daughter particles produced at primary interaction vertex and prompt charmed particles decays associated with inefficiency on the primary muon identification.

Figure 1 shows the probability of discovery at 3 and 4  $\sigma$  significance as a function of  $\Delta m_{13}^2$ .

	Signal $\Delta m_{13}^2 = 2.5 \cdot 10^{-3} \text{ eV}^2$	Signal $\Delta m_{13}^2 = 3.0 \cdot 10^{-3} \text{ eV}^2$	Bckg
$\tau \rightarrow \mu$	2.9	4.2	0.17
$\tau \rightarrow e$	3.5	5.0	0.17
$\tau \rightarrow h$	3.1	4.4	0.24
$\tau \rightarrow 3h$	0.9	1.3	0.17
<i>ALL</i>	10.4	15.0	0.76

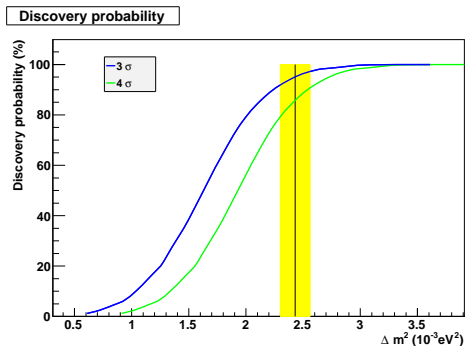


Table 1: See text. The shaded band in the plot marks the region indicated by global analysis after the recent MINOS determination.

The OPERA proposal dates back to 2000, construction started in mid-2003 and the electronics part was completed by the first half of 2007. Detector filling with bricks started in 2007 and was completed by mid-2008.

## 2 Data taking and results

A summary of the first data taking of OPERA is shown in Table 2.

Period	$(10^{18} \text{ p.o.t.})$	Filling	Events (target/external)	Comment
17-30 Aug 2006	0.76	0	0/319	elect. det. commissioning
Oct 2006	0.06	0.1%	0/29	final commissioning
Oct 2007	0.79	40%	38/331	first events in emulsions
Jul-Oct 2008	$\sim 10$	100%	$\sim 1000/3500$	regular running

Table 2: Data taking phases and collected statistics. Full details are given in the text.

The first CNGS technical run started in August 2006. Since brick filling had not started yet, this run was dedicated to the commissioning of the electronic detectors and to alignment and reconstruction algorithms tuning. A sample of 319 neutrino-induced events was collected coming from interactions in the rock surrounding the detector, in the spectrometers and in the target walls. Fine-tuning of the synchronization between CERN and Gran Sasso, performed using GPS clocks, was also possible. The beam spill timing structure composed by two  $10.5 \mu\text{s}$  wide bunches separated by 50 ms could be clearly observed. The zenith-angle distribution of the muon tracks associated to beam  $\nu_\mu$  interactions in the rock was measured to be centered at  $3.4 \pm 0.3(\text{stat.})^\circ$ , in agreement with the value of  $3.3^\circ$  expected from geodesy. Finally, using a Monte Carlo simulation tuned on data from the MACRO experiment, angular shape and absolute normalization of cosmic muons could be reproduced [4].

In October 2006, a new run began but was shortly interrupted ( $0.06 \cdot 10^{18} \text{ p.o.t.}$ ) due to a leak in the closed water cooling system of the reflector in the neutrino beam line.

After repair, a new physics run was possible in October 2007, when OPERA had 40% of the target mass installed (about 550 tons). The beam extraction intensity was limited to 70% of the nominal value due to beam losses which brought severe radiation damage to the CNGS ventilation control electronics. In about 4 days of continuous data taking,  $0.79 \cdot 10^{18} \text{ p.o.t.}$  were delivered and 38 neutrino interactions in the OPERA target were triggered by the electronic detectors with an expectation of  $31.5 \pm 6$ . Out of these 29 had charged-current and 9 neutral-current topology. Out-of-target interactions amounted to 331 events to be compared with an expectation of 303.

The 2007 run provided the opportunity for the first test on real neutrino interactions for the complex chain of brick location, validation, handling, emulsion gridding, development and finally automatic scanning.

The essential interplay between electronic detectors and emulsions could also be carefully tested profiting of this initial sample. Position of bricks obtained from

extensive alignment measurements and mechanical model of structure deformation allowed an effective brick finding of  $80 \pm 7\%$ . Wall finding efficiency was greater than 95% despite the frequent emission of low momentum back-scattered charged particles.

A key tool for brick finding is the Changeable Sheet doublet (CS)[5], consisting of a pair of emulsion films hosted in a box placed outside the brick which acts as an interface between the brick and the electronic target tracker.

The positive finding of tracks compatible with the electronic detector predictions in the CS doublet validates the brick finding algorithm prediction. Following the need for high purity, before installation the CS emulsions underwent a specific treatment called “refreshing” (a period during which storage in a high humidity and temperature environment is applied which allows to “erase” previously recorded tracks). The CS refreshing and assembling of the doublets was done underground to avoid contamination from cosmic tracks<sup>2</sup>. In case of positive validation by the CS the brick is brought to surface and exposed to cosmic rays<sup>3</sup> before development for plate-to-plate fine alignment. Before detaching the CS from the brick, they are exposed to four thin X-ray beams, in order to define their relative alignment.

Among the 38 bricks, 36 had a good CS tagging. The measured residuals between electronic detectors predictions and CS tracks were found to be of the order of a few cm. CS to brick connection was achieved with  $54 \mu\text{m}$  and 9 mrad position and slope accuracy.

The emulsions of the selected bricks were sent to the various automated scanning microscopes spread throughout Europe and Japan (about 40). All the tracks located in the CS were subsequently followed upstream inside the brick (scan-back) up to a “stopping point”. A general scanning (no angular preselection) was subsequently performed in a volume around the stopping point(s) in order to reconstruct the vertex topology. The mechanical accuracy obtained during the brick piling is in the range of  $50\text{-}100 \mu\text{m}$ . The reconstruction of cosmic rays passing through the whole brick allows to improve the definition of a global reference frame, leading the precision to about  $1\text{-}2 \mu\text{m}$ . The technique of marking emulsions with thin lateral X beams to get fast alignment pattern to be used in tracks scan-back and CS internal alignment with Compton tracks have been also successfully applied [5].

In Figure 1 the display of two  $\nu_\mu^{CC}$  vertices reconstructed in the brick is shown. The first one is an interaction with 6-prongs and an electromagnetic shower pointing to the primary interaction vertex. In the second 4-prong vertex a decay of  $\pi^0 \rightarrow \gamma(\rightarrow e^+e^-)\gamma(\rightarrow e^+e^-)$  has been fully reconstructed (with a thickness of 7.8 cm a

---

<sup>2</sup>Refreshing was indeed performed for all emulsions underground (Tono mine) in Japan before their shipment to Italy but, in the case of the large sample of brick emulsions, it was not repeated in Gran Sasso. This was a viable strategy thanks to the fact that the presence of tracks recorded during transportation can be easily dealt with in this case.

<sup>3</sup>This is done in a dedicated area with a properly designed shielding which is intended to suppress the low energy component.

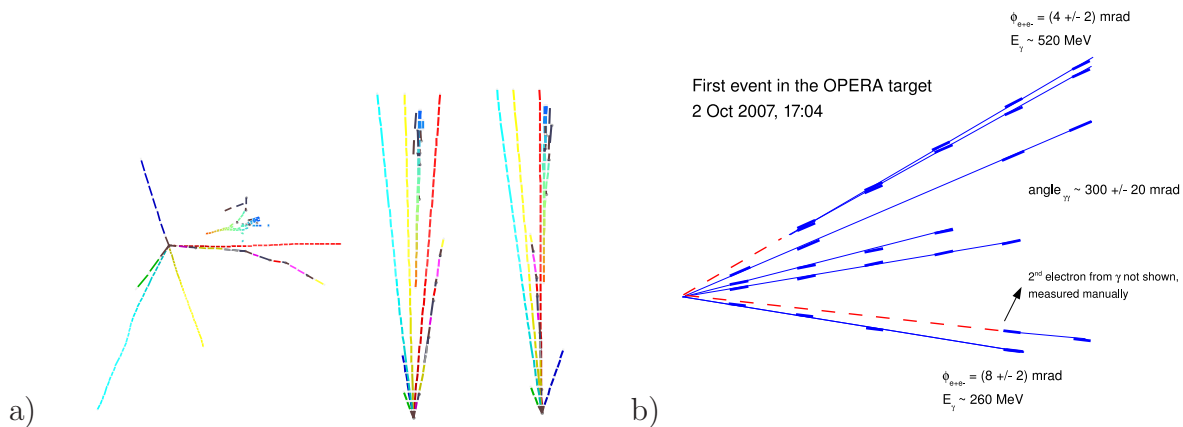


Figure 1: Displays of two  $\nu_\mu^{CC}$  neutrino vertices from the 2007 run reconstructed in the brick. Segments represent emulsion tracks ( $\sim 300 \mu\text{m}$  thick), gaps are due to 1 mm thick lead plates. a) the frontal and two orthogonal lateral views are shown. b) thick dashed lines represent the trajectory of  $\gamma$ s before conversion.

brick amounts to about  $10 X_0$ ). The kinematic analysis leads to an invariant mass measurement  $m_{\gamma\gamma} = (110 \pm 30)$  MeV.

Figure 2 shows the first observed charm candidate. A single prong decay topology is visible. The measured kink decay angle is 0.204 rad and the decay length is 3247  $\mu\text{m}$ . The estimated momentum of the daughter track is  $3.9^{+1.7}_{-0.9}$  GeV ( $p_T = 0.796$  GeV). The muon measured by electronic detectors is unambiguously matched to the primary vertex and lies in a back-to-back configuration in the transverse plane (not shown) with respect to the charmed hadron candidate and fragmentation tracks as expected. An electromagnetic shower is also visible in the display. The observation of one candidate in the sample is statistically in agreement with expectations.

For some selected events tracks from primary vertices were also measured in the adjacent downstream brick thus validating the connection procedure which is of great importance when a detailed kinematic reconstruction of the event is required (mainly through momentum measurement by multiple Coulomb scattering).

### 3 Conclusion and future perspectives

A major revision of the CNGS project has been taken in the beginning of 2008 in order to improve the radiation shielding of the electronics and reduce the beam losses. Meanwhile the OPERA target has been completed by early July 2008 in correspondence with the start of a new long run of CNGS beam. On 1st of October 2008,  $1.0 \cdot 10^{19}$  p.o.t. have been integrated. Analysis is in progress at the time of

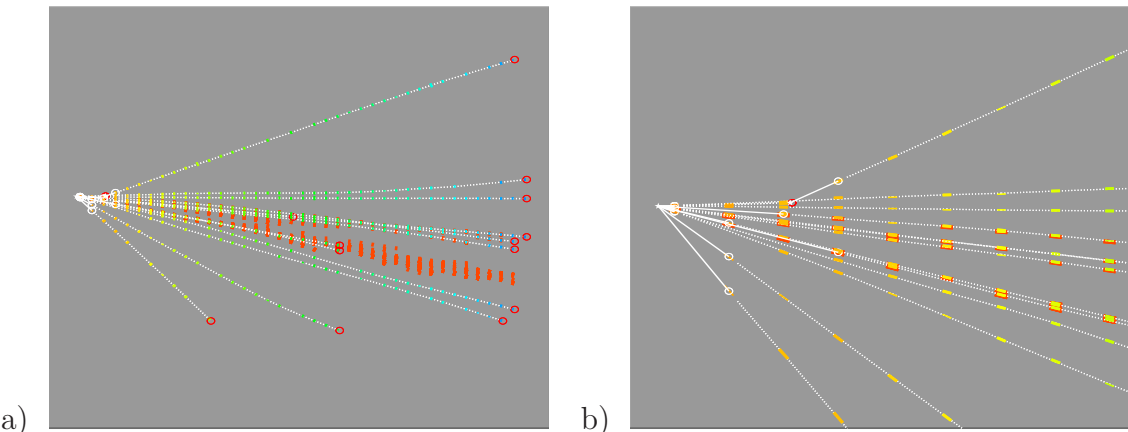


Figure 2: Displays of a charm candidate neutrino vertex in the brick from the 2007 run. Segments represent emulsion tracks ( $\sim 300 \mu\text{m}$  thick), gaps are due to 1 mm thick lead plates. a) the full brick infomation. b) a zoomed view in the primary vertex region.

writing. The collected sample amounts to about 1000 neutrino interactions of which 750 are expected to be  $\nu_\mu^{CC}$  events, 225  $\nu_\mu^{NC}$  events, 42 charm decays, 6  $\nu_e$  or  $\bar{\nu}_e$  events and 0.5  $\nu_\tau$  events.

The concept of the OPERA experiment has been experimentally validated by measuring neutrino events in the detector. Using the charm sample the capability to efficiently reconstruct  $\tau$  decays will be fully exploited. With some dose of luck the first  $\tau$  candidate event could be observed in the data from the current 2008 run.

## References

- [1] M. Guler et al., CERN/SPSC 2000-028, SPSC/P318, LNGS P25/2000, Jul. 2000  
“An appearance experiment to search for oscillations in the CNGS beam”,
- [2] Y. Fukuda et al., Phys. Rev. Lett. 81, 1562 (1998)
- [3] <http://proj-cngs.web.cern.ch/proj-cngs> G. Acquispace at al., CERN-98-02 (1998) R. Bailey et al., CERN-SL/99-034 (1999) A. E. Ball et al., CERN-SL/Note-2000-063 (2000)
- [4] R. Acquaferda et al., “The OPERA 2006 run”, New J. Phys. **8**, 303 (2006).
- [5] A. Anokhina et al, “Emulsion sheet doublets as interface trackers for the OPERA experiment”. JINST 3:P07005, 2008, arXiv:0804.1985v1.

# Heavy Flavour and Strange Particle Physics

Session Convener: *Jean-Marie Brom*  
Session Convener: *Franco L. Fabbri*  
Session Convener: *Sergio Ratti*  
Session Convener: *Gianpaolo Bellini*

*B* decay and *CP* violation: CKM angles and sides  
at the BABAR and BELLE *B*-Factories *Marc Verderi*

New Physics Effects in *B* Decays *Yuan Chao*

Heavy *B* Hadrons *Stefano Giagu*

The Charm Renaissance: D-physics –  
a Selective Review *Guy Wilkinson*

$D^0 - \bar{D}^0$  Mixing: An Overview *Jörg Marks*

Strange Quark Physics at Sixty-Four *Bradley Cox*

Measurement of  $K^+ \rightarrow \pi^+ \nu \bar{\nu}$  at NA62 experiment *Spasimir Balev*

$|V_{us}|$  from kaon decays with the KLOE detector *Mario Antonelli*

Early physics with the LHCb detector *Dirk Wiedner*

# *B* decay and *CP* violation: CKM angles and sides at the BABAR and BELLE *B*-Factories

*Marc Verderi*

*LLR Ecole polytechnique/IN2P3-CNRS*

*Route de Saclay*

*91128 Palaiseau, FRANCE*

## 1 The CKM matrix and Unitarity Triangle

In the Standard Model (SM), the Cabibbo-Kobayashi-Maskawa (CKM) [1] matrix represents the coupling of the  $u, c, t$  up-quarks to the  $d, s, b$  down-quarks in the charged current interactions. It is a  $3 \times 3$  unitarity matrix that can be parameterized by three mixing angles and one *CP*-violating phase, which is the only source of *CP* violation in the SM. The popular Wolfenstein parameterization [2] expresses the CKM matrix in term of the  $\lambda \simeq 0.22$ ,  $A \simeq 0.83$ ,  $\rho$  and  $\eta$  parameters and reflects the matrix hierarchy by a development in power of  $\lambda$ . The parameters  $\rho$  and  $\eta$  describe the *CP* violation,  $\eta$  being the *CP*-violating phase. In this representation<sup>1</sup> the CKM angles are carried by the  $V_{td} = |V_{td}|e^{-i\beta} = A\lambda^3(1 - \rho - i\eta)$  and  $V_{ub} = |V_{ub}|e^{-i\gamma} = A\lambda^3(\rho - i\eta)$  elements, the third angle being  $\alpha = \pi - \beta - \gamma$ .

The Unitarity Triangle (UT) depicts the unitarity condition of the CKM matrix between the first and third columns, namely  $V_{ud}V_{ub}^* + V_{cd}V_{cb}^* + V_{td}V_{tb}^* = 0$ , by a triangle in the complex plane, which apex is  $\rho + i\eta$  and which angles are the previously mentionned  $\alpha(\phi_2)$ ,  $\beta(\phi_1)$ ,  $\gamma(\phi_3)$  angles in the BABAR(BELLE) convention. As all terms in the above sum are of the order  $\lambda^3$ , the UT angles are sizeable.

The sides of the UT are measureable with non-*CP* violating processes, as semileptonic  $B$  decays, or  $B^0\overline{B}^0$  mixing frequency. The angles are measured with *CP* violating processes, like  $B^0 \rightarrow J/\Psi K_S^0$ . The  $\alpha$  and  $\beta$  angles are measured with decays of neutral  $B$  mesons as they undergo  $B^0\overline{B}^0$  mixing which is sensitive to the phase of the (off-shell)  $t$ -quark related  $V_{td}$  through box diagrams. The angle  $\gamma$  can be measured with neutral and charged  $B$  meson decays.

There are three types of *CP* violation (CPV). The first one, so-called “direct” CPV, results from the difference between the amplitudes for a process  $B \rightarrow f$  and its

---

<sup>1</sup>Note that the relative phase between CKM elements does not depend on the matrix representation.

conjugate  $\overline{B} \rightarrow \overline{f}$ . It is possible for both neutral and charged  $B$  meson decays, and is the only possible CPV for charged  $B$  meson decays.

The second type of CPV is in mixing and results from  $\langle B^0 | \overline{B}^0 \rangle \neq \langle \overline{B}^0 | B^0 \rangle$ . With  $|B^0\rangle$  and  $|\overline{B}^0\rangle$  being the  $CP$ -eigenstates, the mass eigenstates  $|B_L\rangle$  and  $|B_H\rangle$  are given by the linear relations  $|B_L\rangle = p|B^0\rangle + q|\overline{B}^0\rangle$  and  $|B_H\rangle = p|B^0\rangle - q|\overline{B}^0\rangle$  where  $p$  and  $q$  are complex coefficients. In the SM, the CPV in mixing is expected to be small with  $|p/q|$  departing from 1 at the  $\sim 10^{-3}$  level, close to present experimental limits.

The last type of CPV happens in interference between mixing and decay. When a same final state,  $f_{CP}$ , with  $CP$ -eigenstate value  $\eta_{f_{CP}}$ , can be reached by both  $B^0$  and  $\overline{B}^0$  mesons, the total amplitude for  $B^0 \rightarrow f_{CP}$  is the sum of the direct amplitude  $A_{CP}(B^0 \rightarrow f_{CP})$  and the amplitude  $A_{mix}(B^0 \rightarrow \overline{B}^0) \times \overline{A}_{CP}(\overline{B}^0 \rightarrow f_{CP})$  for a  $B^0$  to oscillate to a  $\overline{B}^0$  and then to decay to  $f_{CP}$ . With  $\Gamma(B^0(\Delta t) \rightarrow f_{CP})$  (resp.  $\Gamma(\overline{B}^0(\Delta t) \rightarrow f_{CP})$ ) being the decay rate for a  $B$  meson of known flavor  $B^0$  (resp.  $\overline{B}^0$ ) at  $\Delta t = 0$ , to decay to  $f_{CP}$  at  $\Delta t$ , the time-dependent asymmetry  $A_{f_{CP}}(\Delta t) \equiv \frac{\Gamma(B^0(\Delta t) \rightarrow f_{CP}) - \Gamma(\overline{B}^0(\Delta t) \rightarrow f_{CP})}{\Gamma(B^0(\Delta t) \rightarrow f_{CP}) + \Gamma(\overline{B}^0(\Delta t) \rightarrow f_{CP})} = S_{f_{CP}} \sin(\Delta m_{B^0} \Delta t) - C_{f_{CP}} \cos(\Delta m_{B^0} \Delta t)$ , where  $\Delta m_{B^0}$  is the mass difference of the neutral  $B$  meson mass eigenstates, allows to measure the coefficients  $C_{f_{CP}} \equiv \frac{1 - |\lambda_{f_{CP}}|^2}{1 + |\lambda_{f_{CP}}|^2}$ , and  $S_{f_{CP}} \equiv \frac{2 \Im m(\lambda_{f_{CP}})}{1 + |\lambda_{f_{CP}}|^2}$  which are functions of the parameter  $\lambda_{f_{CP}} \equiv \eta_{f_{CP}} \frac{p}{q} \frac{\overline{A}_{CP}}{A_{CP}}$ . A non-zero value for  $C_{f_{CP}}$  signs a direct CPV. Even in the absence of such direct CPV, the asymmetry can be non-zero, as  $S_{f_{CP}}$  is sensitive to the phase of  $\lambda_{f_{CP}}$ . This is notably the case for  $B^0 \rightarrow J/\Psi K_S^0$ .

The  $B$ -Factories design, with a boost of the  $e^+e^- \rightarrow \Upsilon(4S) \rightarrow B\overline{B}$  system along the  $z$  axis, allows to measure  $\Delta t \simeq \Delta z / \langle \beta \gamma \rangle c$  by measuring the distance  $\Delta z$  between the two  $B$  decay vertices,  $\beta$  and  $\gamma$  being the boost parameters (not to be confused with the  $CP$  angles...). The beam energies are  $E_{beam}^{e^-} = 9$  GeV and  $E_{beam}^{e^+} = 3.1$  GeV for BABAR and  $E_{beam}^{e^-} = 8$  GeV and  $E_{beam}^{e^+} = 3.5$  GeV for BELLE. The initial  $B^0$  or  $\overline{B}^0$   $CP$ -flavor of the  $B$  meson decaying to a  $CP$  final state,  $B_{CP}$ , is inferred by a semi-inclusive reconstruction and analysis of the decay products of the other  $B$  meson,  $B_{tag}$ , as follows. The decay time of  $B_{tag}$  defines  $\Delta t = 0$ . At this time, by total antisymmetry of the  $B\overline{B}$  system from the  $1^{--} \Upsilon(4S)$  decay,  $B_{CP}$  is in a pure  $CP$  state, opposite to that of  $B_{tag}$ . The performances of the tagging and vertexing algorithms are determined on large samples of  $B\overline{B}$  events with a self-tagging  $B$  decay meson which is used in place of the  $B_{CP}$  meson. The typical resolution on  $\Delta z$  is about  $170\mu\text{m}$ , largely dominated by the vertex resolution of the semi-inclusive reconstruction of the  $B_{tag}$ , for an average  $\Delta z$  of about  $260\mu\text{m}$ . The effective tagging efficiency  $\epsilon(1 - 2w)^2$ , that includes tagging efficiency  $\epsilon$  and mistag fraction  $w$ , is at the 30% level.

## 2 UT Side Measurements

Measurement of  $|V_{ub}|$  and  $|V_{cb}|$  using semi-leptonic decays is simple at the first sight only. The tree-level quark decay is a short distance process, which properties depend directly on  $|V_{q(=u,c)b}|$  and  $m_b$  in perturbative regime. However, because of quarks binding by soft gluons, non-perturbative long distance interactions of the  $b$  quark with light quarks arise. Two approaches are used. Measurements of inclusive final states  $B \rightarrow X_{q=u,c} l \nu$  experimentally access part of the full phase space, and extrapolation by theory from this experimental to the full phase space is needed. Exclusive measurements  $B \rightarrow \pi, \rho, \dots l \nu$  rely on theory to predict the form factor that enters the decay rate.

The perturbative and non-perturbative corrections that enter the inclusive decay rate  $\Gamma(B \rightarrow X_{qb} l \nu) = \frac{G_F^2 m_b^5}{192\pi^3} |V_{qb}|^2 [[1 + A_{EW}] A_{pert.} A_{nonpert.}]$  are computed as  $\alpha_S$  and  $(1/m_b)$  expansions, respectively. The non-perturbative parameters have to be measured, and depend on the  $m_b$  definition. They can be extracted from the moments  $\langle E_l^n \rangle_{E>E_{cut}} \equiv \frac{1}{\Gamma_q} \int (E_l - \langle E_l \rangle)^n \frac{d\Gamma_q}{dE_l} dE_l$  and  $\langle m_X^n \rangle_{E>E_{cut}} \equiv \frac{1}{\Gamma_q} \int m_X^n \frac{d\Gamma_q}{dm_X} dm_X$  of the lepton energy and hadronic mass spectra, with integration above a minimum lepton energy  $E_{cut}$ . The “kinetic” [3] and “1S” [4] frameworks, based on Heavy Quark Expansion (HQE) and Operator Product Expansion (OPE) provide calculations.

Experimentally, beyond the reconstruction used on the  $B$  signal side, additional criteria can be applied to the other  $B$  meson,  $B_{tag}$ , which allows some trade-off between efficiency and purity. The  $B_{tag}$  can simply be unused, leading to an “Untagged” analysis, or a “Semileptonic tag” can be used, with partial reconstruction of  $B \rightarrow D^{(*)} l \nu$ , or an “Hadronic tag” can be required, with full reconstruction of  $B \rightarrow D^{(*)} \pi/K$ . This last case allows to reconstruct the full kinematics—as the missing neutrino momentum on the signal side can be estimated— $B$  charge and flavor.

### 2.1 $V_{cb}$ inclusive and exclusive

On a sample of 232M  $B\bar{B}$  events sample, BABAR has measured in an inclusive analysis with hadronic tag, the hadronic mass moments  $\langle m_X^k \rangle$ ,  $k = 1, \dots, 6$  and the mixed hadronic energy-mass moments  $\langle n_X^k \rangle$ ,  $k = 2, 4, 6$ ,  $n_X^2 \equiv m_X^2 2c^4 - 2\bar{\Lambda}E_X + \bar{\Lambda}^2$ ,  $\bar{\Lambda} = 0.65$  GeV, for minimal lepton momenta ranging from 0.8 to 1.9 GeV/c [5]. The  $\langle n_X^k \rangle$  moments allow a more reliable extraction of higher-order HQE parameters. The moments are combined in the fit in the “Kinetic” scheme with lepton-energy moments from [6] and photon-energy moments from  $B \rightarrow X_s \gamma$  [7]. This yields to  $|V_{cb}| = (41.88 \pm 0.44_{exp} \pm 0.35_{theo} \pm 0.59_{\Gamma_{SL}}) \times 10^{-3}$  and  $m_b = 4.552 \pm 0.038_{exp} \pm 0.040_{theo}$  GeV, together with a set of non-perturbative parameters. This determines  $|V_{cb}|$  up to a 2% precision.

A recent exclusive measurement of  $V_{cb}$  has been done by BABAR [8] on a sample of 226M  $B\bar{B}$  events with  $B^- \rightarrow D^* e^- \bar{\nu}$ ,  $D^* \rightarrow D^0 \pi^0$ . The differential decay rate  $\frac{d\Gamma}{dw}$ ,

where  $w$  is the dot product of the  $B$  and  $D^*$  four velocities, is measured in order to fit for heavy quark effective QCD correction parameters. One of the parameter,  $\rho_{A_1}^2$ , is uncertain with previous measurements with  $\bar{B}^0 \rightarrow D^{*+} l^- \bar{\nu}$ , and this measurement can help to clarify the situation. BABAR measures  $BR(B^- \rightarrow D^{*0} e^- \bar{\nu}_e) = (5.56 \pm 0.08 \pm 0.41)\%$ ,  $\rho_{A_1}^2 = 1.16 \pm 0.06 \pm 0.08$  –in the center of the range obtained with neutral  $B$  decays– and  $F(1).|V_{cb}| = (35.9 \pm 0.6 \pm 1.4) \times 10^{-3}$ , which, using  $F(1) = 0.919 \pm 0.033$  from Lattice QCD [9], leads to  $|V_{cb}| = (39.0 \pm 0.6 \pm 2.0) \times 10^{-3}$ .

The BELLE [10] and BABAR [11] experiments have measured the  $B \rightarrow D^{**} l \bar{\nu}$  branching ratio as the pollution from this channel is a source of systematic uncertainty in  $|V_{cb}|$  analyses. They both use an hadronic tag for a full  $B$  signal reconstruction. HQET predicts that the rate for the broad  $D_0^*$  channel is  $\sim \frac{1}{10}$  of the narrow  $D_2^*$  narrow. On a 657M  $B\bar{B}$  events sample, BELLE [10] disproves this expectation measuring e.g.  $BR(B^+ \rightarrow \bar{D}_0^{*0} l^+ \nu) = (0.24 \pm 0.04 \pm 0.06)\%$  and  $BR(B^+ \rightarrow \bar{D}_2^{*0} l^+ \nu) = (0.22 \pm 0.03 \pm 0.04)\%$ , which is the first observation of this decay mode.

## 2.2 $V_{ub}$ inclusive and exclusive

The measurement of the inclusive  $B \rightarrow X_u l \bar{\nu}$  decay is complicated by the high background from  $B \rightarrow X_c l \bar{\nu}$  decay which has a rate  $\sim 50$  higher. Taking advantage of  $m_u \ll m_c$ ,  $B \rightarrow X_u l \bar{\nu}$  analyses select regions of phase space free from  $B \rightarrow X_c l \bar{\nu}$  background. This however happens in regions where non-perturbative effects are important. These are related to the “Fermi motion”, i.e.  $b$ -quark motion inside the meson, which is parameterized as a “Shape Function” (SF), extracted from the  $\gamma$  energy spectrum of  $B \rightarrow X_s \gamma$ .

With an hadronic tag technique, and using the  $u$ - wrt  $c$ -quark discriminating variables  $M_X$ , hadronic mass system,  $q^2$ , lepton-neutrino system mass squared, and  $P_+ \equiv E_X - |\vec{P}_X|$ , with the hadronic energy  $E_X$  and momentum  $\vec{P}_X$  calculated in the  $B$  rest frame, BELLE [12] measures on a 275M  $B\bar{B}$  event samples  $|V_{ub}| = (4.09 \pm 0.19_{exp} \pm 0.20_{syst} {}^{+0.14}_{-0.15} {}^{theo} \pm 0.18_{SF})^{-3}$ . BABAR [13] has performed a similar analysis and provide a series of  $|V_{ub}|$  measurements for various theoretical calculations.

A possible systematic uncertainty is due to the weak annihilation (WA) as this process could enhance the decay rate near the endpoint, where the  $|V_{ub}|$  measurement is done. WA may happen for charged  $B$  mesons only. BABAR has compared the partial decay rates of  $B^0 \rightarrow X_u l \bar{\nu}$  and  $B^+ \rightarrow X_u l \bar{\nu}$  in the 2.3–2.6 GeV/ $c$  of the lepton momentum range [14]. Measuring the ratio  $R^{+/0} = 1.18 \pm 0.35_{stat.} \pm 0.17_{syst.}$ , compatible with one, BABAR does not spot significant WA contribution.

Exclusive  $|V_{ub}|$  measurements have been performed by the  $B$ -Factories, with an untagged analysis of  $B \rightarrow \pi l \bar{\nu}$  by BABAR [15] on a 227M  $B\bar{B}$  events sample and a  $D^* l \bar{\nu}$  tag analysis of  $B \rightarrow \pi l \bar{\nu}$  and  $B \rightarrow \rho l \bar{\nu}$  on a 275M  $B\bar{B}$  data sample by

Table 1: BABAR [17] and BELLE [19] results for  $\sin 2\beta (= \sin 2\phi_1)$ ,  $|\lambda|$  and  $A (= -C_{f_{CP}})$ .

<i>BABAR</i>		<i>BELLE</i>	
$\sin 2\beta$	$0.714 \pm 0.032_{stat} \pm 0.018_{syst}$	$\sin 2\phi_1$	$+0.650 \pm 0.029_{stat} \pm 0.018_{syst}$
$ \lambda $	$0.952 \pm 0.022_{stat} \pm 0.017_{syst}$	$A (= -C_{f_{CP}})$	$-0.019 \pm 0.020_{stat} \pm 0.015_{syst}$

BELLE [16]. Recent unquenched lattice QCD results for the form factors are used.

### 2.3 $|V_{td}/V_{ts}|$ from $B_d$ and $B_s$ mixing

An important result, coming from the Tevatron, is  $|V_{td}/V_{ts}|$  with  $B_s$  mixing. The D0 and CDF collaborations have searched for the  $B_s$  oscillation with a 5 standard deviations observation for CDF on the Run II data. The neutral  $B_{q=d,s}$  meson oscillation frequency is related to the mass difference  $\Delta m_q = \frac{G_F^2 m_W^2 \eta S(x_t^2)}{6\pi^2} m_{B_q} f_{B_q}^2 B_{B_q} |V_{tq}^* V_{tb}|^2$ . The  $f_{B_q}$  form factors and  $B_{B_q}$  parameters are known to a  $\sim 15\%$  precision from Lattice calculations, leading to systematical uncertainty on  $V_{td}$ . The ratio  $\xi^2 = \frac{f_d^2 B_{B_d}}{f_s^2 B_{B_s}} = 1.210^{+0.047}_{-0.035}$  is however known to a 4% precision, making  $|V_{td}|/|V_{ts}|$  a more stringent constrain in the  $(\rho, \eta)$  plan than the individual  $|V_{td}|$  or  $|V_{ts}|$ .

Using an “amplitude scan” technique, events are fitted for  $\frac{1}{\tau} e^{-t/\tau} (1 \pm \mathcal{A} \cdot D \cos(\Delta m_s t))$  where the probe parameter  $\mathcal{A}$  becomes compatible with one when  $\Delta m_s$  takes one the correct value during the scan. The CDF result  $\Delta m_s = 17.77 \pm 0.10_{stat} \pm 0.07_{syst} \text{ ps}^{-1}$  leads to  $\left| \frac{V_{td}}{V_{ts}} \right| = 0.2060 \pm 0.0007_{exp}^{+0.0081}_{-0.0060} \text{ theo.}$

## 3 UT Angles Measurements

### 3.1 Measurement of $\beta/\phi_1$

The measurement of  $\beta$  consists in collecting the phase of the  $B^0 \bar{B}^0$  mixing amplitude. The angle  $\beta$  is by far the best measured angle of the UT, with the golden channel  $B^0 \rightarrow J/\Psi K_S^0$ . For this channel and related  $b \rightarrow c\bar{c}s$  quark level transition channels, we have  $\lambda_{f_{CP}} = \eta_{f_{CP}} \frac{q \bar{A}}{p A} = \eta_{f_{CP}} e^{-2i\beta}$ , leading to  $|\lambda_{f_{CP}}| = 1$ ,  $C_{f_{CP}} = 0$ ,  $S_{f_{CP}} = -\eta_{f_{CP}} \sin 2\beta$ . The uncertainty due to penguin pollution is expected to be at the  $\sim 1\%$  level.

The BABAR measurement on  $J/\Psi K_S^0, J/\Psi K^{*0}, \Psi(2S)K_S^0, J/\Psi K_L^0, \eta_c K_S^0, \chi_{c1} K_S^0$  channels on a 383M  $B\bar{B}$  sample is shown in table 1. On a 535M  $B\bar{B}$  event sample, BELLE measures for the  $J/\Psi K_S^0, J/\Psi K_L^0$  channels [18]  $\sin 2\phi_1 = 0.642 \pm 0.031_{stat} \pm 0.017_{syst}$ ,  $A (= -C_{f_{CP}}) = -0.018 \pm 0.021_{stat} \pm 0.014_{syst}$ . BELLE performs a new

measurement for  $\Psi(2S)K_S^0$  on a 657M  $B\bar{B}$  sample [19],  $\sin 2\phi_1 = +0.72 \pm 0.09_{stat} \pm 0.03_{syst}$ ,  $A = +0.04 \pm 0.07_{stat} \pm 0.05_{syst}$ , and provides the new average shown in table 1.

Constrain to the penguin pollution in  $J/\Psi K^0$  can be obtained by SU(3) studying the  $B^0 \rightarrow J/\Psi \pi^0$  channel. This is a  $b \rightarrow c\bar{c}d$  quark-level transition process which carries at the tree level the same weak phase than the  $J/\Psi K^0$  process. If a significant penguin pollution exists, the  $S_{f_{CP}}$  and  $C_{f_{CP}}$  parameters will differ from the expected the  $-\sin 2\beta$  and 0 values, respectively.

On a 466M  $B\bar{B}$  sample, BABAR measures the branching ratio and *CP* parameters [20]  $BR(J/\Psi \pi^0) = (1.60 \pm 0.14_{stat} \pm 0.07_{syst}) \times 10^{-5}$ ,  $S^{J/\Psi \pi^0} = -1.23 \pm 0.21_{stat} \pm 0.04_{syst}$ ,  $C^{J/\Psi \pi^0} = -0.20 \pm 0.19_{stat} \pm 0.03_{syst}$ , which is a  $4\sigma$  evidence for CPV. This is a new measurement. BELLE measures on a 535M  $B\bar{B}$  sample the *CP* parameters [21]  $S^{J/\Psi \pi^0} = -0.65 \pm 0.21_{stat} \pm 0.05_{syst}$ ,  $C^{J/\Psi \pi^0} = -0.08 \pm 0.16_{stat} \pm 0.05_{syst}$ . This is a  $2.4\sigma$  effect from 0 for  $S^{J/\Psi \pi^0}$ .

### 3.2 Measurement of $\alpha/\phi_2$

Significant complications arise in the case of the  $\alpha$  angle measurement because of penguin pollution. For the  $B^0 \rightarrow \pi^+\pi^-$  channel, a pure tree level process would carry a phase  $-2\beta$  from the  $B^0\bar{B}^0$  mixing and  $-2\gamma$  from the tree decay, leading to  $\lambda_{f_{CP}} = \eta_{f_{CP}} \frac{p \cdot \bar{A}}{q \cdot A} = \eta_{f_{CP}} e^{-2i\beta} e^{-2i\gamma} = \eta_{f_{CP}} e^{2i\alpha}$  and  $S_{f_{CP}} = -\eta_{f_{CP}} \sin 2\alpha$ ,  $C_{f_{CP}} = 0$ . The penguin pollution amplitude carries a different weak phase, and is at the 30 to 60% level of the tree amplitude. Denoting by  $T$  and  $P$  the tree and penguin amplitudes, respectively, and by  $\delta = \delta_P - \delta_T$  their relative strong phase, the *CP* parameters become  $\lambda_{f_{CP}} = \eta_{f_{CP}} e^{2i\alpha} \frac{T + Pe^{+i\gamma} e^{i\delta}}{T + Pe^{-i\gamma} e^{i\delta}} = \eta_{f_{CP}} |\lambda_{f_{CP}}| e^{2i\alpha_{eff}}$ ,  $S_{f_{CP}} = \eta_{f_{CP}} \sqrt{1 - C_{f_{CP}}^2} \sin 2\alpha_{eff}$ ,  $C_{f_{CP}} \propto \sin \delta$ . The measurement of the time-dependent asymmetry would only lead to a measurement of  $\alpha_{eff}$ . Extraction of  $\alpha$  from  $\alpha_{eff}$  is possible in principle (up to a 8-fold ambiguity) with an isospin analysis that compares the triangles formed by the amplitudes and by the conjugate amplitudes of  $B^+ \rightarrow h^+ h^0$ ,  $B^0 \rightarrow h^+ h^-$ ,  $h^0 h^0$  [22]. It requires a time-dependent analysis of  $B^0 \rightarrow h^0 h^0$ . Upper bounds on  $\sin^2(\alpha_{eff} - \alpha)$  can also be obtained and are interesting if  $BR(B^0 \rightarrow h^0 h^0)$  is small [23].

On a 383M  $B\bar{B}$  sample, BABAR extracts  $1139 \pm 49$   $B^0 \rightarrow \pi^+\pi^-$  events, and obtains the *CP* parameters  $S_{\pi^+\pi^-} = -0.60 \pm 0.11_{stat} \pm 0.03_{syst}$ ,  $C_{\pi^+\pi^-} = -0.21 \pm 0.09_{stat} \pm 0.02_{syst}$  [24]. BELLE obtains  $1464 \pm 65$  signal events out of a 535M  $B\bar{B}$  events sample and measures  $S_{\pi^+\pi^-} = -0.61 \pm 0.10_{stat} \pm 0.04_{syst}$ ,  $C_{\pi^+\pi^-} = -0.55 \pm 0.08_{stat} \pm 0.05_{syst}$  [25]. Both experiments observe a more than  $5\sigma$  effect on  $S_{\pi^+\pi^-}$ . This makes the CPV well established in this channel. The BABAR and BELLE measurements on  $C_{\pi^+\pi^-}$  differs today by  $2.1\sigma$ .

The *B*-Factories perform an isospin analysis to extract  $\alpha$ , using  $S_{\pi^+\pi^-}$ ,  $C_{\pi^+\pi^-}$ ,  $C_{\pi^0\pi^0}$ ,  $BF_{\pi^+\pi^-}$  and  $BF_{\pi^0\pi^0}$ . The parameter  $S_{\pi^0\pi^0}$  is not used as it would require a challenging time-dependent analysis of the  $B^0 \rightarrow \pi^0\pi^0$  channel. The confidence

Table 2: BABAR and BELLE results for  $B \rightarrow \rho\rho$  analyses. BABAR results for  $\rho^+\rho^-$  are obtained from a 383M  $B\bar{B}$  events sample [27]. The BELLE measurements are performed on 265 and 535M  $B\bar{B}$  event samples [28]. The BABAR analysis of  $B^0 \rightarrow \rho^0\rho^0$  is using a 427M  $B\bar{B}$  events sample. Limits from BELLE [30] for this channel are given in the text. The first error is statistical, the second one systematical.

	$B^0 \rightarrow \rho^+\rho^-$		$B^0 \rightarrow \rho^0\rho^0$
	BABAR	BELLE	BABAR
$BR \times 10^6$	$(25.5 \pm 2.1^{+3.6}_{-3.9})$	$(22.8 \pm 3.8^{+2.3}_{-2.6})$	$(0.84 \pm 0.29 \pm 0.17)$
$f_L$	$0.992 \pm 0.024^{+0.026}_{-0.013}$	$0.941^{+0.034}_{-0.040} \pm 0.30$	$0.70 \pm 0.14 \pm 0.05$
$C_L$	$+0.01 \pm 0.15 \pm 0.06$	$-0.16 \pm 0.21 \pm 0.08$	$+0.4 \pm 0.9 \pm 0.2$
$S_L$	$-0.17 \pm 0.20^{+0.05}_{-0.06}$	$+0.19 \pm 0.30 \pm 0.08$	$+0.5 \pm 0.9 \pm 0.2$

level (CL) curves obtained for  $\alpha$  show a series of ambiguities, as they must. Picking up the SM compatible solution, BABAR obtains  $\alpha = (96^{+11}_{-6})^\circ$  [26] and BELLE  $\alpha = (96 \pm 11)^\circ$  [25].

The *B*-Factories have studied the *CP* asymmetries of  $B^0 \rightarrow \rho^+\rho^-$ . The advantages of this channel are its large branching ratio and small penguin pollution. It is however an *a priori* non pure *CP* channel because of the vector-vector nature of its final state; but the longitudinal polarization fraction was found to be close to one, making this channel an almost pure *CP*-even final state. Experimental complications arise with the presence of two  $\pi^0$ 's in the final state, and because of the large  $\rho$  width. The BABAR and BELLE measurements for  $B^0 \rightarrow \rho^+\rho^-$  are shown in table 2.

In contrast with  $B^0 \rightarrow \pi^0\pi^0$ , the time-dependent analysis of the  $B^0 \rightarrow \rho^0\rho^0$  can be performed, as the  $\rho^0\rho^0$  vertex can be reconstructed. This allows for a full isospin analysis of  $B \rightarrow \rho\rho$ . A preliminary study of the time-dependent analysis of  $B^0 \rightarrow \rho^0\rho^0$  has been performed by BABAR (table 2). This is a new measurement. The low branching fraction indicates that the penguin pollution is small. The full isospin analysis favors  $\Delta\alpha = 11.3^\circ$ . BELLE has performed a new measurement of the  $B^0 \rightarrow \rho^0\rho^0$  branching fraction on a sample of 657M  $B\bar{B}$  events, and finds  $BR(\rho^0\rho^0) = (0.4 \pm 0.4_{stat} \pm 0.2_{syst}) \times 10^{-6}$ , which is turned into the limit  $BR(\rho^0\rho^0) < 1.0 \times 10^{-6}$  at 90% CL [30].

An other  $\alpha$  measurement is performed in a Dalitz analysis of the  $B^0 \rightarrow (\rho\pi)^0 \rightarrow \pi^+\pi^-\pi^0$  channel. Three amplitudes, namely  $B^0 \rightarrow \rho^+\pi^-$ ,  $B^0 \rightarrow \rho^-\pi^+$  and  $B^0 \rightarrow \rho^0\pi^0$  ones, contribute to the final state. Note that the dominant  $B^0 \rightarrow \rho^+\pi^-$  is not a *CP* eigenstate. An isospin analysis, as it requires the two additional amplitudes  $B^+ \rightarrow \rho^+\pi^0$  and  $B^+ \rightarrow \rho^0\pi^+$ , leads to a difficult isospin pentagone analysis. An

other approach was proposed by Snyder and Quinn [31], based on time-dependent Dalitz analysis, assuming isospin symmetry. The amplitude for  $B^0 \rightarrow \pi^+\pi^-\pi^0$ , and related charge conjugate amplitude, are described by

$$A(B^0 \rightarrow \pi^+\pi^-\pi^0) = f_+ A(\rho^+\pi^-) + f_- A(\rho^-\pi^+) + f_0 A(\rho^0\pi^0) \text{ and } \bar{A}(\bar{B}^0 \rightarrow \pi^+\pi^-\pi^0) = f_+ \bar{A}(\rho^+\pi^-) + f_- \bar{A}(\rho^-\pi^+) + f_0 \bar{A}(\rho^0\pi^0),$$

and, in the  $(\rho^-\pi^+, \rho^+\pi^-)$  masses square Dalitz plan, interferences at equal masses provide information on the strong phases between resonances.

On a 375M  $B\bar{B}$  events sample, BABAR [32] has performed a time-dependent Dalitz analysis of  $B^0 \rightarrow (\rho\pi)^0 \rightarrow \pi^+\pi^-\pi^0$ .  $2067 \pm 86$  signal events were found. BABAR measures  $\alpha = (87^{+45}_{-13})^\circ$  (with a mirror solution at  $\alpha + 180^\circ$ .) BELLE [33] has performed both the time-dependant Dalitz and isospin analyses on a 349M  $B\bar{B}$  events sample and obtain the range  $68^\circ < \alpha < 95^\circ$  at 68% CL.

Additional channels to measure  $\alpha$  are studied. The  $B^0 \rightarrow a_1\pi$  channel is considered by both the BABAR and BELLE experiments. It is similar to the  $B \rightarrow \rho\pi$  case as it is not a *CP* eigenstate, and as a quasi two-body approach has to be followed. A quite high branching fraction is measured by both BABAR,  $BR(B^0 \rightarrow a_1\pi) = (33.2 \pm 3.2_{stat} \pm 3.2_{syst}) \times 10^{-6}$  [34], and BELLE  $BR(B^0 \rightarrow a_1\pi) = (29.8 \pm 3.2_{stat} \pm 4.6_{syst}) \times 10^{-6}$  [35]. BABAR extracts  $\alpha_{eff}^{a_1\pi} = (78.6 \pm 7.3)^\circ$ . To further constrain  $\alpha - \alpha_{eff}$  by SU(3) symmetry ( $\pi \leftrightarrow K$ ,  $a_1 \leftrightarrow K_1$ ), studies of  $B \rightarrow a_1K$  are done. BABAR measures  $BR(B^0 \rightarrow a_1K^+) = (16.3 \pm 2.9_{stat} \pm 2.3_{syst}) \times 10^{-6}$  and  $BR(B^0 \rightarrow a_1K^0) = (34.9 \pm 5.0_{stat} \pm 4.4_{syst}) \times 10^{-6}$  [36].

### 3.3 Measurement of $\gamma/\phi_3$

Measurements of  $\gamma$  with charged  $B$  meson decays (no results with neutral  $B$  meson decays presented here) exploit the interferences between the color favored  $B^- \rightarrow K^{(*)-}D^{(*)0}$  and color suppressed  $B^- \rightarrow K^{(*)-}\bar{D}^{(*)0}$  amplitudes that arise when final states common to the  $D^{(*)0}$  and  $\bar{D}^{(*)0}$  mesons are selected. As no penguin pollution exists, these are theoretically clean measurements. The color favored and suppressed  $B$  decay amplitudes are respectively proportional to  $\lambda^3$  and  $\lambda^3 r_B^{(*)} e^{-i\gamma} e^{i\delta}$ , with  $\delta$  being their relative (unknown) strong phase, and  $r_B^{(*)}$  the critical ratio of the suppressed to favored amplitudes, which ranges from 0.1 to 0.2. The angle  $\gamma$  has to be determined together with previous parameters.

The three following methods are used [37]. The Gronau-London-Wyler (GLW) method considers  $D^0/\bar{D}^0$  *CP*-eigenstate final states with *CP*-even states like  $K^+K^-$ ,  $\pi^+\pi^-$ , or *CP*-odd states like  $K_S^0\pi^0$ ,  $K_S^0\omega$ ,  $K_S^0\phi$ . It is based on modes with branching ratio at the  $10^{-6}$  level. The Atwood-Dunietz-Soni (ADS) method considers the  $K^+\pi^-$  final state for the  $D^0/\bar{D}^0$  meson. By combining the favored  $B^- \rightarrow K^-D^0$  amplitude with the doubly-Cabbibbo suppressed  $D^0 \rightarrow K^+\pi^-$  one and the suppressed

Table 3: Updated BABAR measurements of GLW observables on a 383M  $B\bar{B}$  events sample. The  $D^*$  results are preliminary. Errors are statistical and systematical.

	$B^+ \rightarrow DK^+$	$B^+ \rightarrow D^*K^+$
$A_{CP+}$	$+0.27 \pm 0.09 \pm 0.04$	$-0.11 \pm 0.09 \pm 0.01$
$A_{CP-}$	$-0.09 \pm 0.09 \pm 0.02$	$+0.06 \pm 0.10 \pm 0.02$
$R_{CP+}$	$1.06 \pm 0.10 \pm 0.05$	$1.31 \pm 0.13 \pm 0.04$
$R_{CP-}$	$1.03 \pm 0.10 \pm 0.05$	$1.10 \pm 0.12 \pm 0.04$

$B^- \rightarrow K^- \overline{D}^0$  with the favored  $\overline{D}^0 \rightarrow K^+ \pi^-$  one, the ADS method is targeting large  $CP$  asymmetries. This is at the cost of branching ratios at the  $10^{-7}$  level. The Giri-Grossman-Soffer-Zupan (GGSZ) considers three-body final states like  $K_S^0 \pi^+ \pi^-$ ,  $K_S^0 K^+ K^-$ ,  $\pi^0 \pi^+ \pi^-$  and extracts parameters from a Dalitz analysis.

BABAR has provided updated results on the  $B^+ \rightarrow D^{(*)}K^+$  channels with the GLW method [38]. The GLW observables,  $R_{CP\pm} \equiv \frac{\Gamma(B^- \rightarrow D_{CP\pm}^0 K^-) + \Gamma(B^+ \rightarrow D_{CP\pm}^0 K^+)}{[\Gamma(B^- \rightarrow D^0 K^-) + \Gamma(B^+ \rightarrow \overline{D}^0 K^+)]/2} = 1 + r_B^2 \pm 2r_B \cos \delta \cos \gamma$ , and the asymmetry  $A_{CP\pm} \equiv \frac{\Gamma(B^- \rightarrow D_{CP\pm}^0 K^-) - \Gamma(B^+ \rightarrow D_{CP\pm}^0 K^+)}{\Gamma(B^- \rightarrow D_{CP\pm}^0 K^-) + \Gamma(B^+ \rightarrow D_{CP\pm}^0 K^+)} = \pm 2r_B \sin \delta \sin \gamma / R_{CP\pm}$ , with relation  $A_{CP+} R_{CP+} = -A_{CP-} R_{CP-}$ , provide a measurement of  $\gamma$ , but up to an eight-fold ambiguity. The BABAR results are shown in table 3. It can be seen that  $A_{CP+}$  for  $B^+ \rightarrow DK^+$  is  $2.8\sigma$  from no CPV. These results are consistent with  $\gamma = (67.6 \pm 4.0)^\circ$  from SM fit.

BELLE has provided updated results for  $B^+ \rightarrow DK^+$  with the ADS method, on a 657M  $B\bar{B}$  events sample [39]. The observables in the ADS method are  $R_{ADS} \equiv \frac{\Gamma(B \rightarrow D_{supp.} K)}{\Gamma(B \rightarrow D_{fav.} K)} = r_D^2 + r_B^2 + 2r_B r_D \cos \gamma \cos \delta$ ,  $A_{ADS} \equiv \frac{\Gamma(B^- \rightarrow D_{supp.} K^-) - \Gamma(B^+ \rightarrow D_{supp.} K^+)}{\Gamma(B^- \rightarrow D_{supp.} K^-) + \Gamma(B^+ \rightarrow D_{supp.} K^+)} = 2r_B r_D \sin \gamma \sin \delta / R_{ADS}$ , where  $\delta = \delta_B + \delta_D$  is the sum of the relative  $B$  and  $D$  strong phases. No significant signal is observed at this point in the suppressed mode, and BELLE provides the limits  $BR(B \rightarrow D_{supp.} K) < 2.8 \times 10^{-7}$  at 90% CL,  $r_B < 0.19$  at 90% CL.

In the GGSZ method, the  $CP \pm$  amplitudes,  $A_{\pm}(m_-^2, m_+^2)$ , describing the Dalitz plan with coordinates  $m_{\pm}^2 \equiv m^2(K_S^0 \pi^{\pm})$  or  $m^2(K_S^0 K^{\pm})$  or  $m^2(\pi^0 \pi^{\pm})$ , depending on the final state considered, are given by  $A_{\pm}(m_-^2, m_+^2) = |A(B^{\pm} \rightarrow \overline{D}^0/D^0 K^{\pm})| \times [A_D(m_{\pm}^2, m_{\mp}^2) + r_B e^{i\delta_B} e^{\pm i\gamma} A_D(m_{\mp}^2, m_{\pm}^2)]$ , where  $A_D$  is the amplitude for describing the  $D^0$  Dalitz plan. This method allows to extract  $\gamma$  and  $\delta_B$  up to the two-fold ambiguity  $(\gamma, \delta_B) \leftrightarrow (\gamma + \pi, \delta_B + \pi)$ .

Technically, the  $\gamma$ ,  $r_B$  and  $\delta_B$  parameters are extracted using the cartesian coordinates  $x_{\pm} \equiv \kappa r_B \cos(\delta_B \pm \gamma)$ ,  $y_{\pm} \equiv \kappa r_B \sin(\delta_B \pm \gamma)$ , which are Gaussian-behaving and

Table 4: BABAR [40] and BELLE [41] results for the GGSZ analysis obtained on samples of respectively 383 and 657M  $B\bar{B}$  events. Errors are statistical, systematical and, if present, due to the  $D$  Dalitz model.

	<i>BABAR</i>	
	$B^- \rightarrow DK^-$	$B^- \rightarrow D^*K^-$
$x_-, x_-^*$	$+0.090 \pm 0.043 \pm 0.015 \pm 0.011$	$-0.111 \pm 0.069 \pm 0.014 \pm 0.004$
$y_-, y_-^*$	$+0.053 \pm 0.056 \pm 0.007 \pm 0.015$	$-0.051 \pm 0.080 \pm 0.009 \pm 0.010$
$x_+, x_+^*$	$-0.067 \pm 0.043 \pm 0.014 \pm 0.011$	$+0.137 \pm 0.068 \pm 0.014 \pm 0.005$
$y_+, y_+^*$	$-0.015 \pm 0.055 \pm 0.006 \pm 0.008$	$+0.080 \pm 0.102 \pm 0.010 \pm 0.012$
$r_B$	$0.086 \pm 0.035$	$0.135 \pm 0.051$
	<i>BELLE</i>	
$x_-, x_-^*$	$+0.105 \pm 0.047 \pm 0.011$	$+0.024 \pm 0.140 \pm 0.018$
$y_-, y_-^*$	$+0.177 \pm 0.060 \pm 0.018$	$-0.243 \pm 0.137 \pm 0.022$
$x_+, x_+^*$	$-0.107 \pm 0.043 \pm 0.011$	$+0.133 \pm 0.083 \pm 0.018$
$y_+, y_+^*$	$-0.067 \pm 0.059 \pm 0.018$	$+0.130 \pm 0.120 \pm 0.022$
$r_B$	$0.16 \pm 0.04$	$0.21 \pm 0.08$
	$B^- \rightarrow DK^{*-}(\text{BABAR})$	
$x_{s-}, x_{s+}$	$+0.115 \pm 0.138 \pm 0.039 \pm 0.014$	$-0.113 \pm 0.107 \pm 0.028 \pm 0.018$
$y_{s-}, y_{s+}$	$+0.226 \pm 0.142 \pm 0.058 \pm 0.011$	$+0.125 \pm 0.139 \pm 0.051 \pm 0.010$
$\kappa r_s$	$0.163^{+0.088}_{-0.105}$	
	<i>BABAR</i>	<i>BELLE</i>
$\gamma$	$(76 \pm 22 \pm 5 \pm 5)^\circ$	$(76^{+12}_{-13} \pm 4 \pm 9)^\circ$

make the likelihood unbiased. The total decay rate to fit for, is then  $\Gamma_\pm(m_+^2, m_-^2) \propto |A_{D^\pm}|^2 + r_B^2 |A_{D^\mp}|^2 + 2\eta (x_\pm \Re e[A_{D^\pm} A_{D^m p}^*] + y_\pm \Im m[A_{D^\pm} A_{D^m p}^*] +)$  where  $\kappa$  accounts for the  $K^*$  width and  $\eta$  for the parity of  $D^{*0} \rightarrow D^0 \gamma$  wrt  $D^0 \pi^0$ .

An accurate description of the  $D^0$  Dalitz plan is needed. High statistics samples of  $D^{*+} \rightarrow D^0 \pi^+$  are used, tagging the  $D^0/\bar{D}^0$  flavor with the companion pion charge. Updated parameterizations from BABAR and BELLE are detailed in [40, 41] for the  $D^0 \rightarrow K_S^0 \pi^+ \pi^-$  decay, and from BABAR for  $D^0 \rightarrow K_S^0 K^+ K^-$ . Parameterizations are based an isobar approach consisting of a coherent sum of two-body amplitudes and non-resonant contributions.

The BABAR and BELLE results are shown in table 4, and  $3\sigma$  and  $3.5\sigma$  evidences for direct CPV are observed, respectively. It can be noticed that statistical errors on  $\gamma$  are significantly lower for BELLE than for BABAR, despite similar precision on the  $x_\pm^{(*)}, y_\pm^{(*)}$  quantities. This is due to the larger  $r_B^{(*)}$  values obtained by BELLE.

## 4 Conclusion

A remarkable success has been achieved by the  $B$ -Factories, going beyond expectation in some field, like the measurement of  $\gamma$ . BABAR has now finished its data taking, leaving BELLE alone in the “race”, but still many analyses are going on.

The CKM UT is constrained by both measurements of  $CP$ -conserving and  $CP$ -violating quantities, leading to a picture of the CKM sector consistent with the SM. Measurements of semi-leptonic decays benefit from improving experimental techniques and more precise theoretical computations. The angle  $\beta$  is a precision measurement, reaching accuracy of SM calculation. The angle  $\alpha$  will ultimately be limited by penguin pollution. The measurement of  $\gamma$  is reaching the  $13^\circ$  precision.

## References

- [1] M. Kobayashi and T. Maskawa, *Prog. Theor. Phys.* **49**, 652 (1973).
- [2] L. Wolfenstein, *Phys. Rev. Lett.* **51**, 1945 - 1947 (1983).
- [3] D. Benson *et al.* *Nucl. Phys.* **B665**, 367 (2003).
- [4] C. W. Bauer *et al.* *Phys. Rev. D* **70**, 094017 (2004).
- [5] B.Aubert *at al.* arXiv:0707.2670
- [6] B.Aubert *at al.* *Phys.Rev.D***69**, 111104 (2004).
- [7] B.Aubert *at al.* *Phys.Rev.D***72**, 052004 (2005); B.Aubert *at al.* *Phys.Rev.Lett.***97**, 171803 (2006).
- [8] B.Aubert *at al.* *Phys.Rev.Lett.***100**, 231803 (2008).
- [9] S. Hashimoto *et al.* *Phys. Rev. D* **66**, 014503 (2002).
- [10] Dmitri Liventsev *et al.* *Phys.Rev.D***77**, 091503 (2008).
- [11] B.Aubert *at al.* *Phys. Rev. Lett.* **101**, 261802 (2008), reference posterior to this conference.
- [12] I. Bizjak *at al.* *Phys. Rev. Lett.***95**, 241801 (2005).
- [13] B.Aubert *at al.* *Phys. Rev. Lett.* **100**, 171802 (2008).
- [14] B.Aubert *at al.* arXiv:0708.1753
- [15] B.Aubert *at al.* *Phys. Rev. Lett.* **101**, 091801 (2008).

- [16] T. Hokuue *et al.* Phys. Lett. **B648**, 139-148 (2007).
- [17] B.Aubert *et al.* Phys. Rev. Lett. **99**, 171803 (2007).
- [18] K.-F. Chen *et al.* Phys. Rev. Lett. **98**, 031802 (2007).
- [19] H. Sahoo *et al.* Phys. Rev. D **77**, 091103 (2008).
- [20] B.Aubert *et al.* Phys. Rev. Lett. **101**, 021801 (2008).
- [21] S. E. Lee *et al.* Phys. Rev. D **77**, 071101 (2008).
- [22] M. Gronau and D. London, Phys. Rev. Lett. **65**, 3381 (1990).
- [23] Y. Grossman and H. R. Quinn, Phys. Rev. D **58**, 017504 (1998)
- [24] B.Aubert *et al.* Phys. Rev. Lett. **99**, 021603 (2007).
- [25] H. Ishino *et al.* Phys. Rev. Lett. **98**, 211801 (2007).
- [26] B.Aubert *et al.* Phys. Rev. D**76**, 091102 (2007).
- [27] B.Aubert *et al.* Phys.Rev.D **76**, 052007 (2007).
- [28] A. Somov *et al.* Phys. Rev. Lett. **96**, 171801 (2006), A.Somov *et al.* Phys.Rev.D **76**, 011104 (2007).
- [29] B.Aubert *et al.* arXiv:0708.1630.
- [30] C.-C. Chiang, KEK Preprint 2008-22, submitted to PRD(RC).
- [31] A. Snyder and H. Quinn, Phys. Rev. D **48**, 2139 (1993).
- [32] B.Aubert *et al.* Phys. Rev. D **76**, 012004 (2007).
- [33] A. Kusaka *et al.* Phys. Rev. D **77**, 072001 (2008).
- [34] B.Aubert *et al.* Phys. Rev. Lett. **97**, 051802 (2006).
- [35] K.Abe *et al.* arXiv:0706.3279.
- [36] B.Aubert *et al.* Phys. Rev. Lett. **100** 051802 (2008).
- [37] M. Gronau and D. Wyler, Phys. Lett. **B265**, 172 (1991), M. Gronau and D. London, Phys. Lett. **B253**, 483 (1991); D. Atwood, I. Dunietz, and A. Soni, Phys. Rev. Lett. **78**, 3257 (1997); A. Giri, Y. Grossman, A. Soffer, J. Zupan, Phys. Rev. D **68**, 054018 (2003), Bondar, Phys. Rev. **70**, 072003 (2004).

- [38] B.Aubert *et al.* Phys. Rev. D **77**, 111102 (2008); The  $D^*$  results were presented at FPCP08, by D. Kirkby, “Hot topics”, BABAR.
- [39] Y. Horii *et al.* Phys. Rev. D **78**, 071901 (2008).
- [40] B.Aubert *et al.* Phys. Rev. D **78**, 034023 (2008).
- [41] BELLE Collaboration, arXiv:0803.3375.

# New Physics Effects in $B$ Decays

*Yuan Chao*

*Department of Physics  
National Taiwan University  
10617 Taipei, TAIWAN*

## 1 Introduction

The two  $B$ -factories, Belle [1] and BaBar [2], has been played major roles in the  $B$  decays study. Their wonderful design and excellent operation enables their fruitful analysis results. Also recently the Tevatron experiments, CDF and DO, join the game with their  $B_S$  studies.

From the experimental results of  $B$  decay studies, we learn that most of measurements are consistent with the Standard Model (SM). One needs more precise measurements, which relies on large statistics and good analysis tools, to verify the theoretical predictions. Meanwhile, many unanticipated new particles, like  $X$ ,  $Y$  and  $Z$ 's, are discovered as discussed in J. Brodzicka talk. After all, we still have some small room for the New Physics. Some discrepancies from the SM has been found in the measurements of the phases and magnitudes of CKM unitary triangle [3, 4]. There are also various theoretical models that possibly give the contributions. These will relay on further validation with new experimental results.

## 2 Hints from the experiments

The hints of discrepancies between data and standard model are found in the following topics:

### 2.1 Direct CP Violation

In SM,  $CP$  violation arises via the interference of at least two processes with comparable amplitudes and difference  $CP$  phases [3]. The direct  $CP$  violation (DCPV) of  $B \rightarrow K\pi$  comes from the interference of “Tree” and “Penguin” two major processes, shown in Fig. 1.

One would expect a similar DCPV of  $B^\pm \rightarrow K^\pm \pi^0$  to  $B^0 \rightarrow K^+ \pi^-$ . However, from the  $B$ -factories experimental results, the difference is of  $5.2\sigma$  significance with the

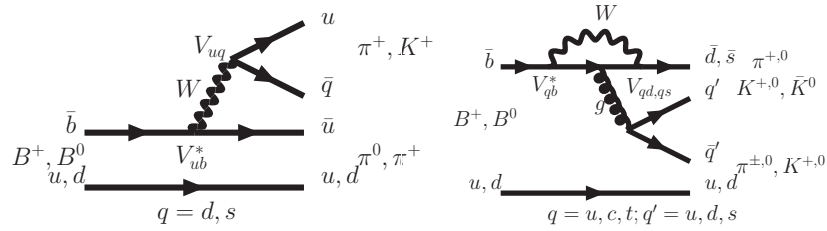


Figure 1: The Feynman diagrams of “Tree” and “Penguin” processes.

world average measurements [5, 6]. This is once called the  $K\pi$  puzzle [7] as the other contribution processes of  $B \rightarrow K^+\pi^0$ , “Color-suppressed Tree” and “Electroweak Penguin”, are theoretically expected to be small [8]. Several theories suggest ways to enhance these two contributions [9]. However, one needs experimental validations on their predictions. A recent publication on *Nature* has a summary on this issue and this is a non-concluded problem.

## 2.2 Radiative and Electroweak Penguins

The radiative  $b \rightarrow s\gamma$  decays would be the most powerful modes to constrain new physics. The deviation would be seen from their decay rates. Experimentally, there are two methods to perform measurements: fully inclusive and semi-inclusive, which sums up the exclusive channels. Belle recently has an update with fully inclusive method and is the current most precise measurement [10]. From the comparison of experimental world averages with next-next-leading-order (NNLO) calculation [11], we find that the agreements of them has been degraded. The most consist Andersen Gardi calculation has quite large uncertainty. On the other hand, BaBar has a recent update with the semi-inclusive method which sums up 16 fully reconstructed exclusive modes [12]. They also provide a DCPV measurement with  $-0.012 \pm 0.030(\text{stat}) \pm 0.019(\text{syst})$ .

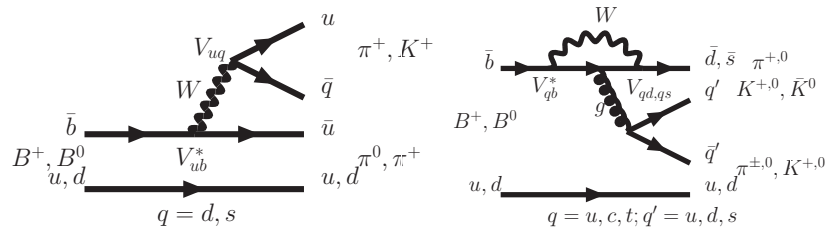


Figure 2: The Feynman diagrams of “Color-suppressed Tree” and “Electroweak Penguin” processes.

### 2.3 Time-dept. CPV in $b \rightarrow s$

The time-dependent  $CP$  violation (TCPV) measures the interference between  $B$  decays into final  $CP$  eigen state and  $B$  mixing into  $\bar{B}$  and decays into the same state. The indirect  $CP$  violation has been established in the  $b \rightarrow c\bar{c}s$  with  $B \rightarrow J/\psi K$  channel [13]. However, the recent results of various  $b \rightarrow sq\bar{q}$  channels shows deviations with a naïve average [14]. Theoretically,  $b \rightarrow sq\bar{q}$  is through “penguin” process and has similar  $CP$  values to  $b \rightarrow c\bar{c}s$  process which is of “tree” process. As there is no KM phase in  $V_{ts}$ , one would expect the same mixing induced  $CP$  measurement. This deviation would imply some non-SM particles in the loop of penguin process. The possible candidates would be the SUSY particles or the K.K. particles [15] of extra dimension. The current deviation of world average is about  $2.2\sigma$ .

### 2.4 Decays with Large Missing Energy

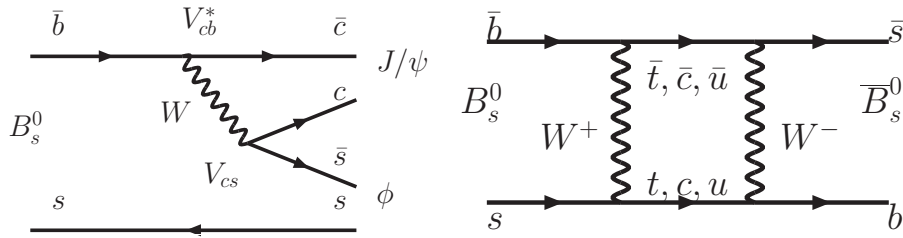
The leptonic  $B$  decays have sensitivity to new physics from charged Higgs as long as the  $B$  decay constant,  $f_B$  is known. For example the decay of  $B \rightarrow \tau\nu$  can be expressed like this:

$$\mathcal{B}(B^+ \rightarrow \tau^+ \nu_\tau) = \frac{G_F^2 m_B}{8\pi} m_\tau^2 (1 - \frac{m_\tau^2}{m_B^2})^2 f_B^2 |V_{ub}|^2 \tau_B$$

From the experimental point of view, the most sensitivity is from  $\tau$  modes with 1-prong. The study is rather difficult as the interesting  $B$  decays a single charged track and neutrinos which can't be seen. One needs to utilize the information from the other  $B$  pair produced in the same event. The current measurements from Belle and BaBar are a combination of  $f_B \cdot |V_{ub}|$  which is of around 1.5% level of uncertainty in average [16]. The difference between the measurements and HPQCD calculation is within  $1\sigma$  [17].

### 2.5 New results from Tevatrons

The process of  $B_S \rightarrow J/\psi\phi$  studied in the Tevatron experiments is very similar to  $B \rightarrow J/\psi K$  as shown in Fig. 3. However, the  $CP$  phase  $\phi_{1S}^{SM}$  (or  $\beta_S^{SM}$ ) is expected to be very small:  $\phi_{1S}^{SM} = \arg(-V_{ts}V_{tb}^*/V_{cs}V_{cb}^*) \sim 0.02$ . Therefore, a non-zero measurement would be a hint of the effect of new physics. Since  $B_S$  is of spin 0 while  $J/\psi$  and  $\phi$  are of spin 1. this leads to three angular momentum states that corresponds to  $CP$  even and  $CP$  odd states. The large  $CP$  violation mixing coefficient seen by CDF and DO indicates hints to new physics [18]. Detailed explanation can be found in S. GIAGU's talk.

Figure 3: The Feynman diagrams of  $B_S$  mixing processes.

### 3 Summary & Conclusion

The success of  $B$ -factories have brought us many fruitful physical results. We also see some unexpected challenges to the SM. There are various hints to new physics that have been pointed out in the previous paragraphs. It's of no doubt that we still need more statistics to further clarifications. Although the operation of BaBar has come to its end early this April, people are now proposing upgrades to the present Belle while constructing a new super  $B$ -factory. Of course, we are also looking forward to the up-coming results in the LHC era.

### References

- [1] Belle Collaboration, A. Abashian *et al.*, Nucl. Instrum. Methods Phys. Res. Sect. A **479**, 117 (2002).
- [2] BaBar Collaboration, B. Aubert *et.al.*, Nucl. Instrum. and Methods (2002)
- [3] M. Kobayashi and T. Maskawa, Prog. Theor. Phys. **49**, 652 (1973)
- [4] N. Cabibbo, Phys. Rev. Lett. 10, 531 (1963)
- [5] BABAR Collaboration, B. Aubert *et.al.*, arXiv:0807.4226 (2008); Belle Collaboration, S.-W. Lin *et.al.*, Nature 452, 332 (2008); CDF Collaboration, M. Morello, Nucl.Phys.Proc.Suppl.170:39-45,2007.
- [6] BABAR Collaboration, B. Aubert *et.al.*, Phys. Rev. **D76**, 091102 (2007) Belle Collaboration, S.-W. Lin *et.al.*, Nature 452, 332 (2008).
- [7] S. Baek and D. London, Phys. Lett. **B653**, 249-253 (2007).
- [8] Y.Y. Keum and A.I. Sanda, Phys. Rev. **D67**, 054009 (2003); M. Beneke and M. Neubert, Nucl. Phys. **B675**, 333-415 (2003).

- [9] C.-W. Chiang, M. Gronau, J.L. Rosner, and D.A. Suprun, Phys. Rev. **D70**, 034020 (2004); Y.-Y. Charng and H-n. Li, Phys. Rev. **D71**, 014036 (2005); W.-S. Hou, M. Nagashima and A. Soddu, Phys. Rev. Lett. 95, 141601 (2005); S. Baek, P. Hamel, D. London, A. Datta and D.A. Suprun, Phys. Rev. **D 71**, 057502 (2005).
- [10] Belle Collaboration, talk by A. Limosani at Moriond EW (2008)
- [11] B. Neubert, Phys. Rev. Lett. 98, 022003 (2007); Misiak, Phys. Rev. Lett. 98, 022002 (2007); A. Gardi, JHEP 0701, 029 (2007).
- [12] BABAR Collaboration, B. Aubert *et.al.*, arXiv:0805.4796v2 (2008).
- [13] BABAR Collaboration, B. Aubert *et.al.*, Phys. Rev. Lett. 87, 091801 (2001); Belle Collaboration, K. Abe *et.al.*, Phys. Rev. Lett. 87, 091802 (2001)
- [14] BABAR Collaboration, PRL 99 (2007) 161802; Belle Collaboration, PRL 98 (2007) 031802; PRD 76 (2007) 091103(R)
- [15] K. Agashe, G. Perez, A. Soni, Phys. Rev. **D71**, 016002 (2005)
- [16] Babar Collaboration, B. Aubert *et.al.*, Phys. Rev. **D77**, 011107 (2008) Belle Collaboration, I. Adachi *et.al.*, BELLE-CONF-0840 (2008).
- [17] G0 Collaboration, D. S. Armstrong *et.al.*, Phys. Rev. Lett. 95, 092001 (2005)
- [18] CDF Collaboration, arXiv:0712.2348, arXiv:0712.2397; D0 Collaboration, arXiv:0802.2255.

# Heavy B Hadrons

*Stefano Giagu  
for the CDF and DO Collaborations  
Sapienza Università di Roma and INFN Roma, 00185-Roma, IT*

## 1 Introduction

The CDF and DO experiments have successfully collected data since start of the Run II at the Tevatron Collider in 2001. The large B-meson production cross-section and the possibility to produce all kind of B hadron states, opened to the two collaborations the possibility to study with high precision the tiny effects of CP-violation in the Heavy B hadrons system, and to search for new physics effects in rare decays, in a way unavailable to the previous generation experiments. A new and largely unknown sector of the Heavy Flavor physics, complementary to the one already tested with precision at the B-factories, as recently pointed out by I. Bigi [1], has begun to be explored in search of possible signs of new physics. In this short note a selection of the most recent results on heavy B hadrons (mostly  $B_s$  mesons) from the Fermilab Tevatron, and from the Belle experiment running at the  $\Upsilon(5S)$  are reviewed.

## 2 CP Violation in $B_s$ mesons at Tevatron

In the neutral  $B_s$  system, the CP asymmetry in  $B_s^0 \rightarrow J/\psi\phi$  decay play the analogous role of the  $B^0 \rightarrow J/\psi K_s^0$  for the  $B_d$  system. Decays of the  $B_s$  meson via  $b \rightarrow c\bar{c}s$  transitions in fact can be used to probe, via interference effects in the mixing and decay amplitudes of the process, the  $\beta_s$  angle of the squashed (bs) unitarity triangle, defined as  $\beta_s = \arg(-V_{ts}V_{tb}^*/V_{cs}V_{cb}^*)$ . An important difference with respect to the  $B_d$  system is that in the Standard Model  $\beta_s$  is expected to be very small ( $\sim 0.02$ ), making the measurement of CP asymmetry in  $B_s^0 \rightarrow J/\psi\phi$  decay very sensitive to new possible physics effects in the mixing phase of the  $B_s^0 - \bar{B}_s^0$  system.

CDF and DO experiments have been able, for the first time, to perform a search for CP violation in the neutral  $B_s$  meson system, by measuring the time-dependent CP asymmetry in the  $B_s^0 \rightarrow J/\psi\phi$  decay mode. The vector-vector final state  $J/\psi\phi$  contains mixtures of polarization amplitudes: the CP-odd  $A_\perp$ , and the CP-even  $A_0$  and  $A_\parallel$  amplitudes. These terms need to be disentangled, using the angular distributions, in order to extract  $\beta_s$ , and their interference provides additional sensitivity [2].

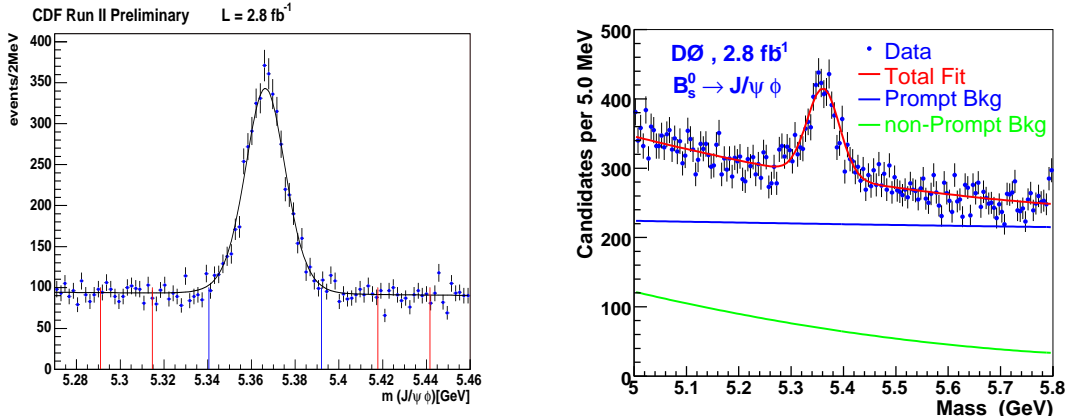


Figure 1: Data samples for the CDF and DO analyses of  $B_s^0 \rightarrow J/\psi\phi$  decay. The CDF experiment reports  $3166 \pm 56$  events, while the DO experiment reports  $1967 \pm 65$  events.

Very recently the CDF collaboration presented a new updated flavor-tagged, time-dependent, analysis, based on  $2.8 \text{ fb}^{-1}$  of integrated luminosity [3], that supersedes results from the previous  $1.7 \text{ fb}^{-1}$  untagged analysis [4], and  $1.35 \text{ fb}^{-1}$  flavor-tagged, time-dependent analysis [5]. The DO collaboration result is also based on a  $2.8 \text{ fb}^{-1}$  sample of flavor-tagged data, and is published in [6]. The  $B_s^0 \rightarrow J/\psi\phi$  signals from the two experiments are shown in Fig. 1.

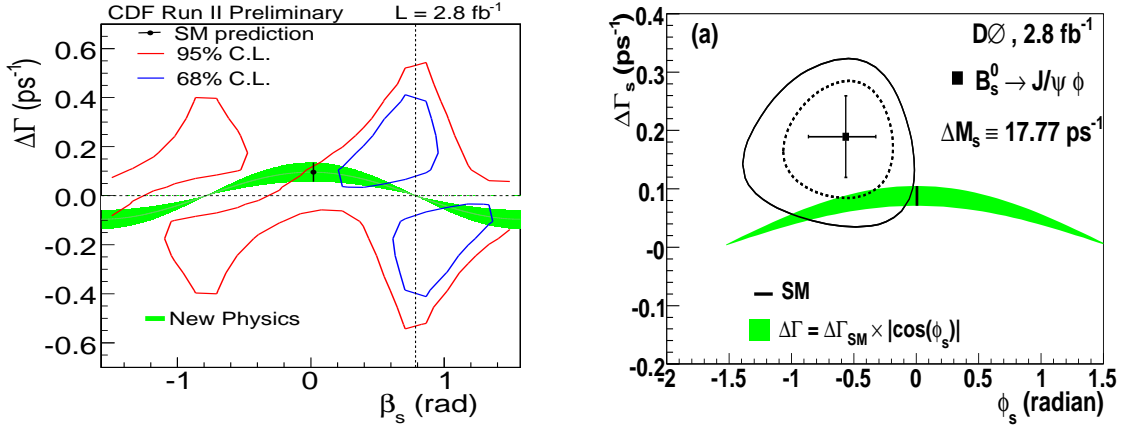


Figure 2: Confidence regions in the space of parameters  $\Delta\Gamma_s$  and  $\beta_s$  for the CDF (left), and DO (right) analyses. The green band corresponds to new physics models, as described in the text.

In the CDF analysis two different fits have been performed, one without using flavor tagging and assuming the Standard Model, which fixes  $\beta_s = 0$ , and a second

one with flavor-tagging and letting  $\beta_s$  to be free. Assuming no CP violation ( $\beta_s = 0$ ) the fit allows to simultaneously measure the decay width difference  $\Delta\Gamma_s$  and the average lifetime of the  $B_s$  meson. The results are reported in Table 1.

Table 1: Standard Model fits in the CDF tagged analysis.

Parameter	CDF measurement (un>tagged)
$c\tau_s = 2c/(\Gamma_H + \Gamma_L)$	$459 \pm 12(stat) \pm 3(syst) \mu m$
$\Delta\Gamma_s = \Gamma_L - \Gamma_H$	$0.02 \pm 0.05(stat) \pm 0.01(syst) ps^{-1}$
$ A_0 ^2$	$0.508 \pm 0.024 \pm 0.008$
$ A_{  }(0) ^2$	$0.241 \pm 0.019 \pm 0.007$

It is worth noticing here that the average  $B_s$  lifetime measurement is consistent with the HQET expectation of equal lifetimes for the  $B_s$  and  $B_d$  mesons. Table 1 reports also the measured polarization amplitudes for the  $B_s^0 \rightarrow J/\psi\phi$  decay, that are consistent with those measured in the similar  $B_d$  decay  $B^0 \rightarrow J/\psi K^{*0}$  [7]. For the CP fit, CDF does not report point estimates for any of the physics parameters, providing instead the confidence region in the  $(\beta_s, \Delta\Gamma_s)$  plane shown in Fig. 2 (left), computed from Monte Carlo using Feldman-Cousins method for confidence intervals. Also shown in the same figure, is the theoretical expectation from the Standard Model (black point), and in presence of new physics (green band). The Standard Model  $p$ -value calculated using the likelihood ratio is of 7%, corresponding to 1.8 Gaussian standard deviations.

Treating  $\Delta\Gamma_s$  as a nuisance parameter, CDF reports confidence intervals for  $\beta_s$ , and find that  $\beta_s$  is within  $[0.28, 1.29]$  at 68% C.L., and within  $[-\pi/2, -1.45] \cup [-1.01, -0.57] \cup [-0.13, \pi/2]$  at 95% CL.

To remove the two-fold ambiguity in the likelihood of the time-dependent, flavor tagged analysis, DO constrained the strong phases of the helicity amplitudes in the  $B_s^0 \rightarrow J/\psi\phi$  decay to the world average values for the  $B^0 \rightarrow J/\psi K^{*0}$  decay, measured at the B-factories [8]. Some justification of the constraint used has been recently showed in [9].

Results of the constrained fits are shown Table 2. In this case three types of fit have been performed: a Standard Model fit which fixes  $\beta_s$  to its expected value, a CP fit with  $\beta_s$  floating, and in addition, a CP fit with the further constraint that  $\Delta\Gamma_s = 2|\Gamma_{12}^s| \cos \phi_s$ , where  $\phi_s = \arg(-M_{12}^s/\Gamma_{12}^s)$ , is the mixing phase of the  $B_s$  system<sup>1</sup>, and  $M_{12}^s$  is the off-diagonal element of the mass matrix governing the flavor oscillations in the  $B_s$  system (related to the mixing frequency by  $\Delta m_s = 2|M_{12}^s|$ ). The average

<sup>1</sup>In the discussion the approximation  $\phi_s \sim -2\beta_s$  has been made. This is a reasonable approximation since, although the equality does not hold in the Standard Model, both are much smaller than the current experimental resolution, whereas new physics contributions add a phase  $\phi_{NP}$  to  $\phi_s$  and subtract the same phase from  $2\beta_s$ , so that the approximation remains valid.

Table 2: CDF results from tagged  $B_s^0 \rightarrow J/\psi\phi$  analysis.

Parameter	CP Fit ( $\phi_s$ floating)	SM Fit ( $\phi_s = 0$ )	NP Fit ( $\Delta\Gamma_s = 2 M_{12}^s  \cos \phi_s$ constraint)
$\tau_s$ (ps)	$1.52 \pm 0.06$	$1.53 \pm 0.06$	$1.49 \pm 0.05$
$\Delta\Gamma_s$ ( $\text{ps}^{-1}$ )	$0.19 \pm 0.07$	$0.14 \pm 0.07$	$0.083 \pm 0.018$
$A_\perp(0)$	$0.41 \pm 0.04$	$0.44 \pm 0.04$	$0.45 \pm 0.03$
$ A_0(0) ^2 -  A_{  }(0) ^2$	$0.34 \pm 0.05$	$0.35 \pm 0.04$	$0.33 \pm 0.04$
$\phi_s = -2\beta_s$	$-0.57^{+0.24}_{-0.30}$	fixed ( $-0.04$ )	$-0.46 \pm 0.28$

lifetime  $\tau_s$ , and the decay amplitudes are consistent with expectations and with the CDF measurements. Confidence regions in the  $(\phi_s (= -2\beta_s), \Delta\Gamma_s)$  space are shown in Fig. 2 (right). The point estimate for the CP violation phase and  $\Delta\Gamma_s$ , obtained by DO are:  $\phi_s = -0.57^{+0.24}_{-0.30}(\text{stat})^{+0.07}_{-0.02}(\text{syst})$  and  $\Delta\Gamma_s = 0.19 \pm 0.07(\text{stat})^{+0.02}_{-0.01}(\text{syst}) \text{ ps}^{-1}$ . The Standard Model  $p$ -value is of 6.6%, and the fluctuation respect to the Standard Model goes in the same direction as CDF.

Experimental sensitivity to new physics effects on the  $B_s$  mixing phase can also be obtained from charge asymmetry measurements in semi-leptonic  $B_s$  decays. The semi-leptonic asymmetry is in fact related to the mixing phase by the relation:

$$A_{SL}^s = \frac{N(\overline{B}_s \rightarrow f) - N(B_s \rightarrow \overline{f})}{N(\overline{B}_s \rightarrow f) + N(B_s \rightarrow \overline{f})} \sim \frac{\Delta\Gamma_s}{\Delta m_s} \tan \phi_s,$$

where  $f$  corresponds to direct  $B_s$  decays  $B_s \rightarrow f$  (e.g.  $D_s^- l^+ \nu_l$ ).

The Standard Model prediction for the semileptonic asymmetry in  $B_s$  decays is very small, at the level of few units in  $10^{-5}$  [10].

At the Tevatron the semileptonic asymmetry has been measured both in inclusive di-muon samples, where  $A_{SL}^s \sim \frac{N_{\mu^+\mu^+} - N_{\mu^-\mu^-}}{N_{\mu^+\mu^+} + N_{\mu^-\mu^-}}$ , or by using the sequential decays sample  $B_s^0 \rightarrow \mu\nu D_s$ . The first method has very high statistical accuracy, but requires knowledge of asymmetries of other contributing processes in addition to the detector charge asymmetries. The second method has less statistical power but ensures that the major contribution to the asymmetry comes from the  $B_s$  decays. Combining the two measurements DO obtains:  $A_{SL}^s = 0.0001 \pm 0.0090$  [11], while the CDF result based on  $1.6 \text{ fb}^{-1}$  di-muon pairs, is:  $A_{SL}^s = 0.020 \pm 0.028$  [12]. At the current level of precision  $A_{SL}^s$  is not able to provide powerful constraints on new physics contributions on the mixing phase.

Both the CDF and DO analyses of the CP violation in  $B_s^0 \rightarrow J/\psi\phi$  decay show a slight disagreement with the Standard Model prediction, and both results fluctuate in the same direction. Recently the DO collaboration has made public the results of the

fit without the strong phase constraints, allowing the HFAG group to combine them with the CDF results [13]. The combined contours are shown in Fig. 3. The  $p$ -value for the combined result is 3.1%, corresponding to 2.2 Gaussian standard deviations.

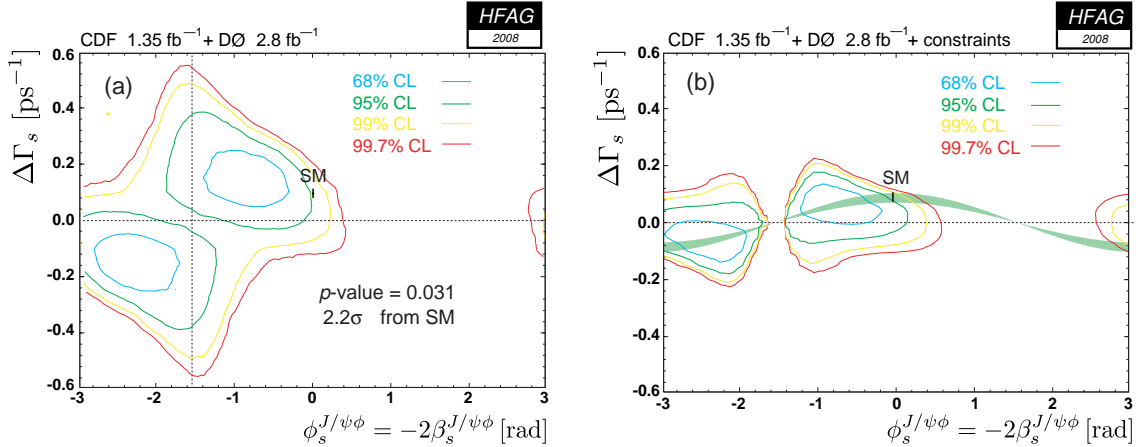


Figure 3: HFAG Combinations of the CDF and DO  $B_s^0 \rightarrow J/\psi\phi$  tagged analyses. The plot on the right use additional experimental input from the CDF and DO measurements of  $A_{SL}^s$ .

### 3 Rare $B_s$ decays at Tevatron and Belle

#### 3.1 Leptonic Two-body Decays at Tevatron

The FCNC process  $B_s^0 \rightarrow \mu^+\mu^-$  is predicted to have a branching ratio of  $\mathcal{B}(B_s^0 \rightarrow \mu^+\mu^-) = (3.42 \pm 0.54) \times 10^{-9}$  in the Standard Model [14], well below the current experimental sensitivity of the Tevatron experiments. The  $B^0 \rightarrow \mu^+\mu^-$  decay is further suppressed by  $|V_{td}/V_{ts}|^2$ , with a predicted branching ratio of  $(1.00 \pm 0.14) \times 10^{-10}$ . Significant enhancements are instead predicted by several new physics models. For example in the minimal super-symmetric standard model (MSSM) the  $B_s^0$  branching ratio is proportional to  $\tan^6 \beta$  where  $\tan \beta$  is the ratio between the vacuum expectation values of the two neutral Higgs fields. In  $R$ -parity violating super-symmetric (SUSY) models an enhancement is possible even at low values of  $\tan \beta$ .

Both Tevatron experiments have dedicated triggers to collect  $B \rightarrow \mu^+\mu^-$  events, and optimized selections for the  $B_s^0 \rightarrow \mu^+\mu^-$  candidates based on sophisticated multivariate analysis techniques. DO combines the discriminant variables in a likelihood ratio, while CDF uses a neural network (NN) discriminant. Both experiments estimate the dominant combinatorial background by a fit to the mass sidebands, while contribution from decays of B mesons to two light hadrons, which could peak

in the signal mass region, is estimated to be an order of magnitude lower than the combinatorial background. Both experiments do not report any significant excess of signal candidates over the expected background, and set 90% C.L. limits calculated with a Bayesian method for a data sample of  $2 \text{ fb}^{-1}$  per experiment:  $\mathcal{B}(B_s^0 \rightarrow \mu^+ \mu^-) < 7.5 \times 10^{-8}$  (DO) [15] and  $\mathcal{B}(B_s^0 \rightarrow \mu^+ \mu^-) < 4.7 \times 10^{-8}$  (CDF) [16]. Because of the superior mass resolution of the tracking system CDF is able to separate  $B_s^0$  and  $B^0$  mesons and to quote a 90% C.L. limit separately for the  $B^0$  decay of  $\mathcal{B}(B^0 \rightarrow \mu^+ \mu^-) < 1.5 \times 10^{-8}$ .

Very recently the CDF experiment reported the results of a search for the  $B_{s,d}^0 \rightarrow e^+ e^-$  channel and for the lepton-flavor violating mode  $B_{s,d}^0 \rightarrow e^+ \mu^-$ . In particular the latter decay modes are strongly suppressed within the Standard Model, in which leptons do not change flavor. These decays are allowed, however, in many models of new physics, such as Pati-Salam leptoquarks model, or in SUSY and Extra Dimension models, where the assumption of a local gauge symmetry between quarks and leptons at the lepton-flavor violation tree-level couplings leads to the prediction of a new force of Nature which mediates transitions between quarks and leptons [17].

Using a  $2 \text{ fb}^{-1}$  data sample, CDF find one event in the search window for the  $B_s^0 \rightarrow e^+ \mu^-$ , with estimated  $0.81 \pm 0.63$  background events, and one event for  $B_s^0 \rightarrow e^+ e^-$ , with  $2.8 \pm 1.8$  estimated background events. By using the  $B^0 \rightarrow K^+ \pi^-$  decay mode as a relative normalization, CDF derives the upper limits at 90% C.L. on the decay branching ratios of  $\mathcal{B}(B_s^0 \rightarrow e^+ \mu^-) < 2.0 \times 10^{-7}$ , and  $\mathcal{B}(B_s^0 \rightarrow e^+ e^-) < 2.8 \times 10^{-7}$  [16]. Finally from the decay branching ratio limits CDF calculate the corresponding lower bound on the Pati-Salam leptoquark mass:  $M_{LQ}(B_s^0) > 47.7 \text{ TeV}/c^2$  at 90% C.L. (see Fig. 4).

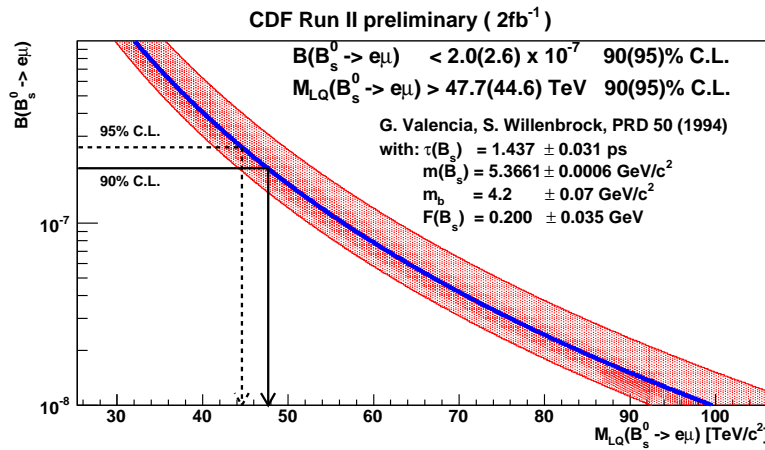


Figure 4: Leptoquark mass limit corresponding to the 90% C.L. on  $\mathcal{B}(B_s^0 \rightarrow e^+ \mu^-)$ .

### 3.2 Charmless Two-body Decays at Tevatron

Non-leptonic decays of  $b$  hadrons into pairs of charmless charged hadrons are effective probes of the CKM matrix, and sensitive to potential new physics effects. The large production cross section of  $b$  hadrons at Tevatron, and the ability of CDF to trigger on fully hadronic decays, allows extending such measurements to  $B_s^0$  and  $\Lambda_b^0$  decays, complementing the  $B^0$  meson case, extensively studied at the B-factories.

CDF analyzed an integrated luminosity of  $\sim 1 \text{ fb}^{-1}$  of pairs of oppositely-charged particles, selected by the displaced track trigger. A sample of 14500  $H_b^0 \rightarrow h^+h^-$  decay modes (where  $H_b^0 = B^0, B_s^0$  or  $\Lambda_b^0$  and  $h = K, \pi, p$ ) was reconstructed after the off-line confirmation of trigger requirements. The invariant mass resolution and the particle identification separation power available in CDF, are not sufficient to disentangle the individual  $H_b^0 \rightarrow h^+h^-$  decay modes on an event-by-event basis, therefore a Maximum Likelihood fit is performed to separate the different components. The fit combines kinematic and particle identification information, to statistically determine both the contribution of each mode, and the relative contributions to the CP asymmetries.

Significant signals are seen for  $B^0 \rightarrow \pi^+\pi^-$ ,  $B^0 \rightarrow K^+\pi^-$ , and  $B_s^0 \rightarrow K^+K^-$ , previously observed by CDF [19]. In addition to that, three new rare decay modes have been observed for the first time  $B_s^0 \rightarrow K^-\pi^+$ ,  $\Lambda_b^0 \rightarrow p\pi^-$  and  $\Lambda_b^0 \rightarrow pK^-$ , with a significance respectively of  $8.2\sigma$ ,  $6.0\sigma$  and  $11.5\sigma$ . No evidence was obtained for  $B_s^0 \rightarrow \pi^+\pi^-$  or  $B^0 \rightarrow K^+K^-$  mode.

Table 3: Branching fractions results. Absolute branching fractions are normalized to the world-average values  $\mathcal{B}(B^0 \rightarrow K^+\pi^-) = (19.4 \pm 0.6) \times 10^{-6}$  and  $f_s/f_d = 0.276 \pm 0.034$  and  $f_\Lambda/f_d = 0.230 \pm 0.052$  [18].

Mode	BR( $10^{-6}$ )
$B^0 \rightarrow \pi^+\pi^-$	$5.02 \pm 0.33 \pm 0.35$
$B_s^0 \rightarrow K^+K^-$	$24.4 \pm 1.4 \pm 3.5$
$B_s^0 \rightarrow K^-\pi^+$	$5.0 \pm 0.7 \pm 0.8$
$\Lambda_b^0 \rightarrow pK^-$	$5.6 \pm 0.8 \pm 1.5$
$\Lambda_b^0 \rightarrow p\pi^-$	$3.5 \pm 0.6 \pm 0.9$
$B_s^0 \rightarrow \pi^+\pi^-$	$0.49 \pm 0.28 \pm 0.36$
$B^0 \rightarrow K^+K^-$	$0.39 \pm 0.16 \pm 0.12$

The absolute branching fractions obtained by CDF normalizing the measurements to the world average value  $\mathcal{B}(B^0 \rightarrow K^+\pi^-) = (19.4 \pm 0.6) \times 10^{-6}$ , are listed in Table 1, while the CP-related measurements are listed in Table 4, where  $f_d$ ,  $f_s$  and  $f_\Lambda$  indicate the production fractions respectively of  $B^0$ ,  $B_s^0$  and  $\Lambda_b^0$  from fragmentation of a  $b$  quark in  $\bar{p}p$  collisions.

Table 4: CP-violation related results.

Mode	Measurement
$A_{CP}(B^0 \rightarrow K^+ \pi^-)$	$-0.086 \pm 0.023 \pm 0.009$
$A_{CP}(B_s^0 \rightarrow K^- \pi^+)$	$0.39 \pm 0.15 \pm 0.08$
$A_{CP}(\Lambda_b^- \rightarrow p K^-)$	$-0.37 \pm 0.17 \pm 0.03$
$A_{CP}(\Lambda_b^0 \rightarrow p \pi^-)$	$-0.03 \pm 0.17 \pm 0.05$

The decays  $\Lambda_b^0 \rightarrow p\pi^-$  and  $\Lambda_b^0 \rightarrow pK^-$  are allowed at tree level in the Standard Model, but are suppressed by the small value of the involved CKM matrix element  $V_{ub}$ . Loop diagram processes can contribute at a magnitude that is comparable to the tree diagram process, leading to sizable direct CP violation. In the Standard Model a  $A_{CP}$  value of  $\mathcal{O}(10\%)$  is predicted.

The measurement of the direct CP violation asymmetries in the  $b$ -baryon decays, presented by CDF, is the first such measurements in this sector. The statistical uncertainty still dominates the resolution and prevents a statement on the presence of asymmetry, whose measured value deviates from 0 at  $2.1\sigma$  level in the  $\Lambda_b^0 \rightarrow pK^-$  decay mode and is fully consistent with 0 in the  $\Lambda_b^0 \rightarrow p\pi^-$  decay mode. In Fig. 5 the invariant mass spectrum in the  $\pi^+\pi^-$  mass hypothesis, and the relative probability density function for the  $\Lambda_b^0 \rightarrow pK^-$  are shown, illustrating the good description of the data by the fit and the powerful  $\Lambda_b^0/\bar{\Lambda}_b^0$  separation.

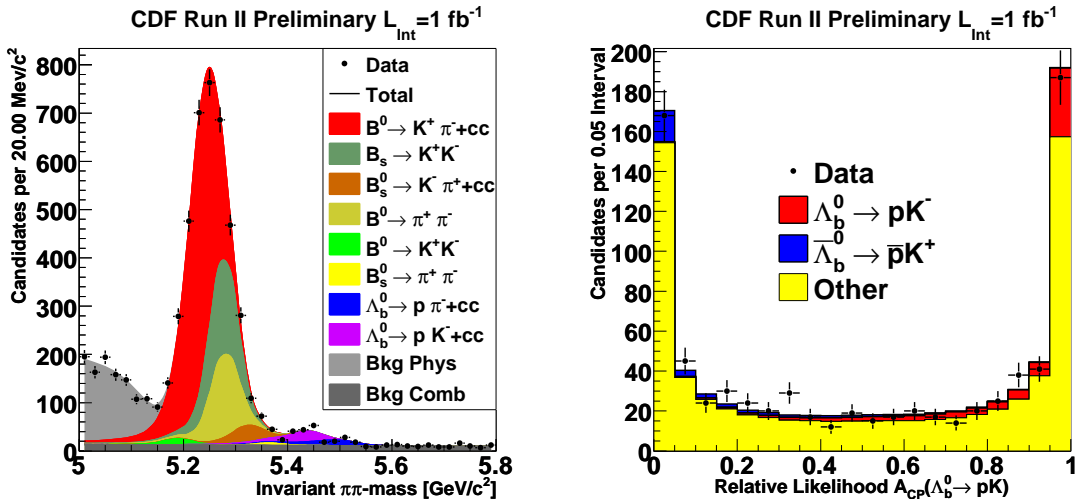


Figure 5: Invariant mass spectrum for  $\pi^+\pi^-$  mass assignment (left) and relative probability density function (pdf) of  $\Lambda_b^0 \rightarrow pK^-$ :  $\text{pdf}(\Lambda_b^0)/[\text{pdf}(\Lambda_b^0) + \text{pdf}(\bar{\Lambda}_b^0)]$  (right).

### 3.3 Radiative $B_s$ penguins at Belle

During the last several years the possibility of performing  $B_s^0$  meson studies at the  $e^+e^-$  colliders running at the  $\Upsilon(5S)$  resonance has been extensively explored. The first evidence for  $B_s^0$  production at the  $\Upsilon(5S)$  was found by the CLEO collaboration [26, 27] using a data sample of  $0.42 \text{ fb}^{-1}$  collected in 2003. This study indicated that practical  $B_s^0$  measurements at the  $\Upsilon(5S)$  are possible with at least  $20 \text{ fb}^{-1}$ , which can be easily collected at B-factories running with  $\sim 10^{34} \text{ cm}^{-2} \text{ sec}^{-1}$  luminosity. To test the feasibility of a  $B_s^0$  physics program the Belle collaboration collected at the  $\Upsilon(5S)$  a sample of  $1.86 \text{ fb}^{-1}$  of data in 2005, and a one of  $21.7 \text{ fb}^{-1}$  in 2006 [28, 29].

The collected samples have been used by Belle to perform searches for exclusive radiative decays of the  $B_s^0$  mesons, that are of great interest, because sensitive to new physics effects and experimentally unaccessible to the Tevatron experiments ,(the presence of low energy photons in the final state makes these kind of decays too hard to be reconstructed in CDF and DO ). In particular Belle searched for the decay modes  $B_s^0 \rightarrow \phi\gamma$  and  $B_s^0 \rightarrow \gamma\gamma$ , using the full  $23.6 \text{ fb}^{-1}$  available data sample [30].

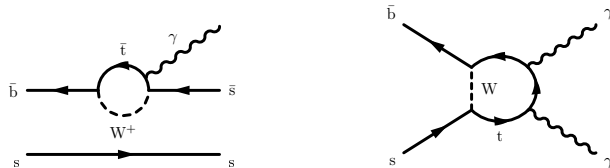


Figure 6: Diagrams describing the dominant SM processes for the  $B_s^0 \rightarrow \phi\gamma$  (left) and  $B_s^0 \rightarrow \gamma\gamma$  (right) decays.

Within the Standard Model (SM) the  $B_s^0 \rightarrow \phi\gamma$  decay is described by the radiative penguin diagram shown in Fig. 6 (left). The branching fraction is predicted to be  $\sim 4 \times 10^{-5}$  [31]. The  $B_s^0 \rightarrow \gamma\gamma$  decay proceed via the penguin annihilation diagram shown in Fig. 6 (right) and is expected to have a much smaller branching ratio, in the range  $(0.5 - 1.0) \times 10^{-6}$ , that can be however enhanced by about an order of magnitude in various new physics models [32, 33, 34], reaching a level not far from the current sensitivity of the Belle experiment.

To extract the signal yields a multi-dimensional un-binned extended maximum likelihood fit is performed to the  $M_{bc}$  and  $\Delta E$  variables.  $M_{bc}$  and  $\Delta E$  are respectively the beam-energy-constrained mass, and the energy difference observable, defined as:  $\Delta E = E_{B_s^0}^{\text{CM}} - E_{\text{beam}}$  and  $M_{bc} = \sqrt{(E_{\text{beam}}^{\text{CM}})^2 - (p_{B_s^0}^{\text{CM}})^2}$ , where  $E_{B_s^0}^{\text{CM}}$  and  $p_{B_s^0}^{\text{CM}}$  are the energy and momentum of the  $B_s^0$  candidate in the  $e^+e^-$  center-of-mass (CM) system, and  $E_{\text{beam}}^{\text{CM}}$  is the CM beam energy.

Fig. 7 shows the  $M_{bc}$  and  $\Delta E$  projections of the fit results of the data, together with the fitted functions. A clear signal of  $18_{-5}^{+6}$  events is seen in the  $B_s^0 \rightarrow \phi\gamma$  mode, with a significance of 5.5 standard deviations, providing the first observation of a  $B_s$

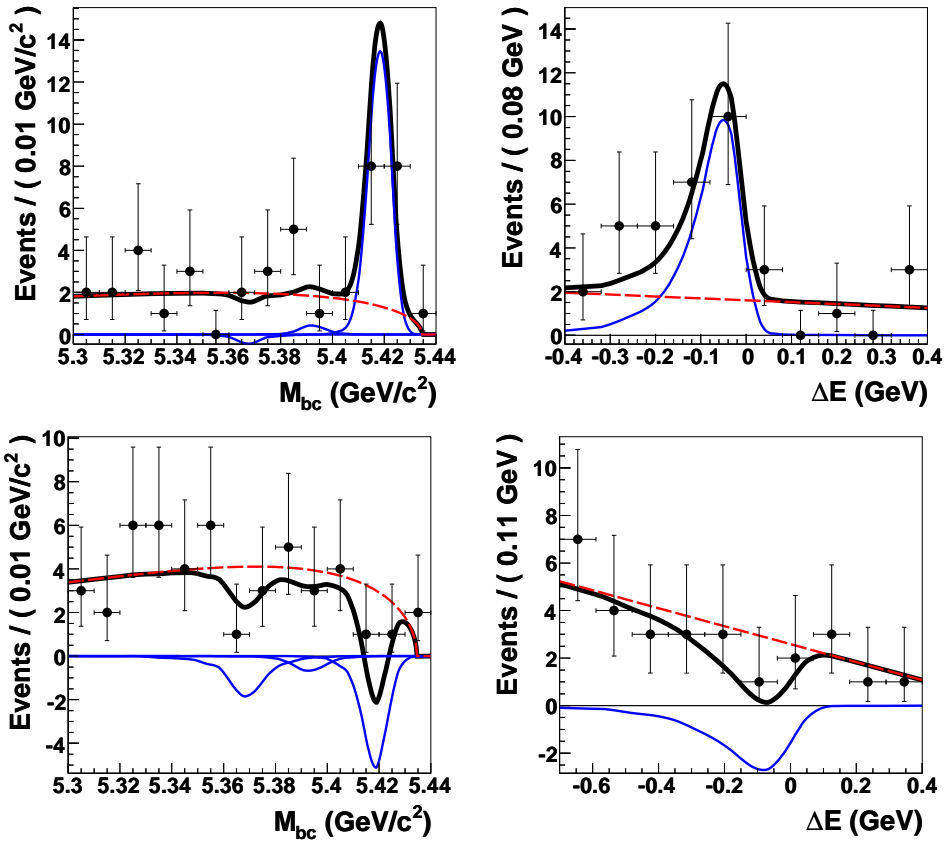


Figure 7:  $M_{bc}$  projection (left) and  $\Delta E$  projection (right) for the  $B_s^0 \rightarrow \phi\gamma$  (top) and  $B_s^0 \rightarrow \gamma\gamma$  (bottom) modes. The thick solid curves are the fit functions (thin solid curves: signal functions, dashed curves: continuum contribution).

penguin radiative decay. The branching fraction is measured to be  $\mathcal{B}(B_s^0 \rightarrow \phi\gamma) = (5.7^{+1.8}_{-1.5}(\text{stat.})^{+1.2}_{-1.1}(\text{syst.})) \times 10^{-5}$ , in agreement with the SM predictions.

No significant signal is observed instead for the  $B_s^0 \rightarrow \gamma\gamma$  mode, and an upper limit at the 90% C.L. of  $\mathcal{B}(B_s^0 \rightarrow \phi\gamma) < 8.7 \times 10^{-6}$  is set.

## References

- [1] I.I. Bigi, arXiv:hep-ph/0701273v1 (2008).
- [2] A.S. Dighe, et al., Eur. Phys. J. C 6, 647 (1999).
- [3] CDF Collab., CDF Public Note 9458 (2008).
- [4] T. Aaltonen et al., CDF Collab., Phys. Rev. Lett. 100 121803 (2008).

- [5] T. Aaltonen et al., CDF Collab., Phys. Rev. Lett. 100 161802 (2008).
- [6] V.M. Abazov et al., DO Collab., arXiv:0802.2255v1 [hep-exp].
- [7] B. Aubert et al., BABAR Collab., Phys. Rev. D76 031102 (2007);  
R. Itoh et al., Belle Collab., Phys. Rev. Lett. 98, 121801, 2007.
- [8] E. Barberio et al., Heavy Flavor Averaging Group, arXiv:0704.0522 [hep-ex].
- [9] J. Rosner and M. Gronau, arXiv:0808.3761v3 [hep-ph], 2008.
- [10] A. Lenz and U. Nierste, JHEP 0706:072 (2007).
- [11] V.M. Abazov et al., DO Collab., Phys. Rev. D76, 057101 (2007).
- [12] The CDF Collab., CDF Public note 9015 (Oct. 16, 2007).
- [13] Heavy Flavor Averaging Group: <http://www.slac.stanford.edu/xorg/hfag/>.
- [14] A.J. Buras, Phys. Lett. B 566, (2003) 115.
- [15] DO Collaboration, Conference Note 5344-CONF.
- [16] T. Aaltonen et al., CDF Collaboration, Phys. Rev. Lett. 100, 101802 (2008).
- [17] J. Pati and A. Salam, Phys. Rev. D 10 275 (1974);  
R.A. Diaz, Eur. Phys. J. C 41, 305 (2005);  
A. Ilakova, Phys. Rev. D 62,036010 (2000);  
G. Valencia and S. Willenbrock, Phys. Rev. D 50, 6843 (1994);  
M. Blanke et al., JHEP 0705, 013 (2007).
- [18] C. Amsler et al., Phys. Lett. B667,1 (2008).
- [19] A. Abulencia et al, CDF Collab., Phys. Rev. Lett., 97, 211802 (2006), hep-ex/0607021.
- [20] A.R. Williamson, J. Zupan, Phys. Rev. D74, 014003 (2006), hep-ph/0601214.
- [21] M. Beneke and M. Neubert, Nucl. Phys. B675, 333 (2003), hep-ph/0308039.
- [22] Xian-Qiao Yu et al., Phys. Rev. D71, 074026 (2005), hep-ph/0501152.
- [23] S. Descotes-Genon, J. Matias and J. Virto, Phys. Rev. Lett. 97, 061801 (2006), hep-ph/0603239.
- [24] S. Baek, D. London, J. Matias and J. Virto, J. High Energy Phys., 612 (2006), hep-ph/0610109.

- [25] R. Mohanta, Phys. Rev. D63, 056006 (2001), hep-ph/0005240.
- [26] M. Artuso et al., CLEO Collaboration, Phys. Rev. Lett. 95, 261801, 2005.
- [27] G. Bonvicini et al., CLEO Collaboration, Phys. Rev. Lett. 96, 022002, 2006.
- [28] A. Drutskoy et al., Belle Collaboration, Phys. Rev. Lett. 98, 052001, 2007.
- [29] A. Drutskoy et al., Belle Collaboration, Phys. Rev. D76, 012002, 2007.
- [30] J. Wicht et al., Belle Collaboration, Phys. Rev. Lett. 100, 121801, 2008.
- [31] P. Ball, G. W. Jones, and R. Zwicky, Phys. Rev. D75, 054004, 2007.
- [32] A. Gemintern, S. Bar-Shalom, and G. Eilam, Phys. Rev. D70, 035008, 2004.
- [33] W. J. Huo, C. D. Lu, and Z. J. Xiao, arXiv:hep-ph/0302177, 2003.
- [34] T. M. Aliev, and E. O. Iltan, Phys. Rev. D58, 095014, 1998.

# The Charm Renaissance: D-physics – a Selective Review

*Guy Wilkinson  
University of Oxford,  
Denys Wilkinson Building,  
Keble Road,  
Oxford, OX1 3RH,  
UNITED KINGDOM*

## 1 Introduction

In recent years, no doubt because of the success of the  $B$ -physics programme at BaBar and Belle, charm has been considered the poor relation of heavy-quark physics. This is now changing: while  $B$ -physics remains the biggest show in town, it is no longer the *only* show. As will be argued, measurements in the  $D$ -sector have a vital, although indirect, role to play in pinning down the value of certain critical parameters of flavour-physics. Furthermore, the charm system provides a powerful laboratory in its own right to search for contributions from non-Standard Model (SM) processes.

Three main reasons can be identified which explain why charm physics is once more, quite correctly, being perceived as an important and exciting discipline:

### 1. Precision CKM Tests

The success of the  $B$ -factories and the Tevatron has meant that CKM unitarity triangle tests are achieving successively higher levels of precision. This progress will continue with the LHCb experiment at CERN. Although the CKM elements being studied are those accessible in  $B$ -decays, charm turns out to be a vital ingredient in the programme.

### 2. Charm Mixing and its Legacy

The discovery of  $D^0 - \overline{D^0}$  oscillations has been the most exciting event of the past couple of years in high energy physics. The higher than expected rate is (arguably) intriguing in its own right, and points the way forward to searches for CP violation (CPV) in the charm sector.

### 3. Recent Discoveries in Spectroscopy

The discovery of several missing charmonium states, and a number of unexpected and possibly exotic resonances (the  $X, Y$  and  $Z$ ) has rekindled interest in the  $c\bar{c}$  system as a laboratory for studying QCD.

In this review we focus on the first two topics. Useful discussion of the third item may be found in [1].

## 2 Facilities and Experimental Attributes

### 2.1 Overview

In reviewing the facilities which have contributed to charm physics studies in recent years, and are expected to do so in future, three complementary strands may be distinguished.

First are the fixed target experiments, most significantly those at Fermilab: E687, E791 and FOCUS. Second are the experiments located on  $e^+e^-$  machines. The majority of results have come from CLEO, BaBar and Belle, with the most important source of  $D$ -meson production being the  $e^+e^-$  continuum lying under the  $\Upsilon(4S)$ . An important special case of  $e^+e^-$  operation is the threshold running pursued by CLEO-c at both the  $\psi(3770)$  and at around 4170 MeV, where  $D_s$  mesons are produced. The significance of these threshold data is explained in more detail below. The BES-III [2] experiment is expected to follow the lead of CLEO-c, and accumulate perhaps 20 times more data over the coming decade. In the more distant future it is hoped that a Super-Flavour Factory [3] will be constructed, which will both increase the charm-from-continuum sample of the  $B$ -factories by 1-to-2 orders of magnitude, and also have the ability to operate at very high luminosity at threshold.

The third important class of facility in which  $D$ -meson properties have been (and will be) studied is that of hadron colliders. The very high production cross-section gives rise to enormous statistics. The Tevatron, and CDF in particular, have published impressive studies exploiting the very large prompt  $D^*$  samples that are available. A recent CDF analysis [4] used this source to reconstruct around 3 million  $D^0 \rightarrow K\pi$  events from  $1.5 \text{ fb}^{-1}$  of data. This programme will continue at LHCb, where the possibilities of harnessing secondary charm from  $B$ -decays has also been explored and shown to be very promising [5]. Plans are being made for an upgraded LHCb experiment [6] which will run at around 10 times the luminosity, and have more efficient triggering, which will therefore provide still larger datasets.

### 2.2 Threshold Running and CLEO-c

Threshold running at  $e^+e^-$  machines has several attractive characteristics:

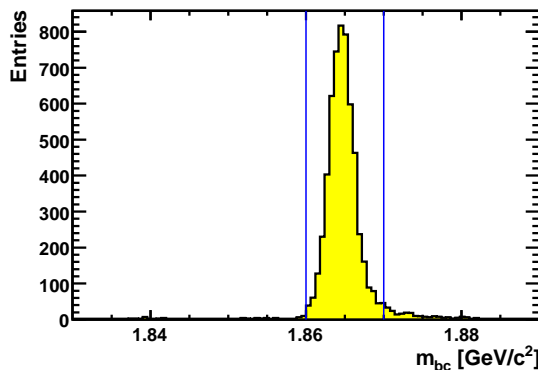


Figure 1: Beam constrained invariant mass of CLEO-c  $D^0 \rightarrow K^-\pi^+\pi^-\pi^+$  events in which the other meson has been reconstructed as  $K^+\pi^-$ . (The tail at high mass arises from signal events in which there has been significant ISR.)

- The environment is very clean, with no additional fragmentation particles produced. This allows for very low backgrounds, particularly in the case where both  $D$ -mesons are reconstructed. Figure 1 shows the beam constrained mass plotted in events where one mesons has been reconstructed in the  $K\pi\pi\pi$  and the other as  $K\pi$ . The background is at the level of 1%.
- Quantum correlation exists between the two  $D$  mesons which can be exploited. For example, at the  $\psi(3770)$  the quantum numbers of the resonance mean that if one  $D$  meson is reconstructed in a CP-even state, for example  $K^+K^-$ , then the CP of the other state is known to be CP-odd. This ability to *CP-tag* decays is the most valuable feature of threshold running, the application of which is explained in Sec. 3.
- If all charged particles and photons are reconstructed then kinematical constraints allow the presence of neutral particles to be inferred, such as  $K_L^0$  mesons and neutrinos. This is useful as it allows CP-tags such as  $K_L^0\pi^0$  to be included in double-tag analyses, and enables the reconstruction of leptonic decays such as  $D_s^+ \rightarrow l^+\nu$ .

CLEO-c, which completed operation in Spring of this year, accumulated  $818 \text{ pb}^{-1}$  of data at the  $\psi(3770)$  and  $586 \text{ pb}^{-1}$  at  $\sqrt{s} = 4170 \text{ MeV}$ .

## 2.3 Experimental Attributes

The desirable attributes needed for a successful  $D$ -physics experiment are essentially the same as those required in  $B$ -physics studies. These include efficient tracking and, if

possible, good calorimetry suitable for  $\gamma$  and  $\pi^0$  reconstruction, hadron identification capabilities to permit  $\pi$ - $K$  discrimination, and – in a hadron collider environment – a trigger system sensitive to the final states of interest. The results discussed in this review come primarily from BaBar, Belle, CLEO-c and CDF – experiments which possess most or all of these characteristics.

### 3 $D$ Decays and the CKM Unitarity Triangle

Our understanding of CP-violating phenomena, as expressed in the context of the Standard Model, is most usefully represented by constraints in the  $(\bar{\rho}, \bar{\eta})$  plane, where at order  $\lambda^2$ , these symbols represent two of the parameters of the CKM-matrix in the Wolfenstein parameterisation [8] multiplied by the factor  $(1 - \lambda^2)$ ,  $\lambda$  being the sine of the Cabibbo angle. All these constraints (with the exception of  $\epsilon_K$ , the CP-violating parameter obtained from kaon decays) come from measurements of  $B$ -meson properties, which are expected to map out a triangle with vertices  $[(0, 0), (1, 0), (\bar{\rho}, \bar{\eta})]$ . The present experimental status is summarised in Fig. 2. All measurements are broadly consistent with each other, indicating the validity of the CKM paradigm. Nonetheless, new physics contributions are not excluded and may become apparent when the experimental precision improves still further – this is one of the principal goals of the flavour physics programme. In surveying where improvement is necessary it is natural to focus on both the angle  $\gamma$ , indicated in Fig. 2, and the so-called ‘mixing’ side opposite to this angle. The geometry of the triangle means that these two quantities are closely linked, for it is the length of the side which largely determines the expected value of  $\gamma$ . Two possible central values are predicted for the value of  $\gamma$  at the one sigma level:  $(55.4^{+2.5}_{-2.2})^\circ$  or  $(67.4^{+3.3}_{-5.6})^\circ$  [7]. Comparison of the measured and expected values of  $\gamma$  is a powerful way to search for new physics. For both quantities it will be seen that, despite the fact that both of these features are measured in  $B$ -decays, crucial input is provided by analyses of  $D$ -decay properties.

#### 3.1 The CKM Angle $\gamma$ and $D$ -decays

The most powerful manner in which to measure the angle  $\gamma$  is with  $B^\pm \rightarrow DK^\pm$  decays. Here two tree diagrams contribute, one of which involves a  $D^0$  meson and the other a  $\bar{D}^0$  meson. If a final state is chosen which is common to both  $D^0$  and  $\bar{D}^0$  then interference occurs that includes terms dependent on the phase difference between the diagrams, which is  $\delta_B - \gamma$ , where  $\delta_B$  is a CP-conserving strong phase. Comparing suitable observables between  $B^-$  and  $B^+$  decays allows  $\gamma$  and  $\delta_B$  to be determined, along with  $r_B$ , a parameter which represents the relative strength of the two diagrams ( $\approx 0.1$ ). Categories of  $D$ -decays which have been proposed for these measurements include CP-eigenstates [9], for example  $K^+K^-$  or  $K_S^0\pi^0$ , Cabibbo favoured

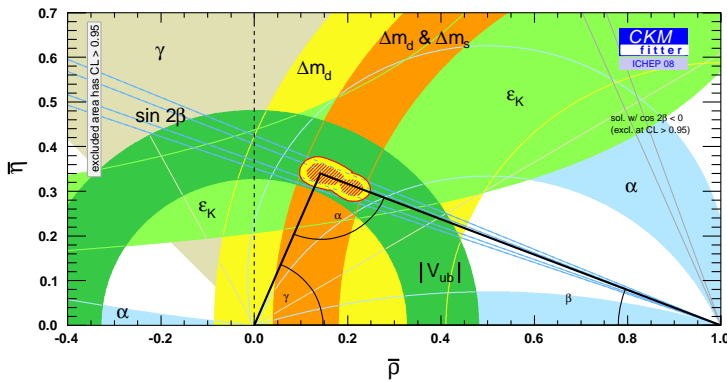


Figure 2: Constraints in the  $\bar{\rho}, \bar{\eta}$  plane as of Summer 2008 [7].

and doubly-Cabibbo suppressed decays (the so-called ‘ADS’ approach [10]), for example  $K^-\pi^+$  or  $K^-\pi^+\pi^-\pi^+$ , and self-conjugate multibody states, such as  $K_S^0\pi^+\pi^-$  [11]. It is this latter method which has yielded the best constraints on  $\gamma$  with the statistics presently available at the  $B$ -factories [12, 13].

In using  $D^0 \rightarrow K_S^0 \pi^+ \pi^-$  decays in a  $B^\pm \rightarrow D K^\pm$  analysis the CP-sensitive observable is the Dalitz plot of the  $D$ -decay. A non-zero value of  $\gamma$  will give rise to differences in the distributions for  $B^+$  and  $B^-$  decays. Examples plots from a recent BELLE analysis [13] are shown in Fig. 3. If the composition of the intermediate resonances involved in the  $D$ -decay is understood, then a comparison of the two plots allows  $\gamma$  to be extracted through an unbinned likelihood fit. In this manner charm physics provides a critical input to the  $\gamma$  measurement.

The  $B$ -factory experiments have devoted a great deal of effort to modelling the  $D^0 \rightarrow K_S^0 \pi^+ \pi^-$  decay for the purposes of the  $\gamma$  measurement. A recent BaBar study [12] has used a sample of 487k flavour tagged  $D^{*\pm} \rightarrow D\pi^\pm$  events to which an isobar model involving ten resonances is fitted. The  $\pi\pi$  and  $K_S^0\pi$  S-wave contributions are described with a K-matrix [14] and LASS [15] parametrisation respectively. Projections of the Dalitz plot, with the model fit superimposed, are shown in Fig. 4. The  $\chi^2$  of the fit is 1.11 for 19274 degrees of freedom. In the  $\gamma$  fit a systematic uncertainty is incurred arising from how well this model represents reality. This error is assigned to be  $7^\circ$ , which is small compared with the statistical uncertainty, but will become limiting with the higher statistics  $B$ -samples expected at LHCb.

An alternative approach is to make a binned fit in which the model predictions are replaced by quantities which are directly measured in double-tagged quantum-correlated D-decays at the  $\psi(3770)$  [16]. If one D-meson is reconstructed in a CP-eigenstate then the other meson will be in the opposite eigenstate, that is a known superposition of  $D^0$  and  $\bar{D}^0$ . So if this meson is reconstructed as  $K_S^0\pi^+\pi^-$  then there

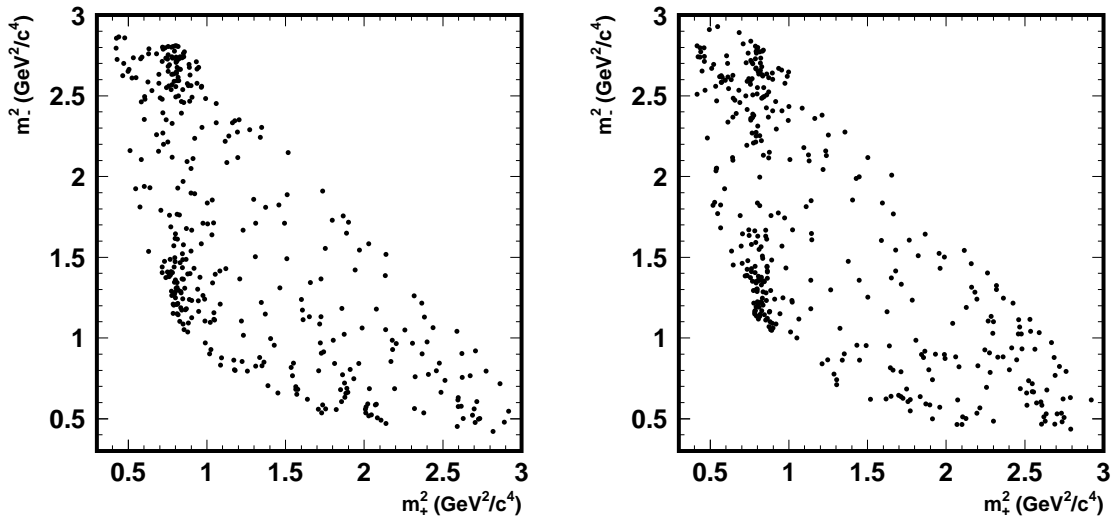


Figure 3: Dalitz plots of  $D^0 \rightarrow K_S^0 \pi^+ \pi^-$  decays arising from the process  $B^\pm \rightarrow D K^\pm$  [13]. Left:  $B^-$ ; right:  $B^+$ . The horizontal axis is the invariant mass squared for the  $K_S^0 \pi^+$  pair, and that of the vertical axis the same for the  $K_S^0 \pi^-$ .

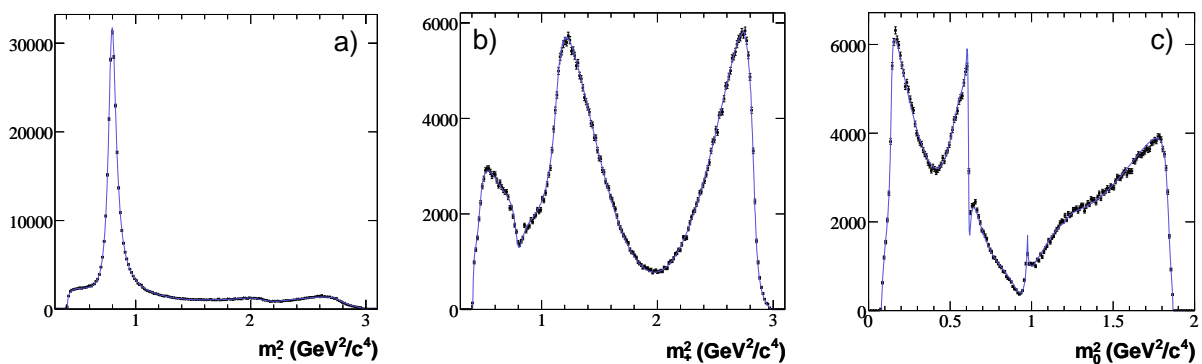


Figure 4: BELLE projections of the Dalitz variables for the decay  $D^0 \rightarrow K_S^0 \pi^+ \pi^-$  with fit result superimposed [12]. Invariant mass squared for the:  $K_S^0 \pi^-$  (a), the  $K_S^0 \pi^+$  (b) and the  $\pi^+ \pi^-$  (c).

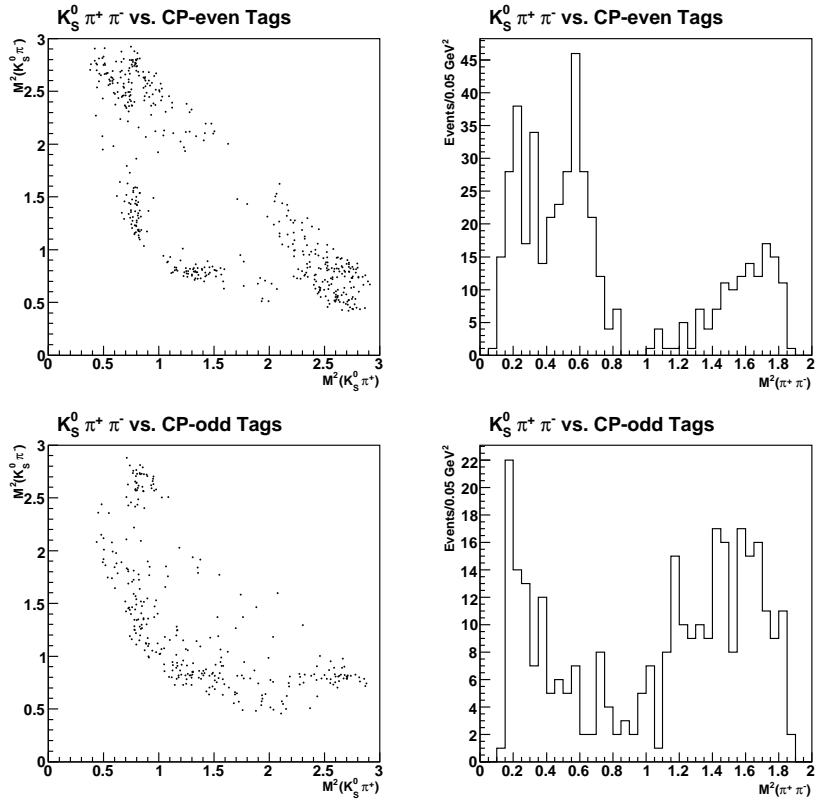


Figure 5: CP-tagged  $D^0 \rightarrow K_S^0 \pi^+ \pi^-$  Dalitz plots and  $\pi^+ \pi^-$  projections from CLEO-c.

will be contributions from  $D^0$ ,  $\overline{D^0}$  and an interference term involving the strong phase difference between the two decay paths. It is this information which is invaluable in the  $\gamma$  measurement and is inaccessible through direct means in flavour-tagged D-decays. Similarly useful input comes from events containing two  $K_S^0 \pi^+ \pi^-$  decays. Quantities required for the  $\gamma$  extraction (the so-called  $c_i$  and  $s_i$  coefficients – see [16]) are measured which are directly related to the relative population of the chosen bins for different combinations of tags. Figure 5 shows  $K_S^0 \pi^+ \pi^-$  Dalitz plots and the corresponding projections made with CLEO-c data for CP-even and CP-odd tags. The difference in structure is apparent, for example the absence of the  $K_S^0 \rho^0$  peak in the events containing a CP-odd tag. Preliminary results exist from CLEO-c [17]; the finite  $\psi(3770)$  sample size will induce a residual error of  $1 - 2^\circ$  on  $\gamma$ . Although the binned treatment leads to some degradation in  $B$ -statistical precision, it is still expected at LHCb that this model independent approach will outperform the model dependent fit after one-year ( $2 \text{ fb}^{-1}$ ) of data-taking [20], with an error dominated by measurement uncertainties alone.

There are other equally important ways in which quantum-correlated  $D$ -decays

can be harnessed for the  $B^\pm \rightarrow DK^\pm \gamma$  analysis, and which are being explored on CLEO-c. These include determinations of the strong phase difference in  $D^0 \rightarrow K-\pi^+$  decays [18], and the *coherence factor* [19] and average strong phase difference in  $D^0 \rightarrow K^-\pi^+\pi^-\pi^+$  and  $D^0 \rightarrow K^-\pi^+\pi^0$  decays [21], all of which are important for the ADS family of  $\gamma$  measurements.

An average of existing measurements with  $B$ -data yields  $\gamma = (67^{+32}_{-25})^\circ$  [7]. LHCb has the potential of reducing this uncertainty to  $2 - 3^\circ$  [22], using a combination of methods, the majority of which will rely critically on the knowledge of the  $D$ -meson decay structure.

### 3.2 The ‘Mixing Side’ and D-Meson Tests of Lattice QCD

The ratio  $|V_{td}/V_{ts}|$  can be used to fix the unitarity triangle side opposite to the angle  $\gamma$ . This ratio is determined from the ratio of oscillation frequencies  $\Delta m_{B_s}$  to  $\Delta m_{B_d}$  in the  $B^0$  and  $B_s$  systems:

$$|V_{td}/V_{ts}| = (f_{B_s}\sqrt{B_{B_s}})/(f_{B_d}\sqrt{B_{B_d}})\sqrt{(\Delta m_{B_d} m_{B_d}/\Delta m_{B_s} m_{B_s})}. \quad (1)$$

Also involved are the meson masses,  $m_{B_{d(s)}}$ , the meson decay constants  $f_{B_{d(s)}}$  and the bag factors  $B_{B_{d(s)}}$ . The ratio  $(f_{B_s}\sqrt{B_{B_s}})/(f_{B_d}\sqrt{B_{B_d}})$  is calculated in lattice QCD [23] to be  $1.23 \pm 0.06$ . It is the uncertainty in this calculation which dominates the knowledge of the length of the side, and hence the prediction for the expected value of  $\gamma$ . For this reason, it is highly desirable to make experimental validations of the lattice QCD calculations. This cannot readily be done in the  $B$ -system, but it is possible to make measurements of  $f_D$  and  $f_{D_s}$ , the form factors for  $D^+$  and  $D_s^+$  decays. Comparison between these results and the lattice calculations then provide a critical test of the lattice approach.

The  $D^+$  and  $D_s^+$  form factors may be measured from leptonic meson decays. The partial width for a  $D^+$  decaying to  $l^+\nu$  is given by

$$\Gamma(D^+ \rightarrow l^+\nu) = \frac{1}{8\pi} G_F^2 f_D^2 m_l^2 m_D \left(1 - \frac{m_l^2}{m_D^2}\right)^2 |V_{cd}|^2 \quad (2)$$

and similarly for  $D_s^+$ , but here involving the parameters  $f_{D_s}$ ,  $m_{D_s}$  and  $|V_{cs}|$ . If the values for the magnitudes of the CKM angles are taken from elsewhere, the form factors may be extracted. Measurements of  $f_{D_s}$  come from CLEO-c [24, 25], BELLE [26] and BaBar [27], and a recent new determination of  $f_D$  has been made by CLEO-c [28]. These are to be compared with the most precise available lattice calculation from [29].

The CLEO-c measurements are based on full-reconstruction techniques which exploit the cleanliness of the threshold environment. In the  $f_D$  analysis, for example, events are considered from the  $\psi(3770)$  running where one charged  $D$  meson is found together with a single other charged track, which is minimum ionising. The missing

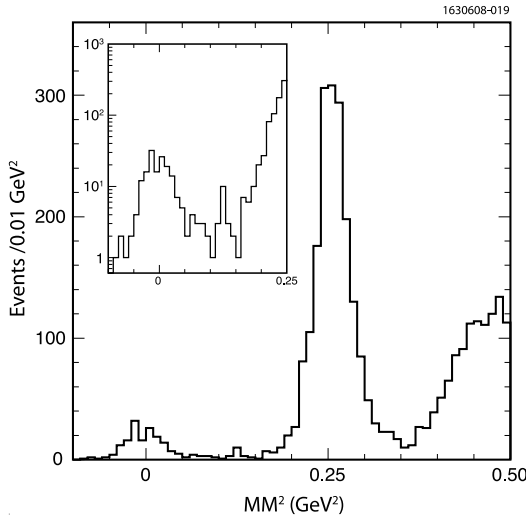


Figure 6: Missing mass squared in the CLEO-c  $D^+ \rightarrow \mu\nu$  analysis [28].

mass for these events is shown in Fig. 6. A peak is seen at zero-missing mass, consistent with  $D^+ \rightarrow \mu^+\nu$  events and clearly separated from the background process  $D^+ \rightarrow K^0\pi^+$ . A small contribution is seen between these two peaks coming from  $D^+ \rightarrow \tau^+(\pi^+\bar{\nu})\nu$ . Using the population of this peak to measure the branching ratio yields a result  $BR(D^+ \rightarrow \mu^+\nu) = (3.82 \pm 0.32 \pm 0.09) \times 10^{-4}$  and a form-factor value which is  $f_D = (205.8 \pm 8.5 \pm 2.5)$  MeV (this result is with the ratio of  $\tau^+\nu$  and  $\mu^+\nu$  decays fixed to the Standard Model expectation) [28]. Similar methods are used for the  $f_{D_s}$  measurement at CLEO-c based on the 4170 MeV dataset, using both muon and tau decays [24, 25]. In [24]  $D_s^+ \rightarrow \mu + \nu$  and  $\tau^+(\pi^+\nu)\nu$  decays from 314 pb<sup>-1</sup> of data are used to determine  $B(D_s^+ \rightarrow \mu^+\nu) = (8.00 \pm 1.3 \pm 0.4) \times 10^{-3}$  and  $f_{D_s} = (274 \pm 13 \pm 7)$  MeV.

At the B-factories the procedure is first to infer the presence of a  $D_s^+$  from the recoiling mass seen against the system of a reconstructed  $D$  and fragmentation particles, and then to look for a muon and compute the invariant mass of what remains. With 548 fb<sup>-1</sup> of data Belle have measured  $B(D_s^+ \rightarrow \mu^+\nu) = (6.44 \pm 0.76 \pm 0.57) \times 10^{-3}$ , implying a form factor result of  $f_{D_s} = (275 \pm 16 \pm 12)$  MeV.

The CLEO result for  $f_D$  is in agreement with the lattice calculation of  $f_D = 207 \pm 4$  MeV [29]. The experimental results for  $f_{D_s}$  are consistent with each other and give a result of  $f_{D_s} = 270 \pm 8$  MeV, which is three sigma above the lattice value of  $f_{D_s} = 241 \pm 3$  MeV. This is an intriguing situation, which could possibly hint at problems in the lattice approach, or even new physics contributions to the  $D_s$  decay [30]. It is therefore imperative to improve still further the experimental precision. New results for  $f_{D_s}$  are expected soon from CLEO-c with the full 4170 MeV

dataset. Updates are also possible from BaBar and Belle. BES-III data will allow for improved measurements of both  $f_{D_s}$  and  $f_D$ .

It is also possible to measure semi-leptonic form factors in  $D$  decays [31], which then allow for another test of lattice QCD predictions.

## 4 Searches for New Physics in Charm Mixing and Decays

The recent discovery of mixing in the  $D^0$  system, after 30 years of experimental effort, is a significant milestone in flavour physics. Here a very brief summary is given; a full review can be found elsewhere at this conference [32]. Attention is now turning to the search for CP violation in the charm sector, which is an outstanding method to probe for evidence of contributions from non-SM processes. Rare charm hadron decays, although not in general allowing for the cleanliness of interpretation that is familiar in B-physics, constitute another area in which beyond-the-SM physics may manifest itself. It must be emphasised that the processes discussed here, suppressed or forbidden in the SM, offer a complementary route to the search for new physics to those pursued elsewhere in flavour physics. In contrast to the kaon and B-meson sectors, rare charm transitions are unique in receiving contributions from loop diagrams involving virtual down-type quarks.

### 4.1 Charm Mixing and CP Violation

$D^0 - \overline{D^0}$  transitions are governed by the two parameters

$$x = \frac{\Delta M}{\Gamma} \quad \text{and} \quad y = \frac{\Delta \Gamma}{2\Gamma}, \quad (3)$$

where  $\Delta M$  and  $\Delta \Gamma$  are the mass and width differences respectively between the two mass eigenstates, and  $\Gamma$  the mean width of these eigenstates. Mixing can be mediated by short or long-distance processes. GIM suppression and the values of the relevant CKM elements make the short-distance contributions tiny in the Standard Model. Box diagrams alone are expected to lead to values of  $x \sim 10^{-5}$  and  $\sim 10^{-7}$  [33]. Long distance effects can however be sizable, particularly for  $y$  where they are expected to be dominant, and able to enhance these values by many orders of magnitude. The only clear signature of new physics therefore would be the observation  $x \gg y$ .

Since 2006 the B-factories have produced results of high precision in a range of complementary strategies sensitive to  $D^0 - \overline{D^0}$  mixing. These have included searches for mixing in the interference between Cabibbo-favoured and doubly-Cabibbo suppressed decays [34] (with an impressive result in the same analysis also emerging from the Tevatron [4]), measurements of the lifetime in decays to CP-eigenstates [35],

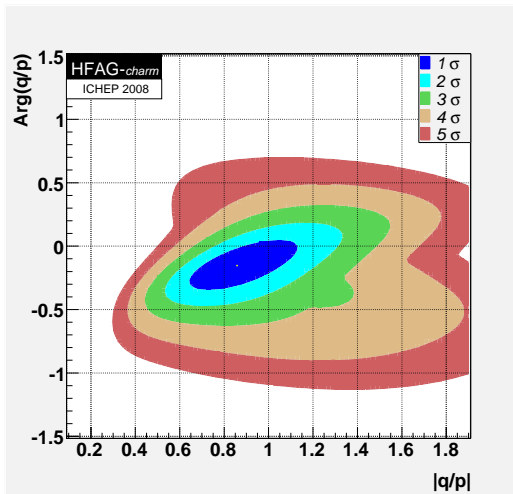


Figure 7: World average results for  $|q/p|$  and  $\phi$  [37].

and mixing-sensitive amplitude analyses of  $D^0 \rightarrow K_S^0 \pi^+ \pi^-$  decays. Although no single measurement has yet yielded a five-sigma discovery in isolation, the cumulative evidence is beyond doubt. A global fit of all results (allowing for CPV) excludes the no-mixing hypothesis at  $9.8\sigma$  and yields parameter values of  $x = 1.00^{+0.24}_{-0.26}$  and  $y = 0.76^{+0.17}_{-0.18}$  [37]. Although these values are larger than many commentators expected [38], they remain in accordance with SM expectations. Nevertheless, the absence of a clear indicator of beyond-the-SM effects can be used to set constraints on a host of new physics models [39]. Furthermore, the larger-than-anticipated value of the oscillation parameters is encouraging in the search for mixing-related CPV.

An unambiguous signature of the existence of new physics processes would be the discovery of CPV, either in the mixing, or in the interference between mixing and decay. The former effect is characterised by a non-zero value of  $\epsilon = |q/p| - 1$ , and the latter by a finite value of  $\phi = \arg(q/p)$ , where  $q$  and  $p$  are the coefficients which relate the mass ( $|D_{1,2}\rangle$ ) and flavour ( $|D^0\rangle$ ,  $|\bar{D}^0\rangle$ ) eigenstates:  $|D_{1,2}\rangle = p|D^0\rangle \pm q|\bar{D}^0\rangle$ . In the SM both  $\epsilon$  and  $\phi$  are negligibly small [40]. Sensitivity to these parameters is achieved by merely generalising the fits of the mixing analyses to allow for CPV contributions. A global average of the present results, displayed in Fig. 7, shows no indication of CPV, with one sigma uncertainties on  $\phi$  and  $\epsilon$  of 0.13 and 0.16 respectively [37]. This precision is already an impressive achievement given the short history of  $D^0$ -mixing studies. Improvements at LHCb and future facilities are eagerly anticipated.

One may look for the effects of direct CPV in a final state  $f$  by searching for

Mode	BaBar	BELLE	CLEO
$K^+K^-$	$0.00 \pm 0.34 \pm 0.13$ [42]	$-0.43 \pm 0.30 \pm 0.11$ [43]	
$\pi^+\pi^-$	$-0.24 \pm 0.52 \pm 0.22$ [42]	$0.43 \pm 0.52 \pm 0.12$ [43]	
$K^+K^-\pi^0$	$1.00 \pm 1.67 \pm 0.25$ [44]		
$\pi^+\pi^-\pi^0$	$0.62 \pm 1.24 \pm 0.28$ [44]	$0.43 \pm 0.41 \pm 1.23$ [45]	
$K^+K^-\pi^+$			$-0.03 \pm 0.84 \pm 0.29$ [46]

Table 1: Recent results in percent for  $A_{CP}^f$  in singly-Cabibbo suppressed  $D$  decays. The uncertainties are statistical and systematic respectively.

non-zero values of the asymmetry  $A_{CP}^f$ :

$$A_{CP}^f = \frac{\Gamma(D \rightarrow f) - \Gamma(\bar{D} \rightarrow \bar{f})}{\Gamma(D \rightarrow f) + \Gamma(\bar{D} \rightarrow \bar{f})}. \quad (4)$$

In the case that the decaying meson is a  $D^0$  then the result includes possible contributions from mixing and mixing-induced CPV, as well as the direct component. Singly-Cabibbo suppressed decays are the most interesting place to look for direct CPV, as gluonic penguins lead to the possibility of significant effects (up to  $10^{-2}$ ) from many new physics models [41], and indeed to non-negligible contributions from the SM itself [40].

Recently there have been results [42, 43, 44, 45, 46] which are achieving sub-percent precision on measurements of  $A_{CP}^f$  for singly-Cabibbo suppressed decays. These results are summarised in Table 1. Although all results are consistent with zero CPV, it is clear that experiments are now entering a very interesting regime. Figure 8 shows the  $D^0$  and  $\bar{D}^0$  mass peaks from the BaBar  $K^+K^-$  and  $\pi^+\pi^-$  analyses, which have around 130k and 64k signal events respectively. What is impressive about these analyses is the manner in which the systematic uncertainties have been controlled. In the  $B$ -factory  $K^+K^-$  and  $\pi^+\pi^-$  analyses [42, 43], for example,  $D^0 \rightarrow K^-\pi^+$  events have been used to calibrate out detector asymmetries associated with the ‘slow pion’ in the  $D^*$  reconstruction, and care has also been taken to remove the effect of the forward-backward asymmetry coming from the  $\gamma - Z$  interference in the  $e^+e^-$  annihilation.

In the case that the decays under study involve more than two particles, then the analysis may be extended to consider final state distributions, which can in principle be more sensitive to CPV than the overall rates. BaBar have done this in a comprehensive manner in their  $K^+K^-\pi^0$  and  $\pi^+\pi^-\pi^0$  study [44], using a variety of techniques to search for differences between  $D^0$  and  $\bar{D}^0$  for the Dalitz plots of the final state particles. In four body decays one can pursue analogous methods or study triple-product correlations [40]. A pilot analysis using the latter approach has been performed by FOCUS for the decay  $K^+K^-\pi^+\pi^-$  [47]. No signal is yet seen of CPV.

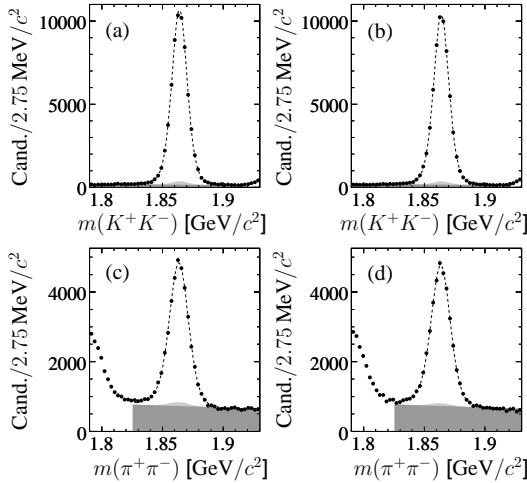


Figure 8: Mass-peaks from BaBar  $A_{CP}^f$  analysis [42]. (a) and (b) show the  $D^0$  and  $\bar{D}^0$  peaks from the  $K^+K^-$  analysis, and (c) and (d) the corresponding peaks from the  $\pi^+\pi^-$  analysis. Solid grey indicates non-peaking background; light grey peaking background.

## 4.2 Rare Charm Decays

The most interesting rare charm decay is the process  $D^0 \rightarrow \mu^+\mu^-$ . In the SM this is extremely suppressed ( $\sim 10^{-13}$ ) but it can be dramatically enhanced in R-parity violating SUSY, which allows for branching ratios up to the level of  $10^{-6}$  [48]. The best existing limit comes from CDF which excludes this decay down to a rate of  $4.3 \times 10^{-7}$  at the 90% C.L. [49] using  $360 \text{ pb}^{-1}$  of data.

As it is the case for the analogous decays in the  $B$  sector, radiative and leptonic modes such as  $D^0 \rightarrow \rho\gamma$ ,  $D^+ \rightarrow \pi^+l^+l^-$  and  $D^0 \rightarrow \rho l^+l^-$  are of interest. (At the time of writing the only ‘rare’ decay of this sort which has been observed is the channel  $D^0 \rightarrow \phi\gamma$ , with a branching ratio of  $2.5^{+0.7}_{-0.6} \times 10^{-5}$  [50].) In general, however, although new physics contributions can be significantly larger than the SM short-range expectations, it is almost certain that the long-distance contributions are often completely dominant, making the absolute branching ratios an unreliable indicator of beyond-the-SM effects. Nevertheless, many channels hold their interest as the kinematical distributions, such as the dilepton invariant mass, or the forward-backward asymmetry, retain their ability to discriminate between the SM and new physics [48]. An example is provided by the dilepton invariant mass distribution in  $D^+ \rightarrow \pi^+l^+l^-$  which has recently been proposed [51] as way in which to test whether leptoquarks can be invoked to explain the tension, discussed in Sec. 3.2, between the lattice and experimental determinations of  $f_{D_s}$ .

## 5 Conclusions

After several years of unjust neglect, charm physics is once more recognised as a discipline with a great deal to contribute to the future of HEP. This sea-change has arisen through three unrelated reasons: recent, unexpected, observations in spectroscopy; the realisation that measurements of  $D$  decay properties are essential technical inputs in the area of precision CKM physics; and the appreciation, given impetus by the discovery of  $D^0 - \overline{D}^0$  mixing, that charm has its own unique discovery potential.

I am grateful to Matt Shepherd for giving many useful suggestions during the preparation of this talk, and the organisers of PIC 2008 in Perugia for a stimulating conference in a beautiful location.

## References

- [1] S. Godfrey and S. Olsen, *The Exotic XYZ Charmonium-like Mesons*, arXiv:0801.3867 [hep-ph].
- [2] D.M. Asner *et al.*, *Physics at BES-III*, arXiv:0809.1869 [hep-ex].
- [3] D.M. Asner, *Charm Physics Opportunities at a Super Flavor Factory*, arXiv:0711.3044 [hep-ex].
- [4] T. Aaltonen *et al.* (CDF Collaboration), Phys. Rev. Lett. **100** (2008) 121802.
- [5] P. Spradlin, G. Wilkinson and F. Xing, *A Study of  $D^0 \rightarrow hh'$  Decays for  $D^0 - \overline{D}^0$  Mixing Measurements*, LHCb-2007-049.
- [6] J. Libby, *LHCb Upgrade*, presentation at ‘Flavour as a Window to New Physics at the LHC’, CERN, May-June 2008.
- [7] J. Charles *et al.* (CKMfitter Group), Eur. Phys. J. **C41** (2005) 1; updated results and plots available at <http://ckmfitter.in23.fr>. All results quoted are from Summer 2008.
- [8] L. Wolfenstein, Phys. Rev. Lett. **51** (1983) 1945.
- [9] M. Gronau and D. London, Phys. Lett. **B 253** (1991) 483; M. Gronau and D. Wyler, Phys. Lett. **B 265** (1991) 172.
- [10] D. Atwood, I. Dunietz and A. Soni, Phys. Rev. Lett. **78** (1997) 3257; D. Atwood, I. Dunietz and A. Soni, Phys. Rev. **D 63** (2001) 036005.

- [11] A. Bondar, Proceedings of BINP Special Analysis Meeting on Dalitz Analysis, 24-26 Sept. 2002, unpublished; A. Giri, Yu. Grossman, A. Soffer and J. Zupan, Phys. Rev. **D 68** (2003) 054018.
- [12] B. Aubert *et al.* (BaBar Collaboration), Phys. Rev. **D 78** (2008) 034023.
- [13] K. Abe *et al.* (BELLE Collaboration), *Updated Measurement of  $\phi_3$  with a Dalitz Plot Analysis of  $B \rightarrow D^{(*)}K$  Decay*, arXiv:0803.3375 [hep-ex].
- [14] E.P. Wigner, Phys. Rev. **70** (1946) 15; S.U. Chung *et al.*, Ann. Phys. **4** (1995) 404; I.J.R. Aitchison, Nucl. Phys. **A 189** (1972) 417.
- [15] D. Aston *et al.* (LASS Collaboration), Nucl. Phys. **B 296** (1988) 493.
- [16] A. Bondar and A. Poluektov, Eur. Phys. J. **C 55** (2008) 51; A. Bondar and A. Poluektov, Eur. Phys. J. **C 47** (2006) 47.
- [17] J. Rademacker, *CLEO-c's Impact on  $\gamma/\phi_3$  from  $B^{\pm(0)} \rightarrow D(K_S^0\pi\pi)K^{\pm(0*)}$* , presentation at ‘CKM 2008’, Rome, September 2008.
- [18] J.L. Rosner *et al.* (CLEO Collaboration), Phys. Rev. Lett. **100** (2008) 221801; D.M. Asner *et al.* (CLEO Collaboration), *Determination of the  $D^0 \rightarrow K^+\pi^-$  Relative Strong Phase Using Quantum-Correlated Measurements in  $e^+e^- \rightarrow D^0\bar{D}^0$  at CLEO*, arXiv:0802.2268 [hep-ex].
- [19] D. Atwood and A. Soni, Phys. Rev. **D 68** (2003) 033003.
- [20] G. Wilkinson,  $\gamma$  at LHCb: *Dalitz Fits in  $B \rightarrow DK$  Decays and Global Precision*, presentation at ‘CKM 2008’, Rome, September 2008.
- [21] J. Libby, *Measurements Related to the ADS Determination of  $\gamma$  at CLEO-c*, presentation at ‘CKM 2008’, Rome, September 2008.
- [22] K. Akiba *et al.*, *Determination of the CKM-Angle  $\gamma$  with Tree-Level Processes at LHCb*, LHCb-2008-031.
- [23] S. Hashimoto, Int. J. Mod. Phys. **A 20** (2005) 5133.
- [24] M. Artuso *et al.* (CLEO Collaboration), Phys. Rev. Lett. **99** (2007) 071802.
- [25] T. Pedlar *et al.* (CLEO Collaboration), *Measurement of  $B(D_s^+ \rightarrow l + \nu)$  and the Decay Constant  $f_{D_s^+}$* , arXiv:0704.0437 [hep-ex].
- [26] L. Widhalm *et al.* (BELLE Collaboration), Phys. Rev. Lett. **100** (2008) 241801.
- [27] B. Aubert *et al.* (BaBar Collaboration), Phys. Rev. Lett. **98** (2007) 141801.

- [28] B.I. Eisenstein *et al.* (CLEO Collaboration), *Precision Measurement of  $B(D^+ \rightarrow \mu^+\nu)$  and the Pseudoscalar Decay Constant  $f_{D^+}$* , arXiv:0806.2112 [hep-ex].
- [29] E. Follana *et al.*, Phys. Rev. Lett. **100** (2008) 062002.
- [30] B.A. Dobrescu and A.S. Kronfeld, Phys. Rev. Lett. **100** (2008) 241802.
- [31] J.Y. Ge *et al.*, *Study of  $D^0 \rightarrow \pi^- e^+ \nu_e$ ,  $D^+ \rightarrow \pi^0 e^+ \nu_e$ ,  $D^0 \rightarrow K^- e^+ \nu_e$ , and  $D^+ \rightarrow \bar{K}^0 e^+ \nu_e$  in Tagged Decays of the  $\psi(3770)$  Resonance*, arXiv:0810.3878 [hep-ex]; D. Cronin-Hennessy *et al.*, *A Study of the Decays  $D^0 \rightarrow \pi^- e^+ \nu_e$ ,  $D^0 \rightarrow K^- e^+ \nu_e$ ,  $D^+ \rightarrow \pi^0 e^+ \nu_e$ , ,and  $D^+ \rightarrow \bar{K}^0 e^+ \nu_e$* , arXiv:0712.0998 [hep-ex]; B. Aubert *et al.* (BaBar Collaboration), Phys. Rev. **D** **76** (2007) 052005; L. Widhalm *et al.* (BELLE Collaboration), Phys. Rev. Lett. **97** (2006) 061804.
- [32] Jörg Marks,  *$D^0 - \bar{D}^0$  Mixing: an Overview*, this conference.
- [33] A. Falk *et al.*, Phys. Rev. **D** **65** (2002) 054034.
- [34] B. Aubert *et al.* (BaBar Collaboration), Phys. Rev. Lett. **98** (2007) 98; B. Aubert *et al.* (BaBar Collaboration), *Measurement of  $D^0 - \bar{D}^0$  Mixing from a Time-Dependent Amplitude Analysis of  $D^0 \rightarrow K^+ \pi^- \pi^0$  Decays*, arXiv:0807.4544 [hep-ex]; L.M. Zhang *et al.* (BELLE Collaboration), Phys. Rev. Lett. **96** (2006) 151801.
- [35] B. Aubert *et al.* (BaBar Collaboration), *Measurement of  $D^0 - \bar{D}^0$  Mixing using the Ratio of Lifetimes for the Decay  $D^0 \rightarrow K^- \pi^+$ ,  $K^- K^+$  and  $\pi^- \pi^+$* , arXiv:0712.2249 [hep-ex]; M. Staric *et al.* (BELLE Collaboration), Phys. Rev. Lett. **98** (2007) 211803; I. Adachi *et al.* (BELLE Collaboration), *Measurement of  $y_{CP}$  in D Meson Decays to CP Eigenstates*, arXiv:0808.0074 [hep-ex].
- [36] K. Abe *et al.* (BELLE Collaboration), Phys. Rev. Lett. **99** (2007) 131803.
- [37] Heavy Flavor Averaging Group (HFAG), August 2008 results, <http://www.slac.stanford.edu/xorg/hfag>.
- [38] A.A. Petrov, *Charm physics: theoretical review*, arXiv:hep-ph/0311371.
- [39] E. Golowich, J. Hewett, S. Pakvasa and A.A. Petrov, Phys. Rev. **D** **76** (2007) 095009.
- [40] I.I. Bigi, *Charm Physics - Like Botticelli in the Sistine Chapel*, arXiv:hep-ph/0107102.
- [41] Y. Grossman, A. Kagan and Y. Nir, Phys. Rev. **D** **75** (2007) 036008.
- [42] B. Aubert *et al.* (BaBar Collaboratio), Phys. Rev. Lett. **100** (2008) 061803.

- [43] M. Staric *et al.* (BELLE Collaboration), *Measurement of CP Asymmetry in Cabibbo Suppressed  $D^0$  Decays*, arXiv:0807.0148 [hep-ex].
- [44] B. Aubert *et al.* (BaBar Collaboration), Phys. Rev. **D 78** (2008) 051102.
- [45] K. Arinstein *et al.* (BELLE Collaboration), Phys. Lett. **B 662** (2008) 102.
- [46] P. Rubin *et al.* (CLEO Collaboration), Phys. Rev. **D 78** (2008) 072003.
- [47] J.M. Link *et al.* (FOCUS Collaboration), Phys. Lett. **B 622** (2005) 239.
- [48] G. Burdman, E. Golowich, J. Hewett, S. Paskvasa, Phys. Rev. **D 66** (2002) 014009.
- [49] CDF Collaboration, *Search for Flavor Changing Neutral Current  $D^0 \rightarrow \mu^+ \mu^-$  Decays Using 360 pb<sup>-1</sup> of CDF Run II Data*, CDF note 9226.
- [50] K. Abe *et al.* (BELLE Collaboration), Phys. Rev. Lett. **92** (2004) 101803.
- [51] S. Fajer and N. Košnik, *Leptoquarks in FCNC Charm Decays*, arXiv:0810.4858 [hep-ph].

# $D^0 - \bar{D}^0$ Mixing: An Overview

*Jörg Marks for the BABAR Collaboration  
Physikalisches Institut der Universität Heidelberg  
Philosophenweg 12, D-69120 Heidelberg, GERMANY*

## 1 Abstract

Recently, the  $B$  factory experiments *BABAR* and *Belle* as well as the CDF collaboration found evidence for mixing in the  $D$  meson system. The current status (beginning of summer 2008) of the experimental results of  $D^0$  mixing is summarized.

## 2 Introduction

The most surprising result of last year's spring conferences on particle physics was the report of the evidence for  $D^0 - \bar{D}^0$  mixing by both the *BABAR* and *Belle* collaborations [1, 2]. At the end of 2007, the CDF collaboration found evidence for  $D^0$  mixing [3] in a different environment but in the same decay channel as *BABAR*.

The first mixing results were obtained in the neutral kaon system [4], 50 years ago. Mixing in the  $B^0$  system [5] was established in 1987 and measurements of the mixing parameters in the  $B_s$  system were published in 2006 by the CDF and D0 collaborations [6].

Within the Standard Model (SM), mainly the first two generations contribute to the  $D^0$  mixing and the mixing parameters and CP violation are expected to be very small. The observation of the  $D^0$  mixing completes the picture of quark mixing, since the  $D^0$  system, in contrast to the other three neutral systems, involves down-type quarks in the mixing loop. On the other hand, non-Standard Model processes could enhance either the mixing or the CP violation or both. Therefore, the measurement of large mixing parameters in the  $D^0$  system or sizable CP violation would be a strong indication for New Physics (NP).

In this paper, we present an overview of  $D^0$  mixing. After an introduction to the charm mixing phenomenology and analysis techniques, results of the mixing parameters and CP violation as related to mixing are summarized. They are obtained from hadronic two-body, multi-body final states and from quantum correlated  $D^0$  decays of the experiments *BABAR*, *Belle*, *Cleo* and *CDF*. Mixing results from semileptonic  $D^0$  decays can be found elsewhere [7, 8].

### 3 Mixing formalism and notation

The neutral mesons are created as eigenstates of the strong interaction and can be distinguished by an internal quantum number, e.g. charm. Due to the weak interaction, an initially defined state of  $|D^0\rangle$  or  $|\bar{D}^0\rangle$  will evolve with time into a mixture of  $D^0$  and  $\bar{D}^0$ . The time evolution can be described by an effective weak Hamiltonian in the time dependent Schrödinger equation

$$i\frac{\partial}{\partial t}\left(\frac{D^0(t)}{D^0(t)}\right) = (M - \frac{i}{2}\Gamma)\left(\frac{D^0(t)}{D^0(t)}\right),$$

where  $M$  and  $\Gamma$  are mass and decay width matrices. The solutions of the Schrödinger equation are the mass eigenstates

$$|D_{1,2}\rangle = p|D^0\rangle \mp q|\bar{D}^0\rangle,$$

with  $p^2 + q^2 = 1$ . They are linear combinations of the flavor eigenstates  $D^0$  and  $\bar{D}^0$ . The mass eigenstates,  $|D_1\rangle$  and  $|D_2\rangle$ , propagate independently in time with their own lifetime  $\Gamma_{1,2}$  and mass  $M_{1,2}$ ,

$$|D_{1,2}(t)\rangle = e^{-i(M_{1,2}-i\Gamma_{1,2}/2)t}|D_{1,2}(t=0)\rangle.$$

The ratios  $x \equiv 2(M_1 - M_2)/(\Gamma_1 + \Gamma_2)$  and  $y \equiv (\Gamma_1 - \Gamma_2)/(\Gamma_1 + \Gamma_2)$  are related to the difference in lifetime and mass of the mass eigenstates. These variables are referred to as mixing parameters and are the observables to be measured.

The probability  $I$  to find the state  $|D^0\rangle$  from an initial state  $|D^0\rangle$  after a time  $t$  is

$$I(D^0 \rightarrow D^0; t) := |\langle D^0 | D^0(t) \rangle|^2 = \frac{e^{-\Gamma t}}{2} [\cosh(\Gamma t) + \cos(\Gamma t)]$$

and the one to find a  $|\bar{D}^0\rangle$  is

$$I(D^0 \rightarrow \bar{D}^0; t) := |\langle \bar{D}^0 | D^0(t) \rangle|^2 = \frac{e^{-\Gamma t}}{2} \left| \frac{p}{q} \right|^2 [\cosh(\Gamma t) - \cos(\Gamma t)].$$

After a certain time, the opposite flavor component appears. Mixing will occur if either the mass difference  $x$  or the lifetime difference  $y$  of the two states is non-zero. Depending on the size of  $x$  and  $y$ , an oscillating behavior can be observed, e.g. as in the case of the  $B_s$  system.

If CP violation is neglected the state  $|D_1\rangle$  ( $|D_2\rangle$ ) is CP-even (CP-odd). However, CP violation in  $D$  mixing can be parametrised in terms of the quantities  $r_m \equiv \left| \frac{q}{p} \right|$  and  $\phi_f \equiv \arg(\frac{qA_f}{pA_f})$ , where  $A_f \equiv \langle f | \mathcal{H}_D | D^0 \rangle$  ( $\bar{A}_f \equiv \langle f | \mathcal{H}_D | \bar{D}^0 \rangle$ ) is the amplitude of

a  $D^0$  ( $\bar{D}^0$ ) to decay into a final state  $f$  and  $\mathcal{H}_D$  is the Hamiltonian of the decay. A value of  $r_m \neq 1$  would indicate CP violation in mixing. A non-zero value of  $\phi_f$  would indicate CP violation in the interference between mixing and decay.

There are two contributions to the charm mixing processes, the short range box contributions and a long range part with on- and off-shell intermediate hadronic states. In contrast to the other neutral systems, the box diagrams of the  $D^0$  system involve loops of down type quarks. Due to the GIM mechanism and the CKM matrix suppression, the lowest-order short distance calculation gives tiny results ( $x_{\text{box}} = \mathcal{O}(10^{-5})$  and  $y_{\text{box}} = \mathcal{O}(10^{-7})$  [10]). Theoretical predictions for the long-range contributions are very difficult, as the  $c$  quark is either not heavy enough or too heavy to be treated by the different theoretical frameworks. Evaluations in the Operator Product Expansion (OPE) framework have shown that the mass and lifetime differences are enhanced with increasing order in the OPE [11] compared to an OPE quark level analysis [12]. This yields  $\mathcal{O} \approx 10^{-3}$  for both  $x$  and  $y$ .

In the SM, CP violation in the charm sector is expected to be small and to be below the sensitivity of the experiments. Any measurement of CP violation in  $D^0$  mixing would be a strong indication of NP.

Calculations within the SM have large uncertainties and, therefore, the ability to detect NP contributions is limited. Nevertheless, the  $D^0$  mixing measurements allow for a restriction of the parameter space of NP models. Golowich et al. (summary in [9]) have explored which NP models yield sizable values for  $x$  and  $y$ . They addressed 21 NP models from various areas and found that in case of 17 models tightened restrictions on the model parameter space can be placed [13].

## 4 Experimental techniques

The most significant measurement of the mixing parameters was performed by the *BABAR* collaboration in the decay  $D^0 \rightarrow K\pi$  [1]. Therefore, basic ideas and techniques of mixing analyses are explained using this decay channel.

### 4.1 Flavor tagging

In order to perform a mixing measurement, the initial state has to be prepared and tagging of the flavor at production time is required. The standard technique in charm physics is the use of  $D^* \rightarrow D^0\pi$  decays<sup>1</sup>. Here, the charge of the pion  $\pi_{\text{tag}}$  determines the flavor of the  $D^0$  at production time.

The flavor at decay time is determined by the final state particle properties. Lets consider the decay of an initial  $D^0$  which decays without mixing as  $D^0 \rightarrow K^-\pi^+$ . In case of mixing, the  $D^0$  converts to a  $\bar{D}^0$  and decays as  $D^0 \rightarrow K^+\pi^-$ . Therefore,

---

<sup>1</sup>The charge conjugate modes are included throughout this paper.

the charge of the  $K$  determines the flavor at decay time and thus if mixing occurred. Events of the decay mode  $D^0 \rightarrow K^-\pi^+$  are classified as right-sign (RS) and events of the decay mode  $D^0 (\rightarrow \bar{D}^0) \rightarrow K^+\pi^-$  are classified as wrong-sign (WS).

Beside the Cabibbo-favored (CF) processes mentioned above, the  $D^0$  also decays doubly Cabibbo-suppressed (DCS) as  $D^0 \rightarrow K^+\pi^-$ . As a consequence, the WS event sample contains not only events which have undergone mixing followed by a CF decay, but also DCS decays. The rate of the DCS events relative to the CF events is suppressed by a factor  $\tan^4(\theta_C)$ , where  $\theta_C$  is the Cabibbo angle. The rate of events with mixing is about another factor hundred smaller. Moreover, both decay amplitudes interfere.

## 4.2 Extracting mixing parameters

While the DCS events decay just exponentially, the mixed decays should have a more complex time structure due to the mixing process. The time evolution of the WS decay rate  $T_{\text{WS}}$  can be approximated by

$$T_{\text{WS}}(t) \propto e^{-\Gamma t} \left( \underbrace{R_D}_{I} + \underbrace{\sqrt{R_D} y' \Gamma t}_{II} + \underbrace{\frac{x'^2 + y'^2}{4} (\Gamma t)^2}_{III} \right) \quad (1)$$

where  $R_D$  is the rate of the DCS events,  $y'$  and  $x'$  denote the mixing parameters and  $\Gamma t$  is the time in units of the  $D^0$  decay time. CP conservation and small mixing parameters are assumed. There are three contributions to  $T_{\text{WS}}$ , the DCS decays (I), the interference of the DCS and mixed decays (II) and the mixed decays (III). Each has a different time dependence. Measuring the time dependence of the WS decay rate allows to determine the mixing parameters  $x$  and  $y$ . Because of the strong phase difference between the CF decay amplitude and the DCS decay amplitude the mixing parameters are only defined up to a phase factor  $\delta_{K\pi}$ . Therefore, the mixing parameters are measured as  $x' = x \sin \delta_{K\pi} + y \cos \delta_{K\pi}$  and  $y' = -x \sin \delta_{K\pi} + y \cos \delta_{K\pi}$ . The phase  $\delta_{K\pi}$  depends on the decay mode and in case of multibody decays it may vary over phase space.

The mixing rate  $R_M$  defined as the time integral over the term III in Eq. 1 is independent of the strong phase ( $x^2 + y^2 = x'^2 + y'^2$ ) and can be measured in semileptonic  $D^0$  decays.

## 4.3 Event selection

The  $Q$  value of the  $D^0$  production process  $D^* \rightarrow D^0 \pi_{\text{tag}}$  is about 6 MeV which leads to a narrow peak in the difference of the  $D^*$  and the  $D^0$  mass ( $\Delta m = m(D^0 \pi_{\text{tag}}) - m(K\pi)$ ). Selecting data in the peak region of the  $\Delta m$  distribution suppresses backgrounds very effectively. The  $D^0$  mass reconstructed from identified kaon and pion

tracks  $m(K\pi)$  is required to be in the expected mass window and the  $D^0$  momentum in the center-of-mass system (CMS) has to be larger than 2.5 GeV in order to remove  $D^0$  mesons from  $B$  decays. The kaon and pion tracks are refit to originate from the same vertex and form a  $D^0$  which is fit together with the slow pion  $\pi_{tag}$  to a common vertex. This provides an event-wise measurement of the  $D^0$  proper time  $\tau$  and the error of the proper time  $\sigma_\tau$ . The typical average value is  $240 \mu\text{m}$  with a resolution of  $100 \mu\text{m}$ .

In the plane of  $\Delta m$  and  $m(K\pi)$ , the *BABAR* analysis selects 1,129,000 RS and 64,000 WS candidates from a data sample of  $384 \text{ fb}^{-1}$ .

## 5 Mixing measurements

### 5.1 $D^0 \rightarrow K\pi$

The RS and WS event candidates in the plane of  $\Delta m$  and  $m(K\pi)$  contain different contributions of signal and backgrounds. Both are described by probability density functions (PDF). Their parameters are determined simultaneously for the RS and WS data sample in an unbinned maximum likelihood fit with four variables  $m(K\pi), \Delta m, \tau, \sigma_\tau$  per event. Figure 1 shows the projections in  $m(K\pi)$  and

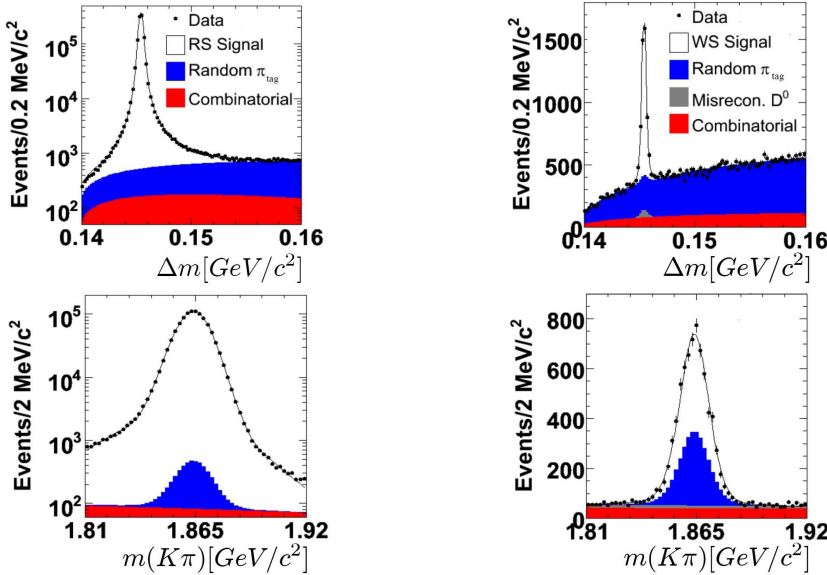


Figure 1:  $m(K\pi)$  (bottom part) and  $\Delta m(K\pi)$  (top part) for wrong-sign candidates (right) and right-sign candidates (left). The fitted PDF's are overlaid. The colored regions represent the different background components [1].

in  $\Delta m(K\pi)$  of the RS and WS candidates. The black points denote the data and the solid lines show the fitted PDF's. The white surface below the curve is the extracted signal. The dominant background component (blue) originates from properly reconstructed  $D^0$  mesons combined with a random slow pion  $\pi_{\text{tag}}$ .

From the fitted signal yields, the WS branching fraction  $R_{\text{WS}}$  in the decay  $D^0 \rightarrow K\pi$  is extracted. The *BABAR* measurement [14] of  $R_{\text{WS}} = (0.353 \pm 0.008 \pm 0.004)\%$  agrees well with the *Belle* result [15] of  $R_{\text{WS}} = (0.377 \pm 0.008 \pm 0.005)\%$ , where the uncertainties are statistical and systematic, respectively.

The WS signal contains mainly DCS events with a small fraction of mixing events. In order to separate the mixing signal,  $D^0$  decay time information is used as described in Sec. 4.2. The  $D^0$  lifetime and the lifetime resolution function is determined from the RS event sample. The WS event sample is fit according to Eq. 1. The result is shown as solid curve in Figure 2. The mixing parameters are measured to be  $R_D =$

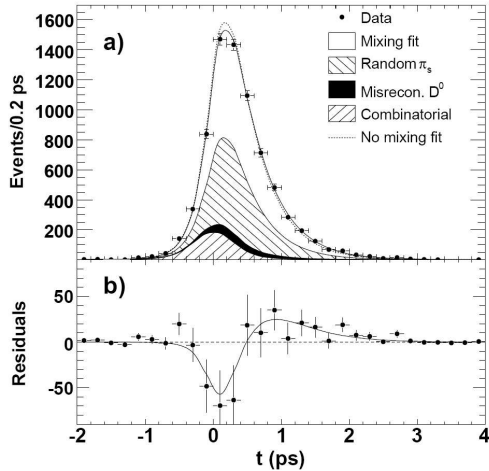


Figure 2: a) Projections of the proper time distribution of the WS candidates and of the fit results. The results of the fit allowing (not allowing) mixing is overlaid as solid (dotted) curve. b) The points represent the difference between the data and the no-mixing fit. The solid curve represents the difference between fits with and without mixing [1].

$(0.303 \pm 0.016 \pm 0.01)\%$ ,  $y' = (0.97 \pm 0.44 \pm 0.31)\%$  and  $x'^2 = (-0.022 \pm 0.03 \pm 0.021)\%$ . The dotted curve shows the fit with the assumption of no-mixing. The histogram in the lower part of Figure 2 displays the difference of the data and the no-mixing fit (dots), while the curve is the difference between the mixing and the no-mixing fit model. The mixing model describes the deviations seen in the residuals. Thus, the deviations of the points from zero can be accounted for by the  $D^0$  mixing. The significance of the mixing signal is evaluated based on the change of the negative log-

likelihood with respect to the maximum. Figure 3 (left part) shows the confidence-level contours calculated from the change in log-likelihood ( $-2\Delta \ln \mathcal{L}$ ) in the two dimensions of  $x'^2$  and  $y'$  considering statistical uncertainties only. The likelihood maximum is indicated as black dot and is located in an unphysical region ( $x'^2 < 0$ ). The most likely physical allowed value ( $x'^2 = 0$  and  $y' = 6.4 \cdot 10^{-3}$ ) has a log-likelihood  $-2\Delta \ln \mathcal{L}$  of 0.7 units. The value of  $-2\Delta \ln \mathcal{L}$  for no-mixing is 23.9 units. Including the systematic uncertainties, this corresponds to a significance of 3.9 standard deviations and thus, constitutes evidence for mixing.

To search for CP violation, Eq. 1 is applied to the WS  $D^0$  and  $\bar{D}^0$  samples separately, fitting for the parameters  $R_D$ ,  $x'^2$  and  $y'$  for  $D^0$  decays (+) and  $\bar{D}^0$  decays (-). Both sets of mixing parameters ( $y'^+ = (0.98 \pm 0.64 \pm 0.45)\%$ ,  $x'^{+2} = (-0.024 \pm 0.043 \pm 0.03)\%$  and ( $y'^- = (0.96 \pm 0.61 \pm 0.43)\%$ ,  $x'^{-2} = (-0.020 \pm 0.041 \pm 0.029)\%$ ) are fully compatible with each other and differ by more than three standard deviations from the no-mixing hypothesis. The values  $R_D = \sqrt{R_D^+ R_D^-} = (0.303 \pm 0.16 \pm 0.10)\%$  and  $A_D = (R_D^+ - R_D^-)/(R_D^+ + R_D^-) = (-2.1 \pm 5.2 \pm 1.5)\%$  are calculated.  $A_D$  is fully compatible with zero. Both sets of mixing parameters do not differ. Therefore, no evidence for CP violation is observed.

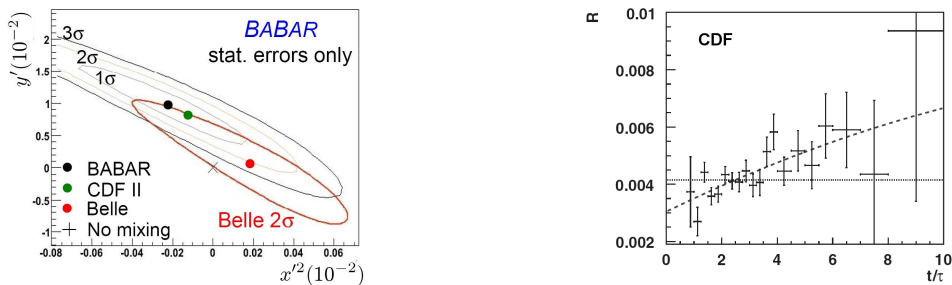


Figure 3: (Left) Comparison of the mixing parameters  $x'^2$  and  $y'$  obtained by *BABAR* (black), *Belle* (red) and *CDF II* (green). The dark curves are the  $1 - 3$  standard deviation likelihood contours from *BABAR*, the red curve is the two standard deviation contour from *Belle* (stat. uncertainties only) [1, 15, 3]. (Right) Ratio of WS and RS  $D^0$  decays as function of normalized proper time as obtained by the *CDF* collaboration. The dashed (dotted) curve is the fit with the mixing (no-mixing) hypothesis [3].

At the end of the year 2007, the *CDF II* collaboration published evidence for mixing in  $D^0 \rightarrow K\pi$  decays using an integrated luminosity of  $1.5 \text{ fb}^{-1}$  in  $p\bar{p}$  collisions [3]. The measurement exploits the time dependence of the number of WS and RS  $D^0$  decays. In the range from 0.75 to 10 units of the  $D^0$  decay time ( $\Gamma t$ ),  $(12.7 \pm 0.3) \cdot 10^3$  WS and  $(3.044 \pm 0.002) \cdot 10^6$  RS signal events are selected. A least-squares parabolic fit of Eq. 1 to  $R = N_{\text{WS}}/N_{\text{RS}}$  in 20 bins of  $\Gamma t$  as shown in the right part of Figure 3 determines the mixing parameters  $R_D = (0.304 \pm 0.055)\%$ ,  $y' = (0.85 \pm$

$0.76\%$  and  $x'^2 = (-0.012 \pm 0.035)\%$ . The no-mixing hypothesis is indicated as dotted line. Despite the different production environment and analysis techniques, the agreement with the *BABAR* mixing results is astonishing (see green dot in the left part of Figure 3). Bayesian probability contours in the  $x'^2 - y'$  plane are calculated. The data are inconsistent with the no-mixing hypothesis with a probability equivalent to 3.8 standard deviations.

The Belle measurement of mixing in  $D^0 \rightarrow K\pi$  published in 2006 is based on an integrated luminosity of  $400 \text{ fb}^{-1}$  [15]. Mixing parameters of  $R_D = (0.364 \pm 0.017)\%$ ,  $y' = (0.06^{+0.40}_{-0.30})\%$  and  $x'^2 = (0.018^{+0.21}_{-0.23})\%$  are obtained. In Figure 3 the results are compared to the *BABAR* and CDF measurements. Belle excludes the no-mixing hypothesis with a significance of two standard deviations considering statistical uncertainties only.

## 5.2 Strong phase $\delta_{K\pi}$

The measurements of the mixing parameters  $x$  and  $y$  are only defined up to a strong phase  $\delta_{K\pi}$  (amplitude ratio of the CF to the DCS decays in  $D^0 \rightarrow K\pi$ ). The CLEO collaboration recently published a measurement of  $\delta_{K\pi}$  using quantum correlated  $D^0\bar{D}^0$  pairs<sup>2</sup> which were produced in  $281 \text{ pb}^{-1}$  of  $e^+e^-$  collisions on the  $\Psi(3770)$  resonance [16]. Two general decay classes are considered, single tags and double tags. For the single tags, one  $D^0$  is reconstructed independently of the other. This class provides uncorrelated decay information. In case of the double tags, both  $D^0$  mesons are reconstructed, and they decay correlated. The final states can be hadronic or semileptonic. Depending on the final state, different enhancement factors to the ratio of the correlated and uncorrelated  $D^0$  decay rates apply. The enhancement factors are functions of the mixing parameters and the strong phase. Therefore, the measurement of the time integrated yields of the correlated and uncorrelated  $D^0$  decays allows to extract the mixing parameters and the strong phase by a fitting procedure. Using external branching fraction measurements in the fit, CLEO obtains  $\cos(\delta_{K\pi}) = 1.03^{+0.31}_{-0.17} \pm 0.06$ . Including additional external measurements of the mixing parameters in the fit provides an alternate measurement of  $\cos(\delta_{K\pi}) = 1.10 \pm 0.35 \pm 0.06$  and allows for a determination of  $x \cdot \sin(\delta_{K\pi}) = (4.4^{+2.7}_{-1.8} \pm 0.29) \cdot 10^{-3}$  and  $\delta_{K\pi} = (22^{+11+9}_{-12-11})^\circ$ .

With these measurements, CLEO established a new technique of time-independent measurements of mixing parameters and the first measurement of the strong phase.

## 5.3 $y_{\text{CP}}$ from lifetime measurements

The decay time  $\tau$  of  $D^0$  mesons (+) and  $\bar{D}^0$  mesons (-) decaying into final states of specific CP (such as  $K^-K^+$  and  $\pi^-\pi^+$ ) can be considered to first order as exponential

---

<sup>2</sup>CLEO uses the inverse amplitude ratio for the definition of the strong phase  $\delta_{K\pi}$ .

with a small correction term that depends on the mixing parameters:

$$\tau^\pm = \frac{\tau^0}{1 + |q/p|(y \cos \phi_f \mp x \sin \phi_f)} ,$$

where  $\tau^0$  is the lifetime of the CF decay  $D^0 \rightarrow K\pi$ . The lifetimes can be combined into the quantities  $y_{CP}$  and  $\Delta Y$ :

$$y_{CP} = \frac{\tau^0}{\tau} - 1 = \frac{\tau(K^-\pi^+)}{\tau(\pi^+\pi^-)} - 1 = \frac{\tau(K^-\pi^+)}{\tau(K^+K^-)} - 1 \quad \Delta Y = \frac{\tau^0 A_\tau}{\tau} ,$$

with  $A_\tau = (\tau^+ - \tau^-)/(\tau^+ + \tau^-)$ . In the limit of CP conservation<sup>3</sup>,  $y_{CP} = \pm y$  and  $\Delta Y = 0$ .

Belle found significantly different decay time distributions for  $D^0$  decays to the CP-eigenstates  $K^+K^-$  and  $\pi^+\pi^-$  compared to the one to the CP-mixed state  $K^-\pi^+$  and measured  $y_{CP} = (1.31 \pm 0.32 \pm 0.25)\%$  with a significance of 3.2 standard deviations including systematic uncertainties [2]. The dataset corresponds to  $540 \text{ fb}^{-1}$ . The measured lifetime asymmetry parameter  $A_\tau = -(0.01 \pm 0.3 \pm 0.15) \cdot 10^{-3}$  reveals no evidence for CP violation.

At the end of 2007, *BABAR* published a measurement of  $y_{CP}$  from the lifetime of the three  $D^0$  decay modes  $K^+K^-$ ,  $\pi^+\pi^-$  and  $K\pi$  [17] using  $384 \text{ fb}^{-1}$  of data. A value of  $y_{CP} = (1.24 \pm 0.39 \pm 0.13)\%$  is obtained, which is evidence for mixing at the three standard deviation level. No indication for CP violation was found, as indicated by the value  $\Delta Y = (-0.26 \pm 0.36 \pm 0.08)\%$ . Combining this result with a previous untagged *BABAR* measurement [18] yields the combined measurement  $y_{CP} = (1.03 \pm 0.33 \pm 0.19)\%$ .

The charm subgroup of the Heavy Flavour Averaging Group (HFAG) provides combined values for mixing parameters [22]. Besides *BABAR* and Belle, results from E791, FOCUS and CLEO contribute to the average values  $y_{CP} = (1.132 \pm 0.266)\%$  and  $A_\tau = -(0.123 \pm 0.248)\%$ . The precision is dominated by the *B* factory experiments. The  $y_{CP}$  measurement clearly indicates  $D^0$  mixing at a lifetime difference which is about 1% and the no-mixing case is excluded at 4.5 standard deviations. There is no indication for CP violation from the averaged asymmetry measurements.

## 5.4 Time-dependent Dalitz analysis

Up to now, we considered only two body decays of the  $D^0$ . CLEO pioneered a method to measure  $x$  and  $y$  from a time-dependent Dalitz analysis of the resonant substructure in the decay  $D^0 \rightarrow K_S^0\pi^+\pi^-$  [19]. This method allows to measure the sign of  $x$ .

---

<sup>3</sup>The sign depends on the CP eigenvalue.

Belle extends the analysis of the self-conjugate process  $D^0 \rightarrow K_S^0\pi^+\pi^-$  to a dataset of  $540 \text{ fb}^{-1}$  [20]. The Dalitz plot is shown in the upper left distribution of Figure 4. It is described by a model containing contributions of 18 different quasi two body decays, which interfere. The time-dependent decay amplitudes of the  $D^0$  and  $\bar{D}^0$  are functions of the Dalitz variables ( $m_+^2(K_S^0\pi^+)$ ,  $m_-^2(K_S^0\pi^-)$ ) and the mixing parameters  $x$  and  $y$ . Therefore,  $x$  and  $y$  can be extracted from an unbinned maximum likelihood fit to the Dalitz variables and the measured  $D^0$  decay time. The data points are shown in Figure 4 and the curves represent the fit results. Assuming negligible CP violation,

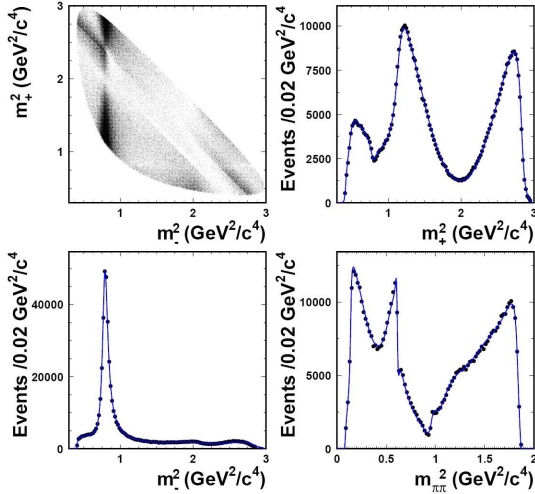


Figure 4: Dalitz plot distribution and the projections in case of data (points with error bars) and the fit result (curve) as obtained by the Belle collaboration [20].

$x = (0.80 \pm 0.29^{+0.09+0.10}_{-0.07-0.14})\%$  and  $y = (0.33 \pm 0.24^{+0.08+0.06}_{-0.12-0.08})\%$  are obtained, where the uncertainties are statistical, experimental systematic and decay-model systematic. The no-mixing case is excluded at 2.2 standard deviations.

Allowing for CP violation, the fit of the additional parameters  $|q/p|$  and  $\phi$  indicates no evidence for CP violation in mixing or interference between mixed and unmixed amplitudes. Since the fit parameters are consistent for both the  $D^0$  and  $\bar{D}^0$  sample, there is also no evidence for direct CP violation.

*BABAR* finds evidence for  $D^0$  mixing using a time-dependent amplitude analysis of the decay  $D^0 \rightarrow K^+\pi^-\pi^0$  in a data sample of  $384 \text{ fb}^{-1}$  [21]. The decay contains WS and RS events (see Sec. 4.1). The signal and background yields are extracted from a binned extended maximum likelihood fit to the  $\Delta m$  and  $m(K\pi\pi^0)$  distributions. The time-dependent relative WS decay rate is a function of the Dalitz variables ( $m_{K^+\pi^-}^2$ ,  $m_{K^+\pi^0}^2$ ) and the mixing parameters in the form  $x'_{K\pi\pi^0} = x \cos \delta_{K\pi\pi^0} + y \sin \delta_{K\pi\pi^0}$  and  $y'_{K\pi\pi^0} = y \cos \delta_{K\pi\pi^0} - x \sin \delta_{K\pi\pi^0}$ , where  $\delta_{K\pi\pi^0}$  is the strong phase between the DCS and the CF amplitude of  $D^0 \rightarrow \rho^-\pi^+$ . The phase  $\delta_{K\pi\pi^0}$  is different from

$\delta_{K\pi}$  and has to be measured elsewhere. From a time-dependent fit to the WS data,  $x'_{K\pi\pi^0} = (2.61^{+0.57}_{-0.68} \pm 0.39)\%$  and  $y'_{K\pi\pi^0} = (-0.06^{+0.55}_{-0.64} \pm 0.34)$  are derived with a correlation of  $-0.75$ . The significance is equivalent to 3.2 standard deviations.

## 6 Combined results

The HFAG determined world average values of the mixing parameters  $x$  and  $y$  in a global fit which takes into account all the relevant data from the various experiments [22]. Most of the more recent results have been presented in this talk. They are dominated by the  $B$  factory measurements with significant contributions from CLEO-c and Tevatron. The no-mixing case is excluded at about seven standard deviations ( $x = (0.91 \pm 0.26)\%$  and  $y = (0.73 \pm 0.18)\%$ ). The mass difference differs from zero by 3 standard deviations, the lifetime difference deviates from zero by about 4.1 standard deviations. The fit also determines  $R_D = (0.3342 \pm 0.0083)\%$ ,  $\delta_{K\pi} = (21.6^{+11.6}_{-12.6})^\circ$  and  $\delta_{K\pi\pi^0} = (30.8^{+25.0}_{-25.8})^\circ$ . The measurement of CLEO of the strong hadronic phase  $\delta_{K\pi}$  discussed in 5.2 was not considered because external measurements of  $R_D$  and  $R_M$  entered in the fitting procedure.

Another set of parameters was determined allowing for CP violation. The values obtained for the CP sensitive parameters  $A_D = -2.2 \pm 2.5$ ,  $|q/p| = 0.86^{+0.18}_{-0.15}$  and  $\phi = (-9.6^{+8.3}_{-9.5})^\circ$  indicate no evidence for CP violation within the current sensitivity of the experiments.

The  $y$  measurement from the  $D^0$  lifetime (see Sec. 5.3) yields  $y > 0$ . Therefore, the  $|D_1\rangle$  as CP-even state lives shorter than the CP-odd state  $|D_2\rangle$ . The sign of  $x$  is measured in the Dalitz analysis (see Sec. 5.4) as  $x > 0$ . Therefore, the CP-even state  $|D_1\rangle$  is heavier than the CP-odd state  $|D_2\rangle$ .

Preliminary Monte Carlo studies of the LHCb collaboration indicate that the statistical uncertainties of the mixing parameters  $x, y$  and  $y_{CP}$  measured in a time-dependent WS analysis of  $D^0 \rightarrow K\pi$  decays and a lifetime analysis of  $D^0$  decays to  $K^-K^+$  and  $K^-\pi^+$  in  $10 \text{ fb}^{-1}$  of data may decrease by a factor five [23].

In summary, three experiments found evidence for  $D^0$  mixing measuring lifetime and mass differences at the level of 1 %. The combined results of all experiments exclude the no-mixing case at seven standard deviations. The measurements are compatible with the SM expectations. It seems likely that the  $D^0$  mixing is dominated by long-distance processes, which are difficult to calculate. Therefore, identifying NP contributions from mixing alone is not easily possible. Neither a single experiment nor the combination of all results provide any hint for CP violation in  $D^0$  mixing.

## References

- [1] B. Aubert et al. (*BABAR Collab.*), Phys. Rev. Lett. **98**, 211802 (2007).

- [2] M. Staric et al. (Belle Collab.), Phys. Rev. Lett. **98**, 211803 (2007).
- [3] T. Aaltonen et al. (CDF Collab.), Phys. Rev. Lett. **100**, 121802 (2008).
- [4] W. F. Fry et al., Phys. Rev. **103**, 1904 (1956).
- [5] C. Albajar et al. (UA1 Collab.), Phys. Lett. B **192**, 247 (1987); H. Albrecht et al. (ARGUS Collab.), Phys. Lett. B **192**, 245 (1987).
- [6] V.M. Abazov et al. (D0 Collab.) Phys. Rev. Lett. B **97**, 021802 (2006); A. Abulencia et al. (CDF Collab.), Phys. Rev. Lett. B **97**, 242003 (2006).
- [7] B. Aubert et al. (*BABAR* Collab.), Phys. Rev. D **72**, 014018 (2007).
- [8] U. Bitenc et al. (Belle Collab.), arXiv:0802.2952 (2008).
- [9] E. Golowich, Proceedings of the CHARM Workshop (2007).
- [10] A. F. Falk et al., Phys. Rev. D **97**, 054034 (2002).
- [11] I.I.Y. Bigi and N.G. Uraltsev Nucl. Phys. B **592**, 92 (2001).
- [12] E. Golowich et al. Phys. Lett. B **625**, 53 (2005).
- [13] E. Golowich et al. Phys. Rev. D arXiv:hep-ph/0705.3650 (2007).
- [14] B. Aubert et al. (*BABAR* Collab.), Phys. Rev. Lett. **98**, 211802 (2007).
- [15] L.M. Zhang et al. (Belle Collab.), Phys. Rev. Lett. **96**, 151801 (2006).
- [16] J. L. Rosner et al. (CLEO Collab.), arXiv:0802.2264 (2008).
- [17] B. Aubert et al. (*BABAR* Collab.), arXiv: 0712.2249 (2007).
- [18] B. Aubert et al. (*BABAR* Collab.), Phys. Rev. Lett. **91**, 221801 (2003).
- [19] D. M. Asner et al. (CLEO Collab.), Phys. Rev. D **72**, 012001 (2005).
- [20] L.M. Zhang et al. (Belle Collab.), Phys. Rev. Lett. **99**, 131803 (2007).
- [21] B. Aubert et al. (*BABAR* Collab.), arXiv: 0807.4544 (2008)
- [22] A. Schwartz et al., arXiv:0803.0082 (2008);  
see <http://www.slac.stanford.edu/xorg/hfag/charm/index.html>.
- [23] P. Spradlin et al. (LHCb Collab.), arXiv:0711.1661 (2007);P. Spradlin et al. (LHCb Collab.), LHCb Pub. Note, LHCb-2007-049 (2008).

# Strange Quark Physics at Sixty-Four

*Bradley Cox*

*Department of Physics*

*University of Virginia*

*Charlottesville, VA 22904*

## 1 Introduction

At a point in time, sixty-four years after the first observation of strange particle by Le Prince Ringuet in the decay of a charged kaon in a cloud chamber [1], strange quark physics is still remarkably robust. The high statistics and precision measurements that are now possible lend themselves to searches for new physics.

There are too many new results in the recent past to cover all the new measurements that deserve attention in this paper. New results in the following areas that have been recently reported and are included in this paper:

- CP violation.
- searches for lepton flavor violation in neutral kaon decays.
- $e,\mu$  universality and new physics in kaon decays.
- $V_{us}$  measurements.

Due to lack of space, beautiful results on quantum coherence and CUSP measurements in kaon decay will not be covered. Lack of space also precludes inclusion of many excellent results bearing on chiral perturbation theory.

The majority of the new results are due to three experiments, KTeV, NA48/2, and KLOE, diagrams of which are shown in Fig. 1. In addition, we are just beginning to see the first results from E391a shown in Fig. 2 (soon to upgraded to experiment E14 at J-PARC). This is the first dedicated experiment designed to search for  $K_L \rightarrow \pi^0 \nu \bar{\nu}$ . The NA48/2 experiment is expected to be followed by NA62 and the KLOE experiment by KLOE II in the future. The future for kaon physics in the US is much more problematic, given the status and priority of the Project X kaon initiative at Fermilab.

With the large statistics and precision measurements of the present generation of experiments, we can ask the question of whether there are any hints of new physics of any kind and if not, do we have a problem developing from the lack of any such evidence at this time. While each high sensitivity search or measurement must be judged on its own merits, as compared with theoretical expectations for new physics levels, a problem with the non-appearance of new physics may be developing.

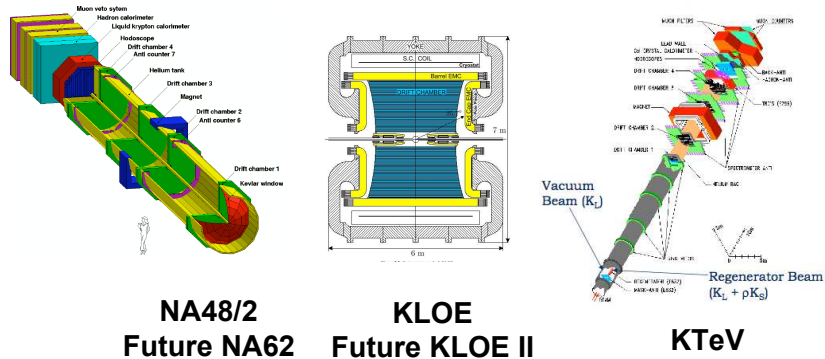


Figure 1: KTeV, NA48/2, and KLOE Experiments.

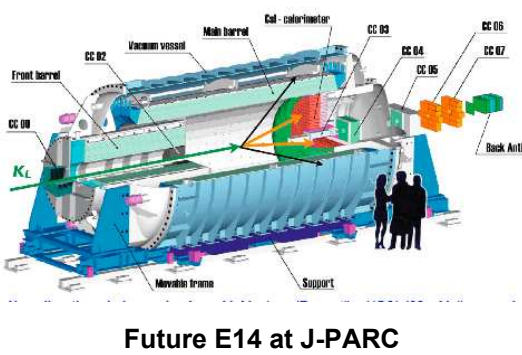


Figure 2: E391a Experiment (to become E14 at J-PARC).

## 2 Direct CP Violation Measurements and Searches in $K_{L,S}$ Decays

### 2.1 Direct CP Detection in $K_{L,S}$ Decays into Di-pions

We have recently seen the completion of the epsilon prime analysis from the entire KTeV data set from 1996, '97 and '98 and the report of a final answer for epsilon prime. Epsilon prime, the parameter whose non-zero value indicates that the weak interaction is direct CP violating, is obtained from the comparison of the charged and neutral two pion decay modes of the  $K_L$  and  $K_S$  mesons. The real part of the ratio of epsilon prime to epsilon (the amplitude for the indirect CP violating decay of the

neutral kaons) can be shown to be related to these decays via the expression

$$Re\left(\frac{\epsilon'}{\epsilon}\right) \approx \frac{1}{6} \left[ \frac{\Gamma(K_L \rightarrow \pi^+ \pi^-) \Gamma(K_S \rightarrow \pi^+ \pi^-)}{\Gamma(K_L \rightarrow \pi^0 \pi^0) \Gamma(K_S \rightarrow \pi^0 \pi^0)} - 1 \right].$$

In order to obtain adequate two body decay statistics for both  $K_S$  and  $K_L$  decays, the KTeV experiment was designed to take data simultaneously using two neutral beams, one of which was a “vacuum” neutral beam composed of a mixture of  $K_L$ ’s and neutrons (and a small number of hyperons) beam and a similar beam in which a regenerator was placed to produce a  $K_{L,S}$  mixture. These two beams passed into an approximately 90 meter decay region where the kaons decayed. The decay products were then detected and measured by a spectrometer just downstream of the decay region. The spectrometer consisted of a drift chamber and large aperture magnet to measure the charge and momentum of the charged pions followed by a CsI calorimeter to identify and measure the energy of the electrons and photons and a muon detector to identify  $\mu$ ’s.

The statistics for each of the four two-body decay modes are shown in Table 1. As can be seen from the table, the most difficult mode to obtain statistics for was the  $K_L \rightarrow \pi^0 \pi^0$  accumulated in vacuum beam operation and is, therefore, the largest contributor to the statistical error.

Decay mode	$K_L$ Vacuum Beam	" $K_S$ " Regenerator Beam
$K \rightarrow \pi^+ \pi^-$	25,107,242	43,674,208
$K \rightarrow \pi^0 \pi^0$	5,968,198	10,180,175

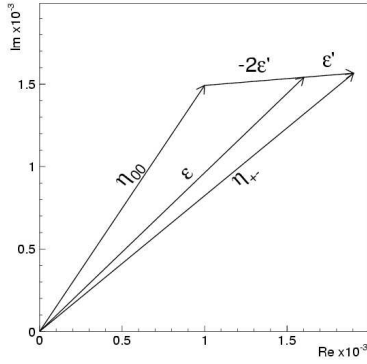
Table 1: Two Body  $K_{L,S} \rightarrow$  di-pion decay mode statistics.

Many systematics were studied for the  $\pi^+ \pi^-$  and  $\pi^0 \pi^0$  modes. The largest contribution to the  $Re\left(\frac{\epsilon'}{\epsilon}\right)$  from the  $\pi^+ \pi^-$  mode is due to an acceptance uncertainty of  $0.57 \times 10^{-4}$  out of a total uncertainty from all systematics from the  $\pi^+ \pi^-$  mode of  $0.81 \times 10^{-4}$ . The largest contribution to the uncertainty in the  $Re\left(\frac{\epsilon'}{\epsilon}\right)$  from the  $\pi^0 \pi^0$  mode was due to uncertainties in the CSI cluster reconstruction and contributed  $0.75 \times 10^{-4}$  to a total uncertainty of  $1.55 \times 10^{-4}$  from the  $\pi^0 \pi^0$  mode. The combined uncertainties from the  $\pi^+ \pi^-$  and  $\pi^0 \pi^0$  modes is  $1.78 \times 10^{-4}$ . The final answer for  $Re\left(\frac{\epsilon'}{\epsilon}\right)$  is

$$Re\left(\frac{\epsilon'}{\epsilon}\right) = [19.2 \pm 1.1(stat) \pm 1.8(syst)] \times 10^{-4}$$

In addition to the determination of  $Re\left(\frac{\epsilon'}{\epsilon}\right)$ , the KTeV experiment has fit for the  $Im\left(\frac{\epsilon'}{\epsilon}\right)$  and several other important neutral kaon parameters. Fig. 3 shows the result of the fit for  $Im\left(\frac{\epsilon'}{\epsilon}\right)$  and Table 2 gives a summary of the neutral kaon parameters extracted from the full data set.

$$\begin{aligned}
\eta_{+-} &= \frac{A(K_L \rightarrow \pi^+ \pi^-)}{A(K_S \rightarrow \pi^+ \pi^-)} = \varepsilon + \varepsilon' \\
\eta_{00} &= \frac{A(K_L \rightarrow \pi^0 \pi^0)}{A(K_S \rightarrow \pi^0 \pi^0)} = \varepsilon - 2\varepsilon' \\
\phi_{SW} &= \tan^{-1} \left( \frac{2\Delta m}{\Delta \Gamma} \right) \\
\phi_{+-} &\approx \phi_\varepsilon + \text{Im}(\varepsilon'/\varepsilon) \\
\phi_{00} &\approx \phi_\varepsilon - 2 \text{Im}(\varepsilon'/\varepsilon) \\
\Delta\phi &\equiv \phi_{00} - \phi_{+-} \approx -3 \text{Im}(\varepsilon'/\varepsilon)
\end{aligned}$$

Figure 3:  $Re(\frac{\epsilon'}{\epsilon})$  vs.  $Im(\frac{\epsilon'}{\epsilon})$ .

Neutral Kaon parameter	
$Re(\frac{\epsilon'}{\epsilon})$	$19.2 \pm 1.1(stat) \pm 1.8(syst)] \times 10^{-4}$
$\Delta m$	$(5269.9 \pm 12.3) \times 10^6 \hbar s^{-1}$
$\tau_S$	$(89.623 \pm 0.047) \times 10^{-12} s$
$\phi_\varepsilon$	$(43.86 \pm 0.63)^\circ$ no CPT constraint
$\phi_\varepsilon - \phi_{SW}$	$(0.40 \pm 0.56)^\circ$ no CPT constraint
$\Delta\phi$	$(0.30 \pm 0.35)^\circ$ no CPT constraint
$\frac{\text{Rate}(K^0 \rightarrow \pi^+ \pi^-) - \text{Rate}(\bar{K}^0 \rightarrow \pi^+ \pi^-)}{\text{Rate}(K^0 \rightarrow \pi^+ \pi^-) + \text{Rate}(\bar{K}^0 \rightarrow \pi^+ \pi^-)}$	$(5.5 \pm 0.5) \times 10^{-5}$

Table 2: Parameters of Neutral Kaon Decays.

## 2.2 Searches for the $K_L \rightarrow \pi^0 \nu \bar{\nu}$ Decay

The  $K_L \rightarrow \pi^0 \nu \bar{\nu}$  decay is a “golden” mode in the sense that this mode is almost 100% direct CP violating with no long distance contributions to the decay amplitude and with hadronic matrix elements that can be determined from kaon modes with larger branching ratios. A measurement of its branching ratio is a measurement of  $\eta$ , the CP violating phase of the CKM matrix. The detection of this mode is very difficult since its signature is essentially two  $\gamma$ ’s plus “nothing” and the Standard Model branching ratio is expected to be of order  $2.76 \pm 0.40 \times 10^{-11}$  [3].

The E391a experiment at KEK that will move to J-PARC and be upgraded to E14 is the first dedicated experiment to attempt to detect and measure the branching ratio for the  $K_L \rightarrow \pi^0 \nu \bar{\nu}$ . In the E-14 experiment a beam of neutrons and  $K_L$ ’s is injected into the experiment where the  $K_L \rightarrow \pi^0 \nu \bar{\nu}$  decays take place in a decay volume surrounded by vetos to eliminate all other decay modes. The main backgrounds are neutron+residual gas  $\rightarrow \pi^0$  and  $K_L \rightarrow \pi^0 \pi^0$  decays where two photons are undetected.

The signal consists of two photons detected in the electromagnetic calorimeter (part of which will be constructed using the KTeV CsI elements). The two photons are required to form a  $\pi^0$  mass and point toward the neutral beam which has small transverse dimensions.

The first results from the E391a version of the experiment have been reported. They improve the existing limits by an order of magnitude. Table 3 lists the new result from E391a and compares it to previous results from KTeV.

Experiment	$\text{BR}((K_L \rightarrow \pi^0\nu\bar{\nu}) \text{ Limit})$
E391a [5]	$< 6.7 \times 10^{-8}$
KTeVII [6]	$< 5.9 \times 10^{-7}$
KTeVVI [7]	$< 1.6 \times 10^{-6}$

Table 3: Branching ratio limit for  $K_L \rightarrow \pi^0\nu\bar{\nu}$ . Note that the KTeVII result was achieved requiring that one of the photons to convert to a Dalitz pair.

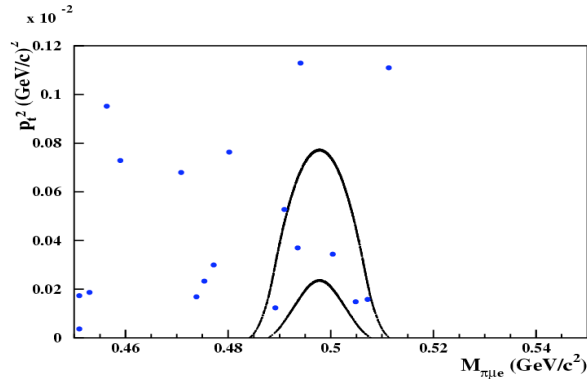
### 3 Search for Lepton Flavor Violation in Neutral Kaon decays

The KTeV experiment has also searched for Lepton Flavor violation in three decay channels,  $K_L \rightarrow \pi^0\mu e$ ,  $K_L \rightarrow \pi^0\pi^0\mu e$ , and  $\pi^0 \rightarrow \mu e$  [2]. The major backgrounds for all three LFV modes were  $Ke3$  or  $Ke4$  decays where a pion decayed or faked a muon. The signal region after physics cuts for the  $K_L \rightarrow \pi^0\mu e$  is shown in Fig. 4. As can be seen, no events were found in the signal region. The same was true for the other two decays, leading to the upper limits for the three decays given in Table 4

mode	upper limit (90% CL)
$\text{BR}(K_L \rightarrow \pi^0\mu e)$	$< 7.56 \times 10^{-11}$
$\text{BR}(K_L \rightarrow \pi^0\pi^0\mu e)$	$< 1.7 \times 10^{-10}$
$\text{BR}(\pi^0 \rightarrow \mu e)$	$< 3.59 \times 10^{-10}$

Table 4: Upper limits for LFV in  $K_L \rightarrow \pi^0\mu e$ ,  $K_L \rightarrow \pi^0\pi^0\mu e$ , and  $\pi^0 \rightarrow \mu e$ .

The result for  $\text{BR}(K_L \rightarrow \pi^0\mu e)$  is 83 times lower than previously obtained. The result for  $\text{BR}(K_L \rightarrow \pi^0\pi^0\mu e)$  is the first upper limit for this mode. Finally, the result for  $\text{BR}(\pi^0 \rightarrow \mu e)$  is a factor of 20 lower than obtained in previous experiments. To see where these searches rank relative to previous LFV searches made using other modes, we show in Fig. 5 a composite of all such searches with these KTeV limits included.

Figure 4: Signal Region for  $K_L \rightarrow \pi^0 \mu e$ .

## 4 Searches for New Physics and e, $\mu$ Universality Violation

The muon and electron differ by only their mass and coupling to the Higgs particle as far as we know at this time. New physics might well be expected to show up in the deviations from predictions in processes whose only difference is in whether an electron or  $\mu$  is involved and are otherwise well determined in the Standard Model. The following three ratios present opportunities to detect such deviations:

- Test of lepton universality for weak vector currents

$$R_{e\mu} = \frac{\Gamma(K_{e3})}{\Gamma(K_{\mu 3})} \rightarrow \frac{G_F^e}{G_F^\mu}$$

- Test of  $H^+$  (scalar)exchange or presence of right handed currents

$$R_{K\pi} = \frac{\Gamma(K \rightarrow \mu\nu)}{\Gamma(\pi \rightarrow \mu\nu)}$$

- Test for LFV due to pseudoscalar weak currents

$$R_K = \frac{\Gamma(K \rightarrow e\nu)}{\Gamma(K \rightarrow \mu\nu)}$$

### 4.1 $R_{e\mu} = \frac{\Gamma(K_{e3})}{\Gamma(K_{\mu 3})}$

Using  $K_{l3}$  branching ratios obtained by KLOE, NA48, KTeV, and ISTRAP+, the FlaviA kaon working group has made new determinations of

$$\frac{g_\mu^2}{g_e^2} = \frac{\Gamma_{\mu 3} I_{e3}(1+\delta_{e3})}{\Gamma_{e3} I_{\mu 3}(1+\delta_{\mu 3})} = \frac{[|V_{us}| f_+(0)]_{\mu 3, obs}^2}{[|V_{us}| f_+(0)]_{e3, obs}^2}$$

Here the I's are kaon structure functions and the  $\delta$ 's are SU(3) and EM theoretical corrections. The results are

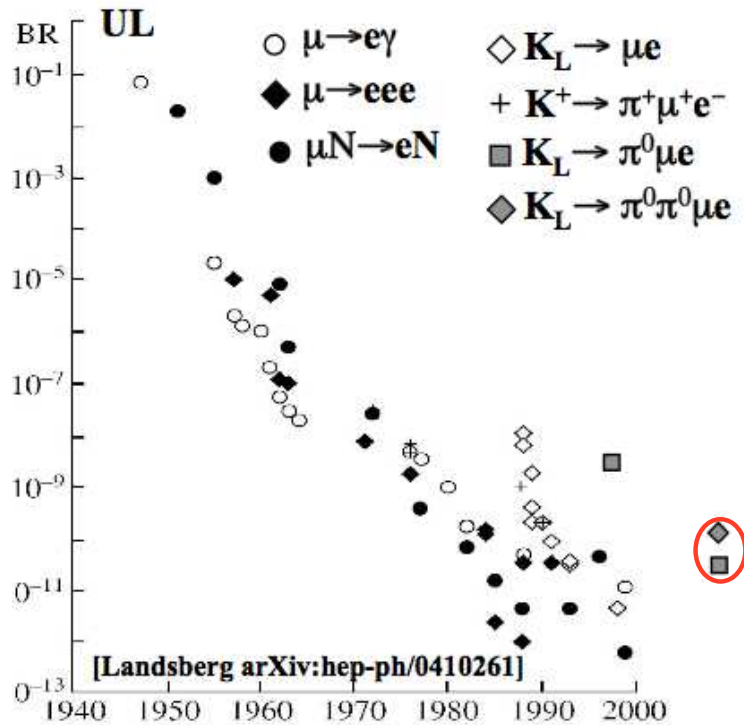


Figure 5: LFV Violation searches over the years [4]

$$\begin{aligned}
 K_L & \quad \frac{g_\mu^2}{g_e^2} = 1.0049(61) \\
 K^+ & \quad \frac{g_\mu^2}{g_e^2} = 1.0029(86) \\
 \text{AVG} & \quad \frac{g_\mu^2}{g_e^2} = 1.0043(52)
 \end{aligned}$$

this can be compared with the result  $\frac{g_\mu^2}{g_e^2} = 0.9998(40)$  extracted from  $\tau \rightarrow l\nu\nu$  decays (PDG07). Thus, we have no evidence for new physics from  $\frac{g_\mu^2}{g_e^2}$  measurements.

#### 4.2 $R_{K\pi} = \frac{\Gamma(K \rightarrow \mu\nu)}{\Gamma(\pi \rightarrow \mu\nu)}$

In the two Higgs doublet models and MSSM, exchanges of  $H^+$  can provide an extra scalar current which could make contributions [8] to  $\Gamma(K \rightarrow l\nu)$  beyond the Standard Model of the form

$$\frac{\Gamma(K \rightarrow l\nu)}{\Gamma_{SM}(K \rightarrow l\nu)} \simeq |1 - \frac{m_K^2}{M_{H^+}^2} (1 - \frac{m_d}{m_s}) \frac{\tan^2 \beta}{1 + \epsilon_0 \tan \beta}|$$

This contribution is supposedly suppressed in  $\pi l2$  compared to  $Kl2$  decays and, thus, could show up as a deviation from the Standard Model expectation for the ratio  $\frac{Kl2}{\pi l2}$  shown below:

$$\frac{\Gamma(Kl2)}{\Gamma(\pi l2)} = \left| \frac{V_{us}}{V_{ud}} \right|^2 \frac{f_K^2 m_K}{f_\pi^2 m_\pi} \left( \frac{1 - \frac{m_l^2}{m_K^2}}{1 - \frac{m_l^2}{m_\pi^2}} \right)^2 \times (1 + \delta_e m)$$

In the Standard model the quantity

$$\left| \frac{V_{us}(Kl2)}{V_{ud}(\pi l2)} \times \frac{V_{ud}(0^+ \rightarrow 0^+)}{V_{us}(Kl3)} \right|$$

is supposed to be equal to one and in the two Higgs doublet (or MSSM) model equal to

$$\left| 1 - \frac{m_K^2}{M_{H^+}^2} \left( 1 - \frac{m_d}{m_s} \right) \frac{\tan^2 \beta}{1 + \epsilon_0 \tan \beta} \right|$$

The present value of this quantity as determined by the FlaviA kaon working group is 1.0018(57), completely consistent with the SM.

### 4.3 $R_K = \frac{\Gamma(K \rightarrow e\nu)}{\Gamma(K \rightarrow \mu\nu)}$

A search for new physics has been done using  $R_K = \frac{\Gamma(Ke2)}{\Gamma(K\mu2)}$ . In the SM this ratio should equal  $2.477(1) \times 10^{-5}$  to an accuracy of 0.04% [9]. Deviations from the SM can be enhanced by helicity suppression [10] and in R-parity violating MSSM, lepton flavor violation can give 1% deviations from the SM. At present, no experiment reaches this level of precision. Current measurements are

KLOE	$R_K = 2.55(5)_{stat}(5)_{sys} \times 10^{-5}$
NA48(2003 data)	$R_K = 2.416(43)_{stat}(24)_{sys} \times 10^{-5}$
NA48(2004 data)	$R_K = 2.455(45)_{stat}(41)_{sys} \times 10^{-5}$

once again, perfectly consistent with the SM. NA62 has collected 100,000  $K\bar{e}2$  events and can possibly achieve a 0.5% precision. The world average of  $R_K = 2.457(32) \times 10^{-5}$  puts significant restrictions on the  $\tan \beta - M_H$  plane according to the FlaviA kaon working group calculations.

## 5 The Status of $V_{us}$

In the recent past, checks of “first row” unitarity of the CKM matrix consistently found unitarity to be significantly violated. Then it was realized by the KTeV experiment that the use of PDG averages for branching ratios for kaon decay modes needed to determine  $V_{us}$  was flawed, and that most major branching ratios needed to be remeasured. This remeasurement has proceeded using the high statistics available from the KTeV, KLOE, and NA48 experiments. Determination of  $|V_{us}| \times f_+(0)$  has been performed by doing global fits and averages of the dominant  $K_L, K_S$ , and  $K^\pm$  using branching ratios, lifetimes, and various parameterizations of the  $K \rightarrow \pi$  hadronic form factors.

### 5.1 Determination of $|V_{us}|$ using $KL3$ Decays

$V_{us}$  can be determined using the  $K_{l3\gamma}$ ) modes (inclusive of radiative effects). The dependence of the partial width for the  $K_{l3\gamma}$ ) on  $|V_{us}| \times f_+(0)$  is given by

$$\Gamma(K_{l3\gamma}) = \frac{C_K^2 G_F^2 M_K^2}{192\pi^3} S_{EW} |V_{us}|^2 |f_+(0)|^2 I_{Kl}(\lambda_{+,0}) (1 + \delta_{SU(2)}^K + \delta_{em}^{Kl})^2$$

In this expression, K can indicate  $K^+$  or  $K^0$  and l either e or  $\mu$ . Determination of  $V_{us}$  requires many inputs as listed in Table 5 below:

Inputs from Theory	Inputs from Experiment
$S_{EW} \equiv$ Short Distance EW Correction	$\Gamma(K_{l3\gamma}) \equiv$ Branching Ratio
$\delta_{SU(2)}^K \equiv$ Form factor correction SU(2) breaking	$I_{Kl}(\lambda) \equiv$ Phase space integral
$\delta_{em}^{Kl} \equiv$ Long distance EM effects	$\lambda \equiv$ form factor dependence on t
$f_+(0) \equiv$ Form factor at t=0	$C_K^2 = 1/2$ for $K^+$ , 1 for $K^0$

Table 5: Inputs for determination of  $|V_{us}| \times f_+(0)$ .

The  $K(e3)$  branching ratios come mainly from the KTeV, Na48, KLOE and ISTRA+ experiments and are in good agreement. The  $K(\mu 3)$  data are not completely consistent from these experiments since the new NA48  $\lambda_0$  form factor is hard to accommodate considering results from other experiments. The form factors (for neutral  $K(l3)$  decays) are defined by

$$\langle \pi^-(k) | \bar{s} \gamma^\mu u | K^0(p) \rangle = (p+k)^\mu f_+(t) + (p-k)^\mu f_-(t)$$

$$\text{where } f_-(t) = \frac{m_K^2 - m_\pi^2}{t} (f_0(t) - f_+(t))$$

and are less well determined at this point. There are three parameterizations of the  $K \rightarrow \pi$  hadronic matrix elements  $f_{+,0}$  commonly used (the  $f_-$  form factor is negligible for  $K_{e3}$ ). The Taylor expansion and the Pole parameterization have the forms given below;

$$\text{Taylor Expansion: } f_{+,0}(t) = f_{+,0}(0)(1 + \lambda'_{+,0} \frac{t}{m_\pi^2} + \frac{1}{2} \lambda''_{+,0} (\frac{t}{m_\pi^2})^2 + \dots)$$

$$\text{Pole parameterization: } f_{+,0}(t) = f_{+,0}(0) \left( \frac{M_{V,S}^2}{M_{V,S}^2 - t} \right)$$

The third approach to obtaining a description of the hadronic matrix element involves a dispersive approach plus  $K\pi$  scattering data to determine both  $f_+(t)$  and  $f_0(t)$ .

Using the branching ratios and the form factors from KTeV, NA48, KLOE and ISTRAP+, the FlaviA kaon working group has performed a global fit for  $|V_{us}|f_+(0)$  the result of which is shown in Fig. 6 below.

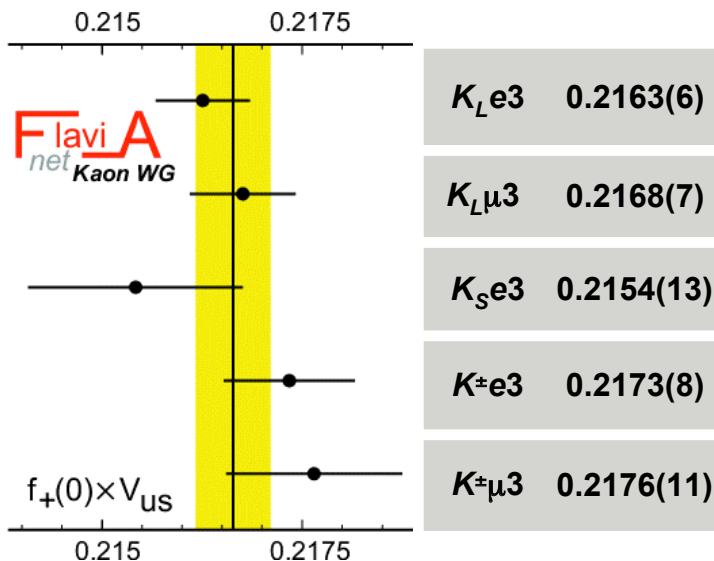


Figure 6: Determination by the FlaviA kaon working group of  $|V_{us}|f_+(0)$ .

The average of the results from each mode is

$$|V_{us}|f_+(0) = 0.2166(5)$$

The ultimate extraction of  $V_{us}$  depends on the theoretical estimates of the the intercept of  $f_+(t)$  at  $t=0$ . There are many attempts to theoretically determine  $f_+(0)$  including the Leutwyler and Roos estimate of  $f_+(0)=0.961(8)$ . Lattice evaluations agree well with this value. Using the RBC-UKQCD07 lattice estimate of  $f_+(0)=0.964(5)$ , the result  $|V_{us}|=0.2246(12)$  is obtained.

## 5.2 Determination of the Ratio $\frac{|V_{us}|^2}{|V_{ud}|^2}$ from $\frac{\Gamma(K_{\mu 2(\gamma)})}{\Gamma(\pi_{\mu 2(\gamma)})}$

The ratio  $\frac{V_{us}}{V_{ud}}$  can be obtained from the ratio of  $K(\mu 2)$   $\pi(\mu 2)$  decays, thereby giving another constraint on  $|V_{us}|$ . The dependence of the ratio of the K and  $\pi$   $\mu 2$  decays on  $\frac{V_{us}}{V_{ud}}$  is given by

$$\frac{\Gamma(K_{\mu 2(\gamma)})}{\Gamma(\pi_{\mu 2(\gamma)})} = \frac{|V_{us}|}{|V_{ud}|} \times \frac{f_K}{f_\pi} \times \frac{M_K(1 - \frac{m_\mu^2}{M_K^2})^2}{m_\pi(1 - \frac{m_\mu^2}{m_\pi^2})^2} \times (1 + \alpha(C_K - C_\pi))$$

In this expression  $C_{K,\pi}$  contains EW radiative corrections. Using the HPQCD-UKQCD07 lattice gauge calculation of  $\frac{f_K}{f_\pi}$  of 1.189(7), the result  $\frac{|V_{us}|}{|V_{ud}|}=0.2321(15)$  is obtained.

## 5.3 Determination of $V_{us}$ from Global Fit

The FlaviA kaon working group has taken into account all information in a global fit for  $V_{us}$ . Fig. 7 shows the fit using  $|V_{us}|=0.2246(12)$ ,  $\frac{|V_{us}|}{|V_{ud}|}=0.2321(15)$ , and  $V_{ud}=0.97418(26)$  [11] with and without a CKM unitarity constraint. The results of the fit with no unitarity constraint are  $V_{us}=0.2253(9)$ ,  $V_{ud}=0.97417(26)$ , and  $1-V_{us}^2-V_{ud}^2=0.0002(6)$ . Applying the unitarity constraint gives  $V_{us}=0.2255(7)$ .

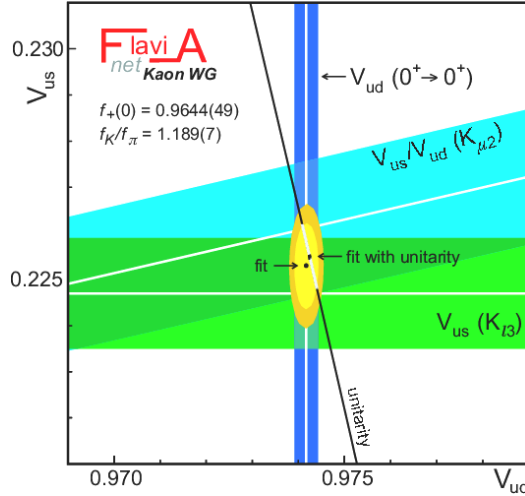


Figure 7: FlaviA kaon working group global fit for  $V_{us}$

## 6 Conclusions

Examining the span of new experimental results, we are forced to conclude that there is no evidence for new physics. There is not yet any hint of CPT violation has been detected or any evidence for lepton flavor violation or violations or  $\mu$ -e universality. However, progress has been made in driving down the limits for LFV to the  $10^{-11}$  level. In addition, KTeV has produced the final result for  $Re \frac{\epsilon'}{\epsilon}$  along with more precise measurements of many other neutral kaon parameters. Improvements in the precision determination of  $V_{us}$  have been achieved using new data from KTeV, NA48/2, KLOE, and ISTRA+ and global fits by the FlaviA kaon working group. Finally, we can expect to see more data in the future from KLOE II, NA62, and E391a.

## 7 Acknowledgements

I would like to thank the organizing committee of this conference, and G. Anzivino, P. Massarotti, M. Moulson, M. Ronquest, T. Spadaro, T. Yamanaka, and E. Worcester from the KTeV, KLOE, NA48, E391a collaborations, and the FlaviA kaon working group for their inputs and the U.S. Department of Energy for support.

## References

- [1] L. Le Prince-Ringuet and M. Lheritier, *Compl. ren.*, 219,618(1944).
- [2] E. Abouzaid et al., Phys. Rev. Lett. **100** 131803(2008).
- [3] M. Smith, [www.inf.infn.it/wg/vus](http://www.inf.infn.it/wg/vus),(2007).
- [4] L.G. Landsberg, arXiv:hep-ph/0410261,(2004)..
- [5] J.K. Ahn et al., arXiv:0712.41164v2 [hep-ex], (2008).
- [6] A. Alavi-Harati et al., Phys. Rev. **D61**, 072006(2000).
- [7] J. Adams et al., Phys. Letters **B447**,240(1999).
- [8] W-S. Hou, PRD**48**,2342(1993).
- [9] V.Cirigliano and I. Rosell, arXiv:0707:4464, (2007).
- [10] A. Maserio, P. Paradisi, R.Petronzio, PRD**74**,011701(2006).
- [11] I.S. Towner and J.C. Hardy, arXiv:0710.3181 [nucl-th], (2007).

# Measurement of $K^+ \rightarrow \pi^+ \nu \bar{\nu}$ at NA62 experiment

*Spasimir Balev*

*Scuola Normale Superiore di Pisa  
56126 Pisa, ITALY*

## 1 Introduction

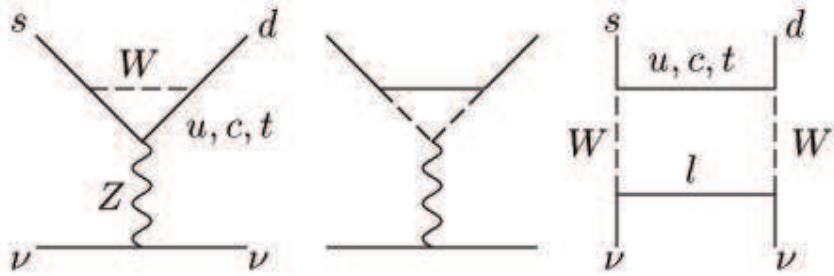
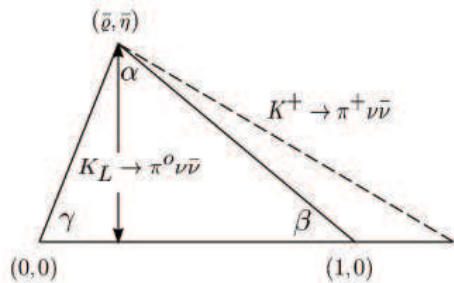
The future program of the experiment NA62 at CERN SPS is currently in advanced stage of development. The main goal of the experiment is to measure the branching ratio of the very rare  $K^+ \rightarrow \pi^+ \nu \bar{\nu}$  decay, by detecting approximately 100 events with 10% background. In this paper is described the motivation of the measurement, the strategy of the experiment, the sources of background and the expected level of their suppression, the main properties of the beam line and necessary detectors.

## 2 Motivation

The  $K^+ \rightarrow \pi^+ \nu \bar{\nu}$  and  $K_L \rightarrow \pi^0 \nu \bar{\nu}$  decays are exceptionally clean modes, dominated by short distance dynamics due to power-like GIM mechanism, and therefore are excellent probes in flavour physics. At the quark level the process  $d \rightarrow s \nu \bar{\nu}$  (see Fig. 1) is realized by combination of  $Z_0$  penguin and double  $W$  exchange. The leading SM contribution to the matrix element is generated by top quark loops and can be computed with negligible theoretical uncertainty. In case of  $K^+ \rightarrow \pi^+ \nu \bar{\nu}$  decay there is a small contribution from charm quark, while the contribution from up quark is negligible in both decay modes. The hadronic matrix element can be extracted from the well measured  $K \rightarrow \pi e \nu$  decays rates with negligible theoretical uncertainty. The current estimations of the branching ratios for the the  $K \rightarrow \pi \nu \bar{\nu}$  decays within the SM are  $BR(K^+ \rightarrow \pi^+ \nu \bar{\nu}) = (8.22 \pm 0.84) \cdot 10^{-11}$  and  $BR(K_L \rightarrow \pi^0 \nu \bar{\nu}) = (2.76 \pm 0.40) \cdot 10^{-11}$  [1].

Measurement of the branching ratios of both  $K^+ \rightarrow \pi^+ \nu \bar{\nu}$  and  $K_L \rightarrow \pi^0 \nu \bar{\nu}$  decay modes leads to determination of  $V_{td}$  element in CKM matrix, i.e. of the Wolfenstein parameters  $(\rho, \eta)$  that define the unitarity triangle (see Fig. 2), independently of the results from  $B$ -physics.

The strong suppression of  $K \rightarrow \pi \nu \bar{\nu}$  decays within SM follows from the absence of tree-level contributions and the hard GIM mechanism. However, this also leads to high sensitivity to possible new-physics effects. Since the cleanliness of these decays

Figure 1: Diagrams of  $d \rightarrow s \nu \bar{\nu}$  process.Figure 2: Connection between the branching ratios of  $K \rightarrow \pi \nu \bar{\nu}$  decays and the unitarity triangle.

modes remains valid in all realistic extensions of SM, a precise measurement of their branching ratios provide sensitive test of the flavour structure of any model beyond SM. Evidence of new physics can be seen in  $K \rightarrow \pi \nu \bar{\nu}$  decays even without significant signals in  $B$ -decays or without particles within LHC reach [2].

Only three  $K^+ \rightarrow \pi^+ \nu \bar{\nu}$  events were discovered by BNL E949 Collaboration. The measured value is compatible with SM prediction:  $(1.47^{+0.30}_{-0.89}) \cdot 10^{-10}$  [3].

The NA62 experiment [4] will use kaon decays in-flight technique, based on the NA48 apparatus and infrastructure, and the same CERN-SPS beam line which produced the kaon beam for all NA48 experiments. The experiment was presented at CERN SPS Committee in September 2005 and in December 2005 the R&D was endorsed by the CERN Research Board. Currently the experiment is in advanced stage of R&D and construction [5] with the data taking expected to begin in 2011.

### 3 Backgrounds

The experimental signature of the studied  $K^+ \rightarrow \pi^+ \nu \bar{\nu}$  decays is a single reconstructed track in the detector downstream the decay volume in time coincidence with

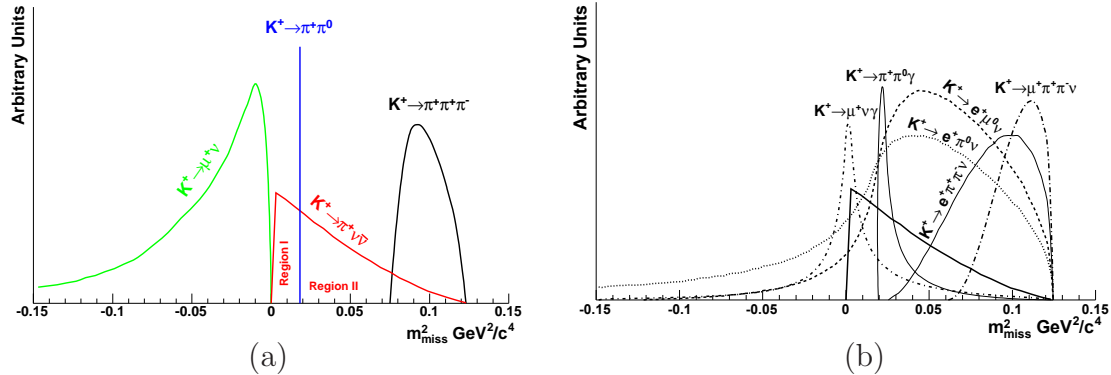


Figure 3: Kinematically constrained (a) and kinematically not constrained (b) backgrounds to  $K^+ \rightarrow \pi^+ \nu \bar{\nu}$  decays.

a kaon measured by the upstream beam tracker. The kinematics of a one-track event can be fully described by the variable  $m_{miss}^2 = (P_K - P_\pi)^2$ , where  $P_K$  and  $P_\pi$  are the four-momenta of the kaon and pion, respectively. Two categories of backgrounds can be considered (see Fig. 3):

- **Kinematically constrained background.** The decays in this category correspond to  $\sim 95\%$  of the total  $K^+$  branching fraction. The  $K^+ \rightarrow \pi^+ \pi^0$  decay splits the kinematical region of the signal in two parts, called region I and region II.  $K^+ \rightarrow \mu^+ \nu$  and  $K^+ \rightarrow \pi \pi \pi$  decays sit on the opposite sides of these regions where cuts must be applied as well. Rejection factor larger than  $10^{12}$  can be achieved only if efficient photon rejection and particle identification complements the kinematical rejection.
- **Kinematically not constrained background.** The rejection of such background profits from relatively small branching fractions. However, photon veto system and particle identification are the only experimental tools available to reduce such a background.

The expected level of background is summarized in Tab. 1. The signal acceptance is found to be 14.4% (3.5% in region I and 10.9% in region II). With a flux of about  $4.8 \cdot 10^{12}$  kaon per year of data taking, the expected number of signal events is 55 events/year.

## 4 The Experimental set-up

The layout of the experimental apparatus is presented in Fig. 4.

The  $K^+$  beam will be produced on a beryllium target from SPS protons with momentum  $400 \text{ GeV}/c$  and intensity  $3.3 \cdot 10^{12}$  protons per pulse. The nominal momentum of the  $K^+$  beam will be  $P_K = 75 \text{ GeV}/c$  with  $\Delta P_K/P_K = 1.2\%$ . The expected fraction of  $K^+$  in the beam is 6.6%. A tungsten radiator 1  $X_0$  thick will be placed on the beam in the first achromat in order to absorb the positron component of the beam.

After the first achromat a differential Cerenkov counter (CEDAR) existing at CERN, will be used after its upgrade for new experimental conditions for kaon tagging, in order to keep the beam background under control.

The beam spectrometer (Gigatracker) will be placed in the second achromat station. It consists of thin silicon micro-pixel detectors for redundant momentum measurement of the incoming beam with 200 ps time resolution, necessary to provide a tight coincidence between incoming kaon and outgoing pion. The Gigatracker will work in rough conditions – near GHz rate of passing particles – hence the name.

A set of ring anti-counters (CHANTI) will be placed after the last Gigatracker station to form a "guard ring" and a large one around the beginning of the decay volume, in order to veto charged particles coming from the collimator.

The decay volume, contained in a vacuum tank, will be surrounded by a set of ring-shaped anti-counters, providing full coverage for photons originating from decay region with angles as large as 48 mrad. Lead-scintillator fibers and lead-scintillator tiles design of this system is now under the study. A lead-glass prototype will be tested in 2008 run of the NA62 experiment.

A magnetic spectrometer, operating in vacuum, will be used to measure the momentum of the out-going pion. The spectrometer is designed with 4 straw chambers with 4 coordinate views each. Chambers should introduce small material contribution (0.5%  $X_0$  per chamber) and have a good spatial resolution (130  $\mu\text{m}$  per view). 36  $\mu\text{m}$  mylar straw tubes with about 10 mm in diameter welded by ultrasound machine and covered with gold inside will be used for these reasons. This spectrometer will

Decay mode	Level of background
$K^+ \rightarrow \pi^+\pi^0$	4.3%
$K^+ \rightarrow \mu^+\nu$	2.2%
$K^+ \rightarrow \pi^+\pi^-e^+\nu$	$\sim 3.0\%$
Other 3-tracks decays	$\sim 1.5\%$
$K^+ \rightarrow \pi^+\pi^0\gamma$	$\sim 2.0\%$
$K^+ \rightarrow \mu^+\nu\gamma$	$\sim 0.7\%$
$K^+ \rightarrow e^+(\mu^+)\nu\pi^0$ and others	negligible
Total background	$\sim 13.7\%$

Table 1: Background levels from various  $K^+$  decay modes.

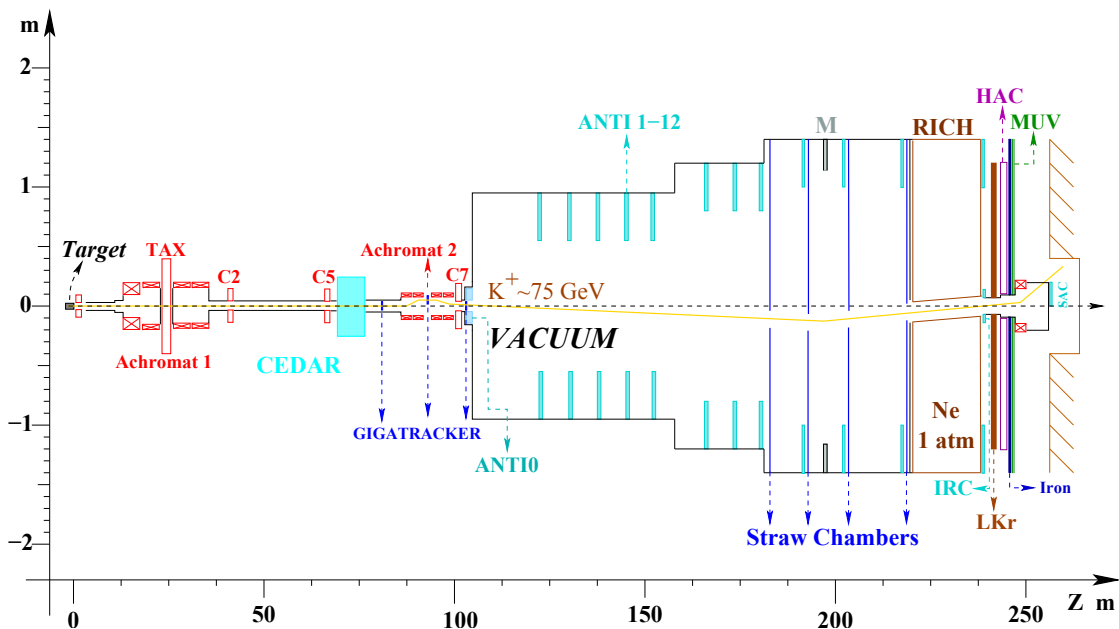


Figure 4: Layout of NA62 experimental apparatus.

be used as well as a veto for high energy negative pion from  $K_{e4}$  decays. The R&D program has been started in 2006, a full length and reduced-size prototype has been constructed, integrated and tested in the NA62 set-up during the 2007 run at CERN. The test continues during the 2008 run of the experiment.

After the magnetic spectrometer a gas Ring Imaging Cerenkov counter (RICH) will be placed, providing muon/pion separation and suppression factor smaller than  $10^{-2}$  in the momentum interval (15–35) GeV/c. The detector will be used also for precise measurement of the pion crossing time with resolution  $\sim 100$  ps, sending signals to the trigger system. In addition RICH will provide redundant measurement of velocity of the charged particles. The detector consists of 18 m long tube with a diameter of 2.8 m, filled with Neon at atmospheric pressure. The Cerenkov radiation will be collected by two mirrors with 17 m of focal length. A full-length prototype 60 cm in diameter has been integrated in the NA62 set-up and tested during the 2007 NA62 run at CERN.

The Liquid Krypton Calorimeter (LKr), built for the NA48 experiment, will be used as part of the photon veto system in the forward region. During test run in 2006 it was shown that inefficiency below  $10^{-5}$  can be reached. A program of consolidation and update of the readout electronics of the LKr is under way.

For muon identification with very small inefficiency will be used a hadron calorime-

ter and muon detector, placed just after LKR. The photon veto system is completed by the Intermediate Ring Calorimeter (IRC), placed at the entrance of LKR, and Small Angle Calorimeter (SAC) at the very end of the detector system, after the muon deflecting magnet, both covering the angular regions around and in the beam. SAC prototype was tested during 2006 and upper limit on its inefficiency was found to be  $6.4 \cdot 10^{-5}$ .

The trigger system of NA62 experiment will be at two levels. The first one (L0) is hardware trigger, which will decrease the events rate from  $\sim 10$  MHz to  $\sim 1$  MHz, employing signals from RICH, photon veto system and the muon detector. The second level (L1/2) is software and its aim is to decrease the rate of the events to kHz level.

## 5 Conclusions

The experiment NA62 is proposed to search for new physics by measuring  $K^+ \rightarrow \pi^+ \nu \bar{\nu}$  branching ratio with 10% accuracy. It is expected that in 2 years of data taking the experiment will collect  $\sim 100$  decays of this mode. Other physical opportunities, like search for lepton flavour violation processes and new low mass particles, as well as tests of lepton universality, are part of the experimental program. The R&D program of the experiment is well advanced and many of the detectors are in prototyping or construction phase.

## References

- [1] The *Flavianet* Kaon WG [<http://www.lnf.infn.it/vus/>].
- [2] A. J. Buras *et al.*, Nucl. Phys. B **714**, 103 (2005) [[arXiv:hep-ph/0408142](https://arxiv.org/abs/hep-ph/0408142)]; G. Isidori *et al.*, JHEP **0608**, 064 (2006) [[arXiv:hep-ph/0604074](https://arxiv.org/abs/hep-ph/0604074)]; M. Blanke *et al.*, JHEP **0701**, 066 (2007) [[arXiv:hep-ph/0610298](https://arxiv.org/abs/hep-ph/0610298)]; A. J. Buras *et al.*, JHEP **0611**, 062 (2006) [[arXiv:hep-ph/0607189](https://arxiv.org/abs/hep-ph/0607189)]; D. Bryman *et al.*, Int. J. Mod. Phys. A **21**, 487 (2006) [[arXiv:hep-ph/0505171](https://arxiv.org/abs/hep-ph/0505171)]; B. Grinstein *et al.*, Nucl. Phys. B **763**, 35 (2007) [[arXiv:hep-ph/0608123](https://arxiv.org/abs/hep-ph/0608123)].
- [3] V. V. Anisimovsky *et al.* [E949 Collaboration], Phys. Rev. Lett. **93**, 031801 (2004) [[arXiv:hep-ex/0403036](https://arxiv.org/abs/hep-ex/0403036)].
- [4] Proposal to measure the Rare Decay at the CERN SPS, CERN-SPSC-2005-013, 11/6/2005
- [5] NA62/P326 Status Report, CERN-SPSC-2007-035, 26/11/2007

# $|V_{us}|$ from kaon decays with the KLOE detector

*Mario Antonelli*

*Laboratori Nazionali di Frascati dell'INFN, Frascati, Italy*

## 1 Introduction

While much emphasis is placed on the search for new physics, we still lack precise information on the validity of certain aspects of the Standard Model itself. In the Standard Model, the coupling of the  $W$  boson to the weak charged current is

$$\frac{g}{\sqrt{2}} W_\alpha^+ (\bar{\mathbf{U}}_L \mathbf{V}_{\text{CKM}} \gamma^\alpha \mathbf{D}_L + \bar{e}_L \gamma^\alpha \nu_e L + \bar{\mu}_L \gamma^\alpha \nu_\mu L + \bar{\tau}_L \gamma^\alpha \nu_\tau L) + \text{h.c.}, \quad (1)$$

where  $\mathbf{U}^T = (u, c, t)$ ,  $\mathbf{D}^T = (d, s, b)$  and  $L$  is for lefthanded. In the coupling above there is only one coupling constant for leptons and quarks. Quarks are mixed by the Cabibbo-Kobayashi-Maskawa matrix,  $\mathbf{V}_{\text{CKM}}$ , which must be unitary. In low energy processes the Fermi coupling constant  $G_F$  is related to the gauge coupling  $g$  by  $G_F = g^2/(4\sqrt{2} M_W^2)$ . In the early sixties only two elements of  $\mathbf{V}_{\text{CKM}}$  were known. From nuclear  $\beta$  decay it was known that  $|V_{ud}| \sim 0.98$  and from strangeness changing decays,  $|V_{us}| \sim 0.26$ , [1].

Precise measurements of leptonic and semileptonic kaon decay rates provide information about lepton universality. Combined with results from nuclear  $\beta$  decay and pion decays, such measurements also provide information about the unitarity of the mixing matrix. Ultimately they tell us whether quarks and leptons do indeed carry the same weak charge. The partial rates  $\Gamma(K \rightarrow \pi e \nu)$  and  $\Gamma(K \rightarrow \pi \mu \nu)$  provide measurements of  $g^4 |V_{us}|^2$ , which, combined with  $g^4 |V_{ud}|^2$  from nuclear  $\beta$  decay and the muon decay rate, test the unitarity condition  $|V_{ud}|^2 + |V_{us}|^2 + |V_{ub}|^2 = 1 \simeq |V_{ud}|^2 + |V_{us}|^2$ . The ratio  $\Gamma(K \rightarrow \mu \nu)/\Gamma(\pi \rightarrow \mu \nu)$  provides an independent measurement of  $|V_{us}|^2/|V_{ud}|^2$ .

### 1.1 Leptonic and Semileptonic kaon decays

The semileptonic decay rates, fully inclusive of radiation, are given by

$$\Gamma(K_{\ell 3(\gamma)}) = \frac{C_K^2 G_F^2 M_K^5}{192\pi^3} S_{\text{EW}} |V_{us}|^2 |f_+(0)|^2 I_{K\ell} \left(1 + \delta_K^{\text{SU}(2)} + \delta_{K\ell}^{\text{EM}}\right)^2. \quad (2)$$

In the above expression, the index  $K$  denotes  $K^0 \rightarrow \pi^\pm$  and  $K^\pm \rightarrow \pi^0$  transitions, for which  $C_K^2 = 1$  and  $1/2$ , respectively.  $M_K$  is the appropriate kaon mass,  $S_{\text{EW}}$

is the universal short-distance electroweak correction [2] and  $\ell = e, \mu$ . Following a common convention,  $f_+(0) \equiv f_+^{K^0\pi^-}(0)$ . The mode dependence is contained in the  $\delta$  terms: the long-distance electromagnetic (EM) corrections, which depend on the meson charges and lepton masses and the SU(2)-breaking corrections, which depend on the kaon species [3].  $I_{K\ell}$  is the integral of the dimensionless Dalitz-plot density.

If the form factors are expanded in powers of  $t$  up to  $t^2$  as

$$\tilde{f}_{+,0}(t) = 1 + \lambda'_{+,0} \frac{t}{m_{\pi^+}^2} + \frac{1}{2} \lambda''_{+,0} \left( \frac{t}{m_{\pi^+}^2} \right)^2, \quad (3)$$

four parameters ( $\lambda'_+$ ,  $\lambda''_+$ ,  $\lambda'_0$  and  $\lambda''_0$ ) need to be determined from the decay pion spectrum in order to be able to compute the phase-space integral.

High-precision lattice quantum chromodynamics (QCD) results have recently become available and are rapidly improving [4]. The availability of precise values for the pion- and kaon-decay constants  $f_\pi$  and  $f_K$  allows use of a relation between  $\Gamma(K_{\mu 2})/\Gamma(\pi_{\mu 2})$  and  $|V_{us}|^2/|V_{ud}|^2$ , with the advantage that lattice-scale uncertainties and radiative corrections largely cancel out in the ratio [5]:

$$\frac{\Gamma(K_{\mu 2(\gamma)})}{\Gamma(\pi_{\mu 2(\gamma)})} = \frac{|V_{us}|^2}{|V_{ud}|^2} \frac{f_K^2}{f_\pi^2} \frac{m_K (1 - m_\mu^2/m_K^2)^2}{m_\pi (1 - m_\mu^2/m_\pi^2)^2} \times (0.9930 \pm 0.0035), \quad (4)$$

where the uncertainty in the numerical factor is dominantly from structure-dependent radiative corrections and may be improved. This ratio can be combined with direct measurements of  $|V_{ud}|$  to obtain  $|V_{us}|$ .

## 2 KLOE's role

The KLOE detector is operated at DAΦNE, the Frascati  $\phi$  factory. DAΦNE is an  $e^+e^-$  collider running at a center of mass energy  $W = m_\phi \sim 1019.45$  MeV.  $\phi$  mesons are produced with a cross section of  $\sim 3 \mu\text{b}$  and decay mostly to charged kaon pairs (49%) and neutral kaon pairs (34%).

The neutral kaon pair from  $\phi \rightarrow K^0\bar{K}^0$  is in a pure  $J^{PC} = 1^{--}$  state. Detection of a  $K_S$  thus signals the presence of, “tags”, a  $K_L$  and vice versa. Thus at DAΦNE we have pure  $K_S$  and  $K_L$  beams of precisely known momenta (event by event) and flux, which can be used to measure absolute  $K_S$  and  $K_L$  branching ratios.

### 2.1 $K_L$ decays

We search for  $K_L$  decays using a beam tagged by detection of  $K_S \rightarrow \pi^+\pi^-$  decays. The  $\pi^+\pi^-$  decays observed near the origin count the number of  $K_L$  mesons, providing

the direction and momentum of each. We have used this technique to measure the BRs for the four main  $K_L$  decay modes, as well as the  $K_L$  lifetime [6].

The errors on the KLOE BR values are dominated by the uncertainty on the  $K_L$  lifetime  $\tau_L$ ; since the dependence of the geometrical efficiency on  $\tau_L$  is known, KLOE can solve for  $\tau_L$  by imposing  $\sum_x \text{BR}K_L \rightarrow x = 1$  (using previous averages for the minor BRs), thereby greatly reducing the uncertainties on the BR values obtained. Our fit makes use of the KLOE BR values before application of this constraint:  $\text{BR}(K_{e3}) = 0.4049(21)$ ,  $\text{BR}(K_{\mu 3}) = 0.2726(16)$ ,  $\text{BR}(K_{e3}) = 0.2018(24)$ , and  $\text{BR}(K_{e3}) = 0.1276(15)$ . The dependence of these values on  $\tau_L$  and the correlations between the errors are taken into account. KLOE has also measured  $\tau_L$  directly, by fitting the proper decay time distribution for  $K_L \rightarrow 3\pi^0$  events, for which the reconstruction efficiency is high and uniform over a fiducial volume of  $\sim 0.4\lambda_L$ . We obtain  $\tau_L = 50.92(30)$  ns [6].

## 2.2 $K_S$ decays

We have measured the ratios  $\text{BR}(K_S \rightarrow \pi e\nu)/\text{BR}(K_S \rightarrow \pi^+ \pi^-)$  separately for each lepton charge, using  $\phi \rightarrow K_L K_S$  decays in which the  $K_L$  is recognized by its interaction in the calorimeter barrel. Semileptonic  $K_S$  decays are identified by time of flight (TOF) of both pion and electron. Our most recent analysis [6] gives about 13,600 signal events.

In a separate analysis, we have used  $K_S$  decays tagged by the  $K_L$  interaction in the EMC barrel to measure  $\text{BR}K_S \rightarrow \pi^+ \pi^-/\text{BR}K_S \rightarrow \pi^0 \pi^0 = 2.2549 \pm 0.0054$  [6]. Together, these measurements completely determine the main  $K_S$  BRs and give:  $\text{BR}(K_S \rightarrow \pi e\nu) = (7.046 \pm 0.091) \times 10^{-4}$  [6].

In our evaluation of  $|V_{us}|$ , we use the KLOE value for  $\text{BR}(K_S \rightarrow \pi e\nu)$  together with the lifetime value  $\tau_S = 0.08958 \pm 0.00005$  ns from the PDG [7].

## 2.3 $K^\pm$ decays

At KLOE,  $\phi \rightarrow K^+ K^-$  events are identified by detecting the abundant two-body decay ( $\text{BR}(K^\pm \rightarrow \pi^\pm \pi^0 + K^\pm \rightarrow \mu^\pm \nu) \sim 84\%$ ) of one of the kaons. As in the analysis of neutral kaon decays, this provides tagging of the kaon of opposite charge. As noted above, the decay  $K \rightarrow \mu\nu$  is of interest in its own right for the determination of  $|V_{us}|$ .

We measure  $\text{BR}(K^+ \rightarrow \mu^+ \nu)$  using  $K^- \rightarrow \mu^- \bar{\nu}$  decays as tags [6]. In  $\sim 34\%$  of some four million tagged events, we find  $\sim 865,000$  signal events giving  $\text{BR}(K^+ \rightarrow \mu^+ \nu(\gamma)) = 0.6366 \pm 0.0009 \pm 0.0015$ .

To measure  $\text{BR}(K_{e3}^\pm)$  and  $\text{BR}(K_{\mu 3}^\pm)$ , we use both  $K \rightarrow \mu\nu$  and  $K \rightarrow \pi\pi^0$  decays as tags.

In all, we find about 300,000  $K_{e3}$  and 160,000  $K_{\mu 3}$  events. We obtain  $\text{BR}(K_{e3}) = (4.965 \pm 0.038 \pm 0.037)\%$  and  $\text{BR}(K_{\mu 3}) = (3.233 \pm 0.029 \pm 0.026)\%$ , with a correlation

of 62.7% [6].

At KLOE, two methods are used to measure charged kaon lifetime. The first is to obtain the decay time from the kaon path length in the DC, accounting for the continuous change in the kaon velocity due to ionization energy losses. A fit to the proper-time distribution in the interval from 15–35 ns ( $1.6\lambda_{\pm}$ ) gives the result  $\tau_{\pm} = 12.364 \pm 0.031 \pm 0.031$  ns. Alternately, the decay time can be obtained from the precise measurement of the arrival times of the photons from  $K^+ \rightarrow \pi^+\pi^0$  decays. In this case, a fit to the proper-time distribution in the interval from 13–42 ns ( $2.3\lambda_{\pm}$ ) gives the result  $\tau_{\pm} = 12.337 \pm 0.030 \pm 0.020$  ns. Taking into account the statistical correlation between these two measurements ( $\rho = 0.307$ ), we obtain the average value  $\tau_{\pm} = 12.347 \pm 0.030$  ns, see [6].

## 2.4 Form factor parameters

$K_{e3}$  form factor(FF) parameters have also been measured [6]. We obtain the vector form factor parameters from binned log-likelihood fits to the  $t$  distribution. Using the quadratic parametrization of eq. 3, we obtain  $\lambda'_+ = (25.5 \pm 1.5 \pm 1.0) \times 10^{-3}$  and  $\lambda''_+ = (1.4 \pm 0.7 \pm 0.4) \times 10^{-3}$ , where the total errors are correlated with  $\rho = -0.95$ .

The measurement of the vector and scalar FF parameters using  $K_L \rightarrow \pi\mu\nu$  decays is reported in Ref. [6]. The FF parameters have been obtained from fits to the distribution of the neutrino energy  $E_\nu$  after integration over the pion energy.

The result of this fit when combined with those from our  $K_{e3}$  analysis is:

$$\begin{aligned} \lambda'_+ &= (25.6 \pm 1.7) \times 10^{-3} \\ \lambda''_+ &= (1.5 \pm 0.8) \times 10^{-3} \\ \lambda'_0 &= (15.4 \pm 2.2) \times 10^{-3} \end{aligned} \quad \left( \begin{array}{ccc} 1 & -0.95 & 0.29 \\ & 1 & -0.38 \\ & & 1 \end{array} \right) \quad (5)$$

The values of the phase-space integrals for  $K_{\ell 3}$  decays are listed in table 1.

Parameters	$I(K_{e3}^0)$	$I(K_{\mu 3}^0)$	$I(K_{e3}^+)$	$I(K_{\mu 3}^+)$
$\lambda'_+, \lambda''_+, \lambda'_0$	0.15483(40)	0.10271(52)	0.15919(41)	0.10568(54)

Table 1: Phase-space integrals for  $K_{\ell 3}$  decays.

## 3 Test of CKM unitarity

Using all of the experimental and theoretical inputs discussed above and the SU(2)-breaking correction from Ref. [8], the values of  $|f_+(0)V_{us}|$  have been evaluated for the  $K_{Le3}$ ,  $K_{L\mu 3}$ ,  $K_{Se3}$ ,  $K_{e3}^\pm$ , and  $K_{\mu 3}^\pm$  decay modes, as shown in table 2. Statistical and systematic uncertainties are added in quadrature everywhere.

Channel	$ f_+(0) V_{us} $	Correlation coefficients					
$K_{Le3}$	0.2155(7)	1					
$K_{L\mu 3}$	0.2167(9)	0.28	1				
$K_{Se3}$	0.2153(14)	0.16	0.08	1			
$K_{e3}^\pm$	0.2152(13)	0.07	0.01	0.04	1		
$K_{\mu 3}^\pm$	0.2132(15)	0.01	0.18	0.01	0.67	1	

Table 2: KLOE results for  $|f_+(0) V_{us}|$ .

with  $\chi^2/\text{ndf} = 7.0/4$  (CL=13%). It is worth noting that the only external experimental input to this analysis is the  $K_S$  lifetime. All other experimental inputs are KLOE results.

Lattice evaluations of  $f_+(0)$  are rapidly improving in precision. The RBC and UKQCD Collaborations have recently obtained  $f_+(0) = 0.9644 \pm 0.0049$  from a lattice calculation with 2 + 1 flavors of dynamical domain-wall fermions [11]. Using their value for  $f_+(0)$ , our  $K_{e3}$  results give  $|V_{us}| = 0.2237 \pm 0.0013$ . A recent evaluation of  $|V_{ud}|$  from  $0^+ \rightarrow 0^+$  nuclear beta decays [10], gives  $|V_{ud}| = 0.97418 \pm 0.00026$  which, combined with our result above, gives  $|V_{ud}|^2 + |V_{us}|^2 - 1 = -0.0009 \pm 0.0008$ , a result compatible with unitarity, which is verified to  $\sim 0.1\%$ . figure 1 shows a compendium of all the KLOE results.

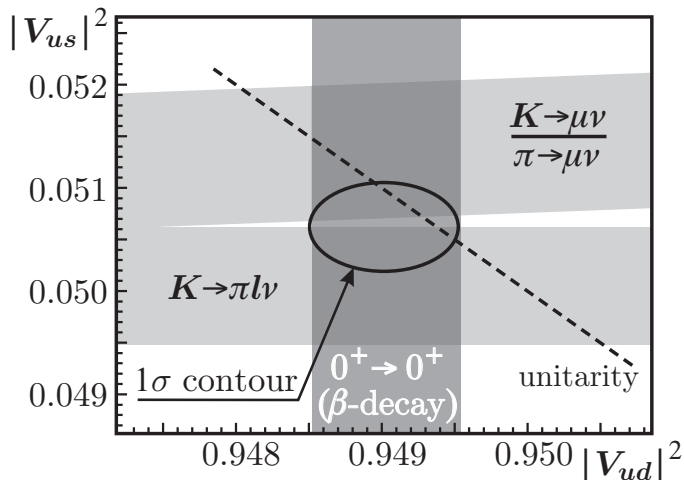


Figure 1: KLOE results for  $|V_{us}|^2$ ,  $|V_{us}/V_{ud}|^2$  and  $|V_{ud}|^2$  from  $\beta$ -decay measurements, shown as  $1\sigma$  wide grey bands. The ellipse is the  $1\sigma$  contour from the fit. The unitarity constraint is illustrated by the dashed line.

Additional information is provided by the determination of the ratio  $|V_{us}/V_{ud}|$ ,

following the approach of eq. 4. From our measurements of  $\text{BR}(K_{\mu 2})$  and  $\tau_{\pm}$  and using  $\Gamma(\pi_{\mu 2})$  from ref. [7], we find  $|V_{us}/V_{ud} \times f_K/f_{\pi}|^2 = 0.07650(33)$ . Using the recent lattice determination of  $f_K/f_{\pi}$  from the HPQCD/UKQCD collaboration,  $f_K/f_{\pi}=1.189 \pm 0.007$  [9], we obtain  $|V_{us}/V_{ud}|^2=0.0541 \pm 0.0007$ . The best estimate of  $|V_{us}|^2$  and  $|V_{ud}|^2$  can be obtained from a fit to the above ratio and our result  $|V_{us}|^2=0.05002 \pm 0.00057$  together with the result  $|V_{ud}|^2 = 0.9490 \pm 0.0005$  from super-allowed  $\beta$ -decays. The fit gives  $|V_{us}|^2 = 0.0506 \pm 0.0004$  and  $|V_{ud}|^2 = 0.9490 \pm 0.0005$  with a correlation of 3%. The fit CL is 13% ( $\chi^2/\text{ndf} = 2.34/1$ ). The values obtained confirm the unitarity of the CKM quark mixing matrix as applied to the first row. We find

$$1 - |V_{us}|^2 - |V_{ud}|^2 = 0.0004 \pm 0.0007 \quad (\sim 0.6\sigma)$$

i.e. the unitarity condition is verified to  $\mathcal{O}(0.1\%)$ , see figure 1. In a more conventional form, the results of the fit are:

$$\begin{aligned} |V_{us}| &= 0.2249 \pm 0.0010 \\ |V_{ud}| &= 0.97417 \pm 0.00026 \end{aligned} \tag{6}$$

Imposing unitarity as a constraint,  $|V_{us}|^2 + |V_{ud}|^2 = 1$ , on the values above and performing a constrained fit we find  $|V_{us}| = 0.2253 \pm 0.0007$  with  $\chi^2/\text{dof}=0.46/1$  corresponding to a CL of 50%.

## References

- [1] N. Cabibbo, Phys. Rev. Lett. **10** (1963) 531.
- [2] A. Sirlin Nucl. Phys. B **196** (1982) 83.
- [3] V. Cirigliano *et al.*, Eur. Phys. J. C **23** (2002) 121.
- [4] C. Davies. talk at Lepton-Photon '07 conference (Daegu, Korea, 2007).
- [5] W. Marciano Phys. Rev. Lett. **93** (2004) 231803.
- [6] F. Ambrosino *et al.* (KLOE Collaboration), JHEP **0804** (2008) 059, and references therein.
- [7] W.-M. Yao. *et al.* (Particle Data Group), J. Phys. G **33** (2006) 1.
- [8] V. Cirigliano et al. Eur. Phys. J. C **23** (2002) 121.
- [9] E. Follana *et al.*, (HPQCD/UKQCD Collaboration), arXiv:0706.1726.
- [10] J.C. Hardy and I.S. Towner, arXiv:0710.3181v1.
- [11] P.A. Boyle *et al.*, (RBC/UKQCD Collaboration), arXiv:0710.5136.

# Early physics with the LHCb detector

*Dirk Wiedner  
(on behalf of the LHCb Collaboration)  
CERN  
Route de Meyrin 385  
CH-1211, Geneva 23 Switzerland*

## 1 Introduction

The Large Hadron Collider beauty experiment [1](fig.1) is a dedicated experiment for the precision measurements of rare decays and CP-violation in the b-sector. It is currently being commissioned at the Large Hadron Collider at CERN. The experimental techniques applied allow for a highly efficient sampling of beauty events.

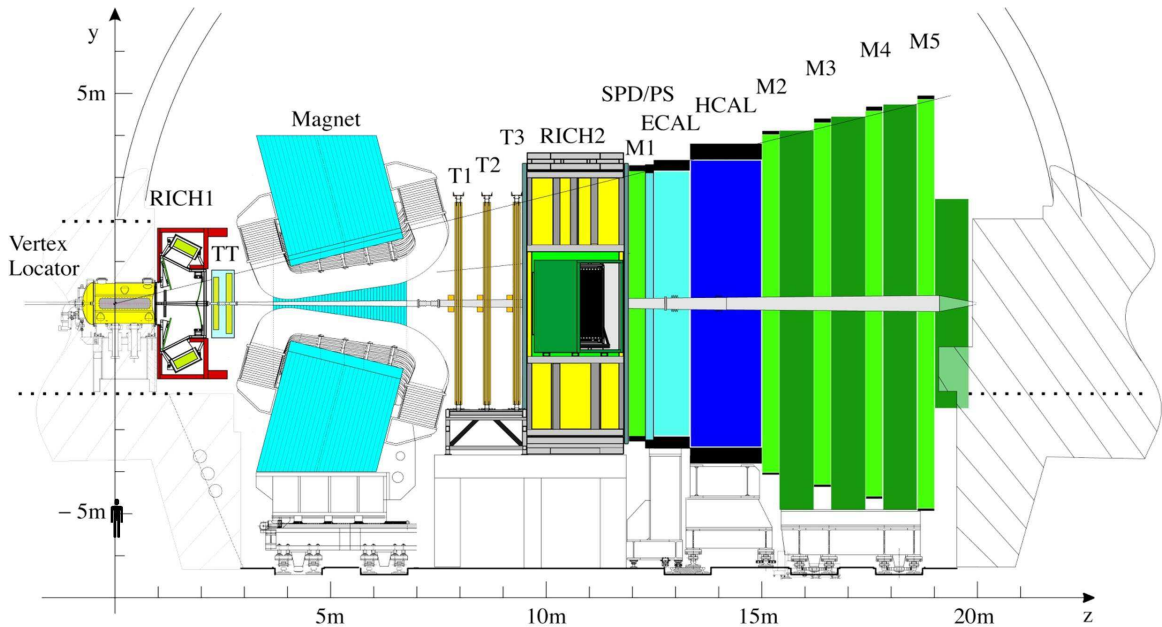


Figure 1: The Large Hadron Collider beauty experiment (LHCb)

## 2 Detector components

Since the  $b\bar{b}$  production in pp collisions at  $\sqrt{s}=14\text{TeV}$  is strongly favoured in the forward region, LHCb has been constructed as a single arm forward spectrometer. The VErtex LOcator (VELO) is a silicon strip detector, see fig.2, placed at a distance of 8 mm around the interaction region. The  $5\mu\text{m}$  hit resolution allows  $30\mu\text{m}$  resolution of the impact parameter. An accuracy of about 40 fs in decay time is achieved for channel  $B_s \rightarrow D\pi$  (fig.3). The good time resolution of the vertex locator permits a clean measurement of  $B_s$  oscillations. Inclusion of the impact parameter measurement in the trigger system leads to early and efficient selection of b-decays.



Figure 2: Vertex Locator (VELO)

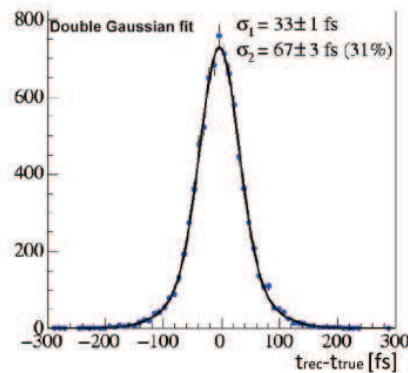


Figure 3: Decay time resolution of the VELO detector for channel  $B_s \rightarrow D\pi$

The momentum and mass measurement is performed with a dipole magnet and tracking stations before and after the magnet. The dipole magnet (fig.4) generates an integrated field of 4 Tm. The VELO together with the Tracker Turicensis (Zurich Tracker, fig.5), the silicon Inner and drift tube Outer Trackers (fig.6) are used to precisely determine the particle momentum with  $\delta p/p = 0.3\%-0.5\%$ . This leads to a mass resolution of  $\sigma \approx 14\text{ MeV}$  for  $B_s \rightarrow \mu\mu$  allowing to efficiently suppress background.

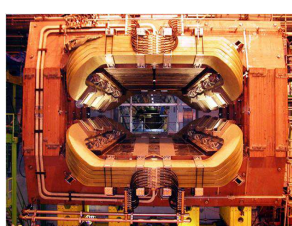


Figure 4: Magnet



Figure 5: Tracker Turicensis

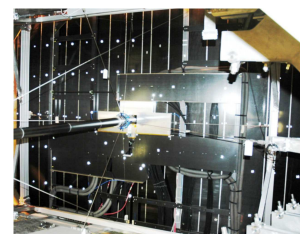


Figure 6: Outer and Inner Tracking detectors

The K- $\pi$  separation is achieved by two Ring Imaging Cherenkov detectors: RICH1 (fig.7) has two different radiators, 5 cm aerogel with a refractive index  $n=1.03$  and  $4\text{ m}^3$  gaseous  $\text{C}_4\text{F}_{10}$  with  $n=1.0014$ , to cover lower and middle momentum range. RICH2 (fig.8) covers the highest momentum range using  $100\text{ m}^3 \text{CF}_4$  with  $n=1.0005$ . As charged particles traverse the medium they emit photons in a cone around their trajectory. The emission angle of the cone depends on the velocity of the particle. If the velocity from the RICH and the momentum from the trackers is known, the particle mass and therefore its identity is determined. The expected kaon identification performance  $P(K \rightarrow K)$  is  $97.29 \pm 0.06\%$  with a fraction of pions misidentified as kaons of  $P(K \rightarrow \pi) = 5.15 \pm 0.02\%$ , see fig.9.

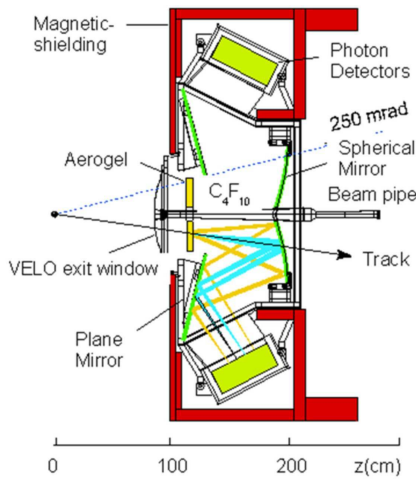


Figure 7: Ring Imaging Cherenkov detector one (RICH1)



Figure 8: Ring Imaging Cherenkov detector two (RICH2)

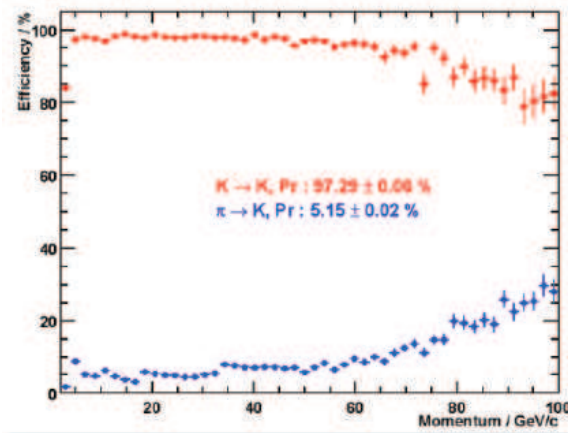


Figure 9: Kaon identification performance

The LHCb calorimeters (fig.10) identify photons, electrons and hadrons by converting them into showers. They supply the Level 0 trigger for high  $E_T$  electrons, photons and hadrons. The rejection of a high background of charged pions requires longitudinal segmentation of the electromagnetic shower detection, i.e. a preshower detector (PS) followed by the main section of the ECAL. The electron trigger must also reject a background of  $\pi_0$ 's with high  $E_T$ , provided by a scintillator pad detector (SPD) plane in front of the PS. The thickness of ECAL was chosen to be 25 radiation lengths for optimal energy resolution, while the hadronic calorimeter has 5.6 interaction lengths. For all calorimeters scintillation light is transmitted to a Photomultiplier (PMT) by wavelength-shifting (WLS) fibers.

The muon system is used for the muon identification and the Level 0 trigger on high  $p_T$  muons. It is composed of five layers of wire chambers (M1-M5), see one layer in fig.11. In M1 also GEM chambers are used in the inner region, where the highest occupancy is expected.

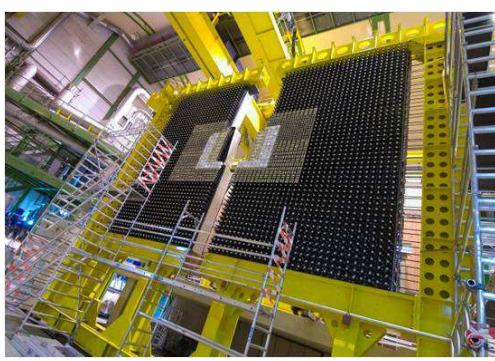


Figure 10: Calorimeter



Figure 11: One layer of muon chambers

The trigger system, designed to efficiently select the events of interest, has two stages. The Level 0 (L0) trigger is implemented in hardware and selects events with high  $p_T$  ( $\mu$ ,  $e$ ,  $\gamma$ ,  $h$ ) at a rate of 1 MHz from an input rate of 40 MHz. The higher level trigger is implemented in software. After L0 confirmation it associates L0 objects with large impact parameter tracks and performs inclusive and exclusive selections. The rate to storage is 2 kHz at an event size of  $\approx 30$  kB.

### 3 First Data

In the first days of data taking starting in 2008, a sample of  $10^8$  minimum bias events is expected to be taken. Only four bunches will be filled leading to a luminosity of  $L=1.1 \times 10^{29} \text{ cm}^{-2} \text{ s}^{-1}$ . This initial data can be used to calibrate the detector [2] and study inclusive particle production, see fig.12. When the detector components are

well understood, the decay  $Z \rightarrow \mu^+ \mu^-$  can be used for luminosity measurement with an expected accuracy of 5% already at  $5 \text{ pb}^{-1}$ . The differential cross section of the decays  $Z \rightarrow \mu^+ \mu^-$  and  $W^\pm \rightarrow \mu^\pm \nu$  will allow the measurement of the Parton Density Function in a phase space priorly inaccessible [3].

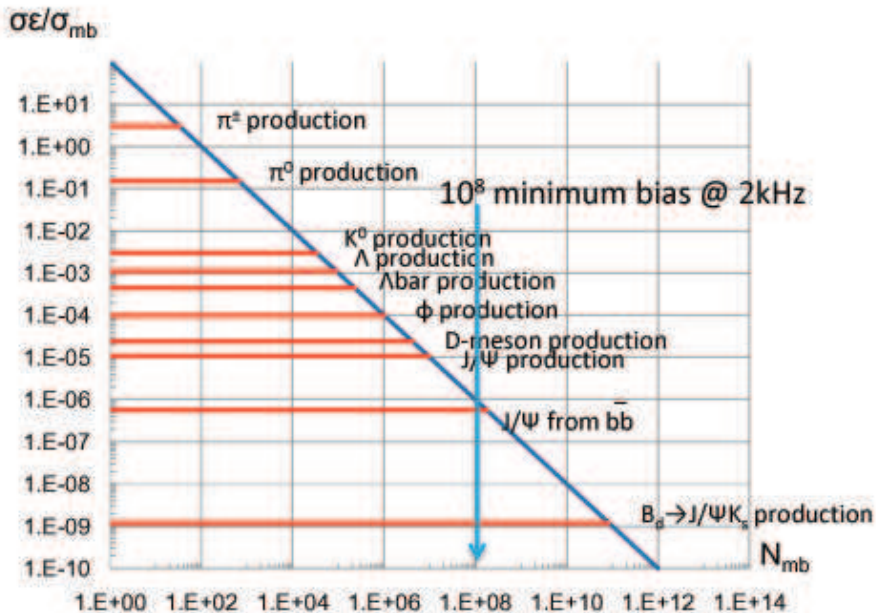


Figure 12: Physics reach vs. integrated luminosity

In the following phase of running with increasing luminosity from  $2 \times 10^{30} \text{ cm}^{-2} \text{s}^{-1}$  to  $2.4 \times 10^{31} \text{ cm}^{-2} \text{s}^{-1}$ , the beauty cross section will be determined amongst others. For this a working muon system, main tracker and VELO will provide the necessary basic information. After measurement of the relative fraction of the prompt and detached  $J/\Psi$ s, the absolute production of  $J/\Psi$  can be determined. From the non prompt  $J/\Psi$  yield the  $b\bar{b}$  cross section will be derived.

This will be followed by the core program of search for new physics in CP-violation and rare decays including very interesting measurements with the expected first  $0.5 \text{ fb}^{-1}$  of data:

- $B_s \rightarrow J/\Psi \phi$  will allow to determine  $B_s$  mixing phase  $2\beta_s$  with  $\approx 0.05$  precision
- $B_s \rightarrow \mu\mu$  will give the BR limit down to SM value
- $B_d \rightarrow K^{0*} \mu\mu$  will have a statistics competitive with B-factories ( $\approx 1800$  events)

## 4 Summary and outlook

The LHCb detector is ready to take data in 2008. It combines good decay time resolution to resolve  $B_s$  oscillations, good mass resolution to efficiently suppress background, an excellent particle identification for  $K-\pi$  separation and an efficient trigger for many  $B$ -decay topologies. Inclusive low  $p_T$  physics will be investigated from day one with a data sample of  $10^8$  minimum bias events. During the subsequent time of increased luminosity, determination of the  $b$ -cross section is envisaged.

The core physics program will make use of  $2\text{ fb}^{-1}$  per year addressing CP violation and rare decays. CP violation measurements include the UT angle  $\gamma$  from trees with a precision of  $5^\circ - 10^\circ$  and from Penguins with  $\approx 10^\circ$  precision, the  $B_s$  mixing phase with an error of  $\sigma(2\beta_s) \approx 0.023$  and  $\beta_s^{eff}$  from Penguins. As mentioned before, examples of the most interesting rare decays which will be studied are  $B_d \rightarrow K^{0*}\mu\mu$ ,  $B_s \rightarrow \phi\gamma$  and  $B_s \rightarrow \mu\mu$ .

## References

- [1] The LHCb Collaboration, “The LHCb Detector At The LHC,” *JINST* **3** (2008) S08005.
- [2] G. Corti, *Nucl. Phys. Proc. Suppl.* **170** (2007) 278.
- [3] S. de Capua, “Large mass dimuon detection in the LHCb experiment,” CERN-THESIS-2006-035.

# Astroparticle Physics

Session Convener:

*Roberto Battiston*

Session Convener:

*Wolfgang Lohmann*

Ultra High Energy Cosmic Rays from earth-based  
observatories

*Sergio Petrera*

Dark Matter Detection and the XENON Experiment

*Elena Aprile*

Cosmic Rays from space based observatories

*Piero Spillantini*

Very High-Energy Gamma Ray Astronomy

*Ullrich Schwanke*

FERMI/GLAST and the Future of High Energy  
Gamma Ray Astronomy

*Vincenzo Vitale*

Ultra-High Energy Particles Astronomy with  
a space-based experiment

*Roberto Pesce*

Antimatter and DM search in space with AMS-02

*Francesca R. Spada*

# Ultra High Energy Cosmic Rays from earth-based observatories

*Sergio Petrera*

*INFN and Physics Department, L'Aquila University  
I-67010 L'Aquila, ITALY*

## 1 Introduction

The origin of the highest energy cosmic rays is one of the most exciting questions of astroparticle physics. Even though a general concept linking magnetic field and size of possible sources (the so called “Hillas plot” [1]) is the basis of our current understanding, up to now there are no generally accepted source candidates known to be able to produce particles of such extreme energies.

At these energies cosmic rays are expected to exhibit a suppression in the energy spectrum because of their interaction with the microwave background radiation (CMB). This feature, known as the Greisen-Zatsepin-Kuz'min (GZK) effect [2], is at about  $\sim 6 \cdot 10^{19}$  eV for protons. It limits the horizon from which these particles can be observed to a distance below about 100 Mpc (depending on the primary mass). The non-observation of the GZK effect in the data of the AGASA experiment [3] has motivated several theoretical and phenomenological models trying to explain the absence of the GZK effect. More recently both HiRes [4] and Auger [5] have shown evidence of a suppression such as expected from the GZK effect with high statistical significance. The recent observation of directional correlations of the most energetic Auger events with the positions of nearby Active Galactic Nuclei [6] complements the observation of the GZK effect very nicely.

Mass composition is another important key to discriminate among different models about the origin of high-energy cosmic rays. Such measurements are difficult due to their strong dependence on hadronic interaction models. Only primary photons can be discriminated safely from protons and nuclei and recent upper limits to their flux largely constrain existing top-down models.

In this paper, prepared for the Physics in Collisions 2008 Conference, each of these topics are exposed and reviewed.

## 2 UHECR Experiments

In the UHE region two detection methods are effective for extensive air showers (EAS): arrays of surface detectors and air fluorescence detectors. A comprehensive review of these experimental methods can be found in [7]. In this Section recent experiments dedicated to the detection of cosmic rays are briefly described.

**AGASA.** The Akeno Giant Air Shower Array, located in Japan at the latitude of about  $35^\circ$  N and altitude of 900 m above sea level was in operation from 1990 until 2004. It was a large surface array [8], designed to measure the front of the cosmic ray showers as they reach ground. The array consisted of 111 plastic scintillators with size of  $2.2 \text{ m}^2$  deployed with separation of 1 km and covering an area of  $100 \text{ km}^2$ . The array was complemented by 27 muon detectors consisting of proportional counters placed below absorbers.

**HiRes.** It is the new and sophisticated version of the pioneering Fly's Eye instrument of the Utah group based on the detection of the fluorescence light from the nitrogen molecules excited by the charged particles of the cosmic ray showers. It was in operation from 1997 until 2006. The HiRes instrument [9] consists of two sites 12.6 km apart located at Dugway in Utah (USA) hosting 22 telescopes at HiRes I and 42 at HiRes II. The telescopes cover the full  $360^\circ$  azimuth and in elevation from  $3^\circ$  up to  $17^\circ$  (HiRes I) and from  $3^\circ$  up to  $31^\circ$  (HiRes II). The main components of each telescope are a spherical mirror of about  $4 \text{ m}^2$  size and an array of 256 photomultipliers as sensitive element. UV filters to cut light outside the 300-400 nm interval of the nitrogen fluorescence were also used.

**Auger.** Two observatories, one in the Northern and one in the Southern hemisphere are foreseen for the Pierre Auger Observatory project, to achieve a full exploration of the sky. The Southern Auger Observatory [10] is located near the small town of Malargüe in the province of Mendoza (Argentina) at the latitude of about  $35^\circ$  S and altitude of 1400 above see level. The Observatory is a hybrid system, a combination of a large surface array and a fluorescence detector. The surface detector (SD) is a large array of 1600 water Cherenkov counters spaced at a distance of 1.5 km and covering a total area of  $3000 \text{ km}^2$ . Each counter is a plastic tank of cylindrical shape with size  $10 \text{ m}^2 \times 1.2 \text{ m}$  filled with purified water. The SD tanks activated by the event record the particle number and the time of arrival. From the times, the direction of each event is determined with an accuracy of about  $1^\circ$ . The fluorescence detector (FD) consists of 24 telescopes located in four stations which are built on the top of small elevations on the perimeter of the site. The telescopes measure the shower development in the air by observing the fluorescence light. Each telescope has a  $12 \text{ m}^2$  spherical mirror with curvature radius of 3.4 m and a camera with 440 photomultipliers. The field of view of each telescope is  $30^\circ \times 30^\circ$ . UV filters were used as in HiRes. The Southern Auger Observatory started to collect data in 2004. The Observatory and has been completed in Summer 2008. The Northern Auger Observatory which is now being designed will

be located in Colorado (USA). We note that the present Auger Observatory is the only detector exploring the Southern hemisphere.

**Telescope Array (TA).** It is being built by a US - Japan - Korea collaboration in Millard County, Utah, USA. Like the Auger Observatory, the TA is a hybrid detector [11]. It covers an area of  $860 \text{ km}^2$  and comprises 576 scintillator stations and three FD sites on a triangle with about 35 km separation each equipped with 12 fluorescence telescopes.

Fig. 1 shows a comparison of the exposures accumulated by various experiments at the end of 2007. More details about the exposure calculations can be found in [12]. It can be seen that the largest exposure has been achieved with the Auger Observatory and it will continue to deliver more than about  $7000 \text{ km}^2 \text{ sr}$  for each year of operation. TA is not shown in the figure since it started full operation since March 2008. It is important to notice the different behaviour with energy of the apertures for

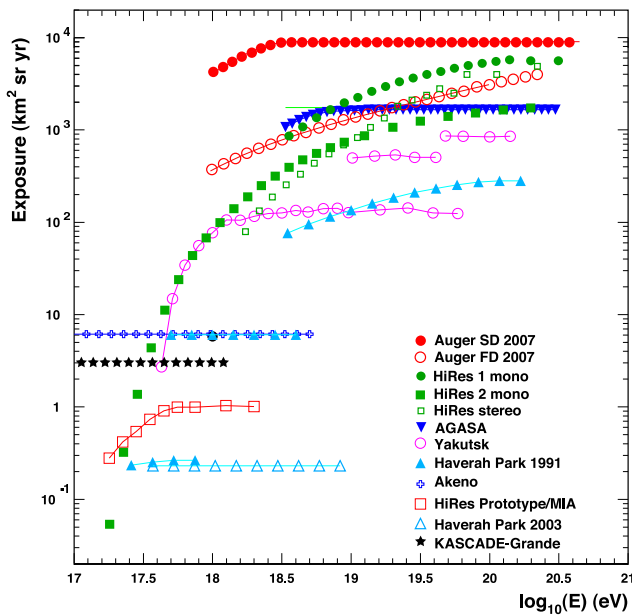


Figure 1: Accumulated exposures of various experiments at the end of 2007 (see ref. [12]).

arrays of surface detectors and fluorescence detectors. In case of arrays of detectors with a regular pattern, the aperture can be calculated in a straight forward and model independent way, once the energy threshold for CR detection and reconstruction is exceeded. The situation is different for fluorescence telescopes. Here, the maximum distance out to which showers can be observed increases with increasing fluorescence light and thereby increasing energy. This condition makes the aperture calculation dependent on Monte Carlo simulation and then on primary mass and on the hadronic

interaction models employed. This dependence can be considerably reduced by applying quality cuts to geometry parameters (e.g. the distance of the shower), but this is possible only if geometry is well determined as in the cases of hybrid or stereo detection.

### 3 The Energy Spectrum

Most of the energy spectrum data available today<sup>1</sup> at UHE are provided by AGASA, HiRes and Auger (see Fig. 2). The two last experiments recently published spectrum analyses [4, 5] showing evidence of a flux suppression as expected by the GZK effect with significances of about 5 and 6  $\sigma$  respectively at slightly different energies (5.6 and  $4 \times 10^{19}$  eV). Shifting the energy scale by about +15% for Auger and about -25% for AGASA with respect to HiRes the three spectra agree rather well up to about  $5 \times 10^{19}$  eV. At higher energies the AGASA data do not exhibit any flux suppression and thus are inconsistent with the other data.

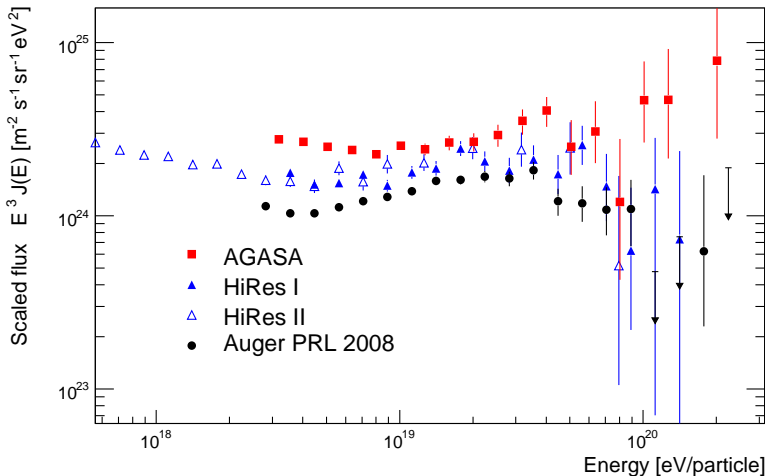


Figure 2: Cosmic ray flux measurements (multiplied by  $E^3$ ) from AGASA [3], HiRes [4] and Auger [5].

Typical uncertainties of the energy scale are on the order of 20  $\div$  25%. Ground arrays like AGASA rely entirely on EAS simulations with their uncertainties originating from the limited knowledge of hadronic interactions. Fluorescence telescopes, such

<sup>1</sup>Spectrum data from instruments with exposure less than  $1000 \text{ km}^2 \text{ sr yr}$  have not been considered in this review.

as operated by HiRes and Auger, observe the longitudinal shower development in the atmosphere. In this way, the atmosphere is employed as a homogenous calorimeter. Nonetheless possible differences in their energy reconstruction are still present because of different assumptions (e.g. fluorescence yield, event reconstruction, analysis cuts).

Even though the Auger spectrum in [5] is based on surface data, the energy calibration is quite new. In fact the method used by Auger to measure the energy spectrum exploits the hybrid nature of the experiment with the aim of using the data itself rather than simulations. For each event the tanks of the SD measure the particle density expressed in units of VEM (Vertical Equivalent Muons) and the times of arrival which are used to determine the axis of the shower. The dependence of the particle density on the distance from the shower axis is fitted by a lateral distribution function (LDF). The LDF fit allows determining the particle density  $S(1000)$ , expressed in units of VEM, at the distance of 1000 m from the axis. This quantity is a good energy estimator [13] in the sense that it is strongly correlated with the energy of the cosmic ray and almost independent of the mass. The energy estimator  $S(1000)$  depends on the zenith angle because of the atmosphere attenuation. The value of  $S(1000)$  corresponding to the median zenith angle of  $38^\circ$  ( $S_{38}$ ) is used as reference and the zenith angle dependence of the energy estimator is determined assuming that the arrival directions are isotropically distributed. This procedure is traditionally called *Constant Intensity Cut*. The absolute calibration of  $S_{38}$  is derived

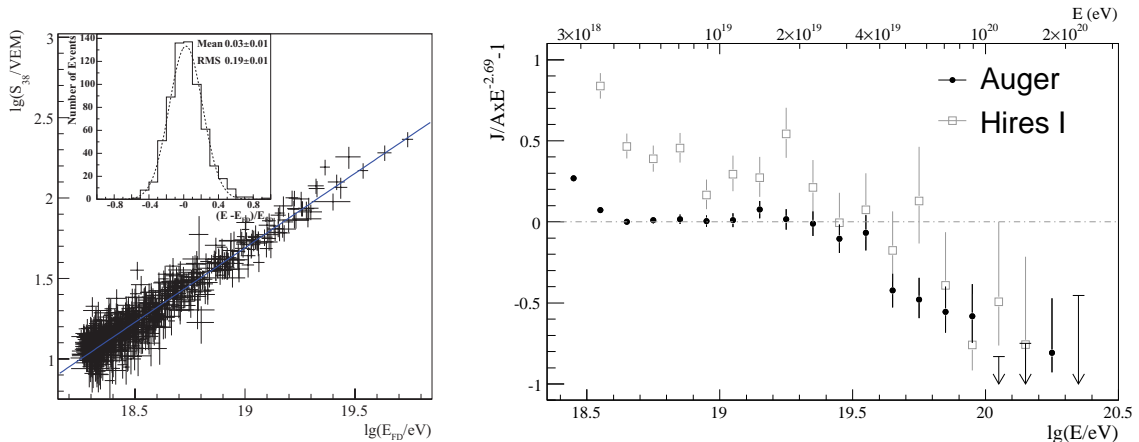


Figure 3: *Left:* Auger calibration of SD data: correlation between surface detector signal and FD energy. The fractional differences between the two energy estimators are inset. *Right:* Fractional difference between Auger and HiRes I data relative to a spectrum with index of 2.69.

from the hybrid events using the calorimetric energy measured by the FD which is then corrected for the missing energy using the mean value between proton and iron (uncertainty about 4% at  $10^{19}$  eV). This absolute calibration, which defines the

energy scale, is at present affected by a systematic error of about 20%, mainly due to uncertainties on the fluorescence yield and on the calibration of the FD telescopes. The energy calibration, obtained from the subset of hybrid events (see Fig. 3) is then used for the full set of events with higher statistics measured by the SD.

The flux suppression in Auger and HiRes as well as the possible difference in their energy scales is evident when plotting the fractional difference with respect to a power law spectrum. Fig. 3, right panel, shows this fact for a spectral index of 2.69 which is the one fitted by Auger below  $4 \times 10^{19}$  eV.

## 4 Primary Composition

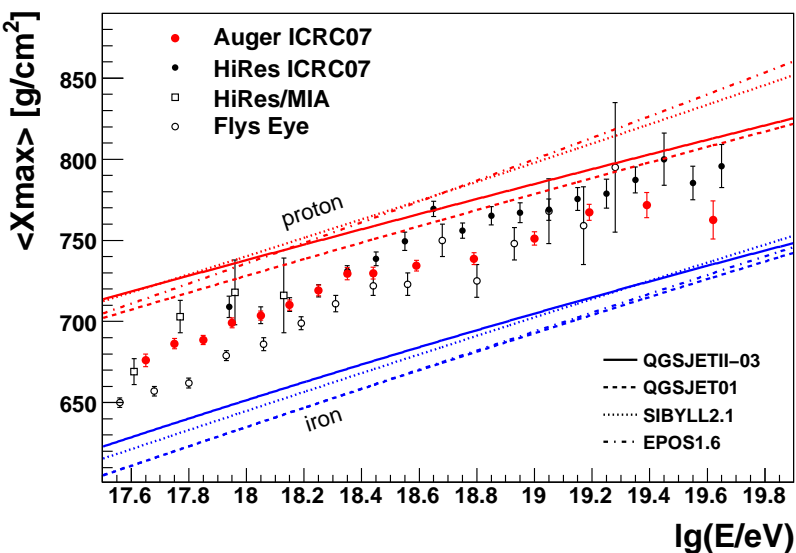


Figure 4:  $\langle X_{max} \rangle$  as a function of energy compared with proton and iron predictions using different hadronic interaction models.

Measuring the composition of cosmic rays is crucial to obtain a full understanding of their acceleration processes, propagation and relation with galactic particles. The atmospheric depth  $X_{max}$  denotes the longitudinal position of the shower maximum, which is directly accessible with the FD. It grows logarithmically with the energy of the primary particle. The behaviour of  $X_{max}$  for different primary particles like photons, protons and heavier nuclei can be conceptually understood in the framework of the Heitler and superposition models [14], which provides good agreement with detailed Monte Carlo simulations. New results based on HiRes-Stereo and Auger hybrid data at the ICRC [15, 16] are reported in Fig. 4. Both data sets agree

very well up to  $\sim 3 \cdot 10^{18}$  eV but differ slightly at higher energies. The differences between the two experiments are within the differences observed between p- and Fe-predictions for different hadronic interaction models. With these caveat kept in mind, both experiments observe an increasingly lighter composition towards the ankle. At higher energies, the HiRes measurement yields a lighter composition than Auger.

Another important issue concerning the primary composition is the search for photons and neutrinos in EAS. The Auger Observatory has set new photon limits with both the hybrid and SD detection methods [17, 18]. The new limits are compared to previous results and to theoretical predictions in Fig. 5 for the photon fraction. In terms of the photon fraction, the current bound at 10 EeV approaches the percent level while previous bounds were at the 10 percent level. A discovery of a substantial photon flux could have been interpreted as a signature of top-down (TD) models. In turn, the experimental limits now put strong constraints on these models. For instance, certain SHDM (Super Heavy Dark Matter) or TD models discussed in the literature [19] predict fluxes that exceed the limits by a factor 10.

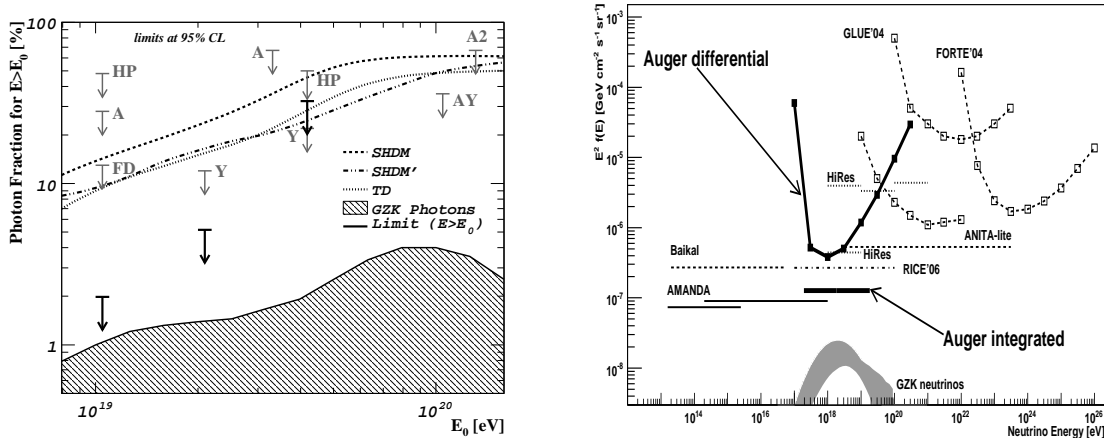


Figure 5: *Left:* The upper limits on the fraction of photons in the integral cosmic ray flux derived from Auger SD (black arrows) along with previous experimental limits (HP: Haverah Park; A1, A2: AGASA; AY: AGASA-Yakutsk; Y: Yakutsk; FD: Auger hybrid limit). Also shown are predictions from top-down models (SHDM, SHDM', TD) and predictions of the GZK photon fraction. For references see [18]. *Right:* Limits at the 90% C.L. for a diffuse flux of  $\nu_\tau$  assuming a 1:1:1 ratio of the 3 neutrino flavors and the expected flux of GZK neutrinos. For references see [20]

Neutrino induced showers can be also identified if they occur deep in the atmosphere under large zenith angles, or by their special topology in the case of Earth-skimming tau neutrinos. Identification criteria have been developed to find EAS that are generated by tau neutrinos emerging from the Earth. Auger has searched for tau

neutrinos in the data collected up to August 2007. No candidates have been found and an upper limit on the diffuse tau neutrino flux has been set. In Fig. 5 this result [20] is shown.

## 5 Arrival Directions

Most of the recent results are from the Auger Collaboration who have started a detailed investigation of the angular directions of the cosmic rays. While no excess has been found from the Galactic Centre in the EeV energy range, evidence for anisotropy has been found in the extreme energy region.

Observation of an excess from the region of the Galactic Centre in the EeV energy region were reported by AGASA [21] and SUGAR [22]. The Auger Observatory is suitable for this study because the Galactic Centre (constellation of Sagittarius) lies well in the field of view of the experiment. The angular resolution of the SD of Auger depends on the number of tanks activated by the shower and it is better than one degree at high-energy. However, with statistics much greater than previous data, the Auger search [23] does not show abnormally over-dense regions around the GC.

A big step towards the discovery of the UHECR sources has been recently made by the Pierre Auger Collaboration [6, 24]. The highest energy events recorded so far were scanned for correlations with relatively nearby AGNs ( $z \leq 0.024$  corresponding to  $D \leq 100$  Mpc) listed in the Véron-Cetty/Véron catalogue [26]. AGNs where used only up to a maximal redshift  $z_{max}$ , which was a free parameter in the correlation scan. Two other free parameters were the minimal energy of the cosmic ray events  $E_{thr}$  and the maximum separation between reconstructed cosmic ray direction and the AGN position  $\psi$ . The scan was performed over data taken during the first two years of stable operation (01/2004 - 05/2006) and a significant minimum of the chance probability calculated assuming isotropic arrival directions was observed. After the parameters of this *explorative scan* ( $z_{max} = 0.018$ ,  $E_{thr} = 56$  EeV,  $\psi = 3.1^\circ$ ) were fixed, the consecutive data set (06/2006-08/2007) was used to verify the correlation signal and the hypothesis of an *isotropic source distribution* could be rejected at more than 99% confidence level. A sky map of the 27 events above the energy threshold of  $E_{thr} = 56$  EeV together with the selected AGN is shown in Fig. 6. Also shown are the events selected during a follow-up analysis of stereo data from the HiRes Collaboration [25], which do not show a significant correlation.

The interpretation of the observed anisotropy is ongoing and a much larger event statistics will be needed to investigate, for example, whether the AGNs act only as tracers for the underlying true sources and whether the angular separation between AGN and UHECR can be related to magnetic deflections.

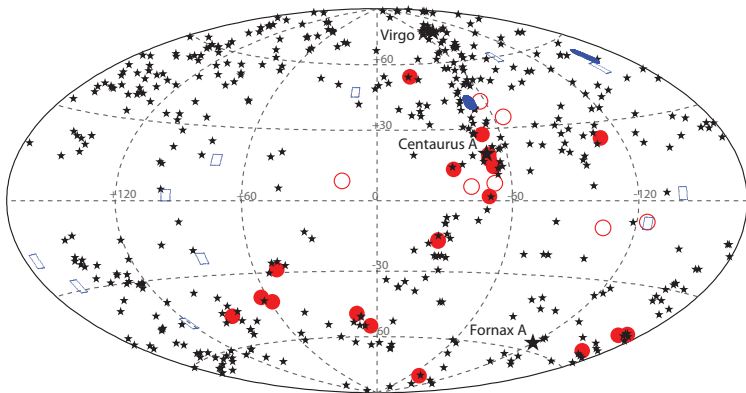


Figure 6: The sky seen with UHECRs with energy above 56 EeV detected with the surface array of Auger (red circles, [6, 24]) and with the HiRes detector in stereo mode (blue squares, [25]) in galactic coordinates. Filled markers denote cosmic rays within  $3.1^\circ$  from AGNs with redshift  $z < 0.018$  (black stars, [26]). The relative exposures of the two experiments are not shown for simplicity. Very roughly Auger (HiRes) is blind to a part of the left (right) side of this plot and then their exposures are rather complementary. Detailed exposures can be found in the original papers.

## 6 Conclusion and outlook

In recent years UHECRs have shown a variety of exciting features: the flux suppression at energies as the one expected for the GZK cutoff and possible correlations with sources are the most attractive. The two phenomena are strictly related one to each other. In particular the correlation scenario is compatible with suitable spectrum shapes and mass compositions in the GZK region. This because cosmic ray propagation through galactic fields and their interactions with the photon background affect not only directions, but also the energy and type of particles observed on Earth.

Coming years are expected to be fruitful. New data will come from the Northern Hemisphere: Telescope Array, now, and Auger North, in a few years, will join this fascinating exploration.

## References

- [1] A. M. Hillas, Annu. Rev. Astron. Astrophys., **22**, 425 (1984).
- [2] K. Greisen, Phys. Rev. Lett. **16**, 748 (1966) and G.T. Zatsepin and V.A. Kuz'min, Sov. Phys. JETP Lett. (Engl. Transl.), **4**, 78 (1966).

- [3] M. Takeda et al. [AGASA Collaboration], *Astropart. Phys.* **19**, 447 (2003).
- [4] R.U. Abbasi et al. [HiRes Collaboration], *Phys. Rev. Lett.* **100**, 101101 (2008).
- [5] J. Abraham et al. [Pierre Auger Collaboration], *Phys. Rev. Lett.* **101**, 061101 (2008).
- [6] J. Abraham et al. [Pierre Auger Collaboration], *Science* **318**, 938 (2007).
- [7] M. Nagano and A. A. Watson, *Rev. Mod. Phys.* **72**, 689 (2000).
- [8] N. Chiba et al., *Nucl. Instrum. Meth.*, **A311**, 338 (1992).
- [9] T. Abu-Zayyad et al., *Nucl. Instrum. Meth.* **A450**, 253 (2000).
- [10] J. Abraham et al., *Nucl. Instrum. Meth.* **A523**, 50 (2004).
- [11] M. Fukushima et al. [Telescope Array Collaboration], Proc. 30th ICRC, Mérida, p. 955 (2007).
- [12] K.-H. Kampert, *J. Phys. Conf. Ser.*, **120**, 062002 (2008).
- [13] D. Newton et al., *Astropart. Phys.* **26**, 414 (2007).
- [14] J. Matthews, *Astropart. Phys.* **22**, 387 (2005)
- [15] Y. Fedorova et al. [HiRes Collaboration], Proc. 30th ICRC, Mérida, p.1236 (2007).
- [16] M. Unger et al. [Pierre Auger Collaboration], Proc. 30th ICRC, Mérida, p.594 (2007).
- [17] J. Abraham et al. [Pierre Auger Collaboration], *Astropart. Phys.* **27**, 155 (2007)
- [18] J. Abraham et al. [Pierre Auger Collaboration], *Astropart. Phys.* **29**, 243 (2008).
- [19] References to theoretical models can be found e.g. in [18].
- [20] J. Abraham et al. [Pierre Auger Collaboration], *Phys. Rev. Lett.* **100**, 211101 (2008).
- [21] M. Teshima et al., Proc. 27th ICRC, Hamburg, vol. 1, p. 337 (2001).
- [22] J.A. Bellido et al., *Astropart. Phys.* **15**, 167 (2001).
- [23] J. Abraham et al. [Pierre Auger Collaboration], *Astropart. Phys.* **27**, 244 (2007).
- [24] J. Abraham et al. [Pierre Auger Collaboration], *Astropart. Phys.* **29**, 288 (2008).

- [25] R.U. Abbasi et al. [HiRes Collaboration], arXiv eprints: 0804.0382v1 (2008).
- [26] M.-P. Véron-Cetty, P. Véron, Astron. Astrophys. **455**, 773 (2006).

# Dark Matter Detection and the XENON Experiment

*Elena Aprile*

*Physics Department and Columbia Astrophysics Laboratory  
Columbia University  
New York, New York 10027*

## 1 Abstract

Observations on all fronts strongly support the view of a universe composed of >96% invisible matter and energy. The invisible matter is non-baryonic, cold and likely in the form of new particles generically referred to as Weakly Interacting Massive Particles (WIMPs), relics from the early universe. One way to detect WIMPs is to measure the nuclear recoils produced in their rare elastic collisions with ordinary matter. The predicted interaction rate ranges from the best sensitivity of existing experiments of  $\sim 1$  evts/kg/yr to  $\sim 1$  evts/1000 kg/yr. Experiments based on noble liquids offer the potential to meet this sensitivity goal, with a combination of large target mass and excellent background rejection at reasonable cost. After a brief overview of the approaches used for dark matter direct detection, I will focus on the recent performance and current status of the XENON experiment.

## 2 Introduction

The nature of dark matter and dark energy, which compose >96% of the universe (see [1], and references therein), is one of the most fundamental questions in physics. The leading candidate for the invisible “dark matter” is relics from the early universe known as Weakly Interacting Massive Particles (WIMPs). Such particles are also predicted by extensions of the standard model of particle physics, such as Supersymmetry (SUSY) [2]. If WIMPs exist, they are also the dominant mass in our own Milky Way, and, though they only very rarely interact with conventional matter, should nonetheless be detectable by sufficiently sensitive detectors on Earth.

In direct detection, one measures the energy, typically a few tens of keV [3], of the nuclear recoil which results from a WIMP-nucleon elastic scattering. A variety of target nuclei and detectors are used in direct detection experiments worldwide.

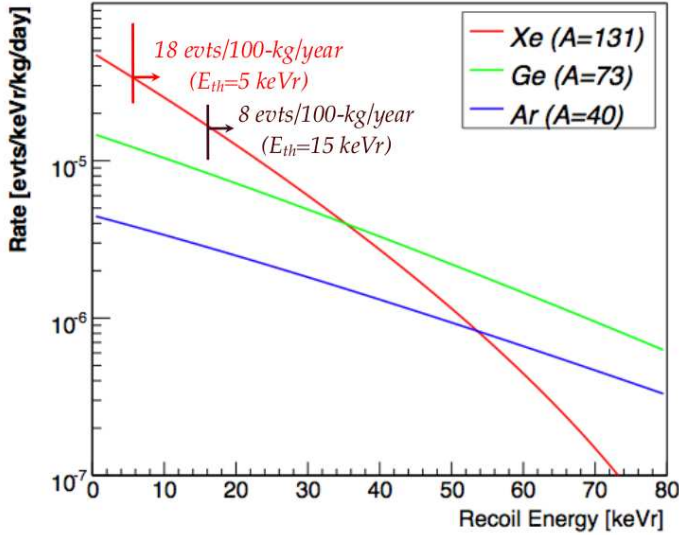


Figure 1: Event rates for a  $100 \text{ GeV}/c^2$  WIMP with spin-independent WIMP-nucleon cross-section of  $10^{-44} \text{ cm}^2$  for different target materials.

For a recent review of the field we refer to the report by the DUSEL S1 Dark Matter Working Group ([4], and references therein). Covering the bulk of the SUSY parameter space for WIMPs will require a sizable increase in sensitivity from the current best experimental limits [7, 6]. An increase in detector mass and exposure, in addition to a reduction in and/or improved rejection of radioactive and cosmogenic backgrounds is necessary.

The predicted event rates for a WIMP mass of  $100 \text{ GeV}/c^2$  and a spin-independent WIMP-nucleon cross-section of  $10^{-44} \text{ cm}^2$  are shown in Fig. 1 for Ge, Xe and Ar targets. The fast fall of the event rate with increasing recoil energy demands a very low energy threshold, around 10 keV. At this energy, the event rate for a Xe target is about 30% higher than for a Ge target, due to the Xe larger atomic number. Cryogenic solid state detectors, based on Ge and Si crystals, have for a long time dominated the field of dark matter direct detection, showing the best background discrimination and reporting stringent spin-independent WIMP-nucleon cross-section ( $4.6 \times 10^{-44} \text{ cm}^2$  at a WIMP mass of  $60 \text{ GeV}/c^2$  [7]).

In recent years, however, the application of cryogenic noble liquids in dark matter searches, has gained new momentum due to their promise for large target mass detectors with possibly as powerful background discrimination as cryogenic crystals. LXe and LAr are especially attractive as they are known to be good scintillators and ionizers, as established in many works. The scintillation mechanism in these liquids is well known [8]. Both excitation and electron-ion pairs recombination produce ex-

cited dimers, which lead to scintillation light ( $\text{Xe}_2^* \rightarrow 2 \text{ Xe} + h\nu$  in the case of Xe). In pure liquids, the light pulse has two decay components due to de-excitation of singlet and triplet states of the excited dimers. These components have decay times which depend strongly on the ionization density of the particle. For alpha-particles in LXe the shorter decay time produced from the de-excitation of singlet states and the longer one from the de-excitation of triplet states, are 4.2 and 22 ns. However, the scintillation for relativistic electrons has only one decay component whose effective decay time is 45 ns. This is due to the slow recombination between electrons and ions produced by relativistic electrons, since this component disappears if some electric field is applied. The decay shape of scintillation light from energetic electrons in LXe, under an electric field of 4 kV/cm, has the usual two decay components, with the short one being 2.2 ns and the longer one being 27 ns. In LAr, these components have decay times which are much more separated, allowing for an easier pulse shape discrimination (PSD) of the scintillation signal as background rejection tool. The ionization electrons which escape recombination can be collected with an applied electric field. The recombination process strongly depends on the ionization density of the radiation and its track structure, so that the ratio of ionization to scintillation in noble liquids is different for electron recoils from gamma and beta background and for nuclear recoils from WIMPs and neutron background. The simultaneous detection of charge and light therefore provides background discrimination in LXe and LAr, in a similar way as the simultaneous detection of charge and phonon signals provides discrimination in cryogenic Ge and Si. In addition to being available in large quantities for cost effective large volume detectors, another advantage of LAr and LXe over cryogenic solid state detectors is their high boiling point, 87K and 165K respectively, which require much less complex cryogenic systems.

I will briefly review the XENON experiment which is based on the simultaneous measurement of charge and light in a Xe two-phase time projection chamber (TPC).

### 3 The XENON Dark Matter Experiment

The goal of the XENON Dark Matter phased program is to realize a very sensitive, low background, dual-phase TPC containing 1000 kg of Xe as fiducial target, to search for both spin-independent and spin-dependent coupling of WIMPs with matter. With an energy threshold of 5 keV, nuclear recoil equivalent, and a total background event rate lower than  $10^{-4}$  evts/kg/keV/yr before any rejection, the sensitivity goal of XENON1T is at the  $10^{-47}$  cm<sup>2</sup> level, or almost four orders of magnitude lower than the current best sensitivity (see Fig. 4).

In the XENON Dark Matter experiment, the simultaneous detection of ionization and scintillation in a liquid xenon 3-D position sensitive time projection chamber is used to identify nuclear recoils, produced by WIMPs (and neutrons), from electron

recoils produced by gamma and beta background, with a rejection power better than 99.5%.

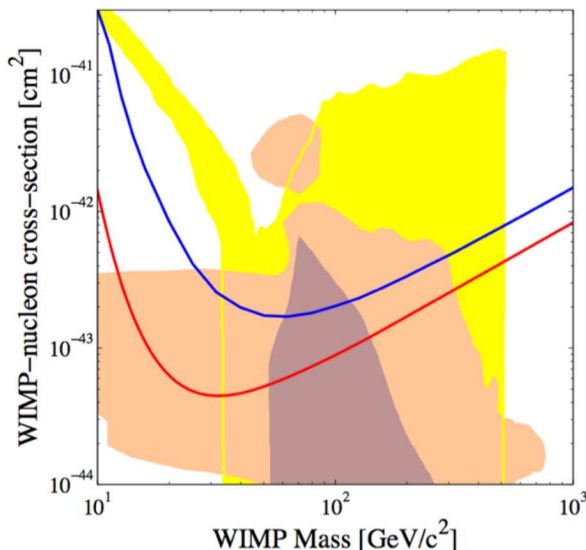


Figure 2: Spin-independent WIMP-nucleon cross-section upper limits (90 % C.L.) versus WIMP mass. Shown curves are for the previously best published limit (upper, blue) and the current work (lower, red). The shaded area is for parameters in the MSSM models (yellow), the Constrained MSSM models (marron) and CMSSM with the recent improved Standard Model prediction for the branching ratio of  $\overline{B} \Rightarrow X_s\gamma$  (brown).

The first prototype detector, XENON10, was deployed at the Gran Sasso Underground Laboratory (LNGS) [9] in Spring of 2006 and the first results from a WIMP search were obtained in Spring 2007, making it the most sensitive dark matter experiment worldwide. Fig. 2 shows the 90% C.L. upper limit on the spin-independent cross-section of a WIMP with nucleons of  $8.8 \times 10^{-44} \text{ cm}^2$  for a WIMP mass of  $100 \text{ GeV}/c^2$  [6]. The result is based on 58.6 live days, acquired between October 2006 and February 2007. The same data were also analyzed for spin dependent coupling of WIMPs to matter [10]. The result for pure neutron couplings are the world's most stringent to date, reaching a minimum cross section of  $5 \times 10^{-39} \text{ cm}^2$  at a WIMP mass of  $30 \text{ GeV}/c^2$  (Fig. 3).

The excellent performance of this first generation TPC has enabled the LXe technology to be at the forefront of dark matter direct detection and the renewed XENON Collaboration is currently pursuing an aggressive second phase of the program with the XENON100 experiment.

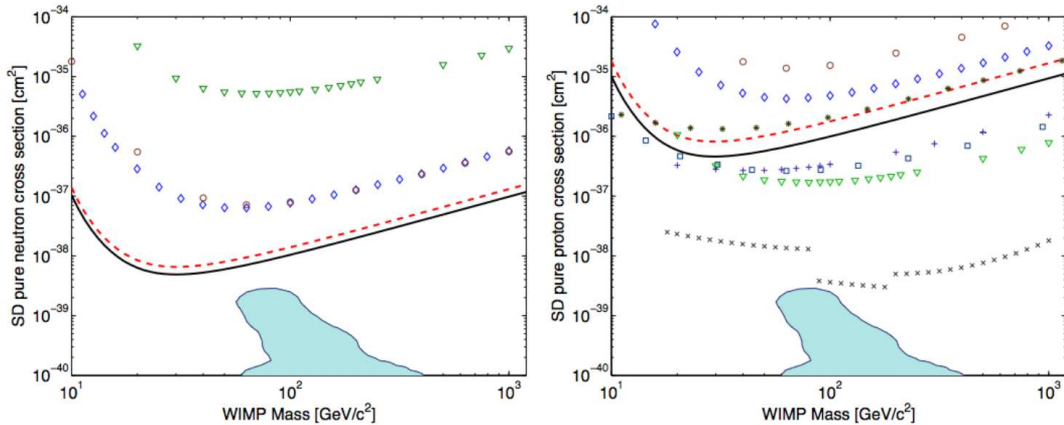


Figure 3: Combined 90% CL exclusion Limits for  $\text{Xe}^{129}$  and  $\text{Xe}^{131}$  for pure neutron (left) and pure proton (right) couplings (solid curves). The dashed curves show the combined Xe limits using the alternate form factor. Also shown are the results from the CDMS experiment (diamonds), ZEPLIN-II (circles), KIMS (triangles), NAIAD (squares), PICASSO (stars), COUPP (pluses) and SuperK (crosses). The theoretical regions (constrained minimal supersymmetric model) are also shown.

The sensitivity reach of the XENON100 experiment is a spin-independent cross section of  $\sim 2 \times 10^{-45} \text{ cm}^2$  within 2009 (see Fig. 4). Following this phase at the 100 kg scale within the phased XENON program, the next step is the realization of the XENON1T TPC, to be operational by 2013 with the projected sensitivity shown in Fig. 4. We have started a design study for the tonne scale experiment, with which we will probe the lowest spin independent WIMP-Nucleon cross section predicted by SUSY.

The XENON100 detector is a dual phase TPC, in which ionization electrons produced by an event in the liquid xenon are efficiently extracted from the liquid to the gas, with subsequent amplification via proportional scintillation. The ratio of the amplitude of the charge and light signals, being quite distinct for nuclear and electron recoils, provides the basis for event-by-event discrimination in the XENON concept. A schematic of the XENON100 TPC is shown in Fig. 5. The XENON100 detector consists of an inner target surrounded by an active LXe veto. Both target and veto are contained in a single double-walled vacuum cryostat made of low activity stainless steel (SS). The total mass of Xe required to fill the detector is 170 kg, of which approximately 70 are in the fiducial volume (target). The light readout is based on the same type of 1 inch square photomultiplier tubes (PMTs) as used in XENON10 (Hamamatsu R8520-06-AL), but with selected low radioactivity materials. The target

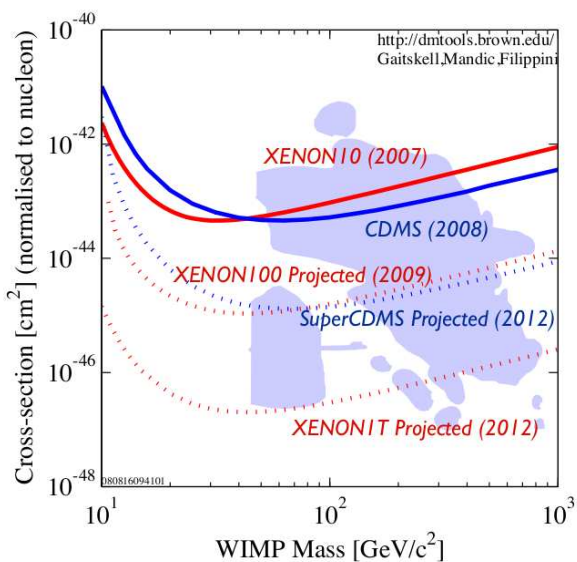


Figure 4: WIMP-nucleon cross-section upper limit (90% C.L.) from direct dark matter search experiments. The projected upper limits are shown as dashed lines.

is enclosed by a teflon structure, made with interlocking panels. Teflon is used as an effective UV light reflector and as an electrical insulator. The TPC is equipped with four wire meshes, two in the liquid and two in the gas. The bottom mesh serves as cathode and the next one positioned just below the liquid level, together with a series of field shaping rings, form the 30 cm drift region. The top two meshes, together with the one below the liquid level, serve to define the gas proportional scintillation region. The wire meshes and top PMT array are mounted in an SS cylinder closed on top, but open at the bottom. The cylinder works like a “diving bell”, keeping the liquid level at a precise height. A positive pressure in the bell is provided by the gas returning from the continuous recirculation system. The “diving bell” system was developed and used to control the liquid level in the XENON10 detector.

A Pulse Tube Refrigerator (PTR) with 170 W cooling power will be used to liquefy and keep the liquid temperature. As demonstrated with XENON10, the PTR provides excellent long time stability of operation, with temperature deviations not exceeding 0.1°C and pressure changes less than 1%. The key difference is that the cryogenic system which was previously mounted on top of the XENON10 cryostat, inside the Pb/Poly shield enclosure, is now moved outside the shield, to minimize background.

An un-vetoed event in the XENON100 TPC will be of interest if it features only two pulses: one from the direct scintillation light in the liquid (S1, with a characteristic width  $>100$  ns) and one from the ionization charge, amplified via scintillation

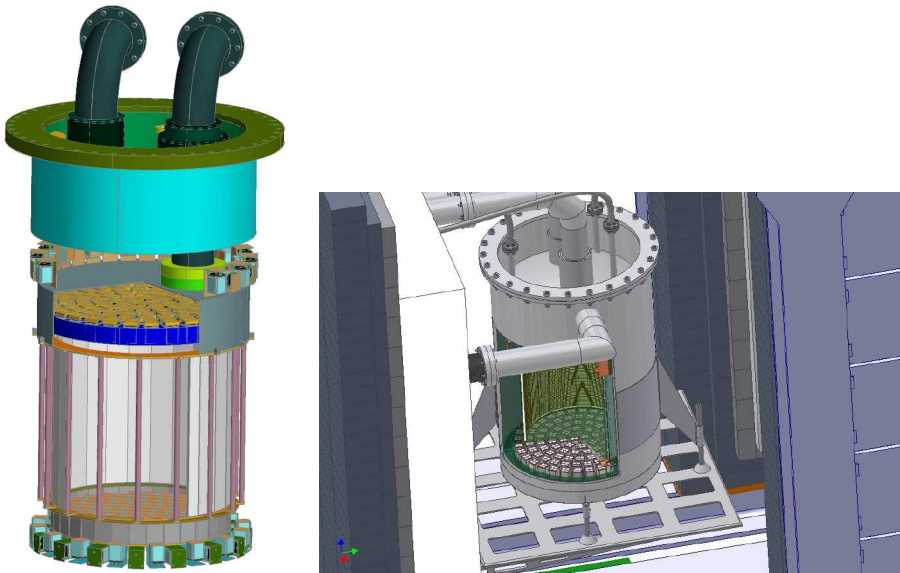


Figure 5: Schematic of the XENON100 TPC (left) and the cryostat inside the shield (right).

in the gas (S2, with characteristic a width of a few  $\mu\text{s}$ ). The two pulses occur within the maximum drift time of 150  $\mu\text{s}$ , for a saturated drift velocity of 2 mm/ $\mu\text{s}$  in LXe.

The greatest challenge for the readout electronics is the large dynamic range required: the system must be able to handle signals ranging from single photoelectrons (scintillation signals in the keV range) up to large S2 pulses from gamma ionization signals (up to thousands of photoelectrons). Moreover, the time difference between S1 and S2 pulses must be measured with sub- $\mu\text{s}$  resolution in a 300  $\mu\text{s}$  range, to provide 3-D position reconstruction throughout the drift volume (we require twice the maximum drift time, to enable triggering either on the S1 or S2 pulse). We have adopted a DAQ design based on CAEN 1724 Flash ADCs, with a sampling rate of 100 MHz. To reduce the large data rate, zero-suppression is implemented with the FPGA (field programmable gate array) available on each board.

High purity liquid xenon is an essential requirement for a TPC like XENON100, with a drift gap of 30 cm. The purity must be preserved at all time during the detector operation in order to ensure stable performance. With XENON10 we have fulfilled this requirement by continuous gas circulation through a high temperature getter, reaching an electron lifetime of  $(1.8 \pm 0.4)$  ms. While more challenging, we expect to achieve similar purity level in XENON100. Similarly demanding, is the requirement for very low level contamination of radioactive  $^{85}\text{Kr}$  in Xe. By using a dedicated cryogenic distillation column, we will reduce the  $^{85}\text{Kr}$  concentration well below the 50 ppt (part per trillion) required by the XENON100 sensitivity goal.

## 4 Summary

The nature of dark matter remains a fundamental mystery, which likely involves new particles and new physics beyond the standard model. In direct detection experiments one searches for the nuclear recoils resulting from the rare collisions of dark matter particles with the nuclei in the detector's target. For the XENON experiment the target is liquid xenon and the detector is a two-phase TPC, capable to measure simultaneously the ionization and the scintillation signals produced by nuclear recoils, in competition with the much larger number of electron recoils resulting from background radiation. The XENON collaboration has completed the commissioning of the XENON100 TPC, which has replaced the XENON10 prototype in the same shield and location at the Gran Sasso Underground Laboratory (LNGS). With a raw exposure of 6000 kg-days, free of background, XENON100 will be able to reach  $\sigma \sim 2 \times 10^{-45} \text{ cm}^2$  at 100 GeV, by the end of 2009. A further reduction in background and an increase in fiducial mass, will enable another order of magnitude improvement in sensitivity by 2012. The next phase will be a detector at the ton scale (XENON1T) with a sensitivity goal at the  $\sigma \sim 10^{-47} \text{ cm}^2$  level for the spin-independent WIMP-nucleon cross section, more than 3 orders of magnitude better than the current best limits from XENON10 [10] and CDMS [7].

## 5 Acknowledgements

My work on the XENON Dark Matter Project is supported by the National Science Foundation with Award No. PHY-0705337 to the Columbia Astrophysics Laboratory.

## References

- [1] D. N. Spergel *et al.*, *Astrophys. J. Suppl.* **170**, 377 (2007).
- [2] A. Bottino, *AIP Conf. Proc.* **751**, 46 (2005).
- [3] J. D. Lewin, P. F. Smith, *Astropart. Phys.* **6**, 87 (1996).
- [4] D. S. Akerib *et al.*, pre-print, astro-ph/0605719v3.
- [5] D. S. Akerib *et al.* (CDMS Collaboration), *Phys. Rev. Lett.* **96**, 011302 (2006).
- [6] J. Angle *et al.* (XENON collaboration), *Phys. Rev. Lett.* **100**, 021303 (2008).
- [7] Z. Ahmed *et al.* (CDMS Collaboration), pre-print, astro-ph/0802.3530v2.
- [8] A. Hitachi *et al.*, *Phys. Rev. B* **27**, 5259 (1983).

- [9] LNGS web page, <http://www.lngs.infn.it>.
- [10] J. Angle *et al.* (XENON collaboration), pre-print, astro-ph/0805.2939v1.

# Cosmic rays from space based observatories

*Piero Spillantini*

*Department of Physics and INFN*

*University of Firenze*

*I-50019 Sesto Fiorentino, ITALY*

## 1 Abstract

Because of the increasing importance of CR research in nuclear physics and in astrophysics, a systematic research program was elaborated by NASA at the beginning of the eighties. The major points were based on experiments borne to space by the shuttle vehicles or on board of the Freedom Space Station (FSS). The loss of the Challenger in 1986, the ending of the FSS program in 1991 and the long lasting shortage of means of transportation to orbit halted the space based part of the program. In last two decades a moderate progress was obtained by balloon borne experiments and by ground based huge area detector arrays. Only recently part of the original program can be recovered in the observation of high energy gamma rays by the launch of the AGILE and GLAST instruments, and in the research on the antimatter component of CRs with the long duration balloon flights of BESS in Antarctica, the going on PAMELA mission and the preparation of the AMS-2 instrument. The preliminary results of the PAMELA are discussed, and the near and far future perspectives considered.

## 2 Historical introduction

About one hundred years ago cosmic rays (CR) offered to physicists projectiles with energies exceeding by more than three orders of magnitude those available by natural radioactivity<sup>1</sup>. The structure of the nuclei could be investigated, mesons discovered

---

<sup>1</sup>A consideration is here worthwhile: electron machines constructed in 19th century could accelerate charged particles up to several keV, i.e. millions of billions of times the higher reachable mechanical kinetic energies, such as the destructive projectile of a powerful gun. They allowed investigating the atomic structure of the matter, and the atomic physics was born. Other three orders of magnitude were offered at the beginning of 20th century by natural radioactivity, whose projectiles have energies up to several MeV and can arrive inside the atoms up to the nucleus. The CR energies are measured in GeV or higher multiple of the eV, what stands for three or more orders of magnitude further.

and studied, nuclear physics born. It took four decades of technological efforts to reproduce CR energy by accelerators and to compete in intensity. After three other decades the technical development of particle detectors allowed to study CR with energies largely exceeding those supplied by accelerators, and CRs again became a useful instrument for elementary particle physics and astrophysics.

Therefore in the seventies the National Academy of Sciences of USA complemented with a CR research program the plan of Great Observatories elaborated by NASA for exploiting the close taking service of the Shuttle fleet [1]<sup>2</sup>

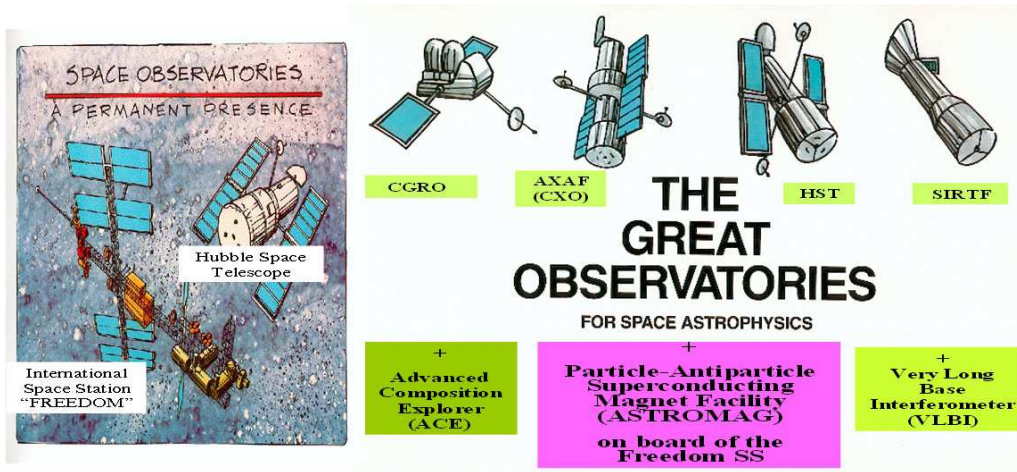


Figure 1: The Great Observatories (NASA brochure, adapted)

It was elaborated a comprehensive program of CR research for the decade 1985-1995 [2], where ground based experiments and theoretical studies were complemented by a robust program of research facilities in space, such that it could be assured a

<sup>2</sup>As soon as scientific instruments could be operated outside the atmosphere the astronomical observation (previously confined to the narrow window of the visible band, and (in the last decades) to the young radioastronomy), could span all the wave lengths of the electromagnetic radiation reaching us from space. The image of the universe was upset, new questions arose, and for answering them it was necessary to provide a **continuous and possibly simultaneous presence in space** of astronomical observatories covering the whole electromagnetic spectrum. The new revolutionary mean of flight planned by NASA, the Shuttle, allowed such an ambitious program. In the '70s were planned and began the realization of the Great Observatories: the Compton Gamma Ray Observatory (CGRO) for gamma rays, launched in 1991, the Advanced X-ray Astrophysics Facility (AXAF) for the X-rays (divided in the two observatories XMM and CXO both launched in 1999), the Hubble Space Telescope (HST) for the optical portion of the spectrum, launched in 1990, and the Space InfraRed Telescope Facility (SIRTF) for the infrared wavelengths, launched in 2003. They were complemented by the Very Large Base Interferometer (VLBI) on ground for the radioastronomy, by the ACE explorer for low energy CR and the ASTROMAG and HNC facilities for the high energy CR on board of the FREEDOM Space Station (see Figure 1).

permanent presence in orbit of instruments for continuous monitoring the electromagnetic and ionizing particle radiation coming from the Universe. Fundamental pieces of this program were (see Figure 2): (a) the Advanced Composition Explorer (ACE) for studying low energy CRs (up to a few GeV/nucleon) outside the magnetosphere that prevents them to approach the Earth; (b) the superconducting magnetic spectrometer ASTROMAG [3] to be used as a facility for CR researches up to energies beyond the PeV/nucleon; (c) the Heavy Nuclei Collector (HNC) [4] for the high charge (up to actinides) CRs. They were completed by a large Cosmic Dust collector. ASTROMAG, HNC and Dust collector were all planned on board of the Freedom Space Station (FSS) that was already under construction and had to take service in 1992 for celebrating the fifth century of the discover of America.

TAB. I - Particle Astrophysics Program for 1985-1995. Schematic from the report of NASA  
Cosmic Ray Program Working Group, dec. '85.

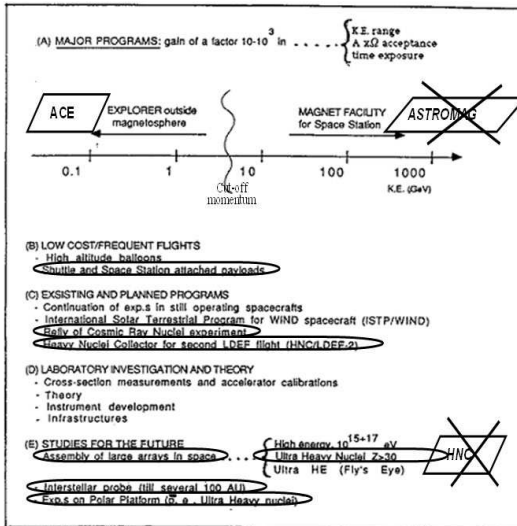


Figure 2: Schematic of the Particle Astrophysics Program for 1985-1995 (table I of the NASA report, adapted). The main facilities are enclosed in a rhombus. The never realized items are pointed out in an oval. The cancelled facilities are crossed.

The original, above mentioned [2], program envisaged by NASA at the beginning in the eighties afforded all the open thematic of CRs observation. They can be summarized in the following points:

- (1) measurement of the fluxes of high Z CR up to actinides (point (E) of the NASA program [2], HNC on FSS);
- (2) determination of the spectra of rare elements and of isotopes (beta decaying, electronic capture decaying) beyond a few GeV/nucleon;

- (3) determination of the spectra of antiparticles up to the hundred GeV region and search for antinuclei;
- (4) determination of the chemical composition around and beyond the knee;
- (5) high statistics measurement of the fluxes of ultra high energy CRs beyond the ankle (point (E) of the NASA program [2])

To the above categories it must be added the detection of the very high energy gammas ( $\geq 1 \text{ GeV}$ ), both because their production is tightly connected to the sources of very high energy CRs, as well for instrumental reasons, as gammas can be measured throughout the produced e+e- pair. The high energy gamma observation was part of the astromag program, with the ASTROGAM experiment [5] dedicated to extend up to about 300 GeV the observations performed by EGRET [6] on board of the CGRO.

For what concerns the electromagnetic observations the great observatories (CGRO, AXAF(CXO+XMM), HST, and SIRTF) were all constructed and launched. Also the ACE explorer for the study of low energy CRs outside the magnetosphere was realized and launched in 1999, and its instruments are producing a rich harvest of valuable data.

For the other facilities the final fate was different. The tragic explosion of the Challenger shuttle in 1986 slowed down the FSS program, which was definitely closed in 1991. The collaborations gathered around the programmed facilities were partially disbanded, and had to rescale their projects, continuing research by ballooning or on board of satellites.

### **3 What could be realized in the last two decades**

Let discuss what has been the progress in the last two decades on the above listed items concerning the high energy CRs.

#### **3.1 Very high energy gamma rays.**

Let begin with very high energy gamma ray observation. Only this year, two decades later, the ASTROGAM program could finally be recovered by the launch of two large acceptance instruments (equipped by calorimeters, but without the help of the strong magnetic field of the astromag facility foreseen in the original program). The AGILE [7] instrument was launched in orbit in April 2008, followed a few months later by the launch of the GLAST [8] instrument.

For the development of the CR researches planned on board of the FSS, namely at the cancelled HNC and ASTROMAG spectrometer facilities, the situation is somewhat differentiated.

### 3.2 Flux measurement of extreme Z cosmic rays.

For the measurement high Z fluxes nothing could be done. The HNC had to follow the inauspicious fate of the FSS. The technique foreseen in this kind of experiment is passive, by recovering the exposed material and etching it for measuring the damage caused by the crossing particle. It was set up and improved in precursor experiments on the LDEF facility and on board of the MIR space station [9], but never could be used in an experiment of conveniently large acceptance. The HNC heritors projects, ENTICE and ECCO [10] planned for the HNX spacecraft, were never founded, and are now hampered by the coming casting off of the shuttle transportation system.

### 3.3 Energy spectra of isotopes and rare components.

The continuation at higher energies of the ACE measurements of the isotopes and rare components does not require a huge acceptance but rather a good determination of the mass, charge and momentum of the incoming nucleus, what makes the instrument somewhat complex. The total acceptance of the dedicated LISA [11] project on the astromag facility was  $\pm 1m^2sr$ , but it could profit of the high intensity of the magnetic field of the spectrometer. In order to pursue the physics program of LISA it was realized by NASA a balloon borne superconducting magnetic spectrometer, ISOMAX [12], that unfortunately was destroyed in a flight accident. No more projects are in view for the next decade and more. The (by-product) data from BESS-Polar long duration balloon experiment and from PAMELA and AMS satellite experiments (see below) promise a good progress for a better understanding of the propagation of the CR in the Galaxy, but will not exhaust the duty of a dedicated experiment.

### 3.4 Chemical composition at knee.

Let now consider the flux of the dominant components of CRs, i.e. the nuclei that can be synthesized in stellar processes, from helium to iron, and subsequently accelerated to be ejected as CR in the interstellar space.

Their chemical composition at very high energy (from  $10^{14}$  to  $10^{16}$  eV/nucleus) is the central problem (the knee problem) of the CR physics. Until now it could not be solved by measuring on the Earth surface the characteristics of the showers produced in the atmosphere. The characteristic of the initial particle cannot be extracted on an event-by-event basis, and the extraction on a statistical basis is strongly model dependent, with contradictory results from different experiments, in spite of the huge investments and long dating efforts of a large community in many countries.

The global primary CR chemical composition and the energy spectra of the most abundant ones can be adequately studied only by detecting them before their interaction with the terrestrial atmosphere, i.e. in balloon borne or satellite borne experiments.

The cancellation of the Freedom SS program in 1991 hampered the SCINATT-MAGIC [13] experiment on ASTROMAG, devoted to the study of the CR chemical composition at the knee. It had to be performed by a suitable application of the nuclear emulsion techniques, developed by members of the proponent Japan-USA collaboration in experiments at accelerators. The collaboration pursued its goal by the series of long duration balloon flights JACEE in Antarctica. These flights, as well those of several other collaborations (RUNJOB and CREAM balloon flight series) gave some precious results up to a few hundreds TeV/nucleus, still too far away from the energy of  $3 \times 10^{15}$  eV of the knee for solving the historical knee problem of CRs. Many satellite borne experiments were in the meantime proposed, ACCESS [14] in USA and several in Russia, but no one was supported or could find the suitable flight occasion. In the next future it will be flown the small NUCLEON experiment [15], which will verify the KLEM method for measuring the energy of VHE shower by thin calorimeters. It will substantially improve the present experimental situation but it is too small for definitively solve the knee problem.

### 3.5 Particle and Antiparticles spectra and search for antinuclei.

Antiparticles are special rare CR components. The hope of observing contributions in their energy spectra (on top of the secondary antiprotons produced in the interactions of particles with the interstellar matter) due to their primordial existence, or to their production from steady sources, or a signal of the so called new physics, increases with energy, and could become significant in the hundred GeV energy region.

The WIZARD collaboration, formed for studying antiparticles and hunting for antinuclei on the astromag facility [16], did not disbanded at the closure of the FSS program, and afforded a program of balloon borne experiments. Several Russian institutions joined this collaboration to form the Russian Italian Mission (RIM) program. This collaboration, after several satellite and MIR borne experiments in life science and solar CRs<sup>3</sup>, constructed and launched the PAMELA [17] experiment<sup>4</sup>, dedicated to the antiparticle studies up to the 100 GeV region.

In the meantime a Japanese-USA collaboration used the prototype of the thin superconducting solenoid designed for the astromag facility in the series of the many balloon borne experiments BESS, mainly dedicated to the high statistic study of the antiparticle fluxes in the low energy region up to a few GeV.

---

<sup>3</sup>In years 1998-2005 were flown small telescopes dedicated to the study of solar CRs (NINA, NINA2) and to life-science studies (Si-eye-1 and Si-eye-2 on board of the MIR Station and Si-eye-3 on board of the ISS)

<sup>4</sup>PAMELA was launched in orbit from Baikonur spaceport in June 2006 and it is now producing the first experimental results (a few articles are in press).

Furthermore a large number of physicists coming from elementary particle researches at accelerators gathered in a large collaboration that performed the precursor experiment AMS-1 [18] on board of the Shuttle and is preparing the AMS-2 [19] experiment that will be installed in the next 2-3 years on the International Space Station (ISS).

A few remarks must here be underlined.

- (a) Antimatter experiments require a strong magnetic field for separating negative particles from positive ones and very good particle identification. They are therefore heavy and can be brought at the top of the atmosphere only by the biggest available balloons, and for a limited time, not more than a few ten hours in each mission. The main reason is that balloons are not closed, but open on the bottom, as mongolfiers, just a thin sheet separating the helium inside from the air outside and not supporting any difference in pressure. A large fraction of the helium is lost from the bottom when the temperature decreases, as it is at sunset, and the balloon falls down. The short duration of the flight hampers the possibility of collecting high statistics at energies higher than 10 GeV. Furthermore the balloons cannot float at altitudes higher than about 40 km, because of the decreasing of external temperature at this altitude; the residual atmosphere of about  $5g/cm^2$  on top of the apparatus produces a background that exceeds the antiproton signal already at few tens GeV.
- (b) A large number of balloon borne experiments were performed in the last two decades, and their results (see them below in Figure 3, compared with new data from the PAMELA experiment) are the maximum that can be collected by the ballooning technique.
- (c) For progressing in statistics and energy range it is necessary a new generation of experiments, or by ballooning in Long Duration Balloon Flights (LDBF) in Antarctica (by flights lasting several weeks, what can largely improve the statistics, but not the covered range in energy because of the CR interaction in the residual atmosphere), or by satellite borne experiments, allowing to increase both the statistics and the explored energy range.
- (d) The above mentioned BESS collaboration is now conducting LDBFs in Antarctica, with a flight every two years. These flights are possible due to the continuous improvements of the superconducting solenoid and of the detectors, that allowed obtaining a payload enough light to be flown by closed balloons (the closed balloons do not loose helium, so that can flight longer, but can carry experiments much lighter than the 3 t carried by the open ones). It is this technical limitation than confines the research of antiparticles of BESS to the low energy region up to a few GeV.

- (e) For what concerns the satellite borne experiments, their realization is not an easy task, and not only for economical reasons. The techniques to be used are not simple and the physicists must have recourse to the help of very expensive industries for the preparation of part of the instrumentation. Furthermore, in general, the spacecraft and the launch vehicle are much more expensive than the instrument. Also the accessory expenditures, such as those for the launch operations, surface transportations and insurances, up and down links to satellite and other various services, are very high and exceed the budgets that particle physics and nuclear physics teams are used to handle. Finally the access to space is very limited, and of interest for many other fields of the human activities, and the research on the field of cosmic rays must compete for resources with other scientific and social investigations in Astrophysics, Astronomy, Physics, Chemistry, Life Science, Earth Observation, Medicine, etc...

The PAMELA and AMS experiment represent indeed the maximum effort that can be afforded on Low Earth Orbit (LEO) experiments. They promise the accurate study of the antiproton and positron spectra up to the hundred GeV energy region, as well a limit of  $10^{-8} - 10^{-9}$  for the antihelium/helium ratio in hunting for antinuclei.

Because of the above mentioned activities, the determination of the spectra of antiparticles and the search for antinuclei are the only items that could register remarkable progresses in the last two decades, and it is worthwhile to have a look to last results and an outlook to the near future.

### **The Pamela experiment and its first preliminary results.**

Before the flight of the Pamela experiment the experimental situation was founded on the results obtained by many balloon borne experiments. Only one experiment [18] was conducted in orbit for a relatively short time on board of the shuttle, precursor of the future AMS-2 experiment [19].

The flight of PAMELA is indeed a real step forward in the field.

The characteristics of the PAMELA instrument are described elsewhere [?]. Here I wish only to underline two its main characteristics: (a) the extraordinary precision of the multistrip silicon tracker, better than 3 micron per point in the bending view of the magnetic spectrometer, allowing to the magnetic spectrometer to reach a Maximum Detectable Rigidity (MDR) of 1 TV; (b) the high granularity of the multistrip silicon calorimeter, 2 mm in each of the 44 layers, supplying a great identification of the electromagnetic particles up to the highest energies.

In this work the preliminary results are presented, based on the data collected from July 2006 to March 2008, a total of about 500 days during the long period of minimum solar activity. All the data are preliminary, because in some case the analysis is still in progress and only statistical error are reported.

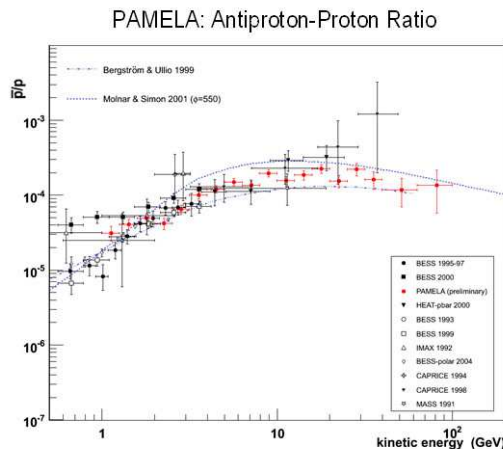


Figure 3: PAMELA: antiproton-proton ratio (preliminary)

The antip/p ratio was determined up to 100 GeV. It confirms, with much smaller errors, the previous results in the whole range (Figure 3), and at higher energies does not contradict the models suggesting the secondary origin of antiprotons by interaction of primary CRs on the interstellar matter of the Galaxy.

Unexpected results were instead obtained for the e+/(e-+e+) ratio. They are reported in Figure 4 up to 10 GeV. It is much lower than previous experiments at low energies and agrees with them at about 10 GeV. Data at higher energies are not reported in the figure because the analysis is still in progress, however we know that the ratio is substantially and continuously increasing up to 100 GeV. This result cannot be explained by secondary production on interstellar matter, but invokes different sources, such as the contribution of a nearby powerful source or dark matter annihilation.

The fluxes of antiprotons and positrons are very low, of the order of  $10^{-4} - 10^{-5}$  of proton flux, what implies the collection of a huge number of protons, several hundreds millions, and of light nuclei, whose spectra can be precisely measured up to very high energies. The spectra registered for proton and helium nucleus are reported in Figure 5. It must be underline that the statistical error is very small in the whole range from a few hundred MeV up to several hundred GeV, what allows to obtain a very precise measurement of the spectral shape and makes possible to study time variation and transient phenomena.

At lower energies, down to the threshold of 80 MeV, the proton spectrum allows to study in detail the decrease of the fluxes of galactic CR due to the solar wind (modulation), which varies depending from the solar activity. As an example, in Figure 6 the proton spectra registered in different times during the period of minimum

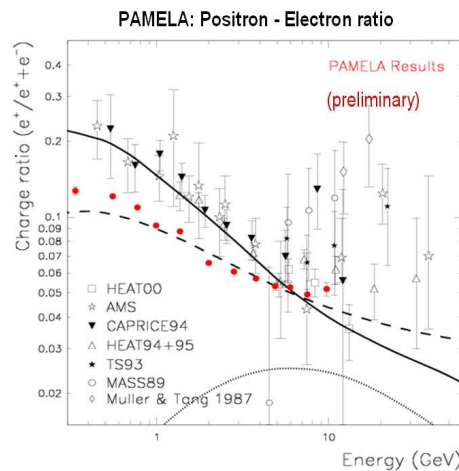
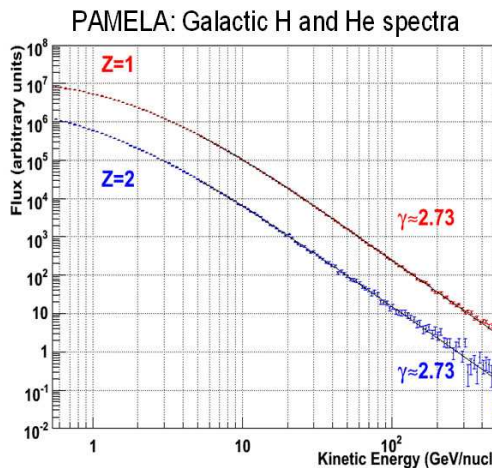
Figure 4: PAMELA:  $e^+/(e^- + e^+)$  ratio (preliminary)

Figure 5: PAMELA: proton and helium energy spectra (preliminary)

solar activity are reported.

Many characteristics of the Galaxy can be inferred from the propagation of CRs, the fundamental tool being the energy spectra of the different nuclei and of different isotopes and their ratios. In Figure 7 is reported the ratio between the B and C nuclei, that can be precisely measured on a very wide energy range, from 300 MeV to 200 GeV in the figure. Analysis for the other nuclei and for light isotopes is in progress.

The high statistics and low energy threshold allow investigating other phenom-

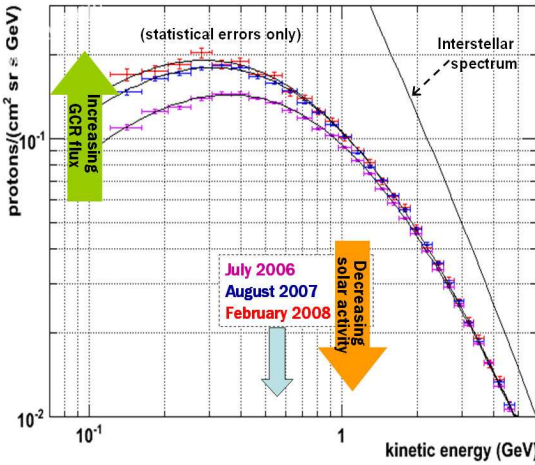


Figure 6: PAMELA: modulation of galactic protons due to solar activity (preliminary)

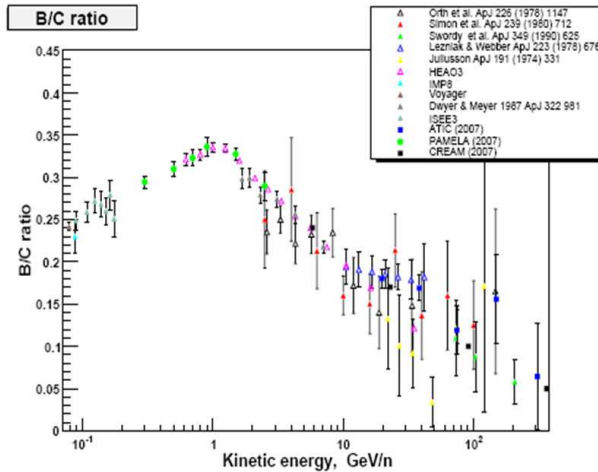


Figure 7: PAMELA: B/C ratio from 300 MeV/n up to 200 GeV/n (preliminary)

ena, such as the trap inside the terrestrial magnetosphere of a portion of the particles (mainly protons) produced in the interactions of primary CR on the terrestrial atmosphere, or the nuclei of solar origin trapped in the radiation belts and approaching the Earth in the region of the Atlantic ocean between South America and Africa (South Atlantic Anomaly, SAA). The study of the CR energy spectrum inside the SAA is extremely interesting, as it is linked to the solar activity and to the propagation of particles through the heliosphere (see in Figure 8 the energy spectra of protons in different SAA regions registered by PAMELA in its over flights).

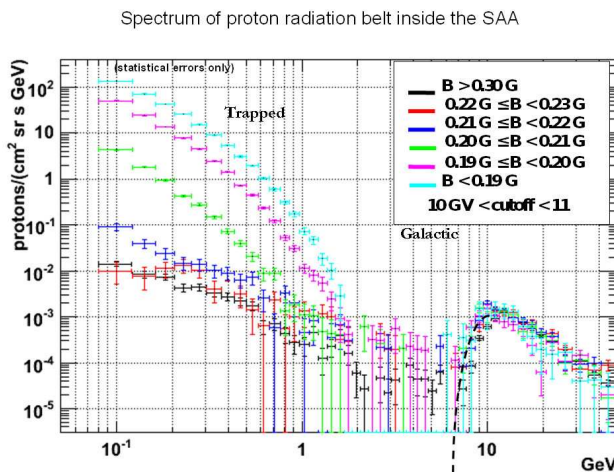


Figure 8: PAMELA: proton energy spectra inside the SAA (preliminary)

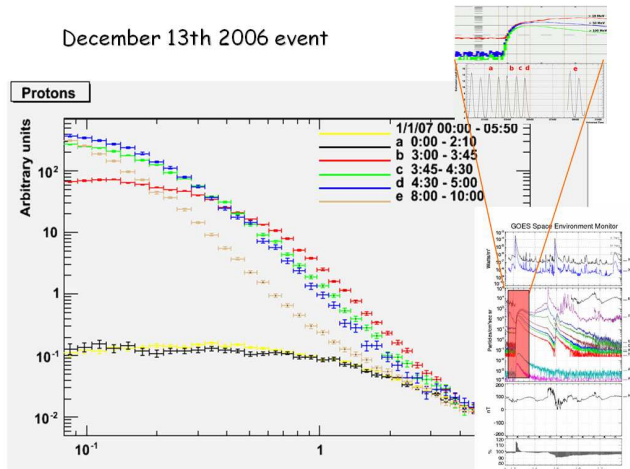


Figure 9: Energy spectra of protons registered by PAMELA in different time intervals (of 45' and 30') during the solar event of December 13th 2006 (preliminary)

Finally the low energy threshold of the instrument (50 MeV for electrons and 80 MeV for protons) allows observing in detail the high energy tail of solar CR, supplying unique information on their propagation through the heliosphere. In Figure 9 it is reported the variation in short intervals of time of the energy spectrum of protons during the solar event of 13 December 2006. It permits an accurate hint on the mechanisms of acceleration of the particles in the vicinity of the Sun.

PAMELA experiment is continuing collecting data, at least until the end of 2009,

increasing the statistics and the energy range explored, in the interesting period of the expected sharp increasing of the solar activity.

### The AMS-2 and an outlook to the near future.

The AMS-2 experiment has a layout similar to PAMELA, but a much larger acceptance, since it was mainly dedicated to hunting for antinuclei, for reaching a limit of  $10^{-9}$  on the antihelium/helium ratio. The large acceptance will greatly improve the statistical errors at the highest energy, allowing also extending the explored energy range beyond the nominal performance of the detector.

PAMELA and AMS-2, both for the wide covered range in energy and the identification capability of the detectors, must be regarded not as thematic experiments but as Space Observatories, which either separately or together will give information on several thematic at 1 AU from the Sun.

The list of the observations, besides the above mentioned measurements of the energy spectra of galactic CRs, up to the TeV region for the proton, and of the antiparticles up to several hundreds GeV, the hunt for antinuclei, the study of the galactic CR modulation in the heliosphere, the study of the time evolution of solar energetic particle fluxes, includes also the search for the dark matter annihilation effects, such as the primary Black Holes evaporation , the variations of the terrestrial radiation belts and of the energetic secondary particle trapped by magnetosphere in correspondence to the different solar events, especially in the SAA region, the acceleration at the heliospheric terminal shock and diffusion through the heliosphere of the anomalous CRs, the existence of nearby electron sources, and the measurement of the Jovian electrons.

### 3.6 What can be foreseen for the far future?

Nothing is foreseen for the measurement of the fluxes of the extremely high Z nuclei. The possibility of exposing on the Moon surface large areas of passive detectors makes this research very attractive as a first generation experiment on the Moon, to be conducted in the phase of the robotic lunar exploration, before the human exploration phase.

No dedicated experiments are foreseen for the measurement of the energy spectra of rare elements and of isotopes. Abundant information will come as by-product of the Pamela and AMS-2 missions and the continuation of the BESS polar flights. However a complex, but relatively small dedicated device on the ISS would be worthwhile, greatly enriching the information on the structure of the Galaxy.

The measurement of the chemical composition at knee can relay, also for the far future, in the improvement of the revision of the computational model (also profiting of the new data expected from the LHC experiments), the patient accumulation of

statistics in the existing on ground arrays and the realization of someones of the proposed new arrays, and the further flights in Antarctica of the CREAM spectrometer.

For the study of antiparticles and the hunting for antinuclei, nothing better than Pamela and AMS-2 is foreseen, and perhaps cannot be foreseen because of insurmountable technical limits. It is in fact not easy to conceive satellite or ISS borne experiments that could significantly move toward higher energies, because mass and complexity dizzy rise with the reachable energies.

For the far future, ten or more years from nowadays, a spectacular progress could be attained for the observation of ultra high energy CR. The construction of the Auger-North array will increase the statistics and energy range of Auger-South. A big step forward will be obtained observing from space the fluorescence light emitted by the huge showers developed by ultra high energy CRs on the terrestrial atmosphere, as the EUSO program [21] (by its steps JEM-EUSO [22], S-EUSO [23] and the precursor TUS [12]) propose to do. If the whole program will be realized up to the end it could be possible to evolve toward an ultra high energy neutrino observatory [?], a new powerful actor in the observation of our Universe, up to its extreme space and time limits, where other probes cannot arrive.

Worthwhile of attention it is also the observation from space of the radio signal of the UHE showers on the regolith of the Moon limb. The methodological experiment LORD [26] will be operated in a few years on board of the LUNA-GLOB lunar satellite for developing the project of a possible UHE neutrino observatory based on this technique.

## References

- [1] Field Committee on Space Astronomy and Astrophysics of the National Research Council of the USA National Academy of Sciences, A strategy for space astronomy and astrophysics for the 80s, USA NAS report, 1979 Astronomy Survey Committee of the USA National Academy of Science, Astronomy and Astrophysics for the 1980s, USA NAS report, August 1982.
- [2] NASA Cosmic Ray Program Working Group, Cosmic Ray Program or the 1980s, NASA report, August 1982, and The particle astrophysics program for 1985-1995, NASA report, October 1985.
- [3] M.A. Green et al., IEEE Transactions in Magnetics, MAG-23, n.2 (1987) 1240  
Astromag Definition Team, The Particle Astrophysics Magnet Facility ASTRO-MAG, NASA report, May 1988 G. Basini et al., Il Nuovo Cimento, 102B (1988) 5.
- [4] P.B. Price, Particle astrophysics: the NASA cosmic ray program for the 1990s

- and beyond (A92-20526), New York, 1990, American Institute of Physics, pp 63-66.
- [5] J. Adams and D. Eichler, Very high energy gamma ray spectroscopy, *Astrophys.J.* 317 (1987) 551.
  - [6] P. Sreekumar et al., *Astrophys. J.* 494 (1998) 494.
  - [7] A. Morselli, et al., XXVI ICRC, OG 4.2.6, 1999 - A. Morselli, et al., Nuclear Physics B 85 (2000) 22 - M. Tavani, et al., AGILE Collaboration, Science with the new generation high energy gamma-ray experiments, in: A. Lionetto, A.Morselli (Eds.), Frascati Physics Series, 45 (2007) 1.
  - [8] A.Morselli, XXXII Rencontres de Moriond, Very High Energy Phenomena in the Universe, Les Arc, France, January 1825, 1997,Editions Frontiers, p. 123 - P. Michelson, et al., in: First GLAST Symposium, Stanford, 2007, AIPCP921, 2007 - A. Morselli, *Nucl. Instr. and Meth. A* 530 (2004) 158.
  - [9] A.J. Weaver et al., *Nature*, 357 (1998) 50 A.J. Westphal et al., *Nucl. Instrum. and Meth.*, B145 (1998) 409 - A.J. Westphal et al., XXVI Int. Cosmic Ray Conf., 4 (1999) 160, Salt Lake City.
  - [10] A.J.Westphal et al., XXVI Int. Cosmic Ray Conf., 4 (1999) 160, Salt Lake City.
  - [11] J.F. Ormes et al., A Large Isotope Spectrometer for Astromag, NASA GSFC, Nov. 1988.
  - [12] J.W.Mitchell et al., XXVI Int. Cosmic Ray Conf., 3 (1999) 113, Salt Lake City; M.Hof et al., *Nucl. Instrum. and Meth.*, A454 (2000) 180; T.Adams et al., XXVII Int. Cosmic Ray Conf. (2001) 1655, Hamburg.
  - [13] T.A.Parnell et al., Spectra, Composition and Interactions of Nuclei above 10 TeV,NASA MSFC, Nov.1988
  - [14] ACCESS-NRA, NASA Research Announcement, NRA 97-OSS-13 J.P. Wefel et al., XXVI Int. Cosmic Ray Conf. (1999) 84, Salt Lake City.
  - [15] D. Podorozhnyi et al., XXVII Int. Cosmic Ray Conf. (2001) 2188, Hamburg.
  - [16] R.L. Golden et al., Wizard: a proposal to measure the cosmic rays including antiprotons, positrons, nuclei and to conduct a search for primordial antimatter, College of Engineering, Editor NMSU, 1988 P. Spillantini et al., *Il Nuovo Cimento*. 103B (1989) 625.
  - [17] O. Adriani et al., XXIV Int. Cosmic Ray Conf., 3 (1995) 591, Rome. [18]

- [18] S. Alhen et al., Nucl. Instrum. and Meth., A350 (1994) 351.
- [19] R. Battiston for the AMS collaboration, XXVII Int. Cosmic Ray Conf. (2001) 2192, Hamburg.
- [20] O. Adriani et al., Nucl. Instrum. and Meth., A478 (2002) 114.
- [21] L.Scarsi et al., Extreme Universe Space Observatory (EUSO) proposal for ESA F2/F3 missions, 2000 EUSO Design Report, ESA/MSM-GU/2000.462/RDA, Dec. 2000 O. Catalano et al., XXVIII Int. Cosmic Ray Conf., 1 (2003) 1081, Tsukuba.
- [22] T. Ebisuzaki et al., The JEM-EUSO project: Observing extremely high energy cosmic rays andneutrinos from the International Space Station, Nucl.Phys.Proc.Suppl.175-176 (2008) 237-240.
- [23] A. Santangelo et al., S-EUSO: a proposal for a space-based observatoryof Ultra-high-Energy cosmic particles, submitted to the ESA CosmicVision 20152025 Program (2007).
- [24] V.V. Alexandrov et al., XXVII Int. Cosmic Ray Conf. (2001) 831, Hamburg - G.K. Garipov et al., Bull. Russ. Acad. Sci. 66 (2002) 1817.
- [25] S.Bottai and P.Spillantini, From the Extreme Universe Space Observatory (EUSO) to the Extreme Energy Neutrino Observatory, 11th Lomonosov Conference on Elementary Particle Physics, August 2003, Moscow, Nuovo Cim. 120B (2005) 887 P.Spillantini et al., EUnO: A neutrino space observatory, 19th European Cosmic Ray Symposium (ECRS 2004), August 2004, Florence, Int.J.Mod.Phys. A20 (2005) 6974. - S.Bottai et al., HE neutrino detection from space. Toward a dedicated neutrino observatory, XXIX Int. Cosmic Ray Conf. 5 (2005) 55, Pune.
- [26] V.A. Tsarev, Detection of ultrahigh-energy cosmic rays by radio method, Physics of Elementary Particles and Nuclei, 35 (2004) 1 V.A. Tsarev, An overview of the LORD experiment, ARENA Workshop, Zeuthen, 2005 V. Chechin, Concept of the LORD instrument, ARENA Workshop, Zeuthen, 2005.

# Very High-Energy Gamma Ray Astronomy

*Ullrich Schwanke  
Institute of Physics  
Humboldt University Berlin  
Newtonstrasse 14  
12489 Berlin, GERMANY*

## 1 Overview

Very high-energy (VHE) gamma ray astronomy explores the non-thermal Universe at energies greater than  $\sim 100$  GeV. This contribution to the XXVIII Physics in Collision Conference describes the status of the field and gives examples (and references) for advances that have been obtained since the last presentation in this conference series [1].

## 2 Experimental Techniques and Experiments

The fluxes of VHE photons are so small that their detection requires collection areas far bigger ( $\mathcal{O}(10^4 - 10^5 \text{ m}^2)$ ) than those of typical satellite-borne experiments ( $\mathcal{O}(1 \text{ m}^2)$ ). The best flux sensitivity is obtained by Imaging Atmospheric Cherenkov Telescopes (IACTs) which detect the Cherenkov light emitted by the showers that are initiated by gamma-rays and hadrons in the atmosphere. The Cherenkov light is imaged onto a camera and can be used to reconstruct the direction, energy and type (photon or hadron) of the incoming particles in a typical  $4^\circ$ -diameter field of view (0.004 sr). Often, the shower is observed by more than one telescope (stereoscopic observation) resulting in a better determination of shower parameters and improved background rejection. Arrival directions are reconstructed with a typical accuracy of  $0.05 - 0.10^\circ$  (depending on energy) while the energy estimate has an error of  $\sim 20\%$ .

The major IACT systems operating at present are CANGAROO ([2], Australia), H.E.S.S. ([3], Namibia), MAGIC ([4], Canary Islands), and VERITAS ([5], Arizona). Their overall duty cycle is  $\sim 15\%$  since observations require cloudless nights with no or little moonshine. A source similar to the Crab Nebula (the standard candle of VHE astronomy) is detected by H.E.S.S. in 30 s. In a typical exposure of 25 hours at a zenith angle of  $20^\circ$ , a source with 1% of the Crab Nebula flux is detected at the  $5\sigma$  level.

At higher energies (few TeV), non-imaging air shower detectors identify showers initiated by photons using different experimental techniques. The so called Water Cherenkov Technique has been pioneered by MILAGRO ([6], New Mexico), while other installations (ARGO and Tibet AS Gamma ([7, 8], Tibet)) use a mixture of resistive plate chambers and scintillators. Unlike the IACTs, the non-imaging experiments cover only the northern hemisphere and have a limited angular resolution ( $\sim 1^\circ$ ). Despite their good duty cycle ( $\sim 90\%$ ) and large field of view ( $\sim 2\text{ sr}$ ) the obtained sensitivity is far lower than those of IACTs; a detection of the Crab Nebula requires an exposure of ( $\sim 3$  months).

### 3 Source Counts and Source Types

In the past 5 years, the number of known VHE gamma ray sources has increased considerably. The *TeV catalogue* [9] lists now  $\sim 70$  sources,  $\sim 50$  of which are galactic. Roughly two thirds of all sources were discovered by the H.E.S.S. array of Cherenkov telescopes that performed a systematic scan of the Galactic plane (see Section 4).

Among the galactic sources, pulsar wind nebulae (see [10] for a review) are the most numerous ( $\sim 10$  detections), followed by supernova remnants (see Section 6). Also detected were 4 TeV binaries [11, 12, 13, 14, 15], at least one stellar association [16], and there a  $\sim 3$  examples where VHE gamma rays were found coincident with molecular clouds. Searches for VHE gamma rays from dwarf galaxies orbiting the Milky Way remained unsuccessful and were used to establish limits [17, 18] in the context of dark matter studies. The Galactic Centre source [19] was recently shown to be spatially separated from a nearby supernova remnant, excluding this explanation for the observed VHE radiation.

The  $\sim 20$  extra-galactic sources are all of the blazar type (see Section 7) with the exception of the giant radio galaxy M87. Searches for VHE radiation from other extra-galactic objects (starburst galaxies and galaxy clusters) have yielded upper limits, indicating that these systems are too faint and/or too far away to be visible for current instruments. Observations of gamma ray burst (following triggers from satellites) were conducted either directly or in follow-up mode. MAGIC managed to observe a GRB only 40 s after its onset, and H.E.S.S. was lucky enough to serendipitously catch a GRB at the edge of its field of view, but searches for an excess of VHE photons remained unsuccessful [20, 21, 22].

### 4 The Milky Way in VHE Gamma Rays

The southern location of the H.E.S.S. experiment and its large field of view ( $5^\circ$  diameter) make it ideally suited for a systematic scan for VHE gamma ray sources in

the inner Galaxy. Such a scan was performed in 2004 and 2005 between  $\pm 30^\circ$  in galactic longitude and  $\pm 2^\circ$  in latitude and led to the discovery of 8 sources[23]. The scan was later extended to  $\pm 3^\circ$  in latitude, and to  $+60^\circ$  and  $-85^\circ$  in longitude, and increased the number of found sources to  $> 14$  [24]. The typical sensitivity obtained by H.E.S.S. in the scan is few per cent of the Crab. A variety of sources -most of them extended- was found and a good fraction of the sources cannot be plausibly associated with sources known from other wavelength bands. Multi-wavelength observations are underway to identify counterparts.

The northern Galaxy was observed by MILAGRO in the years 2000–2007 and the total data set was recently published [25]. The sensitivity level reached by MILAGRO is a factor of 10 worse than that of H.E.S.S., but the observations extend to  $\pm 10^\circ$  in latitude (mainly limited by the usable zenith angle band) and cover  $+30^\circ$  to  $+220^\circ$  ( $= -140^\circ$ ) in longitude. The analysis of the MILAGRO data set (6.5 years of live-time) provided a clear detection of the Crab Nebula and the discovery of seven sources three of which are significant after accounting for trials. Two of the sources are found in the Cygnus region where HEGRA and MAGIC also reported TeV excesses[26, 27], but MILAGRO’s coarse directional resolution makes a detailed comparison difficult. The third source was found in the overlap window of the MILAGRO and H.E.S.S. observations ( $+30^\circ$  to  $+60^\circ$  in longitude). This source (MGRO 1908+06), was recently confirmed by H.E.S.S. [28]. A 15 h exposure revealed a new source (HESS J1908+63) at a significance of  $5.7\sigma$  coincident with the reported MILAGRO detection. The energy spectrum of the fairly strong source (14 % Crab) was measured between 0.4 and 25 TeV and appears hard (spectral index  $\Gamma = 2.05 \pm 0.06$ ), and there is evidence for an association with a SNR and/or molecular clouds. While MILAGRO was unable to derive a spectrum of the source, the MILAGRO excess converted into a differential flux measurement at  $\sim 20$  TeV aligns well with the H.E.S.S. spectrum. These MILAGRO and H.E.S.S. results demonstrate nicely that a consistent picture of our Galaxy at TeV energies is emerging.

## 5 The Crab Nebula and its Pulsar

The numerous detections in the VHE band have significantly improved our understanding of the structure and evolution of pulsar wind nebulae (see [29] for a recent review). We want concentrate here on the well-known Crab Nebula where measurements with the MAGIC telescope have allowed the determination of the spectrum down to 60 GeV and, for the first time in the history of ground-based gamma ray astronomy, the detection of pulsed emission from a pulsar at around  $\sim 25$  GeV.

The Crab Nebula is the remnant of a supernova explosion from 1054 AD. Its diameter is just a few light years, so it appears –at a distance of  $\sim 2$  kpc– point-like for IACTs. Its steady spectrum has been measured over many decades in energy and

is understood in terms of a synchrotron self-Compton (SSC) scenario where electrons accelerated at the pulsar wind termination shock generate a synchrotron spectrum ranging from radio frequencies to GeV energies. The inverse-Compton upscattering of the very same synchrotron photons by the electron population results in a second hump at higher energies than the synchrotron part of the nebula's spectrum. Earlier observations with IACTs detected the falling edge of the inverse Compton hump, but only recently the low energy threshold of the MAGIC telescope has provided evidence for the actual existence of an inverse Compton peak [30]. The MAGIC measurements down to 60 GeV are well described by inverse Compton emission and place the inverse Compton peak at  $\sim 77$  GeV.

The pulsar powering the Crab Nebula (PSR B0531+21) has a period of 33 ms and features the largest energy output ( $5.1 \cdot 10^{38}$  erg s $^{-1}$ ) among all known galactic pulsars. Pulsed emission at the pulsar period has been detected from the radio band up to  $\sim 5$  GeV and appears in two peaks in the phasogram. MAGIC found a first hint for pulsed emission ( $2.9\sigma$ ) in 16 h of standard data-taking. Data-taking with a dedicated pulsar trigger electronics between October 2007 and February 2008 resulted in a 22.3 h data set at an energy threshold that could be reduced from 50 – 60 GeV to 25 GeV. In an analysis of the data set,  $\sim 8500$  photons from pulsed emission could be identified ( $6.4\sigma$ ). An analysis of the energy spectrum of the pulsed photons shows a cutoff around 16–21 GeV which indicates that the emission region must be placed far out in the magnetosphere which disfavours in particular the polar cap emission scenario[31, 32, 33].

The detection of pulsed emission from the Crab Nebula by MAGIC is a very significant result since it demonstrates for the very first time that low-threshold IACTs can bridge the gap to gamma-ray satellites and provide important and novel input to deepen our understanding of the emission processes in the magnetosphere of pulsars.

## 6 Supernova Remnants as Cosmic Ray Sources

Shell-type supernova remnants (SNR) are suspected acceleration sites for hadronic cosmic rays with energies up to the knee. The presence of high-energy electrons had been derived earlier from the detection of non-thermal synchrotron emission at X-ray energies, but the presence of accelerated hadrons in the SNR shock fronts remained hard to prove. H.E.S.S. observations of shell-type SNRs identified the shells of two objects (RX J1713.7–3946 [34, 35, 36] and RX J0852.0–4622[37, 38]) as VHE emitters, and there is a third SNR (RCW 86[39]) where the shell morphology is not as clear. The detection of VHE photons at several 10 TeV and a strong apparent correlation of the VHE emission with X-ray observations are striking evidence that the SNR shells accelerate particles to energies of  $\mathcal{O}(100)$  TeV. A modelling of the multi-wavelength spectra of RX J1713.7–3946 and RX J0852.0–4622 in an electronic

scenario (where the VHE emission is attributed to inverse Compton scattering of electrons on low-energy photon fields) results in rather low magnetic fields (about the size of the  $B$  field in the interstellar medium) which is at odds with the diffusive shock acceleration mechanism and probably also with the thin filaments observed at X-ray energies. While hadronic models (VHE photons from  $\pi^0$  decays generated in the interaction of accelerated with the interstellar medium) can describe the VHE spectra fairly well, there is still lack of evidence that protons are really accelerated at the required efficiency and that the generated hadron spectra extend up to the knee.

In this situation (and facing the small number of available young SNRs) observations at VHE energies have also been extended to older SNRs and it has been tried to identify associations of SNRs and molecular clouds. Only relatively young (up to the Sedov phase) SNRs can shock-accelerate particles to PeV energies, but somewhat older SNRs could be interesting since electrons suffer from stronger energy losses while proton populations might survive and still generate observable signals. Another option is the illumination of nearby dense molecular clouds by high-energy protons that escape the acceleration zone, diffuse out and still interact in the dense molecular cloud while efficient particle acceleration might have ceased in the SNR [40].

Indeed, observations by MAGIC (e.g. IC 444[41]) and H.E.S.S. (e.g. W28[42], HESS J1745–303[43], CTB 37B[44]) have now identified a number of VHE gamma ray sources that appear associated with the shells of SNRs (but are unlikely pulsar wind nebulae), or with molecular clouds whose extent and distance can be inferred from observations in other wavebands (in particular CO observations). A spatial correlation of the VHE sources with molecular clouds and/or regions of maser emissions is observed and is suggestive of a hadronic and SNR-related origin of the VHE emission. Unfortunately, substantial uncertainties on important parameters of SNRs (age, distance, matter density) and clouds (exact kinematic distance, density) do often not allow the firm exclusion of alternative explanations of the observed VHE sources. It appears not unlikely that better instruments with improved sensitivity (in order to boost the source statistics) and wider energy coverage (for a longer lever arm in spectra) will be required to unambiguously identify SNRs as cosmic ray sources.

## 7 Active Galactic Nuclei

New Active Galactic Nuclei (AGN) that emit VHE gamma rays are being discovered by IACTs at a rate of  $\mathcal{O}(5)$  per year. With one exception (M87 [45, 46]), all detected AGN are of the blazar type where the jet is directed toward the observer. The improved source statistics and the detection of spectacular flares (e.g. from PKS 2155–30 where fluxes at the level of  $\sim 15$  Crab, i.e. 100 times the low-state flux [47], were observed) with short rise times ( $\sim 100$  s) resulted in important constraints on the

size of the emission region and provided input for the modelling of the AGN emission. At the same time, the observation of AGN at substantial redshifts ( $z > 0.1$ ) further constrains the amount extra-galactic background light (EGBL) which attenuates the intrinsic AGN spectra by photon-photon pair production over cosmological distances. In particular, a new AGN discovered by H.E.S.S. at  $z = 0.14$  (1ES 0229+200[48]) can be used to show that the Universe is more transparent in the  $2 - 20 \mu\text{m}$  window. If one assumes that the intrinsic spectrum cannot be arbitrarily hard the new data disfavour EGBL models with a high mid infrared flux. It is too early to speak of high-precision cosmology with AGN here (especially given the fact that our understanding of the intrinsic AGN spectra is still far from complete), but it is also clear that the derived constraints are challenging models and direct EGBL measurements. Only recently, the detection of two AGN at redshifts of  $z = 0.212$  (1ES 1011+496[49]) and  $z = 0.538$  (3C279[50]) by MAGIC doubled the range of redshifts where AGN emission can be studied, which should make the EGBL limits even more constraining.

## 8 Summary and Outlook

The current IACTs (notably H.E.S.S., MAGIC and VERITAS) explore the sky with regular observations between  $60 - 100 \text{ GeV}$  and some  $10 \text{ TeV}$  and reach a sensitivity of few per cent Crab. The number of known sources is growing and will soon approach  $\sim 100$ . Scan-type observations of H.E.S.S. in the south and the publication of the complete MILAGRO data set (albeit at a much higher threshold than that of IACTs) for the north provide a first picture of the Milky Way at VHE energies. IACTs collect evidence for SNRs as cosmic ray sources and address fundamental physics question ranging from electrodynamics (pulsar magnetospheres) to cosmology. At the time of writing, the existing IACTs are being upgraded to obtain lower thresholds (H.E.S.S. adds a  $28 \text{ m}$  diameter telescope with an anticipated trigger threshold of  $\sim 25 \text{ GeV}$ ) and better background rejection by stereoscopic observations (MAGIC adds a second  $17 \text{ m}$  diameter telescope). For the next few years, a lot can be expected from these upgrades, the overlap with the recently launched FERMI[51] satellite and studies of the anisotropies reported by AUGER[52]. In the next decade, VHE gamma ray astronomy might enter a new era with the design and construction effort for the Cherenkov Telescope Array (CTA[53]) which is expected to provide an order of magnitude better sensitivity and much wider energy coverage.

## References

- [1] M. Teshima, Talk at the XXVI Physics in Collision conference (2006).
- [2] The CANGAROO website (<http://icrh9.icrr.u-tokyo.ac.jp>).

- [3] The H.E.S.S. website (<http://www.mpi-hd.mpg.de/hfm/HESS>).
- [4] The MAGIC telescope website (<http://wwwmagic.mppmu.mpg.de>).
- [5] The VERITAS website (<http://veritas.sao.arizona.edu>).
- [6] The MILAGRO website (<http://www.lanl.gov/milagro/index.shtml>).
- [7] The ARGO website (<http://argo.na.infn.it>).
- [8] The Tibet AS Gamma Experiment website (<http://www.icrr.u-tokyo.ac.jp/em/index.html>).
- [9] The TeV Catalogue website (<http://www.tevcat.uchicago.edu>).
- [10] Gaensler, B. M., & Slane, P. O., *Ann. Rev. Astron. Astrophys.*, **44**, 17 (2006).
- [11] F. Aharonian *et al.* [The H.E.S.S. Collaboration], *A&A* **460**, 743–749 (2006).
- [12] F. Aharonian *et al.* [The H.E.S.S. Collaboration], *A&A* **442**, 1–10 (2005).
- [13] J. Albert et al., *Science* **312**, 1771 (2006).
- [14] J. Albert et al., *Astrophys. J.* **684**, 1351 (2008).
- [15] J. Albert et al., *Astrophys. J. Lett.* **665**, L51 (2007).
- [16] F. Aharonian *et al.* [The H.E.S.S. Collaboration], *A&A* **467**, 1075–1080 (2007).
- [17] F. Aharonian *et al.* [The H.E.S.S. Collaboration], *Astroparticle Physics* **29**, 55–62 (2008).
- [18] J. Albert et al., *Astrophys. J.* **679**, 428 (2008).
- [19] H.E.S.S. collaboration, *Localising the H.E.S.S. Galactic Center point source*, Proc. 30th International Cosmic Ray Conference, Merida, (2007).
- [20] F. Aharonian *et al.* [The H.E.S.S. Collaboration], Accepted for publication in *Astrophys. J.*
- [21] J. Albert et al., *ApJ Letters* **641**, L9 (2006).
- [22] J. Albert et al., *Astrophys. J.* **667**, 358 (2007).
- [23] F. Aharonian *et al.* [The H.E.S.S. Collaboration], *Science* **307**, 1938–1942 (2005).
- [24] F. Aharonian *et al.* [The H.E.S.S. Collaboration], *Astrophys. Journal* **636**, 777–797 (2006).

- [25] A. A. Abdo et al., *Astrophysical Journal* **664**, L91 (2007).
- [26] F. Aharonian *et al.* [The HEGRA Collaboration], *A&A* **393**, L37 (2002).
- [27] J. Albert et al., *Astrophys. J.* **675**, L25 (2008).
- [28] H.E.S.S. collaboration, *H.E.S.S. Galactic Plane Survey unveils a Milagro Hotspot*, Proc. 30th International Cosmic Ray Conference, Merida, (2007).
- [29] O.C. de Jager, A. Djannati-Ataï, Springer Lecture Notes on Neutron Stars and Pulsars: 40 years after their discovery (2008).
- [30] The MAGIC collaboration: E. Aliu, et al (<http://arxiv.org/abs/0809.2998>).
- [31] Baring, M. G., *Adv. Space Res.*, **33**, 552–560 (2004).
- [32] Thompson, D.J., Bertsch, D.L. & O’Neal, R.H., *Astrophys. J. Suppl. Ser.*, **157**, 324–334 (2005).
- [33] Ruderman, M.A., Sutherland, P.G., Theory of Pulsars- Polar caps, sparks, and coherent microwave radiation, *Astrophys. J.*, **196**, 51–72 (1975).
- [34] F. Aharonian *et al.* [The H.E.S.S. Collaboration], *Nature* **432**, 75 (2005).
- [35] F. Aharonian *et al.* [The H.E.S.S. Collaboration], *A&A* **449**, 223–242 (2006).
- [36] F. Aharonian *et al.* [The H.E.S.S. Collaboration], *A&A* **464**, 235–243 (2007).
- [37] F. Aharonian *et al.* [The H.E.S.S. Collaboration], *A&A* **437**, L7 (2005).
- [38] F. Aharonian *et al.* [The H.E.S.S. Collaboration], *Astrophys. Journal* **661**, 236–249 (2007).
- [39] H.E.S.S. collaboration, *H.E.S.S. observations of the supernova remnant RCW 86*, Proc. 30th International Cosmic Ray Conference, Merida, (2007).
- [40] S. Gabici, F.A. Aharonian and P. Blasi, *Astroph. Space Sci.* **309**, 365–371 (2007).
- [41] J. Albert et al., *ApJ Lett.* **664**, L87 (2007).
- [42] F. Aharonian *et al.* [The H.E.S.S. Collaboration], *A&A* **481**, 401–410 (2008).
- [43] F. Aharonian *et al.* [The H.E.S.S. Collaboration], *A&A* **483**, 509–517 (2008).
- [44] F. Aharonian *et al.* [The H.E.S.S. Collaboration], *A&A* **486**, 829–836 (2008).
- [45] F. Aharonian *et al.* [The H.E.S.S. Collaboration], *Science* **314**, 1424–1427 (2006).

- [46] J. Albert et al., *Astrophys. J. Lett.* **685**, L23 (2008).
- [47] F. Aharonian *et al.* [The H.E.S.S. Collaboration], *Astrophys. Journal Lett.* **664**, L71–L74 (2007).
- [48] F. Aharonian *et al.* [The H.E.S.S. Collaboration], *A&A* **475**, L9–L13 (2007).
- [49] J. Albert et al., *Astrophys. J. Lett.* **667**, L21 (2007).
- [50] MAGIC Collaboration, *Science*, Vol. **320**, 1752 (2008).
- [51] The Fermi telescope website (<http://www-glast.stanford.edu>).
- [52] The Pierre Auger Collaboration et al., *Science* Vol. **318**, 938–943 (2007).
- [53] The CTA website (<http://www.cta-observatory.org>).

# **FERMI/GLAST and the Future of High Energy Gamma Ray Astronomy**

*Vincenzo Vitale*

*(for the LAT Collaboration)*

*Dipartimento di Fisica and INFN*

*Universitá di Tor Vergata*

*I-00133 Roma, ITALY*

## **1 Introduction**

The Fermi Gamma-ray Space Telescope is an observatory for the study of  $\gamma$ -ray emission from astrophysical sources. Fermi has two main instruments: (1) the Large Area Telescope (LAT), a  $\gamma$ -ray imager operating in the energy band between 30 MeV and 300GeV; (2) the Gamma Ray Burst Monitor (GBM), a detector covering the 8keV-20MeV energy range, devoted to the study of the Gamma Ray Bursts. Detailed descriptions of Fermi, which was previously known as GLAST, are in [1], [2] and [3].

Previous studies of the  $\gamma$ -ray sources in the LAT energy band were performed with the Energetic Gamma Ray Experiment Telescope (EGRET) onboard of the Compton Gamma Ray Observatory between 1991 and 2000. EGRET detected 271 sources [4], an half of which unidentified, mainly because of the relatively large errors associated with the source location. The majority of the identified EGRET sources are pulsars (spinning neutron stars, with powerful magnetic field, capable to accelerated particles up to the high energy regime) or Flat Spectrum Radio Quasars and Blazars (active galactic nuclei, with relativistic jets of plasma). Furthermore diffuse galactic and extra-galactic  $\gamma$ -ray emission was detected with EGRET.

The LAT instrument has an effective area five times larger and a much better angular resolution, if compared with EGRET, then Fermi has a sensitivity 30 times better than its predecessor. Fermi scientific objectives span from the detailed study of pulsar, AGNs and diffuse emission, to the search for new classes of  $\gamma$ -ray emitters and the possible signals of new physics, such as from the dark matter (DM). The GBM adds the study of Gamma Ray Bursts, up to GeV energies, to the scientific objectives of the observatory [5].

An international collaboration was set up in order to build and operate Fermi. This collaboration is made of more than 300 members, both astrophysicists and particle physicists, coming from institutions of France, Italy, Japan, Spain, Sweden and

United States of America. Fermi was launched the 11th June of 2008, with a Delta II 7920H rocket, and it is foreseen to be operated for 10 years. In August the observatory was renamed in honour of Enrico Fermi.

## 2 The Large Area Telescope

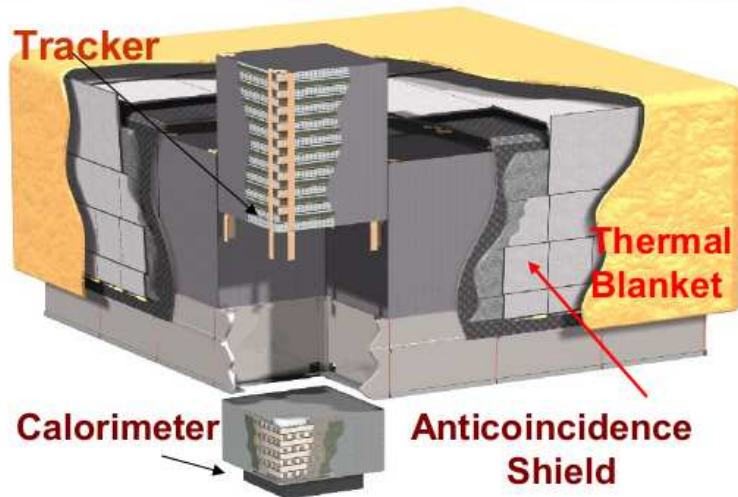


Figure 1: The LAT instrument and the sub-detectors.

LAT is a *pair conversion telescope*. With this type of instrument: (a) the  $\gamma$  rays interact with the instrument mainly by means of electron-positron pair production; (b) the electron and positron trajectories are tracked with precision; (c) the incoming direction of the parent gamma is reconstructed with the electron and positron trajectories; (d) the energy of electron and positron are measured with a calorimeter located at the bottom side of the tracker; (e) the telescope is shielded by an anti-coincidence detector, which covers the tracker and rejects the majority of the charged particles.

LAT is a modular instrument composed by  $4 \times 4$  units dubbed *towers*, with total dimensions of  $1733 \times 1733 \times 970$  mm. Each tower is composed by a tracker and a calorimeter section. The tracker is composed by 18 double planes of single-sided silicon-strip detectors (pitch =  $0.288\mu\text{m}$ ). The first 12 planes are interleaved with  $0.035 X_0$  of tungsten, while the next 4 with  $0.18X_0$  and the last 2 without any converter layer. This pattern is used for optimizing both the gamma ray conversion and the tracking precision. The LAT trackers form a quite large silicon detector with a total surface of  $\approx 80 \text{ m}^2$  and  $8.8 \times 10^5$  readout channels.

Each of the 16 LAT calorimeters contains 96 CsI(Tl) crystals, with dimension of  $326 \times 27 \times 20$  mm, read by two PIN photodiodes. The dynamical range for each crystal is 20MeV - 70GeV. The total depth of the calorimeters is  $8.5X_0$

The LAT anti-coincidence veto (ACD) is composed by 89 plastic scintillator tiles, with an overall efficiency of  $>0.9997$  in response to the passage of charged particles. ACD surrounds the LAT towers. High Energy gamma rays can create secondary charged particles, which might interact with a monolithic veto and severely reduce the telescope sensitivity of a pair conversion telescope (*self-veto effect*). The ACD segmentation is reducing this effect.

The LAT instrument has a large field of view of 2.4sr and an effective area of  $\approx 8000\text{cm}^2$  for normal incidence at 1GeV. Furthermore the silicon detectors provide high angular resolution (0.15, 0.9 and  $3.5^\circ$  of single photon angular resolution, respectively at 10, 1 and 0.1 GeV). These factors allow one to get a sensitivity in order of  $1.6 \times 10^{-9}\text{ph/cm}^2\text{s}$  in two years above 100MeV. Further improvements in respect of the past gamma ray missions are the energy resolution of 10-20 % and the timing accuracy of  $<10\ \mu\text{s}$

### 3 The Indirect Search for Dark Matter with Fermi

The estimated Universe energy content [6] is : 4% of baryonic *ordinary* matter, 23% of *Dark Matter* (DM) and 73% of *Dark Energy*. There are several evidences of the DM existence (see [7],[8],[9],[10],[11],[12]). Non-gravitational DM couplings are studied with: (1) the direct search for DM scattering on ordinary matter; (2) the indirect study of DM annihilation via the secondary products, both charged and neutral ( $e^+$ ,  $\bar{p}$ ,  $\bar{d}$ ,  $\nu$ ,  $\gamma$  rays and lower frequency electro-magnetic radiation). For weakly interacting massive particles (WIMPs) of Majorana the heavy fermions pairs, such as  $b\bar{b}, t\bar{t}, \tau^+\tau^-$ , are favoured as annihilation products [13]. The annihilation in two  $\gamma$  rays is loop-suppressed, with a branching ratio of  $10^{-3}$ - $10^{-4}$ , but  $\gamma$ -ray emission is expected after the decay of heavy fermions.

Then  $\gamma$ -ray observations can be used for the indirect search for annihilating Dark Matter [14]. Many possible observation strategies are currently carried out by the Fermi Dark Matter Working group (see Tab. 1). One of these is the targeting of regions where high DM density is foreseen, such as the Galactic Center or the Spheroidal Dwarf Galaxies.

For example the annihilating DM  $\gamma$ -ray flux, from the Galactic Center (GC) can be expressed as:  $\Phi_{DM} = \sum b_i \frac{dN_{\gamma,i}}{dE_\gamma} \frac{\sigma v}{8\pi m_X^2} \int_{los} \rho^2(l) dl$  where  $\sigma v$  is the DM annihilation cross section times the relative particles velocities,  $m_X$  = DM particle mass,  $\rho(r)$  = DM density as a function GC distance, the integral is performed along the line-of-sight,  $\frac{dN_\gamma}{dE_\gamma}$  = annihilation  $\gamma$ -ray yield and  $b_i$  the branching ratio. DM forms halos with central density enhancements and the Milky Way is embedded in

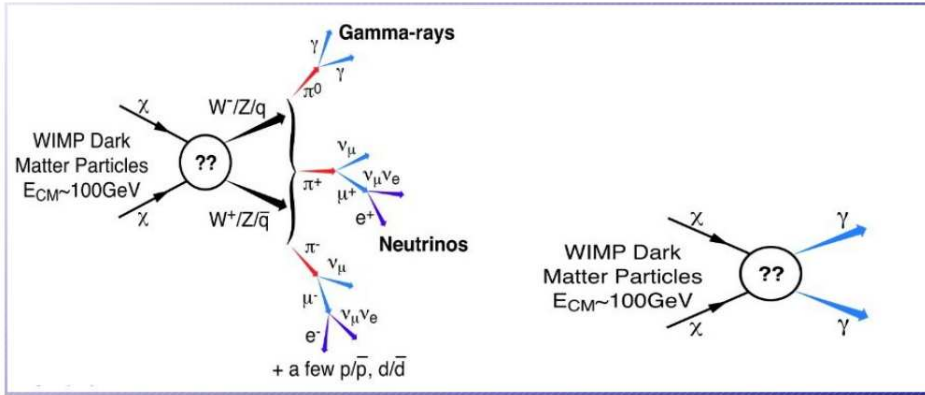


Figure 2: A cartoon on the possible WIMPs annihilation channels, from [14]

one of such structures. The galactic density profile is commonly parametrized as  $\rho(r) = \frac{\rho_0}{(r/R)^\gamma (1+(r/R)^\alpha)^{(\beta-\gamma)/\alpha}}$  with  $R \approx 20$  kpc as scale radius,  $\rho_0$  fixed such as the DM density= 0.3 GeV/cm<sup>3</sup> in the Sun region. The other three parameters are defining the profile type: Navarro-Frenk-White (NFW, [15]) has  $\alpha=1$ ,  $\beta=3$ ,  $\gamma=1$ ; Moore profile [16] has  $\alpha=1.5$ ,  $\beta=3$ ,  $\gamma=1.5$ .

The density profile is essential for the DM indirect study in the  $\gamma$ -ray channel as:(1) the  $\gamma$ -ray flux goes as  $\rho^2$  and can be above or below the detection threshold as function of the profile type; (2) some density profiles might be detected as extended sources. The spatial information and the peculiar energy spectrum, expected by a DM source, will be fundamental in the GC region, where bright  $\gamma$ -ray sources are located. LAT is the most sensitive instrument in the 30MeV-300GeV band, and is well suited for the indirect DM investigations.

## 4 Summary

Fermi was successfully launched the 11th June of 2008, and is now taking data in the nominal regime. Early results have already been published, such as the discovery of a pulsar in CTA 1 [17], more than 12 alerts for flaring AGNs and for the detection of GRB 080916C above 1 GeV [18]. Furthermore the most sensitive indirect search for annihilating DM, in the H.E.  $\gamma$ -ray band is ongoing with the Fermi data. First constraints to the DM theories are expected within 1 year from the launch.

Target	Advantages	Challenges
Galactic Center	good statistics	source confusion galactic diffuse background
Galactic Halo	very good statistics	galactic diffuse background
Galaxy Satellites	low background good source identification	low statistics
Spectral Lines	no astrophysical uncertainties good source identification	low statistics
Extragalactic	very good statistics	galactic diffuse background

Table 1: Main targets for the search for annihilating DM with Fermi [14]

## References

- [1] N.Gehrels et al., 1999, Astroparticle Phys. 11, 277
- [2] W.B.Atwood et al, 1994 N.I.M. A 342, 302
- [3] P.F.Michelson et al., 2007 AIP Conf.Proc. 921, 8
- [4] R.C. Hartman et al, 1999, Ap.J. 123, 79
- [5] N.Omodei et al. 2007 AIP Conf.Proc. 921, 472
- [6] E. Komatsu et. al. arXiv 0803.0547
- [7] A.Borriello et al., MNRAS 323, 285 (2001)
- [8] F.Zwicky, Helv.Phys. Acta 6, 110 (1933)
- [9] J.A. Tyson et al., Astroph.J. 498, L107 (1998)
- [10] D.N. Spergel et al., Astroph.J.Suppl. 170, 377 (2007)
- [11] K.A. Olive et al., Phys.Rept. 333, 389 (2000)
- [12] M. Tegmark et al., Astroph. J. 606, 702 (2004)
- [13] A.Cesarini et al. 2004, Astroparticle Phys. 21, 262
- [14] E.A.Baltz et. al. 2008, JCap 0807, 13
- [15] J.F.Navarro et al., Astroph.J. 462, 563 (1996)
- [16] B. Moore et al., Astroph. J. 524, L19 (1999)

- [17] A.A.Abdo et al, 2008, Science 322, 1218
- [18] GCN 8246 GRB 080916C: Fermi LAT observation

# Ultra-High Energy Particles Astronomy with a space-based experiment

*Roberto Pesce*

*INFN and Department of Physics  
Università degli Studi di Genova  
Via Dodecaneso 33  
I-16146 Genova, ITALY  
e-mail: roberto.pesce@ge.infn.it*

## 1 Introduction

Ultra-High Energy Cosmic Particles (UHECP) with energies in excess of  $10^{19}$  eV, reach the Earth with a very low flux ( $\lesssim 0.01 \text{ particle} \cdot \text{year}^{-1} \cdot \text{km}^{-2} \cdot \text{sr}^{-1}$  for particles with energies  $\gtrsim 10^{20}$  eV). The UHECP physics will not be discussed in this paper (see for example [1]). The Pierre Auger Observatory (PAO) will provide, in the next years, a solid understanding of these phenomena [2]. The PAO south site represents for sure the present of the scientific field, while the forthcoming north site is the near future.

However a next-generation space-based experiment might have the capabilities to increase the event statistics with respect to ground-based experiments, aiming at an instantaneous geometrical aperture of the order of  $10^6 \text{ km}^2 \cdot \text{sr}$ . This requires a big experiment, on a medium/long timescale, whose performances demand for a large amount of R&D in order to setup both the technologies and the knowledge to allow an optimal experiment design.

The scientific scenario, which is becoming available thanks to the PAO, will help to tune the scientific objectives and will drive the unavoidable trade-offs on the objectives, the performances and the design choices.

The relevance of a such post-PAO (south and north) experiment is widely recognized by the HE astroparticle physics community. The inclusion of the UHECP physics in the European Space Agency (ESA) Cosmic Vision2015-2025 program [3] provides a suitable framework for the study of future space missions.

## 2 The required apparatus

The required apparatus is a large aperture, large field-of-view, fast and highly pixelized digital camera detecting with high efficiency near-UV single photons emitted by

the Extensive Air Showers (EAS) generated in the interactions between the primary particles and the atmosphere. The instrument looks downward the Earth at night to observe both the EAS scintillation light and the Cherenkov light diffusely reflected by ground, sea or clouds (see Fig. 1).

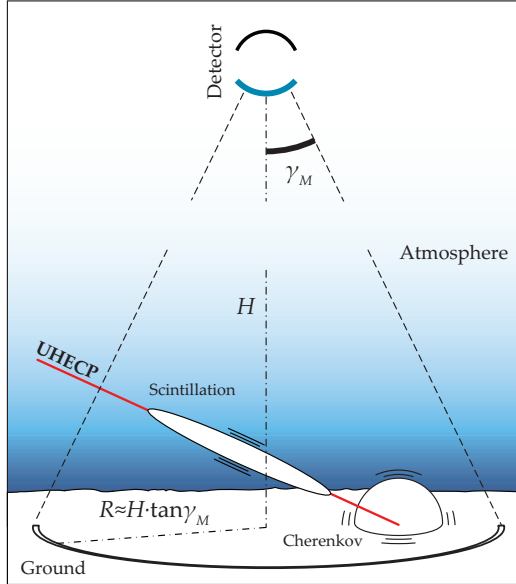


Figure 1: The observational approach of the apparatus.

The detector has to be capable of operating for at least 5-10 years in space. The signal is very small and it is superimposed on a huge background. The continuously changing Field-of-View (FoV) has to be watched by a suitable atmospheric monitoring system, to gather all the information required for the reconstruction of the primary particle.

The main components of the apparatus are:

- a main optics, collecting the light and focusing the EAS image onto a Focal Surface (FS);
- a Photo-Detector (PD) on the FS (photo-sensors, trigger, front-end and back-end electronics, data analysis system), registering the EAS image;
- a calibration system;
- an atmospheric monitoring system;
- other ancillary instrumentation.

Such a challenging experiment needs to exploit novel technologies in order to reach the scientific objectives.

### 3 The EUSO heritage

The current knowledge relies on the studies already conducted in the framework of the Extreme Universe Space Observatory (EUSO)mission phase A [4, 5]. EUSO was proposed to the ESA as a free-flyer satellite in 1999. In 2000 the ESA recommended to consider the accommodation on the Columbus module of the International Space Station (ISS). This accommodation gave rise to many constraints that limited the final EUSO performances: fixed orbit height ( $\sim 400$  km), limits on mass ( $\lesssim 1.5$  ton), volume ( $\lesssim 2.5 \times 2.5 \times 4.5$  m $^3$ ), power consumption ( $\lesssim 1$  kW) and telemetry ( $\lesssim 200$  Mbit/orbit). Therefore the maximum optics diameter was  $\sim 2$  m. EUSO has to be considered as a preliminary exercise. The main lesson is that, in designing such an experiment with so many unknowns, one must keep a safe design margin on the expected performances. The second main lesson is that previously unexpected challenges and critical issues were identified during the phase A study. The EUSO efficiency plateau was reached at  $E \approx 2 \times 10^{20}$  eV [6]. The current scientific scenario look for an experiment with a magnitude order lower energy threshold, so one needs to gain a factor  $10 \div 20$  (at least!) in the threshold.

### 4 The required performances

The improved scientific objectives, with respect to EUSO, imply improved apparatus requirements. It has to be remarked that an accurate experiment optimization is a complex task and it can be carried on only with a detailed study. Therefore only preliminary and conservative estimates are given here. These estimates rely on the EUSO Phase A study, based on end-to-end simulations, from the signal generation and transport to the instrument response and data analysis [5, 6]. The EUSO performances are rescaled to the new experiment using simple and approximate, but reasonably accurate, scaling laws and consolidated expectations based on the new technology developments.

The main physics performance parameter are the instantaneous geometrical aperture, the energy threshold, the energy and angular resolutions and the duty cycle. From the current scientific scenario, the energy threshold has to be of the order of  $\sim 10^{19}$  eV.

The instantaneous geometrical aperture has to be very large and the operational time has to be long enough to get a big exposure providing a number of UHECP larger than it is possible from the Earth. In order to increase the aperture one needs to put the detector in a very high orbit. This weakens the signal, which scales with the square of the distance from the EAS. Therefore the orbital parameters have to be tuned in order to improve the expected performances. Varying the orbital height, for instance using an elliptic orbit, actually extends the observational energy range.

With a free-flyer satellite one has many more degrees of freedom in the choice of orbit than from the ISS.

From the instrumental point of view, the basic performance parameter is the photon collection capability, which strongly affects the main physics performances: the threshold, the energy and angular resolutions and the geometrical aperture, since that with a better photon collection capability one can put the detector on an higher orbit maintaining the same threshold. The photon collection capability depends on the entrance pupil size and on the photon collection efficiency. The latter is affected by the optics efficiency (OE), the photo-detector efficiency (PDE) and many other efficiency factors, which are typically very close to one. So the only parameters capable, *a priori*, to provide a significant improvement are the OE and the PDE. The optics aperture is the only sizable parameter, within the external constraints. Since this is the only parameter affecting the performances that can be dimensioned, the instrument should be designed to have the largest dimensions compatible with a non-deployable photo-detector. Indeed, while large deployable optical systems are currently under development [8], at this moment the developing a deployable photo-detector seems to be a too challenging task.

Provided that suitable technologies are successfully developed, the following goals can be accomplished:

- observed area (at apogee)  $\approx 8 \times 10^5 \text{ km}^2$ ;
- instantaneous geometrical aperture at apogee  $\approx 2 \times 10^6 \text{ km}^2 \cdot \text{sr}$
- the duty cycle is a delicate parameter and a precise value can be only measured; with a guess-estimate we can say that it is of the order of 10%-20%;
- angular granularity corresponding to  $\sim 1 \text{ km}$  at Earth;
- with an entrance pupil diameter of  $\sim 8 \text{ m}$  and a PDE doubled with respect to EUSO ( $\sim 25\%$ ) one can think to reach a threshold  $\lesssim 10^{19} \text{ eV}$  with a statistical uncertainty of  $\sim 10\%$ ;
- angular resolution of few degrees (limited by the EAS visible track length and the number of FS channels).

Some technological developments should be carried on:

- a deployable catadioptric optics;
- high PDE sensors; for example the Geiger-mode Avalanche Photo-Diode (GAPD), provided that the current limitations are successfully overcome [9, 10];
- micro-electronic technologies.

## 5 The Super-EUSO mission

The Super-Extreme Universe Space Observatory (S-EUSO) [7] is an international multi-agency mission, led by ESA. The S-EUSO proposal is based on the technological and mission studies already carried on in the Phase A of the EUSO mission. S-EUSO will observe the EAS from space, shedding light on the origin and sources of UHECP, on their propagation environment and on particle physics at energies well beyond the man-made accelerators. In this sense, such a mission will develop the particle astronomy field, already opened by the PAO. A further scientific fall-out of the mission will be the systematic monitoring of the electromagnetic atmospheric phenomena (e.g. lightnings). In the Table 1 the main parameter of the mission and the experimental apparatus current design are reported.

ORBIT			
perigee radius	$\sim 800$ km	ground velocity	7.5 km/s
apogee radius	$\sim 1000$ km	pointing accuracy	$\sim 3$ deg
inclination	50 deg $\div$ 60 deg	lifetime	5 – 10 years
period	$\sim 100$ min		
OPTICS		FOCAL SURFACE	
mirror diameter	11 m	diameter	4 m
pupil diameter	7 m	number of channels	$\sim 10^6$
f/#	0.7	pixel size	$\sim 4$ mm
granularity at ground	$\sim 0.7$ km	sensor PDE	$\gtrsim 0.25$
field of view	25 deg	power per channel	$\lesssim 2$ mW
throughput	$> 0.7$		

Table 1: Main parameters of the S-EUSO mission (to be optimized).

The required dimensions and the use in space require the optics to be lightweight and deployable. The most versatile configuration is a catadioptric one, e.g. a Schmidt telescope. The focal surface is made by an array of photo-sensors. High PDE is required. The front-end electronics will be a custom ASIC fully integrated with the photo-sensor. Due to the very large span of the energy range (almost three order of magnitudes), two complementary approaches are required: the single photon counting technique at low energies and the charge measurement technique at high energies. The trigger has to be fast and selective in order to tag the EAS signal while rejecting the background in an efficient way.

The observation of the atmosphere inside the FoV (using for instance an infrared camera and/or a LIDAR) will provide key parameters for the EAS reconstruction.

### 5.1 The preparatory program

A careful mission design optimization is required. This implies collecting as many as possible preliminary informations. Therefore it is necessary to follow some preliminary steps: improving the fluorescence yield and Cherenkov albedo measurements through dedicated experiments and characterizing in detail the background via a micro-satellite mission (which can also test some technological issues) [11]. The space approach has to be validated through some preliminary small mission. In this sense the russian TUS [12] and the japanese JEM-EUSO [13] pathfinders are under study.

## 6 Conclusions

A space-based experiment for UHECP detection is very challenging. It is mandatory to clarify the scientific goals for such a post-PAO experiment. The experimental design will require many trade-offs and some preliminary steps (background characterization, etc.) are mandatory.

## References

- [1] P. Bhattacharjee and G. Sigl, Phys. Rept. **327** (2000) 109
- [2] S. Petrera, these proceedings.
- [3] ESA, “Cosmic Vision: Space Science for Europe 2015-2025”, 2005.
- [4] J. Adams, Nucl. Phys. Proc. Suppl. **134** (2004) 15.
- [5] L. Scarsi *et al.*, “EUSO: report on the Phase A study”, 2004
- [6] R. Pesce, “The detection of UHECP on the Earth and from space”, PhD thesis, 2008.
- [7] A. Santangelo *et al.*, “S-EUSO: a proposal for a space-based observatory for UHECP”, 2007.
- [8] P. Mazzinghi *et al.*, Proc. 6th Internat. Conf. on Space Optics, 2006.
- [9] P. Buzhan *et al.*, Nucl. Instrum. Meth. A **504** (2003) 48.
- [10] N. Dinu *et al.*, Nucl. Instrum. Meth. A **572** (2007) 422.
- [11] A. Thea *et al.*, Nucl. Phys. B Proc. Suppl. **166** (2007) 223.
- [12] V. I. Abrashkin *et al.*, Int. J. Mod. Phys. A **20** (2005) 6865.
- [13] Y. Takizawa *et al.*, Nucl. Phys. Proc. Suppl. **166** (2007) 72.

# Antimatter and DM search in space with AMS-02

*Francesca R. Spada*

*Istituto Nazionale di Fisica Nucleare*

*Piazzale Aldo Moro, 5*

*I-00185, Rome, ITALY*

## 1 Introduction

AMS-02 is a space-borne magnetic spectrometer designed to measure with very high accuracy the composition of Cosmic Rays near Earth. With a large acceptance of  $5000 \text{ cm}^2$ , an intense magnetic field from a superconducting magnet (0.7 T) and a very efficient particle identification, AMS-02 will provide the highest precision in Cosmic Rays measurements up to the TeV region.

During a three-years mission on board of the International Space Station, AMS-02 will achieve a sensitivity to the existence of anti-Helium nuclei in the Cosmic Rays of one part in a billion, as well as provide important information on the origin and nature of the Dark Matter.

We review the status of the construction of the AMS-02 experiment and its remarkable discovery capabilities.

## 2 Cosmology with Cosmic Rays

Recent precision measurements of cosmological quantities, such as the Cosmic Microwave Background temperature and polarization [1, 2, 3] and the Supernova luminosity-to-distance relationship, together with Large Scale Structure and structure formation studies [4, 5], allowed to build a *standard cosmological model*, that describes a universe spatially flat, homogeneous and isotropic at large scales.

Our universe consists of ordinary matter and radiation only for a 4.5%: as shown in figure 1, a considerable fraction of the total matter (23%) is in the form of Cold Dark Matter. The largest fraction (73%) consists of Dark Energy, acting like a cosmological constant, whose origin is unknown [6]. The antimatter content of the universe appears to be only  $10^{-6}$  of the matter content [7].

The aim of AMS-02 is to perform precision studies of Cosmic Ray properties such as composition, production, acceleration and propagation mechanisms. Its large

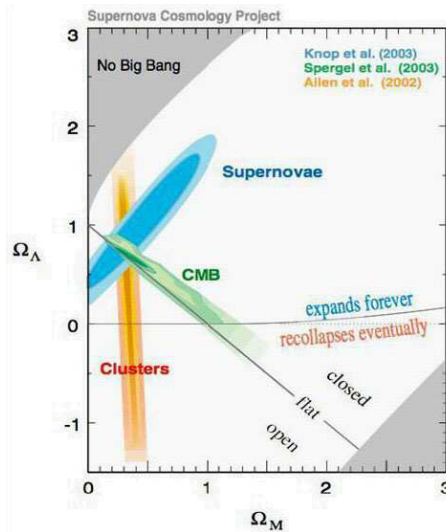


Figure 1: Independent measurements of several cosmological quantities all point in the direction of a universe composed mostly of Dark Matter and Dark Energy.

acceptance, energy resolution and particle identification capabilities allow AMS-02 to search for primordial antimatter by direct detection of antinuclei, and for Dark Matter annihilation products independently in different charged and neutral particles spectra.

### 3 The AMS-02 detector

AMS-02 is designed as a single particle spectrometer with large acceptance, high momentum range and efficient particle identification for reliable operation in space, to provide high statistics spectra of charged particles with nuclei and isotope separation, as well as gamma-ray measurements. It will carry out a 3-years mission taking data above the atmosphere on the International Space Station.

AMS-02 is shown in figure 2. It consists of a fully equipped tracker inside a superconducting magnet (the first ever to operate in space) providing a  $0.8 \text{ T m}^2$  magnetic field. Rigidity is measured up to 3 TeV and nuclei and isotopes are separated up to  $12 \text{ GeV/n}$  for  $Z \leq 26$  or  $A \leq 25$  with a Ring Imaging aerogel/sodium-flouride Cherenkov detector (Agl/NaF RICH), combined with Time of Flight (TOF) and  $dE/dX$  measurements. At 90% positron efficiency, a proton suppression by 3-4 orders of magnitude is achieved with a lead/scintillating fibre sandwich 3D sampling calorimeter (ECAL) based on shower shape information and the matching of shower energy with track momentum. Further proton suppression by 2-3 orders of magnitude up to 300 GeV/c is achieved with a 20 layer fibre fleece Xe/CO<sub>2</sub> proportional wire

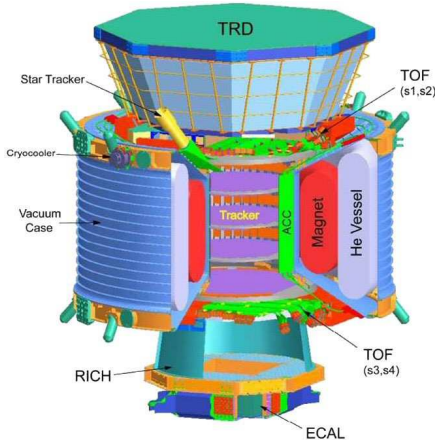


Figure 2: The AMS-02 detector.

straw tube Transition Radiation Detector (TRD). The overall  $10^6$  proton rejection factor is essential for Dark Matter search.

## 4 Indirect search for Dark Matter

A weakly interacting massive particle (WIMP) is the favoured Dark Matter candidate, and supersymmetric extensions of the standard model such as mSUGRA contain a *neutralino* which is stable when R-parity is conserved. AMS-02 is capable of detecting WIMPs indirectly by measuring decay products of neutralino annihilation processes, as an extra source for positrons, antiprotons, antideuterons and gammas on top of standard model predictions from galactic propagation models. With annihilation cross sections proportional to the square of the neutralino density, these measurements are also sensitive to Dark Matter density fluctuations.

Recent measurements of gamma-ray fluxes [8] and the positron fraction [9] have shown deviations from standard model expectations which are consistent with supersymmetric Dark Matter, but controversial within the available statistics and without standard model explanation for the positron excess [10, 11].

AMS-02 will measure the positron spectrum with substantially improved precision for background and signal, in the energy region where an excess has been claimed. Moreover, the simultaneous measurement in other independent channels will increase the sensitivity to Dark Matter detection. The spectra of positrons and antiprotons expected in the AMS-02 sensitivity region are shown in figure 3.

AMS-02 can also detect gamma rays up to 1 TeV either directly in the ECAL, or indirectly as an electron-positron pair after conversion in the material above the tracker, which amounts to 40% of a radiation length. The part of the parameter space

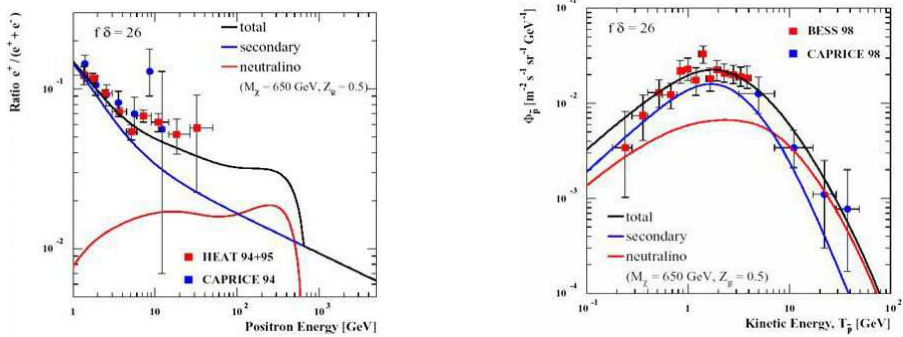


Figure 3: Left: positron flux; right: antiproton flux, in the energy region accessible to AMS-02. The red solid line shows the expected signal for a 650 GeV neutralino.

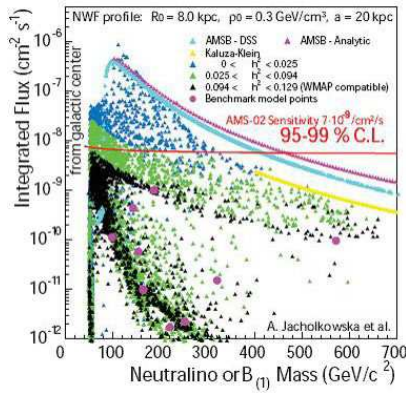


Figure 4: Part of the parameter space from new physics that si within reach of AMS-02 gamma flux measurements.

from new physics that is within reach of AMS-02 gamma measurements in the case of cuspy halo profile or extra enhancements, and even for a standard NFW dark matter halo [12], is shown in figure 4.

## 5 Direct search for antimatter

In the Big Bang theory matter and antimatter are created with equal abundances, and the disappearance of antimatter requires barion number violation and another source of CP violation. Antiparticles are indeed produced in collisions between high energy particles, and are observed in the Cosmic Rays. For example,

$$\phi(e^+)/\phi(e^-) \sim 10^{-1} \text{ at 10 GeV} \quad \phi(p)/\phi(\bar{p}) \sim 10^{-5} \text{ at 10 GeV.}$$

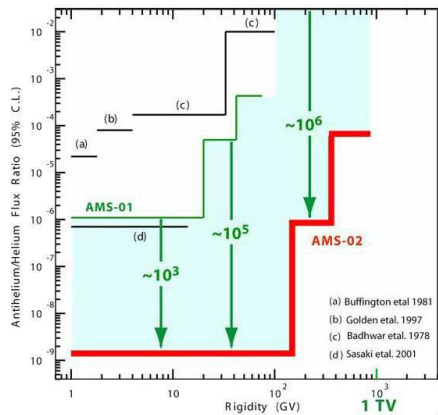


Figure 5: AMS-02 sensitivity to the anti-Helium flux.

However, an anti-Helium nucleus has very low probability of being produced in collisions:

$$\phi(\overline{He})/\phi(He) \sim 10^{-6} - 10^{-8}$$

Anti-Helium detection in the Cosmic Rays would be a clear indication of the existence of an antimatter area somewhere in the universe. AMS-02 will collect in three years  $2 \times 10^9$  nuclei with energies up to 2 TeV, with a sensitivity that reaches anti-Iron. The limit put by the precursor flight AMS-01 will be increased of a factor  $10^3$ , meaning that, if no antinucleus is observed, there is no antimatter to the edge of the observable universe (about 1000 Mpc). The limit on antimatter presence they can be set by AMS-02 is shown in figure 5.

## 6 Status and outlook

AMS-02 will provide a coherent dataset of unprecedented precision for charged Cosmic Rays and gamma rays up to the TeV region.

These data will confirm or disprove with high accuracy the excess in the HEAT positron data in the few GeV region. The multichannel analysis will allow combined fits to the parameters of standard model extensions to establish the nature of Dark Matter. Several models can be constrained and eventually ruled out.

AMS-02 will put a stringent limit on the presence of antimatter: if no antinucleus is observed, the hypothesis of barion asymmetry will be strongly favoured as no antimatter areas are present in the observable universe.

In general, our knowledge of the Cosmic Rays physics will be improved. AMS-02 will perform an accurate study of composition (H, He, B/C,  ${}^9\text{Be}/{}^{10}\text{Be}$ ) and energy spectra, and put significant constraints on galactic propagation model parameters.

It is also worth mentioning the possibility for a search of new types of matter (e.g. strangelets).

The detector integration will be completed in 2008, on schedule to be ready for launch with the Space Shuttle in 2010.

## References

- [1] D. N. Spergel *et al.* [WMAP Collaboration], *Astrophys. J. Suppl.* **170** (2007) 377
- [2] L. Page *et al.* [WMAP Collaboration], *Astrophys. J. Suppl.* **170** (2007) 335 [[arXiv:astro-ph/0603450](#)].
- [3] C. B. Netterfield *et al.* [Boomerang Collaboration], *Astrophys. J.* **571** (2002) 604
- [4] A. G. Riess *et al.* [Supernova Search Team Collaboration], *Astrophys. J.* **607** (2004) 665
- [5] S. Perlmutter, M. S. Turner and M. J. White, *Phys. Rev. Lett.* **83** (1999) 670
- [6] R. A. Knop *et al.* [Supernova Cosmology Project Collaboration], *Astrophys. J.* **598** (2003) 102
- [7] J. Alcaraz *et al.* [AMS Collaboration], *Phys. Lett. B* **461** (1999) 387
- [8] S. D. Hunter *et al.*, *Astrophys. J.* **481** (1997) 205.
- [9] J. J. Beatty *et al.*, *Phys. Rev. Lett.* **93** (2004) 241102 [[arXiv:astro-ph/0412230](#)].
- [10] A. W. Strong, I. V. Moskalenko and O. Reimer, *Astrophys. J.* **613** (2004) 962 [[arXiv:astro-ph/0406254](#)].
- [11] W. de Boer, C. Sander, V. Zhukov, A. V. Gladyshev and D. I. Kazakov, *Phys. Rev. Lett.* **95** (2005) 209001 [[arXiv:astro-ph/0602325](#)].
- [12] A. Jacholkowska *et al.*, *Phys. Rev. D* **74** (2006) 023518

# QCD and Heavy ion Physics

Session Convener:

*Rudiger Voss*

Session Convener:

*Tom Ludlam*

Jet physics at HERA, Tevatron and LHC

*Christophe Royon*

QCD at the HERAscale and implications  
at the Terascale

*Achim Geiser*

Exotic hadron spectroscopy

*Jolanta Brodzicka*

Longitudinal Structure Function  
Measurements from HERA

*Vladimir Chekelian*

Spin structure of the nucleon

*Krzysztof Kurek*

What is the matter created in heavy  
ion collisions?

*Raphael Granier de Cassagnac*

# Jet physics at HERA, Tevatron and LHC

*Christophe Royon*

*IRFU-SPP, CEA Saclay, F91 191 Gif-sur-Yvette, France*

## 1 Introduction

In this short report, we discuss the Jet Physics results and perspectives at HERA, Tevatron and LHC. The different accelerators are complementary as shown in Fig. 1, where the kinematical plane in  $(x, Q^2)$  is displayed ( $x$  and  $Q^2$  are respectively the proton momentum fraction carried by the interacting parton and the transferred energy squared carried by the virtual photon). HERA allows to reach very low values of  $x$  at low  $Q^2$  ( $x \sim 10^{-6}$ ), whereas the Tevatron (and the LHC) very high values of  $Q^2$  at high  $x$  ( $Q^2 \sim 3 \cdot 10^5, 10^8 \text{ GeV}^2$  at the Tevatron and the LHC respectively). In the following, we will benefit from the differences between the accelerators to assess the proton structure in a wide kinematical domain.

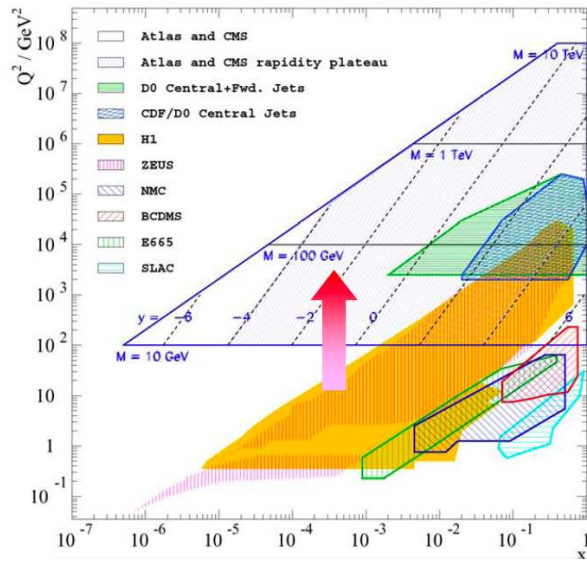


Figure 1: Kinematical domain reached by the experiments at HERA, Tevatron and LHC.

We will start this report by describing the constraints on the proton structure (quark and gluon densities) using inclusive jets at HERA and the Tevatron. The

study of the multijet cross sections will be discussed in the second part of the report since it is a fundamental topic for the LHC and the searches for new particles in the jet channels. Another background related to SUSY and Higgs boson searches is the  $W + b$  jet and  $Z + b$  jet events and we will give the most recent results from the Tevatron. We will finish the report by describing the low  $x$  dynamics which can be probed in forward jets at HERA and Mueller-Navelet jets at the Tevatron/LHC in particular.

## 2 Inclusive jets at HERA and the Tevatron

### 2.1 High $Q^2$ jet measurements at HERA

In addition to the measurement of the proton structure function  $F_2$  which allows to access directly the structure of the proton in terms of quarks and gluons, it is possible to probe the gluon density at high  $x$  using jet measurements at HERA. The H1 and ZEUS collaborations at HERA measured the ratios of the jet and neutral current cross sections [1] to remove many systematic uncertainties as shown in Fig. 2. The jet cross section measurement allows to perform a direct test of the next-to-leading order (NLO) QCD evolution, and allows to constrain the parton distribution functions (PDF) and the values of  $\alpha_S$ . The effect of including or not the jet cross sections in addition to the proton structure function measurements to constrain further the parton density at high  $x$  in the proton is shown in Fig. 3. The uncertainties on the gluon density at high  $x$  are still very large (typically larger than 20% for  $x > 0.3$  at high  $Q^2 \sim 2000$  GeV $^2$ , increasing to 100% at low  $Q^2$ ), and we will study if the Tevatron (and then the LHC) can reduce this uncertainty further.

The H1 and ZEUS collaborations also measured the charged current jet production cross section for jet transverse energies above 100 GeV. A good agreement is found with NLO calculations but in addition to PDF uncertainties, there is a large theoretical uncertainty at high  $x$  which shows the need for NNLO calculations [2].

### 2.2 Inclusive jet cross section measurements at the Tevatron

The inclusive jet cross section measurements at the Tevatron rely on the determination of the jet energy calibration, which leads to the largest systematic uncertainties. Jet measurements are corrected either to particle level or to parton level, depending on the measurements and the collaboration. Jet measurements are performed using either a cone or the  $k_T$  algorithm. The jet energy scale is determined mainly using  $\gamma$ +jet events. In the D0 collaboration, the corrected jet energy is obtained using the following method

$$E_{jet}^{corr} = \frac{E_{jet}^{uncorr} - Off}{Show \times Resp} \quad (1)$$

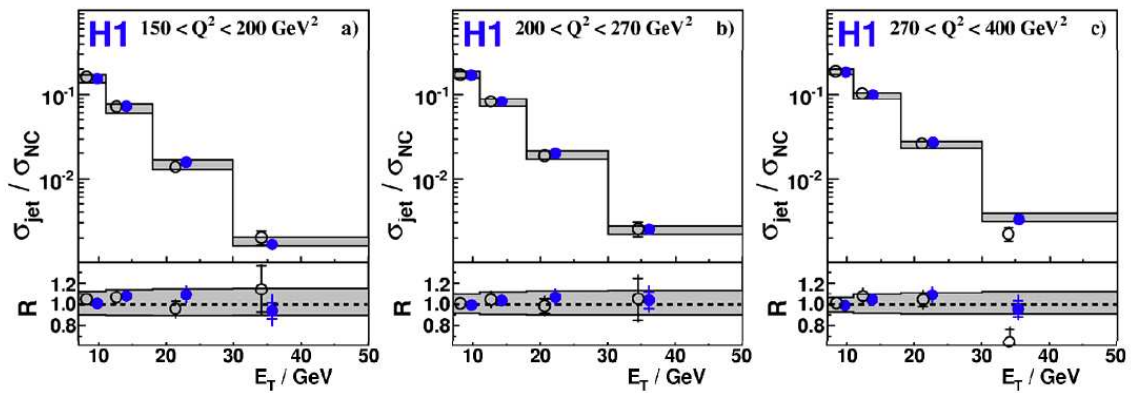


Figure 2: Ratios of the jet production to the neutral current cross sections as a function of jet  $E_T$  in three different  $Q^2$  regions.

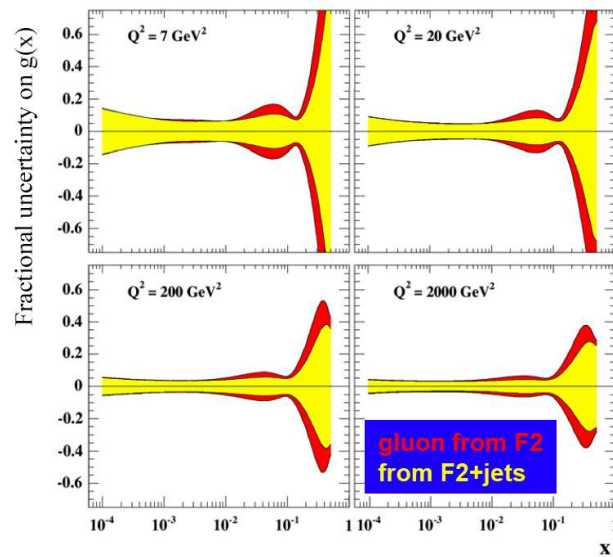


Figure 3: Fractional uncertainty on gluon density in the proton in four different  $Q^2$  bins determined using the proton structure function  $F_2$  data measured at HERA (in red) and the jet cross sections in addition (in yellow).

where  $E_{jet}^{corr}$  and  $E_{jet}^{uncorr}$  are the corrected and uncorrected jet energies respectively. The offset corrections (*Off*) are related to uranium noise and pile-up and are determined using zero-bias data. The showering corrections (*Show*) take into account the energy emitted outside the jet cone because of the detector and dead material and, of course, not the physics showering outside the jet cone which corresponds to QCD radiation outside the cone. The jet response (*Resp*) is the largest correction, and can be subdivided in few corrections. The first step is to equalize the calorimeter response as a function of rapidity, and the jet response is then measured for the central part of the calorimeter only using the  $p_T$  balance in  $\gamma$ +jet events. Some additional small corrections related to the method biases are introduced. One important additional correction deals with the difference in response between quark and gluon jets. The difference was studied both in data and in Monte Carlo (using for instance the  $\gamma$ +jet and the dijet samples which are respectively quark and gluon dominated) and leads to a difference of 4 to 6% as a function of jet  $p_T$ , which is not negligible if one wants a precision on jet energy scale of the order of 1%. This has an important consequence. The jet energy scale is not universal but sample dependent. QCD jets (gluon dominated) will have a different correction with respect to the  $t\bar{t}$  events for instance which are quark dominated. The CDF collaboration follows a method which is more Monte Carlo oriented using beam tests and single pion response to tune their Monte Carlo. At the LHC, it will be possible to use  $Z$ +jets which do not suffer from the ambiguity of photon identification in the detector.

The uncertainties reached by the D0 collaboration concerning the determination of jet energy scale are of the order of 1.2% for jet  $p_T$  between 70-400 GeV and in a wide range of rapidity around zero (the uncertainty is of the order of 2% for a rapidity of 2.5). This allows to make a very precise measurement of the jet inclusive cross section as a function of their transverse momentum.

The measurement of the inclusive jet cross section [3] was performed by the D0 and CDF collaborations at the Tevatron using a jet cone algorithm with a cone size of 0.7 (D0 and CDF) and the  $k_T$  algorithm (CDF). Data are corrected to hadron level (D0) or parton level (CDF). The motivation of this measurement is double: it is sensitive to beyond standard model effects such as quark substructure and to PDFs, especially the gluon density at high  $x$ . Historically, the excess observed by the CDF collaboration in 1995 concerning the inclusive jet  $p_T$  spectrum compared to the parametrisations was suspected to be a signal of quark substructure but it was found that increasing the gluon density at high  $x$  could accommodate these data. This raises the question of PDFs versus beyond standard model effects, and the interpretation of data in general. Data are compared with NLO QCD calculations using either CTEQ6.5M [3] for D0 or CTEQ6.1 for CDF (the uncertainties of the CTEQ6.5M parametrisation are two times smaller). A good agreement is found over six orders of magnitude. The ratio data over theory for the D0 and CDF measurements are given in Figs. 4 and 5. A good agreement is found between NLO QCD and the D0 or CDF measurements with

a tendency of the CTEQ parametrisation to be slightly lower than the data at high jet  $p_T$ . The MRST2004 [3] parametrisation follows the shape of the measurements. Given the precision obtained on jet energy scale, the uncertainties obtained by the D0 collaboration are lower than the PDF ones and will allow to constrain further the PDFs (the uncertainties of the CDF collaboration are about two times larger). The D0 collaboration took also special care of the uncertainty correlation studies, by giving the effects of the 24 sources of systematics in data.

In addition, the CDF collaboration measured the dijet mass cross section [5] above 180 GeV, and up to 1.2 TeV. No excess was found with respect to NLO QCD calculations and this measurement allows to exclude excited quarks below 870 GeV,  $Z'$  (resp.  $W'$ ) below 740 (resp. 840) GeV<sup>1</sup>, and technirho below 1.1 TeV.

The question rises if PDFs can be further constrained at the LHC using inclusive measurements. The PDF uncertainties are typically of the order of 15% for a jet  $p_T$  of 1 TeV, and 25% of 2 TeV for  $1 < |\eta_{jet}| < 2$  (without taking into account the new Tevatron measurements which we just discussed). A typical uncertainty of 5% (resp. 1%) on jet energy scale leads to a systematic uncertainty on 30 to 50% (resp. 6 to 10%) on the jet cross section. A precise determination of the jet energy scale at the LHC will thus be needed to get competitive measurements at the LHC.

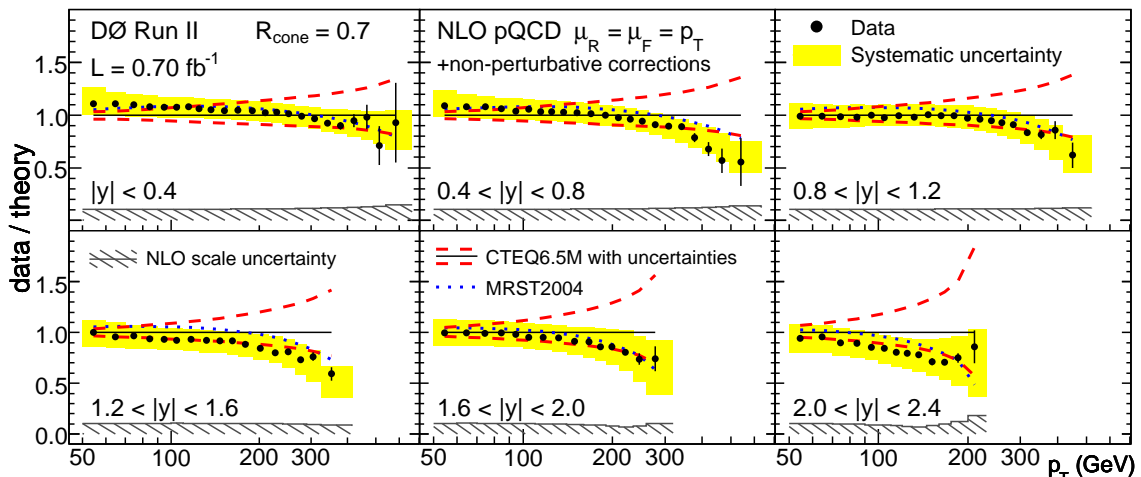


Figure 4: Data over theory for the inclusive  $p_T$  cross section measurement for the D0 collaboration using the 0.7 jet cone. Data are compared to NLO QCD calculations using the CTEQ6.5M parametrisation.

<sup>1</sup>Stronger limits on  $W'$  and  $Z'$  mass limits come from lepton based searches

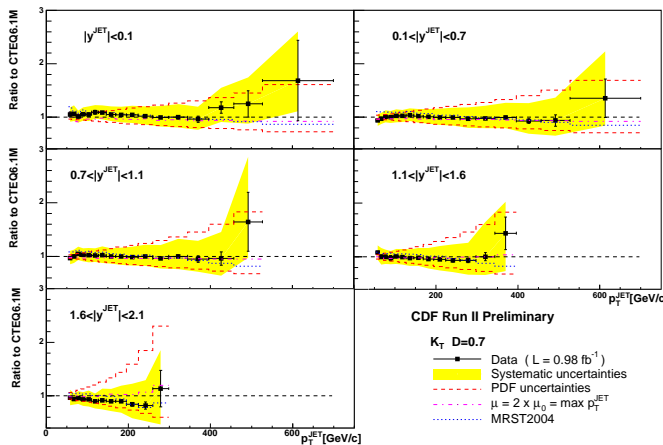


Figure 5: Data over theory for the inclusive  $p_T$  cross section measurement for the CDF collaboration using the  $k_T$  algorithm. Data are compared to NLO QCD calculations using the CTEQ6.1 parametrisation.

### 2.3 How do PDF uncertainties affect LHC potential?

Another question to be raised is to know whether the uncertainty on PDFs (and also of higher order effects) can affect the LHC discovery potential. As an example, let us consider the Higgs boson production. The cross sections are known precisely both for background and signal (typically the uncertainties on  $\sigma(gg \rightarrow H)$  and on  $\sigma(qq \rightarrow Hqq)$  cross sections due to PDFs are respectively less than 5 and 15% over the full Higgs boson mass range). However, there are additional uncertainties related to higher order effects. For example, for Higgs production for a Higgs mass of 120 GeV, NNLO effects are of the order of 9% (for  $Z$  production, it is of the order of 4%). Both sets of uncertainties have to be taken into account in the predictions.

On the other hand, the LHC potential can be affected if the background is poorly known. PDF uncertainties can thus have an impact on searches (extra dimensions, single top, SUSY...). As an example, we can quote the search for  $qqqq$  contact interactions for a given compactification scale which can appear as an excess in the dijet mass spectrum. For a compactification scale of 2 TeV, and 2 extra dimensions, the effect of contact interactions is found to be of the same order as the present PDF uncertainties.

### 3 Multijet cross section measurements at the Tevatron and at HERA

The measurement of multijet cross sections at the Tevatron and at HERA (and later on at the LHC) is fundamental to constrain the PDFs and to tune the Monte Carlo, since it is a direct background entering in many searches for Higgs bosons or new particles at the LHC. We can quote for instance the search for Higgs bosons in association with  $t\bar{t}$ , the measurement of the  $t\bar{t}$  production cross section, the search for  $R$ -parity violated SUSY (which can lead up to 8-10 jets per event...).

#### 3.1 Measurement of $\Delta\Phi$ between jets in D0

The advantage of the measurement of the difference in azimuthal angle between two leading jets in an inclusive QCD sample as was performed in D0 is that there is no need of precise knowledge of jet energy scale (the measurement is dominated by the knowledge of jet angles). The  $\Delta\Phi$  spectrum was measured in four different regions in maximum jet transverse momentum, and a good agreement was found with NLO calculations except at very high  $\Delta\Phi$  where soft radiation is missing [6]. PYTHIA [7] shows a disagreement at small  $\Delta\Phi$ , showing a lack of initial state gluon radiation, while HERWIG [8] shows a good agreement with data.

#### 3.2 Measurement of multijet and $\gamma+$ jet cross sections

The H1 and ZEUS collaborations measured the 2 and 3 jet production cross section relatively to the neutral current one to reduce systematics. A good agreement is found with NLO calculations [9].

The D0 collaboration measured the inclusive production of isolated  $\gamma+$  jets in different detector regions requiring a central photon and a central or a forward jet. It distinguished the cases when the photon and the jet are on the same or opposite side. The cross section has been found in disagreement with NLO QCD expectations both in shape and normalisation and the reason is unclear [10].

#### 3.3 Jet shape measurements in CDF

The jet shape is dictated by multi-gluon emission from primary partons, and is sensitive to quark/gluon contents, PDFs and running  $\alpha_S$ , as well as underlying events. We define  $\Psi$  which is sensitive to the way the energy is spread around the jet center

$$\Psi(r) = \frac{1}{N_{jets}} \sum_{jets} \frac{P_T(0, r)}{P_T^{jet}(0, R)} \quad (2)$$

where  $R$  is the jet size. The energy is more concentrated towards the jet center for quark than for gluon jets since there is more QCD radiation for gluon jets (which means that  $\Psi$  is closer to one for quark jets when  $r \sim 0.3R$  for instance). The CDF collaboration measured  $\Psi(0.3/R)$  for jets with  $0.1 < |y| < 0.7$  as a function of jet  $p_T$  and found higher values of  $\Psi$  at high  $p_T$  as expected since jets are more quark like [11]. This measurement also helps tuning the PYTHIA and HERWIG generators since it is sensitive to underlying events in particular.

The CDF collaboration also studied the jet shapes for  $b$ -jets in four different  $p_T$  bins [12], and the result is given in Fig. 6. The default PYTHIA and HERWIG Monte Carlo in black full and dashed lines respectively are unable to describe the measurement. Compared to the inclusive jet shape depicted in Fig. 6 in full red line for PYTHIA, the tendency of the  $b$ -jet shape is definitely the right one, leading to smaller values of  $\Psi$  as expected, but the measurement leads to a larger difference. The effect of reducing the single  $b$ -quark fraction by 20% leads to a better description of data as shown in green in Fig. 6. The fraction of  $b$ -jets that originate from flavour creation (where a single  $b$ -quark is expected in the same jet cone) over those that originate from gluon splitting (where two  $b$ -quarks are expected in the same jet cone) is different in Monte Carlo and data.

The CDF collaboration also measured the  $b\bar{b}$  dijet cross section as a function of the leading jet  $p_T$  and the difference in azimuthal angle between the two jets and it leads to the same conclusion, namely that PYTHIA and HERWIG underestimate the gluon splitting mechanism [5].

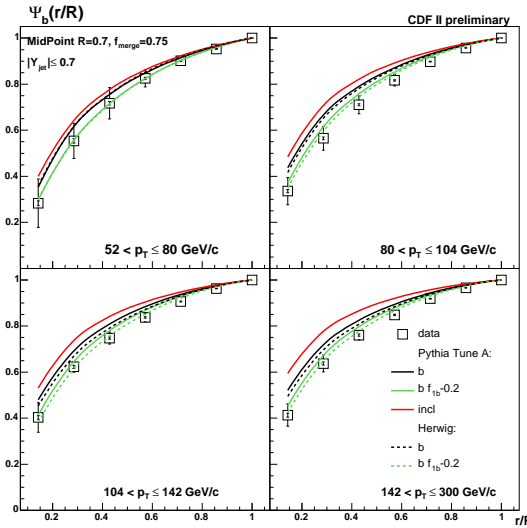


Figure 6: Measurement of the  $b$ -jet shapes and comparison with the predictions of the PYTHIA and HERWIG Monte Carlo (see text).

## 4 Underlying events at Tevatron and LHC

The CDF collaboration measured underlying events at the Tevatron and used these measurements to tune in particular the PYTHIA generator.  $pp$  or  $p\bar{p}$  interactions are namely not as simple as interactions in  $ep$  colliders. In addition to the hard scattering producing dijets, high  $p_T$  leptons..., spectator partons produce additional soft interactions called underlying events. The main consequence is that it introduces additional energy in the detector not related to the main interaction which need to be corrected.

To study this kind of events, the idea is quite simple. It is for instance possible to use dijet events and we can distinguish in azimuthal angle three different regions: the “toward” region around the leading jet direction defined by a cone of 60 degrees around the jet axis, the “away” region in the opposite direction to the jet, and the “transverse” region the remaining regions far away from the jet and the “away” region. In dijet events, the “transverse” region will be dominated by underlying events. The CDF collaboration measured the charged multiplicity and the charged transverse energy as a function of jet transverse energy and used these quantities to tune the PYTHIA Monte Carlo leading to the so called Tune A and Tune AW [5].

Clean Drell Yan events can also be used to tune underlying events [5]. The lepton pair defines the “toward” region while the “away” and “transverse” regions are defined in the same way as for dijets. As an example, we give in Fig. 7 the charged particle density as a function of the transverse momentum of the lepton pair in the three regions compared with the Tune AW of PYTHIA.

At the LHC, one of the first measurements to be performed will be related to the tuning of underlying events in the generators. Present tunings between the different Monte Carlo (PYTHIA, PHOJET, HERWIG) show differences up to a factor six concerning the average multiplicity of charged particles as a function of the  $p_T$  of the leading jet as an example, and it is crucial to tune the Monte Carlo to accomplish fully the LHC program.

## 5 Measurements of the $W$ +jet and $Z$ +jet cross sections at the Tevatron

The measurements of the  $W$ +jet and  $Z$ +jet cross sections are specially important since they are a background for many searches and especially the search for the Higgs boson.

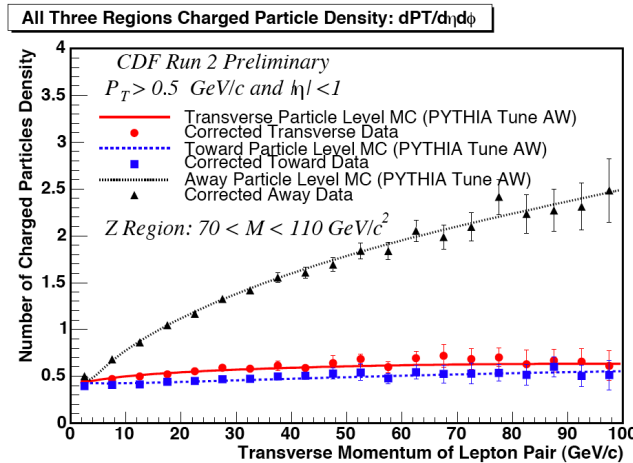


Figure 7: Measurement of the charged particle density for Drell Yan events in the “toward”, “away” and “transverse” regions compared to PYTHIA Tune AW.

## 5.1 Measurements of the $W + X$ cross sections

The D0 collaboration measured the ratio of the  $W + c$  to the inclusive cross section  $0.074 \pm 0.019$  (stat.)  $\pm 0.012$  (syst.) in agreement with NLO calculation [13]. It will be important to redo this measurement with higher statistics since it is directly sensitive to the  $s$ -quark PDF.

The  $W + X$  cross section measurement at the LHC is considered to be one of the “standard” candles with small theoretical uncertainties (the NNLO scale dependence is less than 1%) and could be used even for luminosity measurements. Unfortunately, the PDFs are not so well known in the kinematical region where the  $W + X$  cross section is measured. The average value of  $x$  ( $< x > \sim 7.10^{-3}$  with  $5.10^{-4} < x < 5.10^{-2}$ ) is not in the valence region and thus not in the region where quarks are best known. The differences between PDFs lead to an uncertainty on the  $W + X$  cross section of the order of 8% which is not precise enough to be used as a luminosity monitor. An independant better determination of the PDFs would change the conclusions.

## 5.2 Measurement of the $Z + b$ and $W + b$ cross sections

The motivation to measure the  $Z + b$ -jet cross section is quite clear: this is a direct background for Higgs boson searches and it is also sensitive to the  $b$  quark content of the proton. The measurements of the  $Z + b$ -jet and  $W + b$ -jet cross sections were performed by the CDF collaboration at the Tevatron  $\sigma(Z + b \text{ jets}) = 0.86 \pm 0.14 \pm 0.12 \text{ pb}$  and  $\sigma(W + b - \text{jets}) \times BR(W \rightarrow l\nu) = 2.74 \pm 0.27(\text{stat.}) \pm 0.42(\text{sys.})$

pb in agreement with NLO calculations and PYTHIA predictions [14]. The CDF collaboration also compared the differential distributions in jet  $p_T$  and rapidity as an example and the distributions are found in good agreement with PYTHIA.

## 6 Forward jets and Mueller Navelet jets

### 6.1 Low $Q^2$ jets at HERA

We discussed so far only high  $E_T$  jets at high  $Q^2$  and the question raises about what happens at low  $Q^2$  and how low in  $Q^2$  and jet  $p_T$  is perturbative QCD at NLO reliable. In other words, BFKL [15] effects are supposed to appear at very low  $Q^2$ . The H1 collaboration measured the inclusive jet cross section differentially in  $Q^2$  ( $d\sigma/dQ^2$ ) for jet  $p_T$  greater than 5 GeV and a discrepancy of about a factor 2 between NLO calculations and the measurement is found for  $Q^2 \sim 6$  GeV $^2$ . The reason can be due to missing higher order effects (NNLO) or missing low  $x$  resummation terms present in the BFKL equation [16].

To test further the low  $x$  dynamics, the H1 and ZEUS collaborations measured forward jet production cross sections. The idea is simple: we ask jets to be emitted in the “forward” region, as far as possible in rapidity from the scattered electron. When the jet  $p_T^2$  and the virtual photon  $Q^2$  are close, the DGLAP NLO cross section [17] is expected to be small because of the  $k_T$  ordering of the partons in the ladder in the DGLAP evolution. The BFKL cross section is expected to be much higher since there is no  $k_T$  ordering of the emitted gluons. The kinematical region probed by the H1 collaboration is  $10^{-4} < x < 4.10^{-3}$ ,  $p_T(jet) > 3, 5$  GeV,  $7 < \theta_{jet} < 20$  degrees,  $0.5 < p_T^2/Q^2 < 5$  to enhance the BFKL resummation effects [18]. A discrepancy between NLO QCD prediction and the measurement is found on the differential forward jet  $d\sigma/dx$  cross section at low  $x$  (the discrepancy is about a factor 3 for  $x \sim 0.0005$ . The H1 collaboration also looked at the production cross section of two forward jets and one central jet and some discrepancy is found again at low  $x$ .

To study further how one moves from the BFKL dynamics to the DGLAP one, the H1 collaboration measured the triple differential jet cross section  $d\sigma/dxdp_T^2dQ^2$  [18] as a function of  $x$  for different regions in  $Q^2$  and  $p_T^2$ . The measurement is shown in Fig. 8 [19]. The NLO QCD prediction is displayed in dotted line and describes the cross section at high  $p_T$  but not at low  $p_T$  where it undershoots the data. The LL BFKL prediction leads to a good description at low  $p_T$  (or in the case when  $r = p_T^2/Q^2$  is close to 1 as expected since BFKL effects are dominant in this kinematical region, and overshoots the data at high  $p_T$ . BFKL NLL leads to a good description of data over the full range. In Fig. 8, we display two different resummation schemes for BFKL NLL called S3 and S4 which both lead to a good description [19]. It is worth noticing that implementing the higher-order corrections in the impact factor due to exact gluon kinematics in the  $\gamma^* \rightarrow q\bar{q}$  transition improves further the description of

data [19]. This measurement shows a clear discrepancy with DGLAP NLO calculation and is well described by the NLL BFKL formalism, and it would be nice to know the effects of higher orders corrections of the DGLAP prediction.

The ZEUS collaboration also studied the forward jet cross section. They measure the 3 jet cross section and they see a disagreement with NLO QCD when the jets are in the forward region [18].

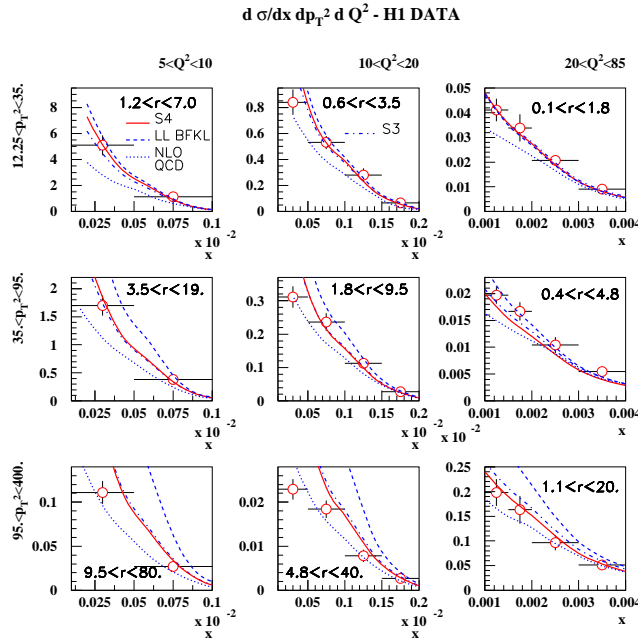


Figure 8: Triple differential cross section measured by the H1 collaboration.

## 6.2 Mueller Navelet jets at the Tevatron and the LHC

The same idea as the forward jets at HERA can be used at the Tevatron and the LHC. Mueller Navelet jets are jets produced in  $pp$  and  $p\bar{p}$  collisions, requiring these two jets to be as far away as possible in rapidity, and to have about the same transverse momentum. For the same reason as for forward jets, the  $k_T$  ordering of the gluons of the ladder ensures that the DGLAP cross section is low whereas the BFKL one is expected to be higher. Another easier observable is the measurement of the difference in azimuthal angle between the two forward jets. Since there are few gluons emitted for the DGLAP evolution, the  $\Delta\Phi$  value is peaked towards  $\pi$  whereas the BFKL expectation will be a flatter distribution in  $\Delta\Phi$  because of the emitted gluons. This

measurement can be performed at the Tevatron and the LHC and can be a test of BFKL resummation effects [20].

## 7 Conclusion

In this short report, we presented many new results from HERA and the Tevatron concerning jet physics and also some expectations for the LHC. In particular, the new measurement of the inclusive jet cross section at the Tevatron is complementary to the HERA jet cross section measurements and is fundamental to constrain further the gluon density at high  $x$ , which is useful for searches at the LHC in the jet channel, especially for a better knowledge of background. The multijet cross section measurements is also in agreement with NLO QCD calculations and is also fundamental for the LHC. The  $\gamma$ +jet cross sections is in discrepancy with NLO calculation and the reason is unclear. The  $W$ +jet and  $Z$ +jet cross sections are in general in agreement with NLO calculations but the uncertainties are still large and will benefit from higher statistics. We finished the report by describing the forward jet and Mueller Navelet jet measurements which are sensitive to low  $x$  resummation effects given by the BFKL equation. Many other topics such as diffraction and the search for diffractive exclusive events in the jet channel by the CDF collaboration, and the implications for the LHC diffractive program were not described because of lack of time [21]

## References

- [1] A. Aktas *et al.*, JHEP 0710:042 (2007); A. Aktas *et al.*, Phys. Lett. B**653** (2007) 134; C. Adloff *et al.*, Eur. Phys. J. C**29** (2003) 497; S. Chekanov *et al.*, Nucl. Phys. B **765** (2007) 1; S. Chekanov *et al.*, Eur. Phys. J. C **42** (2005) 1.
- [2] C. Adloff *et al.*, Eur. Phys. J. C **30** (2003) 1; S. Chekanov *et al.*, Phys. Rev. D **78** (2008) 032004.
- [3] V. M. Abazov *et al.*, Phys. Rev. Lett. 101 (2008) 062001; A. Abulencia *et al.*, Phys. Rev. D **75**, 092006 (2007); Phys. Rev. D **74**, 071103 (2006).
- [4] W.K. Tung *et al.*, JHEP **0702**, 053 (2007); J. Pumplin *et al.*, JHEP **0207**, 12 (2002); D. Stump *et al.*, JHEP **0310**, 046 (2003); A.D. Martin *et al.*, Phys. Lett. B **604**, 61 (2004).
- [5] see <http://www-cdf.fnal.gov/physics/new/qcd/QCD.html>.
- [6] V. M. Abazov *et al.*, Phys. Rev. Lett. 94 (2005) 221801.
- [7] T. Sjöstrand *et al.*, Comp. Phys. Comm. **135**, 238 (2001).

- [8] G. Marchesini *et al.*, Comp. Phys. Comm. **67**, 465 (1992).
- [9] S. Chekanov *et al.*, preprint arXiv:0802.3955; S. Chekanov *et al.*, Nucl. Phys. B **786** (2007) 152; F. D. Aaron *et al.*, Eur. Phys. J. C **54** (2008) 389.
- [10] V. M. Abazov *et al.*, Phys. Lett. B**666** (2008) 435.
- [11] D. Acosta *et al.*, Phys. Rev. D**71** (2005) 112002.
- [12] A. Abulencia *et al.*, preprint ArXiv:0806.1699.
- [13] V. M. Abazov *et al.*, Phys. Lett. B**666** (2008) 23; T. Aaltonen *et al.*, Phys. Rev. Lett. **100** (2008) 091803.
- [14] A. Abulencia *et al.*, Phys. Rev. D**74** (2008) 032008; see <http://www-cdf.fnal.gov/physics/new/qcd/QCD.html>.
- [15] L.N. Lipatov, Sov. J. Nucl. Phys. **23** (1976) 338; E.A. Kuraev, L.N. Lipatov and V.S. Fadin, Sov. Phys. JETP **45** (1977) 199; I.I. Balitsky and L.N. Lipatov, Sov. J. Nucl. Phys. **28** (1978) 822.
- [16] A. Aktas *et al.*, Eur. Phys. J. C**37** (2004) 141.
- [17] G. Altarelli and G. Parisi, Nucl. Phys. B**126** 18C (1977) 298; V.N. Gribov and L.N. Lipatov, Sov. J. Nucl. Phys. (1972) 438 and 675; Yu.L. Dokshitzer, Sov. Phys. JETP **46** (1977) 641.
- [18] A. Aktas *et al.*, Eur. Phys. J. C**46** (2006) 27; S. Chekanov *et al.*, Phys. Lett. B**632** (2006) 13; F. D. Aaron *et al.*, Eur. Phys. J. C **54** (2008) 389; S. Chekanov *et al.*, Eur. Phys. J. C **52** (2007) 515.
- [19] O. Kepka, C. Marquet, R. Peschanski, C. Royon, Eur. Phys. J. C**55** (2008) 259; Phys. Lett. B**655** (2007) 236; C. Marquet, R. Peschanski, C. Royon, Phys. Lett. B**599** (2004) 236; C. Marquet, C. Royon, Nucl. Phys. B**739** (2006) 131; J.G. Contreras, R. Peschanski, C. Royon, Phys. Rev. D**62** (2000) 034006;
- [20] A.H. Mueller and H. Navelet, Nucl. Phys. B**282** (1987) 727; Azimuthal decorrelation of Mueller-Navelet jets at the Tevatron and the LHC, C. Marquet, C. Royon, preprint arXiv:0704.3409; A. Sabio Vera, F. Schwennsen, Nucl. Phys. B**776** (2007) 170.
- [21] T. Aaltonen at al., Phys. Rev. D**77** (2008) 052004; O. Kepka, C. Royon, Phys. Rev. D **76** (2007) 032012; Phys. Rev. D **78** (2008) 073005.

# **QCD at the HERAscale and implications at the Terascale**

*Achim Geiser*

*DESY, D-22603 Hamburg, Germany*

*E-mail: Achim.Geiser@desy.de*

## **1 Introduction**

The HERA data of ep collisions at  $\sqrt{s} = 318$  GeV currently offer one of the best opportunities to test and improve our understanding of the theory of Quantum Chromo Dynamics (QCD). HERA data taking has ended in 2007, but most of the results using the full HERA statistics are still in preparation, and will continue to provide new and improved results.

QCD can be probed in high energy electron proton collisions in several different ways. The study of the structure of the proton yields direct measurements of the parton density functions at high energies. Jet measurements (also covered in a separate contribution [1]) yield complementary insights into higher order QCD corrections, and both taken together allow the (experimentally) most precise determinations of the strong coupling constant,  $\alpha_s$ . The study of semi-inclusive final states like heavy flavour production and diffraction yield further complementary information about both perturbative and non-perturbative QCD. Most of the measurements obtained at HERA (at the “HERAscale”) have direct consequences in the context of current and future measurements at the Tevatron and at the LHC (at the Terascale). The goal of this contribution is to highlight some of the most important of these measurements, and their implications at the Terascale.

## **2 Proton structure**

Understanding the structure of the proton in terms of its gluon and quark constituents has a threefold physics interest:

- to understand the properties of the proton in its own right.
- to understand the details of the underlying theory of QCD.
- to provide a detailed description of this structure in terms of parton densities, which are an essential input to the physics at hadron colliders such as the Tevatron and the LHC.

## 2.1 Kinematics of Deep Inelastic Scattering

The most powerful tool to study the structure of the proton is the so-called Deep Inelastic Scattering (DIS) process, in which a high energy lepton is scattered off a proton with large momentum transfer, exchanging a photon (Fig. 1) or a weak vector boson. In many cases, a measurement of the scattered lepton (e.g. electron) is sufficient to obtain access to the most relevant kinematic variables. These include

- The photon/boson virtuality  $Q^2 = -q^2$ , where  $q = l' - l$ , and  $l, l'$  are the incoming and outgoing lepton four-momenta. For  $Q^2 > m_p^2 \sim 1 \text{ GeV}^2$  details of the proton structure can be resolved, and the resolving power increases with increasing  $Q^2$ .
- The Bjorken scaling variable  $x = \frac{Q^2}{2Pq}$ , where  $P$  is the four-momentum of the incoming or target proton. In the case where the scattering is interpreted to occur off a single light quark (parton) inside the proton (quark-parton model process, QPM, Fig. 1),  $x$  measures the fraction of the proton momentum carried by this parton.
- The inelasticity  $y = \frac{qP}{lP}$ , which is a direct measure of the fraction of the lepton momentum transferred to the exchanged boson. In contrast to  $x$ , this variable remains meaningful even in the limit  $Q^2 < 1 \text{ GeV}^2$  (quasi-real photon), called photoproduction.

The variables  $Q^2$ ,  $x$ , and  $y$  are not independent, and any set of two of them is sufficient to fully describe the lepton part of the scattering. They can be converted into each other via the relation  $Q^2 = xys$ , where  $\sqrt{s}$  is the center-of-mass energy of the lepton-proton system.

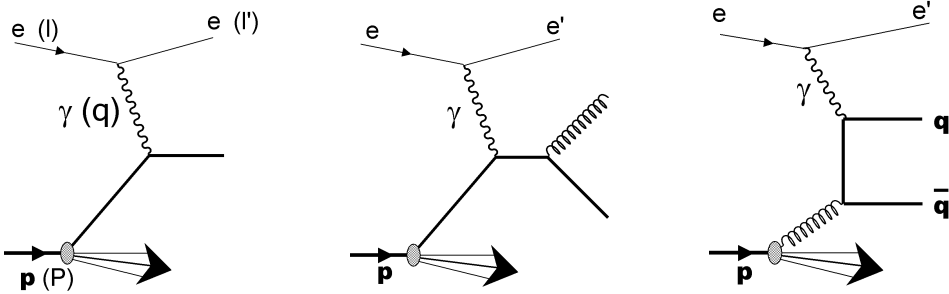


Figure 1: Kinematics of ep scattering for the leading Quark Parton Model process with photon exchange (QPM, left) and graphs for first order QCD corrections: the QCD Compton process (center) and boson gluon fusion (BGF, right).

## 2.2 Structure Functions and Parton Densities

The double differential cross section as a function of  $x$  and  $Q^2$  for the scattering of charged leptons (charge  $\pm 1$ ) off a proton can be parametrized in terms of so-called proton structure functions  $F_2$ ,  $F_L$ , and  $xF_3$

$$\frac{d^2\sigma}{dxdQ^2} = \frac{2\pi\alpha^2}{Q^4x} \quad \left\{ [1 + (1 - y)^2]F_2(x, Q^2) \right. \\ \left. - y^2F_L(x, Q^2) \right. \\ \left. \mp [1 - (1 - y)^2]xF_3(x, Q^2) \right\}$$

In most general terms, this is nothing but a breakdown of the cross section into a complete set of terms with different  $y$ -dependence. It is motivated by the possibility to identify these terms with different physics contributions.

For instance, considering only the simple QPM (0<sup>th</sup> order QCD) graph of Fig. 1, the structure function  $F_2$  can be understood as a direct measurement of the quark plus antiquark content of the proton according to the formula

$$F_2^{em}(x, Q^2) = x \sum_i e_i^2 [q_i(x, Q^2) + \bar{q}_i(x, Q^2)]$$

where  $q_i$  indicates the probability density of finding a quark of flavour  $i$  and momentum fraction  $x$  in the proton (quark density function) at the virtuality scale  $Q^2$ ,  $e_i$  is the quark electric charge, and the sum runs over all flavours. For weak boson exchange the charge coefficients have to be adjusted accordingly, and mass as well as electroweak interference effects have to be taken into account.

Including first order (Fig. 1) and higher order QCD corrections, and/or non-negligible quark masses, such as for heavy quarks, this simple relation gets spoiled. In general, a measurement of the structure functions is thus *not* a direct measurement of the quark densities any more. However, these QCD and mass corrections are calculable and can be unfolded, such that the quark densities can still be extracted. In addition, the gluon density can also be obtained from these corrections, e.g. from the boson-gluon fusion (BGF) contribution (Fig. 1), and from the QCD evolution of the quark densities (Fig. 2). The gluon and quark densities are generically referred to as parton density functions (PDFs). The measurement and extraction of such PDFs is necessary because, due to the smallness of the quark and gluon masses, they can not be obtained from QCD using perturbative methods, and nonperturbative results, e.g. from lattice QCD, are not yet precise enough to be useful.

Note that this leads to varying definitions of the variables  $x$  and  $Q^2$ , depending on the context. In the context of the measurement of nucleon structure functions through electroweak scattering,  $x$  and  $Q^2$  are always strictly defined according to the mathematical definitions in section 2.1. On the other hand, in the PDFs,  $x$

refers to the momentum fraction of the nucleon carried by the parton in the infinite momentum frame, while  $Q^2$  refers to any hard scale at which the parton densities are probed, which can be e.g. the virtuality of a quark or gluon in a purely hadronic interaction. The two definitions coincide only in the simplest form of Quark Parton Model scattering. This is a frequent source of confusion.

The structure function  $F_L$  reflects the (small) contribution from longitudinally polarized photons, and is strongly dependent upon the gluon density. It is only relevant at high  $y$ . For measurements not sensitive to the high  $y$  region, it can often be safely neglected. In regions where it cannot be neglected, one can define the so-called reduced cross section

$$\sigma_r(x, Q^2) = F_2(x, Q^2) - \frac{y^2}{1 + (1 - y)^2} F_L(x, Q^2)$$

which is the quantity actually measured in the experiment, while both  $F_2$  and  $F_L$  are derived quantities. The first direct determination of  $F_L$  was one of the primary goals of the last months of HERA running. Since this is covered by a separate contribution [2] it will not be discussed further here.

The structure function  $xF_3$  is sensitive to quark-antiquark asymmetries related to weak interactions. For neutral current (NC,  $\gamma/Z$  exchange) interactions it is therefore only relevant at high  $Q^2$ , when electroweak interference effects become important. Again, this part and the related electroweak fits are covered by a separate contribution [3].

## 2.3 The structure function $F_2$

Fig. 3 shows a combination of all relevant measurements [4] of the reduced cross section (essentially  $F_2$ ) as a function of  $x$  and  $Q^2$  from HERA I results and fixed target experiments, together with a QCD-based parametrization. The positive slope with respect to  $Q^2$  (so-called scaling violations) at low  $x$  is caused by the splitting of gluons into  $q\bar{q}$  pairs, which becomes visible at high resolution (high  $Q^2$ ), while the negative slope at high  $x$  is caused by gluon radiation from the high  $x$  valence quarks, reducing their effective energy/momentum when looked at with increasing resolution (Fig. 2).

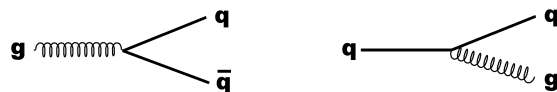


Figure 2: Diagrams contributing to the PDF evolution in leading order QCD. Gluon splitting to quarks (left) and gluon radiation off a quark (right).

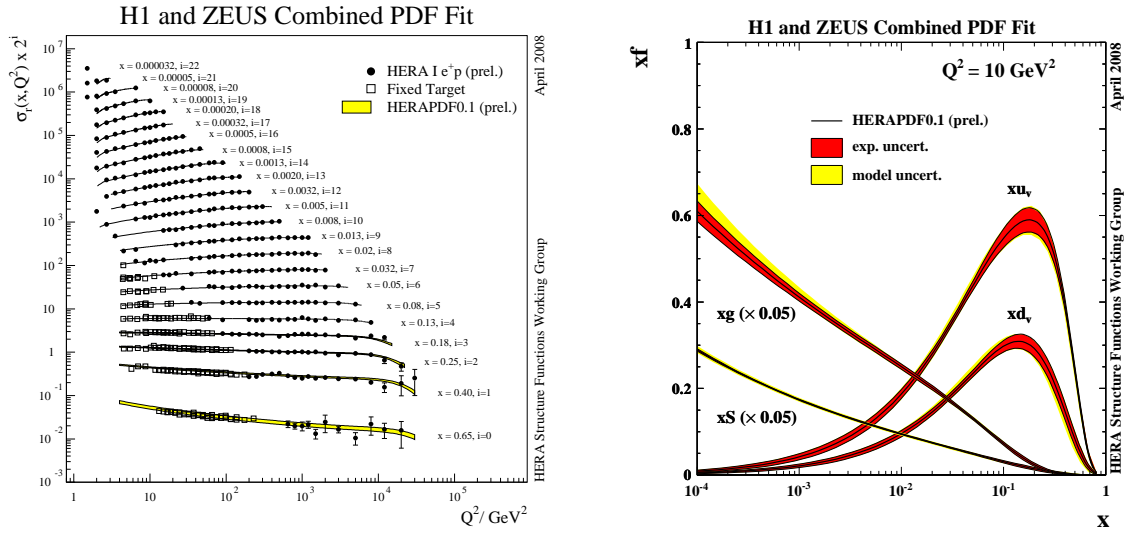


Figure 3: Left: The reduced cross section  $\sigma_r$  as a function of  $Q^2$  for different values of  $x$ , compared to the HERAPDF0.1 fit [4]. For better visibility, offsets have been applied to each curve as indicated in the axis label. Right: The parton density functions ( $u$  and  $d$  valence quarks, sea quarks, and gluons) as a function of  $x$  at  $Q^2 = 10 \text{ GeV}^2$ . For better visibility, the sea and gluon distributions have been scaled down by a factor 20.

This so-called DGLAP parton evolution [5] is predicted by perturbative QCD and uniquely fixes the theoretical parametrization at any  $Q^2$  once a parametrization at a given initial  $Q^2$  is given. Combined with global energy and momentum conservation, this significantly constrains the gluon density function. In addition to a reduction of the statistical error, the combination of data points from ZEUS and H1 also leads to a reduction of the systematic error through the so-called cross-calibration effect [4].

Fig. 3 also shows a parametrization [4] of all these measurements in terms of the parton densities at the scale  $Q^2 = 10 \text{ GeV}^2$ . While the valence quark distributions (difference between quark and antiquark distributions) peak at high  $x$  values, the gluon and sea quark distributions rise strongly at low  $x$ , as expected from the DGLAP parton evolution. The data combination procedure mentioned above allows a very significant reduction of the experimental errors of the parton density extraction, reflected by the small uncertainty bands in Fig. 3. The model uncertainties within the ZM-VFNS scheme (see below), in which these PDFs have been extracted, are also indicated. Further improvements are expected on the experimental side from the inclusion of HERA II data, and on the theoretical side by including heavy quark mass effects.

Fig. 4 shows the kinematic range covered by experiments which contribute to the measurements of the parton densities. In addition to the lepton nucleon scattering

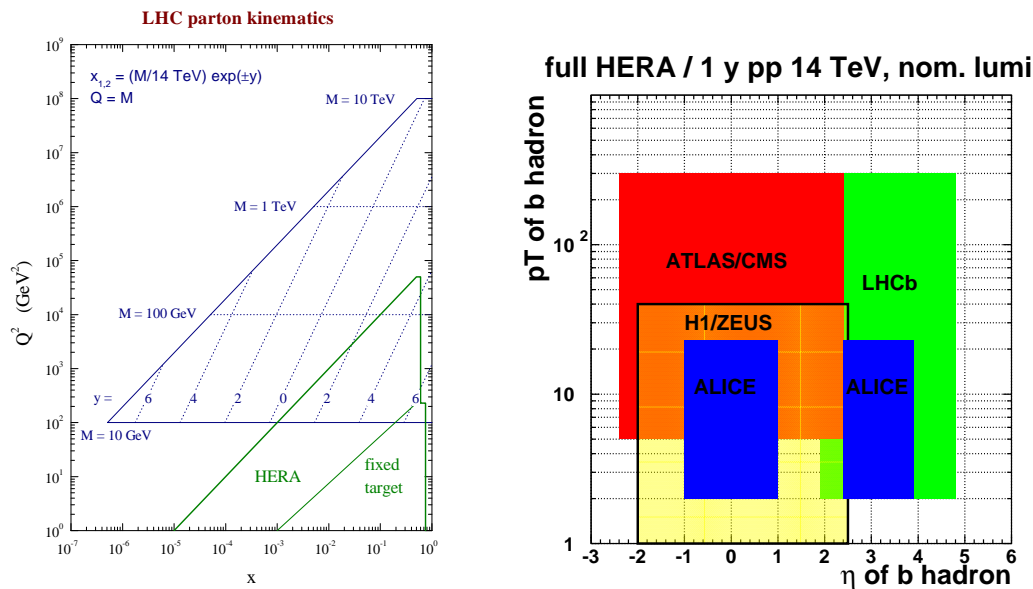


Figure 4: Left: Kinematic plane in  $x$  and  $Q^2$  probed by HERA, fixed target experiments, and the LHC [6]. Right: kinematic acceptance for beauty production at LHC for 1 year of running at nominal luminosity [7] (boxes without boundary) compared to beauty production at HERA for the full final dataset (box with boundary).

experiments, measurements at the Tevatron  $p\bar{p}$  collider also contribute at high  $Q^2$ . The kinematic region relevant for measurements at the LHC is also shown, as a grid indicating the relevant mass and detector rapidity regions. Despite significant overlap between this region and the HERA+Tevatron measurements, a large fraction of the phase space is not covered by direct measurements at other colliders. It therefore has to be (and can be) extrapolated from the measurements at lower  $Q^2$  through QCD parton evolution as explained above. On the other hand, there is also significant overlap in the kinematic coverage for the measurement of specific final states, as illustrated by the example of beauty production in Fig. 4.

Most cross sections at LHC depend on the square of either the quark or the gluon distributions. This illustrates the importance of a precise determination of these PDFs, both through direct measurements and through the detailed understanding of the QCD parton evolution, even at lower energies.

In the early 1980s, the PDFs determined and evolved at leading order (LO) from structure function measurements at fixed target energies [8] were used very successfully to predict the cross sections for W,Z and jets to be expected at the CERN SppS collider. The current state of the art uses next-to-leading order (NLO) QCD evolution to predict the cross sections at LHC from the measurements at HERA (and the

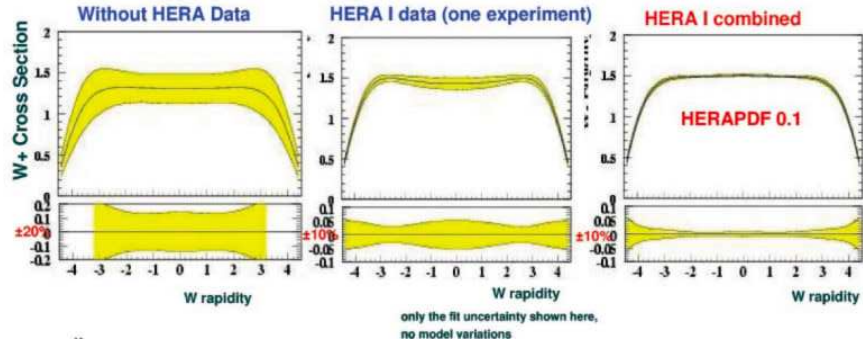


Figure 5: Predictions [9] for  $W$  production at LHC using fixed target data only (left) HERA I data from one of the two experiments (center) and the combined HERAPDF0.1. Only the experimental uncertainties are shown here for illustration.

Tevatron), with first successful attempts to go beyond NLO accuracy.

Predictions for the production of  $W$  bosons at LHC without using HERA data, using the HERA I results from one experiment only, and using the HERAPDF0.1 (with experimental uncertainties only) are shown in Fig. 5. The improvement is obvious.

## 2.4 The heavy flavour contribution to $F_2$

In general, all quark flavours contribute to  $F_2$  at all values of  $Q^2$  and  $x$ . However, if  $m_Q$  is the mass of a heavy quark (charm or beauty), the  $0^{th}$  order QPM process in Fig. 1 is kinematically allowed only for  $Q^2 > (2m_Q)^2$  (“heavy quark threshold”), and its kinematics is strongly affected by the quark mass until  $Q^2 \gg (2m_Q)^2$ . In the latter case the mass becomes negligible, and the theory can be treated as if the heavy quarks were massless. A PDF can be defined for them like for the light quarks (zero mass variable flavour number scheme, ZM-VFNS). For  $Q^2 \lesssim (2m_Q)^2$  a description is possible only in terms of  $1^{st}$  or higher order QCD processes (e.g. the BGF process in Fig. 1), in which the heavy quarks are only produced perturbatively in the matrix element, with no heavy quarks in the PDFs. Since heavy flavour final states are always perturbatively calculable ( $m_Q \gg \Lambda_{QCD}$ ) this so-called fixed flavour number scheme (FFNS) can be analytically continued to the full phase space as an alternative description valid at all<sup>1</sup>  $Q^2$ . In particular, the FFNS approach works down to  $Q^2 \rightarrow 0$  GeV $^2$ , i.e. the photoproduction regime. Of course, the formal values of  $Q^2$  and  $x$  in  $F_2$  become meaningless in this context, and have to be replaced by suitably chosen other kinematic variables. Finally, finite mass effects can be introduced as

<sup>1</sup>It is frequently claimed that the FFNS scheme will stop being valid at high  $Q^2$  due to the occurrence of corrections of the type  $\log(Q^2/m_Q^2)$ . This is correct in principle. However, within most of the kinematic range of HERA, such logs turn out not to be numerically very important.

corrections to the ZM-VFNS scheme at medium  $Q^2$ , and smoothly matched to a pure FFNS treatment at low  $Q^2$ . This so-called general mass variable flavour number scheme (GM-VFNS) is an alternative to the FFNS scheme valid at all  $Q^2 \gtrsim 1 \text{ GeV}^2$ . However, in higher order corrections, the mass treatment differs in different variants of this scheme [10].

At high  $Q^2$ , charm and beauty quark densities can then be extracted in analogy to light quarks, and be applied to other high energy processes such as  $b\bar{b} \rightarrow Z, H$  production at LHC. This contribution to the  $Z$  final state is relevant for the absolute luminosity measurement at LHC, while the Higgs ( $H$ ) boson final state represents an obvious interest by itself.

Heavy flavours such as charm and beauty thus need some special treatment for the interpretation of  $F_2$  in terms of PDFs, and it is interesting to measure their contribution separately. In order to determine the primary quark flavour which has participated in the interaction, this flavour has to be tagged and identified. In contrast to inclusive  $F_2$  measurements, it is thus necessary to measure details of the hadronic final state. The contributions to  $F_2$  which contain a pair of charm or beauty quarks in the final state are often denoted by  $F_2^{c\bar{c}}$  and  $F_2^{b\bar{b}}$ , respectively. A summary of measurements of these contributions are shown in Fig. 6.

Below and around the QPM “threshold” at  $Q^2 \sim (2m_Q)^2$ , an interpretation of  $F_2^{Q\bar{Q}}$  ( $Q = c, b$ ) in terms of quark density functions is not possible. Instead, its interpretation in terms of QCD contributions like the BGF diagram in Fig. 1 can be used to verify the gluon density.

As can be seen from Fig. 6 the spread of the theory predictions due to the choice of scheme, QCD reference scale, value of the heavy quark mass, and other effects is still quite large. While the precision of the data will increase further (so far, only a fraction of the available data has been analyzed) these uncertainties will have to be reduced in order to allow a high precision determination of e.g. the gluon density from these data.

In summary, in view of the increasing precision of the data, no single theoretical scheme has been identified so far which simultaneously and fully satisfactorily treats all aspects of the (at least) three different QCD scales  $Q^2$ ,  $m_Q$ , and  $p_T$  at NLO or beyond. This is known as the multiple hard scale problem. While this often leads to complications for the prediction of heavy-flavour-related cross sections, its effect on the predictability of inclusive cross sections (which contain heavy flavours) is fortunately much smaller, but not negligible.

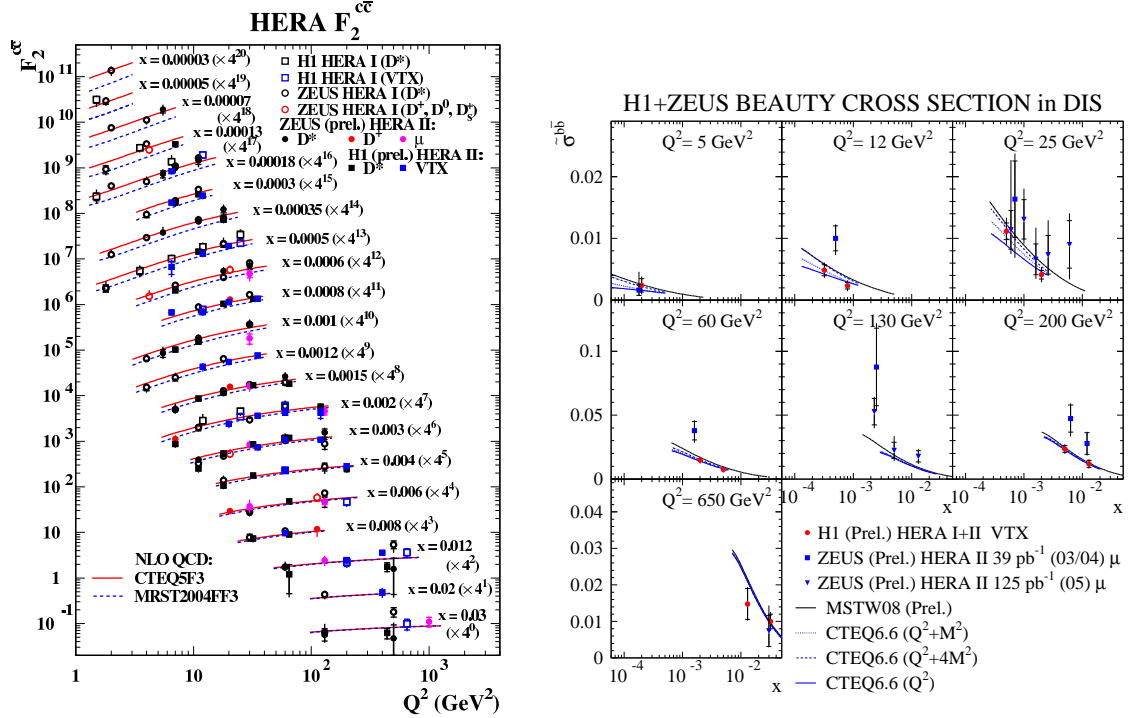


Figure 6: Left: The charm contribution to the proton structure function,  $F_2^{cc}$ , as a function of  $Q^2$  for different values of  $x$ , compared to two FFNS predictions. For better visibility, offsets have been applied to each curve as indicated on the plots. Right: The reduced cross section for the beauty contribution to the proton structure function,  $\tilde{\sigma}^{bb}$ , as a function of  $Q^2$  for different values of  $x$ , compared to different GM-VFNS predictions.

### 3 Global QCD fits and the strong coupling constant

The possibility to test or constrain the gluon distribution through the measurement of heavy flavours, e.g. from boson gluon fusion, was already addressed in the previous section. In a similar way, light quark cross sections can also be used in both DIS and photoproduction if another hard scale is present, such as a high transverse momentum ( $p_T$ ) of the quarks, manifesting itself through the occurrence of high  $p_T$  jets in the final state.

Since jet production is also sensitive to the value of  $\alpha_s$  (NLO calculations are available), a global simultaneous QCD fit to both  $F_2$  and jet cross sections [11] can be made, so far to ZEUS data only. This indeed yields an improved gluon PDF (Fig. 7) as well as one of the currently best measurements of  $\alpha_s$ ,

$$\alpha_s(M_Z) = 0.1183 \pm 0.0028(\text{exp.}) \pm 0.0008(\text{model}) \pm 0.0050(\text{th.})$$

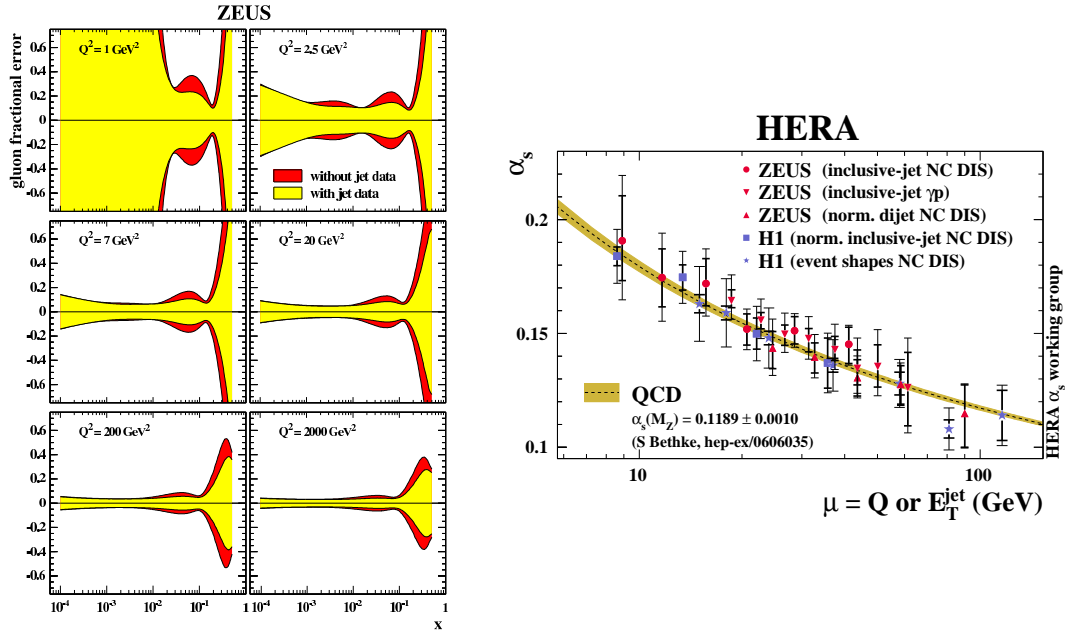


Figure 7: Left: The gluon density from ZEUS data as a function of  $x$  at different values of  $Q^2$ , with and without the inclusion of jet data into the fit. A significant improvement can be seen. Right: Determinations of  $\alpha_s$  at HERA from many different final states. The running of  $\alpha_s$  is clearly visible.

where the first error contains the experimental errors, the second refers to model uncertainties in the  $\alpha_s$  extraction, and the third reflects the usual scale variations of the NLO QCD predictions. Like in most  $\alpha_s$  measurements to NLO, the theoretical uncertainties unfortunately dominate.

Global fits also including charged current data and electroweak effects, which can yield further improvements, are treated elsewhere [3].

Alternative determinations of the strong coupling constant  $\alpha_s$  can be obtained from many dedicated measurements at HERA (Fig. 7). A subset of these measurements, selected to minimize the theoretical uncertainties, has been used for a first combined measurement from both ZEUS and H1 data. The resulting value

$$\alpha_s(M_Z) = 0.1193 \pm 0.0019(\text{exp.}) \pm 0.0026(\text{th.})$$

has an experimental error which is significantly smaller than each of the input measurements, but is still dominated by the theoretical uncertainty.

A recent measurement of H1 [15], aiming at a minimization of the experimental uncertainties, has obtained a value

$$\alpha_s(M_Z) = 0.1193 \pm 0.0014(\text{exp.})^{+0.0047}_{-0.0030}(\text{th.}) \pm 0.0016(\text{pdf}).$$

Combining such results between H1 and ZEUS, and integrating them into global fits, is expected to further reduce the experimental uncertainties. The goal to reduce the theoretical uncertainties through NNLO calculations should thus be of utmost priority. Once available, they will allow the worlds most precise determinations of the strong coupling constant. If supersymmetry is discovered at LHC, this could e.g. be decisive to determine whether the three Standard Model coupling constants can be merged into a single one at some very high scale in the context of supersymmetric Grand Unified Theories.

## 4 Parton dynamics at low $x$

From Fig. 4 it is evident that the very low  $x$  region is particularly relevant for LHC. Since no direct measurements exist in this region, parton evolution from high to low  $x$  and/or low to high  $Q^2$  is needed. A study of the low  $x$  region at HERA reveals that such an evolution is not trivial.

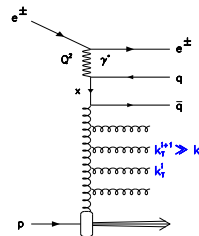


Figure 8: Feynman graph for multijet production at HERA involving an initial state gluon ladder.

Fig. 8 shows the example of a Feynman graph involving multiple initial state gluon radiation (gluon ladder). At HERA, such gluons can lead to detectable jets in the forward (proton) direction [12]. From the theoretical point of view, they can be treated as part of the matrix elements, which then have to be calculated to a very high order, which is difficult in practice. Alternatively, they can be treated as parton showers, using different evolution schemes. In the standard DGLAP [5] scheme, gluon emissions are ordered by increasing virtuality ( $k_T$ -ordering). In the alternative BFKL [13] scheme ordering in  $x$  is used instead. The two schemes can be combined into the CCFM [14] scheme which uses angular ordering. Forward jet measurements in 4-jet final states at HERA [12] show that the leading order matrix element plus next-to-leading log DGLAP parton shower approach partially fails. The NLO ( $O(\alpha_s^2)$ , effectively "LO") plus collinear DGLAP evolution scheme also fails in some cases. Going to NNLO ( $O(\alpha_s^3)$ , effectively "NLO") starts to yield a reasonable but, in the case of H1, still not perfect description. An NNNLO calculation might be needed within the DGLAP approach. Unfortunately a corresponding prediction

using BFKL evolution is not yet available. However, the prediction from the color dipole parton showering model, using  $k-T$  unordered gluons like BFKL, yields a very good agreement. This might indicate that a BFKL-like evolution can be of advantage in the low  $x$  region. Further studies and measurements are needed to quantify the consequences for cross section predictions at the LHC.

More details on this topic can be found in [1].

## 5 Photons and heavy flavours in photoproduction

Further insights into the validity of perturbative QCD can be obtained from the photoproduction of final states including direct photons or heavy flavours. As an example, a summary of measurements of the beauty production cross section is shown in Fig. 9. Reasonable agreement is observed over the full kinematic range. This enhances the confidence in corresponding QCD calculations for the LHC.

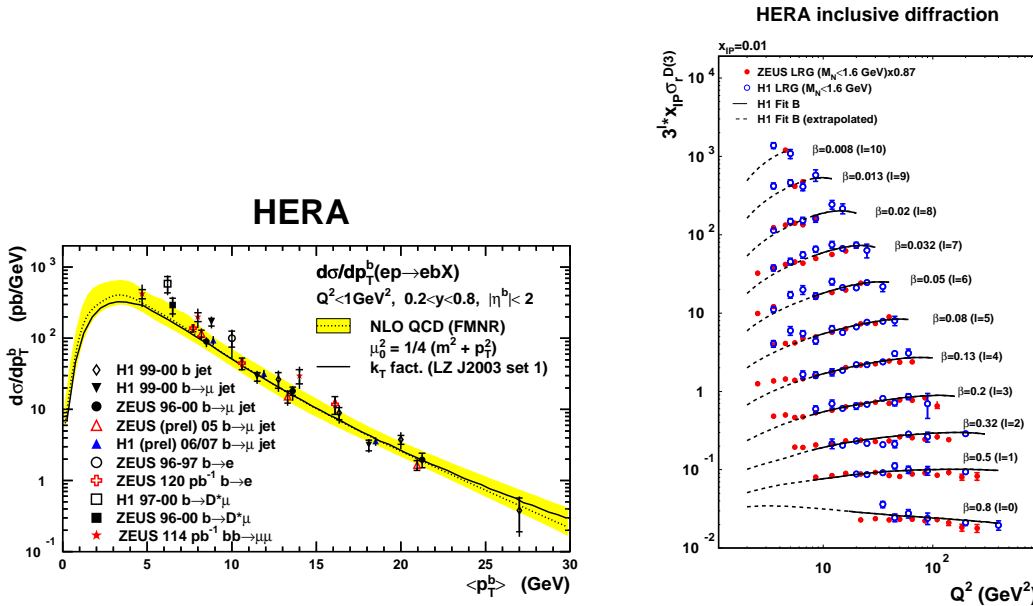


Figure 9: Left: Beauty production cross section at HERA as a function of  $p_T^b$ . QCD predictions from an NLO fixed order calculation [16], and from a calculation using the CCFM approach ( $k_T$  fact.) [17] are also shown. Right: Reduced cross section for inclusive diffractive final states in deep inelastic scattering at HERA [18]. The ZEUS data are scaled by a factor compatible with the relative normalization uncertainty of the two experiments. The continuous lines are the prediction from a QCD fit of part of these data. The dashed lines indicate predictions outside of the validity region of the fit.

## 6 Diffraction

Diffractive production (i.e. via the exchange of a colourless hadronic state with vacuum quantum numbers, sometimes called a pomeron) of vector mesons and/or inclusive hadronic final states yields another handle to study nonperturbative QCD effects and their perturbative evolution at high scales, assuming factorization. A so-called diffractive structure function can then be defined, to be understood as the fraction of the proton structure function yielding diffractive final states.

Diffractive production of vector mesons at HERA is covered in [19]. Inclusive diffraction can be studied in three different ways:

- The detection of a large rapidity gap in the hadronic final state, caused by the colorless exchange.
- The measurement of the mass distribution of the detected hadronic final state ( $M_X$  method).
- Explicit detection of a scattered unbroken proton.

Fig. 9 shows a comparison of the diffractive structure functions measured by ZEUS and H1 using the large rapidity gap method on deep inelastic scattering events. Reasonable agreement is observed. The resulting PDFs can then be used to predict other cross sections at HERA, as well as at the Tevatron and the LHC. Many of these cross sections can currently only be explained by introducing a semi-empirical rapidity gap survival (or suppression) factor. Understanding the QCD origin of this suppression is currently one of the most topical aspects of diffraction, with direct consequences e.g. for the prediction of diffractive Higgs production at the LHC.

## 7 Conclusions

HERA is currently one of the best QCD laboratories. Measurements at HERA (at the “HERAscale”) are generally in good agreement with predictions from perturbative QCD calculations, which represents a great successs of the Standard Model. They also provide valuable information for measurements at the LHC (the Terascale), such as precise parametrisations of the parton density functions, precise determinations of the strong coupling constant, and insights into the treatment of QCD at low  $x$ , the treatment of finite quark masses, and the treatment of diffractive processes. In many cases, the most precise final results with the full HERA statistics are still to come.

## References

- [1] C. Royon, these proceedings
- [2] V. Chekelian, these proceedings
- [3] E. Gallo, these proceedings
- [4] H1 and ZEUS collaborations, *QCD fits using combined H1 and ZEUS inclusive data*, H1prelim-08-045, ZEUS-prel- 08-003 (2008).
- [5] V.N. Gribov and L.N. Lipatov, Sov. J. Nucl. Phys. **15** (1972) 438;  
L. N. Lipatov, Sov. J. Nucl. Phys. **20** (1975) 95;  
G. Altarelli and G. Parisi, Nucl. Phys. **B 126** (1977) 298;  
Yu.L. Dokshitzer, Sov. Phys. JETP **46** (1977) 641.
- [6] W.J. Stirling, CAVENDISH-HEP-08-15, arXiv:0812.2341, dec. 2008.
- [7] A. Dainese et al., Proceedings of HERA and the LHC, p. 357, A. de Roeck and H. Jung (eds.), CERN-2005-014, dec. 2005.
- [8] see e.g. E. Eichten et al., Rev. Mod. Phys. **56** (1984) 579; **58** (1986) 1065.
- [9] A. Cooper-Sarkar, private communication
- [10] R. Thorne and W.K. Tung, Proceedings of HERA and the LHC (to be published), arXiv:0809.0714 [hep-ph].
- [11] ZEUS collaboration, S. Chekanov et al., Eur. Phys. J. **C 42** (2005) 1.
- [12] H1 Collaboration, A. Aktas et al., Eur. Phys. J. **C 48** (2006) 715.  
ZEUS Collaboration, S. Chekanov et al., Nucl. Phys. **B 786** (2007) 152.
- [13] E.A. Kuraev, L.N. Lipatov, and F.S. Fadin, Phys. Lett. **B 60** (1975) 50; Sov. Phys. JETP **44** (1976) 443; Sov. Phys. JETP **45** (1977) 199;  
Ya.Ya. Balitsky and L.N. Lipatov, Sov. J. Nucl. Phys. **28** (1978) 822.
- [14] M. Ciafaloni, Nucl. Phys. **B 296** (1988) 49;  
S. Catani, F. Fiorani and G. Marchesini, Phys. Lett. **B 234** (1990) 339; Nucl. Phys. **B 336** (1990) 18;  
G. Marchesini, Nucl. Phys. **B 445** (1995) 49.
- [15] H1 Collaboration, A. Aktas et al., Phys. Lett. **B 653** (2007) 134.
- [16] S. Frixione, M. L. Mangano, P. Nason and G. Ridolfi, Nucl. Phys. **B 412** (1994) 225; Phys. Lett. **B 348**, 633 (1995);  
S. Frixione, P. Nason and G. Ridolfi, Nucl. Phys. **B 454** (1995) 3.

- [17] A.V. Lipatov, N.P. Zotov Phys. Rev. **D 73** (2006) 114018.
- [18] M. Ruspa, in Proceedings of HERA and the LHC (to be published).
- [19] W. Bartel, these proceedings.

# Exotic hadron spectroscopy

*Jolanta Brodzicka*

*Institute of Nuclear Physics Polish Academy of Sciences  
Krakow, Poland*

## 1 Introduction

The recent discovery of several charmonium and charmonium-like resonances indicates a renaissance of the  $c\bar{c}$  spectroscopy. Majority of these observations have been enabled by the large data samples provided by the  $B$ -factories at SLAC and at KEK. Many of these so called  $XYZ$  states do not fit the conventional  $c\bar{c}$  spectrum which is described, so far successfully, by the quark models. This suggests that some of them might be exotic i.e. be non- $q\bar{q}$  forms of hadrons. In this review the recent experimental evidences of possible exotic states are presented along with discussion on their interpretations proposed.

## 2 Phenomenology introduction

In the constituent quark model hadrons are classified either as mesons formed from quark-antiquark pairs or baryons consisting of three-quark triplets. Forces binding of quarks into hadrons are described by QCD. The potential models incorporating the general features of QCD describe the spectra and properties of the hadrons. In these models quarkonium states are described as quark-antiquark pair bound by single-gluon-exchange dominating at a short distance plus a linear confining potential linearly increasing as the quark separation increases. Adding the higher order corrections allows ones to obtain a picture of quarkonium multiplets including masses of resonances, their transitions, decays, etc. The low lying  $c\bar{c}$  states being discovered over past years have properties that agree quite well with the models' predictions.

The QCD-motivated models predict an existence of hadrons of more complex structure than conventional mesons or baryons such as hybrids and multiquark states of either molecular or tetraquark configuration<sup>1</sup>.

**Molecular state** [1] consists of two mesons weakly bound through pion exchange to form a molecule. Consequence of a loose binding of the comprising mesons is that they tend to decay as if they are free. Molecules are generally not isospin eigenstates.

---

<sup>1</sup>Pentaquarks are not discussed here as there have been no recent experimental results

**Tetraquark** is a tightly bound four-quark state of for example diquark-diantiquark configuration [2] where the comprising quarks group into colour-triplet scalar and vector clusters interacting dominantly by a gluon exchange. Strong decay proceeds through quark's rearrangement to form colour-singlet mesons followed by their dissociation. The  $c\bar{c}$  multiquarks which could be easily distinguished from conventional  $c\bar{c}$  are those of non-zero charge or/and strangeness like for example [ $cd\bar{c}\bar{u}$ ], [ $cd\bar{c}\bar{s}$ ].

**Hybrid mesons** [3] are states which in addition to quarkonium contain an excited gluon and are described by the flux-tube model [4]. The lowest excitations of potential produced by gluons lead to octet of the lowest mass hybrids; some of them bear exotic quantum numbers like  $J^{PC} = 0^{+-}, 1^{-+}, 2^+$ , which are not possible for conventional states. Observation of state of such spin-parity would indicate existence of an exotic resonance. The lowest charmonium hybrids are predicted by lattice QCD to have masses of about  $4.2\text{GeV}/c^2$ , whereas their dominant decays are expected to be open charm decay including  $P$ -wave meson in final state e.g.  $D\bar{D}^{**}$  dominating over  $D\bar{D}^{(*)}$ , and hadronic transition to charmonium via emission of light hadrons:  $c\bar{c} + \pi\pi/\eta$ , etc.

In addition, **thresholds** can also result in structures in cross-sections. At the threshold, for example  $D^{(*)}\bar{D}^{(*)}$ , states with small relative momentum may interact by exchanging pions. Such an attractive interaction can lead to the molecules mentioned; any repulsive interaction could give rise to a virtual state above threshold [5].

The conventional charmonium spectrum is much cleaner with regard to dense spectrum of light states, therefore exotic states containing  $c\bar{c}$  are expected to be identified easier than the ones predicted in the light spectrum. However no unambiguous evidence for exotic states has been found till recently when the  $XYZ$  particles were observed giving a hint of the exotic spectroscopy.

### 3 Experimental opportunities for spectroscopy

The discoveries described in this review have been in the first place enabled by the two  $B$ -factories: PEPII at SLAC and KEKB at KEK. Both are  $e^+e^-$  asymmetric-energy colliders operating most of the time at the  $\Upsilon(4S)$  mass ( $10.58\text{ GeV}$ ). The results presented are based on the large data samples collected by the BaBar detector at the PEPII and the Belle detector at the KEKB. The current data sample accumulated at the  $\Upsilon(4S)$  by Belle amounts to about  $730\text{fb}^{-1}$  and by BaBar:  $430\text{fb}^{-1}$ . Many precious measurements come also from the other experiments: CLEO at the  $e^+e^-$  collider CESR in Cornell, the CDF and  $D\bar{\theta}$  at the  $p\bar{p}$  collider Tevatron in Fermilab.

Although the  $B$ -factories were primarily constructed to study the  $CP$ -violation in  $B$  meson decays, their unexpected bonus has been an significant experimental input to the hadron spectroscopy especially to the charmonia. At the  $B$ -factories the  $c\bar{c}$  states can be produced in numerous production mechanisms such as  $B$  meson decays, initial state radiation, double  $c\bar{c}$  production and two-photon collisions.

The simplest  **$B$  meson decays** yielding charmonium state ( $X_{c\bar{c}}$ ) are  $B \rightarrow KX_{c\bar{c}}$ . They are described by the Cabibbo-favoured  $b \rightarrow c\bar{c}s$  transition, and thus have large branching fractions ( $\mathcal{O}(10^{-3})$ ) assuring large number of detected charmonia. Decays of this type favour production of charmonia bearing  $J^{PC} = 0^{++}$ ,  $1^{--}$  and  $1^{++}$ , while known quantum numbers of parent  $B$  meson allow ones to determine further the spin-parity of the produced  $X_{c\bar{c}}$  by performing angular analysis.

**Initial state radiation** (ISR) process corresponds to the case when the initial  $e^+$  or  $e^-$  radiates photon(s) making the center-of-mass (cm) energy of  $e^+e^-$  annihilation accordingly reduced. If an energy of radiated  $\gamma$  is large enough then  $e^+e^-$  annihilation occurs at the energy being within a range of charmonium masses and allows producing charmonia bearing spin-parity of photon i.e.  $J^{PC} = 1^{--}$ . Although the ISR is a higher-order QED process suppressed by  $\alpha_{em}$ , the very high luminosities of the  $B$ -factories effectively compensate it.

**Double charmonium production**  $e^+e^- \rightarrow X_{c\bar{c}}Y_{c\bar{c}}$  has been found to have much larger cross section than QCD originally predicted. Therefore some of these processes like an inclusive  $J/\psi$  production  $e^+e^- \rightarrow J/\psi X$ , occur to be useful for the charmonium spectroscopy, as it is quite likely that system  $X$  recoiling against  $J/\psi$  is a charmonium state. Because of  $C$ -parity conservation, only  $c\bar{c}$  states with  $C = +$  are produced in association with  $J/\psi$ .

**Two-photon collisions** are produced when both an initial  $e^+$  and  $e^-$  emit photons which afterwards interact with each other. Such  $\gamma\gamma$  interactions can produce states with  $J^{PC} = 0^{-+}$ ,  $0^{++}$ ,  $2^{-+}$  and  $2^{++}$ .

## 4 Experimental evidence

### 4.1 $X(3872)$ : $c\bar{c}$ like state

In 2003 Belle observed the  $X(3872)$  as a narrow peak in the  $M(J/\psi\pi^+\pi^-)$  spectrum in  $B^+ \rightarrow K^+\pi^+\pi^-J/\psi$  decays [6]. The state has been confirmed by CDF and  $D\emptyset$  to be produced in  $p\bar{p}$  collisions, as well as by BaBar [7]. The current PDG values for the  $X(3872)$  mass and upper limit for its total widths are  $m_{X(3872)} = 3871.4 \pm 0.6 \text{ MeV}/c^2$  and  $\Gamma_{X(3872)} < 2.3 \text{ MeV}/c^2$  respectively [8]. Recently the CDF experiment has precisely measured mass of the  $X(3872)$  to be  $m_{X(3872)} = 3871.61 \pm 0.16 \pm 0.19 \text{ MeV}/c^2$  (Fig. 1). In addition to  $J/\psi\pi^+\pi^-$  where dipion mass spectrum (Fig. 1) is consistent with originating from  $\rho \rightarrow \pi\pi$  [9], also evidence of the  $X(3872) \rightarrow J/\psi\pi^+\pi^-\pi^0$  mode proceeding via virtual  $\omega \rightarrow \pi^+\pi^-\pi^0$  has been found [10]. Comparable rates of these decay modes suggest large isospin violation. Also, an evidence of radiative decays to  $J/\psi\gamma$  [10] and recently to  $\psi(2S)\gamma$  [11] indicates  $C$ -parity= + for the  $X(3872)$ . The mentioned properties along with results of the CDF angular analysis [12] strongly favour  $J^{PC} = 1^{++}$  and  $2^{-+}$  for the  $X(3872)$ . As finding charmonium assignment fitting the  $X(3872)$  is very unlikely, exotic interpretations have been suggested.

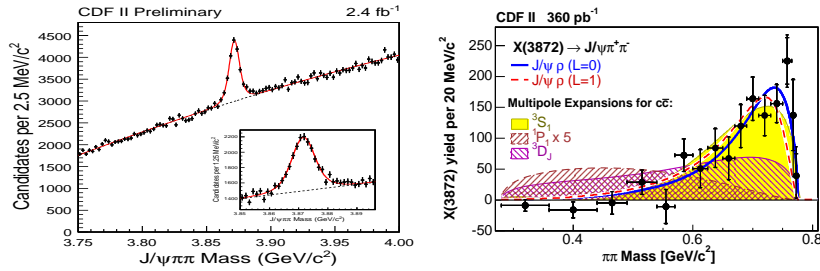


Figure 1:  $M(J/\psi\pi^+\pi^-)$  distribution (left) and  $M(\pi^+\pi^-)$  spectrum (right) for the  $X(3872)$  from CDF.

The  $X(3872)$  mass being in close vicinity of the sum of the  $D^0$  and  $D^{*0}$  masses ( $m_{D^0} + m_{D^{*0}} = 3871.81 \pm 0.36$  MeV/ $c^2$ ) has triggered speculations that  $X(3872)$  is a molecular bound state of  $D^0$  and  $\bar{D}^{*0}$  lying just below the  $D^0D^{*0}$  threshold [13]. Dominating decay modes of such molecule are expected to be  $D^0\bar{D}^0\pi^0$  and  $D^0\bar{D}^0\gamma$  i.e. proceeding through its constituent  $D^{*0}$  decay; also admixtures of  $J/\psi\rho/\omega$  are expected. A narrow near-threshold enhancement which could originate from the  $X(3872)$ , have been observed in the mass distribution of  $D^0\bar{D}^{*0}$  system produced in the  $B \rightarrow KD^0\bar{D}^{*0}$  decays (Fig. 2) [14]. Its mass measured by BaBar to be  $m = 3875.1^{+0.7}_{-0.5} \pm 0.5$  MeV/ $c^2$  is slightly larger than one of the  $X(3872) \rightarrow J/\psi\pi\pi$ . However a new Belle measurement gives  $m = 3872.6^{+0.5}_{-0.4} \pm 0.4$  MeV/ $c^2$  being in good agreement with the current world average for the  $X(3872)$  mass. Branching fraction of  $X(3872) \rightarrow D^0\bar{D}^{*0}$  has been measured to be one order of magnitude larger than for  $X(3872) \rightarrow J/\psi\pi^+\pi^-$ ; this supports the molecular interpretation of  $X(3872)$ . Although the resonance line-shape can be important for investigating the nature of the  $X(3872)$  [15], studying the  $X(3872)$  shape is not feasible with the current statistics. The Flatté parameterization tried for description of the  $D^0\bar{D}^{*0}$  threshold enhancement gives similar results as the Breit-Wigner function (Fig. 2).

Tetraquark explanation of  $X(3872)$  [2] [16] predicts that the neutral doublet should exist corresponding to  $[cu][\bar{c}\bar{u}]$  and  $[cd][\bar{c}\bar{d}]$  states of which former, identified with the  $X(3872)$ , is produced in charged  $B^+ \rightarrow K^+ J/\psi\pi^+\pi^-$  decays, whereas the latter should be observed in neutral  $B^0 \rightarrow K^0 J/\psi\pi^+\pi^-$  decays and have mass differing by a few MeV from the  $X(3872)$ . However recent studies have not revealed any significant mass difference between the  $X$  produced in charged versus neutral  $B$  decays [17]: BaBar measured  $\delta m = 2.7 \pm 1.6 \pm 0.4$  MeV/ $c^2$  whereas Belle:  $\delta m = 0.18 \pm 0.89 \pm 0.26$  MeV/ $c^2$  (Fig. 3). An interpretation of the peak observed in  $D^0\bar{D}^{*0}$  as a missing, heavier partner of the  $X(3872)$  [18] has also failed for its mass from the new Belle study is consistent with the  $X(3872)$ . Charged partner of the  $X(3872)$  predicted by the tetraquark models in the  $J/\psi\pi^+\pi^0$  has not been observed so far [19].

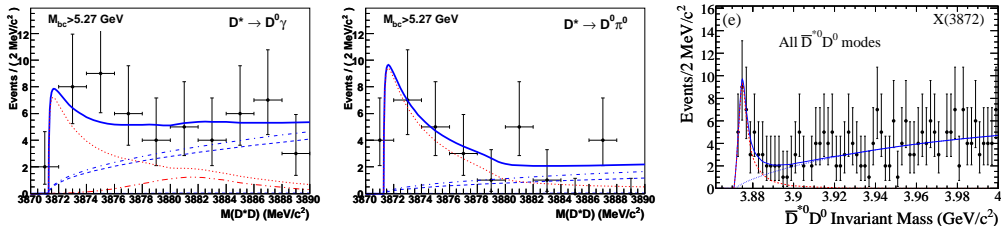


Figure 2:  $M(D^0\bar{D}^{*0})$  distributions for  $B \rightarrow K D^0\bar{D}^{*0}$  decays; left and middle plots are for  $D^{*0} \rightarrow D^0\gamma$  and  $D^{*0} \rightarrow D^0\pi^0$  from Belle; right one is BaBar plot for both  $D^{*0}$  modes combined. Red-dotted line in Belle plots is fit result with the Flatté parameterization used, blue-solid line is fit using the Breit-Wigner function.

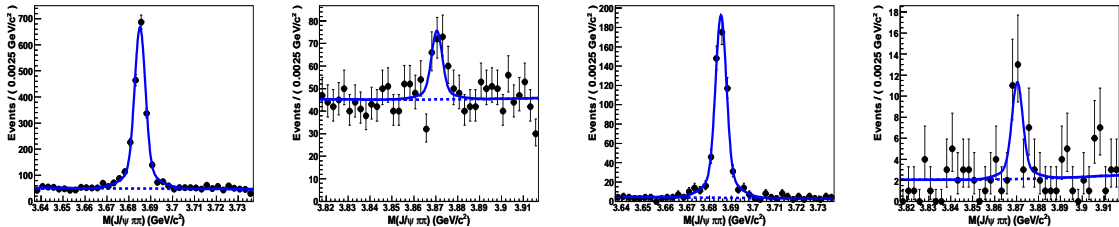


Figure 3:  $M(J/\psi\pi^+\pi^-)$  distribution for the  $\psi(2S)$  (used as a reference) and  $X(3872)$  regions for charged  $B \rightarrow K J/\psi\pi^+\pi^-$  decays (respectively first and second plots to the left) and for neutral ones (third and fourth plots).

Thus, in view of the mentioned experimental results, the molecular interpretation of the  $X(3872)$  seems to be favorable.

## 4.2 Charged charmonium-like $Z$ states

The first charmonium-like state of non-zero electric charge has been observed in the  $\pi^+\psi(2S)$  decay channel in a study of the  $B \rightarrow K\pi^+\psi(2S)$  decays [20]. In the Dalitz plot shown in Fig. 4 there are vertical clusters visible corresponding to the mesons in the  $K\pi^+$  final state like  $K^*(892)$ ,  $K_0^*(1430)$ ,  $K_2^*(1430)$ , whereas an unexpected horizontal band comes from the state in the  $\pi^+\psi(2S)$  system, called the  $Z^+(4430)$ . The  $M(\pi^+\psi(2S))$  projection after the  $K^*$  mass regions being excluded (Fig. 4) exhibits a narrow peak; its Breit-Wigner mass and width obtained from the fit to this projection are:  $m_{Z^+(4430)} = 4433 \pm 4 \pm 2$  MeV/ $c^2$  and  $\Gamma_{Z^+(4430)} = 45^{+18}_{-13} {}^{+30}_{-13}$  MeV/ $c^2$  respectively. It has been checked that the observed peak is not a reflection from any known states and it is too narrow to be produced by any interferences between the  $K\pi^+$  mesons. The statistics available have not been large enough to determine the spin-parity of

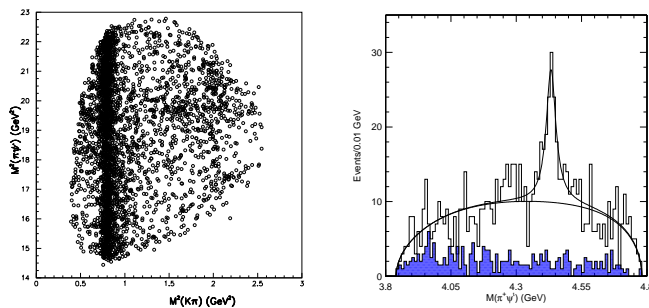


Figure 4:  $M^2(\pi^+\psi(2S))$  vs.  $M^2(K\pi^+)$  Dalitz plot distribution for  $B \rightarrow K\pi^+\psi(2S)$  decays and its  $M(\pi^+\psi(2S))$  projection with the  $K^*$  mass regions vetoed.

the  $Z^+(4430)$  though.

Being a charged state the  $Z^+(4430)$  has minimum quark content ( $c\bar{c}u\bar{d}$ ), thus must be exotic. Theoretical explanations have suggested that since the mass of the  $Z^+(4430)$  is close to the  $D^*\overline{D}_1(2420)$  threshold it could be either an  $S$ -wave threshold effect [21] or a  $D^*\overline{D}_1(2420)$  molecule [22], whereas tetraquark hypothesis considers the  $Z^+(4430)$  to be a diquark-antidiquark state with the  $[cu][\bar{c}\bar{d}]$  configuration [23] and predicts an existence of its neutral partner decaying to  $\psi(2S)\pi^0$  or  $\psi(2S)\eta$ . In the molecular scenario the dominating decay modes should be  $D^*\overline{D}^*\pi$  whereas in the tetraquark one:  $D^{(*)}\overline{D}^*$ ,  $J/\psi\pi$  and  $\psi(2S)\pi$ .

Recently BaBar in their search for the  $Z^+(4430)$  in the  $\pi^+\psi(2S)$  and  $\pi^+J/\psi$  decays modes have not found significant  $Z^+(4430)$  signal in any of the systems studied [24]. This calls for further studies to be resumed by both Belle and BaBar as well as other experiments.

Two other charged resonance-like structures have been observed by Belle in the  $\pi^+\chi_{c1}$  mass distribution near 4.1 GeV/ $c^2$  in the  $\overline{B}^0 \rightarrow K^-\pi^+\chi_{c1}$  decays through full analysis of its Dalitz plot (Fig. 5). In addition to the resonances decaying into  $K^-\pi^+$ , adding two states in the  $\pi^+\chi_{c1}$  system has been necessary to obtain acceptable quality of the Dalitz plot fit. These so called  $Z_1$  and  $Z_2$  states have significance exceeding  $5\sigma$  and their masses and total widths are respectively:  $m_{Z_1} = 4051 \pm 14^{+20}_{-41}$  MeV/ $c^2$ ,  $\Gamma_{Z_1} = 82^{+21}_{-17} {}^{+47}_{-22}$  MeV/ $c^2$ ,  $m_{Z_2} = 4248^{+44}_{-29} {}^{+180}_{-35}$  MeV/ $c^2$ , and  $\Gamma_{Z_2} = 177^{+54}_{-39} {}^{+316}_{-61}$  MeV/ $c^2$ . Both  $J = 0$  and 1 spin hypotheses tested have resulted in similar qualities of the Dalitz plot fit, therefore quantum numbers of the  $Z_1$  and  $Z_2$  have not been determined. The  $M(\pi^+\chi_{c1})$  distribution for  $1.0 < M^2(K^-\pi^+) < 1.75$  GeV $^2/c^4$  where the contributions of the  $Z_1$  and  $Z_2$  are most clearly seen is shown in Fig. 5. Just like in the  $Z^+(4430)$  case, both these states once confirmed will be certain candidates for exotic, most likely multiquark states.

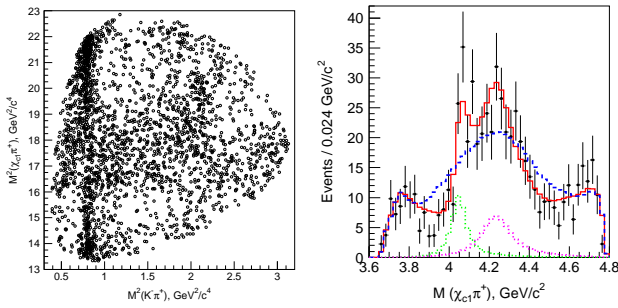


Figure 5: Left:  $M^2(\pi^+\chi_{c1})$  vs.  $M^2(K\pi^*)$  Dalitz plot distribution for  $\bar{B}^0 \rightarrow K^-\pi^+\chi_{c1}$  decays. Right:  $M(\pi^+\chi_{c1})$  distribution for  $1.0 < M^2(K^-\pi^+) < 1.75 \text{ GeV}^2/c^4$ . Blue histogram is the Dalitz plot fit result for the model with all known  $K^*$ 's and without any  $\chi_{c1}\pi^+$  resonance; red histogram represents the fit result with all known  $K^*$ 's and two  $\pi^+\chi_{c1}$  resonances; green and magenta histograms represent the contributions of the  $\pi^+\chi_{c1}$  resonances.

### 4.3 Family of the $1^{--} Y$ states

First member of the family, dubbed  $Y(4260)$ , was discovered by BaBar in the  $J/\psi\pi^+\pi^-$  system produced in the ISR radiation process [28]. Fit to the observed peak with a single Breit-Wigner parameterization (Fig. 6) yields a mass  $m_{Y(4260)} = 4259 \pm 8^{+2}_{-6} \text{ MeV}/c^2$  and a full width  $\Gamma_{Y(4260)} = 88 \pm 23^{+6}_{-4} \text{ MeV}/c^2$ . BaBar also found a broad peak around  $4.32 \text{ GeV}/c^2$  in  $e^+e^- \rightarrow \psi(2S)\pi^+\pi^-$  cross-section (Fig. 6) with parameters distinct from the  $Y(4260)$  [30].

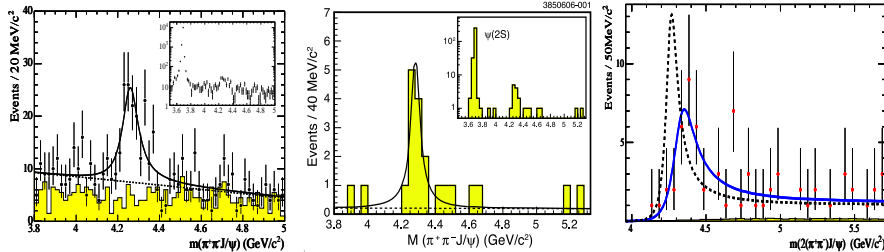


Figure 6:  $M(J/\psi\pi^+\pi^-)$  distribution from BaBar (left) and CLEO (middle) and  $M(\psi(2S)\pi^+\pi^-)$  distribution from BaBar (right).

The  $Y(4260)$  has been confirmed by CLEO [27] and both structures have been observed also by Belle [29] [31]. However Belle in their studies of the cm energy dependent cross-sections for  $e^+e^- \rightarrow J/\psi\pi^+\pi^-$  and  $e^+e^- \rightarrow \psi(2S)\pi^+\pi^-$  observed double-peak structures in each of these systems rather than just single peaks (Fig. 7).

Fit to the  $M(J/\psi\pi^+\pi^-)$  with two coherent Breit-Wigner functions gives parameters of the  $Y(4008)$  and  $Y(4260)$  to be:  $m_{Y(4008)} = 4008 \pm 40^{+114}_{-28} \text{ MeV}/c^2$ ,  $\Gamma_{Y(4008)} = 226 \pm 44 \pm 87 \text{ MeV}/c^2$  and  $m_{Y(4260)} = 4247 \pm 12^{+17}_{-32} \text{ MeV}/c^2$ ,  $\Gamma_{Y(4260)} = 108 \pm 19 \pm 10 \text{ MeV}/c^2$ . The parameters of the  $Y(4260)$  agree well with the BaBar results; the  $Y(4008)$ , seen for the first time, has not been confirmed in the recent BaBar study [24]. Fit with similar parameterization applied to the  $M(\psi(2S)\pi^+\pi^-)$  yields masses and total widths of the so called  $Y(4360)$  and  $Y(4660)$  states:  $m_{Y(4360)} = 4361 \pm 9 \pm 9 \text{ MeV}/c^2$ ,  $\Gamma_{Y(4360)} = 74 \pm 15 \pm 10 \text{ MeV}/c^2$  and  $m_{Y(4660)} = 4664 \pm 11 \pm 5 \text{ MeV}/c^2$ ,  $\Gamma_{Y(4660)} = 48 \pm 15 \pm 3 \text{ MeV}/c^2$ . The  $Y(4360)$  is consistent with the mentioned peak around  $4.32 \text{ GeV}/c^2$  seen by BaBar, whereas the  $Y(4660)$  is a new member of the  $Y$  family.

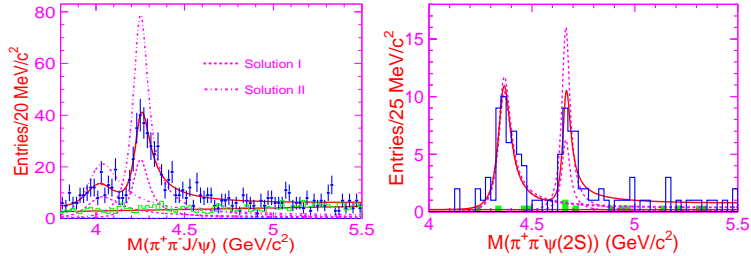


Figure 7:  $M(J/\psi\pi^+\pi^-)$  (left) and  $M(\psi(2S)\pi^+\pi^-)$  (right) distributions from Belle. The dashed curves show the  $Y$  state contributions for the two fit solutions corresponding to the destructive and constructive interferences between the resonances.

All these  $Y$  states, as observed through ISR, have  $J^{PC} = 1^{--}$ . Their parameters do not coincide with any of the vector charmonia observed so far in corresponding mass region ( $\psi(4040)$ ,  $\psi(4160)$ ,  $\psi(4415)$ ) and are inconsistent with the quark model calculations for charmonia. Although the masses of the  $Y$  states are above the threshold for decays to final states like  $D\bar{D}$ ,  $D\bar{D}^*$  or  $D^*\bar{D}^*$ , there are no clear peaks in the cross-sections for  $e^+e^- \rightarrow D^{(*)}\bar{D}^{(*)}$  [32] that could correspond to the  $Y$  states. Instead, their partial decay widths for the hadronic transitions to  $J/\psi\pi\pi$  or  $\psi(2S)\pi\pi$  are very large ( $\mathcal{O}(\text{MeV})$ ) and thus unlikely for the conventional  $c\bar{c}$  states. Other possible interpretations of the  $Y$  states include: charmonium hybrids predicted in this mass region and expected to decay dominantly into  $D\bar{D}_1$ ;  $cq\bar{c}\bar{q}$  tetraquarks,  $D^*\bar{D}^*$ ,  $D\bar{D}_1$  and  $D^*\bar{D}_0^*$  molecules or just  $S$ -wave charm meson thresholds. Moreover coupled-channel effects, rescattering of pairs of charmed mesons, interference of channels near threshold with the conventional charmonia, once understood by theory, could give better insight into the nature of the structures observed. Also, more experimental information on the decay properties is needed, such as searching for other close charm decay modes ( $J/\psi\pi^0\pi^0$ ,  $J/\psi\eta$ ,  $\chi_c\omega$ ), as well as open charm channels especially  $D\bar{D}_1$ .

In addition to interpretations of the exotic candidates observed in the  $c\bar{c}$  system, the models also predict the analogous states in the  $b\bar{b}$  and  $s\bar{s}$  systems. Recent

experimental results seem to support these predictions.

Belle using their data sample collected at the  $\Upsilon(5S)$  mass (10.87 GeV), studied dipion transitions of the  $\Upsilon(5S)$  and found unexpectedly large signals for the  $\Upsilon(1S)\pi^+\pi^-$  and  $\Upsilon(2S)\pi^+\pi^-$  channels [33]. The corresponding partial widths measured are:  $\Gamma(\Upsilon(5S) \rightarrow \Upsilon(1S)\pi^+\pi^-) = 590 \pm 40 \pm 90$  keV,  $\Gamma(\Upsilon(5S) \rightarrow \Upsilon(2S)\pi^+\pi^-) = 850 \pm 70 \pm 160$  keV. They are more than two orders of magnitude larger than corresponding partial widths for the other  $\Upsilon$ 's. This is a similar relation as observed for the  $\Gamma(Y(4260) \rightarrow J/\psi\pi^+\pi^-)$  with regard to the partial widths for the conventional  $c\bar{c}$ . Possible interpretation is that  $b\bar{b}$  analogous of  $Y(4260)$ , called  $Y_b$ , is overlapping the  $\Upsilon(5S)$  and is a source of the anomalous dipion transitions.

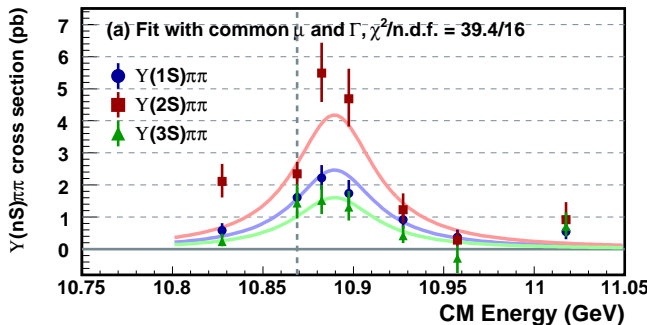


Figure 8: The cm energy dependent cross-section for  $e^+e^- \rightarrow \Upsilon(nS)\pi^+\pi^-$  processes. The curves show fit result, the vertical line indicates the  $\Upsilon(5S)$  mass.

To check this hypothesis, Belle performed an energy scan between 10.83 GeV and 11.02 GeV. Indeed, the measured energy dependent cross-section for the  $\Upsilon(nS)\pi^+\pi^-$  ( $n = 1, 2, 3$ ) production (Fig. 8) has revealed an enhancement which cannot be described by the conventional  $\Upsilon(5S)$  lineshape. Fit using a single Breit-Wigner resonance shape yields a peak mass of  $10889.6 \pm 1.8 \pm 1.5$  MeV/ $c^2$  and a total width of  $54.7^{+8.5}_{-7.2} \pm 2.5$  MeV/ $c^2$  [34]. Explanation other than existence of the  $Y_b$ , suggests mixing of the conventional  $b\bar{b}$  with the threshold followed by rescattering to  $\Upsilon(nS)\pi^+\pi^-$  [35].

#### 4.4 Other XYZ around 4 GeV

The  $Y(3940) \rightarrow J/\psi\omega$  in  $B \rightarrow KJ/\psi\omega$  decays was observed by Belle [36] and recently confirmed by BaBar [37] although a mass and a total width of the  $Y(3940)$  measured by Belle ( $m_{Y(3940)} = 3943 \pm 11 \pm 13$  MeV/ $c^2$ ,  $\Gamma_{Y(3940)} = 87 \pm 22 \pm 26$  MeV/ $c^2$ ) and BaBar (Fig. 9) ( $m_{Y(3940)} = 3914.6^{+3.8}_{-3.4} \pm 2$  MeV/ $c^2$ ,  $\Gamma_{Y(3940)} = 34^{+12}_{-8} \pm 5$  MeV/ $c^2$ ) slightly differ. Large production rates in  $B$  decays ( $\mathcal{O}(10^{-5})$ ) imply  $\Gamma(Y(3940) \rightarrow J/\psi\omega) > 1$  MeV/ $c^2$ , which is larger than for any conventional  $c\bar{c}$  above open charm

threshold. However the  $\chi_{c1}(2P)$  charmonium assignment, suggested by the mass and width of the  $Y(3940)$ , cannot be excluded. This can be tested by searching for the  $D\bar{D}^*$  decay mode which should dominate for  $\chi_{c1}(2P)$ . Possible explanation for the strong  $J/\psi\omega$  decay mode is rescattering through  $D\bar{D}^* \rightarrow J/\psi\omega$ .

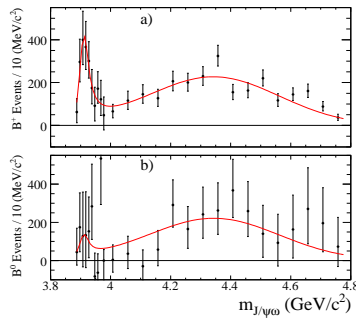


Figure 9:  $M(J/\psi\omega)$  distributions from BaBar for charged (top) and neutral (bottom)  $B \rightarrow KJ/\psi\omega$  decays.

The  $X(3940) \rightarrow D\bar{D}^*$  and  $X(4160) \rightarrow D^*\bar{D}^*$  states have been observed in double charmonium production in association with the  $J/\psi$ :  $e^+e^- \rightarrow J/\psi D^{(*)}\bar{D}^{(*)}$  [39]. As the  $X(3940) \rightarrow J/\psi\omega$  decays have not been observed, it is unlikely that  $X(3940)$  and  $Y(3940)$  are the same state. As the production of  $J = 0$  resonances seems to be favoured over charmonia with a higher spin [38], thus likely assignment for these  $X$  states could be  $\eta_c(3S)$  and  $\eta_c(4S)$ . However measured masses of the  $X$  states:  $m_{X(3940)} = 3942^{+7}_{-6} \text{ MeV}/c^2$  and  $m_{X(4160)} = 4156^{+25}_{-20} \text{ MeV}/c^2$ , are significantly lower than masses predicted by the potential models for the  $\eta_c(3S)$  and  $\eta_c(4S)$  (respectively 4050 and 4400  $\text{MeV}/c^2$ ). This  $\eta_c$  assignment could be tested by performing an angular analysis and searching for these states in  $\gamma\gamma \rightarrow D^{(*)}\bar{D}^{(*)}$ .

## 5 Summary

As it has been presented, there have been many so called  $XYZ$  states observed which cannot be easily accommodated within the conventional  $c\bar{c}$  multiplets and are good candidates for exotic hadrons like molecules, tetraquarks or hybrids. This may suggest that there is a new  $c\bar{c}$  spectroscopy around 4 GeV mass region. Also there is experimental evidence that similar states may exist in other quark sectors for example in the  $b\bar{b}$ .

However there are still many issues to be further studied by both experiment and theory to prove that the  $XYZ$  states are not conventional ones. The most urgent

are: confirmation of the states by other experiments, measurement their quantum numbers and searching for other decay modes. Whereas from the theory side better understanding of the thresholds and coupled channel effects is necessary.

## References

- [1] M.B. Voloshin, L.B. Okun JETP Lett. **23**, 333 (1976); A. De Rujula, H. Georgi *et al.* Phys. Rev. Lett. **38**, 317 (1977); N.A. Tornqvist Z. Phys. C **61**, 525 (1994).
- [2] L. Maiani, F. Piccinini *et al.* Phys. Rev. D **71**, 014028 (2005).
- [3] T. Barnes, F.E. Close *et al.* Phys. Rev. D **52**, 5242 (1995).
- [4] N. Isgur, J.E. Paton Phys. Rev. D **31**, 2910 (1985).
- [5] M.B. Voloshin arXiv:0602233. E. Eichten *et al.* Phys. Rev. D **17**, 3090 (1978); E. Eichten *et al.* Phys. Rev. D **21**, 203 (1980).
- [6] S.K. Choi *et al.* (Belle Collab.) Phys. Rev. Lett. **91**, 262001 (2003).
- [7] D. Acosta *et al.* (CDF Collab.) Phys. Rev. Lett. **93**, 072001 (2004); V.M. Abazov *et al.* D $\emptyset$  Collab.) Phys. Rev. Lett. **93**, 162002 (2004); B. Aubert *et al.* (BaBar Collab.) Phys. Rev. D **71**, 071103 (2005).
- [8] C. Amsler *et al.* (Particle Data Group) Phys. Lett. B **667** 1, (2008).
- [9] A. Abulencia *et al.* (CDF Collab.) Phys. Rev. Lett. **96**, 102002 (2006).
- [10] K. Abe *et al.* (Belle Collab.) arXiv:0505037
- [11] B. Aubert *et al.* (BaBar Collab.) arXiv:0809.0042
- [12] A. Abulencia *et al.* (CDF Collab.) Phys. Rev. Lett. **98**, 132002 (2007).
- [13] E.S. Swanson Phys. Lett. B **588**, 189 (2004); F.E. Close, P.R. Page Phys. Lett. B **578**, 119 (2004); M.B. Voloshin Phys. Lett. B **579**, 316 (2004).
- [14] B. Aubert *et al.* (BaBar Collab.) Phys. Rev. D **77**, 011102 (2008); I. Adachi *et al.* (Belle Collab.) arXiv:0810.0358
- [15] C. Hanhart *et al.* Phys. Rev. D **76**, 034007 (2007); M.B. Voloshin Phys. Rev. D **76**, 014007 (2007); E. Braaten, M. Lu Phys. Rev. D **77**, 014029 (2008).
- [16] D. Ebert, R.N. Faustov, V.O. Galkin Phys. Lett. B **634**, 214 (2006).

- [17] B. Aubert *et al.* (BaBar Collab.) Phys. Rev. D **77**, 111101 (2008); I. Adachi *et al.* (Belle Collab.) arXiv:0809.1224
- [18] L. Maiani, A.D. Polosa *et al.* arXiv:0707.3354
- [19] B. Aubert *et al.* (BaBar Collab.) Phys. Rev. D **71**, 031501 (2007).
- [20] S.K. Choi *et al.* (Belle Collab.) Phys. Rev. Lett. **100**, 142001 (2008).
- [21] J.L. Rosner Phys. Rev. D **76**, 114002 (2007).
- [22] C. Meng, K.T. Chao arXiv:0708.4222; X. Liu, Y.R. Liu *et al.* arXiv:0711.0494
- [23] L. Maiani, A.D. Polosa arXiv:0708.3997
- [24] A.G. Mokhtar (BaBar Collab.) arXiv:0810.1073
- [25] R. Mizuk *et al.* (Belle Collab.) Phys. Rev. D **78**, 072004 (2008).
- [26] T.E. Coan *et al.* (CLEO Collab.), Phys. Rev. Lett. **96**, 162003 (2006).
- [27] Q. He *et al.* (CLEO Collab.) Phys. Rev. D **74**, 091104 (2006).
- [28] B. Aubert *et al.* (BaBar Collab.) Phys. Rev. Lett. **95**, 142001 (2005).
- [29] C.Z. Yuan *et al.* (Belle Collab.) Phys. Rev. Lett. **99**, 182004 (2007).
- [30] B. Aubert *et al.* (BaBar Collab.) Phys. Rev. Lett. **98**, 212001 (2007).
- [31] X.L. Wang *et al.* (Belle Collab.) Phys. Rev. Lett. **99**, 142002 (2007).
- [32] G. Pakhlova *et al.* (Belle Collab.) Phys. Rev. D **77**, 011103 (2008); G. Pakhlova *et al.* (Belle Collab.) Phys. Rev. Lett. **98**, 092001 (2007).
- [33] K.F. Chen *et al.* (Belle Collab.) Phys. Rev. Lett. **100**, 112001 (2008).
- [34] I. Adachi *et al.* (Belle Collab.) arXiv:0804.2063
- [35] F.E. Close arXiv:0801.2646
- [36] S.K. Choi *et al.* (Belle Collab.) Phys. Rev. Lett. **94**, 182002 (2005).
- [37] B. Aubert *et al.* (BaBar Collab.) Phys. Rev. Lett. **101**, 082001 (2008).
- [38] K. Abe *et al.* (Belle Collab.) Phys. Rev. Lett. **98**, 082001 (2007).
- [39] P. Pakhlov *et al.* (Belle Collab.) Phys. Rev. Lett. **100**, 202001 (2008).

# Longitudinal Structure Function Measurements from HERA

Vladimir Chekelian (Shekelyan)  
Max-Planck-Institute für Physik  
Föhringer Ring 6, 80805 Munich, Germany

## 1 Abstract

Measurements of the longitudinal structure function  $F_L$  at the  $ep$  collider HERA are presented. They are derived from inclusive deep inelastic neutral current  $e^+p$  scattering cross section measurements based on data collected in 2007 with the H1 and ZEUS detectors at a positron beam energy of 27.5 GeV and proton beam energies of 920, 575 and 460 GeV. Employing the energy dependence of the cross sections,  $F_L(x, Q^2)$  is measured in the range of negative four-momentum transfer squared  $12 \leq Q^2 \leq 800$  GeV $^2$  and low Bjorken- $x$   $0.00028 \leq x \leq 0.0353$ . The measured longitudinal structure function is compared with higher order QCD predictions.

## 2 Introduction

In the past 15 years, the HERA experiments H1 and ZEUS have extended the knowledge of the proton structure by two orders of magnitude towards high negative four-momentum transfer squared,  $Q^2$ , and to small Bjorken- $x$ . At the end of the HERA operation in 2007, dedicated  $e^+p$  data were collected with lower proton beam energy which allow to measure the longitudinal component of the proton structure. This measurement is directly sensitive to the gluon contribution in the proton. It is essential for completion of the deep inelastic scattering (DIS) program at HERA and for checks of the underlying perturbative Quantum Chromodynamics (QCD) framework used to determine parton distribution functions (PDFs).

The DIS neutral current (NC)  $ep$  scattering cross section at low  $Q^2$  can be written in reduced form as

$$\sigma_r(x, Q^2, y) = \frac{d^2\sigma}{dx dQ^2} \cdot \frac{Q^4 x}{2\pi\alpha^2[1 + (1 - y)^2]} = F_2(x, Q^2) - \frac{y^2}{1 + (1 - y)^2} \cdot F_L(x, Q^2). \quad (1)$$

Here,  $\alpha$  denotes the fine structure constant,  $x$  is the Bjorken scaling variable and  $y$  is the inelasticity of the scattering process related to  $Q^2$  and  $x$  by  $y = Q^2/sx$ , where  $s$  is the centre-of-mass energy squared of the incoming electron and proton.

The cross section is determined by two independent structure functions,  $F_2$  and  $F_L$ . They are related to the  $\gamma^* p$  interaction cross sections of longitudinally and transversely polarised virtual photons,  $\sigma_L$  and  $\sigma_T$ , according to  $F_2 \propto (\sigma_L + \sigma_T)$  and  $F_L \propto \sigma_L$ , therefore  $0 \leq F_L \leq F_2$ .  $F_2$  is the sum of the quark and anti-quark  $x$  distributions weighted by the electric charges of quarks squared and contains the dominant contribution to the cross section. In the Quark Parton Model the value of the longitudinal structure function  $F_L$  is zero, whereas in QCD it differs from zero due to gluon and (anti)quarks emissions. At low  $x$  the gluon contribution to  $F_L$  exceeds the quark contribution and  $F_L$  is a direct measure of the gluon  $x$  distribution.

The longitudinal structure function, or equivalently  $R = \sigma_L/\sigma_T = F_L/(F_2 - F_L)$ , was measured previously in fixed target experiments and found to be small at large  $x \geq 0.2$ , confirming the spin 1/2 nature of the constituent quarks in the proton. From next-to-leading order (NLO) and NNLO [1] QCD analyses of the inclusive DIS cross section data [2, 3, 4], and from experimental  $F_L$  determinations by H1 [5, 6], which used assumptions on the behaviour of  $F_2$ , the longitudinal structure function  $F_L$  at low  $x$  is expected to be significantly larger than zero. A direct, free from theoretical assumptions, measurement of  $F_L$  at HERA, and its comparison with predictions derived from the gluon distribution extracted from the  $Q^2$  evolution of  $F_2(x, Q^2)$  thus represents a crucial test on the validity of the perturbative QCD framework at low  $x$ .

### 3 Measurement Strategy

The model independent measurement of  $F_L$  requires several sets of NC cross sections at fixed  $x$  and  $Q^2$  but different  $y$ . This was achieved at HERA by variation of the proton beam energy.

The measurements of the NC cross sections by H1 and ZEUS are performed using  $e^+p$  data collected in 2007 with a positron beam energy  $E_e = 27.5$  GeV and with three proton beam energies: the nominal energy  $E_p = 920$  GeV, the smallest energy of 460 GeV and an intermediate energy of 575 GeV. The corresponding integrated luminosities are about  $46 \text{ pb}^{-1}$ ,  $12 \text{ pb}^{-1}$  and  $6 \text{ pb}^{-1}$ .

The sensitivity to  $F_L$  is largest at high  $y$  as its contribution to  $\sigma_r$  is proportional to  $y^2$ . The high reconstructed  $y$  values correspond to low values of the scattered positron energy,  $E'_e$ :

$$y = 1 - \frac{E'_e}{E_e} \sin^2(\theta_e/2), \quad Q^2 = \frac{E'^2_e \sin^2 \theta_e}{1-y}, \quad x = Q^2/sy. \quad (2)$$

The measurement in the high  $y$  domain up to  $y = 0.90$  requires the measurement of the scattered positron down to  $E'_e \approx 3$  GeV. Thus, one needs a reliable identification and reconstruction of events with a low scattered positron energy. Furthermore, small energy depositions caused by hadronic final state particles can also lead to fake

positron signals. The large size of this background, mostly due to the photoproduction process at  $Q^2 \simeq 0$ , makes the measurement at high  $y$  especially challenging.

### 3.1 H1 Analysis

H1 performed two independent analyses, at medium [8] and high [9]  $Q^2$ , with the positrons scattered into the acceptance of the backward Spacal calorimeter (the polar angle range of the scattered positron  $\theta_e \gtrsim 153^\circ$ ), corresponding to  $12 \leq Q^2 \leq 90 \text{ GeV}^2$ , and into the acceptance of the Liquid Argon calorimeter (LAr) ( $\theta_e \lesssim 153^\circ$ ), corresponding to  $35 \leq Q^2 \leq 800 \text{ GeV}^2$ .

The scattered positron is identified as a localised energy deposition (cluster) with energy  $E'_e > 3.4 (> 3) \text{ GeV}$  in the Spacal (LAr). The NC events are triggered on positron energy depositions in the Spacal or LAr calorimeters, on hadronic final state energy depositions in the Spacal, and using a new trigger hardware commissioned in 2006. At small positron energies the Spacal trigger is complemented by the central inner proportional chamber (CIP) track trigger which reduces the trigger rate to an acceptable level. The new trigger system includes the Jet Trigger, which performs a real time clustering in the LAr, and the Fast Track Trigger (FTT) [7], which utilizes on-line reconstructed tracks in the central tracker (CT). The combined trigger efficiency reaches 97 – 98% at  $E'_e = 3 \text{ GeV}$  and  $\approx 100\%$  at  $E'_e > 6 - 7 \text{ GeV}$ .

To ensure a good reconstruction of kinematical properties, the reconstructed event vertex is required to be within 35 cm around the nominal vertex position along the beam axis. The primary vertex position is measured using tracks reconstructed in the central tracker system. The positron polar angle is determined by the positions of the interaction vertex and the positron cluster in the calorimeter.

The photoproduction background is reduced by demanding a track from the primary interaction pointing to the positron cluster with an extrapolated distance to the cluster below 6 (12) cm in the medium (high)  $Q^2$  analysis. In the medium  $Q^2$  analysis the fake positron background is reduced by the requirement of a small transverse size of the cluster in the Spacal,  $R_{log}$ , which is estimated using a logarithmic energy weighted cluster radius, and by the requirement that the energy behind the cluster, measured in the hadronic part of the Spacal, may not exceed 15% of  $E'_e$ . For  $E'_e < 6 \text{ GeV}$  in the high  $Q^2$  analysis the following additional requirements are applied: small transverse energy weighted radius of the cluster ( $E_{cra} < 4 \text{ cm}$ ) and matching between the energy of the cluster and the track momentum ( $0.7 < E'_e / P_{track} < 1.5$ ).

Further suppression of photoproduction background is achieved by requiring longitudinal energy-momentum conservation  $\sum_i (E_i - p_{z,i}) > 35 \text{ GeV}$ , where the sum runs over the energy and longitudinal momentum component of all particles in the final state including the scattered positron. For genuine, non-radiative NC events it is equal to  $2E_e = 55 \text{ GeV}$ . This requirement also suppresses events with hard initial state photon radiation. QED Compton events are excluded using a topological cut

against two back-to-back energy depositions in the calorimeters.

In addition, a method of statistical background subtraction is applied for the  $E_p = 460$  and  $575\text{ GeV}$  data at high  $y$  ( $0.38 < y < 0.90$  and  $E'_e < 18\text{ GeV}$ ). The method relies on the determination of the electric charge of the positron candidate from the curvature of the associated track. Only candidates with right (positive) sign of electric charge are accepted. The photoproduction background events are about equally shared between positive and negative charges. Thus, by selecting the right charge the background is suppressed by about a factor of two. The remaining background is corrected for by statistical subtraction of background events with the wrong (negative) charge from the right sign event distributions. This subtraction procedure requires a correction for a small but non-negligible charge asymmetry in the background events due to enlarged energy depositions in the annihilation of anti-protons in the calorimeters.

The small photoproduction background for the  $920\text{ GeV}$  data at  $y < 0.5(0.56)$  in the medium (high)  $Q^2$  analysis is estimated and subtracted using a PHOJET (PYTHIA) simulation normalised to the photoproduction data tagged in the electron tagger located downstream of the positron beam at 6 m.

### 3.2 ZEUS Analysis

ZEUS developed special triggers to record events with low positron energy. The performance of these triggers was demonstrated in a ZEUS measurement of NC cross section at high  $y$  [10].

The scattered positron with energy  $E'_e > 6\text{ GeV}$  is identified in the ZEUS rear calorimeter at radii above  $\approx 28\text{ cm}$  from the beam line. The standard tracking in ZEUS is limited to the particle polar angles of  $\theta \lesssim 154^\circ$ . To suppress large photoproduction background caused by neutral particles (mostly photons from  $\pi^0$  decays) it is crucial to extend this region. A new method is used to define a corridor between the reconstructed vertex of the event and the position of the positron candidate in the calorimeter. Counting hits in the tracking detector within the corridor and comparing it to the number of the traversed layers in the tracker allows to discriminate between charged and neutral particles up to  $\theta \lesssim 168^\circ$ .

The remaining background among positron candidates was estimated using the PYTHIA simulation of photoproduction events. The MC sample was normalised using the rate of identified photoproduction events with a fake positron candidate in the main detector and a signal in the electron tagger located downstream of the positron beam at 6 m.

To ensure a good reconstruction of kinematical properties and to further suppress photoproduction background, the reconstructed event vertex is required to be within 30 cm around the nominal vertex position and the measured value of  $\sum_i(E_i - p_{z,i})$  to be between 42 and 65 GeV.

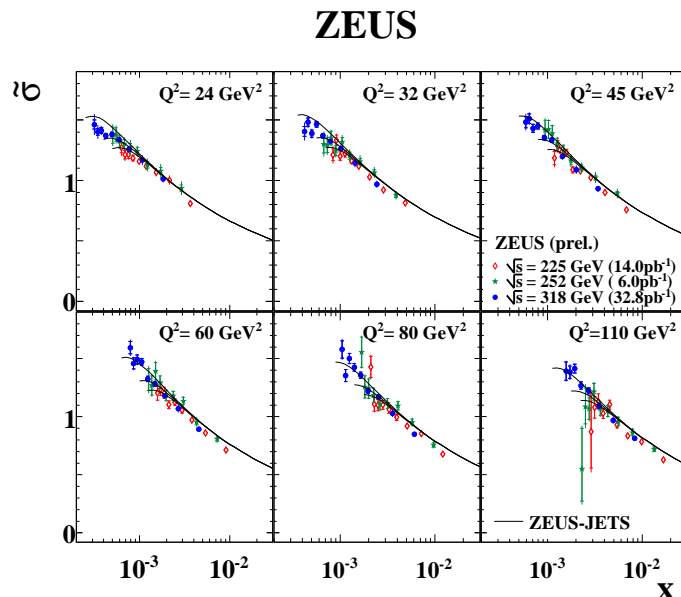


Figure 1: Reduced cross section measured by ZEUS at proton beam energies of 920, 575 and 460 GeV as a function of  $x$  at fixed values of  $Q^2$ .

## 4 HERA Results for $F_L(x, Q^2)$

The reduced NC cross sections measured by ZEUS [11] for three proton beam energies of 460, 575 and 920 GeV are shown in figure 1 as a function of  $x$  at fixed values of  $Q^2$ . They cover the range  $24 \leq Q^2 \leq 110 \text{ GeV}^2$  and  $0.1 \leq y \leq 0.8$  which results in different coverage in  $x$ . The measurements are compared with the NLO QCD predictions based on the ZEUS-JETS QCD fit [12] taking into account the contribution from  $F_L$  which causes a turn over of the expected cross section at lowest  $x$  values measured.

The reduced NC cross sections measured by H1 at medium and high  $Q^2$  ( $35 \leq Q^2 \leq 800 \text{ GeV}^2$ ) in the range  $0.1 \leq y \leq 0.56$  for the  $E_p = 920 \text{ GeV}$  data and  $0.1 \leq y \leq 0.9$  for the 460 and 575 GeV data are shown in figure 2 (left). At  $Q^2 \leq 25 \text{ GeV}^2$  ( $Q^2 \geq 120 \text{ GeV}^2$ ) the measurements are entirely from the medium (high)  $Q^2$  analysis. In the intermediate  $Q^2$  range  $35 \leq Q^2 \leq 90 \text{ GeV}^2$  the cross section is measured at  $E_p = 460(920) \text{ GeV}$  in the medium (high)  $Q^2$  analysis and for the  $E_p = 575 \text{ GeV}$  data the cross section is obtained either using the LAr or Spacal. Small, 1-2%, relative normalisation corrections to the measured cross sections at  $E_p = 460, 575$  and  $920 \text{ GeV}$ , common for both analyses, are derived using measurements at low  $y$  and applied to the cross section points shown in the figure. In this low  $y$  region, the cross sections are determined by  $F_2(x, Q^2)$  only, apart from a small correction for residual  $F_L$  contribution.

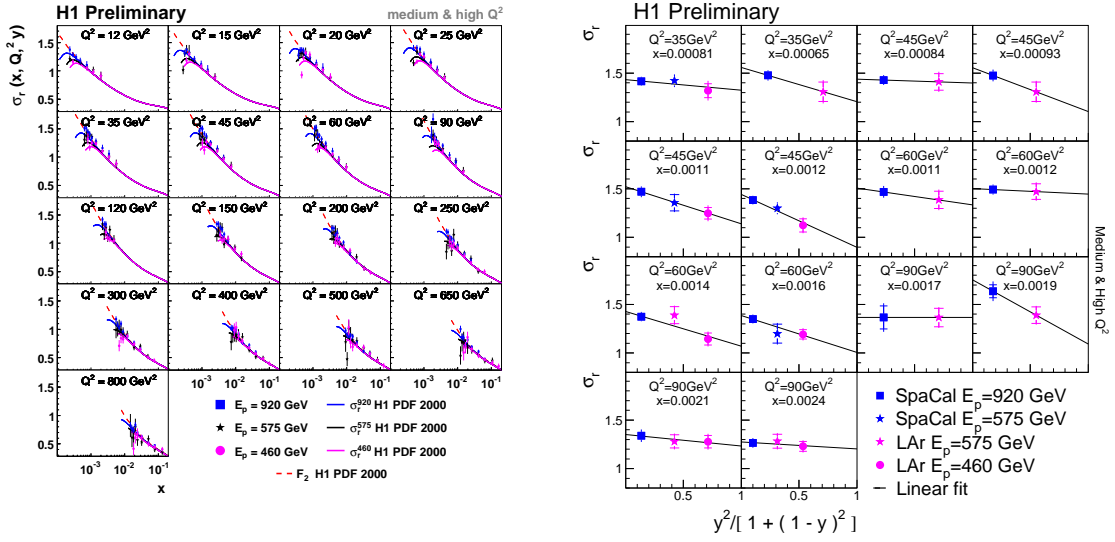


Figure 2: Reduced cross section measured by H1 at proton beam energies of 920, 575 and 460 GeV as a function of  $x$  at fixed values of  $Q^2$  (left) and at fixed values of  $x$  and  $Q^2$  as a function of  $y^2/[1 + (1 - y)^2]$  for measurements which include both the LAr and Spacal data (right). The lines in the right figure show the linear fits used to determine  $F_L(x, Q^2)$  for selected  $Q^2$  and  $x$ .

The longitudinal structure function is extracted from the slope of the measured reduced cross section versus  $y^2/[1 + (1 - y)^2]$ . This procedure is illustrated for the H1 analysis in figure 2 (right) for selected  $Q^2$  and  $x$  values, where both the LAr and Spacal measurements are available. The measurements are consistent with the expected linear dependence, demonstrating consistency of the two independent analyses, which utilize different detectors to measure the scattered positron.

The  $F_L(x, Q^2)$  values are determined in straight-line fits to the  $\sigma_r(x, Q^2, y)$ . The ZEUS result for  $F_L(x, Q^2)$  is shown in figure 3. The result is consistent with the expectation based on the ZEUS-JETS QCD fit [12].

The H1 measurements of  $F_L(x, Q^2)$  with statistical errors better than 10% are shown in figure 4. The central  $F_L(x, Q^2)$  values are determined in the fits using statistical and uncorrelated systematic errors added in quadrature, and statistical (total)  $F_L$  errors - in the fits using statistical (total) errors. The uncertainty due to the relative normalisation of the cross sections is added in quadrature to the total  $F_L(x, Q^2)$  error. This uncertainty is estimated from the effect of a 1% variation of the normalisation of the 920 GeV cross section on the fit result. The measurement of  $F_L(x, Q^2)$  is limited to  $Q^2$  and  $x$  values where the total  $F_L$  error is below 0.4 (1.1) for  $Q^2 \leq 35 (> 35) \text{ GeV}^2$ . The result is consistent with the NLO QCD prediction

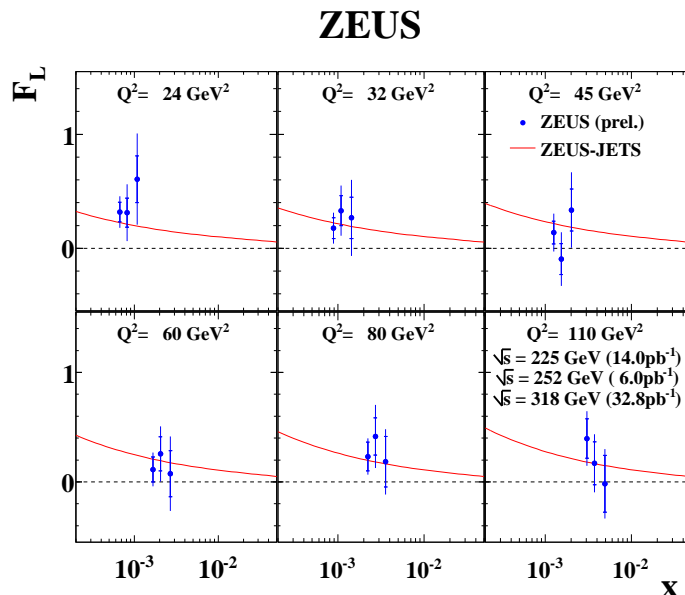


Figure 3:  $F_L(x, Q^2)$  measured by ZEUS as a function of  $x$  at fixed values of  $Q^2$ . The inner and outer error bars are the statistical and total errors, respectively. The curve represents the NLO QCD prediction derived from the ZEUS-JETS fit to previous ZEUS data.

based on the H1 PDF 2000 fit [6] performed using previous H1 cross section data at nominal proton energy.

The H1 measurements of  $F_L(Q^2)$  averaged over  $x$  at fixed  $Q^2$  are presented in figure 5. The average is performed using the total errors of individual measurements. The overall correlated component for the averaged  $F_L$  is estimated to vary between 0.05 and 0.10. The averaged  $F_L$  is compared with the H1 PDF 2000 fit [6] and with the expectations from global parton distribution fit at NNLO (NLO) perturbation theory performed by the MSTW [2] (CTEQ [3]) group and from the NNLO QCD fit by Alekhin [4] (see also figures in [9]). Within the experimental uncertainties the data are consistent with these predictions.

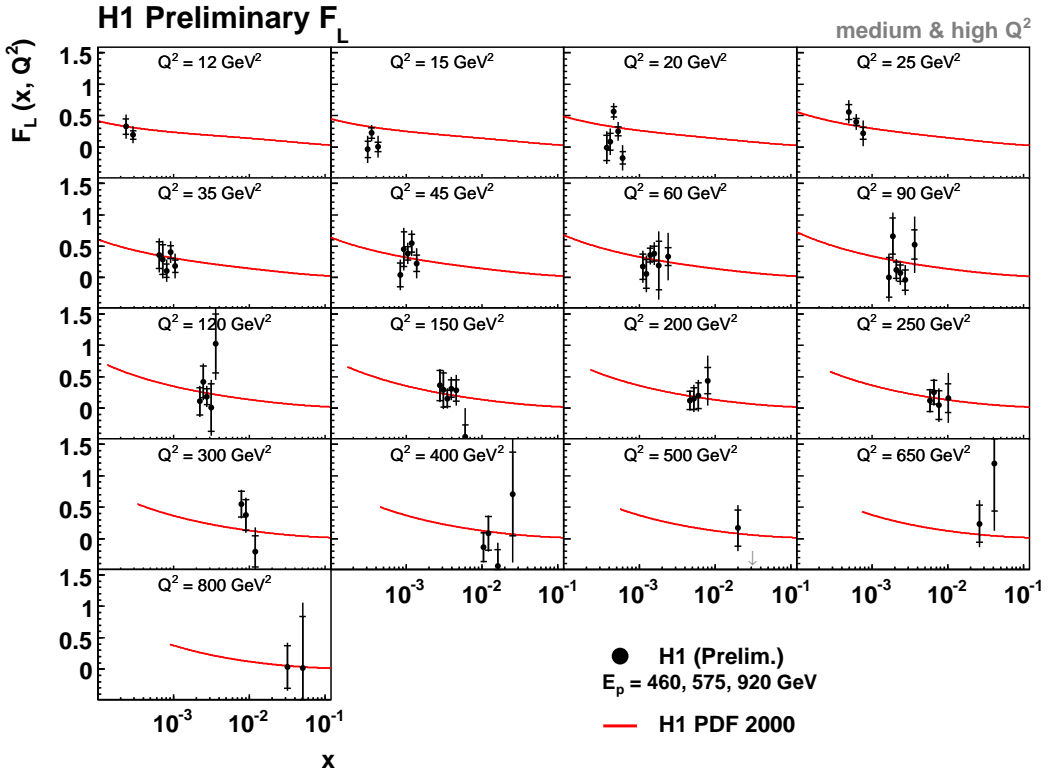


Figure 4:  $F_L(x, Q^2)$  measured by H1 as a function of  $x$  at fixed values of  $Q^2$ . The inner and outer error bars are the statistical and total errors, respectively. The curve represents the NLO QCD prediction derived from the H1 PDF 2000 fit to previous H1 data.

## 5 Summary

The H1 and ZEUS measurements of the longitudinal proton structure function in deep inelastic scattering at low  $x$  are presented. The  $F_L(x, Q^2)$  values are extracted from three sets of cross section measurements at fixed  $x$  and  $Q^2$ , but different inelasticity  $y$  obtained using three different proton beam energies at HERA. For the  $Q^2$  range between 12 and 800  $\text{GeV}^2$ , the  $F_L$  results are consistent at the current level of accuracy with the DGLAP evolution framework of perturbative QCD at low  $x$ .

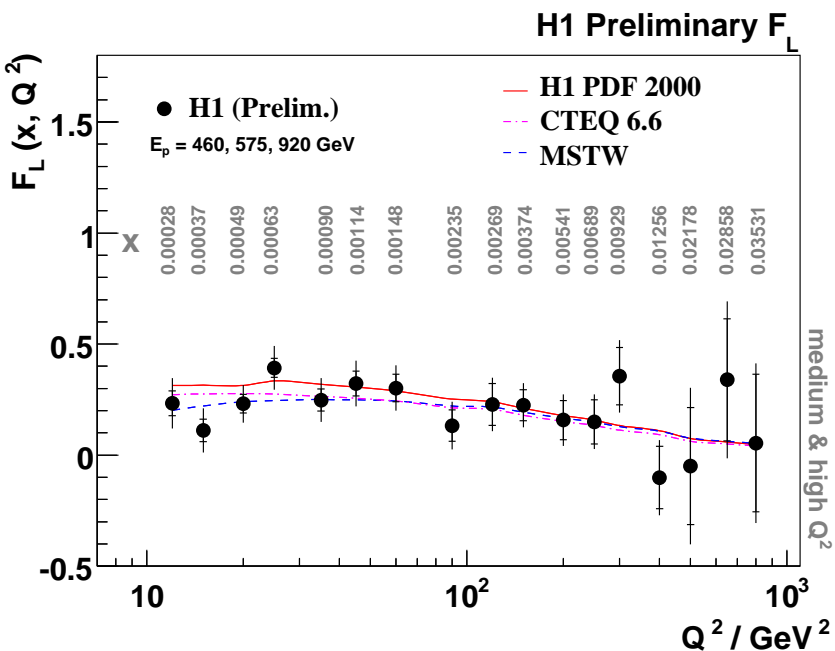


Figure 5: The H1 measurement of  $F_L(Q^2)$  averaged over  $x$  at fixed values of  $Q^2$ . The resulting  $x$  values of the averaged  $F_L$  are given in the figure for each point in  $Q^2$ . The curves represent the QCD predictions.

## References

- [1] S. Moch, J.A.M. Vermaseren and A. Vogt, Phys. Lett. **B606** 123 (2005) and references therein.
- [2] A.D. Martin, W.J. Stirling, R.S. Thorne and G. Watt, Phys. Lett. **B652** 292 (2007).
- [3] J. Pumplin, H.L. Lai and W.K. Tung, Phys. Rev. **D75** 054029 (2007); P.M. Nadolsky *et al.*, arXiv:hep-ph/0802.0007.
- [4] S. Alekhin, K. Melnikov, F. Petriello, Phys. Rev. **D74** 054033 (2006).
- [5] C. Adloff *et al.*, H1 Collaboration, Phys. Lett. **B393** 452 (1997); C. Adloff *et al.*, H1 Collaboration, Eur. Phys. J. **C21** 33 (2001).
- [6] C. Adloff *et al.*, H1 Collaboration, Eur. Phys. J. **C30** 1 (2003).
- [7] A. Baird *et al.*, IEEE Trans. Nucl. Sci. **48** 1276 (2001).

- [8] A. Nikiforov, *Measurement of the Proton  $F_L$  and  $F_2$  Structure Functions at Low  $x$* , 43rd Rencontres de Moriond on QCD and High Energy Interactions, La Thuile, Aosta Valley, Italy (8-15 March 2008);  
B. Antunovic, *Measurement of the Longitudinal Structure Function  $F_L$  at Low  $x$  in the H1 Experiment at HERA*, 16th International Workshop on Deep Inelastic Scattering, London (7-11 April 2008);  
F.D. Aaron *et al.*, H1 Collaboration, Phys. Lett. **B665** 139 (2008).
- [9] V. Chekelian, *Direct  $F_L$  Measurement at High  $Q^2$  at HERA*, 16th International Workshop on Deep Inelastic Scattering, London (7-11 April 2008);  
H1 Collaboration, H1prelim-08-042,  
<http://www-h1.desy.de/h1/www/publications/htmlsplit/H1prelim-08-042.long.html>
- [10] S. Shimizu, *ZEUS High- $y$  Cross Section Measurement and Preparation for Low Energy Running*, Proceedings of the 15th International Workshop on Deep-Inelastic Scattering and Related Subjects, ed. G. Grindhammer and K. Sachs, Verlag Deutsches Elektronen-Synchrotron, April 2007, Munich, Germany, p.289.
- [11] D. Kollár, *Measurement of the Longitudinal Structure Function  $F_L$  at Low  $x$  at HERA with the ZEUS Detector*, 16th International Workshop on Deep Inelastic Scattering, London (7-11 April 2008);  
ZEUS Collaboration, ZEUS-prel-08-001,  
[http://www-zeus.desy.de/public\\_results/publicsearch.html](http://www-zeus.desy.de/public_results/publicsearch.html),  
search-key: ZEUS-prel-08-001.
- [12] S. Chekanov *et al.*, ZEUS Collaboration, Eur. Phys. J. **C42** 1 (2005).

# Spin structure of the nucleon

*Krzysztof Kurek*

*Theoretical Physics Department,  
Institute for Nuclear Studies,  
Hoza 69 pl-00-681 Warsaw, POLAND  
and COMPASS Collaboration*

## 1 The spin degree of freedom

Spin is a fundamental degree of freedom originating from space-time symmetry and plays a critical role in determining the basic structure of fundamental interactions. Spin also provides an opportunity to probe the inner structure of composite systems like a nucleon. After more than 20 years of measurements of the spin-dependent structure functions of the nucleon the third generation of precise polarized experiments is now running and new data are analyzed. Although our knowledge about the spin decomposition in the frame of quark parton model (QPM) and QCD is now more complete and the polarized parton distribution functions (polarized PDFs) are better constrained by data, the driving question for QCD spin physics still has no answer: where does the nucleon spin come from? The famous EMC spin asymmetry measurement [1] and the naive interpretation of the results with help of EllisJaffe sum rule [2] have introduced the so-called spin crisis to Particle Physics : quarks carry only a small fraction of the nucleon helicity. A lot of theoretical work has been done to understand the spin crisis in frame of QCD, e.g. higher order corrections calculated to the EllisJaffe sum rule [3].

The quark helicity distributions  $\Delta q_i(x, Q^2)$  are related to the vector-axial quark current which is not conserved due to the AdlerBellJackiw anomaly. This fact allows to give an explanation of the spin crisis by changing the interpretation of the measurement: instead of the quark spin content  $\Delta\Sigma = \int_0^1 \sum_{i=1}^{n_f} \Delta q_i(x, Q^2) dx$  the flavor-singlet axial current matrix element  $a_0 = \Delta\Sigma - \frac{3\alpha_S}{2\pi} \Delta G$  is measured, where  $\Delta G$  is a gluon helicity inside the nucleon. The spin crisis and the violation of the Ellis-Jaffe sum rule can be then avoided if  $\Delta G$  is large enough. This interpretation was the driving force in the preparation of a series of new polarized DIS type experiments related to - among others - direct measurements of gluon polarization: HERMES in DESY, SMC and COMPASS at CERN, STAR and PHENIX at RHIC. In the light of the new measurements of the gluon polarization the role of the axial anomaly seems to

be marginal as data prefer the gluon contribution to the nucleon's spin to be rather small.

To complete the picture, beside the quark helicities and the gluon polarization also an orbital angular momentum of quarks and gluons can build the longitudinal nucleon spin structure. The definition of the angular momentum of quarks and gluons (orbital as well as total one) is very delicate and nontrivial subject. It should be gauge invariant and expressed in terms of local QCD well defined operators built from quark and gluon fields. This problem was announced to be solved very recently [4].

Complementary measurements to the longitudinal spin structure of the nucleon are performed on transversely polarized targets. The two basic effects which can be accessed with transversely polarized targets are the Collins and the Sivers effect. A new polarized distribution function called "transversity" which is a difference between quark (antiquark) distributions for two different spin orientations relative to the transversely polarized target are associated with such a "transverse" spin proton structure.

Transversity probes the relativistic nature of quarks. For non-relativistic quarks there is no difference of the helicity and transversity distributions because boosts and rotations commute. Relativistic quarks make a difference which can be easily calculated in relativistic models. The good "textbook" example is MIT bag model (for references and calculations see e.g.[5]). The model explains why the naive expectation that  $\Delta\Sigma = 1$  is reduced to  $\sim 0.6$  in the helicity case while for transversity the reduction factor is about 0.83. The nucleon spin decomposition in the case of transversity does not contain gluons; there is no transversity analog of gluon helicity distribution.

In contrast to helicity distributions measured via double-spin asymmetries transverse single-spin asymmetries are studied to extract information about transversity distribution. Due to the fact that transversity is a C-odd and chiral-odd distribution it cannot be accessed in inclusive DIS experiments. The Collins effect [6] uses the spin-dependent part of the hadronization process as a "polarimeter". The Collins chiral-odd and T-even fragmentation function is associated with the correlation between the transverse momentum of the fragmenting quark, the produced hadron and the transversely oriented spin. The Sivers effect [7] is associated with the intrinsic quark transverse momentum in a transversely polarized nucleon. In this case final state interactions produce an asymmetry before the active quark fragments. The Sivers distribution is chiral-even and T-odd and is not universal because it is generated due to final state interactions for DIS and initial state interactions for Drell-Yan process. The Sivers effect requires a correlation of the two QCD amplitudes where two different transverse nucleon spin states produce the same final state. To produce a T-odd effect both amplitudes should have different phases and cannot appear in the so-called tree level approximation. In addition, the two different nucleon spin state amplitudes can give a non-zero correlation if there is non-zero orbital momentum of

the quarks inside the nucleon (see [5] and references therein). The challenge is to disentangle these two effects from the experimental data.

## 2 The cross-section longitudinal asymmetry $A_1$ and $g_1$ structure function

The longitudinal cross-section asymmetry can be decomposed into the virtual photon-deuteron asymmetries  $A_1$  and  $A_2$  as follows:

$$A_{LL} = D(A_1 + \eta A_2) \simeq DA_1, \quad (1)$$

where the photon depolarization factor  $D$  (as well as  $\eta$ ), depends on the event kinematics. All factors which contain  $A_2$  are usually neglected since they are very small in the kinematical range covered by most DIS experiments. However for the JLAB experiments the effects related with  $A_2$  and  $g_2$  are very important and are precisely measured [8]. The spin-dependent structure function  $g_1$  is related to the asymmetry  $A_1$  as follows:

$$g_1 \simeq \frac{F_2}{2x(1+R)} A_1 \quad (2)$$

where  $F_2$  and  $R$  are unpolarized (spin independent) structure functions.

The longitudinal cross-section asymmetry and the  $g_1$  structure function have been measured by many experiments. Here, I will concentrate on the new results from COMPASS, HERMES and - as an example of a very precise measurement from the JLAB facility - new results for the helium spin structure function measured by the E97-110 collaboration at Hall A will be flashed.

The details of the results from the COMPASS experiment can be found in [12] for small  $Q^2$  region and in [13] (large  $Q^2$ ). The experiment was using a 160 GeV polarized muon beam (75% polarization) from the SPS at CERN scattered off a polarized  ${}^6\text{LiD}$  target (polarization: 50%).

The asymmetry and the  $g_1$  structure function for small  $Q^2$  have been calculated for events with  $Q^2 < 1$  ( $\text{GeV}/c$ ) $^2$  and small  $x$  ( $0.00004 < x < 0.02$ ). The data collected in the years 2002-2003 result in a final sample of 300 million events. Systematic errors are mainly due to false asymmetries. The results are consistent with zero in the considered  $x$  range. The statistical precision of  $A_1^d$  and  $g_1^d$  of COMPASS is ten times higher than that of the SMC measurement [10]. The SMC and the COMPASS results are consistent in the region of overlap.

The large  $Q^2$  data collected during the years 2002-2004 result in a sample of 90 million events. The measured  $A_1^d$  asymmetry for  $Q^2 > 1$  ( $\text{GeV}/c$ ) $^2$  (DIS domain) as a function of Bjorken  $x$  as measured in COMPASS and superposed to results of previous experiments at CERN [11], DESY [14] and SLAC [15, 16] is shown in figure 1. The result is consistent with zero for  $x < 0.03$ .

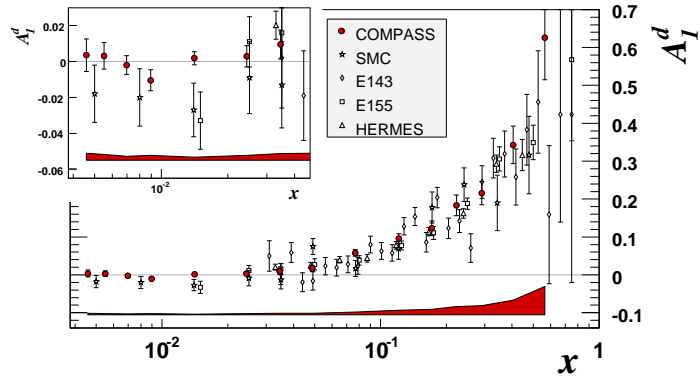


Figure 1: The asymmetry  $A_1^d(x)$  for  $Q^2 > 1$   $(\text{GeV}/c)^2$ . Only statistical errors are shown with a data points. The COMPASS systematic errors are marked by shadowed areas.

In figure 2 the  $g_1$  structure functions for the proton and the deuteron obtained by HERMES collaboration are presented [17] and compared to results of others experiments. The HERMES experiment was using 27.5 GeV electron (positron) beam with polarization 53% on several polarized gas targets (He, H, D). A result for the neutron  $g_1^n$  structure function has been recently published by HERMES [17]. Also a very high precise measurement of the "effective neutron" structure functions  $g_1^n$  and  $g_2^n$  performed on  ${}^3\text{He}$  target has been reported by E97-110 collaboration [8]. The results are presented in figure 3. Note the very precise data also for  $g_2$  and the fact that the measurement is done not in DIS but in the resonance and small  $Q^2$  kinematical regime.

To extract polarized parton distribution functions for quarks and gluons a perturbative QCD analysis is performed. The idea is based on the so-called QCD evolution equations (DGLAP eqs.) which allow to find a link between the  $g_1$  structure function measured at different Bjorken  $x$  and  $Q^2$ . Initial parameterizations of quark combinations and gluons in  $x$  at some fixed  $Q^2$  are assumed and a minimization is performed. Many efforts in the past have been made by several groups, including also COMPASS collaboration [13]. One of the most recent one is a QCD NLO fit done by DSSV group [18]. It is the first time when RHIC proton-proton collision jet data have been included in the fit. The QCD fits allow to estimate the helicity contribution from quarks and gluons to the spin of the nucleon. The DSSV fit predicts  $\Delta\Sigma$  between 0.25 – 0.3 and gluon polarization very close to 0 however still with large error.

Using the experimental values measured by the DIS-type experiments the first moment of  $g_1(x)$ ,  $\Gamma_1$  can be calculated and - with the help of data from weak hyperon decays ( $a_8$  matrix element in the case of deuteron),  $a_0$  can be extracted. Recently

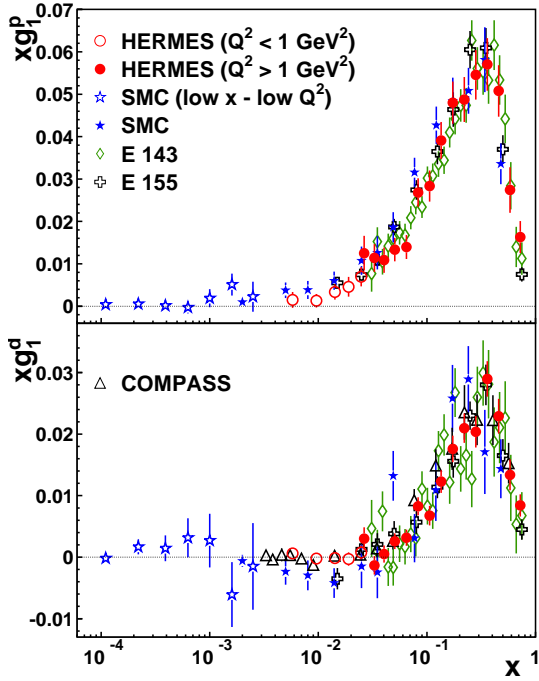


Figure 2: HERMES results on  $xg_1^p$  and  $xg_1^d$  vs  $x$ , shown on separate panels, compared to data from SMC , E143, E155, and COMPASS. The error bars represent the sum in quadrature of statistical and systematic uncertainties.

$\Gamma_1^d$  at  $Q^2 = 3(\text{GeV}/c)^2$  has been calculated from COMPASS deuteron data [13]. The flavor-singlet axial current matrix element,  $a_0$  has been found to be:  $a_0 = 0.35 \pm 0.03(\text{stat.}) \pm 0.05(\text{sys.})$ . Here the value of  $a_8 = 0.585 \pm 0.025$  from [19] has been used. The obtained result is in very good agreement with HERMES result [17] at  $Q^2 = 5(\text{GeV}/c)^2$ :  $a_0 = 0.35 \pm 0.011(\text{theor.}) \pm 0.025(\text{exp.}) \pm 0.028(\text{evol.})$  and with DSSV fit. The combination of the matrix elements:  $\frac{1}{3}(a_0 - a_8)$  is equal to strange quark contribution to the nucleon spin. From the COMPASS inclusive analysis  $\Delta s + \Delta \bar{s} = -0.08 \pm 0.01(\text{stat.}) \pm 0.02(\text{sys.})$  is obtained.

### 3 Semi-inclusive hadron asymmetries

Semi-inclusive measurements (at least one hadron is observed in the final state) allow to extract more information, in particular allow to separate of the flavours of quarks. The prize is that the analysis requires knowledge about fragmentation functions. However, there are very interesting observables called difference asymmetries  $A^{h^+ - h^-}$  [20] which can be interpreted in LO QCD under the assumption of independent fragmen-

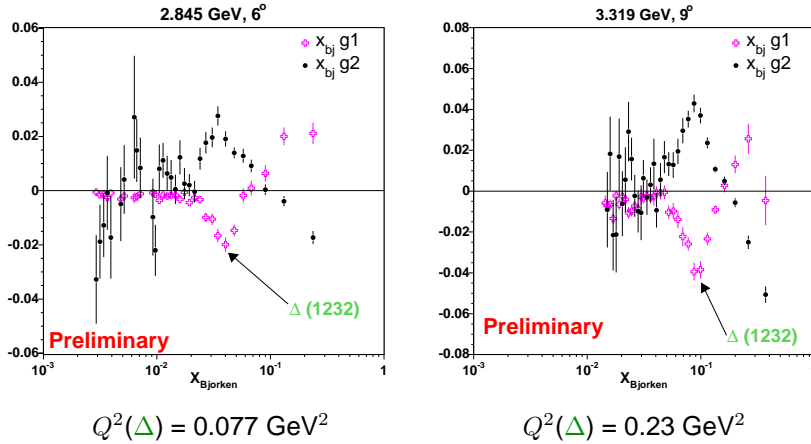


Figure 3: Neutron polarized structure functions  $xg_1^n$  and  $xg_2^n$  as a function of  $x$  from E97-110 experiment at Hall A at JLAB.

tation as the ratio of polarized and unpolarized valence quark distributions:

$$A_d^{\pi^+ - \pi^-} = A_d^{K^+ - K^-} = \frac{\Delta u_v(x) + \Delta d_v(x)}{u_v(x) + d_v(x)}. \quad (3)$$

Here, subscript "d" is related to deuteron target data collected by the COMPASS experiment which were already used in the recently published difference asymmetry analysis [21]. Combining the first moment of the polarized valence quark distribution estimated from the difference asymmetry measurement with first moment of  $\Gamma_1^d$  obtained from inclusive measurements and using again  $a_8$  from [19] it is possible to give an estimate of sea quark polarization.

Comparing the results to the so-called symmetric scenario which assumes that  $\Delta\bar{u} = \Delta\bar{d} = \Delta\bar{s} = \Delta s$  and to the antisymmetric ones where  $\Delta\bar{u} = -\Delta\bar{d}$  it is concluded that the COMPASS data support antisymmetric possibility [21].

The new HERMES semi-inclusive analysis of the strange quark polarization based on the measured kaon asymmetries has been very recently reported [22]. The interesting point is that for this analysis all information necessary (including kaon fragmentation functions) have been extracted from HERMES data alone. The inclusive asymmetry  $A_1^d$  and the kaon asymmetry  $A_1^{d,K}$  as well as kaon multiplicities have been used. Data have been collected on a deuteron target as isoscalarity simplifies the analysis of fragmentation functions. The strange quark polarization  $\Delta s$  has been found to be:  $\Delta s = 0.037 \pm 0.019(\text{stat.}) \pm 0.027(\text{sys.})$  for the  $x$  range from 0.002 till 0.6. The obtained result for  $\Delta s$  is positive in contrast to the COMPASS result from inclusive measurement which is slightly negative.

## 4 The Gluon polarization

As QCD fits are not able to determine the gluon polarization with high precision so far, an alternative method is to extract polarized gluons directly from measured semi-inclusive asymmetries (HERMES, SMC, COMPASS and so-called prompt photon channel at RHIC). The precise measurements of pion and jet asymmetries from RHIC allow also to compare with models of the gluon polarization. This method is inspired by the method used in global QCD analysis and - as it was discussed above - is now used in DSSV fit. The advantage of the direct method is the possibility to determine  $\Delta G/G$  without any assumption on the dependence on the momentum fraction  $x_G$  of the polarized gluon distribution, as it is done in fit-type methods. The experimental challenge is to select the data sample which allows to access gluon-originated subprocesses.

Recently two new results for the gluon polarization from direct measurements have been reported by the COMPASS collaboration. The open-charm channel is the classical way to access gluons for relatively low energies when the charm quark can be considered as heavy, not present inside the nucleon and produced only in hard processes. The measured longitudinal cross section asymmetry of charmed meson ( $D^*$  and  $D^0$ ) production allows to determine  $\Delta G/G$ .

In the LO QCD approximation only the so-called photon-gluon fusion (PGF) process contributes. In COMPASS this channel is experimentally difficult and statistics is very limited. The new result obtained from the 2002 – 2006 data is [23]:  $\Delta G/G = -0.49 \pm 0.27(stat.) \pm 0.11(sys.)$  at a value of  $x_G \simeq 0.11$ , with an asymmetric range of  $0.06 < x_G < 0.22$ , and a scale  $\mu^2 \simeq 13$  (GeV/c) $^2$ .

The alternative way to select PGF events is to observe high- $p_T$  hadron pairs in the final state. The analysis is Monte-Carlo dependent (due to physical background from hard sub-processes different from PGF) and requires very good agreement between data and MC. The big advantage is a large gain in statistics compared to the open-charm channel. The new COMPASS result for the large  $Q^2$  ( $Q^2 > 1$  (GeV/c) $^2$ ) high- $p_T$  analysis [24] is:  $\Delta G/G = -0.08 \pm 0.1(stat.) \pm 0.05(sys.)$  at a value of  $x_G \simeq 0.082$ , with an asymmetric range of  $0.06 < x_G < 0.12$ , and a scale  $\mu^2 \simeq 3$  (GeV/c) $^2$ . Both presented analysis are limited to LO QCD approximation so far.

To illustrate the progress in precision of the RHIC measurements the  $\pi^0$  longitudinal asymmetry obtained from Run 5 and new Run 6 [25] are shown in figure 4. The increasing precision is also seen in the new results from the STAR experiment from jet analysis [26] compared to the published result in [27].

The measured cross sections for different final states in STAR and PHENIX agree with the NLO QCD theoretical predictions very well. This fact justifies the theoretical approach based on QCD calculations and allows to predict asymmetries for different gluon polarization models. The predictions for different models are then compared to data.

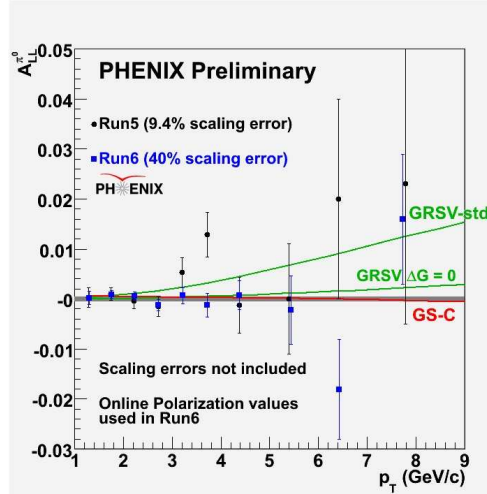


Figure 4: Preliminary Run 6 results for  $\sqrt{s} = 200$  GeV for  $\pi^0 A_{LL}$  asymmetry vs  $p_T$ .

The results presented in this section as well as the results from QCD fits point to a small value of the gluon polarization. Therefore, the role of the axial anomaly seems to be rather marginal.

## 5 Collins and Sivers asymmetries from HERMES and COMPASS

The single hadron spin asymmetries measured on transversely polarized targets allow to investigate the Collins and the Sivers effect. The HERMES results for asymmetries of charged pions measured on a transversely polarized proton target show that both effects are non-zero [28, 29]. These important results indicate that the Collins fragmentation function is non-zero ("polarimeter" in Collins effect) and a signature of the quark orbital angular momentum is seen (Sivers). The results from COMPASS measured on a deuteron target show that both effects are very close to zero [30, 31]. Therefore the cancellation of the effects between proton and neutron in the deuteron target is concluded. Very recently new results on charged hadron asymmetries measured on a proton target in 2007 by COMPASS have been reported [32]. The Collins asymmetries are non-zero and in a good agreement with the HERMES results while the Sivers effect is compatible with zero. This is unexpected result needs to be confirmed with larger statistics.

## 6 Summary

Precise measurements of the spin structure function  $g_1$  show that quarks contribute only about 1/3 to the spin of the nucleon. This result is also confirmed by QCD fits and by an independent measurement of the valence quark polarization. Direct measurements point to a small value of the gluon polarization, however 0.2 – 0.3 is still not excluded. Different types of asymmetries precisely measured at RHIC also indicate that the large gluon polarization scenario is rather excluded and the role of axial anomaly is small. Results for difference asymmetries measured by COMPASS support the so-called antisymmetric scenario:  $\Delta\bar{u} = -\Delta\bar{d}$ . A small positive polarization for strange quarks has been measured by HERMES while COMPASS results based on sum rules give a small negative polarization of the strange sea.

Collins asymmetries measured on a proton target are non-zero for large Bjorken  $x$ . The Collins and the Sivers asymmetries measured by COMPASS on deuteron target are compatible with zero what suggest a cancellation of the effect from the proton and the neutron in the deuteron. Non-zero Sivers asymmetries are observed by HERMES on a proton target while COMPASS results from proton data are compatible with zero. A non-zero Sivers effect can be related to the non-zero total orbital angular momentum of the quarks. Recent results from lattice QCD calculations predict however that the total angular momentum of quarks should be close to zero [33]. In connection with the fact that the gluon polarization seems to be small or zero this leads to a very interesting scenario: a  $\sim 33\%$  of the spin of the nucleon is carried by helicity of the quarks, mainly valence ones; the missing part has to come from orbital angular momentum of gluons. A more "classical" scenario where the gluon polarization is 0.2 – 0.3 is not yet excluded by the data and can also solve the nucleon spin decomposition problem without large total orbital angular momentum of quarks and gluons.

This work was Supported by Ministry of Science and Higher Education grant 41/N-CERN/2007/0

## References

- [1] J. Ashman et al., Phys. Lett. *B*206, 364 (1988), Nucl. Phys. *B*328, 1 (1989).
- [2] J. Ellis, R. L. Jaffe, Phys. Rev. *D*9, 1444 (1974), Phys. Rev. *D*10, 1669 (1974).
- [3] S. A. Larin, Phys. Lett. *B*334, 192 (1994).
- [4] X-S. Chen et al., Phys. Rev. Lett. 100, 232002-1 (2008).

- [5] S. D. Bass, "The spin Structure of the Proton", World Scientific Publishing Co.Pte.Ltd. 2008.
- [6] J. C. Collins, Nucl. Phys. *B*396, 161.
- [7] D. Sivers, Phys. Rev. *D*43, 261.
- [8] V. Sulkosky, talk given at XVI International Workshop on Deep-Inelastic Scattering and Related Subjects, DIS 2008, 7-11 April 2008, University College London.
- [9] X. Zheng et al., Phys. Rev. Lett. 92, 012004,(2004).
- [10] SMC, B. Adeva et al., Phys. Rev. *D*60, 072004 (1999).
- [11] SMC, B. Adeva et al., Phys. Rev. *D*58, 112001 (1998); Erratum *ibid.* *D*62, 079902.
- [12] COMPASS, V. Yu. Alexakhin et al., Phys. Lett. *B*647, 330 (2007).
- [13] COMPASS, V. Yu. Alexakhin et al., Phys. Lett. *B*647, 8 (2007).
- [14] HERMES, A. Airapetian et al., Phys. Rev. *D*75, 012003 (2005).
- [15] E143, K. Abe et al., Phys. Rev. *D*58, 112003 (1998).
- [16] E155, P. L. Anthony et al., Phys. Lett. *B*463, 339 (1999).
- [17] HERMES, A. Airapetian et al., Phys. Rev. *D*75, 0120037 (2007).
- [18] D. de Florian, R. Sassot, M. Stratmann, W. Vogelsang, Phys.Rev.Lett. 101, 072001,(2008)
- [19] Y. Goto et al., Phys. Rev. *D*62, 034017 (2000).
- [20] L. Frankfurt et al., Phys. Lett. *B*230, 141 (1989).
- [21] COMPASS, M. Alekseev et al., Phys. Lett. *B*660, 458 (2008).
- [22] HERMES, A. Airapetian et al, arXiv:0803.2993, Phys. Lett. *B* (in press).
- [23] F. Robinet, talk given at XVI International Workshop on Deep-Inelastic Scattering and Related Subjects, DIS 2008, 7-11 April 2008, University College London.
- [24] M. Stolarski, arXiv:0809.1803, talk given at XVI International Workshop on Deep-Inelastic Scattering and Related Subjects, DIS 2008, 7-11 April 2008, University College London.
- [25] K. Aoki, talk given at XVI International Workshop on Deep-Inelastic Scattering and Related Subjects, DIS 2008, 7-11 April 2008, University College London.

- [26] C. A. Gagliardi, talk given at XVI International Workshop on Deep-Inelastic Scattering and Related Subjects, DIS 2008, 7-11 April 2008, University College London.
- [27] STAR, B. I. Abelev et al., Phys.Rev.Lett. 100, 232003,(2008).
- [28] HERMES, A. Airapetian et al., Phys. Rev. Lett. 94, 012002, (2005).
- [29] D. Hash, talk given at International workshop on hadron and spectroscopy, Torino, Italy, 31.03 02.04.2008
- [30] COMPASS, E.S. Ageev et al., Nucl. Phys. B765, 31,(2007).
- [31] COMPASS, M. Alekseev et al., arXiv:0802.2160, sent to Phys. Lett. B.
- [32] S. Levorato, talk given at Second International Workshop on Transverse Polarisation Phenomena in Hard Processes, Transversity 2008, 28-31.05.2008, Ferrara.
- [33] P. Hagler, talk given at XVI International Workshop on Deep-Inelastic Scattering and Related Subjects, DIS 2008, 7-11 April 2008, University College London.

# What is the matter created in heavy ion collisions?

*Raphael Granier de Cassagnac  
Laboratoire Leprince-Ringuet  
École polytechnique, CNRS/IN2P3  
91128 Palaiseau, France*

## 1 Foreword

Nowadays, the most violent heavy ion collisions available to experimental study occur at the Relativistic Heavy Ion Collider (RHIC) of the Brookhaven National Laboratory. There, gold ions collide at  $\sqrt{s_{NN}} = 200$  GeV. The early and most striking RHIC results were summarized in 2005 by its four experiments, BRAHMS, PHENIX, PHOBOS and STAR, in their so-called *white papers* [1, 2, 3, 4] that will be referenced thereafter. Beyond and after this, a wealth of data has been collected and analyzed, and provided additional elements for an answer to the question raised by my title. It is categorically impossible to give a comprehensive review of these results in a 30 minutes talk or a 10 pages report. I have made the choice to focus on the so-called *hard probes* : jet quenching in sections 2 and 3, quarkonia in section 4 and photons in section 5. Emphasis is put on latest results (some of them being very preliminary) and on the new tools recently made available. A more comprehensive (and slightly older) review can be found in Ref. [5].

One of the obvious manifestation of the collision violence is the transverse (i.e. unboosted by the initial parton longitudinal momenta) energy liberated. Measuring it allows one to estimate the energy density  $\varepsilon$  of the medium after a given time  $\tau_0$ , through the Bjorken formula [6]:  $\varepsilon = dE_T/dy|_{y=0}/\tau_0 A_T$ , where  $A_T$  is the transverse area of the collision. The four RHIC experiments measure consistent values of  $dE_T/dy|_{y=0}$  that correspond to an energy density of at least  $5 \text{ GeV/fm}^3$  at  $\tau_0 = 1 \text{ fm}/c$ . The question of the time to be considered is not trivial, but  $1 \text{ fm}/c$  is a maximum if one cares about the earliest as possible *thermalized* medium. Indeed, hydrodynamical analyses of collective phenomena provide thermalization times between 0.6 and  $1 \text{ fm}/c$ , while the formation time is estimated to be  $0.35 \text{ fm}/c$  and the nucleus-nucleus crossing time is  $0.13 \text{ fm}/c$ . For a detailed discussion of energy density and time scale estimates, see section 2 of Ref. [2]. What matters here is that the *lower* energy density estimate is much higher than the threshold for the transition to a quark gluon plasma, as predicted by QCD on the lattice [7]:  $\varepsilon_c \sim 1 \text{ GeV/fm}^3$ .

This tells us that **the matter should be deconfined**, i.e. made of free quarks and gluons. The following sections review some of the measurements that indicate that it is indeed the case.

## 2 High Transverse Momentum Suppression

Fig. 1 is an illustration of the first and most striking QGP signature seen at RHIC, namely the quenching of jets [8, 9]. Displayed is the nuclear modification factor  $R_{AA}$  defined as the yield of particles seen in A+A collisions, normalized by the same yield from p+p collisions scaled by the average number of binary collisions corresponding to the considered centrality:  $R_{AA} = dN_{AA}/\langle N_{coll} \rangle \times dN_{pp}$ . Hard processes (high  $p_T$  particles in particular) are expected to respect such a scaling ( $R_{AA} = 1$ ). This is indeed the case of the direct photon<sup>1</sup> [12] (purple squares) up to 13 GeV/c, while the corresponding  $\pi^0$  (orange triangles) and  $\eta$  up to 10 GeV/c (red circles) are suppressed by a factor of five. This is understood as an energy loss of the scattered partons going through a very dense matter, and producing softened jets and leading (high  $p_T$ ) particles. The medium is so dense that it cannot be made of individual hadrons, but rather of quarks and gluons. In [13], PHENIX has released  $\pi^0$  modification factors up to 20 GeV/c, and performed a quantitative estimate of the constraints they put on theoretical models. As an example, gluon densities of  $dN_g/dy = 1400^{+270}_{-150}$  are needed to produce such a strong quenching in the model depicted in Ref. [14].

High  $p_T$  suppression is seen for various particles with various  $p_T$  reaches and by the four experiments [1, 2, 3, 4]. It gets stronger for more central collisions. It is not observed in d+Au collisions (in particular for neutral pions [15] to be compared to the ones on Fig. 1) where a moderate enhancement is even seen as a function of  $p_T$ , probably due to multiple scattering of the incoming partons providing additional transverse momentum (the so-called Cronin effect).

In addition, quenching of electrons coming from semi-leptonic decays of heavy flavors (charm and beauty) was also observed [16, 17]. The low  $p_T$  dominant yield scale with the number of collisions ( $R_{AA} \simeq 1$ ) as expected and seen on Fig. 2 (full green circles) but higher  $p_T$  electrons (blue open circles) are quenched by an amount not far from the one of light quarks (red squares). This was a surprise, since energy loss in a gluon medium was expected to be reduced for heavy quarks. In order to reproduce the data, one needs a much higher gluon density than the one required for light flavors ( $dN_g/dy \sim 3500$  [18]). Various hypotheses are made to reinforce the heavy quark quenching (adjunction of elastic energy loss, change in the charm/beauty

---

<sup>1</sup>PHENIX has released preliminary photons up to 18 GeV/c [10], which start to deviate below unity. As discussed in [11], this can be explained by several phenomena (nucleus to proton isospin difference, EMC effect, or quark energy loss prior to photon emission) which have nothing to do with QGP.

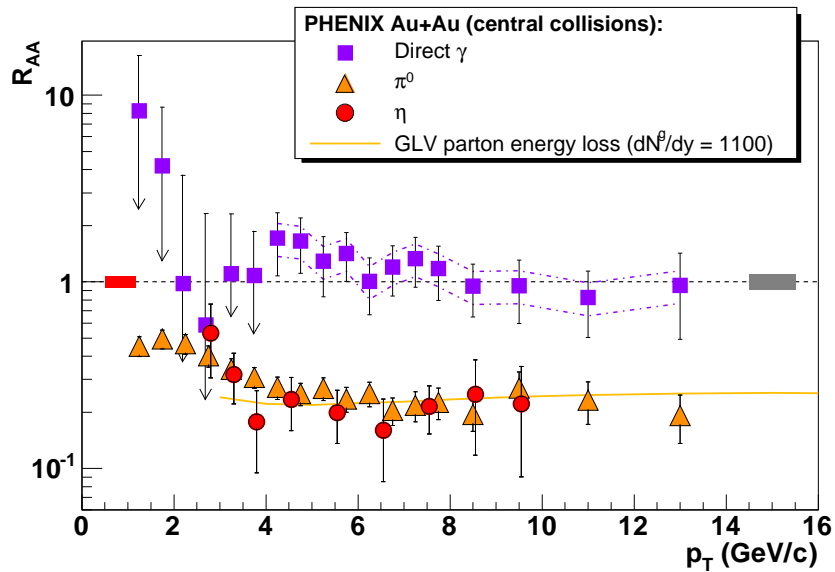


Figure 1: Nuclear modification factors for photon,  $\eta$  and  $\pi^0$  for central collisions, from the PHENIX experiment.

ratio, modification of the strong coupling constant...).

In any case, This quenching of high  $p_T$  particles shows that **the matter they traverse is dense**.

### 3 Back to Back Jets

Another way to look at jets is to consider back to back high transverse momentum hadron correlations. Fig. 3 shows the measurements of such correlations for various collision types performed by the STAR experiment and reported in section 4.2 of Ref. [4]. Displayed are the azimuthal distributions of hadrons around a “trigger” particle of high enough  $p_T$  to reflect the main direction of jets (4 GeV/c for the trigger particle and 2 GeV/c for the others in this example). In  $p+p$  collisions (black histogram), one clearly sees particles belonging to both the narrower same ( $\Delta\phi = 0$ ) and broader opposite ( $\Delta\phi = \pi$ ) jets, while in central  $Au+Au$  collisions (blue stars) the away-side jet disappears [19]. This is also attributed to jet quenching, the away-side jet being absorbed by the dense matter produced at RHIC. As for the high  $p_T$  suppression we saw in the previous section, this effect is not observed in  $d+Au$  collisions (red circles) where away-side hadrons are clearly distinguishable [20].

Jet-induced hadron production has been further and extensively investigated at RHIC and various effects corroborate the jet quenching hypothesis, among which:

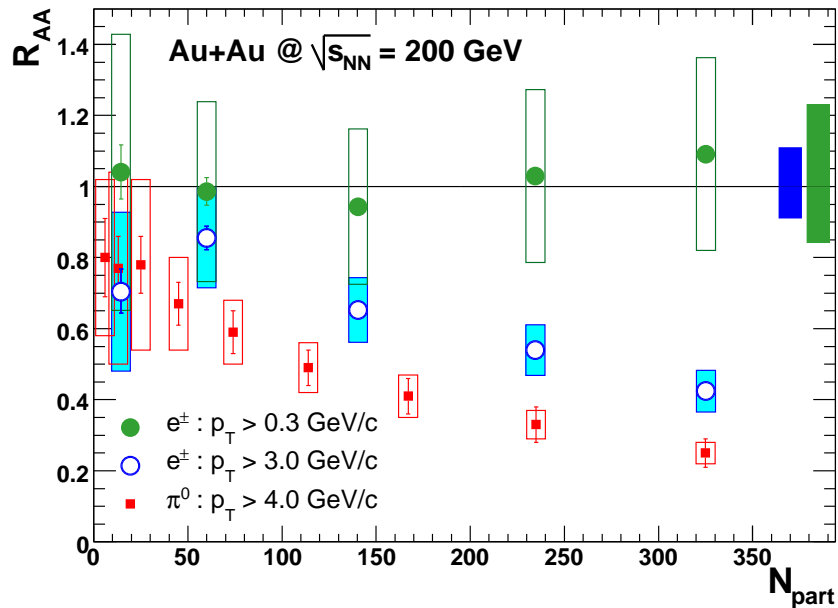


Figure 2: Heavy flavor decay electrons nuclear modification factor, for various  $p_T$  as a function of centrality [16].

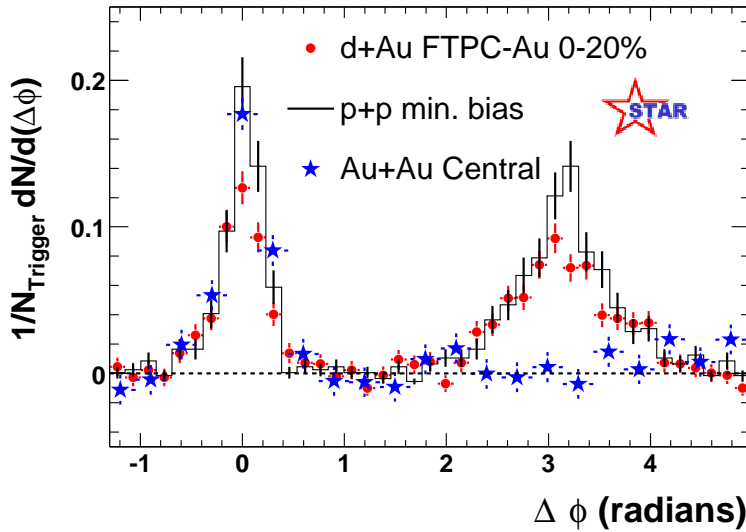


Figure 3: Dihadron azimuthal correlations in  $p+p$ ,  $d+Au$  and  $Au+Au$  central collisions, from the STAR experiment.

- In Au+Au collisions, the away-side disappearance grows with centrality. In fact, the most peripheral collisions exhibit a very similar away-side pattern as in p+p and d+Au collisions.
- The jets emitted in the reaction plane are less suppressed than in the perpendicular direction, where they have more matter to traverse [21]. In fact, the high  $p_T$  (near-side) particles we see in central Au+Au collisions are likely to come from the periphery, the “corona”, of the collision.
- By lowering the  $p_T$  requirements (down to  $\sim 1$  GeV/c), one can find back the away-side jets [22].
- These weakened away-side jets are depleted at  $\Delta\phi = \pi$  and exhibit two displaced maxima around  $\Delta\phi = \pi \pm 1.1$  radians [23, 24]. This camel-back or conical-like shape provides insight in the quenched parton interactions with the medium. Various scenarios are proposed, such as radiative loss [25], Čerenkov-like or Mach-cone emissions [26]. The later allows one to compute an average speed of sound in the medium of  $c_S \sim 0.45$ .
- Analyses of three particles correlations also exhibit the conical pattern [27].
- The near-side jet exhibits a “ridge” along pseudorapidity (thus perpendicular to the azimuthal structure) that suggests the jets are indeed flowing with the expanding matter [22, 24, 28].

In brief, these high  $p_T$  dihadron correlation studies show that **the matter is opaque** to jets to a first approximation, and clearly modifying their remaining structure. In addition to this, two new tools were recently made available, thanks to the statistics accumulation at RHIC:

- The correlation of a jet (or leading hadron) with a high energy photon helps calibrating the jet, since the photon should be unmodified by the medium and thus balancing its initial transverse momentum. Both STAR [29] and PHENIX [30] have seen away side jets and released preliminary analyses of the so called  $I_{AA}$  (or  $I_{CP}$ ), which is the jet particle yield per photon seen in central A+A collisions with respect to p+p (or peripheral A+A). Though limited by statistics,  $I_{AA}$  exhibit a similar suppression as  $R_{AA}$ .
- Another long awaited tool was the full reconstruction of jets in a heavy ion collision environment. It has been shown very recently by the STAR experiment [31]. A very preliminary fragmentation function is derived and show no sizeable modification.

## 4 Quarkonia Suppression

We saw on Fig. 2 that the bulk (low  $p_T$ ) charm production scales to first order with the number of binary collisions. This forms a good baseline for the study of bound states made of charm-anticharm quarks, the more stable of which being the  $J/\psi$  particle. In fact, charmonia were predicted to melt in the QGP, due to Debye screening of the color charge [32]. Furthermore,  $J/\psi$  suppression was indeed observed at lower energy ( $\sqrt{s_{NN}} = 17.3$  GeV) by the NA50 experiment [33] and is the main signature that led CERN to claim for the discovery of QGP. It was thus very awaited at RHIC energies. Fig. 4 shows  $J/\psi$  nuclear modification factors as measured by the PHENIX experiment [34], for both mid (red circles,  $|y| < 0.35$ ) and forward rapidity (blue squares,  $1.2 < |y| < 2.2$ ), as a function of centrality (given by the number of participants  $N_{part}$ ). These results brought two surprises:

- First, the midrapidity result is surprisingly similar to the one observed by the NA50 experiment which also lies close to midrapidity (black crosses,  $0 < y < 1$ ). There is no fundamental reason for this to happen since the energy density for a given  $N_{part}$  is higher at RHIC and should further melt quarkonia.
- Even more surprising is the fact that, at forward rapidity,  $J/\psi$  are further suppressed (by  $\sim 40\%$ ), while any density induced suppression scenario, such as the Debye screening mentioned above would predict the opposite trend.

But one needs to be careful in interpreting these results since  $J/\psi$  are known to be suppressed by regular nuclear matter as it is seen in p+A or d+A collisions [33, 35]. In order to compare two regimes, one thus first needs to subtract these *normal* nuclear matter effects. At RHIC, they are poorly constrained by a relatively low statistics d+Au data set. Several methods, summarized in [35], can nevertheless be used to estimate them. The most data-driven one, inspired by [36] is used to obtain the right part of Fig. 4. The very large error bar displayed as a box is essentially reflecting the large normal suppression uncertainties. It illustrates that the two surprises mentioned above may be caused by normal effects: anomalous suppression could be different at SPS and RHIC, and similar at forward and rapidity at RHIC. More RHIC d+Au data is clearly needed to reduce the normal suppression uncertainty. However, we clearly see that  $J/\psi$  are suppressed beyond normal nuclear effects, both at SPS and RHIC (especially at forward rapidity).

An alternate scenario was (prematurely) proposed to explain the RHIC rapidity difference.  $J/\psi$  could indeed be recreated in the plasma by recombination of independent charm and anticharm quarks (a large variety of recombination or coalescence models [37, 38, 39, 40, 41, 42, 43] exists). This beautiful idea of *reconfinement*, and thus of *deconfinement*, unfortunately do not provide very quantitative predictions of the nuclear modification factors (recombination models suffering from the lack of

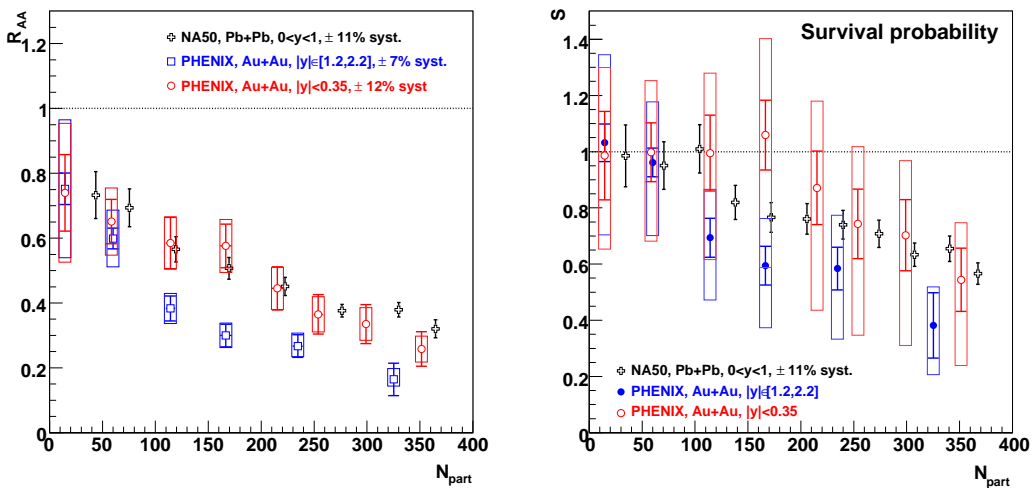


Figure 4:  $J/\psi$  suppression measured by the PHENIX and NA50 experiments, as a function of centrality, given by the number of participants. Left: nuclear modification factor. Right:  $J/\psi$  survival probabilities after normal nuclear effects subtraction.

input charm quark distributions). Other observables ( $p_T$  dependence, elliptic flow, feed-down contributions...) start to be available<sup>2</sup> but so far, they do not allow to conclude.

However, even if the details of the mechanisms responsible for the exact  $J/\psi$  yield at RHIC are not known, we do not need them to reckon that  $J/\psi$  do melt beyond normal nuclear effects, at least in the most central collisions. This is a sign that **the matter is deconfining**.

## 5 Thermal Radiation

A thermalized matter should emit its own thermal radiation. We saw on Fig. 1 that photons are unmodified by the medium and the nuclear modification factor is compatible with unity. This holds for  $p_T > 2$  GeV/ $c$ , but lower  $p_T$  photons exhibit an *enhancement*. The bottom of Fig. 5 shows the p+p photon spectrum (as stars bur from PHENIX) compared to NLO pQCD calculation. The upper spectra are from various centrality selection of Au+Au collisions. The dashed lines are derived from the p+p collisions and scaled up by the number of collisions. The lowest  $p_T$  photons (obtained through an internal conversion method [45]) clearly exhibit an enhancement. Various hydrodynamical models (for a review, see [46]) fairly reproduce the data assuming early (typically at a time of the order of 0.15 to 0.6 fm/ $c$ ) temperature

<sup>2</sup>For a complete recent review on the subject, see Ref. [44].

of 300 to 600 MeV, well above the critical temperature of  $T_c = 190$  MeV provided by lattice QCD [7] as the phase transition boundary to a quark-gluon plasma.

We thus do see thermal photons that demonstrate that **the matter is hot**.

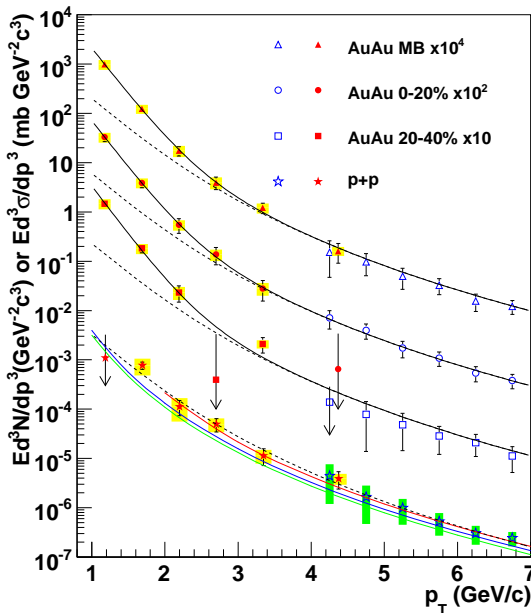


Figure 5: Thermal + perturbative QCD fits to the photon yield in Au+Au collisions, as seen by the PHENIX experiment [45]. The lower points are from p+p collisions and are matched to perturbative QCD only.

## 6 Conclusions

Even if we have not (yet) observed any sharp change in the behavior of the Au+Au observables related to the predicted phase transition, nor numbered degrees of freedom, it is clear that the matter produced at RHIC behaves very differently than ordinary hadronic matter. Indeed, to answer the question raised by my title, we saw that the matter is dense, opaque, deconfining and hot. Other observables [5] show that it is also gluon saturated, strongly interacting and liquid-like, as well as of partonic nature. It is thus very likely to be formed by deconfined quarks and gluons.

## References

- [1] I. Arsene et al. Nucl. Phys. A757 (2005) 1, nucl-ex/0410020.
- [2] K. Adcox et al. Nucl. Phys. A757 (2005) 184, nucl-ex/0410003.
- [3] B. B. Back et al. Nucl. Phys. A757 (2005) 28, nucl-ex/0410022.
- [4] J. Adams et al. Nucl. Phys. A757 (2005) 102, nucl-ex/0501009.
- [5] R. Granier de Cassagnac. Int. J. Mod. Phys. A22 (2008) 6043, arXiv:0707.0328.
- [6] J.D. Bjorken. Phys. Rev. D27 (1983) 140.
- [7] F. Karsch. Lect. Notes Phys. 583 (2002) 209.
- [8] S. S. Adler et al. Phys. Rev. Lett. 91 (2003) 072301, nucl-ex/0304022.
- [9] S. S. Adler et al. Phys. Rev. C75 (2007) 024909, nucl-ex/0611006.
- [10] T. Isobe. J. Phys. G34 (2007) S1015, nucl-ex/0701040.
- [11] F. Arleo. JHEP 09 (2006) 015, hep-ph/0601075.
- [12] S. S. Adler et al. Phys. Rev. Lett. 94 (2005) 232301, nucl-ex/0503003.
- [13] A. Adare et al. Phys. Rev. C77 (2008) 064907, arXiv:0801.4020.
- [14] I. Vitev and M. Gyulassy. Phys. Rev. Lett. 89 (2002) 252301, hep-ph/0209161.
- [15] S. S. Adler et al. Phys. Rev. Lett. 91 (2003) 072303, nucl-ex/0306021.
- [16] A. Adare et al. Phys. Rev. Lett. 98 (2007) 172301, nucl-ex/0611018.
- [17] B. I. Abelev et al. Phys. Rev. Lett. 98 (2007) 192301, nucl-ex/0607012.
- [18] M. Djordjevic et al. Phys. Lett. B632 (2006) 81, nucl-th/0507019.
- [19] C. Adler et al. Phys. Rev. Lett. 90 (2003) 082302, nucl-ex/0210033.
- [20] J. Adams et al. Phys. Rev. Lett. 91 (2003) 072304, nucl-ex/0306024.
- [21] J. Adams et al. Phys. Rev. Lett. 93 (2004) 252301, nucl-ex/0407007.
- [22] J. Adams et al. Phys. Rev. Lett. 95 (2005) 152301, nucl-ex/0501016.
- [23] S. S. Adler et al. Phys. Rev. Lett. 97 (2006) 052301, nucl-ex/0507004.
- [24] A. Adare et al. Phys. Rev. C78 (2008) 014901, arXiv:0801.4545.

- [25] A. D. Polosa and C. A. Salgado. Phys. Rev. C75 (2007) 041901, hep-ph/0607295.
- [26] J. Ruppert and B. Muller. Phys. Lett. B618 (2005) 123, hep-ph/0503158.
- [27] B. I. Abelev et al. arXiv:0805.0622.
- [28] J. Adams et al. Phys. Rev. C73 (2006) 064907, nucl-ex/0411003.
- [29] A. M. Hamed. Hard probes 2008 conference, arXiv:0809.1462.
- [30] M. Nguyen. J. Phys. G35 (2008) 104121, arXiv:0805.1225.
- [31] S. Salur. Hard probes 2008 conference, arXiv:0809.1609.
- [32] T. Matsui and H. Satz. Phys. Lett. B178 (1986) 416.
- [33] B. Alessandro et al. Eur. Phys. J. C39 (2005) 335, hep-ex/0412036.
- [34] A. Adare et al. Phys. Rev. Lett. 98 (2007) 232201, nucl-ex/0611020.
- [35] A. Adare et al. Phys. Rev. C77 (2008) 024912, arXiv:0711.3917.
- [36] R. Granier de Cassagnac. J. Phys. G34 (2007) S955, hep-ph/0701222.
- [37] A. Andronic et al. Nucl.Phys. A789 (2007) 334, nucl-th/0611023.
- [38] R. L. Thews. Eur. Phys. J. C43 (2005) 97, hep-ph/0504226.
- [39] L. Ravagli and R. Rapp. Phys. Lett. B655 (2007) 126, arXiv:0705.0021.
- [40] X. Zhao and R. Rapp. Phys. Lett. B664 (2008) 253, arXiv:0712.2407.
- [41] L. Yan et al. Phys. Rev. Lett. 97 (2006) 232301, nucl-th/0608010.
- [42] O. Linnyk et al. Nucl. Phys. A807 (2008) 79, 0801.4282.
- [43] K. Tywoniuk et al. J. Phys. G35 (2008) 104156, arXiv:0804.4320.
- [44] R. Granier de Cassagnac. J. Phys. G35 (2008) 104023, arXiv:0806.0046.
- [45] A. Adare et al. submitted to Phys. Rev. Lett., arXiv:0804.4168.
- [46] D. d'Enterria and D. Peressounko. Eur. Phys. J. C46 (2006) 451, nucl-th/0503054.

## Discussion

**Question:** When will we have a single simple signature of the quark gluon plasma creation?

**Answer:** In this complicated field, I think that the picture of what the created matter really is can only emerge from a variety of “signatures”, each of which being individually challenged by models, given the very wide phase space offered to theories. I think this variety of signatures is indeed observed at RHIC.

# Higgs Searches and BSM Physics

Session Convener:  
Session Convener:

*Rudiger Voss*  
*Tom Ludlam*

Higgs Searches at the Tevatron

*Anyes Taffard*

Higgs searches at LHC

*Giorgia Mila*

Beyond the Standard Model  
Searches at HERA and the Tevatron

*Stefan Grünendahl*

BSM measurements with Top at LHC: CMS  
sensitivity to Flavour Changing Neutral Currents

*Leonardo Benucci*

$ZZ$  into  $4\ell$  expected sensitivity with the first  
ATLAS data

*Ilektra A. Christidi*

ATLAS RPC commissioning status  
and cosmic ray test results

*Michele Bianco*

# Higgs Searches at the Tevatron

*Anyes Taffard*

*University of California Irvine, CA 92697, U.S.A.  
on behalf of the CDF and DO Collaborations.*<sup>1</sup>

## 1 Abstract

We review the status of the searches for the Higgs boson in the context of the Standard Model and the Minimal SuperSymmetric Standard Model by the CDF and DO experiments at the Fermilab Tevatron proton-antiproton collider, using up to  $2.4 \text{ fb}^{-1}$  of Run II data. Since no evidence of signal above the expected background is observed in any of the various final states examined, limits at 95% confidence level are presented.

## 2 Introduction

In the Standard Model (SM), the Higgs mechanism breaks the electroweak symmetry by introducing a scalar field to generate particle masses. It predicts the existence of a neutral spin 0 boson, the Higgs boson, but not its mass. Direct searches at LEP 2 have excluded a SM Higgs boson with mass below 114.4 GeV at 95% confidence level (C.L.). Indirect measurements from SLD, LEP and the Tevatron, favor a light Higgs boson with mass of  $87^{+36}_{-27}$  GeV at 68% C.L. and constrain its mass to be below 190 GeV at 95% C.L. when including the LEP 2 exclusion [1].

At the Tevatron, SM Higgs production is dominated by gluon fusion, with smaller contributions from W or Z bosons associated productions. Cross sections range from 0.1 to 1 pb. Below 135 GeV (low-mass), the SM Higgs boson decays predominantly to  $b\bar{b}$ . In order to avoid the huge SM QCD multijets background, searches use the associated productions:  $WH$  and  $ZH$ . Above 135 GeV (high-mass), SM Higgs decays predominantly to  $WW^*$ , thus making it possible to use the gluon fusion production.

---

<sup>1</sup>Presented at the Symposium “Physics in Collision”, Perugia, June 25-28, 2008.

Many models beyond the SM, including Supersymmetry, predict larger Higgs production cross sections, some of which within reach in the present data sets [2]. The Minimal Supersymmetric extension of the SM (MSSM) introduces two Higgs doublets separately coupling to up-type and down-type fermions. Out of the eight degree of freedom, three result in the longitudinal components of the  $W^\pm$  and Z bosons and the remaining in five physical Higgs bosons. Two of them are CP-even scalars ( $h, H$ ), where  $h$  is the lightest and SM-like. The other three consist of a charged Higgs pair ( $H^\pm$ ) and a CP-odd scalar (A) the mass of which ( $m_A$ ) is one of the two free parameters of the model at tree-level. In the MSSM, the Higgs production cross section is proportional to square of the second free parameter of the model,  $\tan\beta$ , the ratio of the two vacuum expectation values of the Higgs doublets. Thus, large values of  $\tan\beta$  result in significantly increased production cross section compared to the SM. Additionally, in the large  $\tan\beta$  limit, the heaviest CP-even Higgs boson, H, and the CP-odd Higgs scalar, A, are predicted to be almost degenerate in mass, leading to a further cross section enhancement. The main production mechanism for neutral Higgs bosons ( $\phi = h, H, A$ ) are  $gg, b\bar{b} \rightarrow \phi$  and  $gg, q\bar{q} \rightarrow \phi + b\bar{b}$ , where the branching ratio of  $\phi \rightarrow b\bar{b}$  is around 90% and  $\phi \rightarrow \tau^+\tau^-$  is around 10%. Due to the lower background in the  $\tau$  channel, the overall experimental sensitivity is similar in both channels. Other extension to the SM, such as Top-color [3] or Fermiophobic Higgs model [4], predict an enhanced branching fraction of neutral Higgs bosons to two photons. Extensions of the Higgs sector involving higher isospin multiplets predict the existence of double-charged Higgs bosons, which can be relatively light and hence accessible at the Tevatron.

This document describes the searches for a SM and beyond SM Higgs boson by the CDF and DO collaborations using up to  $2.4 \text{ fb}^{-1}$  of Run II data. The majority of those results are preliminary, and more information can be found on the public pages of CDF [5] and DO [6].

### 3 Standard Model Higgs searches

#### 3.1 Search for $ZH \rightarrow l^+l^-b\bar{b}$

For the low mass region (below 135 GeV) where the Higgs decays predominantly to  $b\bar{b}$ , the cleanest channel is the associated production with a Z boson, where the Z decays leptonically to  $e^+e^-$  or  $\mu^+\mu^-$ . Although the cross section times branching ratio is lower than the associated production with a W boson, this channel offers several tight constraints since  $M_{l^+l^-} = M_Z$  and the lack of direct missing transverse energy ( $\cancel{E}_T$ ) can be used to improve the jet energy resolution. Candidate events are selected by

requiring two high  $P_T$  (typically above 15 GeV) electrons or muons of opposite charge with invariant mass matching that of a Z boson. DO requires two jets with  $E_T > 15$  GeV, while CDF requires additionally that the highest energetic jet passes  $E_T > 25$  GeV. After this pre-selection, the sample is dominated by Z+jets and therefore  $b$ -jets identification is crucial to reduce this background. DO utilises an artificial neural network (NN) tagger based on lifetime information, which performs with efficiencies ranging 50-70% for a mis-identification (also referred to as mistag) rate of 0.3-4.5%. CDF uses a secondary vertex reconstruction algorithm with efficiencies ranging 40-50% for a mistag rate of 0.3-0.5%. To further discriminate signal and background events, DO uses a NN separately trained for 1-tag and 2-tag events using ten kinematic variables (Figure 1). Since no excess of signal is observed, the output of the NN is fitted to extract a 95% C.L. limit corresponding to 17.8 (20.4 expected) above the theoretical SM expectation for  $M_H = 115$  GeV. CDF uses a NN to improve the dijet mass distribution, which essentially is a correction function that re-assigns the  $\cancel{E}_T$  to the jets (Figure 1). Then, a 2-dimensional NN, trained to separate ZH from top background and ZH from Z+jets background, is used separately for single and double tags events. The NN output is fitted to extract a 95% C.L. limit corresponding to 16 (16 expected) above the theoretical SM expectation [7].

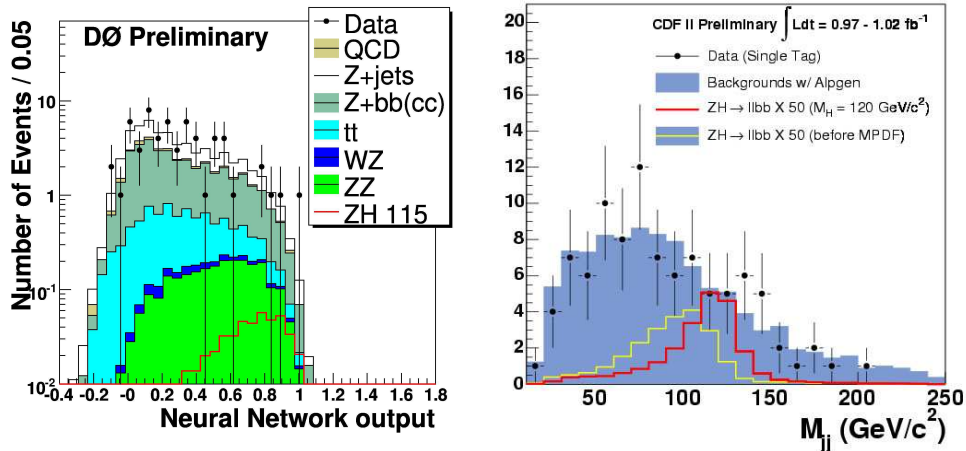


Figure 1: DO NN output for the double tag sample (left). CDF di-jet mass distribution after using the NN correction function (right). The 2 lines histograms show the effect of the correction on a  $ZH$  signal for  $M_H = 120$  GeV.

### 3.2 Search for $ZH \rightarrow \nu\bar{\nu}bb\bar{b}$

Although this channel has a larger branching ratio to neutrinos, it is very challenging to trigger on and background wise. Events are triggered on jets plus  $\cancel{E}_T$  and tight cuts are applied to reject background. DO requires two or three jets with  $E_T > 20$  GeV, where the two leading ones are not back-to-back and with at least 50 GeV of  $\cancel{E}_T$  in the event. CDF asks for two jets only, where the  $E_T$  of the leading jet is above 45 GeV, 25 GeV for the second jet and at least 50 GeV of  $\cancel{E}_T$  not aligned with the jets. Both experiments require that there be no identifies electrons or muons so that the data sample is orthogonal to the  $WH \rightarrow l\nu b\bar{b}$  searches, however, significant event yield from  $WH$  channel remains due to leptonic decay of the  $W$  where the lepton escapes identification. Additionally, angular cuts between the jets and the  $\cancel{E}_T$  are used to reject further the background, and identify a QCD multijets control sample, and  $b$ -tagging requirements are applied to the jets. DO uses a boosted decision tree (DT) technique [8] trained on 25 input variables as the final discriminant (Figure 2). CDF uses two separates NN. The first one uses track-based quantities to discriminate  $ZH$  from QCD multijets background. The second one, used to extract the limit, takes as input the first NN and combines other kinematic variables to discriminate  $ZH$  and  $WH$  from QCD multijet and  $t\bar{t}$  backgrounds (Figure 2). In the absence of any signal, DO sets a limit of 7.5 (8.4 expected) at 95% C.L. above SM expectation, while CDF obtains a limit of 8.0 (8.3 expected) at 95% C.L. Both experiments have performed searches splitting the data

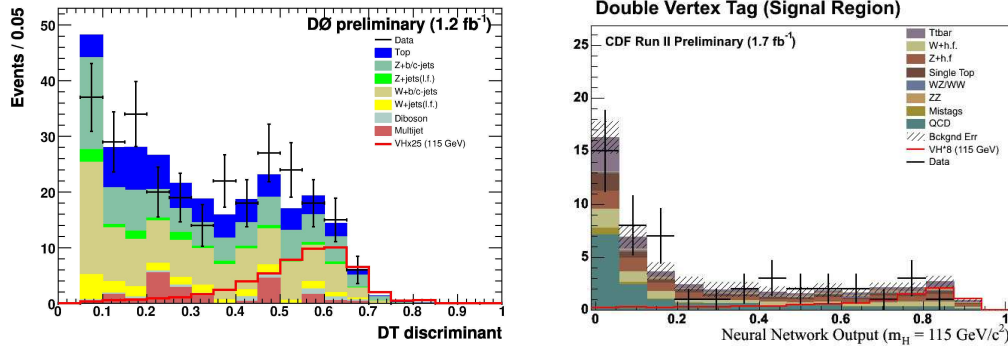


Figure 2: DO DT output (left) and CDF NN output (right) for the double tag sample.

### 3.3 Search for $WH \rightarrow l\nu b\bar{b}$

Searches for Higgs production in associated production with a  $W$  boson decaying leptonically provides the most stringent constraints on the low mass SM Higgs. The

event selection consists on identifying one isolated high- $P_T$  electron or muon,  $E_T > 20$  GeV and two (two or three for DO) jets with  $E_T > 20$  GeV. Additionally, CDF used the  $E_T + \text{jets}$  trigger to identify events with one isolated track which failed the electron or muon identification, thus increasing the Higgs acceptance by 25%. DO uses a NN trained on seven kinematic variables and splits the data into eight exclusive sets based on the number of  $b$ -tagged jets, lepton flavor and the two data periods<sup>2</sup> to optimize the sensitivity. As no excess is observed compared to the expectation, a limit is derived from the eight individual analysis and combined. DO sets a limit of 10.9 (8.9 expected) at 95% C.L. above SM expectation. CDF uses a NN to improve the purity of the single tag sample based on the secondary vertex tagger. In addition, CDF uses a jet probability tagging algorithm which identifies  $b$ -jet by requiring a low probability that the tracks contained in the jets originated from the primary vertex. An event is considered double-tagged if it contains either two secondary vertex tags or one secondary vertex tag and a jet probability tag. Note that the isolated track channel does not make use of neither the NN tagger nor jet probability tagger. CDF uses a NN trained on six kinematics variables and performs the analysis separately on the eight categories of events. In the absence of signal, CDF sets a limit of 6.4 (6.4 expected) 95% C.L. above SM expectation.

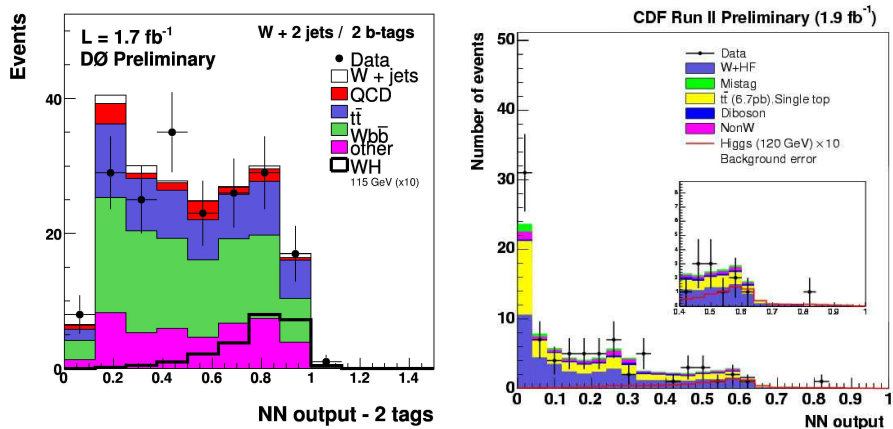


Figure 3: DO NN output (left) and CDF NN output (right) for the double tag sample.

<sup>2</sup>DO detector was upgraded during the Spring 06 Tevatron shutdown. Run IIa dataset corresponds to  $1.04 \text{ fb}^{-1}$ , while Run IIb corresponds to  $0.63 \text{ fb}^{-1}$

### 3.4 Search for $VH, VBF, H \rightarrow \tau^+\tau^- + 2$ jets

CDF performs a novel simultaneous search using the  $\tau$  decay mode of the SM Higgs boson in  $W(\rightarrow q\bar{q}')H(\rightarrow \tau^+\tau^-)$ ,  $Z(\rightarrow q\bar{q})H(\rightarrow \tau^+\tau^-)$ , Vector Boson Fusion (VBF)  $H \rightarrow \tau^+\tau^-$  and  $gg \rightarrow H(\rightarrow \tau^+\tau^-)$ . Candidates events are selected by identifying an isolated electron or muon from the  $\tau$  leptonic decay, one hadronic  $\tau$  and at least 2 jets in an event. In order to further improve the search sensitivity, three NN are used to discriminate the SM Higgs signals from  $Z \rightarrow \tau^+\tau^-$ , top and QCD multijet backgrounds. In the absence of signal, the minimum of the three NN is used to extract a 95% C.L. ranging from 30 to 150 (24 to 112 expected) for Higgs masses of  $110 - 150$  GeV.

### 3.5 Search for $WH \rightarrow WWW^*$

The associated production of SM Higgs with a W boson, where  $H \rightarrow W^+W^-$ , is important in the intermediate mass region ( $125 - 145$  GeV), although this channel suffers from a low branching ratio. Additionally, in some models with anomalous coupling (“fermiophobic Higgs”),  $BR(H \rightarrow WW^*)$  may be close to 100%. The search consists in identifying like-sign high  $P_T$  isolated leptons; one coming from  $H \rightarrow WW$ , the other from the prompt W. CDF scans the two-dimensional plane of the 2<sup>nd</sup> lepton  $P_T$  versus the dilepton system  $P_T$ , while DO performs a counting experiment. Neither experiment sees an excess in the number of events over the SM background expectation and set limits ranging from 20 to 24 times above SM for  $M_H = 160$  GeV and  $M_H = 140$  GeV respectively.

### 3.6 Search for $H \rightarrow W^+W^-$

In the high mass region (above 135 GeV), SM Higgs decays predominantly to  $W^+W^-$ . This channel benefits from a very clean signature with low SM backgrounds thus providing the largest sensitivity for a SM Higgs boson search at the Tevatron. The event selection consists in identifying two opposite charged isolated high  $P_T$  leptons ( $ee$ ,  $\mu\mu$  and  $e\mu$ ),  $\cancel{E}_T > 20, 25$  (DO, CDF) and little jet activities to reduce background from top pair production. The QCD multijet background is further reduced by requiring that the di-lepton mass be above 15 GeV. The remaining background is SM  $WW$  production, and the opening angle between the two leptons,  $\Delta\phi_{ll}$  can be used as a discriminating variable since the leptons from a spin-0 Higgs tend to be more co-linear. DO tunes the various pre-selection criteria thresholds for each di-lepton class and the various SM Higgs masses. To improve the separation between signal and backgrounds, DO uses a NN for each of the di-lepton channel. The input variables consist of various

event or object kinematics, angular variables and a discriminant constructed using the Matrix Element (ME) method in the  $ee$  and  $\mu\mu$  channels (Figure 3). DO obtains a 95% C.L. of 2.1 (2.4 expected) above SM expectation for  $M_H = 160$  GeV. In order to optimize the lepton acceptance, CDF loosen its lepton selection criteria and also identifies isolated track not fiducial to either the calorimeter or muon chambers within  $|\eta| < 1.2$  thus improving the expected signal events by a factor of 1.6. In order to maximize the sensitivity, the ME probabilities are calculated for each selected event to be Higgs signal or  $WW$ ,  $ZZ$ ,  $W\gamma$ ,  $W +$  jet backgrounds and used to construct five likelihood ratio (LR) discriminants. Those LR are used in conjunction with six other kinematics variables as input to a NN (Figure 3). In absence of signal, the NN output is fitted to extract a 95% C.L. of 1.6 (2.5 expected) above SM expectation for  $M_H = 160$  GeV.

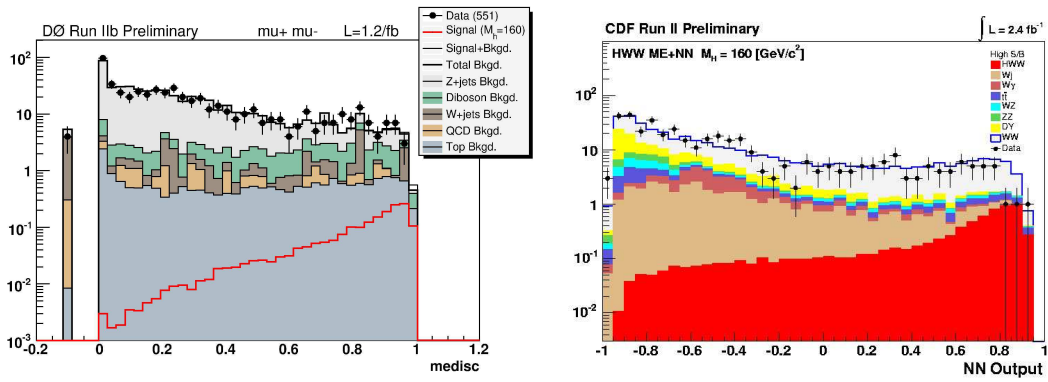


Figure 4: DØ distribution of the ME discriminant (left) after the final selection in  $\mu\mu$  channel for  $M_H = 160$  GeV. Values of  $ME_{disc} < 0$  correspond to events with very small probability of either signal or  $WW$  background. CDF NN output (right) for  $M_H = 160$  GeV for events with high S/B ratio as determined from the LR.

### 3.7 Combine upper limit on Standard Model Higgs boson production

Since no single decay channel and neither experiment has sufficient statistical power to reach the SM prediction over the full mass range, results from all searches for both experiments are combined. In order to simplify the combination, the searches are separated into twenty nine (13 for CDF and 16 for DO) mutually exclusive final states. All systematic uncertainties and their correlations between channels and across the experiments are taken into account to perform several types of combinations, using

$m_H$ (GeV)	110	115	125	135	140	150	160	170	180	190	200
Expected	3.1	3.3	3.8	4.2	3.5	2.7	1.6	1.8	2.5	3.8	5.1
Observed	2.8	3.7	6.6	5.7	3.5	2.3	1.1	1.3	2.4	2.8	5.2

Table 1: Tevatron combined 95% C.L limits on  $\sigma \times BR(H \rightarrow b\bar{b}/W^+W^-)$  for SM Higgs boson production. The limits are reported in units of SM production cross section times branching fraction.

Bayesian and Modified Frequentist approaches, and found to be in agreement within 10%. The results are presented in Table 1 and Figure 4.

## 4 Non Standard Model Higgs searches

### 4.1 Search $\phi \rightarrow \tau^+\tau^-$

DO [9] and CDF have searched for a MSSM Higgs boson decaying to a tau pair, where one of the tau decays leptonically to an electron ( $\tau_e$ ) or muon ( $\tau_\mu$ ) and the other decay either hadronically ( $\tau_h$ ) or leptonically but to a different lepton flavor. Most of the sensitivity in this channel comes from the identification of  $\tau_h$ . DO's tau identification is based on three different NN aimed to optimize the background rejection depending on the hadronic tau types. The  $\tau_h$  decays are subdivided into three types: single charged track matches the energy deposited in the hadronic calorimeter (consistent with  $\tau^\pm \rightarrow \pi^\pm \nu$ ); single charged track matches the energy deposited in the electromagnetic and hadronic calorimeter (consistent with  $\tau^\pm \rightarrow \pi^\pm \pi^0 \nu$ ); three charged tracks with invariant mass less than 1.7 GeV (consistent with  $\tau^\pm \rightarrow \pi^\pm \pi^\pm \pi^\mp (\pi^0) \nu$ ). For the second case of hadronic tau decay, if there is a significant amount of electromagnetic energy, a fourth NN is used to discriminate tau decays from direct electron production. CDF's  $\tau_h$  identification starts by reconstructed a high  $P_T$  “seed” track and then associated to the  $\tau$  candidate additional tracks within a narrow  $\eta - \phi$  cone. The total momentum in the isolation annulus around the  $\tau$ -cone is required to be small. The  $\tau$  momentum is measured by combining the track momenta in the  $\tau$ -cone (typically originating from charged pions), with the electromagnetic calorimeter momenta (typically originating from neutral pions), with a correction to account for the charged-pion contribution to the electromagnetic momenta. Both DO and CDF exploit the visible mass,  $M_{\text{vis}}$  spectrum as a figure of merit, with  $M_{\text{vis}} = \sqrt{(P_{\tau_1} + P_{\tau_2} + \cancel{E}_T)^2}$  and where  $P_{\tau_{1,2}}$  are the four-vector of the visible tau decays.

No excess consistent with a MSSM Higgs is observed in either DO or CDF data, so

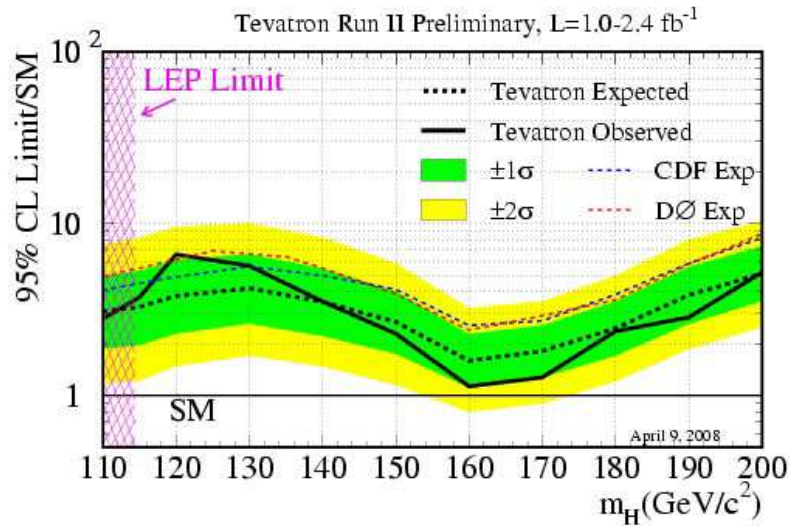


Figure 5: Observed and expected (median, for the background-only hypothesis) 95% C.L. upper limits on the ratios to the SM cross section, as functions of the Higgs boson test mass, for the combined CDF and DO analyses. The limits are expressed as a multiple of the SM prediction for test masses for which both experiments have performed dedicated searches in different channels. The points are joined by straight lines for better readability. The bands indicate the 68% and 95% probability regions where the limits can fluctuate, in the absence of signal. Also shown separately are the expected upper limits obtained for all combined CDF and DO channels.

limits in the  $m_A - \tan \beta$  plane are set for non-vanishing (“ $m_h^{\max}$ ”) or vanishing (“no-mixing”) stop mixing with  $\mu > 0$  and  $\mu < 0$ , where  $\mu$  is the Higgs mixing parameter at the electroweak scale (Figure 4).

## 4.2 Search $b\phi \rightarrow b\bar{b}$

The  $p\bar{p} \rightarrow H \rightarrow b\bar{b}$  process is overwhelmed by direct  $b\bar{b}$  production, therefore searches in this Higgs decay mode use the process  $gb \rightarrow Hb \rightarrow bbb$  and  $q\bar{q}/gg \rightarrow bbH \rightarrow bbb$ . Both DO and CDF require three identified  $b$ -jets in the final state. The  $b$ -jet energy resolution is important to reconstruct the Higgs mass from the background continuum. The dominant background are QCD multijet events with two real  $b$ -quarks and a “ $b$ ”, “ $c$ ” or “fake” tag. DO uses a NN  $b$ -tagger to identify  $b$ -jets. The background

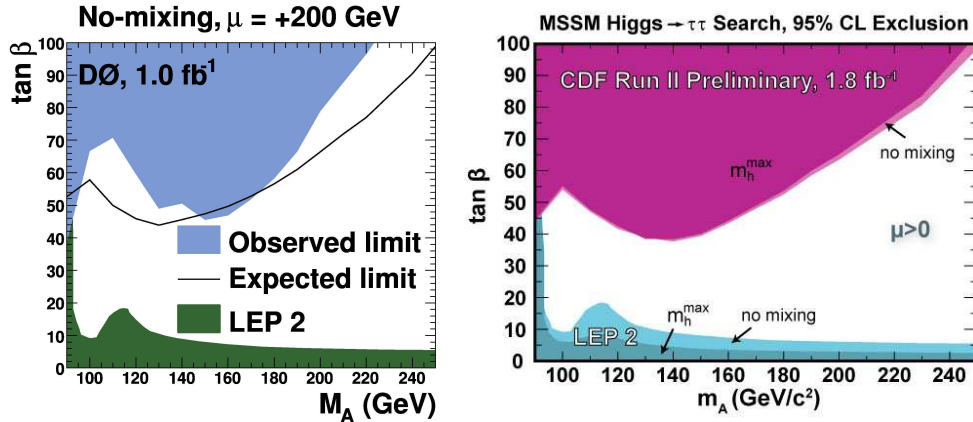


Figure 6: DO (left) and CDF (right) limits in the  $m_A - \tan \beta$  plane. DO examines the no-mixing and  $m_h^{\max}$  (not shown) scenarios for  $\mu > 0$ . The  $m_h^{\max}$  limits are similar. CDF examines the  $m_h^{\max}$  and no-mixing for  $\mu > 0$  and  $\mu < 0$  (not shown). The  $\mu < 0$  limits are similar.

is estimated separately for three, four and five-jets channels using the measured  $b$ -jet identification efficiency and control samples with and without identified  $b$ -jets. A likelihood based on six variables is used to discriminate Higgs signal from background, where the cut on the likelihood varies depending on the jet multiplicity and the Higgs boson mass. The resulting invariant mass spectrum from the two leading jets shows good agreement between data and predicted background. Limits are set in the  $m_A - \tan \beta$  plane for  $\mu \pm 200$  for the  $m_h^{\max}$  (negative  $\mu$  only) and no-mixing scenarios (Figure 7) [10]. CDF identifies  $b$ -jets using the secondary vertex tagger and the invariant mass of the reconstructed vertex since the vertex mass is higher for  $b$ -jet than for light-flavor jet. The mass distribution for four background types ( $bbb$ ,  $bbx$ ,  $bcb$ ,  $bqb$ ) are predicted using a combination of data and PYTHIA Monte Carlo simulation. Those background templates are used in a binned maximum-likelihood to fit the data without using any absolute normalisation. The invariant mass spectrum of the two leading jets shows no deviations from the expected background only hypothesis and limits are set in the  $m_A - \tan \beta$  plane for  $\mu = -200 \text{ GeV}$  in the  $m_h^{\max}$  scenario (Figure 7).

### 4.3 Search for Fermiophobic and doubly charged Higgs

DO searched for fermiophobic Higgs boson produced by vector-boson fusion or in association with a  $W$  or  $Z$  boson, where for  $m_H < 100 \text{ GeV}$ , the Higgs boson predominantly decays to photon pairs [11]. The search consists in identifying two high

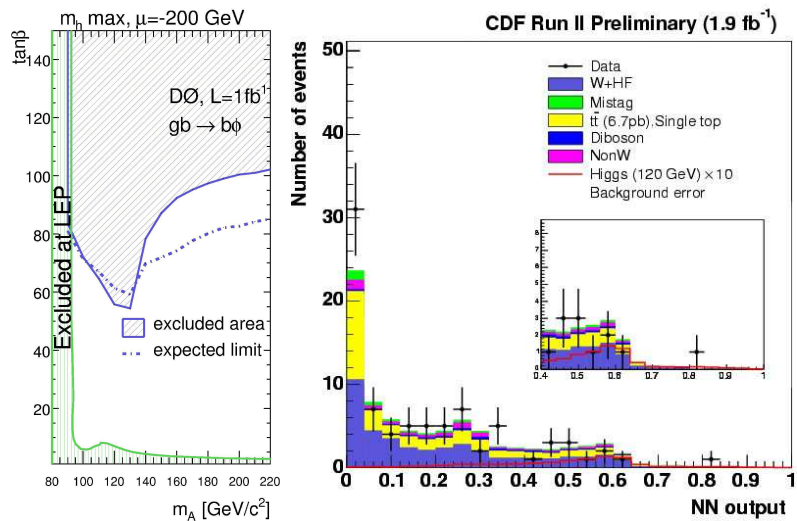


Figure 7: DO (left) and CDF (right) limits in the  $m_A - \tan\beta$  plane. DO examines for  $\mu \pm 200$  GeV, no-mixing (not shown) and  $m_h^{\max}$  scenarios ( $\mu < 0$  only). CDF examines the  $m_h^{\max}$  scenario for  $\mu = -200$  GeV.

$E_T$  isolated photon. The dominant background come from direct photon production or events where jets are misidentified as photons, and are estimated using a combination of data and MC simulation. Since no excess of events is observed in the di-photon invariant mass, a 95% C.L. upper limit on the branching ratio of a fermiophobic Higgs to di-photon is set (Figure 8). This search significantly extends sensitivity into region not accessible at LEP.

Scenarios such as left-right symmetry models, Higgs triplet models and Little Higgs models, predict the existence of doubly-charged Higgs ( $H^{\pm\pm}$ ) which couples to like-sign dilepton pairs. At the Tevatron, doubly-charged Higgs are produced predominantly in pairs. Events with four lepton in the final state have negligible background and therefore searches typically require fewer than four leptons to increase the acceptance. DO has performed a search in the three muon final state [12], where at least two muons are like-sign. Since no excess is observed in the same sign dimuon invariant mass, the distribution is used to extract a 95% C.L upper limit on the doubly charged Higgs production cross section (Figure 8). The limit excludes  $m_{H^{\pm\pm}} > 150$  (127) GeV for Higgs bosons couple to left-(right-) handed muons with 100% branching ratio. This result increases the previous mass limit obtained at LEP and complements CDF.

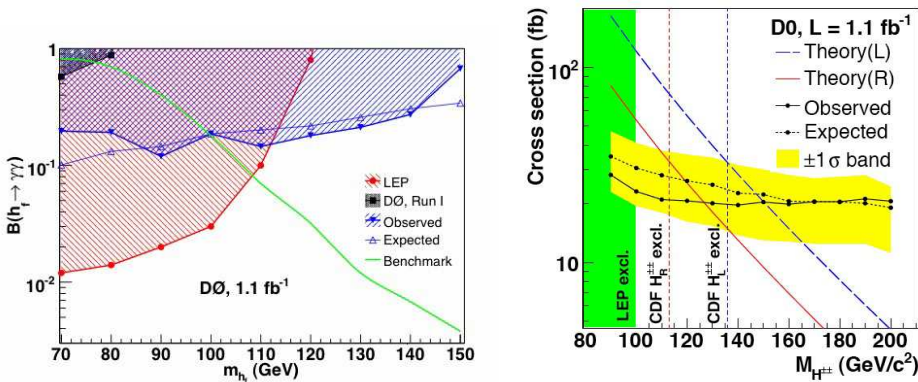


Figure 8: Limits on  $BR(h_f \rightarrow \gamma\gamma)$  as a function of the Higgs mass (left). Shaded region correspond to the excluded values of the branching ratio. Cross section limit as a function of  $m_{H^{\pm\pm}}$  at 95% C.L (right).

## 5 Conclusions and prospects

CDF and DO have performed searches for the SM and non-SM Higgs bosons over a wide range of masses with an integrated luminosity up to  $2.4 \text{ fb}^{-1}$ . Since no excess of signal above the expected backgrounds were observed, limits were set.

Both experiments have brought a variety of improvements to the analyses: trigger and lepton identification optimisation, dijet mass resolution,  $b$ -tagging algorithms, splitting classes of events, advance analysis techniques (NN, DT, ME), all of which permitted to improve on the limit faster than the gain from increasing luminosity. In the case of a SM Higgs, a Tevatron combined limit was produced and shows that exclusion of a SM Higgs around 160 GeV is around the corner.

The search for non-SM Higgs bosons show very promising sensitivity and have already produce powerful limits. Analysis techniques are well advanced but additional improvements could help obtained even more stringent limits. Additionally, both experiments plan on working toward combining their results from the different channels. With the expected  $6 - 7 \text{ fb}^{-1}$  of data per experiment by the end of Run II, it is expected the Tevatron could probe down to  $\tan \beta$  around 20 for low  $m_A$ .

I would like to thank my colleagues from the DO and CDF Collaborations for providing the material for this talk and the organisers of PIC 2008 for a very enjoyable and interesting conference.

## References

- [1] <http://lepewwg.web.cern.ch/LEPEWWG/>
- [2] D.J.H. Chung *et al.*, Phys. Rept. **407** (2005) 1-203, and references therein.
- [3] C.T. Hill, Phys. Lett. **B266** (1991) 419.
- [4] H.E. Haber, G.L. Kane, T. Sterling, Nucl. Phys. **B161** (1979) 493.
- [5] <http://www-cdf.fnal.gov>
- [6] <http://www-d0.fnal.gov>
- [7] T. Aaltonen *et al.* (CDF Collaboration), arXiv:0807.4493 (2008).
- [8] L. Breiman *et al.*, “Classification and Regression Trees”, Wadsworth (1984); Y. Freund and R.R. Shapire, “Experiments with new boosting algorithms” in Machine Learning: Proceedings of the Thirteenth International Conference, pp. 148-156 (1996); V.M. Abazov *et al.*, Phys. Rev. Lett. **98** (2007) 181802
- [9] V. Abazov *et al.* (DO Collaboration), Phys. Rev. Lett. **101** (2008) 071804
- [10] V. Abazov *et al.* (DO Collaboration), arXiv:0805.3556
- [11] V. Abazov *et al.* (DO Collaboration), Phys. Rev. Lett. **101** (2008) 051801
- [12] V. Abazov *et al.* (DO Collaboration), Phys. Rev. Lett. **101** (2008) 071803

# Higgs searches at LHC

*Giorgia Mila  
on behalf of the ATLAS and CMS collaboration  
Department of Physics  
University of Torino, ITALY*

## 1 Introduction

In the Standard Model (SM) the elementary particles acquire their mass through the Higgs mechanism. This mechanism foresees the existence of the Higgs boson a scalar particle which couples to massive particles. Its mass is the only yet unknown parameter of the SM. Constraints on its value come from the theory and from the experimental results from LEP [1]. In the SM the allowed mass range is  $114.4 \text{ GeV}/c^2 \div 1 \text{ TeV}/c^2$  and the production cross section is of the order of a few pb.

The Large Hadron Collider (LHC) is the machine designed for its discovery. Thanks to its high center of mass energy (14 TeV) the LHC will be able to explore the whole allowed mass range while its high instantaneous luminosity ( $10^{34} \text{ cm}^{-2}\text{s}^{-1}$ ) will allow to assess the small cross sections involved in the Higgs production.

## 2 Higgs production and decay channels

Figure 1 shows the tree level diagrams of the four main Higgs production channels in p-p collisions and their cross sections, as a function of the Higgs mass, for a center of mass energy of 14 TeV. The gluon-gluon fusion is the dominant process over the whole mass spectrum. Its cross section suffers of high QCD corrections and large uncertainties due to the gluon structure functions. The Vector Boson Fusion (VBF) cross section is about one order of magnitude lower than the  $gg$  fusion one for a large range of the Higgs masses. The two processes become comparable for high values of the Higgs mass. This process has a well known next-to-leading-order cross section, small QCD corrections and a very clear experimental signature, due to the presence of the two spectator jets with high invariant mass in the forward region. The remaining production processes have very small cross sections, orders of magnitude lower than

those of  $gg$  and VBF. They will be used for the Higgs discovery in association with particular Higgs decay modes to exploit final states with a clear signature.

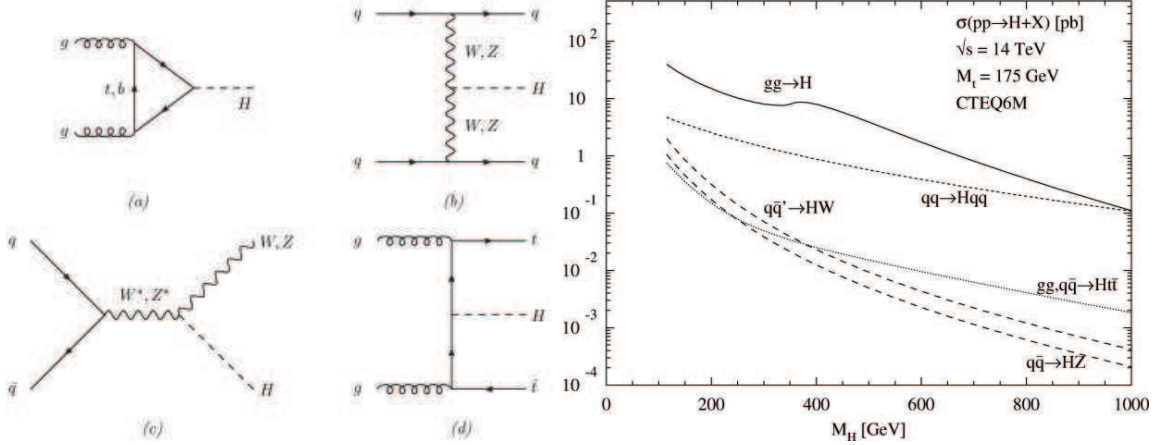


Figure 1: [Left side] Higgs boson production mechanisms at tree level in proton-proton collisions: (a) gluon-gluon fusion; (b) Vector Boson Fusion, (c)  $W$  and  $Z$  associated production (or *Higgsstrahlung*); (d)  $t\bar{t}$  associated production. [Right side] Higgs boson production cross sections at  $\sqrt{s} = 14$  TeV as a function of the Higgs boson mass. The cross sections are calculated using HIGLU [2]; they contain higher order corrections and the CTEQ6m [6] p.d.f. has been adopted.

The branching ratio of all the possible Higgs decay channels as a function of the Higgs mass is shown in Figure 2. For Higgs masses up to 150  $\text{GeV}/c^2$  fermionic decay modes are dominating. When the decay channels into vector boson pairs open up, they quickly dominate. At high masses (above 350  $\text{GeV}/c^2$ ) also  $t\bar{t}$  pairs can be produced.

Depending on the Higgs mass, ATLAS [3, 4] and CMS [2], the two general purpose experiments at the LHC, have been developed different strategies for its search. The experimental techniques and the expected sensitivity are discussed in the following.

### 3 Higgs Searches at the LHC

#### 3.1 Low mass region

The most promising discovery channels for  $M_H < 130 \text{ GeV}/c^2$  are the decay modes into a pair of photons or  $\tau$  leptons thanks to their clear signature.

The first process suffers of a very high background coming from Drell-Yan  $e^+e^-$ ,

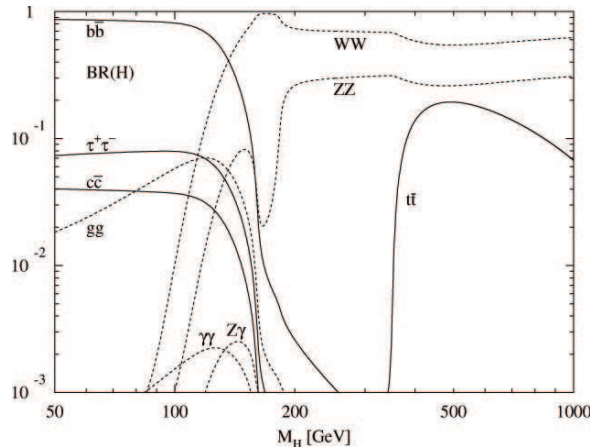


Figure 2: Branching ratios for different Higgs boson decay channels as a function of the Higgs boson mass. They are calculated with the program HDECAY [7] which includes the dominant higher order corrections to the decay width.

$pp \rightarrow \gamma\gamma$ ,  $pp \rightarrow jets + \gamma$ ,  $pp \rightarrow jets$  where one or more jets are misidentified as  $\gamma$ . The suppression of the last two contributions will require a good understanding of the performance of the electromagnetic calorimeter and a reliable modeling of the amount of material in front of it.

The analysis on the  $H \rightarrow \tau\tau$  decay mode focus on the VBF production channel because of its higher signal over background ratio. The most promising final state is the one with one  $\tau$  decaying into leptons and the other into hadrons. The irreducible backgrounds to this process are the QCD and EW production of two  $\tau$  leptons from  $Z$  or  $\gamma^*$  with associated jets. Contributions also come from  $W+multi-jets$  production and  $t\bar{t}$  events in which one of the jets can be misidentified as a  $\tau$  jet. The signature is characterized by the hadronically decaying  $\tau$  (associated to a little ( $\Delta R=0.4$ ) isolated jet), the leptonically decaying  $\tau$  (identified from the electron or the muon with highest transverse momentum  $p_t > 15$  GeV/c) and the two quarks emitting the bosons in the VBF process which have a high energy and rapidity gap.

The high branching ratio of the Higgs boson into a pair of  $b$  quarks can only be exploited in the study of the Higgs production via  $t\bar{t}$  fusion. The most promising final states have at least one of the two  $t$  quark decaying leptonically thanks to the clear signature offered by the presence of at least one high  $p_t$  lepton from one of the two  $W$ , missing energy and 4  $b$ -tagged jets (of which two from the Higgs). The 4 jets are the responsible of a very high background, mostly composed by  $ttbb$ ,  $Zbb$ ,  $tt + N_{jets}$  and multi-jets QCD events and are the main sources of uncertainty. A pioneer novel study [8] has obtained good results on the signal over background ratio

by reconstructing the  $H \rightarrow b\bar{b}$  decay (produced through VBF) asking the presence of a central high  $p_t$  photon in the final state.

### 3.2 High mass region

This region corresponds to values of the Higgs boson mass above the threshold of  $2M_w$ , where the Higgs analysis are focused on the Higgs decays into a couple of vector bosons.

The main channels of interest are those where the two vector bosons decay leptonically. The clear experimental signature of these events compensates for their low branching ratio, which is about one order of magnitude lower than the hadronic ones.

In the  $H \rightarrow WW \rightarrow l\nu l\nu$  channel it is not possible to reconstruct the  $H$  invariant mass due to the presence of the two neutrinos. Since the signal selection can not exploit this variable other techniques must be used for the discrimination and a good control of the background shape is mandatory. The final state presents 2 isolated high  $p_t$  leptons pointing to the primary vertex, high missing energy and no hadronic activity. The signal selection relies mainly on the request of a central jet veto, high missing energy and of a small angle between the two leptons due to the V-A structure of the weak interaction.

The  $H \rightarrow ZZ \rightarrow 4l$  ( $l =$  muons or electrons) channels are the "golden channels" for the Higgs discovery. The main backgrounds are:  $t\bar{t}$ ,  $Zb\bar{b}$  and the irreducible  $ZZ^*/\gamma^*$ . The trigger and the offline cuts rely on the presence of isolated charged leptons coming from the primary vertex, with high transverse momentum. The instrumental backgrounds become negligible with the request of lepton isolation and using different cuts on the sorted lepton transverse momenta. The irreducible background can be suppressed applying cuts on angular variables. The main sources of systematic uncertainties come from the choice of the PDF and the QCD scale, the NLO versus the LO dynamics, the isolation cut and its efficiency, the electron reconstruction efficiency, the energy and the momentum scale and the charge identification.

As discussed above, the VBF production channel becomes important in the very high mass region thanks to its clear experimental signature given by the two spectator jets and the Higgs decay products, which allows a good rejection of dominant background coming from  $V + njets$ ,  $VV + njets$  and  $t\bar{t}$  production. These jets are well separated in pseudo-rapidity and have a very high invariant mass.

Moreover, the Vector Boson Fusion cross section (with or without a production of an Higgs particle) is an extremely interesting process because the cross section  $\sigma(pp \rightarrow VVjj)$  and the polarization of the VV pair depend sensitively on the presence or

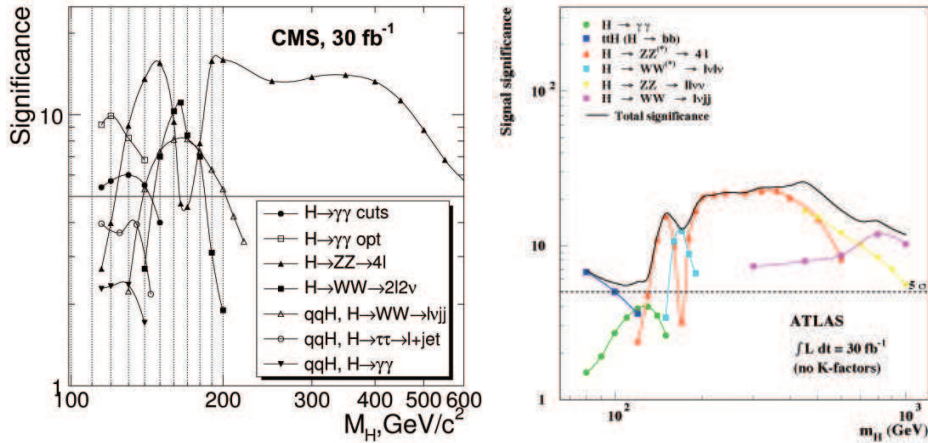


Figure 3: The signal significance as a function of the Higgs Boson mass for  $30 \text{ fb}^{-1}$  of the integrated luminosity for the different Higgs Boson production and decay channels. Analysis results from CMS [9] (left) and ATLAS [10] (right).

absence of a light Higgs in the physical spectrum. If a massive Higgs boson exists, a resonance will be observed in the  $VV$  invariant mass spectrum in correspondence of the Higgs mass. In the absence of the Higgs particle the SM predicts that the scattering amplitude of longitudinally polarized vector bosons grows linearly with  $s$  and violates unitarity at about  $1 - 1.5 \text{ TeV}$ . This means that the measurement of the cross section at large  $M(VV)$  could provide information on the existence of the Higgs boson independently of its direct observation.

### 3.3 Higgs discovery significance

The Higgs expected significance in the different channels, after an integrated luminosity of  $30 \text{ fb}^{-1}$ , is showed in Figure 3 for the ATLAS and CMS experiments.

In the low Higgs mass region CMS will focus on the  $H \rightarrow \gamma\gamma$  channel, relying on its excellent electromagnetic calorimetric system, while ATLAS can exploit the performance of its hadronic calorimeter investigating the  $qqH \rightarrow q\bar{q}\tau\tau$  channel. In the high Higgs mass region both ATLAS and CMS will concentrate their efforts in the study of decay modes into a pair of vector bosons. The highly performant tracker system of the CMS experiment plays a key role in these analysis. Combining the results of both experiments, it is foreseen that, for Higgs masses larger than  $140 \text{ GeV}/c^2$ , the significance will be close to  $5\sigma$  already after an integrated luminosity of  $1 \text{ fb}^{-1}$ . For a light Higgs the situation is instead more complex because of the need to combine several channels. The minimum luminosity for the discovery will be around  $5 \text{ fb}^{-1}$ . It is

however important to remark that these values of luminosity refer to a scenario where the two experiments have already reached a deep understanding of their detectors, of the systematic uncertainties involved in the measurements and of the accuracy of the simulation of signal and background processes.

## References

- [1] The LEP collaborations, the LEP Electroweak Working Group and the SLD Heavy Flavour Group, "A combination of Preliminary Electroweak Measurements and Constraints on the Standard Model", LEPEWWG 2003-01.
- [2] M. Spira, "HIGLU: a Program for the Calculation of the Total Higgs Production Cross Section at Hadron Collider via Gluon Fusion Including QCD Corrections", DESY T-95-05 (1995), hep-ph/9510347.
- [3] G. Aad et al. (ATLAS Collaboration), JINST 3, S08003 (2008).
- [4] ATLAS Collaboration, Expected Performance of the ATLAS Experiment, Detector, Trigger and Physics, CERN-OPEN-2008-020, Geneva, 2008, to appear.
- [5] The CMS Collaboration (R. Adolphi et al), JINST 3, S08004 (2008).
- [6] J. Pumplin, D.R. Stump, J. Huston, H.L. Lai, P. Nadolsky and W.K. Tung, "New generation of parton distribution with uncertainties from global QCD analysis" JHEP 0207:012, (The CTEQ Collaboration).
- [7] A. Djouardi, J. Kalinowski and M.Spira,"HDECAY; a Program for Higgs Boson Decay in the Standard Model and its Supersymmetric Extension", DESY 97-079 (1997), hep-ph/9704448.
- [8] E. Gabrieli, F. Maltoni, B. Mele, F. Piccinini and R. Pittau, "Higgs Boson Production in Association with a Photon in Vector Boson Fusion at the LHC", Nucl. Phys. B781 (2007) 64.
- [9] The CMS Collaboration, "CMS Physics: Technical Design Report. Volume II: Physics Performance", CERN/LHCC 2006-021, CMS TDR 8.2 (2006).
- [10] The ATLAS Collaboration, "ATLAS detector and physics performance Technical Design Report", CERN/LHCC 99-14. ATLAS TDR 14 (1999).

# Beyond the Standard Model - Searches at HERA and the Tevatron

*Stefan Grünendahl*

*Fermi National Accelerator Laboratory  
PO Box 500, Batavia, IL 60510, USA*

*(FERMILAB-CONF-08-577-E)*

## 1 Introduction

Searches for Physics beyond the Standard Model have entered an exciting new phase: the complete HERA data samples obtained until the end of operations in the Summer of 2007 are now available for analysis. ZEUS and H1 have each collected about  $0.5\text{ fb}^{-1}$  of lepton proton data, distributed over electron and positron running, and over different lepton beam polarisations (see Table 2). At the same time the Tevatron proton-antiproton collider is accumulating data at unprecedented rates, with current analyses based on up to  $3\text{ fb}^{-1}$ . The Tevatron experiments D $\emptyset$  and CDF have each already recorded over  $4\text{ fb}^{-1}$  (Fall 2008), and are aiming for a total of  $8\text{ fb}^{-1}$  of  $\bar{p}p$  collisions at 2 TeV center-of-mass energy for Tevatron Run II.

I am presenting recent updates (from the last 12 months) on searches, grouped loosely into three classes: well-established ‘traditional’ searches, mostly for very specific signatures and models, more recent and/or more generalized searches for broader classes of phenomena, and newer searches that strive to be model-independent. Table 1 provides an overview of the analysis updates presented here.

## 2 Specialised Searches

### 2.1 Leptoquarks

Leptoquarks carry both lepton and quark quantum numbers and are present in many Grand Unified Theories, Technicolor and other extensions of the Standard Model. At

exp.	analysis	channel	$\mathcal{L} [fb^{-1}]$	updated	limit/result	ref.
DØ	LQ1	2 e + 2 jets	1	6/14/08	$m_{LQ1} > 292 GeV$	[1]
H1	LQ1	e + jet	0.449	4/08	$m_{LQ1}$ vs $\lambda$ (contour)	[2]
DØ	LQ2	$2\mu + 2 \text{ jets}$ $\mu\nu + 2 \text{ jets}$	1	8/29/08	$m_{LQ2} > 316 GeV$	[3]
CDF	LQ	2 jets + $\not{p}_T$	2	4/03/08	$m_{LQ1/2} > 179 GeV$ $m_{LQ3} > 169 GeV$	[4]
DØ	LQ3	$\tau + b$	1.05	6/21/08	$m_{LQ3} > 210 GeV$	[5]
CDF	TC	$\rho_T \rightarrow \pi_T W$ $l\nu b\bar{b}$ )	1.9	4/11/08	contour	[6]
CDF	mSUGRA	$\tilde{\chi}_1^\pm \tilde{\chi}_2^0$	2	1/10/08	$m_{\tilde{\chi}_1^\pm} > 145 GeV$	[7]
DØ	mSUGRA	trileptons	$\leq 1.7$	7/31/07	$m_{\tilde{\chi}_1^\pm} > 145 GeV$	[8]
CDF	$\tilde{q}, \tilde{g}$	jets + $\not{p}_T$	2	2/14/08	$m_{\tilde{q}} = m_{\tilde{g}} > 392 GeV$ $m_{\tilde{g}} > 280 GeV$ for $m_{\tilde{q}} \leq 600 GeV$	[9]
DØ	$\tilde{q}, \tilde{g}$	jets + $\not{p}_T$	2.1	1/24/08	$m_{\tilde{g}} > 308 GeV$ $m_{\tilde{g}} > 379 GeV$	[10]
CDF	stop	(e, $\mu$ ) + b + $\not{p}_T$	2.7	7/22/08	contour	[11]
DØ	stop	2 c + $\not{p}_T$	1	3/14/08	contour	[13]
DØ	stop	e + $\mu$ + 2b + $\not{p}_T$	1.1	4/1/08	contour	[12]
DØ	GMSB	di-photon	1.1	10/21/07	$m_{\tilde{\chi}_1^0} > 125 GeV$ $m_{\tilde{\chi}_1^\pm} > 229 GeV$	[14]
DØ	$W'$	e $\nu$	1	10/16/07	$m_{W'} > 1 TeV$	[15]
CDF	$W'$	t $\bar{b}$	1.9	12/20/07	$m_{W'} > 800 GeV$	[16]
DØ	$W'$	t $\bar{b}$	0.9	5/30/08	$m_{W'} > 731 GeV$	[17]
CDF	$Z'$	2 e	2.5	3/6/08	$m_{Z'} > 966 GeV$	[18]
CDF	LED	mono- $\gamma$ /jet	2/1.1	2/21/08	$m_D > 950 GeV$ (n=6)	[19]
DØ	LED	mono- $\gamma$	2.7	7/23/08	$m_D > 831 GeV$ (n=6)	[20]
DØ	Z+ $\gamma$	$\gamma + ee$ or $\mu\mu$	1.1/1.0	6/3/08	contour	[21]
CDF	$t't'$	e $\nu jjjj$	2.3	3/7/08	$m_{t'} > 284 GeV$	[22]
CDF	same sign tt	various	2	5/8/08	$\xi < 0.85$ for $m_\eta = 200 GeV$	[23]
CDF	$q^*$	dijets	1.1	3/19/08	$260 < m_{q^*} < 870 GeV$	[24]
DØ	$e^*$	e $e\gamma$	1	1/6/08	$m_{e^*} > 756 GeV$	[25]
H1	$e^*$	e $\gamma, eZ, \nu W$	0.475	5/08	contour	[26]
H1	$\nu^*$	$\nu\gamma, \nu Z, eW$	0.184	2/08	contour	[27]
Zeus	iso.leptons	e/ $\mu$ + $\not{p}_T$	0.5	7/08	no excess	[29]
Hera	multileptons	leptons	0.5	6/08	no excess	[30]
DØ	di-em vertices	2e/2 $\gamma$	1.1	6/13/08	limits	[31]
CDF	Vista/Sleuth	various	2.0	2/28/08	no dev. found	[32]

Table 1: Searches Summary as of Summer 2008

Period	Beams	Electron energy (GeV)	Proton energy (GeV)	$\sqrt{s}$ (GeV)	$\mathcal{L}$ (pb $^{-1}$ )
1994–1997	$e^+p$	27.5	820	300	48.2
1998–1999	$e^-p$	27.5	920	318	16.7
1999–2000	$e^+p$	27.5	920	318	65.1
2003–2004	$e^+p$	27.5	920	318	40.8
2004–2006	$e^-p$	27.5	920	318	190.9
2006–2007	$e^+p$	27.5	920	318	142.4

Table 2: Zeus beam configurations time line, from [29].

a hadron collider, leptoquarks of all three generations are produced in pairs via the strong interaction. At Hera production of the first generation LQ1 is proportional to the non-SM lepton-quark coupling. D0 has updated its search for leptoquarks of the first generation, coupling to electrons and up and down quarks, with results based on  $1\text{ fb}^{-1}$  [1]. Fig. 1 compares the distribution of the sum of the transverse energies of leptoquark decay products for SM backgrounds and for a hypothetical 250 GeV leptoquark; no excess is visible. Scalar leptoquarks with masses less than 292 GeV are excluded at 95% confidence level (cf. Fig. 2). H1 [2] has updated its LQ1 results a while ago. Fig. 3 shows the exclusion contours for two different LQ variants.

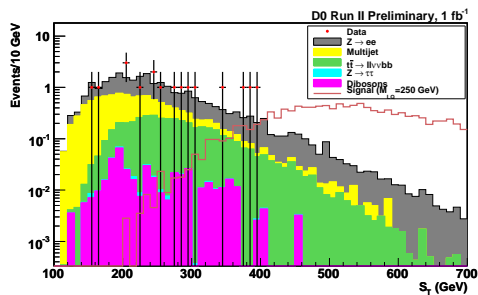


Figure 1: Sum of LQ decay transverse energies

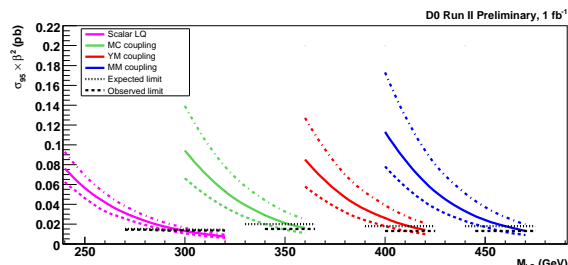


Figure 2: D0 LQ1 exclusion limits

Both D0 and CDF have also updated their results for second generation leptoquark searches. While the D0 analysis [3] requires a single muon accompanied by two jets and missing transverse energy  $\not{p}_T$ , CDF searches in the (exclusive) dijet plus missing transverse energy channel and thus sets limits on first, second and third generation leptoquarks [4]. For results see the references and table 1.

D0 has a recent  $\tau$  based analysis for third generation leptoquarks [5], which yields a limit of 210 GeV for a third generation leptoquark at a branching fraction of  $\beta = 1$

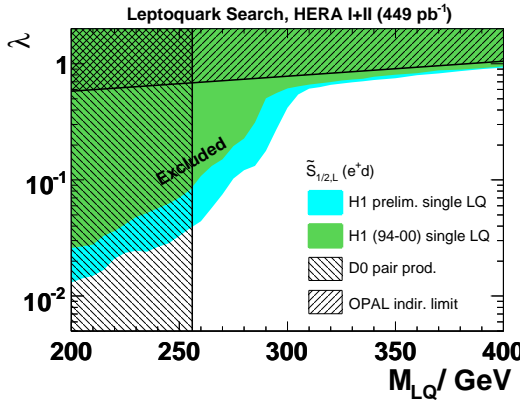


Figure 3: H1 LQ1 exclusion limits

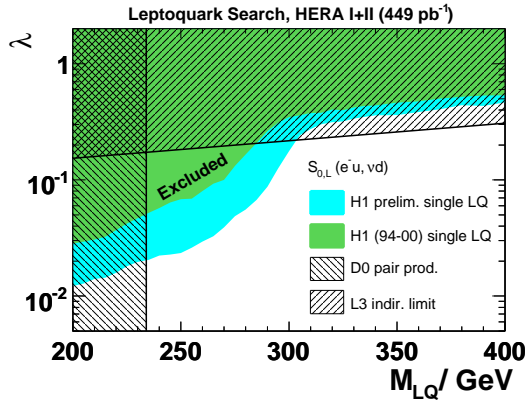


Figure 4: H1 LQ1 exclusion limits

into the charged lepton channel (Fig. 5).

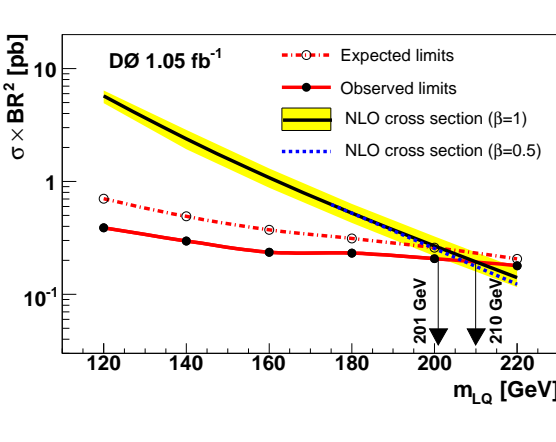
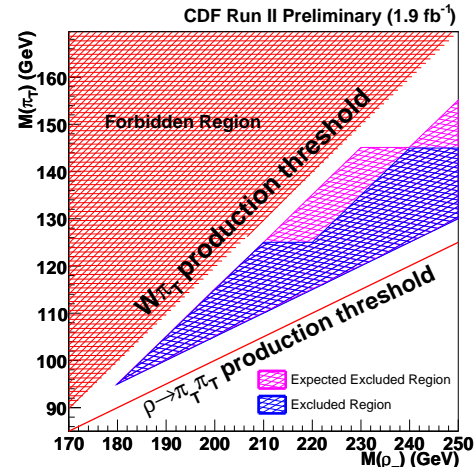


Figure 5: DØ LQ3 exclusion limit

Figure 6: CDF Techni- $\rho$  exclusion limit

## 2.2 Technicolor

Pursuing a signal very similar to that for associated production of W + Higgs, CDF has recently studied the decay of a hypothetical techni- $\rho$  into a techni-pion plus W and then further into W plus b jets [6]. From data corresponding to  $1.9 \text{ fb}^{-1}$ , CDF excludes a new region in the  $m_{\rho_T}$  -  $m_{\pi_T}$  plane (Fig. 6).

## 2.3 SUSY

Ever since its invention in the last century, supersymmetry has been the most copious source of hypothetical particles.

### Trileptons

A stalwart among the searches beyond the standard model is the quest for chargino and neutralino pair production via decay of an off-shell W. Both CDF and D $\emptyset$  have updates to their trilepton analyses available [7, 8]. Masses up to about 145 GeV are excluded.

### Squarks and Gluinos

More stringent (higher) limits can be set on squarks and gluinos, due to their strong production. With a little bit more than 2 inverse femtobarns analysed, D $\emptyset$  excludes squarks below 392 GeV and gluinos below 327 GeV [10], and CDF [9] is not far behind.

### Stop

In some models, the supersymmetric partner of the top quark is the lightest of the squarks. Among them, CDF and D $\emptyset$  have studied three different potential decay paths of this hypothetical particle:

1.  $\tilde{t}_1 \rightarrow c\tilde{\chi}_1^0 \rightarrow 2 \text{ c jets} + \not{p}_T$  [13]
2.  $\tilde{t}_1 \rightarrow b\tilde{\chi}_1^\pm \rightarrow b\tilde{\chi}_1^0 l\nu \rightarrow 2 \text{ leptons (1 isolated), 2 jets (1 btag)}, \not{p}_T$  [11]
3.  $\tilde{t}_1 \rightarrow b\tilde{l}\tilde{\nu} \rightarrow e + \mu + 2b + \not{p}_T$  [12]

Regions of SUSY parameter space extending almost to  $m_{\tilde{t}_1} = 180 \text{ GeV}$  have been excluded.

### Gauge-Mediated Symmetry Breaking

D $\emptyset$  is making extended use of the ‘EM pointing’ technique it pioneered in Run I, using the lateral and depth segmentation of its electromagnetic calorimeter to associate electromagnetic showers with a particular primary vertex (Fig. 13). This helps in

suppressing multiple interaction background, which can otherwise become a problem at the high luminosities (several  $10^{32} s^{-1} cm^{-2}$ ) the Tevatron is routinely achieving these days. Using this technique, a search for signs of GMSB yielding two photons plus missing transverse energy based on  $1.1 fb^{-1}$  sets limits of  $m_{\tilde{\chi}_1^\pm} > 229 GeV$  and  $m_{\tilde{\chi}_1^0} > 125 GeV$  [14].

## 2.4 W'

Only slightly younger than the W itself are searches for its heavier reincarnation, the W'. The latest D $\emptyset$  result in the electron channel [15] pushes the mass limit into the TeV region. Both D $\emptyset$  and CDF are also searching for a W' decaying to top plus bottom [16, 17]. Here the limits are still a bit shy of the TeV boundary.

## 2.5 Z'

The only update falling into our time window is from CDF: in [18] CDF searches the  $e^+e^-$  mass spectrum for deviations from the standard model prediction, using narrow resonances (width compatible with the detector mass resolution) as templates. The largest deviation found has a significance of  $2.5\sigma$ . A Z' with SM couplings is ruled out up to a mass of 966 GeV.

# 3 Recent Additions to the Searches Repertoire

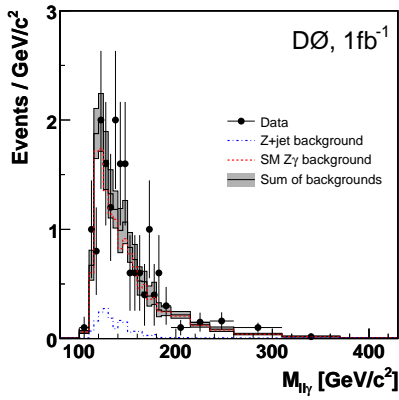
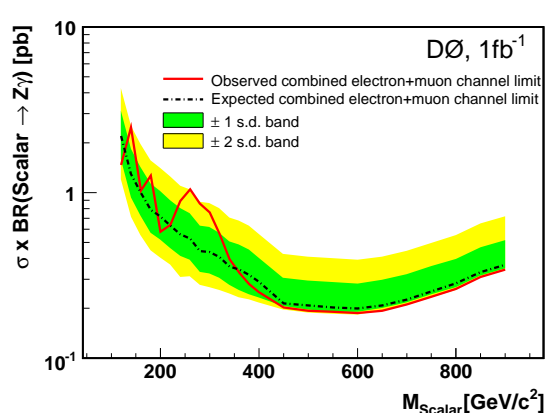
## 3.1 Large Extra Dimensions

Both D $\emptyset$  and CDF search for large extra dimensions in the monophoton and mono-jet final states. D $\emptyset$  recently updated their monophoton analysis (again using EM pointing) [20] based on a sample corresponding to  $1.05 fb^{-1}$ , and CDF has new combined results for monophotons and monojets using  $1.1 fb^{-1}$  and  $2.0 fb^{-1}$ , respectively. Lower limits on the  $M_D$  parameter are about 1 TeV, depending on the number of extra dimensions, and are better than the combined LEP limits for  $4 \leq n_D \leq 8$ .

## 3.2 Z + $\gamma$

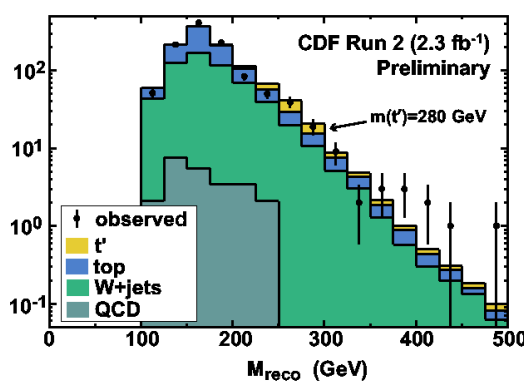
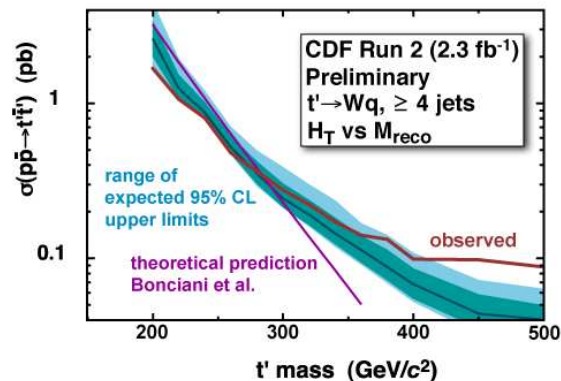
D $\emptyset$  has published a search for scalar or vector particles decaying into Z +  $\gamma$ , based on data corresponding to  $1 fb^{-1}$  [21]. Fig. 7 shows the invariant mass spectrum and

Fig. 8 the resulting exclusion limit.

Figure 7: DØ  $Z + \gamma$  mass spectrum for  $ee\gamma$  and  $\mu\mu\gamma$  combinedFigure 8: DØ  $Z + \gamma$  exclusion contour

### 3.3 Fourth Generation

Part of the emerging ‘top quark factory’ output are searches for new particles coupling predominantly to top quarks, like members of the fourth generation, or new scalars leading to ‘maximal flavour violation’ (see below). CDF has searched for a  $t'$  in  $2.3 \text{ fb}^{-1}$  of data [22], with the expected outcome, and is excluding  $t'$  masses below 284 GeV (Fig. 9).

Figure 9: CDF  $Z t'$  mass spectrum.Figure 10: CDF  $Z t'$  exclusion limit.

### 3.4 Maximal Flavour Violation

New scalars decaying to like sign top quark pairs are being excluded in the mass range from 180 to 300 GeV for couplings to the top quark above 0.79 (180 GeV) to 1.32 (300 GeV) in a new CDF analysis [23].

## 4 Global/Model-Independent Searches global searches

### 4.1 Excited Electrons & Quarks

CDF [24] has searched for bumps in the dijet mass spectrum using  $1.13\text{ fb}^{-1}$  of data, and excludes excited quarks with masses between 260 and 870 GeV. D $\emptyset$  published a search [25] for excited electrons decaying to  $e\gamma$ ; based on data from  $1\text{ fb}^{-1}$  they exclude  $e^*$  up to 756 GeV, for a compositeness scale of 1 TeV.

At Hera, lepton compositeness can be studied via gauge mediated or contact interaction production of excited electrons and neutrinos. In [26] the H1 collaboration describes a search for excited electrons decaying into  $e\gamma$ ,  $eZ$  or  $\nu W$ , using the full statistics accumulated at Hera. No deviations from the standard model are found, and a region is excluded in the plane of the mass of the composite particle versus  $f/\Lambda$ , the ratio of the (SU(2)=U(1)) coupling strength to the compositeness scale (Fig. 11).

The companion paper [27] sets limits resulting from a H1 search for excited neutrinos, based on  $184\text{ pb}^{-1}$  of  $e^-p$  running at Hera.

### 4.2 Isolated and Multi-Leptons

After an initial report [28] by H1 of a  $3\sigma$  excess in the production of isolated leptons, an update using the full Hera statistics of  $504\text{ pb}^{-1}$  is now available from Zeus [29]. No significant excess is found.

Both H1 and Zeus have updated their high- $p_T$  multilepton studies to the full Hera statistics, and report no significant excess beyond standard model sources [30].

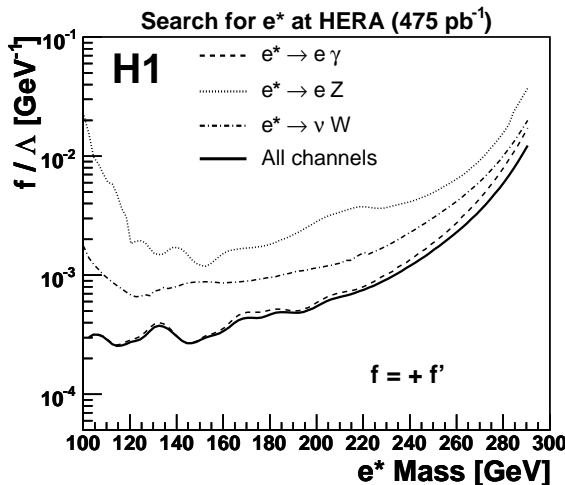


Figure 11: H1  $e^*$  exclusion region: breakdown by channel.

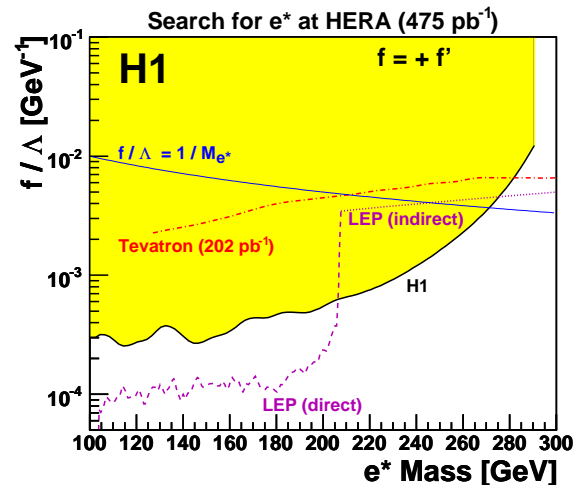


Figure 12: H1  $e^*$  exclusion region: comparison to other limits.

### 4.3 Long-lived Particles decaying to Diphotons or Dielectrons at the Tevatron

DØ has updated its search for long lived particles yielding two electromagnetic clusters [31]. Using the EM pointing technique described above removes any dependence on tracking efficiency and thus extends the decay lengths covered significantly over a similar CDF analysis, despite the much smaller tracking volume (Fig. 14).

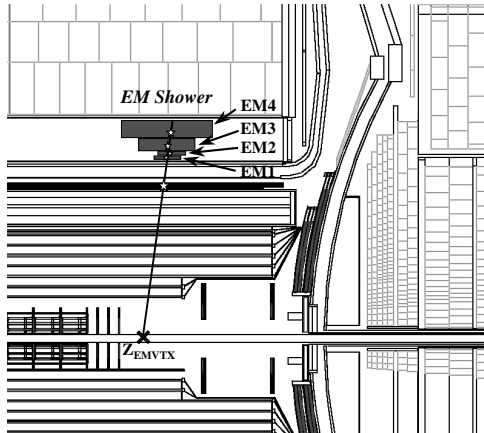


Figure 13: DØ EM pointing technique

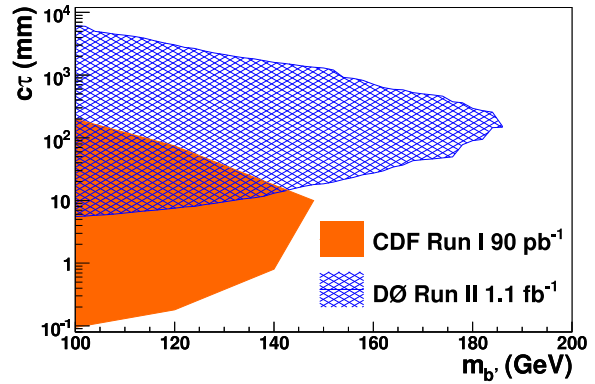


Figure 14: DØ exclusion contour for long-lived particles decaying to two photons or electrons.

## 4.4 Global Spectra Analysis and Bump Hunt at the Tevatron

Initially conceived at D $\emptyset$  as Sherlock/Sleuth and used for beyond-the-Standard-Model searches at D $\emptyset$  and H1, model-independent searches for EW-scale new phenomena have received a big boost by the continued development at CDF. In a recent update [32] CDF describes the search for deviations from the standard model using the VISTA/Sleuth global comparison machinery. Using VISTA, roughly 4 million events from  $2\text{ fb}^{-1}$  were partitioned into about 400 exclusive final states, and the populations of those states as well as about 20,000 kinematic distributions were compared to standard model predictions. About 5000 mass spectra were scoured for mass bumps. No significant deviations from the Standard Model were found, after initial deficiencies in the event modeling and the detector description (in particular the imperfect modeling of 3-jet final states) were accounted for.

Sleuth was then used to specifically examine the high  $p_T$  tails of 87 kinematic distributions for any excess not explained by SM sources. The probability to observe deviations as large or larger than the ones seen due to purely SM sources was quantified as 8%. Thus, no new physics is required yet.

## 5 Summary

A very vibrant and diverse program of searches for physics beyond the Standard Model has led to many updates in the last 12 months from the large data sets amassed by the Hera and Tevatron collaborations. The final results from Hera, based on integrated luminosities of 500/pb for each of H1 and Zeus, have begun to arrive. Tevatron updates based on up to 3 events per fb have been shown. With both CDF and D $\emptyset$  aiming for total integrated luminosities of  $8\text{ fb}^{-1}$ , a lot more data are expected. These ever increasing data samples are complemented by advances in analysis techniques, pushing the limits of discovery ever further.

## References

- [1] <http://www-d0.fnal.gov/Run2Physics/WWW/results/prelim/NP/N62/>
- [2] [http://www-h1.desy.de/h1/www/publications/htmlsplit/  
H1prelim-07-164.long.html](http://www-h1.desy.de/h1/www/publications/htmlsplit/H1prelim-07-164.long.html)
- [3] <http://www-d0.fnal.gov/Run2Physics/WWW/results/final/NP/N08G/>,  
<http://arxiv.org/abs/0808.4023>, FERMILAB-PUB-08/334-E, sub. to PLB

- [4] [http://www-cdf.fnal.gov/physics/exotic/r2a/20080403.dijetmet/dijet\\_mssm\\_lq/dijet\\_met\\_2fb.html](http://www-cdf.fnal.gov/physics/exotic/r2a/20080403.dijetmet/dijet_mssm_lq/dijet_met_2fb.html)  
[http://www-cdf.fnal.gov/physics/exotic/r2a/20080403.dijetmet/dijet\\_mssm\\_lq/dijet\\_met\\_2fb.html](http://www-cdf.fnal.gov/physics/exotic/r2a/20080403.dijetmet/dijet_mssm_lq/dijet_met_2fb.html)
- [5] <http://www-d0.fnal.gov/Run2Physics/WWW/results/final/NP/N08E/>,  
<http://arxiv.org/abs/0806.3527>, FERMILAB-PUB-08/201-E, sub. to PRL
- [6] [http://www-cdf.fnal.gov/physics/new/hdg/results/technicolor\\_080411/](http://www-cdf.fnal.gov/physics/new/hdg/results/technicolor_080411/)
- [7] [http://www-cdf.fnal.gov/physics/exotic/r2a/20080110.trilepton\\_dube](http://www-cdf.fnal.gov/physics/exotic/r2a/20080110.trilepton_dube)
- [8] <http://www-d0.fnal.gov/Run2Physics/WWW/results/prelim/NP/N57/>
- [9] [http://www-cdf.fnal.gov/physics/exotic/r2a/20080214.squark\\_gluino/squark\\_gluino.html](http://www-cdf.fnal.gov/physics/exotic/r2a/20080214.squark_gluino/squark_gluino.html)  
[http://www-cdf.fnal.gov/physics/exotic/r2a/20080214.squark\\_gluino/squark\\_gluino.html](http://www-cdf.fnal.gov/physics/exotic/r2a/20080214.squark_gluino/squark_gluino.html)
- [10] <http://www-d0.fnal.gov/Run2Physics/WWW/results/final/NP/N07H/>,  
<http://arxiv.org/abs/0712.3805>, FERMILAB-PUB-07/668-E, PLB 660, 449 (2008)
- [11] [http://www-cdf.fnal.gov/physics/new/top/2008/tprop/Stop/Dilepton\\_Stop\\_Quark\\_Search\\_2Point7invfb.html](http://www-cdf.fnal.gov/physics/new/top/2008/tprop/Stop/Dilepton_Stop_Quark_Search_2Point7invfb.html) [http://www-cdf.fnal.gov/physics/new/top/2008/tprop/Stop/Dilepton\\_Stop\\_Quark\\_Search\\_2Point7invfb.html](http://www-cdf.fnal.gov/physics/new/top/2008/tprop/Stop/Dilepton_Stop_Quark_Search_2Point7invfb.html)
- [12] <http://www-d0.fnal.gov/Run2Physics/WWW/results/prelim/NP/N61/>
- [13] <http://www-d0.fnal.gov/Run2Physics/WWW/results/final/NP/N08B/>,  
<http://arxiv.org/abs/0803.2263>, FERMILAB-PUB-08/063-E, PLB 665, 1 (2008)
- [14] <http://www-d0.fnal.gov/Run2Physics/WWW/results/final/NP/N07F/>,  
<http://arxiv.org/abs/0710.3946>, FERMILAB-PUB-07/560-E, PLB 659, 856 (2008)
- [15] <http://www-d0.fnal.gov/Run2Physics/WWW/results/final/NP/N07D/>,  
<http://arxiv.org/abs/0710.2966>, FERMILAB-PUB-07/499-E, PRL 100, 31804 (2008)
- [16] [http://www-cdf.fnal.gov/physics/new/top/2007/singletop/Wprime/Public\\_2fb.html](http://www-cdf.fnal.gov/physics/new/top/2007/singletop/Wprime/Public_2fb.html)  
[http://www-cdf.fnal.gov/physics/new/top/2007/singletop/Wprime/Public\\_2fb.html](http://www-cdf.fnal.gov/physics/new/top/2007/singletop/Wprime/Public_2fb.html)

- [17] <http://arXiv.org/abs/0803.3256>, Phys. Rev. Lett. 100, 211803 (2008)
- [18] [http://www-cdf.fnal.gov/physics/exotic/r2a/20080306.dielectron\\_duke/  
pub25/duke.html](http://www-cdf.fnal.gov/physics/exotic/r2a/20080306.dielectron_duke/pub25/duke.html)  
[http://www-cdf.fnal.gov/physics/exotic/r2a/20080306.dielectron\\_duke/  
pub25/duke.html](http://www-cdf.fnal.gov/physics/exotic/r2a/20080306.dielectron_duke/pub25/duke.html)
- [19] [http://www-cdf.fnal.gov/physics/exotic/r2a/20071213.gammamet/  
LonelyPhotons/photonmet.html](http://www-cdf.fnal.gov/physics/exotic/r2a/20071213.gammamet/LonelyPhotons/photonmet.html)  
[http://www-cdf.fnal.gov/physics/exotic/r2a/20071213.gammamet/LonelyPhotons/  
photonmet.html](http://www-cdf.fnal.gov/physics/exotic/r2a/20071213.gammamet/LonelyPhotons/photonmet.html)
- [20] <http://www-d0.fnal.gov/Run2Physics/WWW/results/prelim/NP/N63/>
- [21] <http://www-d0.fnal.gov/Run2Physics/WWW/results/final/EW/E08C/>,  
<http://arxiv.org/abs/0806.0611>, arxiv:0806.0611, FERMILAB-PUB-08-154-E, accepted by PLB.
- [22] <http://www-cdf.fnal.gov/physics/new/top/2008/tprop/Tprime2.3/public.html>
- [23] <http://www-cdf.fnal.gov/physics/exotic/r2a/20080508.mxfv/index.html>
- [24] [http://www-cdf.fnal.gov/physics/exotic/r2a/20080214.mjj\\_resonance\\_1b](http://www-cdf.fnal.gov/physics/exotic/r2a/20080214.mjj_resonance_1b)
- [25] <http://www-d0.fnal.gov/Run2Physics/WWW/results/final/NP/N08A/>,  
arXiv:0801.0877, FERMILAB-PUB-08/007-E, Phys.Rev.D77,091102 (2008).
- [26] [http://www-h1.desy.de/h1/www/publications/htmlsplit/  
DESY-08-052.long.html](http://www-h1.desy.de/h1/www/publications/htmlsplit/DESY-08-052.long.html), DESY-08-052, arxiv:0805.4530, H1-169, Phys. Lett. B666 (2008) 131-139.
- [27] [http://www-h1.desy.de/h1/www/publications/htmlsplit/  
DESY-08-009.long.html](http://www-h1.desy.de/h1/www/publications/htmlsplit/DESY-08-009.long.html), DESY-08-009, arxiv:0802.1858, H1-168, Physics Letters B663 (2008) 382-389.
- [28] V. Andreev et al. [H1 Collaboration], Phys. Lett. B 561 (2003) 241 [hep-ex/0301030]
- [29] [http://www-zeus.desy.de/physics/exo/ZEUS\\_PUBLIC/zeus-pub-08-005/](http://www-zeus.desy.de/physics/exo/ZEUS_PUBLIC/zeus-pub-08-005/),  
arxiv:0807.0589, see also <http://www-h1.desy.de/psfiles/confpap/EPS2007/H1prelim-07-162.ps> <http://www-h1.desy.de/psfiles/confpap/EPS2007/H1prelim-07-162.ps> (H1 & Zeus Summer 2007).

- [30] <http://www-h1.desy.de/h1/www/publications/htmlsplit/DESY-08-065.long.html>,  
arxiv:0806.3987, H1-171, Phys. Lett. B668 (2008) 268-276. see also ZEUS-prel-07-022, [http://www-zeus.desy.de/øsamu/public/electron\\_eps2007\\_public.htm](http://www-zeus.desy.de/øsamu/public/electron_eps2007_public.htm) and ZEUS-prel-08-006.
- [31] <http://www-d0.fnal.gov/Run2Physics/WWW/results/final/NP/N08D/>,  
arXiv:/0806.2223, Fermilab-PUB-08/169-E, accepted by Phys. Rev. Lett. ; see  
[http://www-cdf.fnal.gov/physics/exotic/r2a/20040826.mumulxy\\_longlifez/](http://www-cdf.fnal.gov/physics/exotic/r2a/20040826.mumulxy_longlifez/)
- [32] [http://www-cdf.fnal.gov/physics/exotic/r2a/20080228.vista\\_sleuth/publicPage.html](http://www-cdf.fnal.gov/physics/exotic/r2a/20080228.vista_sleuth/publicPage.html)  
[http://www-cdf.fnal.gov/physics/exotic/r2a/20080228.vista\\_sleuth/publicPage.html](http://www-cdf.fnal.gov/physics/exotic/r2a/20080228.vista_sleuth/publicPage.html)

# BSM measurements with Top at LHC : CMS sensitivity to Flavour Changing Neutral Currents

*Leonardo Benucci*  
*Universiteit Antwerpen*  
*2020 Antwerp, BELGIUM*

## 1 Top quark and New Physics

Top quark was discovered at Fermilab in the 1995-96 [1], completing the three-families structure of the Standard Model (SM) and opening the new field of top quark physics. Since the beginning of the study phase, this object has appeared to be a very special one.

Top quark is distinguished by a large mass ( $172.4 \pm 0.7$  (stat)  $\pm 1.0$  (syst)GeV, [2]) that is intriguingly close to the scale of electroweak (EW) and a Yukawa coupling surprisingly close to 1. Within the Minimal Standard Model, top quark processes are known with high accuracy with no need for phenomenological parameters, decay occurs mostly through the  $t \rightarrow bW$  channel and, since the top mass width is larger than the QCD scale, no top-hadrons are formed. These unique properties suggest that the top quark can be considered a very clean laboratory where to constrain the SM and to look beyond it.

Several properties of the top quark have already been examined at the  $p\bar{p}$  collider Tevatron at Fermilab (up to now the only place where it is directly produced),  $e^\pm p$  collider HERA at DESY and  $e^+e^-$  collider LEP at CERN. Despite the very important reaches and limits of these measurements, most of them suffer from the small sample of top quarks collected. It is here that the Large Hadron Collider (LHC) comes into the game.

Whereas the center-of-mass energy at LHC is seven times higher than the Tevatron, the cross section for  $t\bar{t}$  production is more than a hundred times larger and amounts to  $833 \pm 83$  (PDF)  $\pm 50$  (stat) pb at next-to-leading order [3]. This large cross section, combined with the significantly enhanced single-top production, implies that during the stable low-luminosity run ( $\mathcal{L} = 2 \times 10^{33}\text{cm}^{-2}\text{s}^{-1}$ ) a rate around 4 top quarks per second will be reached. About 800,000 events will be likely obtained after  $1\text{fb}^{-1}$ ,

then several millions of events can be accumulated each year. Therefore, LHC can well be renamed as a “top factory”. Having a so powerful machine at hand, several top quark properties will be examined with a much better precision and entirely new measurements can be contemplated. Among the possible new couplings, the Flavour Changing Neutral Currents (FCNCs) are one of the most interesting processes.

At a fundamental level, FCNCs consist in couplings of the type  $tVq$ , where  $V$  is a neutral gauge boson ( $V = \gamma, Z^0, g$ ) and  $q$  is a  $u$  or  $c$  quark. Since in the SM these anomalous couplings are absent at tree-level and occur only at loop level, rates for FCNC processes in the top sector are extremely small (with Branching Ratios from  $10^{-14}$  to  $10^{-14}$ , [5, 6]), because of the strong loop suppression and the high masses of the gauge bosons. Therefore, the top quark plays a unique role compared to the other quarks – for which the expected FCNC transitions are much larger – and *any experimental evidence for a top quark FCNC interaction would signal the existence of new physics.*

Several scenarios beyond the SM have been proposed in recent years. In many new physics models as the two Higgs Doublet Models (2HDM), the Minimal Supersymmetric Standard Model (MSSM) with and without R-parity conservation, SUperSimmetrY (SUSY) top-assisted technicolor (TC), left-right (LR) asymmetry model and quark singlets (QS), enhancements in FCNC decays can arise, either from a large virtual mass or from the couplings involved in the loop. A summary of the predicted Branching Ratios for the most promising models is in Tab. 1.

The aim of this study is to determine the sensitivity and discovery reach of the CMS experiment [14] at LHC for this channel, in both the  $t \rightarrow Zq$  and  $t \rightarrow \gamma q$  neutral decays ( $t \rightarrow qg$  is not studied because of its very high QCD background). The strategy to reveal these signals on top of the SM background is based on a series of optimized cuts and is assessed in Sec. 2. A full set of systematic effects, originating from detector or theoretical uncertainties, are added to the simulation and their impact on the analysis is established in Sec. 3. Then a closer look is given to the relevant background and efforts are performed (Sec. 4) to find a specific control region that can be addressed in the future samples, thus allowing to measure directly

	2HDM-III [7, 8]	MSSM with $R$ [4]	MSSM with $\not{R}$ [9]	TC2 [10]	LR [11]	QS [12, 13]
$\text{BR}(t \rightarrow qg)$	$10^{-4}$	$10^{-4}$	$10^{-3}$	$10^{-3}$	$10^{-5}$	$10^{-7}$
$\text{BR}(t \rightarrow q\gamma)$	$9 \cdot 10^{-4}$	$10^{-6}$	$10^{-5}$	$10^{-7}$	$10^{-6}$	$10^{-8}$
$\text{BR}(t \rightarrow qZ)$	$10^{-6}$	$10^{-5}$	$10^{-4}$	$10^{-4}$	$10^{-4}$	$10^{-4}$

Table 1: Branching Ratios for FCNC top quark decays as predicted within some SM extensions. Only the order of magnitude is quoted here.

the background when data will be available. In the conclusion (Sec. 5) results are presented and comparison with current limits are showed. Full details of the work are in Ref. [15].

## 2 Analysis of the FCNC signals

The features that mostly make different the FCNC signal from the background events are: the presence of an isolated, high transverse momentum charged leptons ( $p_T > 10 \div 20 \text{ GeV}$ ) coming from vectorial boson decays; a high-energy isolated photon in the  $t \rightarrow q\gamma$  case; large missing energy ( $\cancel{E}_T > 30 \div 40 \text{ GeV}$ ) from undetected neutrinos in  $W$  decays; two hard jets, typically with transverse momentum  $p_T > 50 \div 60 \text{ GeV}$ , coming from the fragmentation of  $b$  and  $q$  quarks.

The anomalous top decay has been studied by simulating the production of a  $t\bar{t}$  pair from gluon-gluon and quark-antiquark annihilation, then requiring the SM decay for one top ( $t \rightarrow bW$ ) and FCNC decay for the other. The  $t\bar{t}$  signal has been generated with TOPREX 4.11 [16], while PYTHIA [17] was used for modeling of quark and gluon hadronization. Only leptonic decay channels of  $Z$  and  $W$  bosons have been studied, where the lepton could be either  $e$  or  $\mu$ ; hadronic bosons decays as well as decays to  $\tau$  leptons are not considered because of the large QCD background. Both initial and final state radiation (ISR and FSR) were simulated with CTEQ5L parton density functions (PDFs). The generated events were passed through the full detector simulation and digitization, taking into account low luminosity pile-up.

Several SM processes contributing as background have been studied:  $t\bar{t}$  production with both top quarks following the standard decay, single-top quark production ( $t$ -channel),  $Z/W + \text{jets}$ ,  $(W/Z)(W/Z) + \text{jets}$ ,  $Zb\bar{b}$  and QCD multi-jet production.

The off-line selected leptons have to be considered isolated when the isolation variable (defined in Ref. [14]) is less than 0.07. High- $p_T$  jets are assumed to come from a  $b$ -jet if they have more than 2 tracks and a discriminator value (defined again in Ref. [14]) larger than 2. This choice allows to maximize the  $b$ -jet purity while containing the mis-tag with jets from  $u/c$  quarks below few percent.

For the FCNC  $t \rightarrow \gamma q$  channel the main selection cuts have been optimized as: *a*) ‘single electron or single muon’ or ‘single-photon’ criteria at the first level (L1) trigger and High Level Trigger (HLT); *b*) one isolated  $\mu^\pm$  (with  $p_T > 20 \text{ GeV}$ ) or an  $e^\pm$  (with  $p_T > 30 \text{ GeV}$ ), plus more than  $25 \text{ GeV}$  of missing transverse energy, forming a transverse invariant mass  $M_T(l-\cancel{E}_T) < 120 \text{ GeV}$  and a transverse momentum greater than  $65 \text{ GeV}$  for  $p_T(e-\cancel{E}_T)$  or  $50 \text{ GeV}$  for  $p_T(\mu-\cancel{E}_T)$ ; *c*) only one jet compatible with  $b$ -jet with  $p_T > 50 \text{ GeV}$ , that in combination with the  $W$  candidate gives an invariant transverse mass  $M_T(bW) < 220 \text{ GeV}$ ; *d*) the isolated photon selected from the trigger satisfying  $p_T > 90 \text{ GeV}$ ; *e*) at least one jet incompatible with coming from  $b$  quark

and harder than 60GeV; *f*) the combination of the photon and the light jet in the range  $100 < M(q\gamma) < 250$ GeV. A fit of the invariant mass shape with a Gaussian and a linear+exponential function (Fig. 1, left) can be used to estimate the combinatorial background. The signal efficiency turns to be  $(4.0 \pm 0.4)\%$  and the only process surviving from the SM events is the top pair inclusive decay with an isolated lepton (efficiency  $(1.7 \pm 0.1) \cdot 10^{-5}$ ).

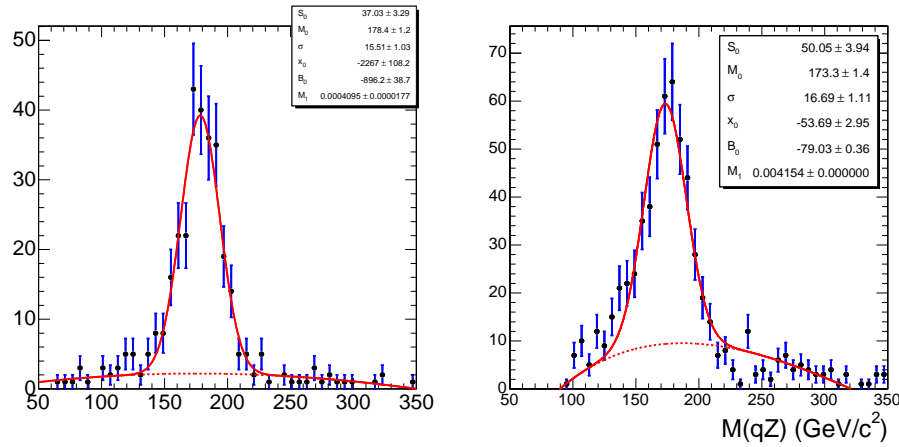


Figure 1: The result of the fit on the  $t \rightarrow q\gamma$  (left) and  $t \rightarrow qZ$  (right) signal distribution with a Gaussian summed to a linear plus exponential function.

For the FCNC  $t \rightarrow qZ$  channel the main selection cuts are: *a*) ‘double electron or double muon’ trigger criteria at L1 and HLT levels; *b*) two isolated  $e^\pm$  (with  $p_T > 20$ GeV) or  $\mu^\pm$  (with  $p_T > 15$ GeV), having an invariant mass  $\pm 10$ GeV around the nominal  $Z$  mass; *c*) a third lepton with same quality cuts, which, in combination with the missing transverse energy ( $\cancel{E}_T > 35$ GeV) has a transverse mass less than 120GeV; *d*) only one jet compatible with  $b$ -jet with  $p_T > 60$ GeV; *e*) the invariant transverse mass of the  $M_T(bW) < 220$ GeV; *f*) at least one jet which is incompatible with coming from a  $b$  quark and satisfying  $p_T > 60$ GeV; *g*) invariant mass of this jet and the  $Z$  in the range  $100 < M(qZ) < 250$ GeV. The resulting distribution is presented in Fig. 1 (right), and the number of signal events corresponds to a  $(4.4 \pm 0.4)\%$  efficiency. The relevant background sources are the di-leptonic  $t\bar{t}$  decay and the  $Zb\bar{b}$  production (both with efficiency  $\sim 10^{-5}$ ), that may give origin to the third lepton from the decay of one  $b$ -jet.

### 3 Study of systematic effects

Since in this study the background will be counted in specific ‘control regions’, systematic effects affecting the absolute background rate have no relevance and only the variables that mark the difference between the control and the signal region are considered.

The uncertainty on the jet energy scale (considered as 3% for  $p_T(\text{jet}) > 50\text{GeV}$ ) is one of the most important effects, because the number of detected jets can vary in about 15% in both the light and the  $b$ -jet selection and a different occurrence of events with a single tagged jet (both light and  $b$ -tagged) is induced. Fluctuations related to tracker and muon chambers uncertainties, electromagnetic energy scale and missing energy uncertainty have been simulated and found to be below 1% in all background samples. The impact on the efficiency for  $b$ -jet is not an issue here, because the effect of asking a  $b$ -tagged object will be directly included in the control region definition. For what concerns the theoretical description of the signal and background processes, the analysis has found to be sensitive to the description of the heavy quarks fragmentation, since changing the parameter of the Lund model (according with prescriptions in Ref. [18]) can worse the efficiency about 9% for the  $b$ -jets and 11% for the light ones. On the other hand, the fact that the main background is  $t\bar{t}$  (having exactly the same initial state of the signal and a final state differing only in one jet contents) is instrumental in absorbing the impact of many theoretical uncertainties, as those on ISR/FSR, PDF and underlying event. The residual effects can be measured in a top pair-rich region and subtracted from the signal region.

### 4 Background estimation driven from data

When the amount of surviving background in both channels is evaluated by counting the number of event filling the last selection, several uncertainties are included, as high statistical fluctuations due to the small number of events, luminosity uncertainties, theoretical error in the cross sections. Here the problem is faced adopting the common solution, to identify specific control regions (suitable to be searched for in future data samples with the lowest systematic error) almost signal-free and rich in only one type of background process. Due to the increased background statistic, with these techniques errors from Monte Carlo are much reduced.

The  $t\bar{t}$  (di-leptonic) background for the  $t \rightarrow qZ$  analysis has been evaluated by requiring the double lepton ( $e^\pm/\mu^\pm$ ), a large missing energy  $\cancel{E}_T > 85\text{GeV}$ (to minimize contamination from  $Zb\bar{b}$ ) and one  $b$ -jet at least. These events can be used to form a region corresponding to the right side of the  $M(l\bar{l})$  distribution (Fig. 2, left) where the contaminations from  $Zb\bar{b}$  (blue line) and signal (upper plot) are negligible. If the

cut on missing energy is removed and at least two b-jets are required, a region around the  $Z$  peak to evaluate  $Zb\bar{b}$  amount is obtained. Here the fraction of  $t\bar{t}$  events under the peak is significant, but it can be derived from the data-driven estimation above. When the number of events in these control regions is rescaled to the signal one (using factors as 3<sup>rd</sup> lepton and light jet efficiency, different  $\cancel{E}_T$  cut and  $b$ -jet multiplicity) the total background is  $19.8 \pm 1.6$  (stat)  $\pm 2.7$  (syst)  $\pm 2.0$  (theor) events after  $10 \text{ fb}^{-1}$ .

The  $t\bar{t} \rightarrow l + X$  process for the  $t \rightarrow q\gamma$  analysis can be measured from a fit of the  $M(bW)$  invariant mass shape, in a sample having high  $W$  boost ( $p_T(W) > 85 \text{ GeV}$ ) and at least two hard light jets, in order not to suffer from single-top contamination. Rescaling from the different  $p_T(W)$  cut and  $b$ -jet multiplicity, the top pair background in the signal region after  $10 \text{ fb}^{-1}$  is  $33.2 \pm 4.6$  (stat)  $\pm 1.0$  (syst)  $\pm 3.0$  (theor) events.

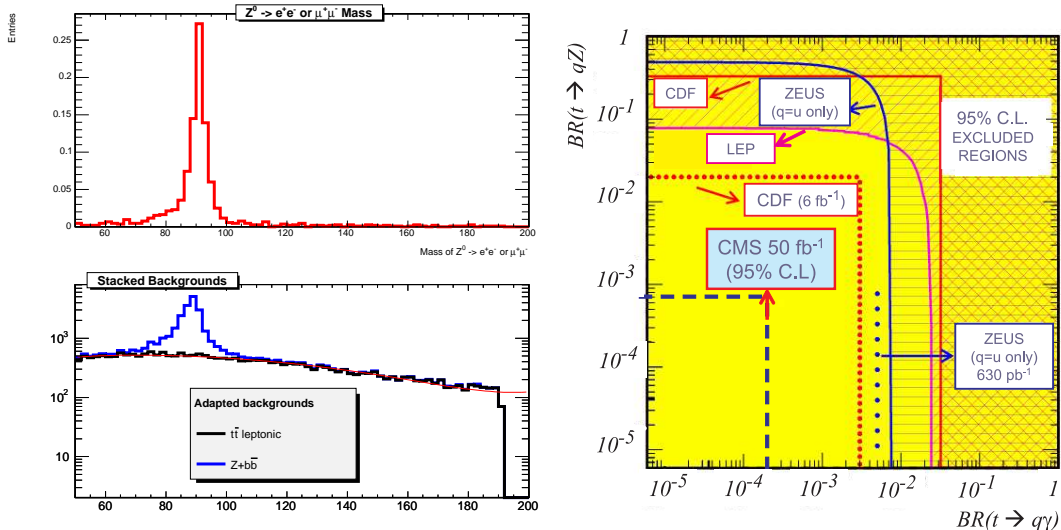


Figure 2: Left: Invariant mass of two same-sign opposite-flavour leptons in the control region defined in the text. A polynomial fit is superimposed to the  $t\bar{t}$  background. Right: The 95% C.L. exclusion plot of the analysis after  $50 \text{ fb}^{-1}$ , compared with the current limits to  $t \rightarrow q\gamma$  and  $t \rightarrow qZ$  branching ratios.

## 5 Sensitivity estimation and conclusions

To evaluate the sensitivity reach of the analysis, the  $S_{12}$  function [19] is adopted as a significance estimator and corrections from statistical and theoretical errors are included as in Ref. [20]. For a given significance (or confidence level C.L.) and integrated luminosity  $L$ , a minimum number  $N_{min}$  of  $t \rightarrow qZ/\gamma$  events is obtained from that estimator. The related Branching Ratio  $BR_{FCNC}$  comes from the formula

$N_{min} = L \cdot \epsilon_S \sigma(t\bar{t}) \cdot BR_{SM} \cdot BR_{FCNC}$ , where  $BR_{SM}$  is the SM decay from the other top quark and signal efficiency  $\epsilon_S$  is optimized in the analysis procedure for each cut. After  $50 \text{ fb}^{-1}$ , a  $t \rightarrow q\gamma$  ( $t \rightarrow qZ$ ) decay can be discovered at  $3\sigma$  if  $BR$  is larger than  $1.65(10.4) \cdot 10^{-4}$ , while the 95% C.L. exclusion limit is  $1.19(7.6) \cdot 10^{-4}$ . When these results are compared with the current limits as depicted in Fig. 2 (right), an improvement larger than one order of magnitude can be appreciated. It is worth to observe that even after  $1 \text{ fb}^{-1}$ , 95% C.L. limits for the  $t \rightarrow qZ(\gamma)$  will be about  $1.0 \cdot 10^{-2}(8.4 \cdot 10^{-4})$ , exceeding the sensitivity expected from CDF at the end of Tevatron life ( $6 \text{ fb}^{-1}$ ) and falling below the bounds determined from CP and EW observables. For integrated luminosities larger than some tens of  $\text{fb}^{-1}$ , constraints firstly on 2HDM and then on top-color and R-violating models can be obtained. Due to the fact that different theories predict different orders of enhancement, the measurements of such processes at the LHC will not only shed light on new physics, but also may indicate some favor for a specific model.

## References

- [1] [CDF Collaboration], Phys. Rev. Lett. **73**, 225 (1994), [hep-ex/9405005](#)
- [2] Tevatron Electroweak Working Group, [0808.1089v1 \[hep-ex\]](#)
- [3] W. Beenakker, *et al.*, Phys. Rev. D **40**, 54 (1989)
- [4] J. J. Cao, G. Eilam *et al.*, [hep-ph/0702264v3](#)
- [5] B. Mele, S. Petrarca, A. Soddu, Phys. Lett. B **435**, 401 (1998)
- [6] C.-S. Huang, X.-H. Wu and S.-H. Zhu, Phys. Lett. B **452**, 143 (1999).
- [7] D. Atwood, L. Reina and A. Soni, Phys. Rev. D **55**, 3156 (1997)
- [8] R. A. Diaz, R. Martinez, J-A. Rodriguez, [hep-ph/0103307](#)
- [9] J. M. Yang, B.-L. Young and X. Zhang, Phys. Rev. D **58**, 055001 (1998)
- [10] H. Zhang, [0712.0151 \[hep-ph\]](#)
- [11] M. Frank and I. Turan, Phys. Rev. D **72**, 035008 (2005)
- [12] J. A. Aguilar-Saavedra, Acta Phys. Pol. B **35**, 2695 (2004)
- [13] J. A. Aguilar-Saavedra, B. M. Nobre, Phys. Lett. B **553**, 251 (2003)
- [14] [CMS Collaboration], CERN-LHCC 2006/001 (2006)

- [15] L. Benucci, CMS Thesis 2008/010 (2008)
- [16] S. R. Slabospitsky, L. Sonnenschein, Comput. Phys. Commun. **148**, 87 (2002)
- [17] T. Sjöstrand, *et al.*, Comput. Phys. Commun. **135**, 238 (2001)
- [18] P. Bartalini, R. Chierici, A. De Roeck, CMS Note 2005/013 (2005)
- [19] S. I. Bityukov and N. V. Krasnikov, Nucl. Instr. and Meth., A **452**, 518 (2000)
- [20] [CMS Collaboration], J. Phys. G: Nucl. Part. Phys., **34**, 995 (2007).

# $ZZ$ into $4\ell$ expected sensitivity with the first ATLAS data

*Ilektra A. Christidi  
(on behalf of the ATLAS collaboration)  
Department of Physics  
Aristotle University of Thessaloniki  
54124 Thessaloniki, GREECE*

## 1 Introduction

In the Standard Model (SM),  $ZZ$  production proceeds through the t- and u-channel  $q\bar{q}$  scattering diagrams shown in Figure 1. It is of great interest to measure its cross-section at LHC energies because this process is an irreducible background to the SM Higgs decay channel  $H \rightarrow ZZ$ , and it provides a unique opportunity to test the SM by measuring the neutral Triple Gauge Coupling (TGC) strength, which is zero at tree level in the SM.

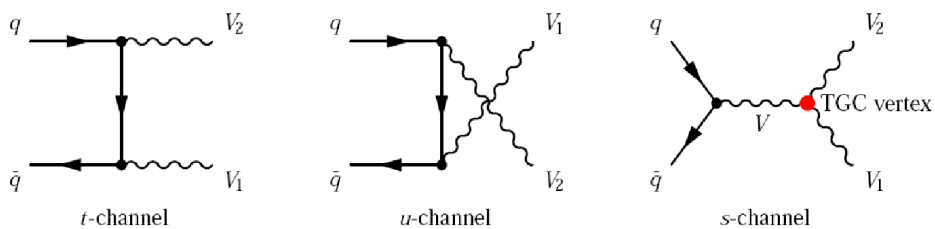


Figure 1: Feynman diagrams of  $ZZ$  production at leading-order for  $(V, V_1, V_2) = (Z^{(*)}, Z, Z)$  or  $(\gamma^{(*)}, Z, Z)$ . The rightmost diagram is forbidden in the SM.

In this note we study the expected ATLAS sensitivity to  $ZZ$  production at 14 TeV c.m. energy with simulated data, via the four lepton final states  $pp \rightarrow ZZ \rightarrow 4e, 4\mu, 2e2\mu$ , taking into account both the on-mass and off-mass shell  $Z$  bosons. More details can be found in [1].

The signal channel is characterised by four high  $p_T$ , isolated leptons. Background contributions to this channel come mainly from:

- $t\bar{t}$  pair production where both  $W$  bosons decay leptonically and the other two lepton candidates come from the remaining  $b$ -jet.
- Production of  $b$ -jets associated with a  $Z$  boson, where the boson decays leptonically and is accompanied by leptons from the heavy quark jets ( $Zb\bar{b}$ ).

Reconstructed muons not originating from  $Z$  decays are usually decay products of  $b$  quarks, whereas electrons are often misidentified jets.

These backgrounds can be very effectively suppressed as shown in this analysis, giving an expected signal to background ratio of  $O(100)$  ( $O(10)$ ) for on-shell (off-shell)  $Z$  bosons, and a signal significance of  $O(7)$  with  $1 \text{ fb}^{-1}$  of data.

## 2 Signal and background MC Samples

Table 1 summarizes the signal and background samples used in this analysis, generated with full detector simulation and reconstruction. The  $ZZ \rightarrow 4\ell$  signal NLO sample includes only on-shell  $Z$  bosons, therefore it is used for the TGC studies only and not for the cross-section studies, which are performed with the Pythia LO sample. For both the signal samples the  $Z$  bosons, as well as the taus, are forced to decay leptonically and the sample is restricted at generator level to lepton  $|\eta| < 3.0$  and  $p_T > 5 \text{ GeV}$  for all 4 leptons. For the background samples, filter cuts requiring 4 leptons in the final state were applied.

Process	Generator	Events	Filter eff.	K-factor	$\sigma(\text{fb}) \times \text{BR}$
$ZZ \rightarrow 4\ell$	Pythia(v6.3) [2]	43000	0.219	1.35	159
$ZZ \rightarrow 4\ell$	MC@NLO/Jimmy [3]	49250	1.000	-	66.8
$Zb\bar{b} \rightarrow 4\ell$	Acer/Pythia [4]	313689	0.009	1.42	52000
$t\bar{t} \rightarrow 4\ell$	MC@NLO/Jimmy	152701	0.007	-	833000

Table 1: Signal and background MC data samples summary table. The cross-section times Branching Ratio (BR) given in the last column is before the filter cut and does not include the K-factor for LO generators.

## 3 Event Selection

A set of pre-selection cuts is applied to reconstructed muons and electrons, then possible  $Z$  candidates are formed from the leptons which pass those pre-selection

cuts. More cuts are applied to the lepton pairs, and finally one  $ZZ$  pair is selected.

### Pre-selection cuts

Muon tracks are required to be well reconstructed by the Muon Spectrometer (MS) and the Inner Detector (ID) combined, or the MS alone outside the ID's acceptance [5]. Basic kinematic cuts are also applied ( $p_T > 6$  GeV,  $|\eta| < 2.7$ ).

The electrons should be reconstructed as an electron-like cluster in the calorimeters matched to a track in the ID, with  $0.5 < E/p < 3.0$ . The kinematic cuts are similar to those for muons ( $p_T > 6$  GeV,  $|\eta| < 2.5$ ).

After pre-selection, lepton pairs of the same flavor and opposite charge are formed and pairs whose leptons have  $\Delta R = \sqrt{\Delta\eta^2 + \Delta\phi^2} < 0.2$  are rejected. The remaining pairs are combined to form  $ZZ$  candidates and each event is required to have at least two legitimate pairs.

### Isolation and maximum $p_T$ cuts

The two main criteria which are used to discriminate signal from background are the lepton  $p_T$  and isolation. For muon isolation, the isolation ratio  $I = \frac{E_{T,0.4}}{E_T^\mu}$  is required to be  $< 0.2$  for each muon of the pair, where  $E_{T,0.4}$  is the transverse energy in a cone of radius  $\Delta R = 0.4$  around the muon track, and  $E_T^\mu$  is the transverse energy of the muon. For electron isolation, cuts on shower shape in the Electromagnetic Calorimeter are applied to each electron. All pairs must have at least one lepton with  $p_T > 20$  GeV.

### Mass cut

In order to eliminate background from leptons not originating from  $Z$  decays, a cut of 70-110 GeV on the reconstructed  $Z$  invariant mass is applied. For the  $ZZ$  case, both candidate  $Z$  bosons are required to satisfy this cut, whereas for  $ZZ^*$  only one. The other  $Z$  candidate has to have an invariant mass greater than 20 GeV, making the  $ZZ$  sample a subset of the  $ZZ^*$  sample.

The cut flow described above and the respective efficiencies for the  $4\mu$  event topology is given in Table 2 for the signal and the backgrounds as an example.

## 4 Results

The  $4\ell$  invariant mass distributions for signal and background after all cuts are shown in Figure 2 for  $ZZ$  and  $ZZ^*$ . All plots are normalized to  $10 \text{ fb}^{-1}$  integrated luminosity.

The expected number of signal and background events for each of the three final state configurations is given in Table 3 for the  $ZZ$  and  $ZZ^*$  cases, for an integrated

	$ZZ \rightarrow 4\mu$ signal (%)	$Zb\bar{b}$ background (%)	$t\bar{t}$ background (%)	
	$ZZ^*$	$ZZ$	$ZZ^*$	$ZZ$
Lepton Preselection		71	6.3	3.2
Pair formation, $\Delta R$		99	77	63
Isolation, $p_T^{max}$		81	1.3	0.13
$Z$ Mass region	92	73	25	2.0
Total	52	41	0.0156	0.0013
				0.0007

Table 2: Signal and background selection cut efficiencies for the  $4\mu$  final state. The efficiency in every step is the number of events remaining after the cut divided by the number of events before the cut.

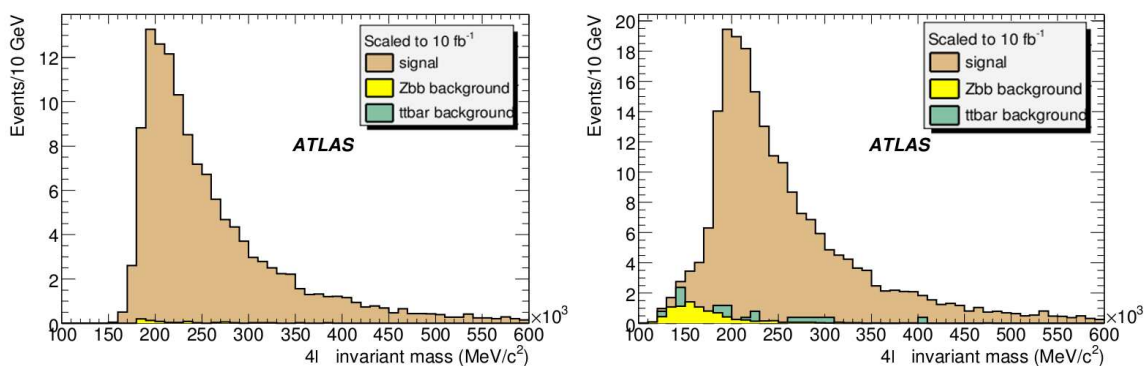


Figure 2: Final invariant mass of  $4\ell$  for signal and backgrounds, for  $ZZ$  (left) and  $ZZ^*$  (right), normalized to  $10 \text{ fb}^{-1}$ .

luminosity of  $1 \text{ fb}^{-1}$ . The uncertainties shown are only the statistical ones. The signal-to-background ratio is 66.5 (8.7) and the statistical significance 7.7 (6.6) for the  $ZZ$  ( $ZZ^*$ ) case. The significance  $s$  is calculated as  $s = \frac{\text{sig}}{\sqrt{\text{bkg}}}$ , where  $\text{sig}$  is the expected number of signal events and  $\text{bkg}$  is the 95% Poisson limit for a mean of 0 (2) background events (for a conservative result, given the small statistics).

## 5 Systematic uncertainties

The expected numbers of events are subject to both theoretical and experimental uncertainties. The major theoretical uncertainties on the production cross-sections come from the PDF uncertainties and the QCD factorization scale uncertainties (for NLO calculations). The effect of varying the PDF's on the calculated cross-sections is about 4% (from 14.74 pb with CTEQ6M to 15.32 pb with MRST03).

The main experimental systematic effects arise from the uncertainties of the luminosity determination, the lepton identification and trigger efficiencies and energy/momentum resolutions, the jet energy scale and resolutions, and background model and estimate. The luminosity uncertainties could be controlled to  $\sim 5\%$  [6]. The lepton acceptance uncertainty is about 2-3% mainly due to the isolation requirement, which involves the hadronic jet energy uncertainties. Thanks to the very low background level expected for the  $ZZ \rightarrow 4\ell$  process, the background uncertainty should be less than 2%, despite the limited MC statistics available for the background measurement.

## 6 Triple Gauge Couplings (TGC)

While the Standard Model  $ZZZ$  and  $ZZ\gamma$  triple gauge boson couplings are zero at tree level, anomalous couplings may contribute. The on-shell  $ZZ$  final state is used to probe the neutral anomalous TGC sensitivity (see diagram in Figure 1). The most general form of the  $ZZV$  ( $V = Z, \gamma$ ) vertex function is described in [7] and depends on the couplings  $f_i^V$  ( $i = 4, 5$ ), which are dimensionless complex functions.

The most dramatic signature of anomalous couplings in diboson production is an increase in the cross-section at high values of gauge boson  $p_T$  and diboson transverse mass. The following results are obtained by using the  $p_T(Z)$  distributions only.

A binned likelihood fitting method using the  $p_T(Z)$  spectrum is used to extract the 95% C.L. intervals of anomalous coupling parameters. Expected events are determined from full NLO MC, weighted by the LO Monte Carlo [7] results for different anomalous coupling parameters.

Random samples are generated according to this expectation, which give the observed number of events  $n$ . For each  $p_T(Z)$  bin, a likelihood is constructed, based on Poisson statistics convolved with Gaussian probabilities ( $g_{sig}$  and  $g_{bkg}$ ) to model the signal

	4 $\mu$ events		4e events		2 $\mu$ 2e events		Total	
	$ZZ^*$	$ZZ$	$ZZ^*$	$ZZ$	$ZZ^*$	$ZZ$	$ZZ^*$	$ZZ$
Signal	5.72	4.52	3.17	2.59	7.56	6.18	16.5	13.3
$Zb\bar{b}$	0.11	0.009	0.48	0.042	0.28	0.035	0.87	0.086
$t\bar{t}$	0.08	0.04	0.52	0.04	0.44	0.04	1.03	0.12
Total bgr	0.19	0.049	1.00	0.082	0.72	0.075	1.90	0.20

Table 3: Expected signal and background  $ZZ$  and  $ZZ^*$  events for  $\mathcal{L}=1 \text{ fb}^{-1}$ .

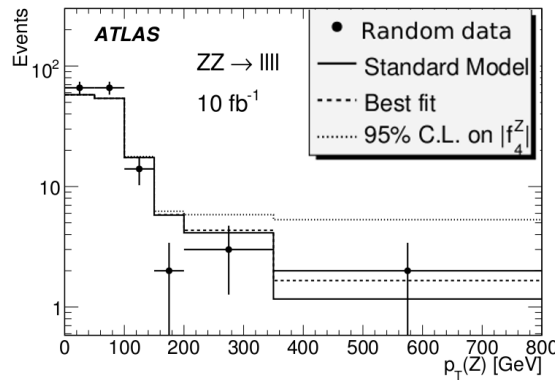


Figure 3: Example of a fit to one random sample with the likelihood method.

and background uncertainties. This likelihood

$$L = \int_{1-3\sigma_{bkg}}^{1+3\sigma_{bkg}} \int_{1-3\sigma_{sig}}^{1+3\sigma_{sig}} g_{sig} g_{bkg} \frac{(f_{sig}\nu_{sig} + f_{bkg}\nu_{bkg})^n e^{-(f_{sig}\nu_{sig} + f_{bkg}\nu_{bkg})}}{n!} df_{sig} df_{bkg}$$

is determined as a function of the coupling  $f_i^V$  in each bin of the measured spectrum. Summing over bins, a total log-likelihood is formed and its maximum determines the most likely value for the anomalous TGC. An example fit is shown in Figure 3.

The expected 95% C.L. intervals on anomalous couplings for  $10 \text{ fb}^{-1}$  integrated luminosity are  $[-0.010, 0.010]$ ,  $[-0.010, 0.010]$ ,  $[-0.012, 0.012]$ , and  $[-0.013, 0.012]$  for  $f_4^Z$ ,  $f_5^Z$ ,  $f_4^\gamma$  and  $f_5^\gamma$  respectively, using the  $ZZ \rightarrow \ell\ell\ell\ell$  final state alone. These limits improve slightly if they are combined with  $ZZ \rightarrow \ell\ell\nu\nu$ . The values of the scale  $\Lambda$  and the power  $n$  used for those couplings [7] are 2 TeV and 3 respectively. To calculate the limit in each parameter, other anomalous couplings are set to zero. Thus it should be possible to improve the LEP limits [8] on all TGC parameters by an order of magnitude.

## Acknowledgements

This work is partially supported by the European Commission, through the ARTEMIS Research Training Network, contract number MRTN-CT-2006-035657.

## References

- [1] ATLAS Collaboration, "Expected Performance of the ATLAS Experiment, Detector, Trigger and Physics", CERN-OPEN-2008-020, Geneva, 2008, to appear.
- [2] T. Sjostrand *et al.*, Comput. Phys. Commun., **135**, 238259 (2001).
- [3] S. Frixione and B.R.Webber, JHEP 0206 (2002) 029;  
S. Frixione, P. Nason and B.R.Webber, JHEP 0308 (2003) 007.
- [4] B.P. Kersevan and E. Richter-Was, Comput. Phys. Commun., **149**, 142 (2003).
- [5] ATLAS Collaboration, G. Aad *et al.*, "The ATLAS Experiment at the CERN Large Hadron Collider", JINST 3 (2008) S08003.
- [6] M. Dittmar, F. Pauss, D. Zuercher, Phys. Rev. D 56 (1997) 7284-7290.
- [7] U. Baur and D. Rainwater, Phys. Rev. **D62** 113011 (2000).
- [8] The LEP Collaborations ALEPH, DELPHI, L3, OPAL and the LEP Electroweak Working Group, CERN-EP/2006-042,p.52, 2006; hep-ex/0612034.

# ATLAS RPC commissioning status and cosmic ray test results

*Michele Bianco*

*on behalf of ATLAS RPC-LVL1 collaboration*

*Department of Physics, University of Salento & INFN Lecce  
73100 Lecce, ITALY*

The muon trigger system of the ATLAS experiment consists of several sub-systems and each of them need to be tested and certified before LHC operation. In the barrel region Resistive Plate Chambers [1] are employed. RPC detector and its level-1 trigger electronics are designed to detect and select high momentum muons with high time resolution and good tracking capability for a total surface of about  $4000\text{ m}^2$ . The commissioning phase provided an unique opportunity to demonstrate, before LHC start-up, the functionality of the muon trigger components such as detector chambers, level-1 trigger electronics, detector slow control system, data acquisition chain, software and computing. We present the status of ATLAS RPC detector, the problems met during the commissioning and the solutions found and, finally, its performances as obtained by acquiring cosmic rays.

## 1 Introduction

Muon identification capability and high accuracy in muon momentum measurements are crucial requirements for the ATLAS experimental program. The ATLAS Muon Spectrometer [2] was designed to achieve a standalone muon momentum measurements with good resolution, high efficiency and over a wide range of transverse momentum, pseudo-rapidity, and azimuthal angle. RPC were chosen as muon trigger detector for the barrel region (up to  $\text{abs}(\eta)=1$ ). They are gaseous detectors operated at atmospheric pressure, covering about  $4000\text{ m}^2$  and arranged in three concentric layers, each one consisting of two active gas volumes.

The on-line muon selection algorithm is based on fast measurement of charged particle trajectory deflections due to the magnetic field. By measuring the deviation of the trajectory from the straight line (“infinite momentum track”) interpolated from the interaction point to the middle RPC layer (Figure 1), one can estimate the curvature of the charged particle trajectory in the toroidal magnetic field.

The trigger selection algorithm is based on the definition of allowed geometrical roads (*Coincidence Windows*) around the infinite momentum track projected on the inner and outer RPC layers (respectively Low- $p_t$  and High- $p_t$  planes in Figure 1).

In the ATLAS barrel sub-system two muon trigger thresholds are chosen:

- 1) Low- $p_t$  muon triggers ( $6 < p_t < 20$  GeV) built-up from coincidence signals coming only from the middle RPC station and requiring a 3 out of 4 majority logic.
- 2) High- $p_t$  muon triggers ( $> 20$  GeV) built-up only in presence of a Low- $p_t$  trigger and requiring in addition a spatial coincidence with the outer chamber with a 1 out of 2 majority logic.

The system was designed with 3  $p_t$  programmable thresholds applied in parallel, both for Low- $p_t$  and High- $p_t$ . The lower available  $p_t$  threshold value is limited by the cabling and it corresponds at about 5 GeV.

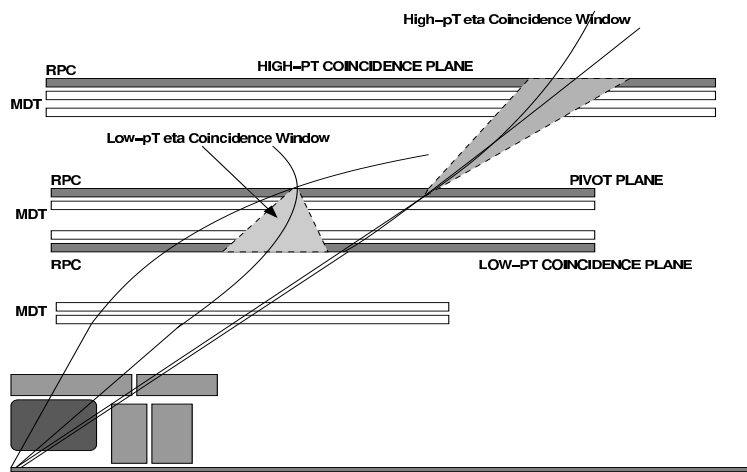


Figure 1: Level-1 muon trigger algorithm in the ATLAS barrel region implemented by three RPC layers.

## 2 ATLAS RPC commissioning

In order to assure the proper functionality of the apparatus, each hardware and software component was subject to several tests. Due to the high level of interdependence between different parts: gas system, electrical service cabling, power system, slow control system, data acquisition and off-line monitoring, a well defined commissioning schedule was followed and specific diagnostic tools were used.

## 2.1 Hardware components commissioning

The hardware commissioning can be divided in three main parts: **gas system, electrical service cabling and power system**.

- **Gas system:** The gas system is a recirculating system with a constant fraction of fresh gas mixture at the input. The total amount of gas volume, including also the gas pipes, is about  $18\ m^3$ . The gas mixer, humidification and purification modules and the gas analysis apparatus are located on surface, while in the experimental cavern are located the 5 distribution gas racks for a total number of 128 gas lines.

During the commissioning each gas line was checked at every step to avoid the presence of gas leaks. About 1 % of the gas inlets glued on the volume inside the chambers were found broken after the installation phase. The most accessible ones were repaired, the 22 gas volume, on about 4000, with the remain gas inlets broken were isolated from the gas manifold and disconnected from the high voltage distribution system. These few gas inlet will be repaired during the winter shutdown.

A gas chromatography facility was installed on surface building in order to monitor the gas mixture purity and composition. Since May 2008 the gas system is complete and working in a stable way in recirculating mode.

- **Electrical service cabling:** A huge amount of work was done in the experimental cavern to connect each RPC chamber and level-1 trigger tower to the electrical service cables in order to power the detector.

All electrical cables were tested on both sides, before the connection to the chambers and racks, using specific tools made available by the DCS software. This procedure reduced significantly the amount of mapping errors of such a complicated system. Before the cavern closure for LHC start-up, all standard RPC chambers were cabled and tested by cosmics, special RPC chambers (less than 5 % of the total coverage) will be connected and tested during the winter shutdown.

- **Power system:** In order to power all the RPC chambers and level-1 trigger towers, a complex power system was setup in the service and experimental caverns. In the service cavern three 1527 CAEN mainframes control by 17 branch controller modules, all the electronic boards directly installed in the experimental cavern. In the experimental cavern 29 racks were arranged, each one containing several crates were the electronic boards are located. To assure the correct operations and control of every electronic board, each crate must be powered by two separate 48 volt power lines, one for the control system and the

other one for the power distribution.

To provide the power distribution twenty four 3486 CAEN generators were installed in the experimental cavern, while for the control line two 3485 CAEN generators were installed in the service cavern. The control lines are back-up against utility power cut by a Uninterruptible Power Supply (UPS) system. The ATLAS RPC and level-1 power system uses about 300 electronic boards, all of them installed, tested and connected to the final distribution power system.

## 2.2 Software components commissioning

The software parts could be divided in two separate components: **DCS** and **DAQ**, which interact directly with the hardware of the apparatus, and the **off-line software**, which accurately monitor the detector performances.

- **DCS and DAQ system:** The RPC Detector Control System (DCS) is implemented as a finite-state machine in a common ATLAS framework that allows slow control and monitoring of the detector. The DCS commissioning had followed in parallel the hardware commissioning of the system, leading its evolution. Since the first ATLAS combined run period RPC DCS was employed extensively through its Graphical User Interface (GUI) thanks to its advanced stage. The full service chain is remotely controlled and monitored from the ATLAS counting room in the same integrated framework. In particular, the end-user can manage in a simple way all RPC and trigger electronics parameters and voltage supplies, and monitor the gas system parameters and environmental quantities. A direct connection to on-line database is implemented and the automatic data archive is under implementation. The RPC detector is fully integrated in the ATLAS level-1 trigger and data acquisition systems. It routinely provides cosmic ray triggers for the other sub-detectors, during combined data taking periods. The corresponding trigger rates are directly related to the position and orientation of the operated trigger towers with respect to the main shafts, where most of the cosmic rays are coming. Trigger roads were implemented in both views for most of the trigger towers before the LHC startup. Up to now RPC triggers were delivered to the MCTPI (Muon Central Trigger Processor Interface) for Low- $p_t$  trigger conditions in the non-bending view only. Muon triggers will be delivered for both views after the fine RPC time calibration. Since spring 2008, several high rate tests were performed and RPC level-1 trigger system were able to provide trigger up to 100 kHz, which corresponds to the running conditions for the ATLAS 2009 upgrade.

- **Off-line analysis software:** RPC off-line data analysis is performed in the ATLAS standard software framework named ATHENA [3]. During the commissioning the off-line code was optimized and debugged by real cosmic rays data. The readout channel mapping were cross checked and accurately verified to describe the hardware. Being a part of the Muon Off-Line Monitoring package, the RPC monitoring code automatically runs at the CERN Tier0 facility, where data are processed just after being available on the central data storage. Run by run all relevant quantities characterizing the RPC detector are measured such as efficiency, cluster size and noise. Moreover, general and specific plots are stored and displayed on the web to asses the RPC data quality.

### 3 Cosmics ray test results

Since Fall 2006 cosmic muons were acquired with the ATLAS muon spectrometer [4]. This intense activity allowed to debug and characterize the RPC detector in an extensive way. In Figure 2 the RPC readout strip cluster size and detection efficiency measured by cosmic rays during commissioning are shown.

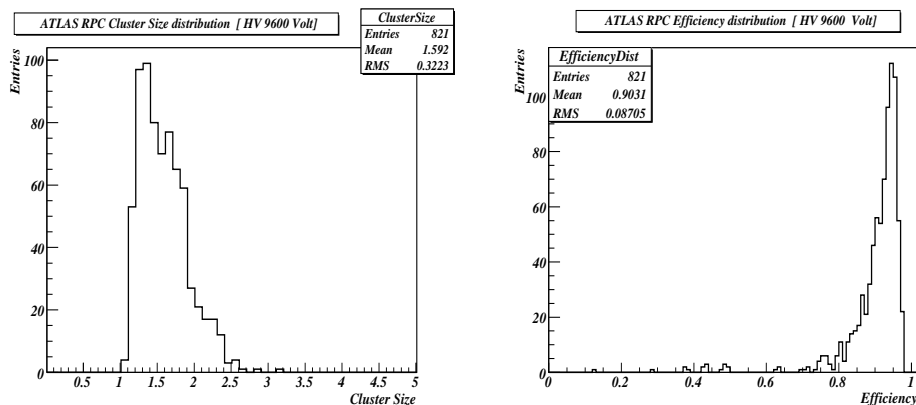


Figure 2: Distribution of the RPC readout strip panel average cluster size and detection efficiency for a high voltage of 9600 V and nominal voltage front-end threshold ( $T=20^{\circ}\text{C}$  and  $P=980\text{ mbar}$ ).

By then onwards we participated at several ATLAS combined data taking periods before LHC start-up. Over a year's work with cosmic rays enabled to characterize all the muon spectrometer aspects and verify its functionality. In particular, correlations between precision tracking chambers and trigger chambers were extensively studied

in order to verify if data corruptions and synchronization problems were presents (see Figure 3.a).

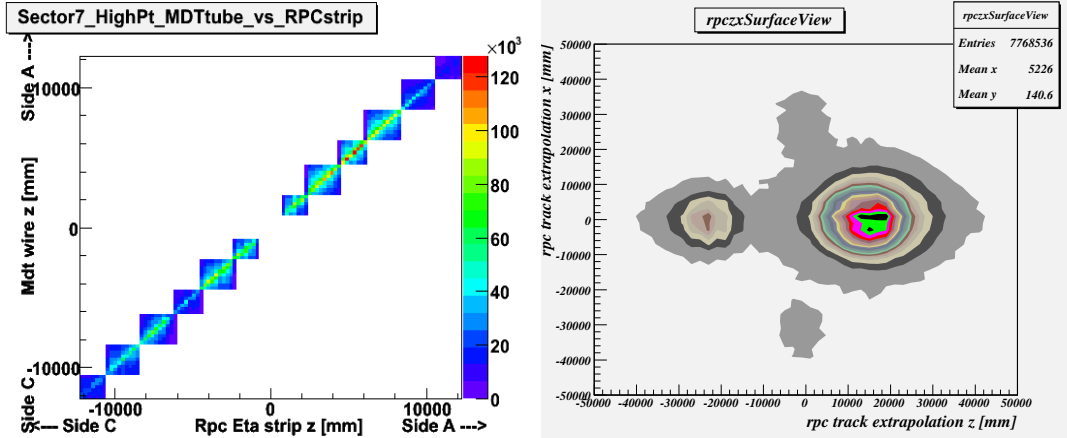


Figure 3: Hit spatial correlation along the beam (z axis) of adjacent MDT multi-layers and RPC planes (a). Extrapolation on surface of the cosmic muon triggered and reconstructed by the ATLAS RPC detector. In addition to the two main ATLAS shaft ( $z=0$  axis), the ATLAS service lifts are also clearly visible (b).

In Figure 3.b is shown the extrapolation on the earth surface of the RPC-only tracks reconstructed with the RPC off-line monitoring. The plot shows that most cosmic muons reach the experimental cavern going through the two main conduits used to lift down the single components of the apparatus (located along the  $z=0$  axis), but some of them are coming from the two secondary conduits hosting service lifts (located along the  $x=0$  axis).

## 4 Conclusions

The ATLAS RPC commissioning was completed before LHC start-up. All hardware and software elements were installed, verified and certified, allowing a wide use of the detector as cosmic ray trigger source for all ATLAS commissioning. Nevertheless, during the winter shutdown further RPC detector improvements are scheduled.

## 5 Acknowledgments

We are indebted to the RPC/LVL1 technical staff for their highly qualified contribution in designing and setting up the whole system. We are grateful to the CERN technical staff for the continuous and promptly support during detector installation and commissioning phase.

## References

- [1] R. Santonico R. Cardarelli: **Development of resistive plate counters**. Nuclear Instruments and Methods, 187 (1981) 377.
- [2] ATLAS Muon Collaboration, **ATLAS Muon Spectrometer Technical Design Report**. CERN/LHCC/97-22, (1997).
- [3] ATLAS Computing Group, **ATLAS Computing Technical Design Report**. ATLAS TDR-017, CERN/LHCC/2005-022, (2005).
- [4] G. Chiodini, *et al.* “**RPC cosmic ray tests in the ATLAS experiment**” Nuclear Instrum.Meth.A 581 (2007) 213-216.

# Poster Session

Study of the Behavior of the Nuclear  
Modification Factor in Freeze-out State

*Muhammad Ajaz et al.*

Hidden Valley Higgs Decays in the  
ATLAS Detector

*Guido Ciapetti*

Mini-Bias and Underlying Event Studies  
at CMS

*Yuan Chao*

ATLAS Trigger Menu for Early  
Data-Taking

*Marc-André Dufour & Bilge Demirköz*

Level-3 Calorimetric Resolution available  
for the Level-1 and Level-2  
CDF Triggers

*Virginia Greco et al.*

Measurement of Branching Fractions  
of the inclusive decay  $D^0 \rightarrow \Phi X$   
and of the exclusive decays  
of the  $D^0$  involving a  $K^+K^-$

*Gerhard Leder & Franz Mandl*

The Liquid Argon Jet Trigger  
of the H1 Experiment at HERA

*Bob Olivier*

A new very inclusive trigger selection  
for the SM WH discovery channel  
at CDF

*Pierluigi Totaro*

# Study of the Behavior of the Nuclear Modification Factor in Freeze-out State

*M. Ajaz<sup>\*,1</sup>, M. K. Suleymanov<sup>1,2</sup>, E. U. Khan<sup>1</sup>, M. Q. Haseeb<sup>1</sup>, K. H. Khan<sup>1</sup>, Z. Wazir<sup>1</sup>*

<sup>1</sup> *Department of Physics  
COMSATS Institute of Information Technology  
44000 Islamabad, Pakistan*

<sup>2</sup> *Veksler - Baldin Laboratory of High Energy  
Joint Institute for Nuclear Research  
141980, Dubna, Russia*

\* rph\_f06\_013@comsats.edu.pk

## 1 Introduction

One of the latest trends in the advancement of experimental high-energy physics is to identify the Quark Gluon Plasma (QGP) [1] predicted qualitatively by the Quantum Chromodynamics (QCD) [2]. QGP is considered to be a state of strongly interacting matter under extreme conditions (high temperatures and/or densities of the baryons). This can be brought about under laboratory conditions during collisions of relativistic heavy nuclei by increasing energies and varying masses of colliding nuclei. This leads to a continuing quest of leading research centers on high-energy physics to create new accelerators of heavy nuclei and enhance the energies of existing accelerators.

Strongly interacting matter may be subject to a series of phase transitions with increasing temperature and/or density of the baryon among which is the first-order phase transition of restoration of a specific symmetry of strong interactions—chiral symmetry that is strongly violated at low temperatures and/or densities of the baryon charge. However, to create necessary laboratory conditions and pick up a "signal" of formation of the QGP phase, one needs a lot of intellectual and material resources. The well known time evolution of central heavy ion collisions is shown in Fig. 1. Here the five states are shown as: I-pre-interaction state; II-parton-parton interaction one; III-mixed phase; IV-QGP phase ; V-freezout. In each state the matter can

be characterized by different temperature and density. Apart from these parameters, there could be another very interesting parameter, namely the transparency ( $Tr$ ) of matter, to characterize these states. We believe that the appearance and changing of the transparency could give the necessary information for identification the QGP formation.

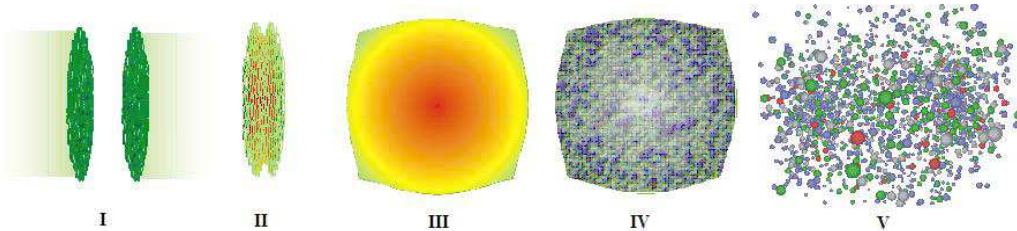


Figure 1: Time evolution of the central heavy ion collisions.

In Ref. [3] a signal on mixed phase formation is considered as an important point to identify QGP because such a state must contain real particles which can interact with matter and therefore could be detected.

## 2 Nuclear Modification Factor

In this paper we discuss some ideas connected with identification of the QGP using the information coming from the freezout state. The main idea is that the values of transparency ( $Tr$ ) for different states of time evolution of heavy ion collisions are different ( $Tr_{III}$ ,  $Tr_{IV}$  and  $Tr_V$ ).

To characterize the  $Tr$  it is convenient to use the nuclear modification factor ( $R$ ). A comparison of yields in different ion systems by using nuclear modification factors (involving Central and Peripheral collisions) should provide information on the hadronization [5] (see Fig. 2.  $R$  highlights the particle type dependence at intermediate  $p_T$  as was suggested by coalescence models [6] leading to the idea that hadrons result from the coalescence of quarks in the dense medium. Fig. 3 shows the recent results from RHIC on heavy flavor production [7].

It is supposed that  $Tr_{III-V} \sim R_{III-V}$ . To restore the time scale we are going to use the values of temperature because they must be different for III-V states.

If the states of III-V will appear critically so the regime change have to be observed in the behavior of  $R$  as a function of temperature.

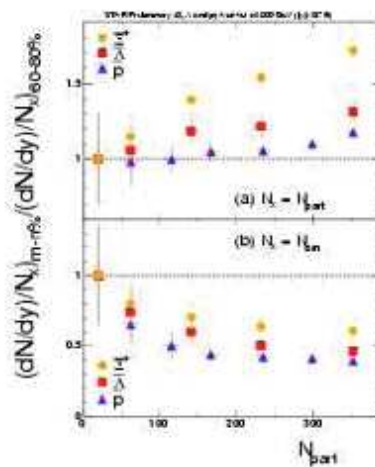


Figure 2: Yields of some baryons as a function of the centrality (expressed with the number of participants) in Au+Au collisions normalized to the most peripheral point and to  $N_{part}$  (upper frame) and  $N_{bin}$  (lower frame).

### 3 Results

To confirm the above idea we use data coming from different heavy ion generators and experiments. Fig. 4 shows the result of the study of the behavior of  $R$  function defined as a ratio of the yields of different particles at central to peripheral collision as a function of the thermal freeze out temperature ( $T_{th}$ ) produced in Au-Au collisions at RHIC energies. The data is simulated using the Fast Hadron Freezout Generator (FASTMC) [4]. The FASTMC hadron generation allows one to study and analyze various observables for stable hadrons and hadron resonances produced in

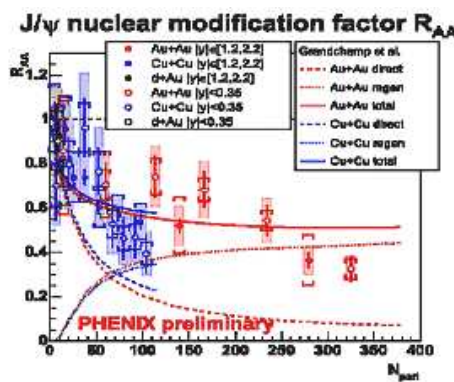


Figure 3: Nuclear modification factor as function of a number of participant.

ultra-relativistic heavy ion collisions. Particles can be generated on the chemical or thermal freeze-out hyper surface represented by a parametrization or a numerical solution of relativistic hydrodynamics with given initial conditions and equation of state [4]. There are two regions in the behavior of  $R$  as a function of the  $T_{th}$  (see Fig. 4). In the first region one can see that in the freeze out state  $R$  is almost a linearly increasing function of the  $T_{th}$  independent of the types of particles and the second region is a straight line, which has no dependence on  $T_{th}$ , it can be regarded as a regime change.

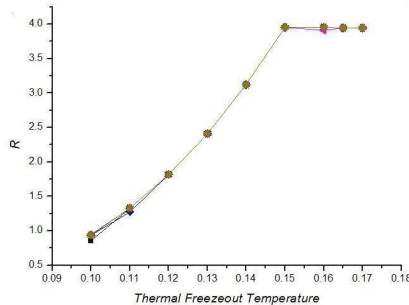


Figure 4: Nuclear Modification Factor as a function of thermal freezeout temperature.

## References

- [1] S. Jeon and V. Koch Review for Quark-Gluon Plasma 3 eds. R. C. Hwa and X.-N. Wang (World Scientific, Singapore, 2004).
- [2] Walter Greiner, Andreas Schafer, (1994). Quantum Chromodynamics. Springer. ISBN 0-387-57103-5.
- [3] A. N. Sissakian, A. S. Sorin, M. K. Suleymanov, V. D. Toneev , G. M. Zinovjev. Phys.Part.Nucl.Lett.**5**, 1-6 (2008)
- [4] N. S. Amelin et. al., arXiv:0711.0835 (2007)
- [5] Christelle Roy for the STAR Collaboration, POS (HEP2005) 141.
- [6] D. Molnar et al., Phys. Rev. Lett. **91**, 092301 (2003)
- [7] A. A. P. Suaide. Brazilian Journal of Physics **37** N 2C, 731-735 (2007)

# Hidden Valley Higgs Decays in the ATLAS Detector

*Guido Ciapetti*

*(on behalf of the ATLAS Collaboration)*

*Dipartimento di Fisica Universita' Sapienza and INFN Sezione di Roma*

## 1 Introduction

A number of extensions of the Standard Model result in particles that are neutral, weakly-coupled and have macroscopic decay lengths that can be comparable with LHC detector dimensions[1, 2, 3]. These long lived particles occur in many models; in the Hidden Valley (HV) Scenario a new sector is weakly coupled to the Standard Model and results in neutral long lived HV particles ( $\pi_v^0$ ) that decay to heavy quark pairs and tau pairs. These particles can be produced in Higgs boson decays, SUSY processes and  $Z'$  decays.

We present the results of a first study of the ATLAS Detector performance for the Higgs decay  $h^0 \rightarrow \pi_v^0 \pi_v^0$ , where  $\pi_v^0$  is neutral and has a displaced decay mainly to bottom quarks. The initial goal of our study is to obtain benchmark triggers for processes with such non-standard signatures in the ATLAS apparatus.

## 2 The Hidden Valley Scenario

We begin with some general discussion of the scenario [4]. To the Standard Model is appended a hidden sector, the “v-sector” for short, and a communicator (or communicators) which interacts with both sectors. A barrier (perhaps the communicator’s high mass, weak couplings, or small mixing angles) weakens the interactions between the two sectors, making production even of light v-sector particles (“v-particles”) rare at low energy. At the LHC, by contrast, production of v-particles, through various possible channels, may be observable. The communicator can be any neutral particle or combination of particles, including the Higgs boson, the  $Z$  boson,  $Z'$  bosons, neutralinos, neutrinos, or loops of particles charged under both Standard Model and v-sector gauge groups.

The study presented here uses the following parameters:

$m_{h^0} = 140$  GeV<sup>1</sup>,  $m_{\pi_v} = 40$  GeV and  $c\tau_{\pi_v} = 1.5$  m. With these parameters approximately 40% of the decays occur in the ATLAS Inner Detector (ID), 48% in the Calorimeters (ECal and HCal) and the remaining 12% in the Muon Spectrometer (MS) system.

### 3 Detector Signatures and Triggers

A simulation of typical HV Higgs decays  $h^0 \rightarrow \pi_v^0 \pi_v^0$  in the ATLAS Detector is shown in Figure 1. Due to the displaced vertices with tracks non pointing to the interaction region and to the low Higgs mass, the standard ATLAS triggers [5] are able to select only a very small fraction of these events, as can be seen in Table 1. A signature driven trigger strategy is therefore required.

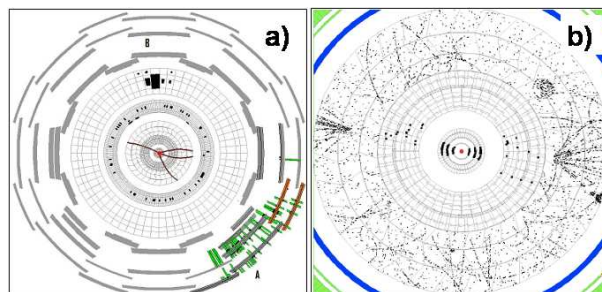


Figure 1: Event display for typical  $h^0 \rightarrow \pi_v^0 \pi_v^0$  decays. a) decays in the MS and in HCal; b) decays in the ID.

We consider three detector regions to illustrate the trigger signatures of Hidden Valley particles: 1)Decays in the MS from the end of the HCal to the first muon trigger plane;

<sup>1</sup>At this mass value Higgs production is dominated by gluon fusion (gg). We have also investigated Vector Boson Fusion (VBF) and the W-Higgs production mechanism.

Process	Calorimeter triggers	Muon trigger	Total
$h^0 \rightarrow \pi_v^0 \pi_v^0$	4.4%	2.2%	4.7%

Table 1: ATLAS standard triggers efficiency, normalized to the whole sample; Total is the union of Calorimeter and Muon triggers.

2)Decays in the Calorimeters from the end of the ECal to the end of HCal; 3)Decays in the ID beyond the pixel layers to the end of the Transition Radiation Tracker (TRT). Decays in the beam pipe and pixel layers are not considered due to the predominant irreducible Standard Model  $b\bar{b}$  background.

### 3.1 Decays in Muon Tracker

Decays occurring near the end of the HCal and before the first muon trigger plane result in a large number of hadrons traversing a narrow  $(\eta, \phi)$  region of the Muon Spectrometer. The Level-1 muon trigger will return several RoIs<sup>2</sup> clustered in a small  $\Delta R(\eta, \phi)$  area. The muon RoIs from this decay topology will not usually have an associated track in the inner tracker and most will not survive the Level-2 muon trigger. However, this ROI cluster event signature can be used as a stand-alone Level-2 trigger object to select these late decays. Plotted in Figure 2 is the average number of

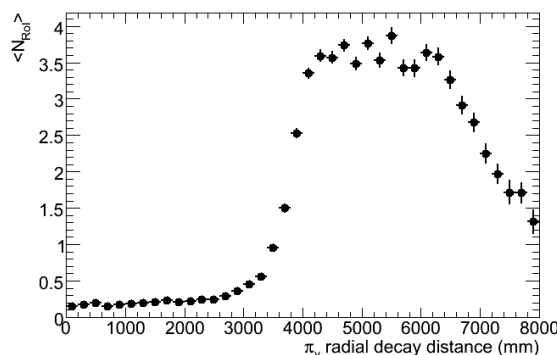


Figure 2: Average number of Level-1 muon RoIs contained in a cone of  $\Delta R=0.4$  around the  $\pi_v$  line of flight vs  $\pi_v$  radial decay distance.

Level-1 muon RoIs contained in a cone of radius  $\Delta R=0.4$  around the  $\pi_v$  line of flight, as a function of the  $\pi_v$  radial decay distance,  $L_R$ . As the  $\pi_v$  decay vertex approaches the end of the HCal (4500mm), the average number of muon RoIs contained in the cone plateaus at  $\sim 3.5$  until the  $\pi_v$  decays close to the first trigger plane (7000mm), at which point the charged hadrons are not spatially separated enough to give multiple unique RoIs.

<sup>2</sup>ATLAS Level-1 trigger object, which defines a Region of Interest, ROI, in  $(\eta, \phi)$  to be examined at Level-2.

### 3.2 Decays in the Calorimeters

Events with  $\pi_v$  decays in the Calorimeters near the end of the ECal are characterized by jets with few or no tracks and unique energy distributions. These events often have little energy deposited in the first part of the ECal. This leads to jets with more energy deposited in the HCal than in the ECal. The logarithm of the hadronic to electromagnetic energy ratio,  $\log_{10}(E_{HAD}/E_{EM})$ , for jets from  $\pi_v$  decays as a function of the  $\pi_v$  decay distance can be seen in Figure 3. As the  $\pi_v$  decays closer to the end of the ECal (2200mm), the ratio changes from a characteristic (for Standard Model jets) negative to a positive value.

Because most jets with  $\log_{10}(E_{HAD}/E_{EM}) \geq 0.5$  are produced by  $\pi_v$ 's decaying in

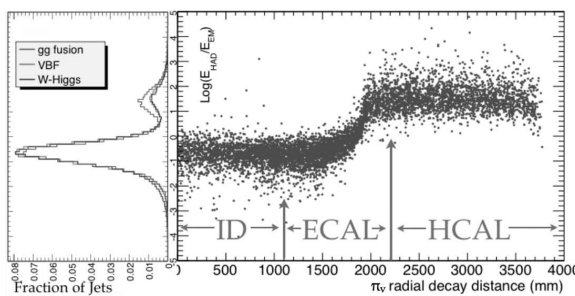


Figure 3:  $\log_{10}(E_{HAD}/E_{EM})$  vs  $\pi_v$  decay distance,  $L_R$ .

the calorimeter, one would expect to find a lack of activity in the Inner Detector. Using the Level-2 tracking algorithm, we find that the 95% of jets with  $|\eta| \leq 2.5$  and a  $\log_{10}(E_{HAD}/E_{EM}) \geq 0.5$  have zero tracks reconstructed in a region of  $0.2 \times 0.2$  ( $\delta\eta \times \delta\phi$ ) around center of the jet RoI. In contrast, less than 25% of the Standard Model QCD jets with  $\log_{10}(E_{HAD}/E_{EM}) \geq 0.5$  have zero reconstructed tracks.

### 3.3 Decays in the Inner Detector

Displaced decays in the TRT result in low tracking efficiency because tracking requires seed hits in the pixel and silicon strip layers. This suggests that a jet with no tracks reconstructed in the ID at Level-2 may be a good trigger object to select  $\pi_v$  that decay beyond the pixel layers. To reduce Standard Model QCD jets background we require that a Level-1 muon RoI is contained in a cone of radius  $\Delta R = 0.4$  around the jet axis, which selects a semileptonic  $b\bar{b}$  decay.

$\log_{10}(E_{HAD}/E_{EM})$	Trackless jets	Muon cluster	Total HV triggers	All triggers
5.0%	3.8%	9.0%	15.7%	18.5 %

Table 2: HV specific triggers efficiency, normalized to the whole sample. All triggers is the union of the three specific HV triggers and of the standard ATLAS triggers

## 4 Conclusions

We have implemented in the ATLAS simulation package the new signature based triggers. The resulting trigger acceptances are shown in Table 2. With these new triggers ATLAS will be able to select  $\sim 20\%$  of events with displaced decays from  $h^0 \rightarrow \pi_v^0 \pi_v^0$ .

Standard Model QCD processes are a potential source of significant background at the trigger level. The same trigger objects have been applied to a simulated di-jet samples, resulting in a negligible ( $\sim 6 \text{ nb}$ ) cross section acceptance at Level-2.

One important issue is to ensure that our triggers, particularly the muon triggers, be associated with the correct beam crossing. In our model most of the  $\pi_v$  have  $\beta > 0.7$ , introducing a delay well inside the 25 ns bunch crossing separation.

Long lived particles predicted by a number of Standard Model extensions are challenging to the ATLAS Detector, in particular for the online trigger selection. We have shown that by implementing new signature based triggers it is possible to increase the selection efficiency with a negligible background rate from Standard Model processes.

I would like to thank Matt Strassler (Rutgers University) for his central contributions at all stages of this work. It is a pleasure to thank the organizers of the PIC08 conference in Perugia.

## References

- [1] See as example: A. Nisati, S. Petrarca, G. Salvini, ATL-MUON-97-205; S. Ambrosanio, B. Mele, S. Petrarca, G. Polesello, A. Rimoldi, ATL-PHYS-2002-006; S. Tarem et Al., ATL-PHYS-PUB-2005.022; J. Ellis, A.R. Raklev, O.K. Oye, ATL-PHYS-PUB-2007-016; S. Tarem, S. Bressler, H. Nomoto, A. Di Mattia, ATL-PHYS-PUB-2008-01.
- [2] L. J. Hall and M. Suzuki, Nucl. Phys. B **231**, 419 (1984).

- [3] S. Dimopoulos, M. Dine, S. Raby and S. D. Thomas, Phys. Rev. Lett. **76**, 3494 (1996) [arXiv:hep-ph/9601367]; C. H. Chen and J. F. Gunion, Phys. Rev. D **58**, 075005 (1998) [arXiv:hep-ph/9802252].
- [4] M. J. Strassler and K. M. Zurek, Phys. Lett. B 651 (2007) 374-379; M. J. Strassler and K. M. Zurek, Phys. Lett. B 661 (2008) 263-267; M. J. Strassler, arXiv:hep-ph/0607160.
- [5] The ATLAS Collaboration, G. Aad et al., 2008 JINST 3 S08003.
- [6] C. Adorisio et al., ATL-MUON-PUB-2007-005.

# Mini-Bias and Underlying Event Studies at CMS

*Yuan Chao*

*Department of Physics  
National Taiwan University  
10617 Taipei, TAIWAN*

## 1 Introduction

The Tevatron experiments provide us very good information for the quantum chromodynamics (QCD) modelings of event generators. However, in the LHC era, the collisions is in different region of phase-space from that of Tevatron. A naïve rescaling of cross-sections will not work. The current modeling of non-trivial interplay of perturbative and non-perturbative aspects based on Tevatron data have large discrepancies when extrapolated to the LHC energy. This study is devoted to the proton-proton dynamics exploration: discriminating among different QCD Monte Carlo models.

## 2 The Minimum Bias events and triggers

From the experimental point of view, a minimum bias events (MB) correspond to a non-single diffractive inelastic interaction. Meanwhile a totally inclusive trigger, or called zero bias trigger, corresponds to a randomly reading out from the detector whenever a collision is possible. The later is only efficient when the luminosity is high enough such that a reasonable probability of collisions occur during a bunch crossing.

For events with one and only one collision occurs is called “ideal data”, which have no piled-ups, during a bunch crossing. This kind of events is important for underlying events (UE) study as no influence from multiple p-p interactions.

The average number of collisions, constituting the pile-up, per beam bunch can be described as:

$$\langle N_{int.} \rangle = L_{inst.} \times \sigma / f_{rev.}$$

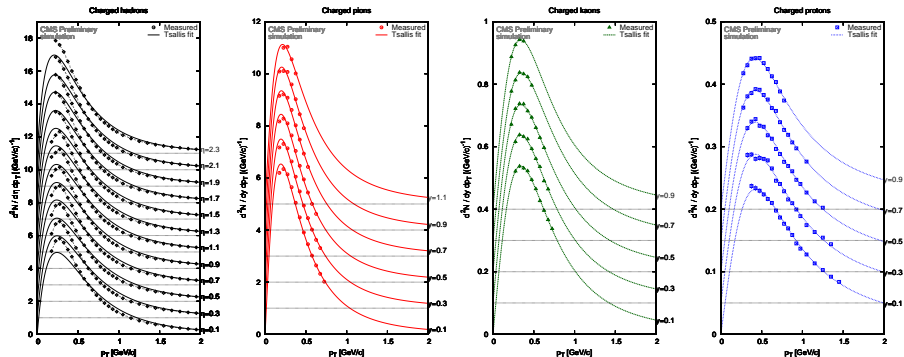
The cross-section  $\sigma$ , includes both elastic and inelastic, is  $\sim 100$  mb at LHC with mostly low  $p_T$  particles and low multiplicity. So the averaged number is about 35 events per bunch-crossing for luminosity  $L=1034 \text{ /cm}^2/\text{sec.}$

## 2.1 Minimum-Bias Trigger

The MB trigger in CMS is using the Hadron Forward (HF) calorimeter. It has a geometrical coverage from 3 to 5 in absolute value of pseudo-rapidity  $\eta$  and consists of 18 wedges per side with tower size  $0.175 \times 0.175$  in  $\eta$  and  $\phi$ . A trigger based on minimum 10 towers with energy threshold greater than 1.4 GeV gives 90% efficiency.

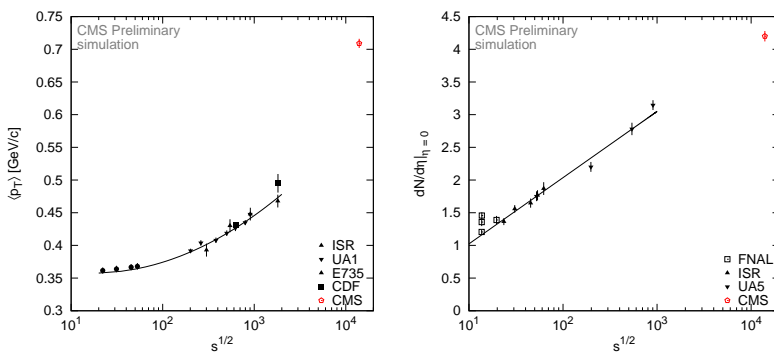
## 2.2 Charged Hadron Spectra

A study on the charged hadron spectra on MB events has been performed. The measured differential yields of unidentified charged particles as well as pions, kaons and protons are shown as a function of  $p_T$  and in narrow  $\eta$  bins. Tsallis function fits are also superimposed. The results are using a sum of both positive and negative charged particles and assuming symmetric  $\eta$  bins.



## 2.3 Energy dependency

The density of charged hadrons at  $\eta \sim 0$  follows the trend from lower energies, which is linear in  $\log \sqrt{s}$ . CMS expected to see an averaged 4.2 charged hadrons in the central region. Meanwhile the averaged transverse momentum of charged hadrons at lower energies is described by a quadratic function in  $\log \sqrt{s}$ . The expected average  $p_T$  is about 0.7  $\text{GeV}/c$  for CMS.



### 3 Underlying Events

The “underlying events” (UE) is everything in a single proton-proton interaction except for the hard scattering component. It’s not a minimum-bias event on top of the hard process. What happens to the beam remnants after the hard scattering is an important issue. The UE has the same production vertex so it’s tied to the process of interest. Its activity also grows with the process energy scale as a “pedestal effect”.

UE phenomenology has been studied with CDF data using “charged jet” from iterative cone algorithm on mass-less tracks. With various energy scale in  $p_T$  of the charged jet, multiplicity and  $p_T$  density has been studied in the transverse region. As we can easily tell from the following plots, the activities in this region have less influence from the hadron event.

Clear dependency on  $p_T$  can also be seen for charged jets in the toward region.

#### 3.1 Underlying Event Models

The UE event modeling has both non-perturbative and perturbative aspects. The former ones include initial-state radiation (ISR), final-state radiation (FSR) and beam remnants together with multiple parton-parton interaction, while the later part have the following considerations: allowing more than one parton-parton interaction per pp-scattering (MPI); regularizing QCD two-to-two cross section cut-off on  $p_T$ , e.g. Pythia DW and DWT tunes; variable impact parameter models; and color reconnection models, e.g. Pythia S0. However, the current models based on Tevatron data have different behavior when extrapolating to LHC.

From an experimental point of view, one can use a topological structure of hadron-hadron collisions to probe the UE activities out of the hard scattering component.

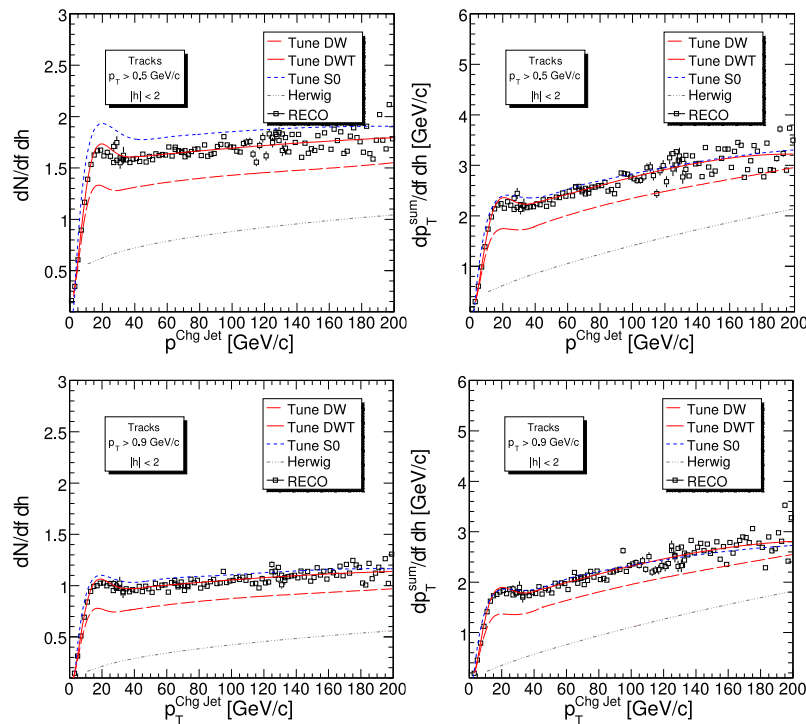
The activities near the transverse plane to the jet direction has the smallest influence from the hard scattering and provides the most sensitivity to the UE contributions.

### 3.2 Results

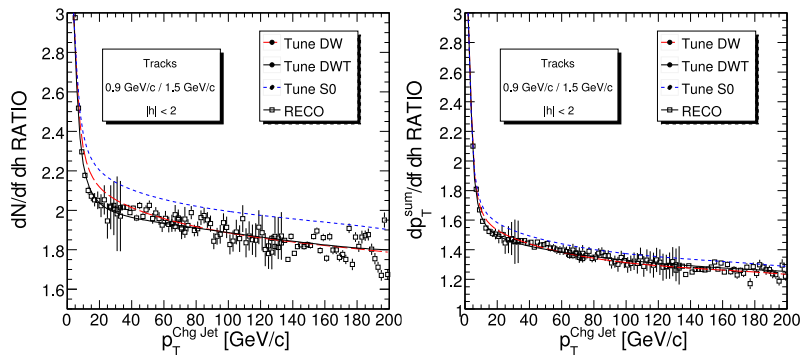
Herwig (without MPI), Pythia tunes DW, DWT, and with MPI), all predict observed results from the Tevatron. One can discriminate between these scenarios at LHC energies by looking at the density of charged particles  $dN/d\eta d\phi$  and the momentum density  $dp_T^{sum}/d\eta d\phi$  in the transverse region.

Density of charged particles and momentum of the leading charged particle jet using a track reconstruction threshold of 0.9 GeV/c is shown. Data points from different triggers are superimposed (Minimum Bias, JET20, JET60, JET120) and correspond to the corrected reconstruction level profiles using tune data). The lines correspond to the different generator level tunes: DW, DWT, S0 and HERWIG.

By lowering the  $p_T$  threshold to 0.5 GeV/c it is possible (largely due to MB data) to distinguish between DW/DWT and S0 as well.



With  $100 \text{ pb}^{-1}$  of data it should be possible to discern between Herwig DW, and the two other Pythia tunes (DWT, SO) using a  $p_T$  threshold of 0.9 GeV/c.



## 4 Conclusion

The UE study can help us to discriminate between various QCD models which will facilitate the improvement and tuning of Monte Carlo models at LHC start-up. It will also open prospects for the exploration of QCD dynamics in proton-proton collisions at 10 TeV.

## References

- [1] “*LHC Machine*”, Lyndon Evans and Philip Bryant (editors), JINST 3 S08001 (2008)
- [2] “*The CMS experiment at the CERN LHC*” The CMS Collaboration, S Chatrchyan *et al.*, JINST 3 S08004 (2008)
- [3] “*Measurement of charged hadron spectra in proton-proton collisions at  $\sqrt{s} = 14$  TeV*”, PAS-QCD-07-001
- [4] “*Measurement of the Underlying Event in Jet Topologies using Charged Particle and Momentum Densities*”, PAS-QCD-07-003

# ATLAS Trigger Menu for Early Data-Taking

*Marc-André Dufour*  
*Department of Physics*  
*McGill University*  
*Montreal, Quebec, Canada*

*Bilge Demirköz*  
*Conseil Européen Recherche*  
*Nucléaire (CERN)*  
*Geneva, Switzerland*

*For the ATLAS Collaboration*

## 1 Introduction

The ATLAS trigger system is based on three levels of events selection that selects the physics of interests from an initial bunch crossing rate of 40 MHz. During nominal LHC operation at a luminosity of  $10^{34}\text{cm}^{-2}\text{s}^{-1}$ , decisions must be taken every 25 ns with each bunch crossing containing about 23 interactions [1]. The selections in the three trigger levels must provide sufficient rejection to reduce the rate down to 200 Hz to be compatible with the offline computing power and storage capacity [2], [3]. The LHC is expected to begin operation in spring 2009 with a peak luminosity of  $10^{31}\text{cm}^{-2}\text{s}^{-1}$  with a reduced number of bunches. Operations are expected to quickly ramp up to higher luminosities, hence the trigger needs to adapt to the changing beam conditions while preserving the interesting physics and detector requirements.

We present the status of the preparation of the trigger menu for early data taking and show how we plan to deploy the trigger system from the first collision to the nominal luminosity. We also show expected rates and physics performance obtained from simulated data.

## 2 Trigger system

The ATLAS trigger system comprises of three levels (LVL1, LVL2, and EF) and selects events of physics interest while reducing the rate from the 40 MHz collision rate to approximately 200 Hz.

The level-1 trigger (LVL1) is a hardware trigger using data from the calorimeter and the muon trigger chambers. The LVL1 central trigger processor (CTP) receives the

multiplicity of objects above a certain threshold (e.g. muon, electromagnetic cluster, jet and missing transverse energy) identified by the sub-systems. The CTP makes a decision based on the multiplicity of various thresholds. Threshold values and the logic used in the CTP are configurable. However, the number of different thresholds for each type of objects and the number of independent trigger logic (trigger item) is fixed by hardware design to a maximum of 256.

The level-2 trigger (LVL2) is a software-based trigger running on  $\sim$ 1000 computing nodes. The LVL2 system receives the results of the LVL1 trigger items and the threshold information. The threshold information is used to identify the region of interest (RoI) where the LVL1 observed interesting objects. Execution of algorithms at LVL2 is controlled by the HLT steering software which runs the algorithm on each RoI. Algorithms then request data from the detector readout system belonging to the RoI. The average execution time per event must be below  $\sim$ 40 ms.

The event filter (EF) execution is also controlled by the HLT steering. At EF, algorithms similar to the ones in the offline reconstruction are executed after the event building has finished. This feature allows algorithms to access the full event data. The event processing time must be less than a few seconds at this stage.

Events passing the event filter selection are directed to different streams depending on which trigger chain accepted the event. Events assigned to different streams will be written out into different files to allow for separate offline reprocessing of events based on the event type. Event streaming is done inclusively, i.e. if an event passes several triggers in different streams, that same event will be written into several streams.

A fraction of the collected data goes to the calibration stream to record a sample dedicated to detector calibration, or for express stream. The express stream will be used for fast reconstruction to validate data.

### 3 Physics program

The physics program in ATLAS extends to a broad range of physics. Measurements of the Standard Model of particle physics will be possible at much higher energies than at any other particle collider. Hence, Quantum Chromodynamics (QCD) jet productions, electroweak processes (e.g. W/Z production), B-Physics, top-quarks, etc. will all be studied in great details [1].

However, the experiment must also be sensitive to other possible physics beyond the Standard Model (SM) (e.g. SUSY, Extra-dimension models, etc.) or to other predictions from the SM that have not yet been observed, such as the Higgs particle.

The three-level trigger must thus collect a wide range of physics processes ranging from low-transverse momentum events, such as in B-physics, to high-transverse momentum events, such as in beyond SM searches with various final states.

During early data-taking, it will be crucial to record a wide variety of events in order to calibrate the trigger system, and to understand the trigger response. To accomplish this task, the trigger reconstructs basic physics objects: muons, electrons, photons, hadronic  $\tau$ 's, jets/b-jets, energy sum, missing energy, B-physics and minimum bias signatures. In order to improve the selection of events and reduce the acceptance rates, the trigger also includes requirements based several basic objects.

## 4 Startup strategy

The LHC accelerator and the ATLAS experiment are expected to start operation in fall 2009. We expect to have the first  $pp$ -collision at the LHC by summer 2009. The first LHC operation will be done at low luminosity ( $\mathcal{L}=10^{31}\text{cm}^{-2}\text{s}^{-1}$  or less), quickly ramping up to higher luminosities (up to  $\mathcal{L}=10^{33}\text{cm}^{-2}\text{s}^{-1}$ ). The ATLAS experiment is preparing several trigger menus from the first collision to higher luminosity running, namely for the luminosity of  $10^{31}$ ,  $10^{32}$  and  $10^{33}\text{cm}^{-2}\text{s}^{-1}$ . Different prescale sets are being prepared for each menu to deal with the luminosity changes during the run.

During the early LHC running period at low luminosity, the trigger can be run with many low threshold items in order to understand the HLT selection algorithm performance with real data. To this end, when possible the HLT algorithms are executed but events are accepted regardless of the algorithms' decision.

## 5 Trigger performance for $\mathcal{L}=10^{31}\text{cm}^{-2}\text{s}^{-1}$

In order to probe the lower energy range of the full spectrum of collision events obtained at the LHC, the trigger uses low-threshold but prescaled triggers. However, for physics searches unprescaled triggers are required.

The strategy of sampling the lower energy range of the physics spectrum available in the events can be observed in the selected jets distribution (figure 1). In this figure, the lower energy plateau of accepted jets is selected with prescaled triggers, while the higher energy tail is unprescaled so as to be used in physics analysis. Figure 2 shows the approximated individual and cumulative rates at which events are recorded by different groups of triggers based on Monte Carlo simulations.

## 6 Summary

A trigger menu for initial collisions is being prepared, and will be used as a solid starting point for recording first collisions at the LHC. Although the menu will initially need to evolve very quickly, the experience and tools resulting from the current trigger menu studies will be essential to cope with the stringent demands that the LHC will

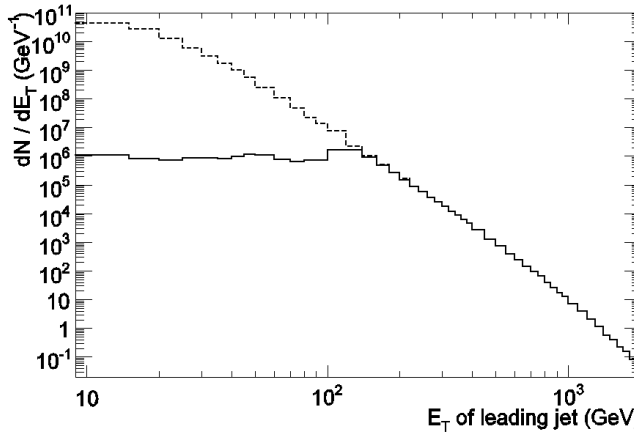


Figure 1: The transverse momentum spectrum of jets selected by the jet triggers (solid line), and of the full spectrum of jets in the Monte Carlo simulation (dashed line).

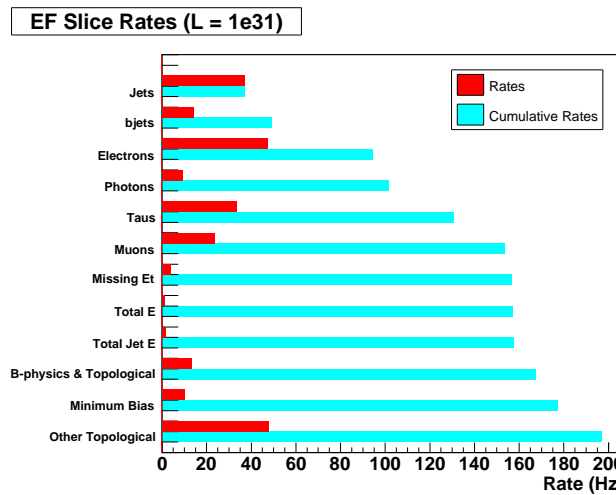


Figure 2: The overall approximated output rates of the EF for different groups of triggers for a luminosity of  $10^{31} \text{cm}^{-2}\text{s}^{-1}$ .

impose on both software and hardware used in this experiment.

## References

- [1] [ATLAS Collaboration], “ATLAS: Detector and physics performance technical design report. Volume 1”
- [2] R. Goncalo [ATLAS TDAQ Collaboration], J. Phys. Conf. Ser. **110**, 092013 (2008).
- [3] T. Kono [ATLAS Collaboration], arXiv:0808.4102 [hep-ex].
- [4] [ATLAS Collaboration], “ATLAS high-level trigger, data acquisition and controls: Technical design report”

# Level-3 Calorimetric Resolution available for the Level-1 and Level-2 CDF Triggers

*A. Canepa<sup>a</sup>, M. Casarsa<sup>b</sup>, V. Cavaliere<sup>c</sup>, G. Cortiana<sup>d</sup>, S. Donati<sup>c</sup>, G. Flanagan<sup>e</sup>, V. Greco<sup>c</sup>, P. Giannetti<sup>c</sup>, H. Frisch<sup>f</sup>, D. Kropf<sup>f</sup>, T. Liu<sup>b</sup>, M. Piendibene<sup>c</sup>, C. Pilcher<sup>f</sup>, L. Ristori<sup>c</sup>, V. Rusu<sup>b</sup>, L. Sartori<sup>c</sup>, M. Vidal<sup>g</sup>.*

*<sup>a</sup>University of Pennsylvania, USA; <sup>b</sup>Fermilab, USA; <sup>c</sup>Physics Dept and INFN Pisa, Italy; <sup>d</sup>Physics Dept and INFN Padova, Italy; <sup>e</sup>Purdue University, USA; <sup>f</sup>University of Chicago, USA; <sup>g</sup>CIEMAT, Spain.*

## 1 Abstract

As the Tevatron luminosity increases, sophisticated selections are required to be efficient in selecting rare events among a very huge background. To cope with this problem, CDF has pushed the Level 3 calorimeter algorithm resolution up to Level 2 and, when possible, even to Level 1, increasing efficiency and, at the same time, keeping under control the rates. This strategy increases the purity of the Level2 and Level1 samples and produces free-bandwidth that allows to reduce the thresholds. The global effect is an improvement of the trigger efficiency, most notably on important SM Higgs channels. The Level 2 upgrade improves the cluster finder algorithm and the resolution of the Missing Transverse Energy (MET) calculations. The improved MET resolution will be soon available also at Level 1. We describe the CDF Level 2 and Level 1 calorimeter upgrades, the architecture and the trigger performances. The Level 2 upgraded system is running as the official one since August 2007, the Level 1 is under commissioning.

## 2 Overview of the CDF Calorimeter Trigger

The CDF trigger [1] for Run II is a three level system: each stage must reject a sufficient fraction of the events to allow processing at the next level with acceptable dead time. The Level 1 and Level 2 triggers use custom-designed hardware to find physics objects in a subset of the event information. The Level 1 decision is taken on the basis of a limited reconstruction of the muon, track and calorimeter information.

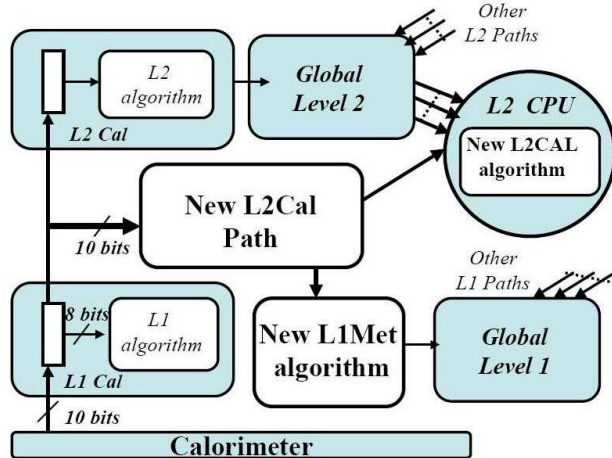


Figure 1: Hardware configuration (L1 and L2) for the Calorimeter Trigger upgrade.

When an event is accepted by the Level 1 trigger, all data are moved to one of four Level 2 data buffers. At the same time, subsets of detector information are sent to the Level 2 trigger system, where some limited event reconstruction is performed and a Level 2 decision is made inside a dedicated PC. Upon a Level 2 accept, the full detector is readout and data are sent to the Level 3. The Level 3 trigger uses the full detector information for complete event reconstruction in a farm of x86 PCs. Only the events accepted at L3 will be sent to mass storage. The goal of the calorimeter trigger (both at Level 1 and Level 2) is to trigger on electrons, photons, jets, total transverse energy (SumET) as well as missing transverse energy (MET).

A coordinate system is defined by the polar angle  $\theta$ , measured from the proton direction, and the azimuthal angle  $\phi$ , measured from the Tevatron plane. The pseudo-rapidity is defined as  $\eta = \ln(\tan(\theta/2))$ . All calorimeter tower energy information, including both electromagnetic (EM) energy and hadronic (HAD) energy, is digitized every 132 ns and the physical towers are summed into trigger towers. So, the entire detector is represented as a  $24 \times 24$  map of trigger towers in the  $\eta - \phi$  plane. The tower energy information is then sent to both L1 and L2 calorimeter trigger systems with 10-bit energy resolution. The Level 1 calorimeter (L1CAL) subsystem only uses 8 of the 10 available bits for each trigger tower; it also calculates global SumET and MET using that lower resolution.

The main task of the existing L2CAL was to find clusters using the transverse energy ( $E_T$ ) of trigger towers. The cluster finding algorithm was based on a simple algorithm, implemented in dedicated hardware, which forms clusters by simply combining contiguous regions of trigger towers with non-trivial energy. Such algorithm has worked well at lower luminosity, but now, at high instantaneous luminosity, large “fake clus-

ters” are likely to be formed: this because the occupancy of the detector increases since towers which are unrelated to any jet activity have their  $E_T$  boosted above clustering thresholds. One more limitation of the existing hardware-based L2CAL system is that it does not re-calculate SumET and MET using the full 10-bit resolution energy information available, instead it uses the SumET and MET information directly from current L1CAL (based on 8-bit resolution). This design feature limits its trigger selection capability, or rejection power, for triggers with global transverse energy requirements.

## 3 The Calorimeter Trigger Upgrade

### 3.1 Hardware Architecture

The full 10 bit resolution calorimeter trigger tower energy information is now received, preprocessed and merged by a set of electronic boards, before being sent to the Level 2 decision CPU, where a more sophisticated cluster finding “cone” algorithm (replacing the old “pac-man” one) can reconstruct jets. At the same time the MET and SumET are calculated exploiting the full 10 bits resolution of the trigger tower energy information.

The system is based on the PULSAR [2], a general purpose VME board developed at CDF and already used for other upgrades [3]. It is equipped with three FPGA chips (APEX 20K400BC-652-1XV [4]): two DataIO and one Control. A first set of 18 identical Pulsars receives the raw (full 10-bit resolution) trigger tower energy information from L1CAL, over 288 LVDS cables, through a new Pulsar Mezzanine card, specifically designed for this upgrade. The trigger tower data are converted into 32-SLINK format [5] and delivered to a second set of 5 SLINK Merger Pulsars, which receive and merge the eighteen SLINK channels into four and then send the data to the Level 2 decision PC, using FILAR [6].

The same bunch of 18 Pulsar boards can be used to perform a first step of the MET and SumET calculation (with 10 bit resolution) for the Level1. The results are sent to an additional LVDS Pulsar board, which completes the MET and SumET calculation and makes the L1 trigger calorimeter decision within the L1 timing constraints( $5.5\mu s$ ). The LVDS Pulsar boards start to elaborate the L2 information when they receive back the global L1 decision (see figure 1).

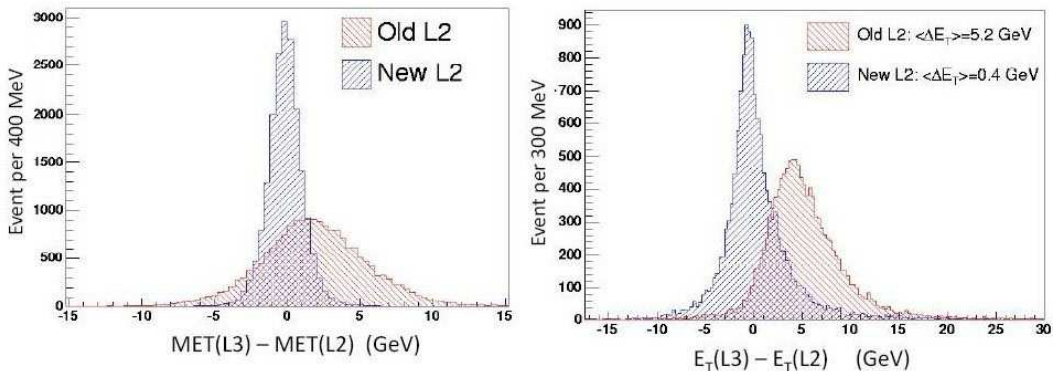


Figure 2: Difference between L2 and L3 MET (left) and Jet transverse energy (right) for existing and upgraded L2CAL. The average luminosity is  $180 \times 10^{30} \text{ cm}^{-2} \text{s}^{-1}$ .

### 3.2 Performances

The Pulsar-based calorimeter trigger upgrade has improved both Jet and MET measurements at Level2; at Level1 it will improve the MET measurement too. Figure 2 shows the difference between Level2 and Level3 in MET and Jet transverse energy, for the existing system as well as for the upgraded one, with data taking at an average luminosity of  $180 \times 10^{30} \text{ cm}^{-2} \text{s}^{-1}$ . The same MET difference has been measured between the future L1CAL system and L3. These improvements allow a significant rate reduction and higher efficiency in Jet and MET based triggers, both at Level1 and Level2. As an example, figure 3(a) shows the Level 2 JET40 trigger cross section growth with luminosity before and after the upgrade. In figure 3(b) we can see the trigger efficiency curve for the Level2 JET15 (Jet with  $E_T$  above 15 GeV) trigger, in the upgraded L2CAL system and in the existing one.

## 4 Conclusions

We have presented the design, the hardware implementation and the performance of the Pulsar-based new L2CAL system for CDF experiment. It makes the full resolution calorimeter trigger tower information directly available to the Level 2 decision CPU, where a more sophisticated algorithm is implemented. Both Level 2 jets and MET are made nearly equivalent to offline quality, thus significantly improving the performance and flexibility of the jet and MET related triggers. We have also presented the under-commissioning L1CAL upgrade, easily obtained exploiting the flexibility of the same Pulsar boards used for the L2CAL. We foresee many opportunities for additional improvements in trigger purity and efficiency, most notably for physics

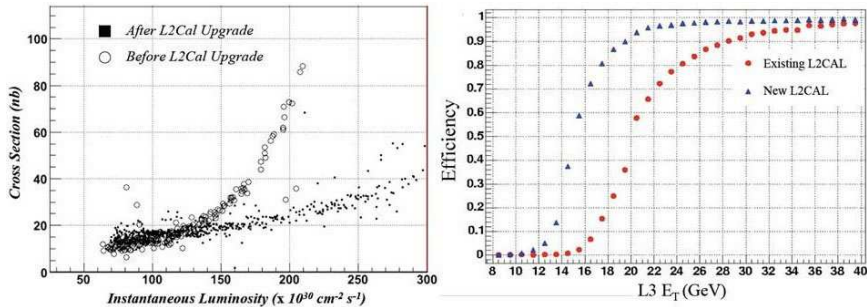


Figure 3: (a)Cross Section of the jet trigger selection requiring jets above 40 GeV as a function of the Instantaneous Luminosity: upgraded L2CAL vs existing L2CAL. (b)Efficiency verse  $E_T$  for Level 2 Jet trigger with 15 GeV threshold, existing L2CAL system and new L2CAL.

triggers searching for Higgs and new physics.

## References

- [1] R. Blair et al (CDF II collaboration), *The CDF RunII Detector Technical Design Report*, FERMILAB-PUB-96/390 E, 1996.
- [2] Pulsar project web page: <http://hep.uchicago.edu/~thliu/projects/Pulsar>.
- [3] K.Anikeev et al., *CDF Level 2 Trigger Upgrade*, IEEE Trans. on Nucl. Sci., Vol.53, No 2, 2006 pp.653-658.
- [4] ALTERA Pub, *APEX 20K Programmable Logic Device Family*, Data Sheet v.5.1, 2004.
- [5] SLINK web page: <http://hsi.web.cern.ch/HSI/s-link>, Data Sheet v.5.1, 2004.
- [6] FILAR web page: <http://hsi.web.cern.ch/HSI/s-link/devices/filar/Welcome.html>.

# Measurement of Branching Fractions of the inclusive decay $D^0 \rightarrow \Phi X$ and of the exclusive decays of the $D^0$ involving a $K^+K^-$

*Gerhard Leder and Franz Mandl*

*Institute for High Energy Physics of the OeAW*

*Nikolsdorfergasse 18 A-1050 Wien, Austria*

*(Belle Collaboration)*

## 1 Introduction

The branching fractions (BF) of inclusive decay modes are notoriously difficult to measure and therefore generally not very well known. For instance, in 2006 the branching fraction of the decay  $D^0 \rightarrow \Phi X$  still had an uncertainty of about 50%. A novel method of reconstructing completely events has been developed, which is especially suitable for evaluating inclusive (also useful for exclusive - ) branching fractions. Since the branching fractions obtained are still highly preliminary, **we will present mainly this method**, which leads to the "best" measurement of  $\text{BF}(D^0 \rightarrow \Phi X)$  confirming the present value of PDG2008 [1]. All exclusive decays of the  $D^0$  involving a  $K^+K^-$  are compatible with the PDG2008 listings.

## 2 Data, Analysis Strategy and Event Selection

Our analysis is based on data collected by the Belle detector [2] at the asymmetric-energy KEKB storage rings [3] with a center of mass (CM) energy of 10.58 GeV ( $\Upsilon(4S)$ ) and 60 MeV below, corresponding to a total integrated luminosity of 490  $\text{fb}^{-1}$ .

The analysis strategy follows closely that adopted for the study on semileptonic decays  $D^0 \rightarrow h\nu$ , were  $h=\pi$  or  $K$  [4]. We seek events of the type  $e^+e^- \rightarrow D_{\text{tag}}^{(*)} D_{\text{sig}}^{*-} X \{D_{\text{sig}}^{*-} \rightarrow \bar{D}_{\text{sig}}^0 \pi^-\}$ , where  $X$  may include additional  $\pi^\pm$ ,  $\pi^0$ , or  $K^\pm$  mesons (inclusion of charge-conjugate states is implied throughout this report). The  $D^0$  is then tagged

by fully reconstructing the remainder of the event. Each candidate is assembled from a fully reconstructed “tag-side” charm meson ( $D_{\text{tag}}^{(*)}$ ) and additional particles ( $X$ ), with the requirement that the combination be kinematically consistent with  $e^+e^- \rightarrow D_{\text{tag}}^{(*)} D_{\text{sig}}^{*-} X$ . To the  $D_{\text{tag}}^{(*)} X$  is added a charged slow pion that is kinematically consistent with  $\pi_s^-$  from  $D_{\text{sig}}^{*-} \rightarrow \bar{D}_{\text{sig}}^0 \pi_s^-$ . Candidate  $D_{\text{tag}}^{(*)} X \pi_s^-$  combinations passing the analysis criteria thus provide a tag of  $\bar{D}_{\text{sig}}^0$  and its momentum without having used any of its decay products. The  $D_{\text{tag}}^{(*)}$  is reconstructed in the modes  $D^{*+} \rightarrow D^0 \pi^+$ ,  $D^+ \pi^0$  and  $D^{*0} \rightarrow D^0 \pi^0, D^0 \gamma$ , with  $D^{+/0} \rightarrow K^-(n\pi)^{++/+} \{n = 1, 2, 3\}$ . Each  $D_{\text{tag}}$  and  $D_{\text{tag}}^*$  candidate is subjected to a mass-constrained vertex fit to improve the momentum resolution. We require a successful fit of each  $D_{\text{tag}}$  candidate; furthermore, if this candidate is a daughter of a successfully fitted  $D_{\text{tag}}^*$  candidate, the event is treated as  $D_{\text{tag}}^* D_{\text{sig}}^{*-} X$ , otherwise it proceeds as  $D_{\text{tag}} D_{\text{sig}}^{*-} X$ . The candidate  $X$  is formed from combinations of unassigned pairs of pions and kaons, conserving total electric charge and strangeness. The 4-momentum of  $D_{\text{sig}}^{*-}$  (decaying into  $\bar{D}_{\text{sig}}^0 \pi^-$ ) is found by energy-momentum conservation, assuming a  $D_{\text{tag}}^{(*)} D_{\text{sig}}^{*-} X$  event. Its resolution is improved by subjecting it to a fit of the  $X$  tracks and the  $D_{\text{tag}}^{(*)}$  momentum, constrained to originate at the run-by-run average collision point, while the invariant mass is constrained to the nominal mass of a  $D_{\text{sig}}^{*-}$ . All possible combinations yielding  $X$  are tried. A candidate is rejected if the confidence level (fd<sub>s2cl</sub>) of this fit is less than 0.1% (corresponding to  $\pm 3.3\sigma$  of mass resolution).

In a correctly reconstructed signal event, the **remaining** particles not yet used have to be decay products of the  $D_{\text{sig}}^0$ . Since the  $D_{\text{sig}}^0$  has been reconstructed without use of any of these decay products, this method is ideal for studying various inclusive decay modes.

### 3 Study of the $D^0$ sample

Background lying under the  $\bar{D}_{\text{sig}}^0$  mass peak (i.e. fake- $\bar{D}_{\text{sig}}^0$ ) is estimated using a wrong sign (WS) sample where the tag- and signal-side  $D$  candidates have the same flavor. Fig.1 top left shows the invariant mass (“md0”, GeV) of the  $D_{\text{sig}}^0$  candidate prior to the mass-constrained fit of the  $D_{\text{sig}}^0$ . The line is the mass distribution for the right sign (RS) sample, black that of WS. Obviously most of the background is cancelled in the difference; a possible remaining background is studied with MC below. The RS and WS  $m_{D^0}$  distributions for “good” events (confidence level of  $D_{\text{sig}}^0 > 0.1\%$ ) (fd<sub>2cl</sub>) are shown in Fig.1 top right. Bottom left shows the RS-WS mass distribution representing the **canonical  $D^0$  sample** for all present studies.

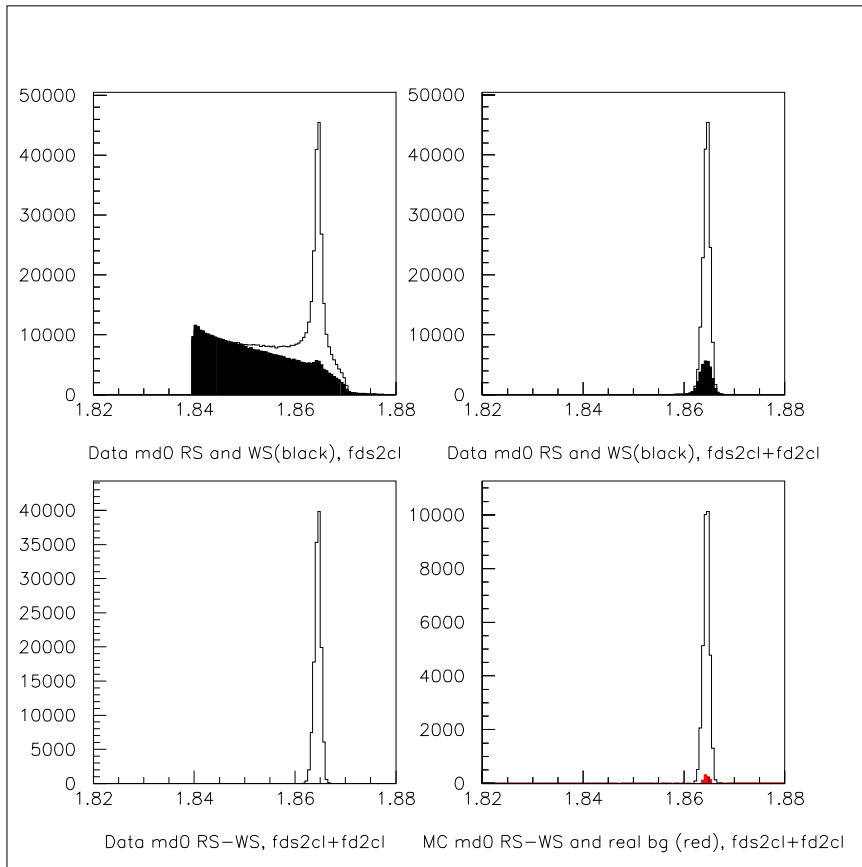


Figure 1: **Unfitted  $D^0$  masses ("md0")**, GeV. Explanations in the text.

To evaluate the amount of possible background ("no  $D_{sig}^0$  events") still contained in the RS-WS  $D_{sig}^0$  sample (bottom right part of Fig.1) a MC sample of  $e^+e^- \rightarrow \gamma \rightarrow q\bar{q}$ , where  $q = c, s, u, d$ , containing about 35% of the data statistics, is used. The line is the canonical distribution, which can be compared to bottom left. Using generator information the true identity and origin of the particles supposedly coming from  $D^0$  subsamples can be identified: Fig.1 bottom right red shows this (very small) background of "no  $D^0$  events" amounting to about 3.5%, i.e. no particle originates, directly or indirectly, from a  $D_{sig}^0$ .

## 4 Evaluation of branching fractions of $D^0$ decays

Invariant mass  $m(K^+K^-)$  and missing mass spectra of  $K^+K^-$  are studied. In order to understand the background the charm MC is used. In Fig. 2 it is demonstrated that

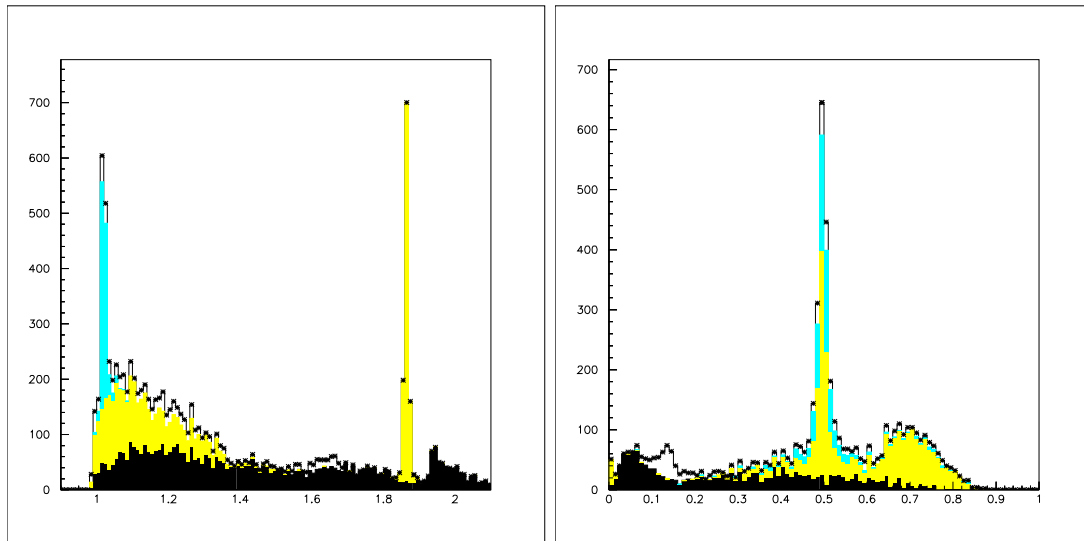


Figure 2: **MC:** Invariant mass (Left) and missing mass (Right) spectra of  $K^+K^-$ . **Yellow:**  $D^0 \rightarrow K^+K^-X$ . **Blue:**  $D^0 \rightarrow \Phi(K^+K^-)X$ . **Black:** One kaon has been wrongly identified by particle identification. **White:** Mainly  $D^0 \rightarrow K^*(890)\pi^0$

the background of misidentified particles (black) consists of wrong identifications. In Fig. 2, left,  $m(K^+K^-)$  exhibits under the  $\Phi$  signal a further background contribution stemming from decays  $D^0 \rightarrow K^+K^-X$  (yellow, left part). The yellow signal to the right around  $m(D^0)$  comes from the exclusive decay  $D^0 \rightarrow K^+K^-$ . One can approximate the non-physics background in the data by purposely misidentifying a pion as a kaon. Clear background-free signals are obtained by subtracting the two kinds of backgrounds described above.

The MC simulations displayed in Fig. 2 have shown that the background of misidentified particles is smooth and non peaking. As an example we show for data in Fig. 3, that for  $D^0 \rightarrow \Phi X$  similar results for the "direct fit" of Fig. 3 left (no

background subtraction) are obtained compared with background subtraction as a cross-check (Fig. 3 right). Similar procedures are applied for the missing mass spectra of  $K^+K^-$  and for  $K^+K^-\pi^0$ . Nine different branching fractions for  $D^0$  decays involving a  $K^+K^-$  pair have been evaluated. Since the branching fractions obtained are presently under review, we do not quote quantitative results. The procedure described above leads to the "best" measurement of  $BF(D^0 \rightarrow \Phi X)$  confirming the present value of PDG2008 [1]. All exclusive decays of the  $D^0$  involving a  $K^+K^-$  are compatible with the PDG2008 listings.

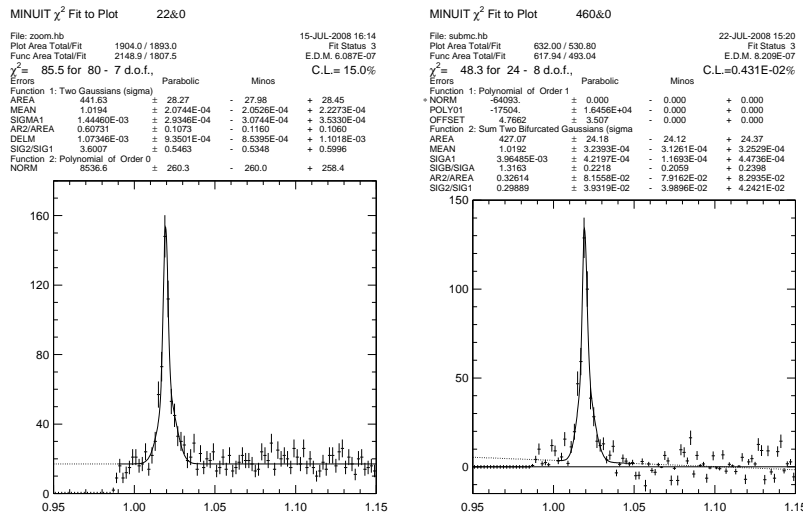


Figure 3: **Data: Fits** of  $m(K^+K^-)$  around  $m(\Phi)$ : **Left:** no background subtraction.  
**Right:** with background subtraction.

## References

- [1] Amsler et al. (Particle Data Group), Phys. Lett. **B667**, 1 (2008).
  - [2] A.Abashian et al. (Belle), Nucl. Instrum. Methods Phys. Res., Sect. **A 479**, 117 (2002).
  - [3] S.Kurokawa and E. Kikutani (Belle), Nucl. Instrum. Methods Phys. Res., Sect. **A 499**, 1 (2003) and other paper in this volume..
  - [4] L. Widhalm et al. (Belle), Phys. Rev. Lett. **97**, 061804 (2006).

# The Liquid Argon Jet Trigger of the H1 Experiment at HERA

*Bob Olivier*

*Max-Planck-Institut für Physik (Werner-Heisenberg-Institut)  
Föhringer Ring 6, D-80805 München, Germany*

## 1 Abstract

The Liquid Argon Jet Trigger, installed in the H1 experiment at HERA implements in 800 ns a real-time cluster algorithm by finding local energy maxima, summing their immediate neighbors, sorting the resulting “jets” by energy, and applying topological conditions. It operated since the year 2006 and drastically reduced the thresholds for triggering on electrons and jets.

## 2 Introduction

After the luminosity upgrade of the HERA machine in the years 2000–2001 (HERA–2), a significant increase of the background rates was expected and indeed observed. While parts of the H1 detector were upgraded during the year 2001 as well, the H1 data logging rate to permanent storage (about 10 Hz) remained a stringent constraint for the data acquisition system. The aim of the upgrade of the digital part of the LAr trigger, the Jet Trigger[1], was to complement the existing global LAr calorimeter trigger with a system that performs real-time clustering to avoid summing-up noise distributed over large parts of the calorimeter, thus allowing for triggers on even lower energy depositions while keeping the trigger rates within the required bounds.

## 3 Jet Trigger Algorithm

The Jet Trigger identifies the localized energy depositions of electrons, photons and bundles of hadrons in the LAr calorimeter, and uses these energy clusters (“jets”),



Figure 1: Details of the installed hardware in the electronic trailer of the H1 experiment: View of the Jet Trigger ADC-Calculation-Storage unit composed of 8 crates, one for each of the 8 octants of the LAr calorimeter. The system receives the analog trigger towers and transfers the digitized signals to the Bump Finder Unit via a bit-serial link.

including their topological information, for a fast event selection. The “jets” are found by identifying trigger towers with a local energy maximum. Around this maximum the immediate neighboring towers are summed and added to the center. The resulting local “jets” are the basis of the trigger decision. Such a local concept improves the sensitivity for low-energy depositions in the calorimeter. The “jets” are then sorted by energy in decreasing order. The 16 highest energy “jets” are used to provide flexible and optimized triggers based on discrimination of individual jet energies, counting jets with energies above certain thresholds, and determination of topological correlations between the jets.

## 4 Jet Trigger Realization

The realization of the above algorithm was implemented in the following way. The input of the jet trigger is 1200 analog trigger towers received at the 10 MHz HERA bunch crossing rate. The clock generation is performed by a Clock Distribution and Configuration Card with adjustable phases to minimize the overall system latency.

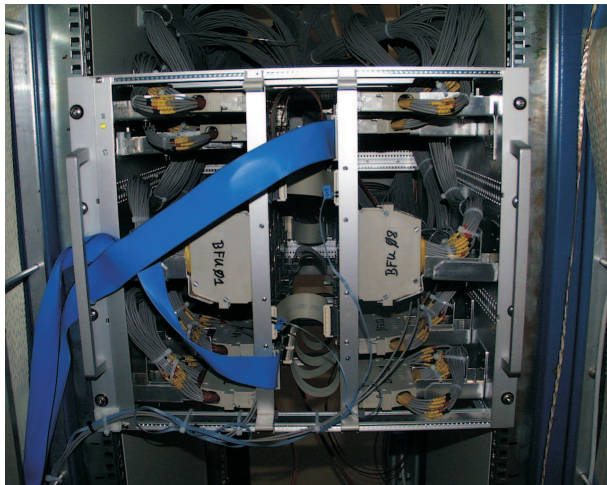


Figure 2: View into the Bump Finder crate containing 2 units, one for each calorimeter hemisphere. In the Bump Finder unit the “jets” are found in real-time. The Primary Sorting Unit presorts the jets from one quadrant according to their energies and sends its output to the Secondary Sorting Unit.

The ADC-Calculation-Storage unit (see figure 1) digitizes the 1200 input towers to 8 bit accuracy each, transforms the energies into transverse energies, and sums the electromagnetic and hadronic energies. The resulting 440 outputs are transferred via a bit-serial link to the so-called Bump Finder Unit (see figure 2). This unit searches for local maxima of energy and sums them with their immediate neighbors. This search and summing is done, for each input tower, in a completely parallel fashion. The resulting 116 energy maxima are sorted by decreasing energy first quadrant-wise, then detector-wise, by the Primary and Secondary Sorting Units. The programmable Trigger Element Generator (see figure 3) applies conditions on the 16 highest energies and their locations. These conditions are local (energy and polar angle criteria on each individual jet, azimuthal and polar angle differences between jets), and global (total energy and missing energy in the event).

In total, the Jet Trigger consists of about 550 FPGAs with 75 M Gates, computing 300 G operations/s. The 12 GB/s raw data rate is reduced to 16 trigger element bits per bunch cross, corresponding to a data reduction factor of 600. Each unit performs its function within 1 to 3 bunch crossings. The total latency is 800 ns.

## 5 Jet Trigger Results

The Jet Trigger operation started in the summer of 2006 and accumulated about  $100 \text{ pb}^{-1}$  of luminosity until the end of the HERA-2 program in July 2007. It

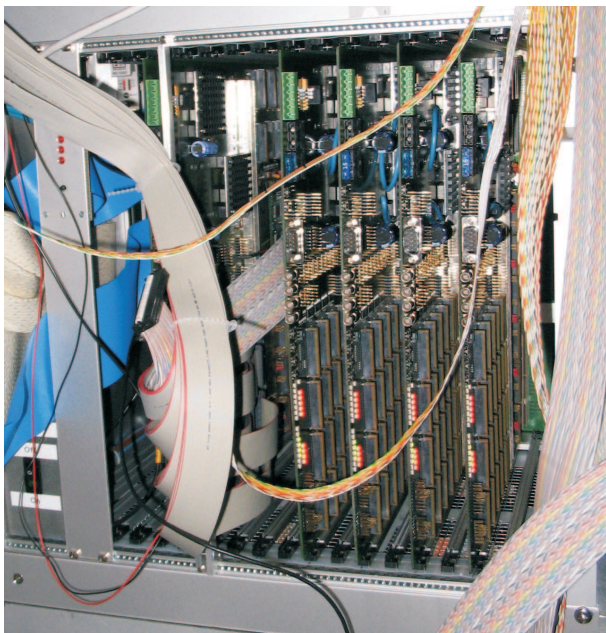


Figure 3: View into the crate housing the Secondary Sorting Unit and the 4 Trigger Element Generator units. In the Secondary Sorting Unit the presorted lists from the four quadrants are finally sorted by energy and transferred to the Trigger Element Generator units which apply topological conditions to the jets.

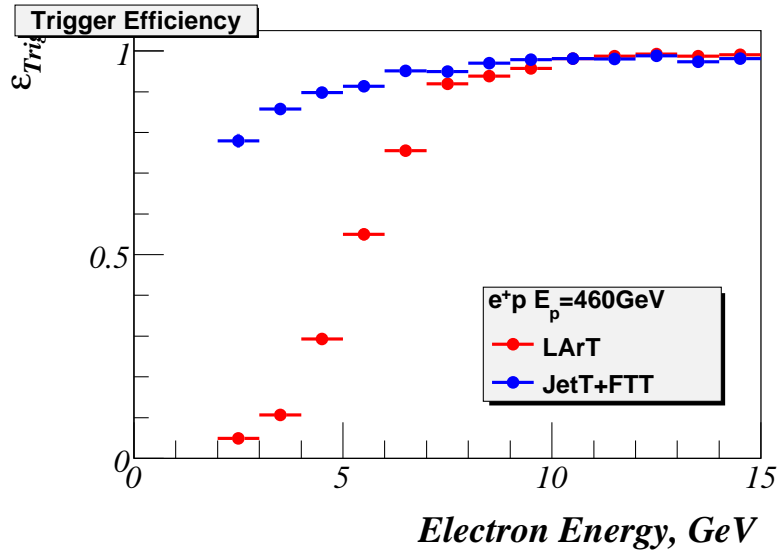


Figure 4: Efficiency to trigger on electrons as a function of the electron energy for both the “old” LAr trigger (red) and the Jet Trigger (blue). Note the decrease of efficient triggering from 6 GeV to 2 GeV.

opened the phase space for events containing a single forward jet of at least 8 GeV at low angle below 30 degrees. The energy-sorted jet information was combined with track-based triggers to successfully perform b-tagging with a track threshold of 1.5 GeV. The Jet Trigger was used to successfully decrease the electron triggering threshold from 6 GeV down to 2 GeV (see figure 4) and to perform the world's first measurement of the longitudinal structure function  $F_L$  of the proton.

## References

- [1] A. Dubak, AIP Conf. Proc. **899** (2007) 573.

# A new very inclusive trigger selection for the SM WH discovery channel at CDF

*Pierluigi Totaro*

*Università degli Studi di Trieste and INFN, Sezione di Trieste  
Trieste, ITALY*

## 1 Introduction

In order to increase the sensitivity of CDF to the low mass Standard Model (SM) Higgs Boson produced in association with a W boson, a new trigger based on calorimetric requirements has been designed, exploiting the enhanced capabilities of the upgraded CDF trigger system. This new trigger, named MET\_DIJET, is meant to be complementary to the standard WH selections and it is demonstrated to provide an effective gain in signal efficiency at trigger level.

## 2 The CDF Detector and its Trigger System

CDF II is a large multi-purpose detector, installed at the B0 interaction point of the Tevatron collider. It consists of an inner silicon vertex detector, which provides three-dimensional track reconstruction; an outer multiwire drift chamber, designed to measure particle momenta; a superconducting solenoidal magnet which supplies a uniform 1.4 T magnetic field inside the trackers; electromagnetic and hadronic calorimeters segmented in projective towers; drift chambers and scintillator counters to detect muons escaping the calorimeters and additional steel absorbers.

CDF is organized in a three level trigger system. Level-1 and Level-2 use custom-designed hardware to find physics objects based on subsets of the detector information. Level-3 uses the full detector information to reconstruct complete events in a processor farm. The goal of each stage is to reject a sufficient fraction of events to allow processing at the next stage with acceptable deadtime. At the Tevatron proton and antiproton bunches collide at a maximum rate of 2.53 MHz, so that maximum accept rates for the whole trigger system are 35 kHz for Level-1, 600 Hz for Level-2 and 100 Hz for Level-3.

A detailed description of the CDF detector and its trigger architecture can be found elsewhere [1].

### 3 Underlying strategy of the new WH trigger

The experimental signature of  $WH \rightarrow l\nu b\bar{b}$  events, with  $l = e, \mu, \tau$ , is characterized by two energetic jets coming from the Higgs boson decay, a high transverse momentum ( $p_T$ ) lepton and a large missing transverse energy ( $\cancel{E}_T$ ), due to the undetected neutrino, coming from the W.

Current CDF analyses [2] are mainly based on high- $p_T$  lepton samples (e.g. electron and muons with  $p_T > 18$  GeV/c), where the tight lepton selections allow to keep under control the trigger rates, with the disadvantage of a compromised signal efficiency. The capabilities of recent hardware upgrades of CDF, like the improved Level-2 calorimetric trigger energy resolution and the new sophisticated trigger cone clustering algorithms [3], give the possibility to explore new complementary strategies for the WH channel. The idea is an implementation of a new trigger path, based entirely on calorimetric requirements: a selection which relies only on missing energy and jet information allows to recover sizably the WH efficiency at analysis level, by using looser offline lepton definitions. Moreover, alternative and more powerful identification tools, like neural networks, can be adopted without biases potentially introduced by the trigger requirements.

On the other hand, such an approach keeps the drawback of a higher acquisition rate. An optimization procedure was performed and the results represent a compromise between good signal efficiency and the maximum reasonable acquisition rate at disposal, which must be kept under control at all three trigger levels. Considering the total available bandwidth, we set *a priori* the following approximate rate limits for the new MET\_DIJET at the maximum expected luminosity of  $3 \times 10^{32} cm^{-2}s^{-1}$ : 2000 Hz at Level-1, 100 Hz at Level-2 and 30 Hz at Level-3. The choice of the most suitable variables, on which operates the trigger selection, and their cut values, are driven by these rate limits.

In order to predict the efficiency of a given set of cuts, we used a Monte Carlo sample of WH events with full detector and trigger simulation, where the W is forced to decay leptonically and the Higgs is forced to decay into  $b\bar{b}$ .

The background is estimated in the SingleTower10 data sample. This trigger path requires at least one calorimeter tower with a total energy deposit of at least 10 GeV at Level-1. The efficiency of this sample for WH is very high (about 97%) so it is a very good starting point for any trigger study aimed at WH. The predicted acquisition rate, as a function of instantaneous luminosity, is obtained as the product of the unprescaled rate of the SingleTower10 times the reduction factor caused by the

simulated set of trigger cuts.

## 4 Trigger cuts optimization

- At Level-1 we added a cut on the missing transverse energy,  $\cancel{E}_T > 15$  GeV, to the request of a tower with  $E_T > 10$  GeV, reaching a global efficiency of 87.3%. The expected corresponding rate at  $300 \times 10^{30} cm^{-2}s^{-1}$  is about 1900 Hz.
- At Level-2 we implemented a multiparameter optimization procedure, which maximizes the signal efficiency at a fixed background reduction factor, scanning the  $\cancel{E}_T$  and jet  $E_T$  variables. The final Level-2 selection is: at least two jets with  $E_T \geq 3$  GeV and  $\cancel{E}_T \geq 28$  GeV, with a WH efficiency of 71.3% and a rate of about 80 Hz at  $300 \times 10^{30} cm^{-2}s^{-1}$  of luminosity.
- At Level-3 we decided to keep the selection as simple as possible. The single cut on missing transverse energy at 30 GeV satisfies already the bandwidth constraint: we obtain a cross-section of about 35 Hz at  $300 \times 10^{30} cm^{-2}s^{-1}$ , where the corresponding global efficiency for WH is 63.9%.

Table 1 summarizes the final MET\_DIJET trigger selection.

L1	$\cancel{E}_T^{L1} > 15$ GeV at least one trigger tower with $E_T > 10$ GeV
L2	$\cancel{E}_T^{L2} > 28$ GeV two jets with $E_T > 3$ GeV and $ \eta  \leq 3.6$
L3	$\cancel{E}_T^{L3} > 30$ GeV

Table 1: MET\_DIJET trigger selection.

## 5 Trigger performances

Before the final implementation, a first version of the MET\_DIJET trigger with similar requirements and an additional precautionary prescale factor of 10 was tested. Figure 1 shows the on-line measured cross-sections (coloured dots) for Level-1 and

Level-2 selections of this test version, as a function of instantaneous luminosity, compared with the estimated distributions (points with error bars). The full line is a second order polynomial fit of the estimated cross-section points, while dashed lines connect points corresponding to the same rate. Plots indicate that rates are kept under control, as desired, and that our model well simulates the real behaviour of the trigger, over a wide range of instantaneous luminosity.

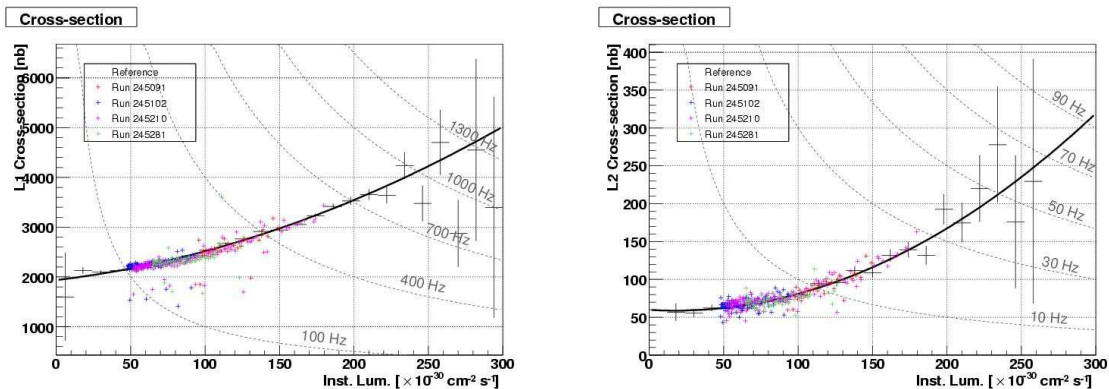


Figure 1: Measured and predicted cross-sections for the Level-1 (left) and Level-2 (right) selections of the new MET\_DIJET trigger, as a function of instantaneous luminosity. Predicted points have been fit to a second order polynomial. Dashed lines connect points corresponding to the same rate.

Trigger efficiencies for WH signal, evaluated for different Higgs mass hypotheses in the range 110-130  $\text{GeV}/c^2$ , are reported in table 2, along with the expected number of Higgs bosons collected in  $5 \text{ fb}^{-1}$ .

$M_H [\text{GeV}/c^2]$	110	115	120	130
L1 efficiency	86.2%	87.0%	87.3%	88.8%
L2 efficiency	69.8%	70.8%	71.3%	73.6%
L3 efficiency	61.6%	63.0%	63.9%	65.9%
Higgs in $5 \text{ fb}^{-1}$	148	123	105	66

Table 2: MET\_DIJET trigger efficiency for WH, for different Higgs mass hypotheses.

We also considered the efficiency separately for all the leptonic decay modes of the W boson, with a Higgs mass of  $120 \text{ GeV}/c^2$ , as shown in table 3. By taking into account

the signal overlap between different WH trigger selections, we evaluated the effective gain in efficiency provided by the MET\_DIJET. Cumulative efficiencies are reported in table 4.

	<i>WH</i>		
	$e\nu_e b\bar{b}$	$\mu\nu_\mu b\bar{b}$	$\tau\nu_\tau b\bar{b}$
L1 efficiency	91.8%	85.5%	84.5%
L2 efficiency	75.8%	71.2%	66.9%
L3 efficiency	66.3%	65.7%	59.5%
Higgs in $5 \text{ fb}^{-1}$	36	36	33

Table 3: MET\_DIJET trigger efficiency for WH ( $M_H=120 \text{ GeV}/c^2$ ), separately for the three leptonic decay modes of W boson.

WH efficiency		
	lepton-based triggers	cumulative with MET_DIJET
e	61.2%	85.4%
$\mu$	22.1%	74.5%
$\tau$	11.3%	62.8%

Table 4: WH efficiency ( $M_H=120 \text{ GeV}/c^2$ ) for the lepton-based CDF triggers, and cumulative values with the introduction of the new MET\_DIJET.

## 6 Conclusions

We designed and implemented a new calorimetric trigger, optimized for the detection of a low mass SM Higgs Boson, produced in association with a W boson. We demonstrated that this new online selection, complementary to the high  $p_T$ -based lepton triggers, allows to consistently increase the efficiency for all three leptonic decay modes of the W boson. We also estimated the MET\_DIJET trigger rate sustainable up to  $300 \times 10^{30} \text{ cm}^{-2} \text{ s}^{-1}$  at Level-1, Level-2 and Level-3, and tested the validity of our prediction model. The trigger was approved in Autumn 2007 and officially introduced in the CDF trigger table. By the end of Tevatron Run II we expect to collect about  $5 \text{ fb}^{-1}$  of data with this new selection, with a significant contribution to the SM Higgs analyses of CDF.

## References

- [1] R.Blair *et al.*[CDF Collaboration], FERMILAB-Pub-96/390-E.
- [2] A.Abulencia *et al.*[CDF Collaboration], FERMILAB-PUB-08-070-E
- [3] A.A.Bhatti *et al.*,FERMILAB-CONF-07-165-E.



# PIC 2008 Scientific Program

## Wednesday 25 June 2008

### **Registration (25 June 16:30-19:00)**

### **Welcome party (25 June 19:00-21:00)**

## Thursday 26 June 2008

### **Session 1 (26 June 09:00-13:15)**

- Conveners: (9-10.50) Mantovani G.; (11.15-13.15) Przysiezniak H.

time	[id]	title	presenter
09:00	[1]	1-A Welcome Address	MANTOVANI, Giancarlo
09:05	[2]	1-B Tribute to Beate Naroska	BARTEL, Wulfrin
09:20	[3]	1-C TOP quark cross sections	DELIOT, Frederic
10:05	[4]	1-D TOP quark properties	DATTA, Mousumi
10:50		Coffee break and Poster session	
11:15	[5]	1-E W-Z physics from the Tevatron	BOLTON, Tim
12:00	[6]	1-F EW constraints from HERA	GALLO, Elisabetta
12:45	[7]	1-P1 ZZ into 4l measurements with the first ATLAS data	CHRISTIDI, Elektra
13:00	[8]	1-P2 Status of the ATLAS RPC commissioning and cosmic test results	BIANCO, Michele

### **Session 2 (26 June 14:30-17:50)**

- Conveners: (14.30-16.15) Appel J.; (16.35-17:50) Simak V.

time	[id]	title	presenter
14:30	[9]	2-A New developments in solar neutrino physics	BELLINI, Gianpaolo
15:15	[10]	2-B Short base-line neutrinos	PATTERSON, Ryan
15:45	[11]	2-C Ultra high-energy neutrinos	NICHOL, Ryan
16:15		Coffee break	
16:35	[12]	2-D Underground nuclear astrophysics and the Sun	BROGGINI, Carlo
17:05	[13]	2-E Cosmic rays from space-based observatories	SPILLANTINI, Piero
17:35	[14]	2-P1 OPERA: waiting for the tau	LONGHIN, Andrea

## Friday 27 June 2008

### Session 3 (27 June 09:00-13:30)

- Conveners: (9-10.45) Brom J.M.; (11.15-13.30) Fabbri F.L.

time	[id] title	presenter
09:00	[15] 3-A B decay and CP violation (CKM angles and sides)	VERDERI, Marc
09:45	[16] 3-B New physics effects in B decays	CHAO, Yuan
10:30	[17] 3-P1 Early physics with the LHCb detector	WIEDNER, Dirk
10:45	Coffee break and Poster session	
11:15	[18] 3-C Heavy B Hadrons	GIAGU, Stefano
12:00	[19] 3-D Charm physics	WILKINSON, Guy
12:45	[20] 3-E D0-D0bar mixing: an overview	MARKS, Joerg

### Session 4 (27 June 14:45-17:50)

- Conveners: (14.45-16) Ratti S.P.; (16.20-17:50) Bellini G.

time	[id] title	presenter
14:45	[21] 4-A Strange particle physics	COX, Brad
15:30	[22] 4-P1 Measurement of the br. ratio K+ into pi+nu+nubar at NA62	BALEV, Spasimir
15:45	[23] 4-P2 Vus and lepton universality from K decays with the KLOE detector	ANTONELLI, Mario
16:00	Coffee break	
16:20	[24] 4-B UHE Cosmic rays from earth-based observatories	PETRERA, Sergio
16:50	[25] 4-C Dark matter	APRILE, Elena
17:20	[26] 4-D Long base-line neutrino experiments	THOMPSON, Mark

## Saturday 28 June 2008

### **Session 5 (28 June 09:00-13:15)**

- Conveners: (9-10.30) Battiston R.; (11-13.15) Lohmann W.

time	[id] title	presenter
09:00	[27] 5-A High-energy cosmic gamma rays	SCHWANKE, Ullrich
09:45	[28] 5-P1 GLAST and the future of HE Gamma astronomy	VITALE, Vincenzo
10:00	[29] 5-P2 Ultra HE particle astronomy with a space-based experiment	PESCE, Roberto
10:15	[30] 5-P3 Antimatter and dark matter search with AMS-02	SPADA, Francesca
10:30	Coffee break and Poster session	
11:00	[31] 5-B Jet physics	ROYON, Christophe
11:45	[32] 5-C Hard scale QCD from HERA	GEISER, Achim
12:30	[33] 5-D Exotic hadron spectroscopy	BRODZICKA, Jolanta

### **Session 6 (28 June 14:30-18:30)**

- Conveners: (14.30-16) Voss R.; (16.20- 18.30) Ludlam T.

time	[id] title	presenter
14:30	[34] 6-A Longitudinal structure function measurement from HERA	CHEKELYAN, Vladimir
15:00	[35] 6-B Spin structure of the nucleon	KUREK, Krzysztof
15:30	[36] 6-C Heavy ion collisions	GRANIER DE CASSAGNAC, Raphael
16:00	Coffee break	
16:20	[37] 6-D Higgs searches at the Tevatron	TAFFARD, Anyes
17:05	[38] 6-P1 Higgs searches at the LHC	MILA, Giorgia
17:20	[39] 6-E BSM searches at HERA and the Tevatron	GRUENENDAHL, Stefan
18:05	[40] 6-P2 BSM measurements with Top at LHC	BENUCCI, Leonardo
18:20	[41] Presentation of the next PIC venue	YAMAZAKI, Yuji

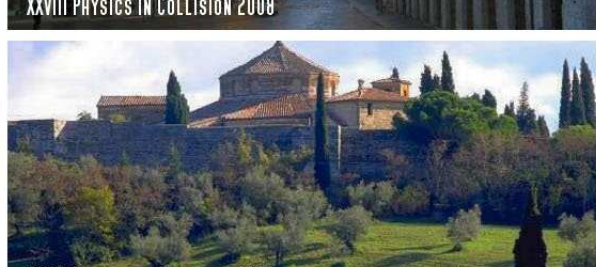
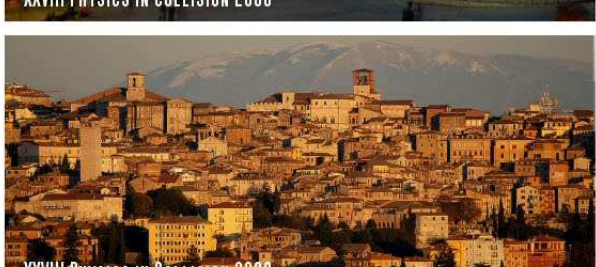
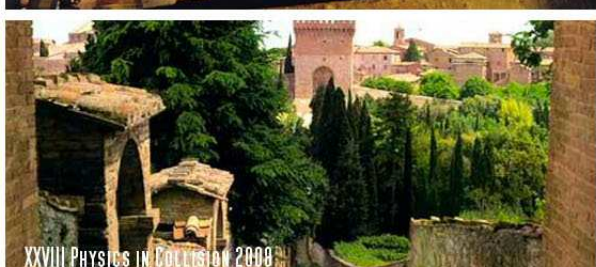
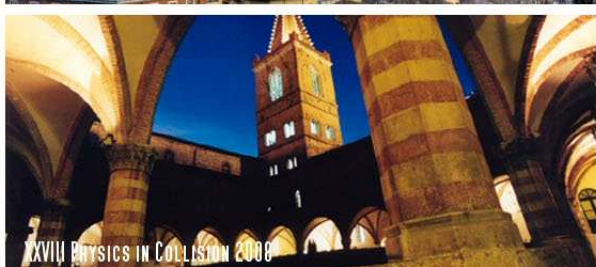


# List of Participants

Muhammad AJAZ	COMSATS Islamabad (PK)
Behcet ALPAT	INFN Perugia (IT)
Giovanni AMBROSI	INFN Perugia (IT)
Mario ANTONELLI	LNF Frascati (IT)
Giuseppina ANZIVINO (LOC)	Univ. and INFN Perugia (IT)
Jeffrey APPEL (IAC)	FERMILAB (US)
Elena APRILE	Columbia Univ. (US)
Spasimir BALEV	INFN and SNS Pisa (IT)
Wulfrin BARTEL	DESY Hamburg (DE)
Roberto BATTISTON	Univ. and INFN Perugia (IT)
Gianpaolo BELLINI (IAC)	Univ. and INFN Milano (IT)
Leonardo BENUCCI	Univ. Antwerpen (BE)
Bruna BERTUCCI (LOC)	Univ. and INFN Perugia (IT)
Michele BIANCO	Univ. and INFN Lecce (IT)
Maurizio BIASINI	Univ. and INFN Perugia (IT)
Reiner BLAES	Univ. H.te Alsace (FR)
Tim BOLTON	Kansas St.Univ. (US)
Bruno BORGIA	Univ. and INFN Roma Sapienza(IT)
Jolanta BRODZICKA	INP Cracow (PL)
Carlo BROGGINI	INFN Padova (IT)
Jean-Marie BROM (IAC)	IPHC Strasbourg (FR)
Dusan BRUNCKO	IEP SAS Kosice (SK)
Claudia CECCHI (LOC)	Univ. and INFN Perugia (IT)
Yuan CHAO	Nat. Taiwan Univ. Taipei (TW)
Vladimir CHEKELIAN	Max-Planck I. Mnchen (DE)
Guido CIAPETTI	Univ. and INFN Roma Sapienza (IT)
Stefano CIPRINI (LOC)	Univ. and INFN Perugia (IT)
Claudio CONTA	Univ. and INFN Pavia (IT)
Bradley COX	Univ. of Virginia (US)
Elektra CHRISTIDI	Aristotle Univ. Thessaloniki (GR)
Mousumi DATTA	FERMILAB (US)
Frédéric DÉLIOT	IRFU Saclay (FR)
Marc Andr DUFOUR	McGill Univ. Montreal (CA)
Franco L. FABBRI	LNF Frascati (IT)
Emanuele FIANDRINI	Univ. and INFN Perugia (IT)
Elisabetta GALLO	INFN Firenze (IT)
Luca GAMMAITONI (LOC)	Univ. and INFN Perugia (IT)
Achim GEISER	DESY Hamburg (DE)
Stefano GIAGU	Univ. and INFN Roma Sapienza (IT)

Raphael GRANIER DE CASSAGNAC	LLR Palaiseau (FR)
Virginia GRECO	Univ. and INFN Siena (IT)
Stefan GRÜNENDAHL	FERMILAB (US)
Claude GUYOT	IRFU Saclay (FR)
Krzysztof KUREK	SINS Warsaw (PL)
Wolfgang LOHMANN (IAC)	DESY Zeuthen (DE)
Andrea LONGHIN	Univ. and INFN Bari (IT)
Thomas LUDLAM (IAC)	Brookhaven N. Lab. Upton (US)
Franz MANDL	HEPHI Vienna (AT)
Giancarlo MANTOVANI (CHAIR)	Univ. and INFN Perugia (IT)
Jörg MARKS	Univ. Heidelberg (DE)
Joachim MEYER	DESY Hamburg (DE)
Giorgia MILA	Univ. and INFN Torino (IT)
Thomas MLLER	Univ. Karlsruhe (DE)
Ryan NICHOL	Univ. College London (GB)
Bob OLIVIER	Max-Planck I. Mnchen (DE)
Ahmimed OURAOU	CEA-Saclay (FR)
Ryan PATTERSON	CALTECH (US)
Roberto PESCE	Univ. and INFN Genova (IT)
Sergio PETRERA	Univ. and INFN L'Aquila (IT)
Helenka PRZYSIEZNAIK (IAC)	Univ. Montreal (CA)
Sergio RATTI	Univ. and INFN Pavia (IT)
Christophe ROYON	IRFU Saclay (FR)
Attilio SANTOCCHIA (LOC)	Univ. and INFN Perugia (IT)
Ullrich SCHWANKE	Humboldt Univ. Berlin (DE)
Vladislav SIMAK (IAC)	FJFI-CVUT Prague (CZ)
Francesca SPADA	Univ. and INFN Roma Sapienza (IT)
Piero SPILLANTINI	Univ. and INFN Firenze (IT)
Pavol STRIZENEC	IEP SAS Kosice (SK)
Anyes TAFFARD	Univ. CAL Irvine (US)
Geoffrey TAYLOR	Univ. Melbourne (AU)
Mark THOMPSON	Univ. Cambridge (GB)
Pierluigi TOTARO	Univ. and INFN Trieste (IT)
Marisa VALDATA	Univ. and INFN Perugia (IT)
Marc VERDERI	LLR Palaiseau (FR)
Didier VILANOVA	CEA Saclay (FR)
Vincenzo VITALE	Univ. and INFN Roma Tor Vergata (IT)
Rdiger VOSS (IAC)	CERN (CH)
Dirk WIEDNER	CERN (CH)
Guy WILKINSON	Univ. Oxford (GB)
Yuji YAMAZAKI	Univ. Kobe (JP)





econf/C080625

[www.slac.stanford.edu/econf/C080625](http://www.slac.stanford.edu/econf/C080625)

[www.pg.infn.it/pic2008](http://www.pg.infn.it/pic2008)